

# Toward Numerically Exact Computation of Conductivity in the Thermodynamic Limit of Interacting Lattice Models

Jeremija Kovačević,<sup>1</sup> Michel Ferrero<sup>2,3</sup>, and Jakša Vučičević<sup>1</sup>

<sup>1</sup>*Scientific Computing Laboratory, Center for the Study of Complex Systems, Institute of Physics Belgrade, University of Belgrade, Pregrevica 118, 11080 Belgrade, Serbia*

<sup>2</sup>*CPHT, CNRS, Ecole Polytechnique, Institut Polytechnique de Paris, Route de Saclay, 91128 Palaiseau, France*

<sup>3</sup>*Collège de France, 11 place Marcelin Berthelot, 75005 Paris, France*



(Received 31 January 2025; accepted 6 June 2025; published 2 July 2025)

Computing dynamical response functions in interacting lattice models is a long-standing challenge in condensed matter physics. In view of recent results, the dc resistivity  $\rho_{dc}$  in the weak-coupling regime of the Hubbard model is of great interest, yet it is not fully understood. The challenge lies in having to work with large lattices while avoiding analytical continuation. The weak-coupling  $\rho_{dc}$  results were so far computed at the level of the Boltzmann theory and at the level of the Kubo bubble approximation, which neglects vertex corrections. Neither theory was so far rigorously proven to give exact results even at infinitesimal coupling, and the respective dc resistivity results differ greatly. In this Letter we develop, cross-check and apply two state-of-the-art methods for obtaining dynamical response functions. We compute the optical conductivity at weak coupling in the Hubbard model in a fully controlled way, in the thermodynamic limit, and without analytical continuation. We show that vertex corrections persist to infinitesimal coupling, with a constant ratio to the Kubo bubble. We connect our methods with the Boltzmann theory, and show that the latter applies additional approximations that lead to quantitatively incorrect scaling of  $\rho_{dc}$  with respect to the coupling constant.

DOI: [10.1103/mm38-zttx](https://doi.org/10.1103/mm38-zttx)

Strongly correlated electronic systems often display rich, yet remarkably universal phase diagrams [1–10]. One of the most puzzling universal phenomena is the strange-metallic linear-in-temperature dc resistivity [9,11–19]. It appears in unconventional and high-temperature superconductors, in the regime where their critical temperature  $T_c$  is the highest [1,11,12,16,19]. In other cases, strange metals are associated with quantum critical points [9,17,20–22]. This raises the question of whether there is an intimate connection between criticality, transport properties, and the magnitude of the superconducting  $T_c$ . To make sense of the vast experimental data, one must be able to compute the conductivity in interacting lattice models, which is a difficult, long-standing task. The main challenge is to find a way to obtain controlled results on the real frequency axis and, at the same time, avoid finite lattice-size effects. Exact diagonalization based methods [finite-temperature Lanczos (FTLM) [23–25]], linked cluster expansions [26–28], and the density-matrix renormalization group [29] are all inherently limited to small lattice sizes. Quantum Monte Carlo methods, on the other hand, either require analytical continuation [30–32] or are effectively limited to atomic problems [33–37]. In the special case of Hall resistivity, expansions in terms of thermodynamic quantities allow for progress [38,39]. In this Letter, however, we formulate a general and systematic way forward.

The workhorse model for the description of the cuprates (and many other classes of correlated systems) is the Hubbard model [2,7,10,14,21,40–43]. Early works [21] have shown that the infinite-dimensional Bethe-lattice Hubbard model roughly describes the normal phase resistivity in LSCO at moderate to high temperature. However, the physics at low temperature is expected to be dominated by the dimensionality of the model, and thus of primary interest is the Hubbard model on the 2D square lattice. At very strong coupling and high temperature, small 2D lattices become representative of the thermodynamic limit, and FTLM was used to obtain numerically exact results [23,24]. However, to address the questions of strange-metallic behavior and its connection to quantum critical points [1,12,13,16,18,20,22], one must be able to perform computations at lower temperature and, perhaps, lower coupling, a regime where small-cluster methods fail.

Recent works [32,44] have indicated that the ground-state phase diagram of the (nearest-neighbor hopping) square-lattice Hubbard model features a quantum critical line, delineating an ordered stripe ground state. The quantum critical line passes through zero coupling at zero doping (i.e., half-filling). At this point, charge and spin susceptibility diverge [45], and both the Boltzmann theory [46,47] and the Kubo bubble [45] predict a linear-in-temperature resistivity down to the lowest accessible temperature. This finding is in line with numerous

observations of linear resistivity in the vicinity of quantum critical points [12,13,16,18,20,22]. Kiely and Muller [46] have argued that the linear-resistivity strange metal observed at half-filling and weak coupling is connected to the strange metal in the cuprates, corresponding to the strong coupling and finite doping regime of the Hubbard model.

However, our recent results [45] have shown a strong quantitative disagreement between Boltzmann theory and the Kubo bubble, casting doubt on whether either of the theories captures correctly even the qualitative behavior of resistivity. To resolve the phenomenology at weak coupling, better methods are needed.

In this Letter, we address the conductivity in the square lattice Hubbard model. We develop two state-of-the-art methodologies and fully avoid finite-size effects and the uncontrolled analytical continuation [24,31,48].

First, we make use of the real-frequency diagrammatic Monte Carlo (RFDiagMC) [49–52], which relies on constructing a power-series expansion for a given physical quantity; the resulting Feynman diagrams are computed up to a given order and then the series is (re)summed. The imaginary-time integrals in Feynman diagrams are solved analytically (which circumvents analytical continuation), while spatial degrees of freedom are summed over using (quasi) Monte Carlo [36,53,54]. The thermodynamic limit is treated directly.

Next, we devise three different nonequilibrium protocols, where we perturb the system with small external fields and compute the current response as a function of time; we then use the results to reconstruct the optical and dc conductivity in a manner of “inverse linear response theory.” In practice, we solve the Kadanoff-Baym equations to obtain the Green’s function, given an approximation for the self-energy as input. We do this calculation for lattices as large as  $60 \times 60$  and confirm convergence of the results with lattice size.

Our diagrammatic series expansion and the corresponding non-equilibrium results are in excellent agreement, which confirms the validity of both implementations. As the coupling constant approaches zero, we observe that vertex corrections to dc conductivity do not vanish, but rather diverge with the same power-law scaling as the Kubo bubble contribution, meaning that they remain quantitatively important even at infinitesimal coupling. Vertex corrections are, however, not very big relative to the Kubo bubble. Nevertheless, neither the Kubo bubble approximation nor the Boltzmann equation yield quantitatively correct results, even at infinitesimal coupling.

**Model**—We are treating the square lattice Hubbard model. The Hamiltonian reads

$$H = -t \sum_{\langle ij \rangle, \sigma} c_{\sigma,i}^{\dagger} c_{\sigma,j} - \mu \sum_{\sigma,i} n_{\sigma,i} + U \sum_i n_{\uparrow,i} n_{\downarrow,i}, \quad (1)$$

where  $i, j$  enumerate lattice sites,  $c^{\dagger}/c$  are creation or annihilation operators,  $\sigma = \uparrow, \downarrow$  denotes spin,  $t$  is the nearest-neighbor hopping amplitude, set to  $t = 0.25$ . The particle-number operator is denoted  $n_{\sigma,i} = c_{\sigma,i}^{\dagger} c_{\sigma,i}$ , and  $\mu$  is the chemical potential, which is used to tune the average occupancy of the sites. The coupling constant is denoted  $U$ . In practice, we absorb the Hartree shift in the chemical potential,  $\tilde{\mu} = \mu - U \langle n_{i,\sigma} \rangle$ , and thus  $\tilde{\mu} = 0$  corresponds to half-filling. We assume  $\hbar = e = 1$ .

**Nonequilibrium approach**—We consider the time evolution of the Hubbard model, which was in a thermal state at times  $t < 0$ , and was then subjected to an external perturbation starting from time  $t = 0$ . Given an approximation for the self-energy, the Green’s function can be computed by solving the Kadanoff-Baym equations [we use the code package NESSi [55] and cross-check with our own implementation; see Supplemental Material (SM) [56] for details]. Kadanoff-Baym equations are formulated on the three-piece time contour as [57]

$$G(t, t') [-i \overleftarrow{\partial}_{t'} - h(t')] - \int_C d\bar{t} G(t, \bar{t}) \Sigma(\bar{t}, t') = \delta_C. \quad (2)$$

Here,  $G$  is the full Green’s function,  $\Sigma$  is the self-energy, and  $h$  is the single-particle Hamiltonian, which introduces an external electric field through the vector potential  $\mathbf{A}$ , namely  $\mathbf{E} = -\partial_t \mathbf{A}$ . We restrict ourselves to fields along the  $x$  direction [assuming site positions to be  $\mathbf{r}_i = (x_i, y_i)$ , with  $x_i, y_i \in \mathbb{Z}$ ] and the corresponding longitudinal response [58]. The time-diagonal elements in the lesser component of the Green’s function contain information about the uniform current, i.e.,  $\langle j(t) \rangle = -(i/N) \sum_{\sigma, \mathbf{k}} v_{\mathbf{k}-\mathbf{A}(t)} G_{\sigma, \mathbf{k}}^<(t, t)$  [57,59], and  $v_{\mathbf{k}}$  is the  $x$  component of the velocity of an electron in the plane-wave state  $\mathbf{k}$ .

On the other hand, the time evolution of the current following application of a weak electric field can be computed based on the knowledge of the retarded current-current correlation function in equilibrium [60],  $\Lambda$ , as

$$\langle j(t) \rangle = \int_{-\infty}^t dt' \Lambda(t - t') A(t') - K A(t), \quad (3)$$

with  $K = -\langle E_{\text{kin}} \rangle / 2$ , i.e., minus the average kinetic energy per site per spatial dimension. The first term is the paramagnetic part of the current; the second term is the diamagnetic part (see SM for details). Alternatively, if one knows the optical conductivity  $\sigma$ , the current response is computed as

$$\langle j(t) \rangle = \int_{-\infty}^t dt' \sigma(t - t') E(t'). \quad (4)$$

The current-current correlation function is related to the optical conductivity through  $\sigma(t) = K \theta(t) - \int_0^t dt' \Lambda(t')$ , or  $\partial_t \sigma = -\Lambda$  (for  $t > 0$ ). The optical conductivities in time



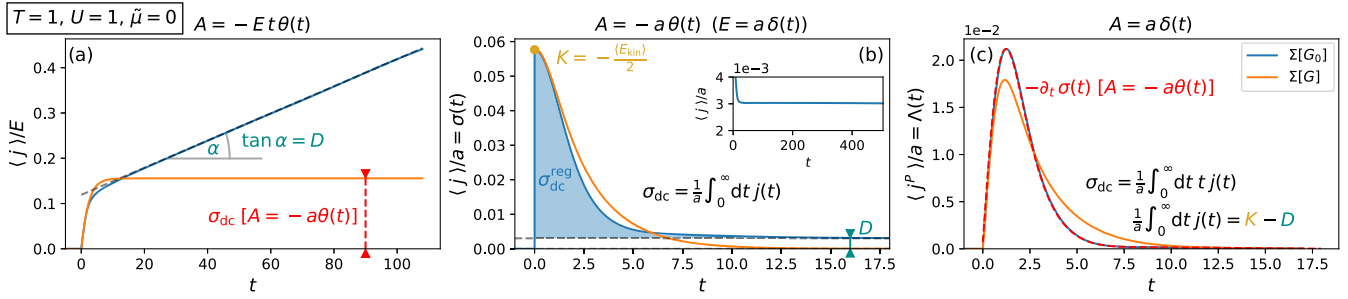


FIG. 1. Example of nonequilibrium, inverse linear response theory. Plots show current response vs time in three different nonequilibrium protocols: (a) constant electric field  $E$ , (b) short pulse of electric field, and (c) short pulse of vector potential  $A$ . Protocol (a) allows to extract  $\sigma_{dc}$ ; (b) and (c) yield the full  $\sigma(t)$  [and thus  $\sigma(\omega)$ ]. Different curves correspond to different self-energy approximations, namely  $\Sigma[G]$  and  $\Sigma[G_0]$ . The red dashed lines in panels (a) and (c) are comparisons with the protocol (b). In protocol (c), we show the paramagnetic part of the current  $j^p$  as only this part is relevant. All three protocols yield consistent results. In the  $\Sigma[G_0]$  approximation, we observe a finite charge stiffness  $D$ . The inset in panel (b) enlarges the long-time tail, showing clearly that  $\sigma(t \rightarrow \infty) = D$ .

and frequency domains are connected via Fourier transformation  $\sigma(\omega) = \int_{-\infty}^{\infty} dt e^{i\omega t} \sigma(t)$ , and the dc conductivity is simply  $\sigma_{dc} \equiv \sigma(\omega = 0)$ .

We devise nonequilibrium protocols that will allow us to invert the linear response [Eqs. (3) and (4)] for  $\Lambda(t)$  and  $\sigma(t)$ , compute them based on the current response, and reconstruct  $\sigma(\omega)$ . The three protocols are (a) constant electric field, (b) short pulse of electric field and (c) short pulse of vector potential. The corresponding expressions for the vector potential  $A(t)$  are given in Fig. 1. We use weak fields and make sure we probe the linear response regime (see SM for details).

**Self-energy approximation**—We compute the self-energy perturbatively in powers of  $U$ , and truncate at second order. The first-order self-energy in the Hubbard model is instantaneous (the Hartree shift) and can be absorbed in the single-particle Hamiltonian  $h$ . What remains to be computed is a single Feynman diagram,

$$\Sigma_{ij}(t, t')[G] = U^2 G_{ij}(t, t') G_{ij}(t, t') G_{ji}(t', t). \quad (5)$$

However, one may still choose to compute the diagram self-consistently or not, i.e., the propagator appearing in the self-energy diagram can be considered to be the fully dressed propagator ( $G$ ) or the bare propagator ( $G_0$ ). The self-consistent approximation corresponds to an approximation of the Luttinger-Ward functional and is guaranteed to respect charge and energy conservation laws. The two approximations for the self-energy must become indistinguishable as  $U \rightarrow 0$ , but at any finite  $U$ , they may yield different results.

**Results**—Our nonequilibrium theory is illustrated in an example in Fig. 1. We find that the three protocols yield perfectly consistent results [e.g., in Figs. 1(a) and 1(c) we show in red the comparison to the protocol (b) result]. However, the two self-energy approximations lead to drastically different results. Most importantly, the  $\Sigma[G_0]$  approximation yields infinite conductivity. This manifests

differently in the three different protocols. In the case of constant electric field, this means there is no stationary state and the current keeps growing with time. In the short electric field pulse case, the current does not decay to zero, but to a finite constant instead [as shown on Fig. 1(a), the constant is in perfect agreement with the slope of the linear growth of the current in the protocol (a)]. This indicates that the infinite conductivity is due to a finite charge stiffness  $D$ , which is when the optical conductivity can be separated in two parts as  $\sigma(t) = \sigma^{\text{reg}}(t) + D\theta(t)$ , with the regular part  $\sigma^{\text{reg}}(t)$  decaying to zero at long times [60,61]. In frequency domain this means  $\text{Re}\sigma(\omega) = \pi D\delta(\omega) + \text{Re}\sigma^{\text{reg}}(\omega)$ . In the short vector potential pulse case, the current does decay to zero, but the charge stiffness can be deduced from the obtained current-current correlation function based on the relation  $\int_0^\infty dt \Lambda(t) = K - D$ . Regardless of the  $\Sigma$  approximation, the optical sum rule  $\sigma(t = 0^+) = K = (1/\pi) \int d\omega \text{Re}\sigma(\omega)$  is satisfied [Fig. 1(b), SM]. To confirm that our results indicate charge stiffness, rather than a large conductivity, we have studied how  $\sigma(\omega)$  changes in the presence of a small fermionic bath (see SM).

**Cross-checking with RFDiagMC**—To cross-check the nonequilibrium results, we employ our new implementation of the RFDiagMC method for the computation of correlation functions in equilibrium. To do this, we first need to determine the diagrammatic content of the current-current correlation function that we effectively compute in our nonequilibrium calculations (in principle, in neither the  $\Sigma[G_0]$  nor the  $\Sigma[G]$  case will the diagrammatic content correspond to the bold perturbation theory for the current-current correlation function). Given an approximation for the self-energy, one can express the generalized two-particle susceptibility  $\chi$  as a functional derivative of the Green's function with respect to an applied external field,  $\chi = (\delta G / \delta \phi)$  [62]. In the case of the  $\Sigma[G]$  approximation, this yields the self-consistent Bethe-Salpeter equation, with  $\chi$  appearing on both sides of the equation. In the case of  $\Sigma[G_0]$ , one finds a closed expression where the

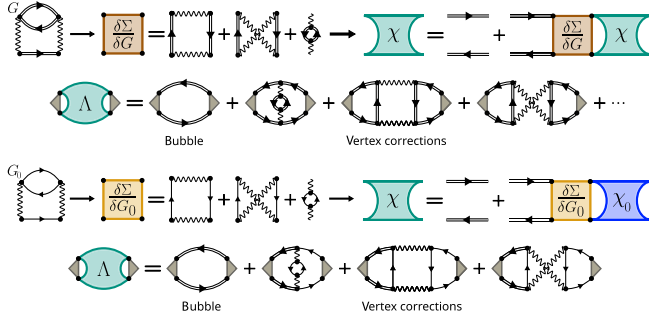


FIG. 2. Diagrammatic content of the current-current correlation function effectively computed in our nonequilibrium theory based on different diagrammatic approximations for the self-energy.

noninteracting  $\chi_0 = G_0 G_0$  appears on the rhs instead. The current-current correlation function  $\Lambda$  is obtained by connecting the legs of the generalized susceptibility  $\chi$  to two current vertices  $v$ . We see that in the case of  $\Sigma[G]$ ,  $\Lambda$  effectively contains infinitely many skeleton diagrams of all even orders with all propagators being the full Green's functions. Up to second order, all nonzero bold-skeleton diagrams are captured. However, odd orders are not captured, and at order 4 and above not all skeleton diagrams are captured. In the  $\Sigma[G_0]$  case, one obtains only three second-order diagrams, which are skeleton, but all propagators except two are bare. See Fig. 2 and SM for details.

The  $\Lambda$  diagrams from Fig. 2 can be computed using RFDiagMC, and we denote these theories as  $\Sigma[G]$  and  $\Sigma[G_0]$ . The comparison with nonequilibrium results is then

made by comparing  $\sigma^{\text{reg}}(\omega)$  and  $D$ . Both can be computed from  $\Lambda$ , namely  $\text{Re}\sigma^{\text{reg}}(\omega \neq 0) = \text{Im}\Lambda(\omega)/\omega$ ,  $\sigma_{\text{dc}}^{\text{reg}} = [\partial \text{Im}\Lambda(\omega)/\partial \omega]_{\omega \rightarrow 0}$  and  $D = K - \text{Re}\Lambda(\omega = 0)$ . The results are presented in Fig. 3(a). We see excellent agreement. In the case of  $\Sigma[G]$  effective  $\Lambda$  diagrams, it was enough to do only second-order vertex correction diagrams to reach agreement, which means that fourth and higher order diagrams are all negligible. In the case of  $\Sigma[G_0]$ , the charge stiffness was found to be below statistical error. In the case of  $\Sigma[G_0]$ , the charge stiffness entirely comes from vertex corrections.

**Perturbation theory for  $\Lambda$** —Now that we have established the validity of our implementation, we can also use RFDiagMC to solve the perturbation theory for the current-current correlation function. We take a given self-energy approximation, construct the dressed Green's function, and then compute *all* the bold-skeleton diagrams, up to a given order (including the odd orders). We denote such theories as  $\Lambda$ -pert. with a given  $\Sigma$  approximation. We find that third-order diagrams are practically negligible at  $U = 0.1$  (see SM), and the series is most likely converged already at second order. Therefore, our  $\Lambda$ -pert.  $\Sigma[G]$  theory gives the same result as the noneq.  $\Sigma[G]$  theory. However, the  $\Lambda$ -pert.  $\Sigma[G_0]$  approximation is different from the nonequilibrium  $\Sigma[G_0]$  theory because the vertex correction diagrams we compute are different. The results for all three distinct theories (as well as the Boltzmann theory) are compared in Fig. 3(b).

**Discussion and prospects for future work**—We observe a clear trend that  $\Lambda$ -pert.  $\Sigma[G_0]$  and  $\Sigma[G]$  results become the same as  $U \rightarrow 0$  [Fig. 3(b)]. This indicates that the  $\Lambda$ -pert.

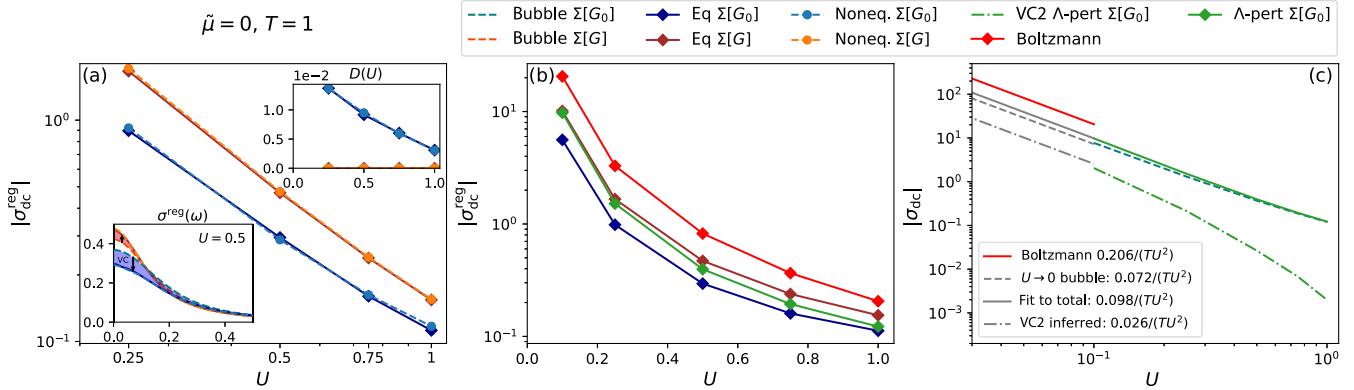


FIG. 3. Main results showing the comparison between different theories and the divergence of vertex corrections in the  $U \rightarrow 0$  limit. (a) Cross-check between equilibrium and the corresponding nonequilibrium theories showing perfect agreement in terms of the regular part of the dc conductivity  $\sigma_{\text{dc}}^{\text{reg}}$  (main panel), optical conductivity  $\text{Re}\sigma^{\text{reg}}(\omega)$  (lower inset), and the charge stiffness  $D$  (upper inset). The lower inset also shows the contribution of the vertex corrections to  $\text{Re}\sigma^{\text{reg}}(\omega)$  (positive in  $\Sigma[G]$  approximation, negative in  $\Sigma[G_0]$  approximation, vanishing at high frequency). (b) Comparison between two possible  $\Lambda$ -perturbation ( $\Lambda$ -pert.) theories (brown and green), the theory consistent with nonequilibrium (noneq.)  $\Sigma[G_0]$  approximation (blue), and the Boltzmann theory (red), showing that different  $\Lambda$ -pert. theories become indistinguishable as  $U \rightarrow 0$ , while the noneq.  $\Sigma[G_0]$  and the Boltzmann remain different. (c) Small- $U$  scaling of the results. Gray lines display the strict  $U \rightarrow 0$  scaling: the dashed gray line denotes the bubble computed in this limit, using the approach explained in [45]; the full gray line is a fit to the total result (full green line); the dash-dotted line is inferred from the previous two; the scaling of Boltzmann results is taken from [46].

series is not sensitive to the precise choice of the  $\Lambda$  approximation—as our second-order  $\Sigma[G]$  and  $\Sigma[G_0]$  converge in the weak-coupling limit, so do the corresponding low-order bold-skeleton perturbation theories for  $\Lambda$ . However, we observe that (non)eq.  $\Sigma[G_0]$  and Boltzmann theory results remain different as  $U \rightarrow 0$ .

To understand this, it is important to note that the  $\Lambda$  diagrams that are effectively being computed in our noneq.  $\Sigma[G_0]$  theory do not form a proper low-order perturbation theory. Even though  $\Sigma[G_0]$  becomes exact as  $U \rightarrow 0$  (and is even expected to perform best at low but finite coupling [63,64]; see also SM), the current response one gets from it is most likely never exact, no matter how low the value of  $U$ . The vertex corrections introduced this way subtract from  $\sigma_{dc}^{\text{reg}}$ , which is opposite to what is found in noneq.  $\Sigma[G]$  and the previous work with FTLM [24]. The failure of  $\Sigma[G_0]$  is relevant for Ref. [48] where in a similar theory, at low doping and high temperature, vertex corrections are also found to suppress dc conductivity instead of enhance it (see SM).

On the other hand, the Boltzmann theory is equivalent to our noneq.  $\Sigma[G]$  theory, plus additional approximations. Most importantly, the Green's function appearing in the collision integral and the second-order self-energy is simplified by the quasiparticle approximation (leading to expressions formally similar to our  $\Sigma[G_0]$ ; see SM for details). Therefore, the Boltzmann theory cannot be more accurate than our noneq.  $\Sigma[G]$  theory, and the additional approximations likely lead to the quantitatively wrong scaling we observe at  $U \rightarrow 0$ .

Our main finding is that the vertex corrections to dc conductivity do not vanish, even as  $U \rightarrow 0$ . It appears that both the bubble and the vertex corrections diverge at small  $U$  as  $1/U^2$ , but with a different prefactor, meaning that, as  $U$  is reduced, the ratio between the bubble and the vertex corrections remains fixed. This happens despite the  $U^2$  prefactor in second-order vertex correction diagrams (VC2). The reason is that the frequency dependence  $\text{Im}\Lambda^{\text{VC2}}(\omega)/U^2$  becomes singular at  $\omega = 0$  as  $U \rightarrow 0$  (we have checked this by computing  $\Lambda$  diagrams with the bare propagators; see SM). It is possible that a similar scenario happens at higher orders as well, and that *all orders* of perturbation contribute to  $\sigma_{dc}$  even at infinitesimal coupling. Our results, however, suggest that third-order vertex corrections to  $\sigma_{dc}$  at  $U = 0.1$  are at least 2 orders of magnitude smaller than second order. At  $U \approx 0.1$ – $0.25$ , the difference between  $\Lambda$ -pert.  $\Sigma[G]$  and  $\Lambda$ -pert.  $\Sigma[G_0]$  results appears to be only due to the difference in the self-energy, not due to lack of convergence of the  $\Lambda$  series.

Our findings show that neither the Boltzmann theory nor the Kubo bubble are exact in the weak-coupling limit. To fully confirm the strange-metal phenomenology that these two theories predict at  $U \rightarrow 0$  and half-filling [45], we need to be able to do calculations at temperatures of order 0.001–0.1. This will require further optimization in both our

RFDiagMC and noneq.  $\Sigma[G]$  theories, which are currently limited to about  $T > 0.05$ . Our nonequilibrium approach can be pushed to lower temperatures by using compression methods [65,66], and the preliminary results are encouraging. With additional optimization outside of the scope of the current Letter, we should also be able to push RFDiagMC to lower temperatures and stronger coupling. The path forward is clear, at least in principle: one should attempt to converge the bare series for the equilibrium  $\Sigma[G_0]$ , then use it to dress the Green's function, and then try to converge the bold-skeleton series for  $\Lambda$ .

Computations were performed on the PARADOX supercomputing facility (Scientific Computing Laboratory, Center for the Study of Complex Systems, Institute of Physics Belgrade).

*Acknowledgments*—We acknowledge useful discussions with Hugo Strand, Nenad Vukmirović, Rok Žitko, Antoine Georges, André-Marie Tremblay, and Jérôme Leblanc. The authors also acknowledge the access granted to the HPC resources of TGCC and IDRIS under the allocations A0170510609 attributed by GENCI (Grand Equipement National de Calcul Intensif) and to the high performance computing resources of IDCS (Infrastructure, Données, Calcul Scientifique) under the allocation CPHT 2024. J. V. and J. K. acknowledge funding provided by the Institute of Physics Belgrade, through a grant by the Ministry of Science, Technological Development and Innovation of the Republic of Serbia. J. V. and J. K. acknowledge funding by the European Research Council, Grant No. ERC-2022-StG:101076100.

*Data availability*—The data that support the findings of this article are not publicly available upon publication because it is not technically feasible and/or the cost of preparing, depositing, and hosting the data would be prohibitive within the terms of this research project. The data are available from the authors upon reasonable request.

- 
- [1] B. Keimer, S. A. Kivelson, M. R. Norman, S. Uchida, and J. Zaanen, *Nature (London)* **518**, 179 (2015).
  - [2] P. Limelette, P. Wzietek, S. Florens, A. Georges, T. A. Costi, C. Pasquier, D. Jérôme, C. Mézière, and P. Batail, *Phys. Rev. Lett.* **91**, 016401 (2003).
  - [3] Y. Kurosaki, Y. Shimizu, K. Miyagawa, K. Kanoda, and G. Saito, *Phys. Rev. Lett.* **95**, 177001 (2005).
  - [4] F. Kagawa, K. Miyagawa, and K. Kanoda, *Nature (London)* **436**, 534 (2005).
  - [5] M. Dumm, D. Faltermeier, N. Drichko, M. Dressel, C. Mézière, and P. Batail, *Phys. Rev. B* **79**, 195106 (2009).
  - [6] B. J. Powell and R. H. McKenzie, *Rep. Prog. Phys.* **74**, 056501 (2011).
  - [7] T. Furukawa, K. Miyagawa, H. Taniguchi, R. Kato, and K. Kanoda, *Nat. Phys.* **11**, 221 (2015).
  - [8] E. Y. Andrei and A. H. MacDonald, *Nat. Mater.* **19**, 1265 (2020).



- [9] Y. Cao, D. Chowdhury, D. Rodan-Legrain, O. Rubies-Bigorda, K. Watanabe, T. Taniguchi, T. Senthil, and P. Jarillo-Herrero, *Phys. Rev. Lett.* **124**, 076801 (2020).
- [10] T. Li, S. Jiang, L. Li, Y. Zhang, K. Kang, J. Zhu, K. Watanabe, T. Taniguchi, D. Chowdhury, L. Fu, J. Shan, and K. F. Mak, *Nature (London)* **597**, 350 (2021).
- [11] H. Takagi, B. Batlogg, H. L. Kao, J. Kwo, R. J. Cava, J. J. Krajewski, and W. F. Peck, *Phys. Rev. Lett.* **69**, 2975 (1992).
- [12] R. A. Cooper, Y. Wang, B. Vignolle, O. J. Lipscombe, S. M. Hayden, Y. Tanabe, T. Adachi, Y. Koike, M. Nohara, H. Takagi, C. Proust, and N. E. Hussey, *Science* **323**, 603 (2009).
- [13] A. Legros, S. Benhabib, W. Tabis, F. Laliberté, M. Dion, M. Lizaïre, B. Vignolle, D. Vignolles, H. Raffy, Z. Z. Li, P. Auban-Senzier, N. Doiron-Leyraud, P. Fournier, D. Colson, L. Taillefer, and C. Proust, *Nat. Phys.* **15**, 142 (2018).
- [14] R. Krishna Kumar, X. Chen, G. H. Auton, A. Mishchenko, D. A. Bandurin, S. V. Morozov, Y. Cao, E. Khestanova, M. Ben Shalom, A. V. Kretinin, K. S. Novoselov, L. Eaves, I. V. Grigorieva, L. A. Ponomarenko, V. I. Fal'ko, and A. K. Geim, *Science* **357**, 181 (2017).
- [15] R. K. Kumar, A. Mishchenko, X. Chen, S. Pezzini, G. H. Auton, L. A. Ponomarenko, U. Zeitler, L. Eaves, V. I. Fal'ko, and A. K. Geim, *Proc. Natl. Acad. Sci. U.S.A.* **115**, 5135 (2018).
- [16] C. G. Wang, R. Zhou, and G.-q. Zheng, in *Proceedings of the International Conference on Strongly Correlated Electron Systems (SCES2019)* (Physical Society of Japan, Tokyo, 2020), [10.7566/JPSCP.30.011028](https://arxiv.org/abs/10.7566/JPSCP.30.011028).
- [17] G. Grissonnanche, Y. Fang, A. Legros, S. Verret, F. Laliberté, C. Collignon, J. Zhou, D. Graf, P. A. Goddard, L. Taillefer, and B. J. Ramshaw, *Nature (London)* **595**, 667 (2021).
- [18] A. Jaoui, I. Das, G. Di Battista, J. Díez-Mérida, X. Lu, K. Watanabe, T. Taniguchi, H. Ishizuka, L. Levitov, and D. K. Efetov, *Nat. Phys.* **18**, 633 (2022).
- [19] J. Ayres, M. Berben, M. Čulo, Y.-T. Hsu, E. van Heumen, Y. Huang, J. Zaanen, T. Kondo, T. Takeuchi, J. R. Cooper, C. Putzke, S. Friedemann, A. Carrington, and N. E. Hussey, *Nature (London)* **595**, 661 (2021).
- [20] S. A. Grigera, R. S. Perry, A. J. Schofield, M. Chiao, S. R. Julian, G. G. Lonzarich, S. I. Ikeda, Y. Maeno, A. J. Millis, and A. P. Mackenzie, *Science* **294**, 329 (2001).
- [21] J. Vučičević, D. Tanasković, M. J. Rozenberg, and V. Dobrosavljević, *Phys. Rev. Lett.* **114**, 246402 (2015).
- [22] P. Cha, N. Wentzell, O. Parcollet, A. Georges, and E.-A. Kim, *Proc. Natl. Acad. Sci. U.S.A.* **117**, 18341 (2020).
- [23] J. Kokalj, *Phys. Rev. B* **95**, 041110 (2017).
- [24] J. Vučičević, J. Kokalj, R. Žitko, N. Wentzell, D. Tanasković, and J. Mravlje, *Phys. Rev. Lett.* **123**, 036601 (2019).
- [25] I. Vasić and J. Vučičević, *Phys. Rev. B* **110**, 064501 (2024).
- [26] M. Rigol, T. Bryant, and R. R. P. Singh, *Phys. Rev. Lett.* **97**, 187202 (2006).
- [27] E. Khatami and M. Rigol, *Phys. Rev. A* **84**, 053611 (2011).
- [28] B. Tang, E. Khatami, and M. Rigol, *Comput. Phys. Commun.* **184**, 557 (2013).
- [29] D.-W. Qu, Q. Li, S.-S. Gong, Y. Qi, W. Li, and G. Su, *Phys. Rev. Lett.* **133**, 256003 (2024).
- [30] P. J. H. Denteneer, R. T. Scalettar, and N. Trivedi, *Phys. Rev. Lett.* **83**, 4610 (1999).
- [31] E. W. Huang, R. Sheppard, B. Moritz, and T. P. Devereaux, *Science* **366**, 987 (2019).
- [32] F. Šimković, R. Rossi, A. Georges, and M. Ferrero, *Science* **385**, 6715 (2024).
- [33] M. Schiró, *Phys. Rev. B* **81**, 085126 (2010).
- [34] G. Cohen, E. Gull, D. R. Reichman, and A. J. Millis, *Phys. Rev. Lett.* **115**, 266802 (2015).
- [35] R. E. V. Profumo, C. Groth, L. Messio, O. Parcollet, and X. Waintal, *Phys. Rev. B* **91**, 245154 (2015).
- [36] M. Maček, P. T. Dumitrescu, C. Bertrand, B. Triggs, O. Parcollet, and X. Waintal, *Phys. Rev. Lett.* **125**, 047702 (2020).
- [37] C. Bertrand, D. Bauernfeind, P. T. Dumitrescu, M. Maček, X. Waintal, and O. Parcollet, *Phys. Rev. B* **103**, 155104 (2021).
- [38] A. Auerbach, *Phys. Rev. B* **99**, 115115 (2019).
- [39] I. Khait, S. Bhattacharyya, A. Samanta, and A. Auerbach, *npj Quantum Mater.* **8**, 75 (2023).
- [40] M. Qin, T. Schäfer, S. Andergassen, P. Corboz, and E. Gull, *Annu. Rev. Condens. Matter Phys.* **13**, 275 (2022).
- [41] H. Terletska, J. Vučičević, D. Tanasković, and V. Dobrosavljević, *Phys. Rev. Lett.* **107**, 026401 (2011).
- [42] X. Deng, J. Mravlje, R. Žitko, M. Ferrero, G. Kotliar, and A. Georges, *Phys. Rev. Lett.* **110**, 086401 (2013).
- [43] J. Vučičević and R. Žitko, *Phys. Rev. Lett.* **127**, 196601 (2021).
- [44] H. Xu, H. Shi, E. Vitali, M. Qin, and S. Zhang, *Phys. Rev. Res.* **4**, 013239 (2022).
- [45] J. Vučičević, S. Predin, and M. Ferrero, *Phys. Rev. B* **107**, 155140 (2023).
- [46] T. G. Kiely and E. J. Mueller, *Phys. Rev. B* **104**, 165143 (2021).
- [47] U. Schneider, L. Hackermüller, J. P. Ronzheimer, S. Will, S. Braun, T. Best, I. Bloch, E. Demler, S. Mandt, D. Rasch, and A. Rosch, *Nat. Phys.* **8**, 213 (2012).
- [48] D. Bergeron, V. Hankevych, B. Kyung, and A.-M. S. Tremblay, *Phys. Rev. B* **84**, 085128 (2011).
- [49] J. Vučičević, P. Stipsić, and M. Ferrero, *Phys. Rev. Res.* **3**, 023082 (2021).
- [50] J. Vučičević and M. Ferrero, *Phys. Rev. B* **101**, 075113 (2020).
- [51] A. Taheridehkordi, S. H. Curnoe, and J. P. F. LeBlanc, *Phys. Rev. B* **99**, 035120 (2019).
- [52] M. Grandadam and J. P. F. LeBlanc, [arXiv:2303.04964](https://arxiv.org/abs/2303.04964).
- [53] I. Sobol', *USSR Computational Mathematics and Mathematical Physics* **7**, 86 (1967).
- [54] H. U. R. Strand, J. Kleinhenz, and I. Krivenko, *Phys. Rev. B* **110**, L121120 (2024).
- [55] M. Schüler, D. Golež, Y. Murakami, N. Bittner, A. Herrmann, H. U. Strand, P. Werner, and M. Eckstein, *Comput. Phys. Commun.* **257**, 107484 (2020).
- [56] See Supplemental Material at <http://link.aps.org/supplemental/10.1103/mm38-zttx> for details.
- [57] H. Aoki, N. Tsuji, M. Eckstein, M. Kollar, T. Oka, and P. Werner, *Rev. Mod. Phys.* **86**, 779 (2014).
- [58] J. Vučičević and R. Žitko, *Phys. Rev. B* **104**, 205101 (2021).
- [59] A. Amaricci, C. Weber, M. Capone, and G. Kotliar, *Phys. Rev. B* **86**, 085110 (2012).



- [60] D. M. Kennes, E. Y. Wilner, D. R. Reichman, and A. J. Millis, *Phys. Rev. B* **96**, 054506 (2017).
- [61] T. Kaneko, S. Yunoki, and A. J. Millis, *Phys. Rev. Res.* **2**, 032027(R) (2020).
- [62] G. Baym and L. P. Kadanoff, *Phys. Rev.* **124**, 287 (1961).
- [63] E. Kozik, M. Ferrero, and A. Georges, *Phys. Rev. Lett.* **114**, 156402 (2015).
- [64] J. Gukelberger, L. Huang, and P. Werner, *Phys. Rev. B* **91**, 235114 (2015).
- [65] J. Kaye and D. Golež, *SciPost Phys.* **10**, 091 (2021).
- [66] J. Kaye and H. U. R. Strand, *Adv. Comput. Math.* **49**, 63 (2023).

# Supplemental Material: Towards numerically exact computation of conductivity in the thermodynamic limit of interacting lattice models

Jeremija Kovačević,<sup>1</sup> Michel Ferrero,<sup>2,3</sup> and Jakša Vučičević<sup>1</sup>

<sup>1</sup>Scientific Computing Laboratory, Center for the Study of Complex Systems,

Institute of Physics Belgrade, University of Belgrade, Pregrevica 118, 11080 Belgrade, Serbia

<sup>2</sup>CPHT, CNRS, Ecole Polytechnique, Institut Polytechnique de Paris, Route de Saclay, 91128 Palaiseau, France

<sup>3</sup>Collège de France, 11 place Marcelin Berthelot, 75005 Paris, France

(Dated: May 27, 2025)

## I. KADANOFF-BAYM EQUATIONS

Here, we briefly discuss Kadanoff-Baym (KB) equations and their numerical solution.

In order to calculate the non-equilibrium Green's function  $G_{\mathbf{k}}$  in a given self-energy approximation  $\Sigma_{\mathbf{k}}$  we solve the Dyson equation on the L-shaped contour  $\mathcal{C}$  (Fig. 1) in the complex time plane

$$G_{\mathbf{k}} = G_{0\mathbf{k}} + G_{0\mathbf{k}} * \Sigma_{\mathbf{k}} * G_{\mathbf{k}} \quad (1)$$

where  $*$  represents contour convolution, and  $G_{0\mathbf{k}}$  is the bare Green's function given by

$$G_{0\mathbf{k}}^{-1} = [i\partial_t - \varepsilon_{\mathbf{k}}(t)] \delta_{\mathcal{C}} \quad (2)$$

where  $\varepsilon_{\mathbf{k}}(t)$  is the time dependent dispersion relation, and  $\delta_{\mathcal{C}}$  is the delta function on the contour  $\mathcal{C}$ . We assume that the eigenstates of the non-interacting Hamiltonian do not change with time. By writing the Dyson equation in terms of contour components of  $G$  one obtains Kadanoff-Baym equations<sup>1,2</sup>

$$[-\partial_{\tau} - \varepsilon_{\mathbf{k}}(0^-)]G_{\mathbf{k}}^{\text{M}}(\tau) - \int_0^{\beta} d\bar{\tau} \Sigma_{\mathbf{k}}^{\text{M}}(\tau - \bar{\tau})G_{\mathbf{k}}^{\text{M}}(\bar{\tau}) = \delta(\tau) \quad (3)$$

$$[i\partial_t - \varepsilon_{\mathbf{k}}(t)]G_{\mathbf{k}}^{\text{R}}(t, t') - \int_{t'}^t d\bar{t} \Sigma_{\mathbf{k}}^{\text{R}}(t, \bar{t})G_{\mathbf{k}}^{\text{M}}(\bar{t}, t') = \delta(t - t') \quad (4)$$

$$[i\partial_t - \varepsilon_{\mathbf{k}}(t)]G_{\mathbf{k}}^{\text{A}}(t, \tau) - \int_{t_0}^t d\bar{t} \Sigma_{\mathbf{k}}^{\text{R}}(t, \bar{t})G_{\mathbf{k}}^{\text{A}}(\bar{t}, \tau) = Q_{\mathbf{k}}^{\text{A}}(t, \tau) \quad (5)$$

$$[i\partial_t - \varepsilon_{\mathbf{k}}(t)]G_{\mathbf{k}}^{\text{G}}(t, t') - \int_{t_0}^t d\bar{t} \Sigma_{\mathbf{k}}^{\text{R}}(t, \bar{t})G_{\mathbf{k}}^{\text{G}}(\bar{t}, t') = Q_{\mathbf{k}}^{\text{G}}(t, t') \quad (6)$$

with

$$Q_{\mathbf{k}}^{\text{A}}(t, \tau) = \int_0^{\beta} d\bar{\tau} \Sigma_{\mathbf{k}}^{\text{A}}(t, \bar{\tau})G_{\mathbf{k}}^{\text{M}}(\bar{\tau}, \tau) \quad (7)$$

$$Q_{\mathbf{k}}^{\text{G}}(t, t') = \int_{t_0}^{t'} d\bar{t} \Sigma_{\mathbf{k}}^{\text{G}}(t, \bar{t})G_{\mathbf{k}}^{\text{A}}(\bar{t}, t') - i \int_0^{\beta} d\bar{\tau} \Sigma_{\mathbf{k}}^{\text{A}}(t, \bar{\tau})G_{\mathbf{k}}^{\text{G}}(\bar{\tau}, t'). \quad (8)$$

The complex contour  $\mathcal{C}$  describes a physical setup where at the initial time  $t_0$  the system is in a thermal equilibrium state. After the initial time, external fields may be applied to drive the

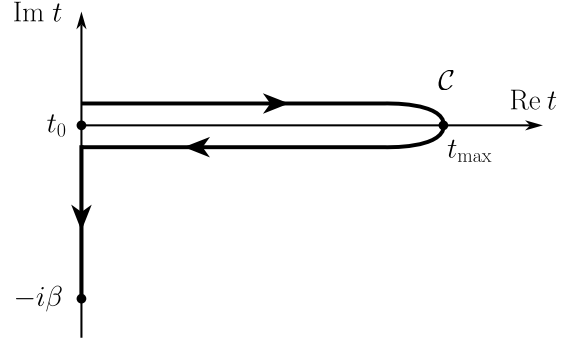


Figure 1. L-shaped contour  $\mathcal{C}$  in the complex time plane.

system out of equilibrium. The evolution of the system after the initial time is described by the real parts of the contour.

Every KB equation Eq. 3 - Eq. 6 has a conjugate version, derived from the conjugate Dyson equation

$$G_{\mathbf{k}} = G_{0\mathbf{k}} + G_{\mathbf{k}} * \Sigma_{\mathbf{k}} * G_{0\mathbf{k}}. \quad (9)$$

Finding the solution of the KB equations amounts to solving a system of coupled Volterra integral equations of the second kind<sup>1-3</sup>. To do this calculation we use the NESSi package<sup>1</sup>, and in some special cases we crosscheck the results with our own implementation. NESSi implements a version of the implicit Runge-Kutta method for solving Volterra equations where the global error scales as  $\mathcal{O}(\Delta t^5)$  with size of the time step  $\Delta t$ . The complexity of these methods scales as  $\mathcal{O}(N_t^3)$  with the number of time points  $N_t$  and as  $\mathcal{O}(N_{\mathbf{k}})$  with the number of  $\mathbf{k}$ -points  $N_{\mathbf{k}}$  due to translational invariance.

## II. SELF-ENERGY

We will now discuss the calculation of the self-energy approximations used in this paper. As mentioned in the main text, we use two different self-energy approximations both represented by the expression

$$\Sigma_{ij}[G](t, t') = U^2 G_{ij}(t, t') G_{ij}(t, t') G_{ji}(t', t) \quad (10)$$

and differentiate between bold  $\Sigma[G]$  and bare  $\Sigma[G_0]$  approximation depending on whether the propagator used is fully dressed or bare. The fully dressed propagator is  $G$  which solves the Dyson equation, while the bare propagator is  $G_0$  given by Eq. 2. Since  $\Sigma[G]$  is calculated using the

fully dressed propagator  $G$  this makes the KB equations self-consistent and we apply an iterative procedure to solve them.

The self-consistent calculation of the bold  $\Sigma[G]$  approximation can be done in two different ways. In the first approach, for one time step  $(t_i, t_j)$  a loop  $\Sigma_{\mathbf{k}}[G] \rightarrow G_{\mathbf{k}}[\Sigma[G]] \rightarrow G_{\mathbf{r}} \rightarrow \Sigma_{\mathbf{r}}[G] \rightarrow \Sigma_{\mathbf{k}}$  is iterated over until convergence is reached. In this case convergence is determined by the condition  $\Delta G(t_i, t_j) = \|G(l) - G(l-1)\| < \epsilon$ , where  $l$  is the iteration index and  $\epsilon$  is a small number. For different time steps  $(t_i, t_j)$  and  $(t'_i, t'_j)$  a different number of iterations might be needed to reach the same level of convergence. At least in principle, this allows one to reduce the overall number of computational steps.

The other possible approach, that we use in this paper, is to simply, in each iteration  $l$ , calculate  $\Sigma_{\mathbf{k}}[G] \rightarrow G_{\mathbf{k}}[\Sigma[G]] \rightarrow G_{\mathbf{r}} \rightarrow \Sigma_{\mathbf{r}}[G] \rightarrow \Sigma_{\mathbf{k}}$  on the entire contour, until convergence is reached. In this way, the convergence criterion can be changed to reflect physically relevant quantities: in our case we are primarily interested in the current  $j$ , so we take  $\Delta j = \|j(l) - j(l-1)\| < \epsilon$  as the condition.

For a given propagator  $G_{ij}$  the calculation of the expression Eq. 10 obviously scales as  $\mathcal{O}(N_t^2)$  with the number of discrete time points  $N_t$ , and as  $\mathcal{O}(N_{\mathbf{r}}^2)$  with the number of

sites  $N_{\mathbf{r}}$ . In order to obtain  $\Sigma_{\mathbf{k}}$  from  $\Sigma_{\mathbf{r}}$  and  $G_{\mathbf{r}}$  from  $G_{\mathbf{k}}$ , we use fast Fourier transforms which scale as  $\mathcal{O}(N_{\mathbf{r}} \log N_{\mathbf{r}})$ . This is faster than using a  $\mathbf{k}$ -space expression equivalent to Eq. 10, because it scales as  $\mathcal{O}(N_{\mathbf{k}}^3)$ .

### III. DERIVATION OF THE BOLTZMANN EQUATION FOR LATTICE MODELS

In this section we present a derivation of the Boltzmann equation starting from Kadanoff-Baym equations for lattice models coupled to external electromagnetic fields.

Coupling (discrete) lattice models to electromagnetic fields described by gauge potentials  $(\phi, \mathbf{A})$  is done by the Peierls substitution. This introduces a change in the one-particle Hamiltonian

$$H(t) = \sum_{ij, \sigma} h_{ij}(t) c_{i\sigma}^\dagger c_{j\sigma} \quad (11)$$

$$h_{ij}(t) = t_{ij} e^{i\mathbf{A}(t) \cdot (\mathbf{r}_i - \mathbf{r}_j)} + \delta_{i,j} \phi(\mathbf{r}_i) \quad (12)$$

where  $t_{ij}$  is a non-local hopping amplitude and where the vector potential the vector potential  $\mathbf{A}$  is assumed to be slowly varying in space.

We start from the KB equation for the lesser component of the Green's function and its conjugate version in site space

$$\sum_l [i\delta_{il} \vec{\partial}_t - h_{il}(t)] G_{lj}^<(t, t') - \sum_l \int_{t_0}^t d\bar{t} \Sigma_{il}^R(t, \bar{t}) G_{lj}^<(\bar{t}, t') = Q_{ij}^<(t, t') \quad (13)$$

$$\sum_l G_{il}^<(t, t') [-i\delta_{lj} \overleftarrow{\partial}_{t'} - h_{lj}(t')] - \sum_l \int_{t_0}^{t'} d\bar{t} G_{il}^<(t, \bar{t}) \Sigma_{lj}^A(\bar{t}, t') = \tilde{Q}_{ij}^<(t, t') \quad (14)$$

with

$$Q_{ij}^<(t, t') = \sum_l \int_{t_0}^{t'} d\bar{t} \Sigma_{il}^<(t, \bar{t}) G_{lj}^A(\bar{t}, t') - i \sum_l \int_0^\beta d\tau \Sigma_{il}^\gamma(t, \tau) G_{lj}^\tau(\tau, t')$$

$$\tilde{Q}_{ij}^<(t, t') = \sum_l \int_{t_0}^t d\bar{t} G_{il}^R(t, \bar{t}) \Sigma_{lj}^<(\bar{t}, t') - i \sum_l \int_0^\beta d\tau G_{il}^\gamma(t, \tau) \Sigma_{lj}^\tau(\tau, t').$$

Subtracting Eq. 14 from Eq. 13 we get

$$\begin{aligned} i\partial_t G_{ij}^<(t, t') + i\partial_{t'} G_{ij}^<(t, t') &= \sum_l h_{il}(t) G_{lj}^<(t, t') - G_{il}^<(t, t') h_{lj}(t') \\ &+ \sum_l \int_{t_0}^t d\bar{t} \left( \Sigma_{il}^R(t, \bar{t}) G_{lj}^<(\bar{t}, t') - G_{il}^R(t, \bar{t}) \Sigma_{lj}^<(\bar{t}, t') \right) \\ &+ \sum_l \int_{t_0}^{t'} d\bar{t} \left( \Sigma_{il}^<(t, \bar{t}) G_{lj}^A(\bar{t}, t') - G_{il}^<(t, \bar{t}) \Sigma_{lj}^A(\bar{t}, t') \right) \\ &- i \sum_l \int_0^\beta d\tau \left( \Sigma_{il}^\gamma(t, \tau) G_{lj}^\tau(\tau, t') - G_{il}^\gamma(t, \tau) \Sigma_{lj}^\tau(\tau, t') \right). \end{aligned} \quad (15)$$

We focus on the first term on the right-hand side and introduce

$$S_{ij}(t, t') = \sum_l h_{il}(t) G_{lj}^<(t, t') - G_{il}^<(t, t') h_{lj}(t') \quad (16)$$

$$= (\phi(\mathbf{r}_i) - \phi(\mathbf{r}_j)) G_{ij}^<(t, t') + \sum_l t_{il}(t) G_{lj}^<(t, t') - G_{il}^<(t, t') t_{lj}(t') \quad (17)$$

where  $t_{ij}(t) = t_{ij} e^{i\mathbf{A}(t) \cdot (\mathbf{r}_i - \mathbf{r}_j)}$ .

Now we perform the Fourier transform  $S_{\mathbf{k}} = \frac{1}{N_r} \sum_{ij} S_{ij}(t, t') e^{i\mathbf{k} \cdot (\mathbf{r}_i - \mathbf{r}_j)}$ , and depending on the gauge we obtain different expressions. In the  $\phi$ -gauge defined by  $\phi(\mathbf{r}_i) = -\mathbf{E} \cdot \mathbf{r}_i$ ,  $\mathbf{A} = 0$  we get

$$S_{\mathbf{k}}^\phi(t, t') = i\mathbf{E} \cdot \nabla_{\mathbf{k}} G_{\mathbf{k}}^<(t, t') \quad (18)$$

In the  $A$ -gauge, defined by  $\phi = 0$ ,  $\mathbf{A}(t) = -t\mathbf{E}$  we get

$$S_{\mathbf{k}}^A(t, t') = (\varepsilon_{\mathbf{k}+\mathbf{A}(t)} - \varepsilon_{\mathbf{k}+\mathbf{A}(t')}) G_{\mathbf{k}}^<(t, t') \quad (19)$$

The two choices of the gauge are physically equivalent. The

standard Boltzmann equation is derived in the  $\phi$ -gauge.

Since we are interested in finding the Boltzmann equation, i.e. the equation of motion for the non-equilibrium distribution function  $\langle n_{\mathbf{k}} \rangle$  we concentrate on equal times  $t' = t$  where

$$\left( \partial_t i G_{\mathbf{k}}^<(t, t') + \partial_{t'} i G_{\mathbf{k}}^<(t, t') \right) \Big|_{t'=t} = -\partial_t \langle n_{\mathbf{k}}(t) \rangle \quad (20)$$

and

$$S_{\mathbf{k}}(t, t) = -\mathbf{E} \cdot \nabla_{\mathbf{k}} \langle n_{\mathbf{k}}(t) \rangle. \quad (21)$$

Putting this back into the equation Eq. 15 we get

$$\begin{aligned} \partial_t n_{\mathbf{k}}(t) - \mathbf{E} \cdot \nabla_{\mathbf{k}} n_{\mathbf{k}}(t) = & - \int_{t_0}^t d\bar{t} \left( \Sigma_{\mathbf{k}}^R(t, \bar{t}) G_{\mathbf{k}}^<(\bar{t}, t) - G_{\mathbf{k}}^R(t, \bar{t}) \Sigma_{\mathbf{k}}^<(\bar{t}, t) \right. \\ & \left. + \Sigma_{\mathbf{k}}^<(t, \bar{t}) G_{\mathbf{k}}^A(\bar{t}, t) - G_{\mathbf{k}}^<(t, \bar{t}) \Sigma_{\mathbf{k}}^A(\bar{t}, t) \right) \\ & + i \int_0^\beta d\tau \left( \Sigma_{\mathbf{k}}^\top(t, \tau) G_{\mathbf{k}}^\top(\tau, t) - G_{\mathbf{k}}^\top(t, \tau) \Sigma_{\mathbf{k}}^\top(\tau, t) \right). \end{aligned} \quad (22)$$

where we have dropped the average brackets  $\langle \dots \rangle$  for the sake of brevity. In order to further simplify this expression we concentrate on the limit of long times, i.e. times long after the initial state, by taking  $t_0 \rightarrow -\infty$ . In this limit, the mixed terms vanish. Applying this and the relations

$$G^R(t, t') = \theta(t - t') (G^>(t, t') - G^<(t, t')) \quad (23)$$

$$G^A(t, t') = \theta(t' - t) (G^<(t, t') - G^>(t, t')) \quad (24)$$

in equation Eq. 22 we get the *Boltzmann equation*

$$\partial_t n_{\mathbf{k}}(t) - \mathbf{E} \cdot \nabla_{\mathbf{k}} n_{\mathbf{k}}(t) = -I_{\mathbf{k}}(t) \quad (25)$$

where

$$\begin{aligned} I_{\mathbf{k}}(t) = & \int_{-\infty}^t d\bar{t} \left( \Sigma_{\mathbf{k}}^>(t, \bar{t}) G_{\mathbf{k}}^<(\bar{t}, t) + G_{\mathbf{k}}^<(t, \bar{t}) \Sigma_{\mathbf{k}}^>(\bar{t}, t) \right. \\ & \left. - \Sigma_{\mathbf{k}}^<(t, \bar{t}) G_{\mathbf{k}}^>(\bar{t}, t) - G_{\mathbf{k}}^>(t, \bar{t}) \Sigma_{\mathbf{k}}^<(\bar{t}, t) \right) \end{aligned} \quad (26)$$

is the collision integral.

#### A. Quasi-particle approximation for the collision integral in the Hubbard model

Under the assumption of a stationary state, real time components of the Green's function and the self-energy depend only on the time difference  $t - t'$ . The collision integral Eq. 26 becomes independent of time and can be further simplified

$$I_{\mathbf{k}} = \int_{-\infty}^{\infty} d\bar{t} \left( G_{\mathbf{k}}^<(\bar{t}) \Sigma_{\mathbf{k}}^>(-\bar{t}) - G_{\mathbf{k}}^>(\bar{t}) \Sigma_{\mathbf{k}}^<(-\bar{t}) \right) \quad (27)$$

where the integration variable in equation Eq. 26 has first been shifted  $\bar{t} \rightarrow t - \bar{t}$  and then for the first and third term a change of variables  $\bar{t} \rightarrow -\bar{t}$  was also made.

The quasi-particle approximation now assumes that the



spectral function is a delta peak at  $\omega = \varepsilon_{\mathbf{k}}$ . Therefore,

$$G_{\mathbf{k}}^<(t) = \int \frac{d\omega}{2\pi} e^{-i\omega t} G_{\mathbf{k}}^<(\omega) \quad (28)$$

$$= \int \frac{d\omega}{2\pi} e^{-i\omega t} n(\omega) A_{\mathbf{k}}(\omega) \quad (29)$$

$$\approx \int \frac{d\omega}{2\pi} e^{-i\omega t} 2\pi \langle n_{\mathbf{k}} \rangle \delta(\omega - \varepsilon_{\mathbf{k}}) \quad (30)$$

$$= n_{\mathbf{k}} e^{-i\varepsilon_{\mathbf{k}} t}. \quad (31)$$

Similarly

$$G_{\mathbf{k}}^>(t) = (1 - n_{\mathbf{k}}) e^{-i\varepsilon_{\mathbf{k}} t}. \quad (32)$$

Furthermore, if the self-energy is assumed to be given by the second order diagram  $\Sigma[G]$  (as we assume in our calculations) it can be expressed in momentum space as

$$\Sigma_{\mathbf{k}}^<(t) = \frac{U^2}{N^2} \sum_{\mathbf{k}', \mathbf{q}} G_{\mathbf{k}-\mathbf{q}}^<(t) G_{\mathbf{k}'+\mathbf{q}}^<(t) G_{\mathbf{k}'}^>(-t). \quad (33)$$

Plugging this back in the collision integral Eq. 27, and applying the QP approximation we get

$$\begin{aligned} I_{\mathbf{k}}^{\text{QP}, \phi} &= \frac{2\pi U^2}{N^2} \sum_{\mathbf{k}', \mathbf{q}} \delta(\varepsilon_{\mathbf{k}} - \varepsilon_{\mathbf{k}-\mathbf{q}} - \varepsilon_{\mathbf{k}'+\mathbf{q}} + \varepsilon_{\mathbf{k}'}) \\ &\times \left[ n_{\mathbf{k}}(1 - n_{\mathbf{k}-\mathbf{q}})(1 - n_{\mathbf{k}'+\mathbf{q}})n_{\mathbf{k}'} \right. \\ &\quad \left. - (1 - n_{\mathbf{k}})n_{\mathbf{k}-\mathbf{q}}n_{\mathbf{k}'+\mathbf{q}}(1 - n_{\mathbf{k}'}) \right] \end{aligned} \quad (34)$$

which is also known as the Fermi golden rule. The equation Eq. 25 together with Eq. 34 is the starting point of the calculations in Ref. 4.

#### IV. DIAGRAMMATIC CONTENT OF NON-EQUILIBRIUM THEORIES

Here we derive the diagrammatic content for the current-current correlation function that we effectively compute in our non-equilibrium theories based on a diagrammatic approximation for the self-energy. Linear response of the system to

external fields  $\phi$  is obtained by considering a general four-point correlation function  $\chi^5$ . For convenience, we introduce a general source field  $\phi_{\alpha\beta}(t, t')$  which can later be easily modified to represent a scalar or a vector potential.

All correlation functions of an interacting theory coupled to the source field  $\phi$  can be obtained from the generating functional

$$\mathcal{Z}[\phi] = \text{Tr} \left[ \mathcal{T}_C e^{-i \int_C dt H(t)} e^{-i \iint_C dt_1 dt_2 c_{\alpha}^{\dagger}(t_1) \phi_{\alpha\bar{\beta}}(t_1, t_2) c_{\bar{\beta}}(t_2)} \right] \quad (35)$$

through its functional derivatives with respect to the source field  $\phi$ . Green's function is then defined as

$$G_{ij}^{\phi}(t_1, t_2) = -\frac{\delta \ln \mathcal{Z}[\phi]}{\delta \phi_{ji}(t_2, t_1)} = -i \langle \mathcal{T}_C c_i(t_1) c_j^{\dagger}(t_2) \rangle_{\phi}. \quad (36)$$

On the other hand, the Green's function can be obtained from the knowledge of the self-energy  $\Sigma$ , using the Dyson equation

$$G_{ij}^{-1, \phi}(t_1, t_2) = G_{0ij}^{-1}(t_1, t_2) - \phi_{ij}(t_1, t_2) - \Sigma_{ij}^{\phi}(t_1, t_2). \quad (37)$$

The four-point correlation function  $\chi$  is defined with the second functional derivative of  $\mathcal{Z}[\phi]$

$$\chi_{ijkl}(t_1, t_2, t_4, t_3) = -i \frac{\delta G_{ij}^{\phi}(t_1, t_2)}{\delta \phi_{lk}(t_4, t_3)} \quad (38)$$

$$\begin{aligned} &= -i G_{kl}^{\phi}(t_3, t_4) G_{ij}^{\phi}(t_1, t_2) \\ &\quad + i \langle c_l^{\dagger}(t_4) c_k(t_3) c_i(t_1) c_j^{\dagger}(t_2) \rangle \end{aligned} \quad (39)$$

Using a representation of the unit operator

$$G_{ij}^{-1, \phi}(t_1, \bar{t}_2) G_{jk}^{\phi}(t_1, \bar{t}_2) = \delta_{i,k} \delta(t_1 - t_2) \quad (40)$$

we can write

$$\begin{aligned} \chi_{ijkl}(t_1, t_2, t_4, t_3) &= -i \frac{\delta G_{i\bar{m}}^{\phi}(t_1, \bar{t}_5)}{\delta \phi_{kl}(t_4, t_3)} G_{\bar{m}\bar{n}}^{-1, \phi}(\bar{t}_5, \bar{t}_6) G_{\bar{n}j}^{\phi}(\bar{t}_6, t_2) \end{aligned} \quad (41)$$

$$= i G_{i\bar{m}}^{\phi}(t_1, \bar{t}_5) \frac{\delta G_{\bar{m}\bar{n}}^{-1, \phi}(\bar{t}_5, \bar{t}_6)}{\delta \phi_{kl}(t_4, t_3)} G_{\bar{n}j}^{\phi}(\bar{t}_6, t_2) \quad (42)$$

$$\begin{aligned} &= -i G_{ik}^{\phi}(t_1, t_4) G_{lj}^{\phi}(t_3, t_2) \\ &\quad - i G_{i\bar{m}}^{\phi}(t_1, \bar{t}_5) \frac{\delta \Sigma_{\bar{m}\bar{n}}^{\phi}(\bar{t}_5, \bar{t}_6)}{\delta \phi_{kl}(t_4, t_3)} G_{\bar{n}j}^{\phi}(\bar{t}_6, t_2). \end{aligned} \quad (43)$$

For bold  $\Sigma[G]$  approximation Eq. 43 is transformed by the chain rule to

$$\begin{aligned} \chi_{ijkl}(t_1, t_2, t_4, t_3) &= -i G_{ik}^{\phi}(t_1, t_4) G_{lj}^{\phi}(t_3, t_2) \\ &\quad + G_{i\bar{m}}^{\phi}(t_1, \bar{t}_5) \frac{\delta \Sigma_{\bar{m}\bar{n}}^{\phi}(\bar{t}_5, \bar{t}_6)}{\delta G_{\bar{p}q}^{\phi}(\bar{t}_7, \bar{t}_8)} \chi_{\bar{p}q\bar{l}k}(\bar{t}_7, \bar{t}_8, t_4, t_3) G_{\bar{n}j}^{\phi}(\bar{t}_6, t_2) \end{aligned} \quad (44)$$

which is the Bethe-Salpeter equation. The diagrammatic content of  $\chi$  is then determined by the diagrammatic content of the functional derivative  $\delta \Sigma / \delta G$ , which is also known as the irreducible vertex in the particle-hole channel,  $\Gamma^{\text{ph}}$ . The diagrammatic content of  $\Gamma^{\text{ph}}$  can be obtained straightforwardly if the self-energy is approximated in terms of Feynman diagrams.

In the case of a bare  $\Sigma[G_0]$  approximation using the chain rule in Eq. 43 we get a different equation

$$\begin{aligned} \chi_{ijkl}(t_1, t_2, t_4, t_3) = & -iG_{ik}^\phi(t_1, t_4)G_{lj}^\phi(t_3, t_2) \\ & + G_{im}^\phi(t_1, t_5) \frac{\delta \Sigma_{\bar{m}\bar{n}}^\phi(\bar{t}_5, \bar{t}_6)}{\delta G_{0\bar{p}\bar{q}}^\phi(\bar{t}_7, \bar{t}_8)} \chi_{\bar{p}\bar{q}lk}^0(\bar{t}_7, \bar{t}_8, t_4, t_3) G_{\bar{n}j}^\phi(\bar{t}_6, t_2) \end{aligned} \quad (45)$$

where

$$\chi_{\bar{p}\bar{q}lk}^0(t_7, t_8, t_4, t_3) = -i \frac{\delta G_{0\bar{p}\bar{q}}^\phi(t_7, t_8)}{\delta \phi_{kl}(t_4, t_3)} = -i G_{0\bar{p}\bar{q}}^\phi(t_7, t_8) G_{0\bar{p}\bar{q}}^\phi(t_7, t_8). \quad (46)$$

Equation Eq. 45 represents a closed expression for calculating the correlation function  $\chi$ .

#### A. Connection between $\sigma$ , $\Lambda$ , $D$ , $K$ and the f-sum rule

In order to obtain the optical conductivity  $\sigma$  we are interested in computing the retarded current-current correlation function

$$\Lambda(t - t') = i \langle [j(t), j(t')] \rangle \theta(t - t'), \quad (47)$$

where  $j(t)$  is the current density along the arbitrarily chosen  $x$  direction

$$j(t) = \frac{1}{N} \sum_{\mathbf{r}} j_x(\mathbf{r}, t). \quad (48)$$

If the four-particle correlation function  $\chi$  is known, the current-current correlation function can be obtained by connecting the legs of  $\chi$  to the current vertex  $v$ . For example, if the coupling of the system to the electric field is described by an additional term

$$\sum_k \phi_k(t) v_{ijk} c_i^\dagger c_j \quad (49)$$

in the Hamiltonian, then we can calculate the dynamical response correlation function as

$$\Lambda_{ij}(t_1, t_2) = \sum_{i', i'', j', j''} v_{i, i', i''} \chi_{i', i'', j', j''}(t_1, t_1^+, t_2, t_2^+) v_{j, j', j''}. \quad (50)$$

For the explicit expression for the current vertex see Refs. 6 and 7.

The current-current correlation function determines the linear response to an applied field through the relation

$$\langle j(t) \rangle = \int_{-\infty}^{\infty} \Lambda(t - t') A(t') dt' - K A(t), \quad (51)$$

where  $A(t)$  is the vector potential and  $K = -\frac{\langle E_{\text{kin}} \rangle}{2}$ , with  $\langle E_{\text{kin}} \rangle$  the average kinetic energy per site. With the knowledge of  $\Lambda$ , the optical conductivity is obtained from

$$\sigma(\omega) = -i \frac{\Lambda(\omega) - K}{\omega + i\eta} \quad (52)$$

$$= \mathcal{P} \left( \frac{\Lambda(\omega) - K}{i\omega} \right) - \pi \delta(\omega) [\Lambda(\omega = 0) - K] \quad (53)$$

If we focus on the real part, we have

$$\text{Re } \sigma(\omega) = \mathcal{P} \left( \frac{\text{Im} \Lambda(\omega)}{\omega} \right) - \pi \delta(\omega) [\Lambda(\omega = 0) - K] \quad (54)$$

Here we have used the fact that  $\Lambda(\omega = 0)$  is purely real.

From Eq. 54, we see that we can express the optical conductivity as the sum of a regular part and a Drude peak at  $\omega = 0$  (due to charge-stiffness,  $D$ )

$$\text{Re} \sigma(\omega) = \text{Re} \sigma^{\text{reg}}(\omega) + D \pi \delta(\omega), \quad (55)$$

where

$$\sigma^{\text{reg}}(\omega) = \mathcal{P} \left( \frac{\text{Im} \Lambda(\omega)}{\omega} \right) \quad (56)$$

$$D = K - \Lambda(\omega = 0). \quad (57)$$

This is compatible with a real-time expression for  $\sigma(t)$  reading

$$\sigma(t) = \sigma^{\text{reg}}(t) + D \theta(t). \quad (58)$$

Note that  $\sigma(t)$  is purely real.

The optical conductivity obeys the f-sum rule

$$\int_{-\infty}^{\infty} \frac{d\omega}{2\pi} \text{Re} \sigma(\omega) = \frac{K}{2} = -\frac{\langle E_{\text{kin}} \rangle}{4} \quad (59)$$

but this also implies the value of  $\sigma(t = 0^+)$ . This is because it is sufficient to consider only the real part of  $\sigma(\omega)$  in its Fourier

transformation. Namely

$$\begin{aligned}
\sigma(t) &= \mathcal{F}^{-1}[\sigma(\omega)] \\
&= \int \frac{d\omega}{2\pi} e^{-i\omega t} \sigma(\omega) \\
&= \int \frac{d\omega}{2\pi} e^{-i\omega t} (\text{Re}\sigma(\omega) + i\text{Im}\sigma(\omega)) \\
&= \int \frac{d\omega}{2\pi} e^{-i\omega t} \text{Re}\sigma(\omega) \\
&\quad + i \int \frac{d\omega}{2\pi} e^{-i\omega t} \mathcal{P} \left( \int \frac{d\omega'}{\pi} \frac{\text{Re}\sigma(\omega')}{\omega - \omega'} \right) \\
&= \int \frac{d\omega}{2\pi} e^{-i\omega t} \text{Re}\sigma(\omega) \\
&\quad + i\mathcal{P} \left( \int \frac{d\omega'}{\pi} \text{Re}\sigma(\omega') e^{-i\omega' t} \int \frac{d\omega}{2\pi} \frac{e^{-i(\omega - \omega')t}}{\omega - \omega'} \right) \\
&= \int \frac{d\omega}{2\pi} e^{-i\omega t} \text{Re}\sigma(\omega) \\
&\quad + \text{sgn}(t) \mathcal{P} \left( \int \frac{d\omega'}{2\pi} \text{Re}\sigma(\omega') e^{-i\omega' t} \right) \\
&= 2\theta(t) \mathcal{F}^{-1}[\text{Re}\sigma(\omega)]
\end{aligned} \tag{60}$$

where  $\mathcal{F}$  denotes the Fourier transform. Therefore, the f-sum rule Eq.59 implies

$$\begin{aligned}
\sigma(t = 0^+) &= 2 \int \frac{d\omega}{2\pi} e^{-i\omega 0^+} \text{Re}\sigma(\omega) \\
&= 2 \int \frac{d\omega}{2\pi} \text{Re}\sigma(\omega) \\
&= K
\end{aligned} \tag{61}$$

where we have used the fact that  $\text{Re}\sigma(\omega)$  decays faster than  $\omega^{-1}$ .

Let us finally note that in the non-interacting case  $U = 0$ , we have  $\Lambda = 0$ . The conductivity has no regular part, and it reads

$$\sigma(\omega) = i \frac{K}{\omega + i\eta}, \tag{62}$$

which means that  $D = K$ .

## V. STUDY OF THE EFFECTS OF THE FERMIONIC BATH ON $\rho_{dc}$

In this appendix we explore the effect on  $\rho_{dc}$  of coupling our model to an external fermionic bath.

We take the bath to be an infinite non-interacting system in equilibrium at temperature  $T$ . The full Hamiltonian of the system coupled to a fermionic bath reads

$$H = H_{\text{sys}} + H_{\text{mix}} + H_{\text{bath}} \tag{63}$$

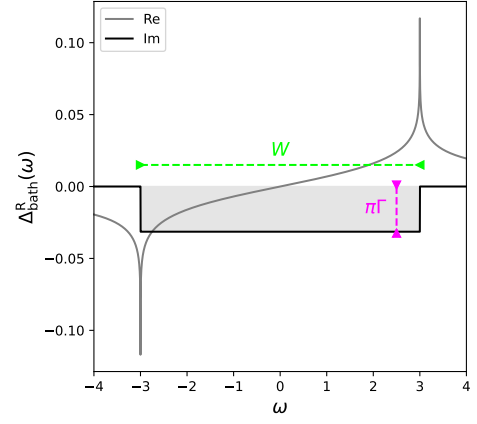


Figure 2. Our choice of the hybridization function  $\Delta_{\text{bath}}(\omega)$  as defined in Eq. 69.

where

$$H_{\text{mix}} = V \sum_{i,p} (c_i^\dagger b_{i,p} + c_i b_{i,p}^\dagger) \tag{64}$$

describes the hybridization between the system and the bath, and

$$H_{\text{bath}} = \sum_{i,p} \epsilon_p b_{i,p}^\dagger b_{i,p} \tag{65}$$

is the bath Hamiltonian. With this, the Green's function of the bath is

$$G_{\text{bath}}(t - t') = -i \sum_p \langle \mathcal{T}_C b_{i,p}(t) b_{i,p}^\dagger(t') \rangle_{\text{bath}}. \tag{66}$$

As the bath is in thermal equilibrium, the Green's function is fully defined from the knowledge of the retarded Green's function, which we choose as

$$G_{\text{bath}}^{\text{R}}(\omega) = \frac{1}{W} \left[ \ln \left| \frac{\frac{W}{2} + \omega}{\frac{W}{2} - \omega} \right| - i\pi\theta \left( \frac{W}{2} - |\omega| \right) \right]. \tag{67}$$

The bare Green's function with the additional bath is

$$\mathcal{G}_{0\mathbf{k}}^{-1}(t, t') = G_{0\mathbf{k}}^{-1}(t, t') - \Delta_{\text{bath}}(t - t') \tag{68}$$

where the hybridization function is

$$\Delta_{\text{bath}}(t - t') = V^2 G_{\text{bath}}(t - t'). \tag{69}$$

For convenience we introduce a coupling constant  $\Gamma = \frac{V^2}{W}$  and keep  $W$  constant. Retarded component of the hybridization function is presented in the Fig. 2.

We calculate  $\rho_{dc}$  for different values of  $\Gamma$  using the constant electric field protocol  $A = -Et\theta(t)$ . For different self-energy approximations the system behavior is drastically different, see Fig. 3.

In the case of the bold  $\Sigma[G]$  approximation we can calculate the  $\Gamma = 0$  point because the system reaches a stationary state, as illustrated in the main text.

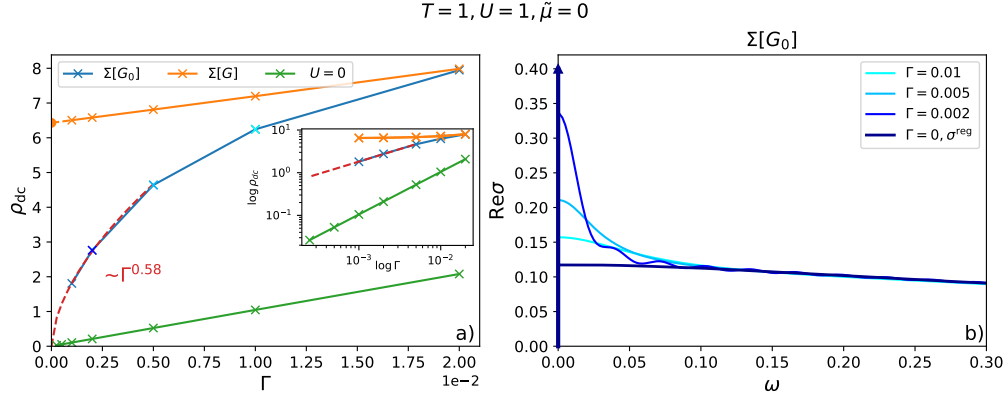


Figure 3. a)  $\rho_{dc}$  vs. the bath coupling  $\Gamma$  for different theories; b)  $\text{Re}\sigma(\omega)$  for different couplings  $\Gamma$  in the  $\Sigma[G_0]$  approximation.

On the other hand, if we use the bare  $\Sigma[G_0]$  approximation, we cannot calculate  $\rho_{dc}$  for  $\Gamma = 0$  because the current grows indefinitely. Due to this, we compute the results at several small values of  $\Gamma$  and then extrapolate to  $\Gamma = 0$ . The results fit to a power law form, indicating  $\rho_{dc}(\Gamma = 0) = 0$ , see Fig. 3a. This is in stark contrast with the  $\Sigma[G]$  approximation where  $\rho_{dc}$  has a finite value at  $\Gamma = 0$ .

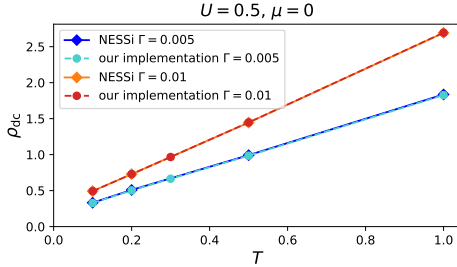


Figure 4. Comparison of  $\rho_{dc}(T)$  for different implementations of Kadanoff-Baym equations.

In Fig. 3b the optical conductivity  $\text{Re}\sigma(\omega)$  in the bare approximation is presented. We explore the  $\Gamma \rightarrow 0$  limit and we see that  $\sigma$  develops a delta peak at  $\omega = 0$  for  $\Gamma = 0$ , elucidating the presence of charge stiffness in this approximation.

As an additional check, we created our own implementation of the Kadanoff-Baym equations for this setup and compared it to the NESSI implementation (Fig. 4) and the results are in excellent agreement. In our implementation the initial thermal state is at  $T = \infty$ . This approach is possible because the system gets cooled down to temperature  $T$  due to the coupling with the bath, and indeed we observe a stationary state in our results.

In practice, because the initial state is at infinite temperature,  $\beta = 0$ , the imaginary part of the contour drops out, as well as all the mixed terms. This leaves us with only two KB equations, one for  $G^<$  and the other one for  $G^>$ . The system then evolves to a stationary state at temperature  $T$  due to the coupling with the bath. We solved KB equations using the implicit Runge-Kutta method of the 4-th order where the global error scales as  $\mathcal{O}(\Delta t^4)$ . NESSI has better error scaling

$\mathcal{O}(\Delta t^5)$ , this did not make a difference in the final results.

## VI. INVERSE LINEAR RESPONSE THEORY

In this appendix we will discuss our approach to using non-equilibrium protocols for calculating  $\rho_{dc}$ .

As mentioned in the main text, we use three different non-equilibrium protocols for calculating  $\rho_{dc}$ . They are presented in Table I.

Table I. Non-equilibrium protocols to extract  $\sigma(\omega)$

a) Constant electric field	$A = -Et \theta(t)$	$\sigma_{dc} = \langle j(t \rightarrow \infty) \rangle / E$
b) Short pulse of elec. field	$A = -a\theta(t)$	$\sigma(t) = \langle j(t) \rangle / a$
c) Short pulse of vec. pot.	$A = a\delta(t)$	$\Lambda(t) = \langle j(t) \rangle / a$

We consider two equivalent linear response equations for the uniform current<sup>8,9</sup>

$$\langle j(t) \rangle = \int_{-\infty}^t dt' \sigma(t-t') E(t') \quad (70)$$

$$\langle j(t) \rangle = \int_{-\infty}^t dt' \Lambda(t-t') A(t') - K A(t), \quad (71)$$

where  $K = -\frac{\langle E_{kin} \rangle}{2}$  with  $\langle E_{kin} \rangle$  the average kinetic energy per site and  $E(t)$  the electric field. If we apply protocol b) to Eq. 70 and protocol c) to Eq. 71 we get

$$\langle j(t) \rangle = a\sigma(t) \quad (72)$$

$$\langle j(t) \rangle = a\Lambda(t). \quad (73)$$

After solving KB Eqs. 3-6 in a given protocol we get the current  $j(t)$ , which we then use in Eqs. 72 and 73 to obtain the correlation functions. In this way, we have *inverted* the linear response Eqs. 70 and 71.

In the case of the constant electric field protocol a) we assume a stationary state, and we can write

$$\langle j(t \rightarrow \infty) \rangle = E \int_{-\infty}^{\infty} dt' \sigma(t-t') \quad (74)$$

$$= E\sigma_{dc}. \quad (75)$$



### A. Diamagnetic response in the protocol c)

In the Fig. 5 we present the paramagnetic and diamagnetic parts of the current calculated in the protocol c). The paramagnetic part is used in the calculation of the current-current correlation function  $\Lambda$  (see Fig.1 in the main text). The diamagnetic part is non-zero only during the initial pulse of the vector potential. In our calculations we use the duration of the pulse  $\Delta t_{\text{pulse}}$  as the control parameter and show that there is no dependence of the obtained results on  $\Delta t_{\text{pulse}}$ , see Section VII.

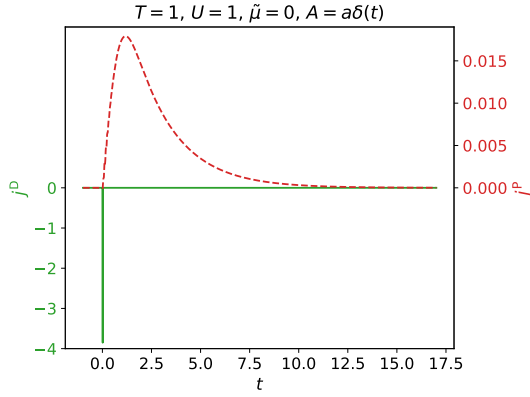


Figure 5. Diamagnetic  $j^D$  and paramagnetic  $j^P$  parts of the current in the protocol c).

## VII. BENCHMARKS

Here we will discuss the dependence of the results on the numerical parameters.

Fig. 6 shows the dependence of the calculated current  $\langle j(t) \rangle$  on the linear lattice size  $L$  and temperature  $T$  in different approximations in the b) protocol. We see the current displays large finite size effects for both approximations.

In the  $\Sigma[G_0]$  approximation, at a higher temperature  $T = 1$  in Fig. 6a we can see that the current is strictly positive for all lattice sizes, while this is not necessarily the case for the lower temperature  $T = 0.1$  (Fig. 6c). Also, it can be seen that the charge stiffness does not decrease with increasing lattice size.

In the  $\Sigma[G]$  approximation the current changes sign due to finite size effects regardless of the temperature, see Figs. 6b and 6d. We see that in this case charge stiffness decreases with linear lattice size  $L$ . In the insets of Fig. 6 we show  $\sigma_{dc}^{\text{reg}}$  which is obtained as  $\frac{1}{a} \int dt (\langle j(t) \rangle - D)$ . One can see that finite size effects are not strong in terms of  $\sigma_{dc}^{\text{reg}}$ , even though  $\sigma(t) - D$  does appear noticeably different; the reason is that there is a cancellation of difference between shorter and longer times.

In the  $\Sigma[G_0]$  approximation we also see "revivals" occurring for a long time after the field pulse, while in the  $\Sigma[G]$  approximation no revivals are observed at any lattice size  $L$ .

Fig. 7a shows the current  $\langle j(t) \rangle$  in the bare  $\Sigma[G_0]$  approximation calculated using the b) protocol for different time steps  $\Delta t$ .

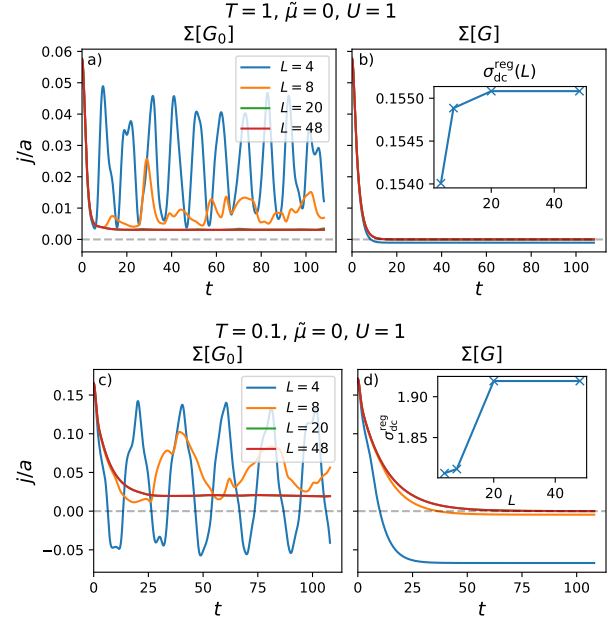


Figure 6.  $j/a$  in the b) protocol as a function of the linear lattice size  $L$  in different self-energy approximations and at different temperatures.

Fig. 7b and 7c present  $\langle j(t) \rangle$  in  $\Sigma[G]$  approximation calculated using the b) and a) protocol for two different values of the parameters  $a$  and  $E$ , respectively. Fig. 7d shows  $\langle j(t) \rangle$  in the c) protocol for different durations of the applied pulse  $\Delta t_{\text{pulse}}$ . Note that in the b) protocol we do not have a finite duration of the applied field, but rather exactly  $\Delta t_{\text{pulse}} = 0$ ; this means we have no additional numerical parameter to control the results with respect to.

In conclusion, the calculated currents do not depend significantly on the numerical parameters and we have reached a linear regime.

## VIII. LOCAL SELF-ENERGY

In the case of local approximations of the Luttinger-Ward functional, the irreducible vertex  $\delta\Sigma/\delta G$  featured in the Bethe-Salpeter equation Eq. 44 is fully local. On lattices that preserve inversion symmetry this ensures that the vertex corrections for the uniform current-current correlation function  $\Lambda$  cancel out<sup>6,10</sup>. Therefore, as an additional check, we compare non-equilibrium and Kubo bubble values of  $\rho_{dc}$  in the local self-energy  $\Sigma[G_0^{\text{loc}}]$  approximation in Fig. 8. We see excellent agreement between these theories.

## IX. CHARGE STIFFNESS IN $\Sigma[G_0]$ APPROXIMATION

In this section we discuss the charge stiffness  $D$  that is present in the non-equilibrium  $\Sigma[G_0]$  approximation.

Charge stiffness develops at all the temperatures and at all the couplings we examined, Fig. 9. We see that the charge

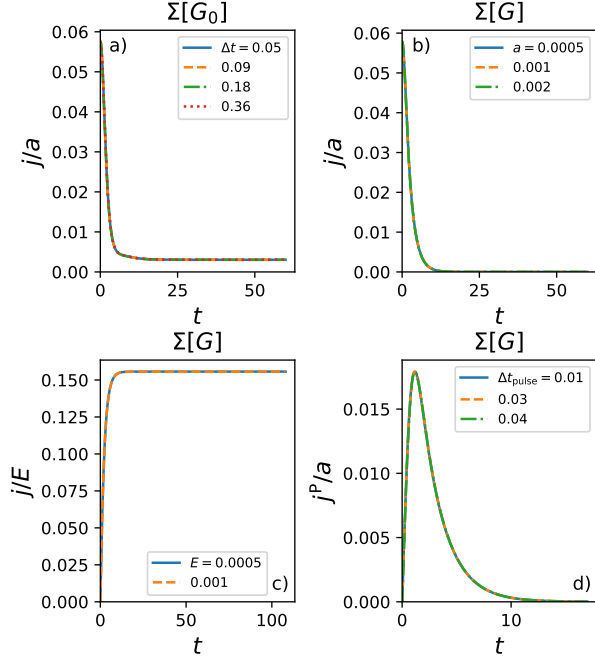


Figure 7. a)  $j/a$  in the b) protocol for different time steps  $\Delta t$ ; b)  $j/a$  in the b) protocol for different values of the parameter  $a$ ; c)  $j/E$  in the a) protocol for different  $E$ ; d)  $j/a$  in the c) protocol for different durations of the applied pulse  $\Delta t_{\text{pulse}}$ .

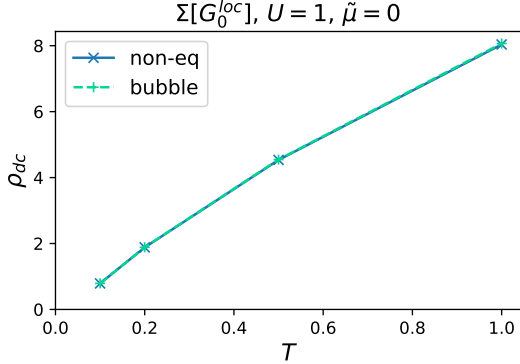


Figure 8. Comparison of  $\rho_{\text{dc}}(T)$  for the non-equilibrium  $\Sigma[G_0^{\text{loc}}]$  approximation and the bubble approximation.

stiffness increases with smaller couplings, and at  $U = 0$  we have  $D = K$ . This is clearly understood, by taking into account that at  $U = 0$ ,  $\Lambda(\omega) = 0$  (see Section XIII), and therefore the entire optical conductivity  $\sigma(\omega)$  is contained in the charge stiffness peak at  $\omega = 0$ . We confirm that, at  $U = 0$ ,  $D = K$ , by looking at results of protocol b) with  $\Sigma = 0$ , and comparing to  $K$  computed as

$$K = -\frac{\langle E_{\text{kin}}(U=0) \rangle}{2} = -\sum_{\mathbf{k}} n_F(\varepsilon_{\mathbf{k}}) \varepsilon_{\mathbf{k}}. \quad (76)$$

In the b) protocol, charge stiffness manifests as a non-

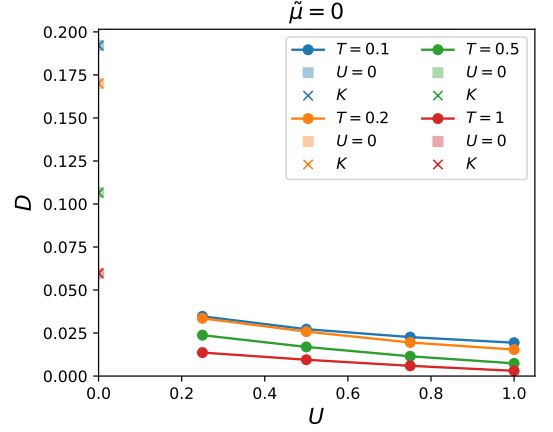


Figure 9. Charge stiffness  $D$  in the  $\Sigma[G_0]$  approximation. The  $U = 0$  point is calculated using the short pulse of electric field protocol.  $K$  is calculated according to Eq. 76. Colors on the plot indicate the temperature  $T$ .

physical stationary state with constant current. In our  $\Sigma[G_0]$  approximation, we observe such a stationary state. The density distribution in the Brillouin zone  $\langle n_{\mathbf{k}} \rangle$  in this state is different from the initial equilibrium one, as can be seen in Fig. 10. One can see that it does not have the full symmetry of the lattice. Due to this, the contribution to the uniform current of different  $\mathbf{k}$ -points does not cancel out.

## X. $\Sigma[G](\omega)$ AND $\Sigma[G_0](\omega)$ COMPARISON

Here we compare two different self-energy approximations used in the paper. We focus on thermal equilibrium state and compute  $\Sigma[G_0]$  using a separate well-optimized code implemented in frequency domain<sup>11</sup>. We compute  $\Sigma[G]$  by solving the self-consistent KB equations, but without any external fields. The resulting  $\Sigma$  is then Fourier transformed from time domain to frequency domain. In Fig. 11 a comparison of the bare  $\Sigma[G_0]$  and the bold  $\Sigma[G]$  approximations is presented for two different temperatures. In Fig. 12 we compare two different approximations for different values of  $U$ . In the limit  $U \rightarrow 0$  we see that  $\Sigma[G] \rightarrow \Sigma[G_0]$ . We also see that  $\Sigma[G]$  has in general a smoother frequency dependence and longer high-frequency tails.

## XI. LIMITATIONS OF SELF-ENERGY APPROXIMATIONS

In this section we will discuss some limitations of self-energy approximations that we used.

We expect both  $\Sigma[G]$  and  $\Sigma[G_0]$  approximations to be valid only for weak couplings. In Ref. 12 and Ref. 13 authors show how for moderate couplings, our second order  $\Sigma[G_0]$  is found to be in better agreement with numerically exact results than the second order  $\Sigma[G]$ . However, we document here that there is a hard cutoff value of  $U$  beyond which  $\Sigma[G_0]$  starts giving

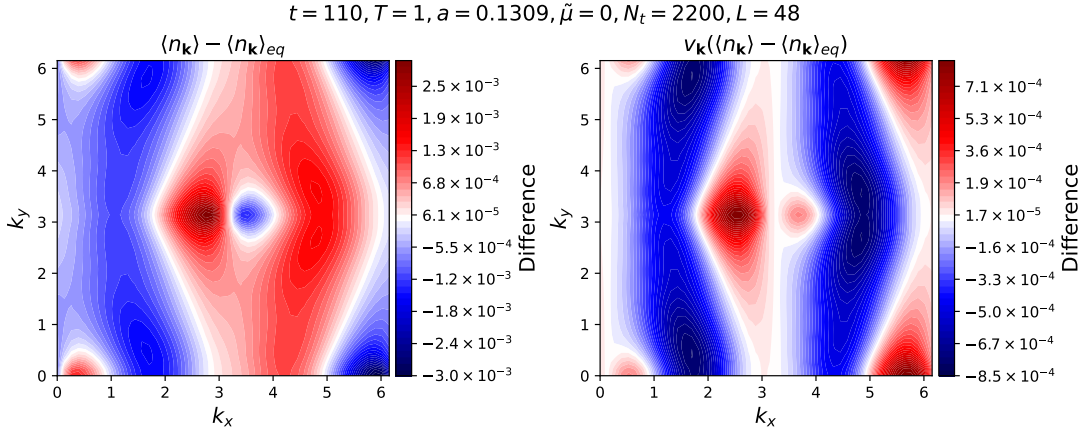


Figure 10. Characterization of the unphysical stationary state in case of the bare  $\Sigma[G_0]$  approximation.

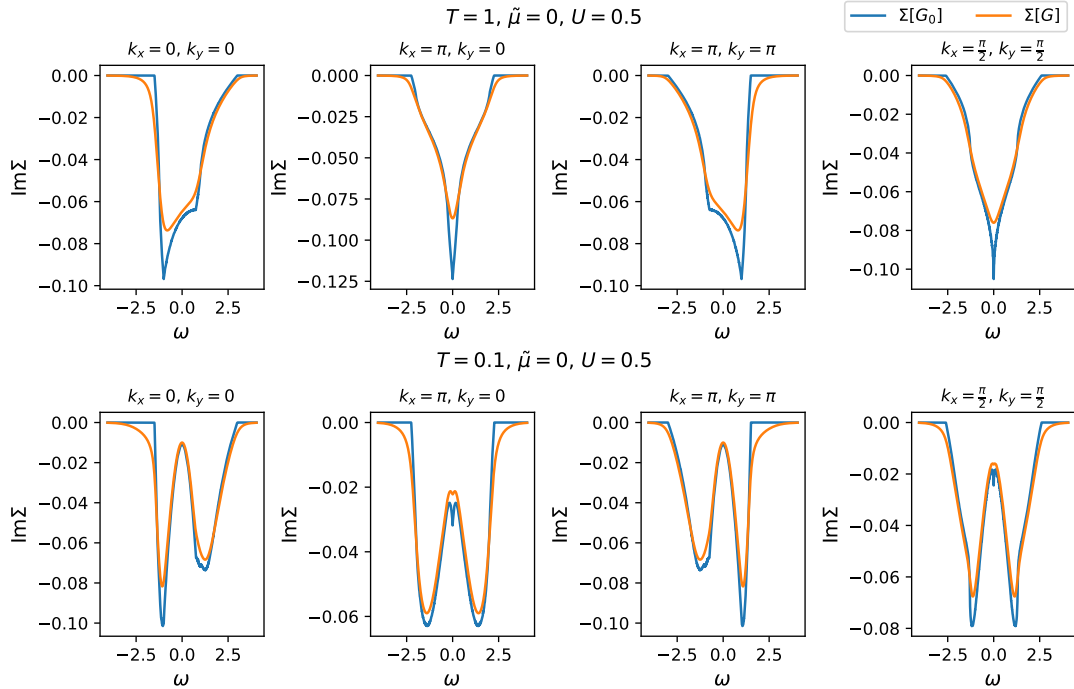


Figure 11. Comparison of different self-energy approximations for two different temperatures.

unphysical results for the Green's function. By contrast, the  $\Sigma[G]$  approximation does not have such a limitation, albeit the convergence of the iterative  $\Sigma[G]$  solution is not guaranteed at strong couplings.

The limitation of the  $\Sigma[G_0]$  approximation comes from the fact that  $\text{Im}\Sigma(\omega)$  always goes to exactly zero at some finite (and not very large) frequency. At large  $U > U_{\text{max}}$  this leads to the appearance of unphysical coherent states at certain wave vectors. To understand this, we need to look at the expression for the Green's function

$$G(\omega) = \frac{1}{\omega + \mu - \varepsilon_{\mathbf{k}} - U^2 \text{Re}\tilde{\Sigma}_{\mathbf{k}}(\omega) - iU^2 \text{Im}\tilde{\Sigma}_{\mathbf{k}}(\omega)} \quad (77)$$

where we have pulled the  $U^2$  factor out of the self-energy  $\tilde{\Sigma} \equiv \Sigma/U^2$ . We see that the real part of the denominator can have zeros  $\omega^*$  such that  $\text{Im}\Sigma(\omega^*) = 0$ , yielding a delta peak structure in the Green's function, which would correspond to an infinitely long lived state. This can lead to infinite conductivity, even if there is no charge stiffness. Fig. 13b illustrates on one example the real part of the denominator of  $G$  and its root  $\omega^*$ . It can be seen that the root  $\omega^*$  is at a frequency where  $\text{Im}\Sigma(\omega^*) = 0$ . This is in contrast with the smaller value of  $U$ , see Fig. 13a, where there are no roots  $\omega^*$  for which  $\text{Im}\Sigma(\omega^*)$  vanishes. In Fig. 13c  $U_{\text{max}}$  is presented as a function of temperature for different chemical potentials  $\tilde{\mu}$ . We conclude that, regardless of the accuracy of the second order  $\Sigma[G_0]$  approx-

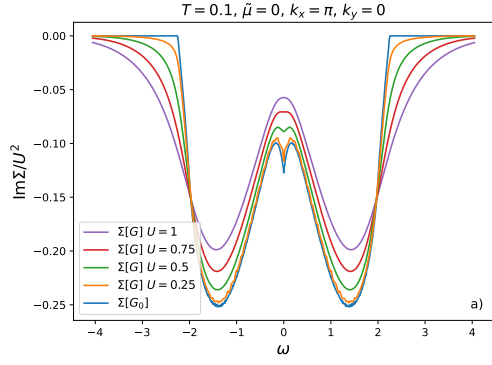


Figure 12. Comparison between  $\Sigma[G_0]$  and  $\Sigma[G]$  for different couplings  $U$ .

imation in terms of describing the correct  $\Sigma$  at low frequency, it cannot be safely used for the computation of spectral and transport properties beyond about  $U \approx 1.3$ .

## XII. REAL-FREQUENCY DIAGRAMMATIC MONTE CARLO (RFDIAGMC)

The basis for our RFDiagMC calculations is explained in Ref. 14. The idea is that imaginary-time integrals in a general Feynman diagram  $D$  can be solved analytically, to arrive at a general expression of the form:

$$D(i\omega_n) = \sum_{l,p} \frac{\mathcal{A}_{lp}}{(i\omega_n - \mathcal{E}_{lp})^p} \quad (78)$$

This is a sum of poles of various orders  $p$ , with amplitude  $\mathcal{A}$  at energy  $\mathcal{E}$ . The analytical continuation is then trivially performed, by replacing the Matsubara frequency by the complex frequency  $i\omega_n \rightarrow z$ . We can then take  $z = \omega + i0^+$  to retrieve the contribution of the diagram to the retarded correlation function,  $D^R(\omega)$ . By binning the pole amplitudes on a uniform real-frequency grid, we can ultimately avoid using any broadening. The only numerical parameter in the calculation is the frequency resolution with which we accumulate the results.

In this paper, we have performed two important generalizations of the algorithm, compared to our work in Ref. 14. First, our algorithm is now general for an arbitrary physical quantity, which allows us to compute both the self-energy diagrams and the current-current correlation function diagrams. Second, the propagators in the diagram can now be the dressed Green's functions, as is necessary for computation of bold skeleton diagrams. Our algorithm can work with fully general propagators of the form:

$$G(\tau) = \eta s_\tau \int d\omega \rho(\omega) n_\eta(-s_\tau \omega) e^{-\omega \tau} \quad (79)$$

where  $\eta = \pm 1$  for bosons/fermions,  $s_\tau$  is the sign of  $\tau \in [-\beta, \beta]$ , with  $\beta$  the inverse temperature, and  $\rho(\omega) =$

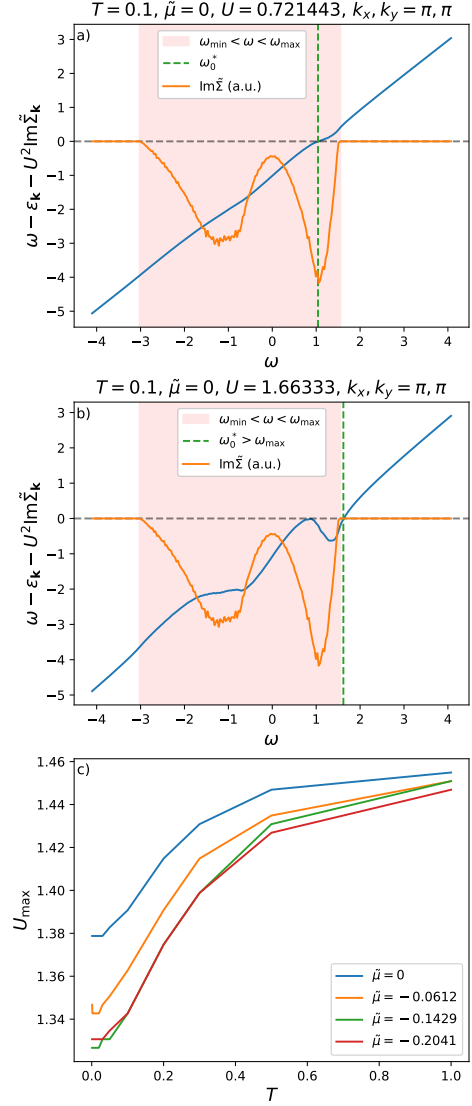


Figure 13. a) Real part of the denominator of  $G$  and imaginary part of the self-energy for  $U < U_{\max}$ ; b) Real part of the denominator of  $G$  and imaginary part of the self-energy for  $U > U_{\max}$ ; c)  $U_{\max}$  at different temperatures and chemical potentials. On all plots  $\text{Im}\Sigma$  is given in arbitrary units (a.u.).

$-\frac{1}{\pi} \text{Im}G^R(\omega)$  is the corresponding spectral function, obtained from the retarded Green's function  $G^R$ . In practice, this means that in the expressions that are being evaluated, now we have additional frequency integrals to be solved numerically. At this point, one must consider whether it is better to solve the diagrams directly on the three-piece contour. When solving bold skeleton diagrams using our approach, one essentially replaces a smaller number of time-integrals by a larger number of frequency integrals. However, the frequency integrals appear much easier to solve. The real-time integrands are highly oscillatory, and the integration domain is infinite. Real-time integrations are a difficult problem that has not yet been solved in the lattice context. By contrast, the frequency integrals do not contribute to the sign problem as  $\rho(\omega)$  is pos-



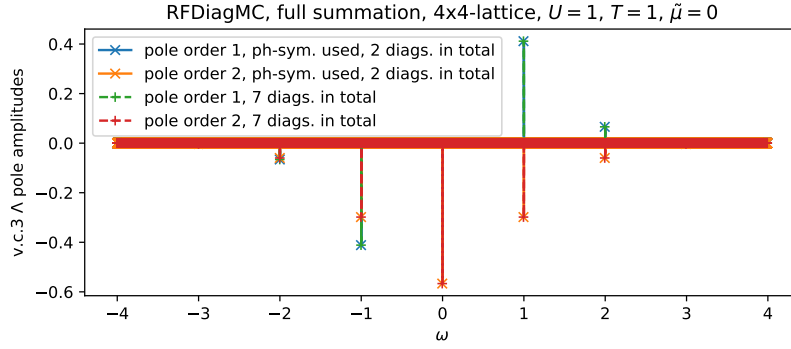


Figure 14. Benchmark of our algorithm for identifying the minimal set of diagrams: The results shown are the third order vertex corrections, computed for a small lattice, using the bare propagator and the full momentum summation to eliminate any statistical errors. The results are computed with and without making use of the particle-hole symmetry which reduces the number of diagrams from 7 to 2, and they show perfect agreement.

itive definite (as long as we work in momentum basis) and the integration domain is very restricted ( $\rho(\omega)$  is sharply peaked if the self-energy used to dress the propagator is small; the problem thus becomes easier at weaker coupling). By using the product of spectral functions  $\rho(\omega)$  of all the propagators in a diagram as Monte Carlo weight, we can successfully perform the frequency integration.

#### A. Specifics of numerical integration in the case of $\Lambda$ diagrams

We start from the general expression for a  $\Lambda$  diagram that we solve. At present, we restrict ourselves to the  $xx$ -component of the uniform current-current correlation function. The diagram topology we denote  $\Upsilon$ , and the order of the diagram  $N$ . For the sake of simplicity of the presentation, we assume there are no instantaneous self-energy insertions and that the lattice is two-dimensional, but our code is not limited in either sense. We label the diagram in imaginary time and momentum space. Therefore, our starting point is the following:

$$\Lambda_{\Upsilon}(\tau) = (-1)^{N_{\text{bub}}^{\Upsilon}} (-U)^N \prod_{i=2}^{N-1} \int_0^{\beta} d\tau_i \times \quad (80)$$

$$\times \int_{\text{BZ}} \frac{d\mathbf{k}_1}{(2\pi)^2} \cdots \frac{d\mathbf{k}_N}{(2\pi)^2} v_{\mathbf{k}_1}^x v_{\mathbf{k}_2}^x \prod_{j=1}^{2N+2} G(\tilde{\mathbf{k}}_j, \tilde{\tau}_j - \tilde{\tau}'_j)$$

We have  $N$  different imaginary times  $\tau$  enumerated by  $i$ , but  $\tau_1$  and  $\tau_N$  are the outer times. We can always set  $\tau_{i=1}$  to zero, and then  $\tau_N \equiv \tau$  is the external time appearing on the l.h.s. We have as many internal momenta as the interacting vertices ( $N$ ), and  $2N+2$  propagators  $G$ , at momenta  $\tilde{\mathbf{k}}_j = \sum_{i=1}^N c_{ji}^{\Upsilon} \mathbf{k}_i$  and attached to times  $\tilde{\tau}_j, \tilde{\tau}'_j \in \{\tau_1, \dots, \tau_N\}$  (dependent on the topology  $\Upsilon$ ). The overall sign of the diagram is determined by the number of fermionic loops,  $N_{\text{bub}}^{\Upsilon}$ . When propagators are dressed with dynamical self-energy, each propagator then brings an additional integral over frequency,  $\omega_j$ . At any  $\mathbf{k}$ , the propagator is of the general form Eq. 79. The time integrals

(including over the external time to perform the Fourier transform to Matsubara frequency) we perform analytically using a symbolic algebra algorithm. This we can do on-the-fly, but we have also devised an optimization procedure that relies on performing the analytical integration in advance (we simplify and store the resulting expressions in the form of highly optimized, algorithmically generated code). The resulting analytical expression  $\mathcal{I}$  is analytically continued by  $i\omega_n \rightarrow z$ . We finally arrive at the expression that is numerically evaluated

$$\Lambda_{\Upsilon}(z) = (-1)^{N_{\text{bub}}^{\Upsilon}} (-U)^N \prod_{j=1}^{2N+2} \int d\omega_j \times \quad (81)$$

$$\times \int_{\text{BZ}} \frac{d\mathbf{k}_1}{(2\pi)^2} \cdots \frac{d\mathbf{k}_N}{(2\pi)^2} v_{\mathbf{k}_1}^x v_{\mathbf{k}_2}^x \rho_{\tilde{\mathbf{k}}_j}(\omega_j) \mathcal{I}(\{\omega_j\}, T; z)$$

It turns out that it is very important that the momentum integrations are performed in a continuous BZ, i.e. in the true thermodynamic limit. We have shown in our previous work<sup>14</sup> that finite-size lattice calculations lead to noisy structures in frequency spectra. We have observed similar behavior also in the context of our current-current correlation function calculations - yet, here we are here interested in the derivative of  $\text{Im}\Lambda(\omega)$  at  $\omega = 0$ , where this function is nearly singular, and rapidly changes slope in a very narrow frequency window. Any noise coming from finite lattice size could easily affect our  $\sigma_{\text{dc}}$  estimates.

The propagator in our main RFDiagMC calculations is dressed by the second order self-energy, either  $\Sigma[G]$  or  $\Sigma[G_0]$ . The self-energy is computed in advance, on a large lattice. During the Monte Carlo sampling, we interpolate  $\Sigma$  linearly on-the-fly, as needed to construct the dressed propagator  $G$  that enters the diagram. In the case of the  $\Sigma[G]$  approximation, we have computed the self-consistent self-energy in real time (in absence of any field, with the lattice size  $48 \times 48$ ), and then performed the Fourier transform to real frequency. In the case of the  $\Sigma[G_0]$ , we have performed the calculation in frequency using a separate, highly accurate and efficient code we had developed previously<sup>11</sup> (with the lattice size  $64 \times 64$ ).

We use Sobol sequence<sup>15</sup> quasi Monte Carlo for the summation over inner momenta  $\mathbf{k}$ , and for each given choice of

momenta, we perform a weighted Monte Carlo over frequencies (the integration over frequency is the inner loop; at order 2 we have 6 propagators, and therefore 6-dimensional continuous-frequency-space to integrate over). The weighting function here, as already indicated, is the product of the spectral functions  $\prod_j \rho_{\mathbf{k}_j}(\omega_j)$  corresponding to each of the propagators, at the corresponding momenta (set in the outer loop). The “update” step in the weighted Monte Carlo over frequencies is a shift in one randomly selected frequency. The shift is chosen randomly from the interval  $[-\Delta\omega_{\max}, \Delta\omega_{\max}]$ . The Markov chain is thus trivially balanced.

The initial values of frequencies  $\omega_j$  for a given choice of inner momenta  $\mathbf{k}_i$  are chosen to be the quasiparticle (qp) energies (i.e. the solution to  $\omega_{j,\text{init}} - \varepsilon_{\mathbf{k}_j} - \text{Re}\Sigma_{\mathbf{k}_j}(\omega_{j,\text{init}}) = 0$  for each of the propagators; note that here we have absorbed the Hartree shift and the chemical potential in the dispersion  $\varepsilon_{\mathbf{k}}$ ). In the case of lower  $U$  the maximal shift  $\Delta\omega_{\max}$  must be taken smaller to avoid high rejection rates, because the spectral weight is more concentrated around the qp energy. We usually take  $2^{18}$   $\mathbf{k}$ -samples, and as many frequency samples for each choice of momenta. This means we are in total taking  $2^{36} \approx 6.8 \times 10^{10}$  samples.

### B. Use of symmetries

The calculation of vertex correction diagrams is expensive. We have used symmetries to reduce the overall number of diagrams to be computed. In general, the current-vertex symmetry  $v_{\mathbf{k}} = -v_{-\mathbf{k}}$  will make contributions of certain diagrams zero. Due to this symmetry all first order vertex correction diagrams drop out. The bosonic symmetry of the correlation function itself  $\Lambda(\tau) = \Lambda(-\tau)$  means that diagrams which are topologically the same up to the exchange of terminals (current vertices) will yield the same contribution, and it is sufficient to compute only one of them. Finally, at half-filling, one can use particle-hole symmetry to further reduce the number of diagrams<sup>16</sup>. However, this will only hold for fully dressed diagrams (not possible in the case of partially dressed diagrams one effectively obtains in our non-eq.  $\Sigma[G_0]$  theory). At half-filling, in total, we need to compute a single diagram at order 2 (out of 4 possible diagrams), and 2 diagrams at order 3 (out of 11 possible diagrams).

To check the validity of our simplifications, we have performed calculations of all diagrams and compared to the results obtained using the minimal set of diagrams, on examples which are not numerically expensive. In Fig. 14 we show the calculation of 3rd order vertex correction diagrams with the bare-propagators, on a small  $4 \times 4$  lattice, with and without the use of ph-symmetry, and show how the results agree perfectly. The momentum summations are here performed fully.

### C. Accumulation of the results

We accumulate the pole amplitudes  $\mathcal{A}_{l,p}$  on a dense uniform frequency grid  $\omega_l = l\Delta\omega$ . After the calculation is done, we resample the amplitudes by merging adjacent bins, until

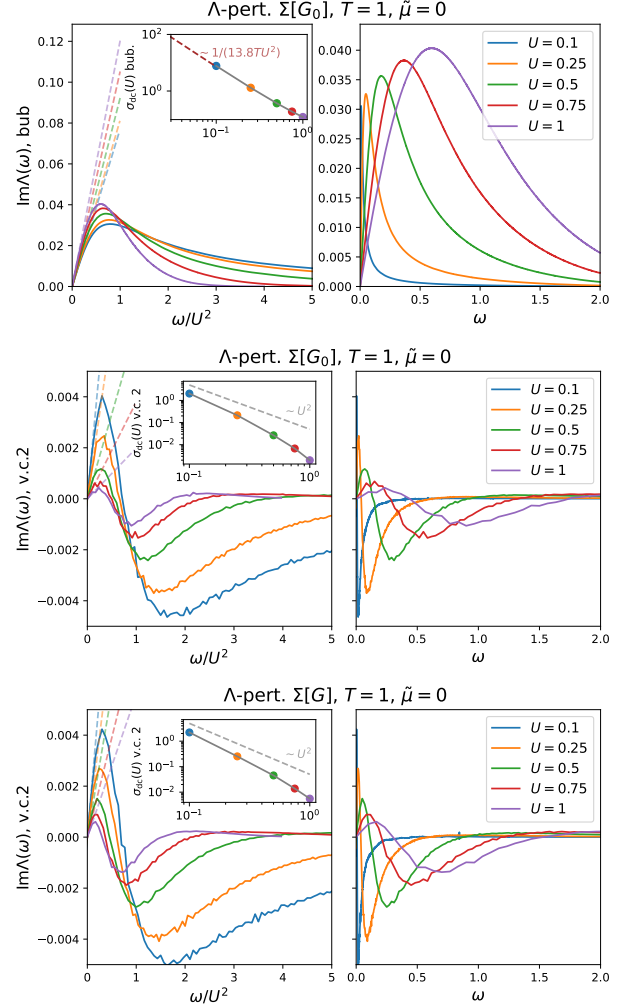


Figure 15. Raw current-current correlation function results for different values of  $U$ . First row: Kubo bubble contribution, second and third rows: second-order vertex corrections computed with the propagator dressed with two different self-energy approximations. In the left column, frequency axis has been rescaled by  $U^2$  for easier inspection. The  $\sigma_{\text{dc}}$  contribution is the angle at  $\omega = 0$ , indicated by the dashed line, and shown as a function of  $U$  in the insets.

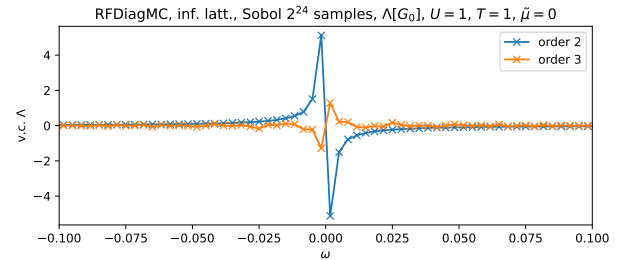


Figure 16. Vertex corrections to the current-current correlation function at second and third order, computed using bare propagators. There is a discontinuity (jump) at  $\omega = 0$ , which yields an infinite contribution to  $\sigma_{\text{dc}}$ . This indicates that the bare series for  $\Lambda(\omega \approx 0)$  is not convergent.

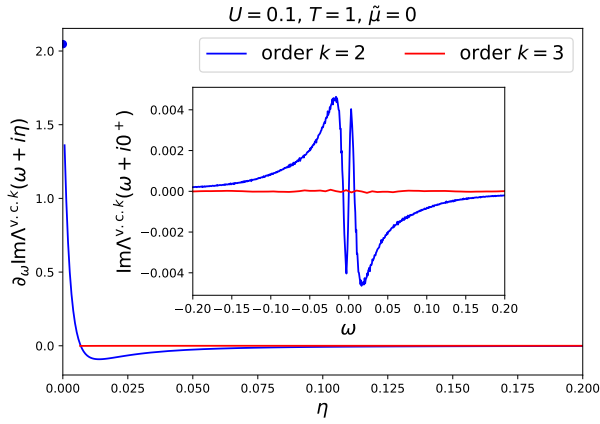


Figure 17. Comparison of the second and third order vertex corrections, computed using propagators dressed with  $\Sigma[G_0]$ . Inset: frequency dependence of the imaginary part. Main panel: contribution to  $\sigma_{\text{dc}}$  as a function of the broadening  $\eta$ . Third order contribution to  $\sigma_{\text{dc}}$  appears to be below the statistical error bar.

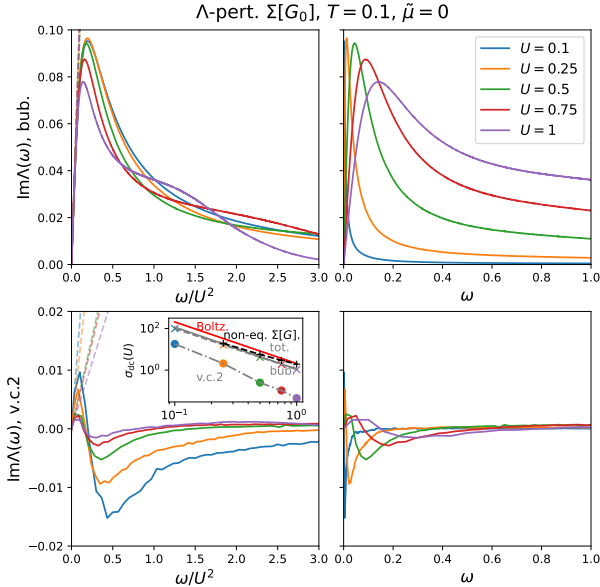


Figure 18. Results at  $T = 0.1$ , showing that all of our conclusions stand even at lower temperature. The agreement between  $\Lambda$ -pert  $\Sigma[G_0]$  and non-eq.  $\Sigma[G]$  at low  $U$  is excellent. It is interesting that the Boltzmann theory becomes worse at low temperature, and that the vertex corrections become relatively smaller.

we get smooth curves. The imaginary part *without any broadening* is obtained using the expression<sup>14</sup>

$$\text{Im} \Lambda(\omega_l + i0^+) \approx \frac{\pi}{\Delta\omega} \sum_p \frac{(-1)^p}{(p-1)!} \tilde{\partial}_l^{p-1} \mathcal{A}_{l,p} \quad (82)$$

and the real part  $\text{Re} \Lambda(\omega_l)$  is reconstructed using Kramers-Kronig relations (in particular we need  $\text{Re} \Lambda(\omega = 0)$  for the estimate of charge stiffness).

### XIII. VERTEX CORRECTIONS

In this section we discuss and show the raw results for the bubble and vertex correction contributions to the current-current correlation function  $\Lambda(\omega)$ .

In Fig. 15 we show our main  $\text{Im} \Lambda(\omega)$  results. It is clear that as  $U$  is reduced, the bubble vanishes, but at the same time the slope at  $\omega = 0$  diverges. Ultimately, if we take exactly  $U = 0$  and compute the bubble with the bare propagators, we get  $\Lambda(\omega) = 0$ , as already mentioned in Appendix IX.

Similarly, the vertex correction diagrams become more and more singular around  $\omega = 0$  as  $U \rightarrow 0$ . We have checked that, when vertex correction diagrams are computed with the bare propagator, one observes a true discontinuity (jump) in  $\text{Im} \Lambda(\omega)$  at  $\omega = 0$ , see Fig. 16, which means that contributions of individual diagrams to  $\sigma_{\text{dc}}$  become of the form  $0 \times \infty$  as  $U \rightarrow 0$ . If for diagrams at order  $k$ , the divergence is  $1/U^{k+2}$  or faster, these vertex correction diagrams will contribute even at infinitesimal coupling. Of course, there is an overall prefactor which is expected to decrease with increasing  $k$ , and the contribution of high orders may be small and even negligible.

The calculation of 3rd order vertex corrections to high enough precision to extract  $\sigma_{\text{dc}}$  is currently not possible. We find that  $\text{Im} \Lambda^{\text{v.c.}, 3}(\omega)$  is overall 2 orders of magnitude smaller than  $\text{Im} \Lambda^{\text{v.c.}, 2}(\omega)$  (see Fig. 17). We believe it is highly unlikely that v.c. of 3rd order (and higher) contribute significantly. Further optimizations in our code will be necessary to fully resolve this question.

We have checked that all the phenomenology we have observed is qualitatively the same also at lower temperature (see Fig. 18).

#### A. Sign of the vertex corrections

The common wisdom is that vertex corrections ought to increase conductivity, because they account for scattering processes which reduce the lifetime of quasiparticles (and thus reduce the bubble contribution), but do not reduce the current. However, these processes are mostly relevant in the dc context. Indeed we see that the vertex corrections to optical conductivity are positive at low frequency, become smaller and change sign at intermediate frequency, and then vanish at high frequency (see Fig. 19, left panels). The same behavior was observed in the previous publication of one of us<sup>17</sup> at strong coupling and high temperature. It is interesting that in the Bose-Hubbard model, the  $\omega$ -dependence of v.c. is very similar, but with an overall opposite sign<sup>18</sup>. In our  $\Sigma[G_0]$  theory, the sign is also the opposite at low frequency, but we do not observe the change of sign at intermediate frequency (see Fig. 19, right panels).

<sup>1</sup> M. Schüler, D. Golež, Y. Murakami, N. Bittner, A. Herrmann, H. U. Strand, P. Werner, and M. Eckstein, [Computer Physics Communications](#) **257**, 107484 (2020).

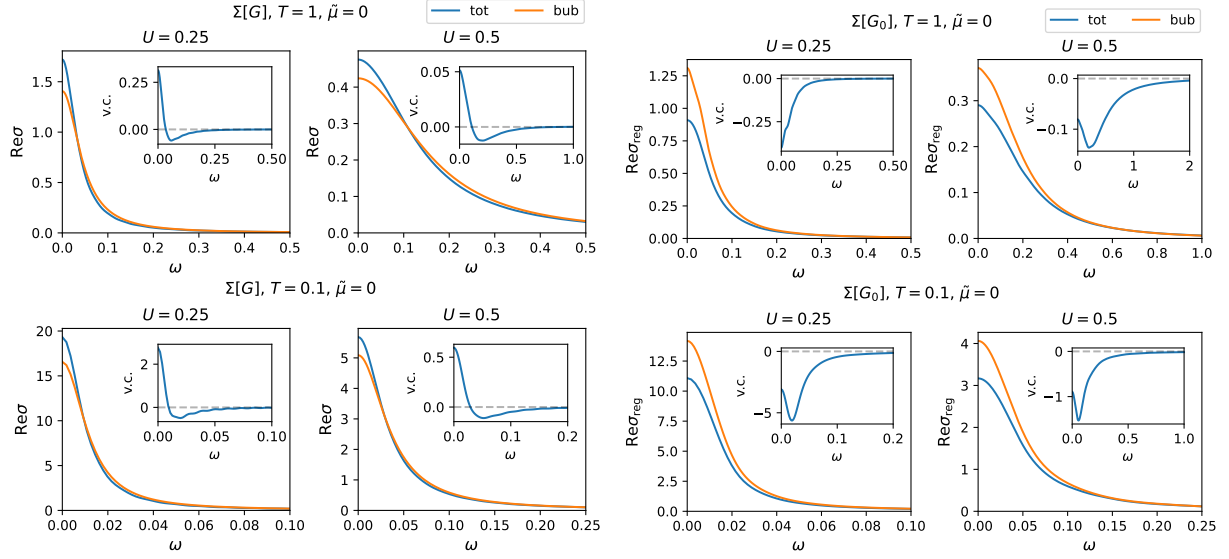



Figure 19. Optical conductivity and the frequency dependence of the vertex corrections.

- <sup>2</sup> H. Aoki, N. Tsuji, M. Eckstein, M. Kollar, T. Oka, and P. Werner, *Rev. Mod. Phys.* **86**, 779 (2014).
- <sup>3</sup> N. Tsuji and P. Werner, *Phys. Rev. B* **88**, 165115 (2013).
- <sup>4</sup> T. G. Kiely and E. J. Mueller, *Phys. Rev. B* **104**, 165143 (2021).
- <sup>5</sup> G. Baym and L. P. Kadanoff, *Physical Review* **124**, 287 (1961).
- <sup>6</sup> J. Vučković and R. Žitko, *Phys. Rev. B* **104**, 205101 (2021).
- <sup>7</sup> H. Hafermann, E. G. C. P. van Loon, M. I. Katsnelson, A. I. Liechtenstein, and O. Parcollet, *Phys. Rev. B* **90**, 235105 (2014).
- <sup>8</sup> D. M. Kennes, E. Y. Wilner, D. R. Reichman, and A. J. Millis, *Phys. Rev. B* **96**, 054506 (2017).
- <sup>9</sup> G. Stefanucci and R. van Leeuwen, *Nonequilibrium Many-Body Theory of Quantum Systems: A Modern Introduction* (Cambridge University Press, 2013).
- <sup>10</sup> A. Khurana, *Phys. Rev. Lett.* **64**, 1990 (1990).
- <sup>11</sup> J. Vučković, S. Pédin, and M. Ferrero, *Phys. Rev. B* **107**, 155140 (2023).
- <sup>12</sup> E. Kozik, M. Ferrero, and A. Georges, *Phys. Rev. Lett.* **114**, 156402 (2015).
- <sup>13</sup> J. Gukelberger, L. Huang, and P. Werner, *Phys. Rev. B* **91**, 235114 (2015).
- <sup>14</sup> J. Vučković, P. Stipsić, and M. Ferrero, *Phys. Rev. Res.* **3**, 023082 (2021).
- <sup>15</sup> I. Sobol', *USSR Computational Mathematics and Mathematical Physics* **7**, 86–112 (1967).
- <sup>16</sup> A. Taheridehkordi, S. H. Curnoe, and J. P. F. LeBlanc, *Phys. Rev. B* **101**, 125109 (2020).
- <sup>17</sup> J. Vučković, J. Kokalj, R. Žitko, N. Wentzell, D. Tanasković, and J. Mravlje, *Phys. Rev. Lett.* **123**, 036601 (2019).
- <sup>18</sup> I. Vasić and J. Vučković, *Phys. Rev. B* **110**, 064501 (2024).

# Conductivity in the Bose-Hubbard model at high temperatures

Ivana Vasić  and Jakša Vučičević

*Institute of Physics Belgrade, University of Belgrade, Pregrevica 118, 11080 Belgrade, Serbia*



(Received 30 April 2024; revised 16 July 2024; accepted 18 July 2024; published 1 August 2024)

Quantum simulations are quickly becoming an indispensable tool for studying particle transport in correlated lattice models. One of the central topics in the study of transport is bad-metal behavior, characterized by the direct-current resistivity linear in temperature. In the fermionic Hubbard model, optical conductivity has been studied extensively, and a recent optical lattice experiment demonstrated bad-metal behavior in qualitative agreement with theory. Far less is known about transport in the bosonic Hubbard model. We investigate the conductivity in the Bose-Hubbard model and focus on the regime of strong interactions and high temperatures. We use numerically exact calculations for small lattice sizes. At weak tunneling, we find multiple peaks in the optical conductivity that stem from the Hubbard bands present in the many-body spectrum. This feature slowly washes out as the tunneling rate gets stronger. At high temperature, we identify a regime of  $T$ -linear resistivity, as expected. When the interactions are very strong, the leading inverse-temperature coefficient in conductivity is proportional to the tunneling amplitude. As the tunneling becomes stronger, this dependence takes quadratic form. At very strong coupling and half filling, we identify a separate linear resistivity regime at lower temperature, corresponding to the hard-core boson regime. Additionally, we unexpectedly observe that at half filling, in a big part of the phase diagram, conductivity is an increasing function of the coupling constant before it saturates at the hard-core-boson result. We explain this feature based on the analysis of the many-body energy spectrum and the contributions to conductivity of individual eigenstates of the system.

DOI: [10.1103/PhysRevB.110.064501](https://doi.org/10.1103/PhysRevB.110.064501)

## I. INTRODUCTION

Cold atoms in optical lattices have provided a clean and tunable realization of the Hubbard model [1]. The focus of early experiments was on studying phase transitions within the model, but various aspects of nonequilibrium dynamics have also been explored in this setup. In particular, a lot of effort has been invested in performing transport measurements with cold atoms [2–4]. Transport measurements in optical lattices are of great interest as they allow us to isolate the effects of strong correlations from the effects of phonons and disorder in a way that is not possible in real materials.

Particular attention is paid to linear-in-temperature resistivity, which is believed to be related to the superconducting phase and/or quantum critical points in cuprates and more general strongly correlated systems [5–10]. This phenomenon has been studied theoretically in different versions of the Fermi-Hubbard model and in different parameter regimes [11–17]. The onset of resistivity linear in temperature was addressed in more general terms from the theoretical side in Refs. [18–20]. In experiment with fermionic cold atoms in optical lattices, the  $T$ -linear resistivity has also been observed to span a large range of temperature, in qualitative agreement with theory [4]. However, transport in bosonic lattice models has been less studied from both theoretical and experimental perspectives.

Bosonic transport in the strongly interacting regime of the Bose-Hubbard model was addressed in a cold-atom setup by investigating expansion dynamics induced by harmonic-trap removal [21,22] and by studying center-of-mass oscillations induced by trap displacement [23,24]. However these studies

did not focus on optical conductivity. Optical conductivity of bosons at zero and low temperature was calculated in early papers [25–27]. The conductivity of two-dimensional hard-core bosons was addressed in Refs. [28,29], and a large temperature range with linearly increasing resistivity was found. The conductivity of strongly correlated bosons in optical lattices in a synthetic magnetic field was obtained in Ref. [30]. The regime of resistivity linear in temperature was recently investigated for the Bose-Hubbard model at weak coupling [31]. The dynamical response within the scaling regime of the quantum critical point and universal conductivity at the quantum phase transition were investigated theoretically in an attempt to establish a clear connection with ADS-CFT mapping [32,33]. In addition to cold-atom studies, bosonic transport properties have been studied in the context of an emergent Bose liquid [34–36]. Transport properties of nanopatterned film arrays have been analyzed in terms of bosonic strange metal featuring resistivity linear in temperature down to low temperatures [37].

In this paper, we study conductivity in the Bose-Hubbard model [1,25] in relation to optical lattice experiments with bosonic atoms. We consider the strongly interacting regime and focus on high temperatures, away from any ordering instabilities. We consider small lattice sizes of up to  $4 \times 4$  lattice sites and employ averaging over twisted boundary conditions to lessen the finite-size effects. We control our results by comparing different lattice sizes, as well as by checking sum rules to make sure that charge stiffness is negligible. We also use both the canonical and grand-canonical ensembles and compare the results. To solve the model, we use exact diagonalization and finite-temperature Lanczos method [38].



We compute and analyze the probability distribution of the eigenenergies (the many-body density of states), the spectral function, and the optical and the direct-current (DC) conductivities, as well as some thermodynamic quantities. Where applicable, we compare results to the hard-core limit and the classical limit, as well as to the results obtained with the bubble-diagram approximation. Our results show several expected features. First, the many-body density of states, spectral function, and optical conductivity all simultaneously develop gaps and corresponding Hubbard bands as the coupling is increased. Next, we clearly identify the linear DC resistivity regime at high temperature and find the connection between the slope and the tunneling amplitude, along the lines of Ref. [20]. Furthermore, at lower temperatures and high coupling, we identify a separate linear resistivity regime corresponding to hard-core-like behavior, which can be expected on general grounds. We also find some unexpected features: we observe nonmonotonic behavior in the DC conductivity as a function of the coupling constant, which we map out throughout the phase diagram.

This paper is organized as follows: In Sec. II, we briefly describe our method of choice. In Sec. III we present our results: In Sec. III A we address the many-body density of states, and in Sec. III B we show some thermodynamic properties of the Bose-Hubbard model in the high-temperature regime. In Sec. III C we calculate the optical conductivity for finite interaction strength, and in Sec. III D we investigate the dependence of the direct-current conductivity on microscopic parameters of the Bose-Hubbard model and temperature. In Sec. III E we explain the observed features using an analysis of the Kubo formula from Ref. [20]. Then in Sec. III F we compare our results for half filling with the results for hard-core bosons [28]. We discuss the finite-size effects in Sec. III G and compare the results obtained with the canonical ensemble with the results obtained with the grand-canonical ensemble in Sec. III H. In Sec. III I we compare our results obtained for small lattices with the result of the often used bubble-diagram approximation. Finally, we summarize our findings in Sec. IV.

## II. MODEL AND METHODS

Cold bosonic atoms in optical lattices are realistically described by the Bose-Hubbard model [1]:

$$H = -J \sum_{\langle ij \rangle} (b_i^\dagger b_j + \text{H.c.}) + \frac{U}{2} \sum_i n_i(n_i - 1), \quad (1)$$

where  $J$  is the tunneling amplitude between nearest-neighbor sites of a square lattice and  $U$  is the on-site density-density interaction. Unless stated differently, our units are set with the choice  $U = 1$ . Throughout this paper, we set lattice constant  $a = 1$ ,  $\hbar = 1$ , and  $k_B = 1$ . We also assume that the effective charge of particles is  $q = 1$ .

The quantitative finite-temperature phase diagram of the model on a square lattice was obtained in Ref. [39]. At integer filling, a quantum phase transition between a Mott insulator state and a superfluid is found [in particular, for filling  $n = 1$  boson per site, the transition occurs at  $(J/U)_c \approx 0.0597$ ]. At finite temperature a Berezinskii-Kosterlitz-Thouless (BKT)

transition describes the loss of superfluidity [40]. In this paper we work in the high-temperature regime, where we expect only normal (noncondensed) states and short-range correlations.

The Bose-Hubbard model represents only a low-energy effective description of the full continuum Hamiltonian for bosonic particles in a periodic potential [1]. For this reason, the practicality of the high-temperature limit considered throughout the paper is provisional. We assume that temperatures are high in comparison with the effective parameters  $J$  and  $U$  but that they are small enough to keep all the higher single-particle bands of the full model unoccupied. The applicability of this condition will depend on actual experimental parameters, such as the lattice constant and lattice depth.

In the cold-atom realization of Bose-Hubbard models, the constituent particles are charge neutral. However, the current can be induced and the conductivity can be probed either by implementing a linear potential or by using artificial gauge fields to introduce a time-dependent vector potential, which would correspond to a constant electric field [41,42]. We consider the retarded current-current correlation function at finite temperature  $T = 1/\beta$ ,

$$C_{xx}(t) = -i\theta(t)\langle [J_x(t), J_x] \rangle_\beta, \quad (2)$$

where the current operator is given by

$$J_x = -iJ \sum_{\langle ij \rangle_x} (b_i^\dagger b_j - \text{H.c.}), \quad (3)$$

with the summation only over nearest neighbors along the  $x$  direction. The partition function is  $Z(\beta) = \text{Tr}(e^{-\beta H})$ , and averaging is performed as

$$\langle X \rangle_\beta = \frac{1}{Z(\beta)} \text{Tr}(e^{-\beta H} X). \quad (4)$$

In the linear response regime, the conductivity is given by the Kubo formula [43,44]:

$$\sigma_{xx}(\omega) = \frac{i}{\omega} \left[ \langle -E_{\text{kin}}^x \rangle_\beta + C_{xx}(\omega) \right], \quad (5)$$

where  $C_{xx}(\omega) = \int_{-\infty}^{\infty} dt e^{i\omega t} C_{xx}(t)$  and  $\langle E_{\text{kin}}^x \rangle_\beta$  is the average kinetic energy along the  $x$  direction. Note that for the real conductivity from Eq. (5), we need the imaginary part of the correlation function  $\text{Im} C_{xx}(\omega)$ . The DC conductivity is obtained as  $\sigma_{\text{DC}} = \text{Re} \sigma_{xx}(\omega \rightarrow 0)$ .

In the following we rely on numerically exact approaches for small lattice sizes. We use exact diagonalization to obtain the eigenenergies  $E_n$  and eigenstates  $|n\rangle$  of the Hamiltonian  $H$  and calculate

$$\begin{aligned} \text{Re} \sigma_{xx}(\omega) &= \frac{\pi}{Z(\beta)\omega} \sum_{n,m} |\langle n | J_x | m \rangle|^2 (e^{-\beta E_n} - e^{-\beta E_m}) \\ &\quad \times \delta(\omega + E_n - E_m). \end{aligned} \quad (6)$$

For larger lattice sizes, we apply the finite-temperature Lanczos method [38]. We employ averaging over twisted boundary conditions to lessen the finite-size effects [45,46]. This is done by introducing in the model an external homogeneous gauge field (vector potential). Formally, this amounts to setting the same complex phase for each of the hopping amplitudes in a given direction. In particular, for the hopping along



the  $x$  direction to the first neighbor on the right we use  $J_{ij} = J \exp(i\theta_x/L_x)$ , and for the hopping to the left we use  $J_{ij} = J \exp(-i\theta_x/L_x)$ . The same is done for the  $y$  direction. Physically, this corresponds to switching to a moving (inertial) reference frame. Note that the expression for the current operator from Eq. (3) in this case reads [47]

$$J_x = -i \sum_{\langle ij \rangle_x} (J_{ij} b_i^\dagger b_j - \text{H. c.}). \quad (7)$$

We randomly sample values of  $\theta_x$  and  $\theta_y$  in the range  $(0, 2\pi)$  and perform averaging over the obtained eigenstates for these different values of total flux in Eq. (6).

Due to the expected onset of charge stiffness in finite systems and, more generally, longer-range correlations at low temperature, we expect our method to be limited to the regime of high temperature and relatively strong interactions (corresponding to a smaller ratio  $J/U$ ). For a crosscheck of the validity of our numerical approaches, we rely on a comparison of different lattice sizes (Sec. III G) and the sum rule [48]

$$\int_0^\infty d\omega \text{Re } \sigma_{xx}(\omega) = \frac{\pi}{2} \langle -E_{\text{kin}}^x \rangle_\beta. \quad (8)$$

Indeed, we find that the sum rule is satisfied at temperatures  $T/U \geq 1$  and tunneling  $J/U \leq 0.2$ . In this regime we find that the results no longer significantly change with increasing lattice size (Sec. III G); thus, our results are expected to be reasonably representative of the thermodynamic limit.

Finally, we control the results with respect to the choice of the statistical ensemble. A comparison of the results obtained with the grand-canonical and canonical ensembles is given in Sec. III H. We do not find a substantial difference in the results between the two statistical ensembles; thus, we choose to work in the canonical ensemble, as it allows us to consider larger lattices. Unless stated differently, the results presented in this paper are for the canonical ensemble.

### III. RESULTS

#### A. Eigenstate spectrum

We first consider the many-body density of states of the model (1) defined by

$$g(E) = \sum_n \delta(E - E_n). \quad (9)$$

We show our numerical results for fillings  $n = 1/2$  and  $n = 1$  in Fig. 1(a).

The classical limit  $J = 0$  is simple to understand. The many-body spectrum features energies  $E_n^{J=0} = nU$ ,  $n = 0, 1, \dots$ , with huge degeneracies. The Hilbert space dimension is  $\dim \mathcal{H} = \binom{L+N_p-1}{N_p}$ , where  $L$  is the number of lattice sites and  $N_p$  is the number of particles. For  $N_p < L$ , there are  $\binom{L}{N_p}$  states with zero energy,  $\binom{L}{1} \binom{L-1}{N_p-1}$  states (a single site occupied by two bosons) with energy  $E_n = U$ , and so on. The number of different energy levels is set by the system size that we consider. As the ratio  $J/U$  increases from zero, these macroscopic degeneracies are slowly resolved, and the bands obtain a finite width. This is precisely what we observe in the numerical data, as shown in Fig. 1(a), but we find that separate many-body bands do persist up to a finite value

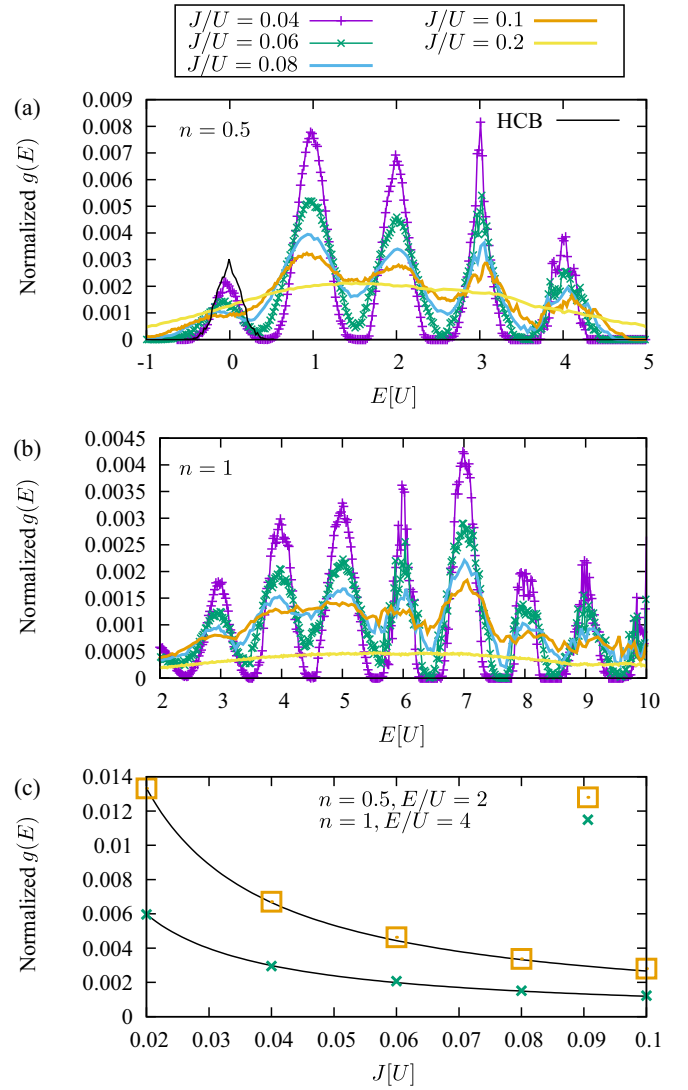


FIG. 1. The normalized many-body density of states defined in Eq. (9) for (a)  $n = 0.5$ ,  $L_x = 4$ ,  $L_y = 3$ , and  $N_p = 6$  and (b)  $n = 1$ ,  $L_x = 3$ ,  $L_y = 3$ , and  $N_p = 9$ . The black solid line in (a) gives the corresponding density of states for the case of hard-core bosons. We use 100 random realizations of the twisted boundary conditions. In (c) we plot the height of the peak at energies  $E = 2U$  (for half filling) and  $E = 4U$  (for unit filling). The black solid lines give the fitted  $(J/U)^{-1}$  dependence.

of  $J/U \approx 0.05$ , regardless of filling. Around this value, the peaks in  $g(E)$  (found around  $E = nU$ ) have heights roughly proportional to  $1/J$  [see Fig. 1(c)]. As  $J$  increases further, the density of states turns into a wide, bell-shaped curve, as shown in Fig. 1(b) for unit filling at  $J/U = 0.2$ . This particular feature of the spectrum has been considered for a related one-dimensional model in Ref. [49]. We also observe that for  $n = 1/2$ , the lowest many-body band can be reasonably approximated by hard-core bosons.

#### B. Thermodynamic properties

We investigate thermodynamic properties for  $T/U \geq 1$ , as this regime has not been discussed in much detail in the literature. Our numerical results indicate that in this regime,

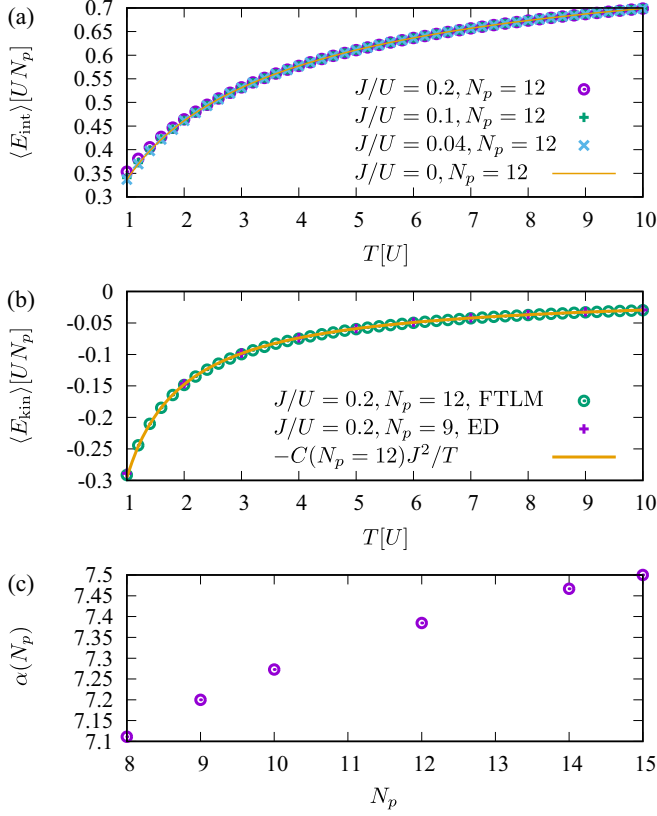


FIG. 2. (a) Interaction energy, Eq. (10), as a function of temperature. (b) Kinetic energy, Eq. (15), as a function of temperature. (c) The coefficient  $\alpha(N_p)$  from Eq. (15) as a function of system size. System size  $L_x = 4, L_y = 3$ ; number of particles  $N_p = 12$ .

thermodynamic quantities approach the results of the atomic limit  $J = 0$ . In particular, the interaction energy

$$\langle E_{\text{int}} \rangle_\beta = \frac{U}{2} \left\langle \sum_i n_i(n_i - 1) \right\rangle_\beta \quad (10)$$

is very weakly dependent on the tunneling  $J/U$ , as shown in Fig. 2(a), for the tunneling range that we consider  $0 \leq J/U \leq 0.2$  and close to the single-site  $J = 0$  value. From the numerical results, we find that the average value of the kinetic energy

$$\langle E_{\text{kin}} \rangle_\beta = \left\langle -J \sum_{\langle ij \rangle} b_i^\dagger b_j + \text{H.c.} \right\rangle_\beta \quad (11)$$

can be reasonably approximated by the leading order in the high-temperature expansion

$$\langle E_{\text{kin}} \rangle_\beta \approx \frac{\text{Tr}(1 - \beta H) E_{\text{kin}}}{\text{Tr}(1 - \beta H)} \quad (12)$$

$$\approx -\beta \frac{\text{Tr} E_{\text{kin}}^2}{\text{dim} \mathcal{H}} \quad (13)$$

$$= -\alpha(N_p) N_p J^2 / T, \quad (14)$$

$$\alpha(N_p) = \frac{1}{\text{dim} \mathcal{H}} \sum_{\langle ij \rangle} \text{Tr} n_i(n_j + 1), \quad (15)$$

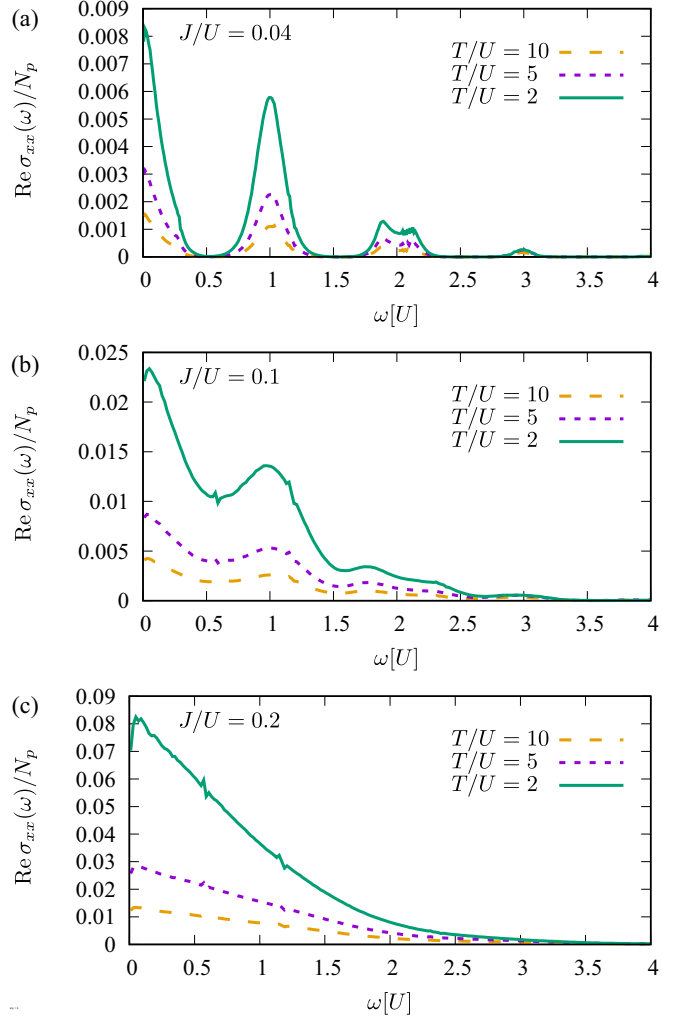


FIG. 3. Optical conductivity  $\text{Re} \sigma_{xx}(\omega)$  as a function of frequency. Parameters are (a)  $J/U = 0.04$ , (b)  $J/U = 0.1$ , and (c)  $J/U = 0.2$ ;  $L_x \times L_y = 4 \times 3$ ; and  $N_p = 6$ .

where  $N_p$  is the number of particles in the system and  $\text{dim} \mathcal{H}$  is the dimension of the Hilbert space. The coefficient  $\alpha(N_p)$  is size dependent [see Fig. 2(c)].

### C. Optical conductivity

We present numerical results for the optical conductivity in Fig. 3 for bosons with  $J/U = 0.04, 0.1, 0.2$  and temperatures  $T/U = 2, 5, 10$ . We check that within this range of physical parameters the sum rule given in Eq. (8) is satisfied with accuracy better than 1%. For the weak tunneling amplitude  $J/U = 0.04$  we observe that the conductivity exhibits multiple peaks at  $\omega \sim nU, n = 1, 2, 3, \dots$  that stem from the energy bands of the Hubbard model, as shown in Fig. 1. As temperature is lowered, the higher-energy peaks become smaller relative to the low-energy peaks, which is clearly expected. However, in absolute terms, the optical conductivity gets smaller with increasing temperature at all frequencies. As the tunneling gets stronger the peaks merge, but the multippeak structure is still visible at intermediate hopping  $J/U = 0.1$ . Finally, for  $J/U = 0.2$  the conductivity takes a simpler form

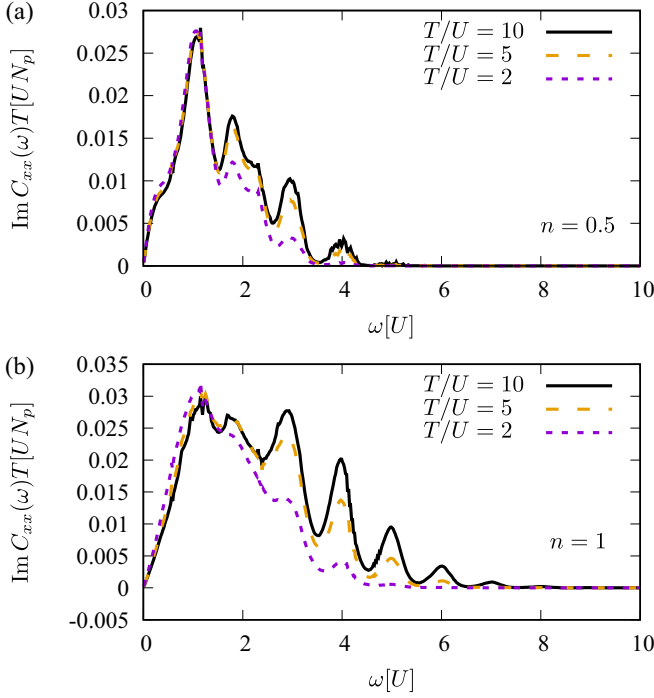


FIG. 4. Imaginary part of the current-current correlation function  $\text{Im } C_{xx}(\omega)$  multiplied by temperature  $T$  for a better comparison as a function of frequency  $\omega$ . Parameters are (a)  $N_p = 6$  and (b)  $N_p = 12$ ,  $J/U = 0.1$ , and  $L_x \times L_y = 4 \times 3$ .

[see Fig. 3(c)]. In Fig. 4 we show that at low frequency, the current-current correlation function scales with temperature in a simple way, but the behavior is more complicated at higher frequencies.

#### D. DC limit and $T$ -linear resistivity

We now focus on the range of small  $\omega$ . We have seen that the strong interaction  $U$  introduces gaps in the many-body spectrum that translate into peaks in the optical conductivity. In order to address the role of tunneling  $J$  in more detail, we replot numerical data in Fig. 5 by showing the current-current correlation  $\text{Im } C_{xx}(\omega)/J^2$  as a function of  $\omega/J$ . The rescaling by  $J^2$  is motivated by the basic definition of the current-current correlation function from Eq. (2). We find that for up to  $J/U \approx 0.08$  numerical data overlap near  $\omega = 0$  and are very weakly dependent on  $J/U$ . We further analyze and explain this feature in Sec. III E.

In order to extract the DC conductivity  $\sigma_{\text{DC}}$  from the current-current correlation function, we consider small but finite  $\omega$  and perform a linear fit,  $\lim_{\omega \rightarrow 0} \text{Im } C_{xx}(\omega)(T) \approx \sigma_{\text{DC}}(T) \times \omega$ . For numerical purposes we perform the fitting in the range  $\omega \in (0, J)$ .

In Fig. 6 we plot the DC conductivity as a function of inverse temperature  $\beta$ . Overall, we find that the normalized conductivity  $\sigma_{\text{DC}}/N_p$  decreases with filling from  $n = 1/2$  to  $n = 1$  in this strongly interacting regime. This is easily understood because, at integer fillings, the model is expected to have maximal resistivity (at integer filling, low temperature, and strong enough coupling, the model is in the Mott insulating

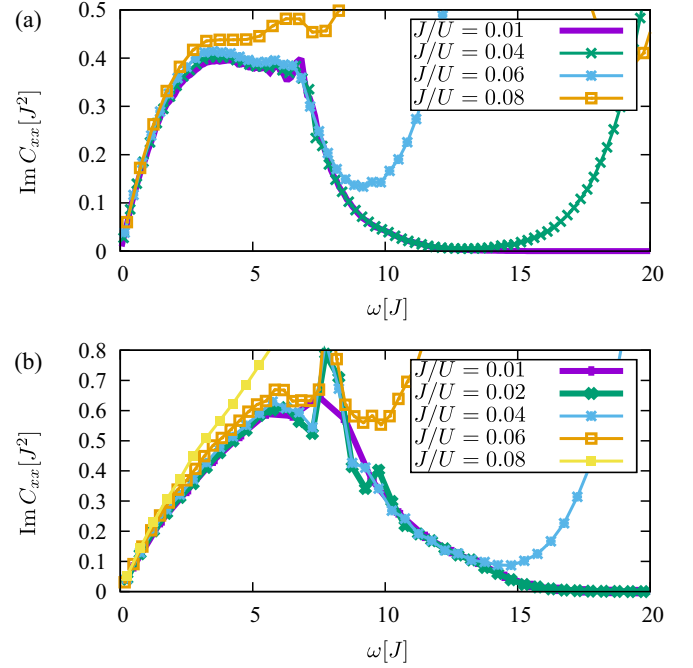


FIG. 5. Imaginary part of the current-current correlation function  $\text{Im } C_{xx}(\omega)$  as a function of frequency,  $T/U = 10$ . Parameters are (a)  $L_x \times L_y = 4 \times 3$  and  $N_p = 6$  and (b)  $L_x \times L_y = 3 \times 3$  and  $N_p = 9$ .

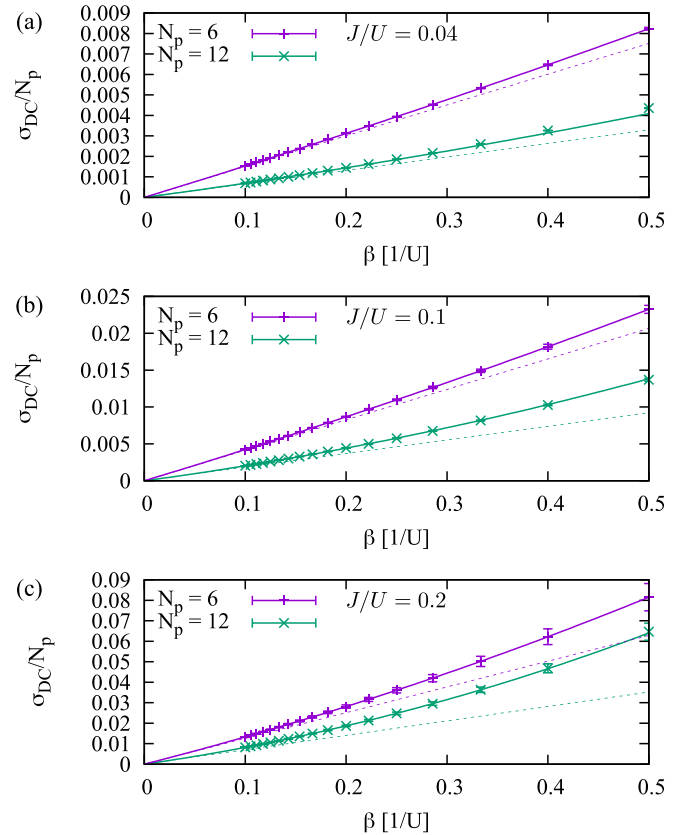


FIG. 6. DC conductivity  $\sigma_{\text{DC}}$  as a function of inverse temperature  $\beta$  for (a)  $J/U = 0.04$ , (b)  $J/U = 0.1$ , and (c)  $J/U = 0.2$ . System size  $L_x \times L_y = 4 \times 3$ . The solid lines give fits according to Eq. (16), and the dashed lines give the leading linear dependence in  $\beta$ .

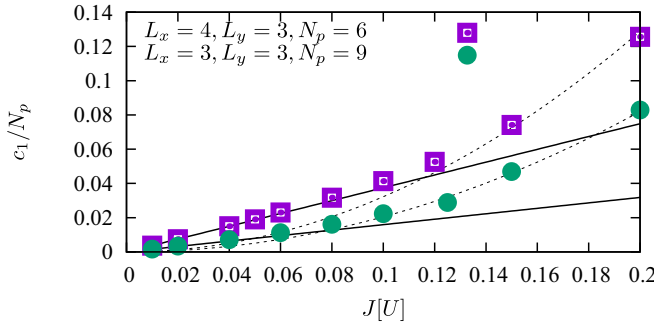


FIG. 7. The coefficient  $c_1$  introduced in Eq. (16) versus tunneling amplitude  $J/U$ . The solid lines give linear fits, and the dashed lines present quadratic functions.

phase). More importantly, we observe at high temperature a clear linear regime  $\sigma_{\text{DC}} \sim \beta$ , i.e.,  $\rho_{\text{DC}} \sim T$ .

In general, it is expected that a finite-size system with a bounded spectrum exhibits resistivity linear in temperature in the limit  $T \rightarrow \infty$  (or  $\sigma_{\text{DC}}$  linear in the inverse temperature  $\beta$ ) [18,20]. When working within the canonical ensemble in the strongly interacting limit, the upper bound of the Bose-Hubbard model is close to  $N_p(N_p - 1)U/2$ , where  $N_p$  is the number of particles, and all the bosons occupy the same site. Within the grand-canonical ensemble we control the average density by reducing the chemical potential  $\mu$ , and in this way we effectively limit the highest-energy state.

The key question is how far down in the temperature range resistivity linear in temperature persists. In particular, for hard-core bosons it has been shown that higher-order corrections become strong only at low temperatures in the vicinity of the BKT phase transition [28]. To determine where quadratic corrections to  $\sigma_{\text{DC}} \sim \beta$  start to play a role, we fit our result to

$$\sigma_{\text{DC}}(\beta) \approx c_1\beta + c_2\beta^2 \quad (16)$$

in the range  $\beta U \in (0.1, 0.2)$ . We find that this approximation works well even for a wider range  $\beta U \in (0.1, 0.5)$ . For weak hopping  $J/U \leq 0.1$ , in agreement with the observation from Fig. 5, we find that  $c_1 \sim J$ , or

$$\sigma_{\text{DC}} \sim J/T. \quad (17)$$

A closely related result for the fermionic model was derived using a high-temperature expansion in Ref. [13]. For stronger hopping it holds that  $c_1 \sim J^2$ , as shown in Fig. 7. The subleading term  $c_2$  becomes more prominent as the ratio  $J/U$  gets stronger.

### E. The analysis of the Kubo formula

We explain the numerically identified features of the conductivity using the framework introduced in Ref. [20]. Starting from the Kubo formula, Eq. (6), we consider small enough  $\omega \rightarrow 0$ . Following the previous numerical analysis, in the following we use small but finite  $\omega$ . We approximate the Dirac delta function from Eq. (6) as  $\delta(x) \approx \theta(\Delta\omega/2 - |x|)/\Delta\omega$ , where  $\theta$  is the Heaviside function and the bin width  $\Delta\omega$  is chosen to accommodate a reasonably large number of energy levels of our finite-size system. By rewriting Eq. (6)

and taking the limit  $\omega \rightarrow 0$ , we obtain

$$\begin{aligned} \sigma_{\text{DC}} &= \lim_{\omega \rightarrow 0} \frac{\pi(1 - e^{-\beta\omega})}{\omega Z(\beta)} \sum_{n,m} \delta(E_n - E_m - \omega) |\langle n | J_x | m \rangle|^2 e^{-\beta E_n} \\ &= \frac{\pi\beta}{Z(\beta)} \lim_{\omega \rightarrow 0, \Delta\omega \rightarrow 0} \frac{1}{\Delta\omega} \sum_{n,m: |E_n - E_m - \omega| < \Delta\omega/2} |\langle n | J_x | m \rangle|^2 e^{-\beta E_n} \\ &= \frac{\beta}{Z(\beta)} \sum_n \lim_{\omega \rightarrow 0} f_n(\omega) e^{-\beta E_n}, \end{aligned} \quad (18)$$

where

$$f_n(\omega) = \lim_{\omega \rightarrow 0, \Delta\omega \rightarrow 0} \frac{\pi}{\Delta\omega} \sum_{m: |E_n - E_m - \omega| < \Delta\omega/2} |\langle n | J_x | m \rangle|^2. \quad (19)$$

Using the high-temperature expansion in Eq. (18), we find approximate results for the coefficients  $c_1$  and  $c_2$  introduced in Eq. (16),

$$c_1 \approx \langle f_n(\omega) \rangle_n \equiv \frac{1}{\dim \mathcal{H}} \sum_n f_n(\omega), \quad (20)$$

$$c_2 \approx \langle f_n(\omega) \rangle_n \langle E_n \rangle_n - \langle f_n(\omega) E_n \rangle_n, \quad (21)$$

where  $\langle A_n \rangle_n \equiv \frac{1}{\dim \mathcal{H}} \sum_n A_n$ . By a numerical inspection, we find that estimates for the coefficients  $c_1$  and  $c_2$  obtained in this way do match numerical data. Based on the approximation in Eq. (20), we infer that  $c_1 \sim J$  behavior is related to the presence of bands in the many-body spectrum. The bands' density of states is inversely proportional to  $J$  (see Fig. 1), and consequently, the number of available states within a frequency bin  $\Delta\omega$  in Eq. (19) is inversely proportional to the tunneling  $J$ . For stronger  $J$  a quadratic dependence  $c_1 \sim (J/U)^2$  appears as the band structure is washed out (Fig. 7). Following Ref. [20], we perform coarse graining of the coefficients  $f_n(\omega)$  from Eq. (19),

$$f(E, \omega) = \frac{1}{g(E)} \sum_n \delta(E_n - E) f_n(\omega), \quad (22)$$

where  $g(E)$  is the many-body density of states, Eq. (9). An almost flat line, an indicator of the invariance of  $f(E, \omega)$  with energy  $E$ , ensures resistivity linear in temperature far down in  $T$ , as shown in Ref. [20]. In Fig. 8(a) we present the coarse-grained coefficients  $f(E, \omega)$  for  $J = 0.1$  and  $U = 2$  and  $U = 4$ . In both cases the many-body spectrum consists of bands centered around  $0, U, 2U, \dots$ . Within each band  $f(E, \omega)$  is roughly constant and weakly dependent on  $U$ . As  $U$  gets weaker, the gaps between bands are closed, and the function  $f(E, \omega)$  acquires more features; see Fig. 8(b) for  $U = 1$ . Because the function  $f(E, \omega)$  deviates from an averaged flat line throughout the spectrum, at first glance resistivity linear in temperature is found only at high temperatures. This observation is in agreement with the data presented in Fig. 6, where the regime of linear resistivity is found roughly at  $T \geq 5U$  ( $\beta \leq 0.2$ ). However, in the next section we discuss another regime of linear resistivity found at lower temperatures when the hard-core description becomes relevant.

### F. Comparison with hard-core bosons

Conductivity of hard-core bosons at half filling was investigated in Ref. [28]. It was found that a Gaussian function

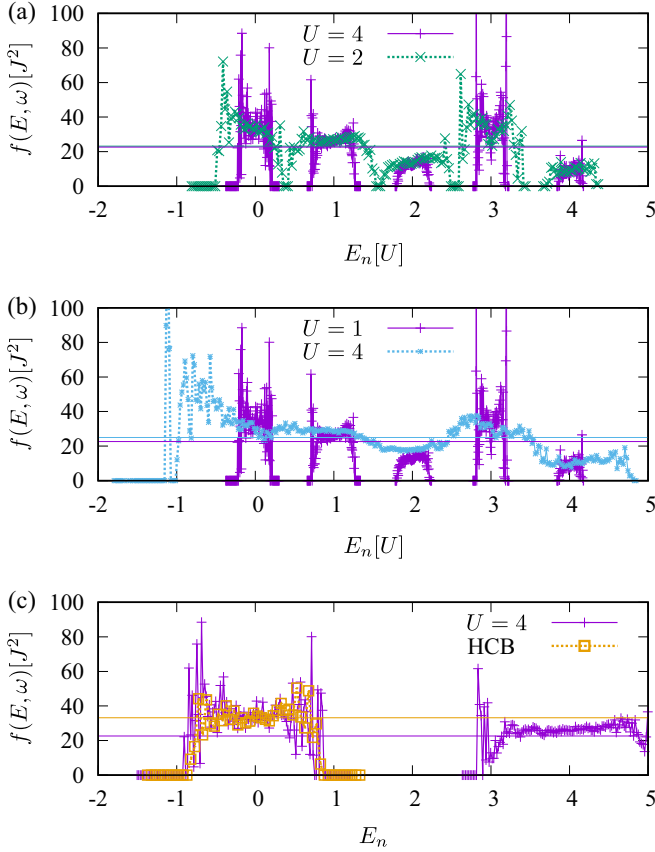


FIG. 8. The function  $f(E, \omega)$  as defined in Eq. (22) for  $J = 0.1$  and  $U = 4$  and (a)  $J/U = 0.1$  and  $U = 2$ , (b)  $J/U = 0.1$  and  $U = 1$ , and (c) hard-core bosons with  $J = 0.1$ . Parameters are  $L_x \times L_y = 4 \times 3$ ,  $N_p = 6$ ,  $\omega/J = 0.35$ , and  $\Delta\omega/U = 0.01$ . The horizontal lines show averaged values of  $f(E, \omega)$  over the full spectrum.

approximates well optical conductivity as a function of frequency. In order to reach the limit of hard-core bosons here we consider bosons at half filling ( $n = 1/2$  bosons per lattice site). We keep fixed hopping rate  $J = 0.1$  and change the value of local interaction  $U$ . In Fig. 9(a) we show that for a low enough ratio  $T/U$ , for example, for  $U = 4$  and  $T = 1$ , our results for the optical conductivity at half filling approach the result for hard-core bosons for  $\omega/U < 1$  as expected. The contribution of higher Hubbard bands is absent in the hard-core model.

The same applies to the DC conductivity, as shown in Fig. 9(b). Reference [28] showed that the resistivity of hard-core bosons is linear in temperature down to very low temperatures close to the BKT transition. Our considerations from the previous section are in line with this conclusion, as we find that the hard-core bosons exhibit a nearly constant function  $f(E, \omega)$  [see Fig. 8(c)], which closely corresponds to the function  $f(E, \omega)$  of the lowest band of the full model. As expected, when the temperature is low enough with respect to  $U$ , only the lowest band of the full model is occupied, and bosons can be described as hard-core particles. Consequently, the DC conductivity starts off as a linear function of the inverse temperature  $\beta$ , exhibits a transitional behavior for a range of intermediate  $\beta$  values, and changes into a linear

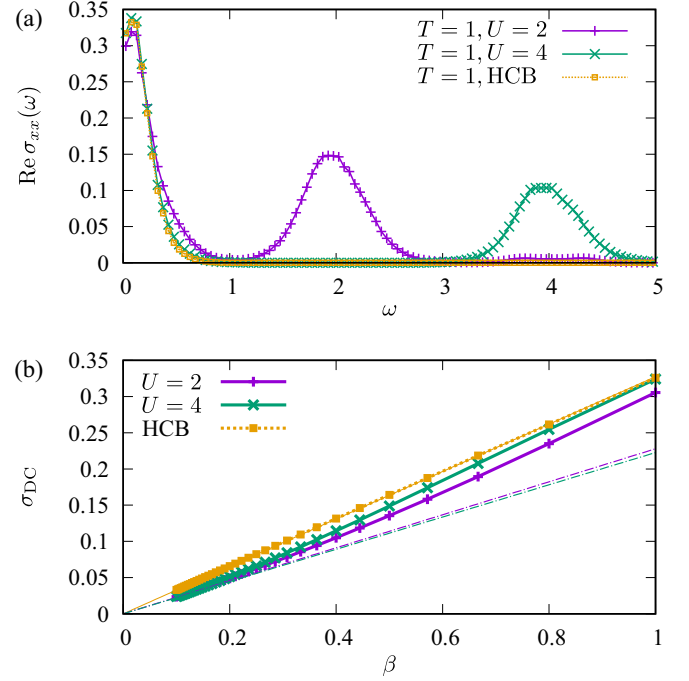


FIG. 9. (a) The conductivity  $\text{Re } \sigma_{xx}(\omega)$  vs frequency  $\omega$  for half filling at  $T = 1$  for hard-core bosons,  $U = 2$  and  $U = 4$ . (b) The DC conductivity as a function of inverse temperature  $\beta$ . The dot-dashed lines give the leading-order high-temperature result  $\sigma_{\text{DC}} \approx c_1 \times \beta$  for  $U = 4$  and  $U = 2$ . Parameters are  $J = 0.1$ ,  $L_x \times L_y = 4 \times 3$ , and  $N_p = 6$ .

function corresponding to hard-core-boson behavior at large  $\beta$  (low  $T$ ).

Now we investigate in more detail how the DC conductivity of hard-core bosons is reached by varying parameter  $U$  of the full model and temperature  $T$ . We present data for the DC conductivity as a function of temperature  $T$  and interaction  $U$  in Fig. 10. As we plot the DC conductivity multiplied by temperature  $T$ , for hard-core bosons we find an almost perfect constant within the considered temperature range [see Fig. 10(a)]. This constant is reached for  $U = 8$  at  $T = 2$  and for  $U = 4$  at  $T = 1$ . What we find surprising is the  $U$  dependence of the conductivity: we find that  $\sigma_{\text{DC}} T$  exhibits a minimum at some finite  $U$  before reaching the hard-core-boson result [see Fig. 10(b)].

This behavior can be traced back to the result from Fig. 8(c), where we saw that the average value of  $f(E, \omega \rightarrow 0)$  of hard-core bosons overestimates the result of the full model. We rewrite Eq. (18) as

$$\sigma_{\text{DC}} T = \frac{1}{\sum_n e^{-\beta E_n}} \sum_n \lim_{\omega \rightarrow 0} f_n(\omega) e^{-\beta E_n} \quad (23)$$

and consider the strongly interacting limit where the function  $f_n(\omega \rightarrow 0)$  can be approximated by a sum of rectangular functions centered around  $0, U, 2U, \dots$ , as presented in Fig. 8(a). From Fig. 8(a) we observe that from the several lowest Hubbard bands, it is the lowest band that has the highest value of  $f(E, \omega \rightarrow 0)$ . From Eq. (23) we infer that at fixed temperature, as we increase the interaction strength  $U$ , both the numerator and the denominator of the last expression are



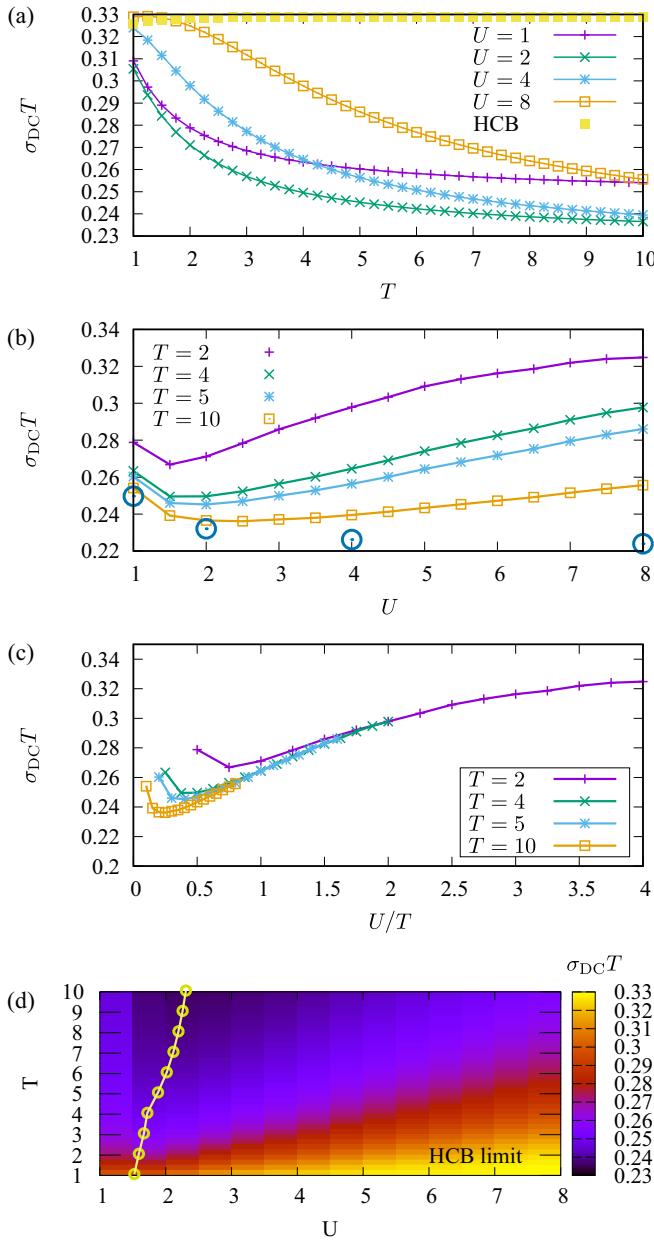


FIG. 10. The DC conductivity multiplied by temperature  $T$  as a function of (a) temperature  $T$ , (b) interaction  $U$ , and (c) the ratio  $T/U$ . The large blue circles in (b) give the value of the coefficient  $c_1$  introduced in Eq. (20) as a function of  $U$ . (d) The color map gives the DC conductivity multiplied by temperature  $T$ . The limit of hard-core bosons is reached in the bottom right corner of the plot. The yellow circles in (d) give the location of minima in  $\sigma_{\text{DC}}T$  as a function of  $U$ . The solid line is a guide to the eye. Parameters are  $J = 0.1$ ,  $L_x \times L_y = 4 \times 3$ , and  $N_p = 6$ .

reduced. Yet the partition function  $Z(\beta)$  decays faster because each term  $e^{-\beta E_n} \sim e^{-\beta nU}$  in the numerator is multiplied by a factor  $f_n < 1$  (and gets smaller with increasing  $n$ ), while in the denominator it is multiplied by 1. Therefore, the conductivity increases with increasing  $U$ , and we reach the limit of hard-core-boson conductivity from below. This is a striking and highly counterintuitive observation. We have checked that

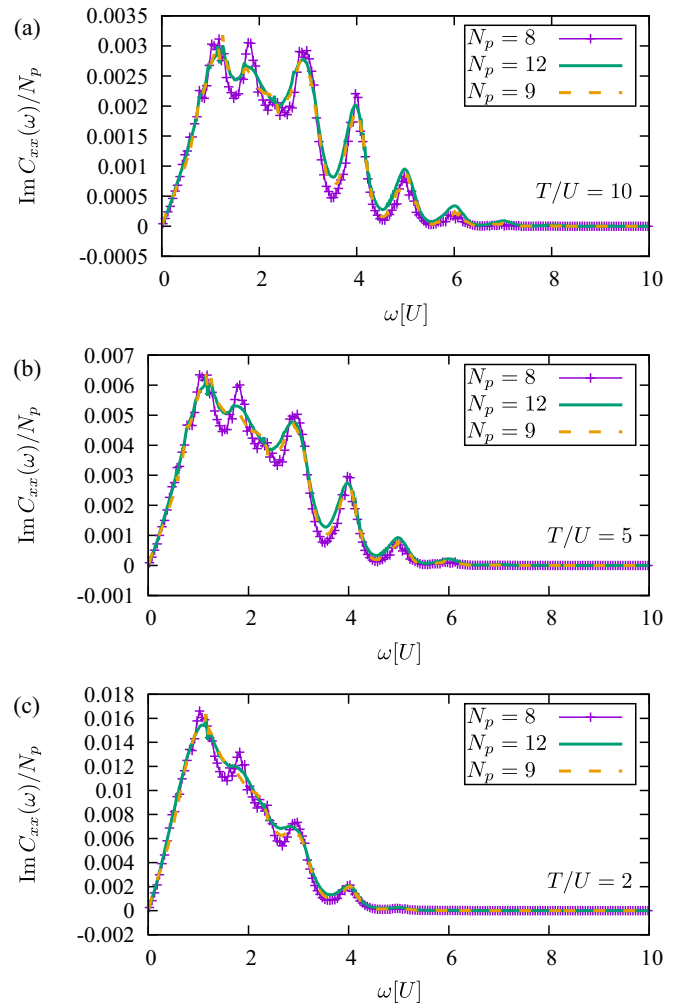


FIG. 11. The current-current correlation function vs frequency  $\omega$  for unit filling and three different system sizes:  $L_x \times L_y = 4 \times 2$ ,  $L_x \times L_y = 3 \times 3$ , and  $L_x \times L_y = 4 \times 3$ . Parameters are  $J/U = 0.1$  and (a)  $T/U = 10$ , (b)  $T/U = 5$ , and (c)  $T/U = 2$ .

this feature persists even when calculations are done in the grand-canonical ensemble and when the size of the lattice is changed, but it still might be an artifact of the finite size of the system.

### G. Finite-size effects

While that lattice sizes that we consider are too small to quantitatively predict results in the thermodynamic limit, we expect that the main features of the optical conductivity that we observe remain valid. For example, at high temperature we do expect DC conductivity to take the form  $\sigma_{\text{DC}}^{\text{th}} \sim J/T$ , yet the exact values of the tunneling  $J$  and temperature  $T$  where this behavior changes into a more complex dependence are possibly system size dependent.

In Fig. 11 we compare the current-current correlation functions for three different lattice sizes at several values of temperatures. Overall, the results show good agreement, and the main discrepancies are found close to  $\omega \rightarrow 0$ . By comparing the results for the two largest available lattice sizes

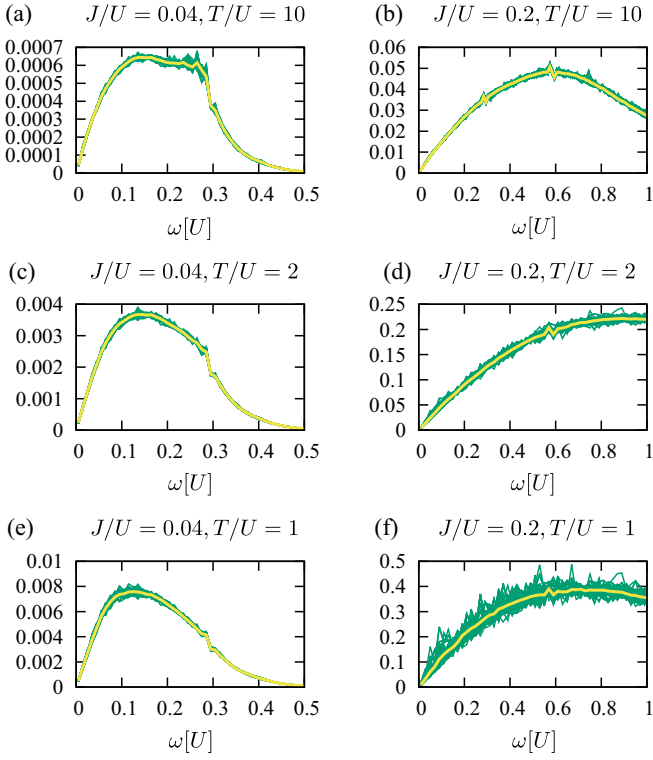


FIG. 12. The current-current correlation function  $\text{Im}C_{xx}(\omega)$  vs frequency  $\omega$  for half filling and  $J/U = 0.04$  (left column) and  $J/U = 0.2$  (right column). Parameters are (a) and (b)  $T/U = 10$ , (c) and (d)  $T/U = 5$ , and (e) and (f)  $T/U = 2$ . Lattice size  $L_x \times L_y = 4 \times 3$ , and  $N_p = 6$ . The thin lines give results for each of the 100 boundary conditions separately. The thick line is the averaged value.

and assuming that finite-size results approach the thermodynamic limit as  $\sigma_{\text{DC}}(N_p) \approx \sigma_{\text{DC}}^{\text{th}} + \text{const}/N_p$ , we estimate the relative errors of  $\sigma_{\text{DC}}$  with respect to the result in the thermodynamic limit  $\sigma_{\text{DC}}^{\text{th}}$  to be roughly of the order of 10%. In particular, for  $N_p = 8$  and  $L_x \times L_y = 4 \times 4$ ,  $\Delta\sigma_{\text{DC}}/\sigma_{\text{DC}} \approx 3\%$  at  $J/U = 0.04$  and  $T/U = 10$ ,  $\Delta\sigma_{\text{DC}}/\sigma_{\text{DC}} \approx 12\%$  at  $J/U = 0.04$  and  $T/U = 1$ , and  $\Delta\sigma_{\text{DC}}/\sigma_{\text{DC}} \approx 15\%$  at  $J/U = 0.2$  and  $T/U = 10$ . Another way to claim that finite-size effects are under control is to explore in more detail the role of boundary conditions. In our study we implement the so-called twisted boundary conditions, as introduced in [45,46]. We emphasize that the dependence of the results on the choice of the gauge is a measure of finite-size effects. The variance of the results with respect to a random choice of the gauge field being small is a good indication that the results are well representative of the thermodynamic limit.

As we typically implement 100 twisted boundary conditions [45,46,50], in Fig. 12 we plot the results for the imaginary part of the current-current correlation function for all the different boundary conditions separately, together with their averaged value. At high  $T$  we find very weak dependence on the boundary conditions already for lattice size  $L_x \times L_y = 4 \times 3$ , as can be seen in the top row of Fig. 12. However, the dependence gets stronger with decreasing temperature, as shown in the bottom row of Fig. 12, and it increases with the ratio  $J/U$ .

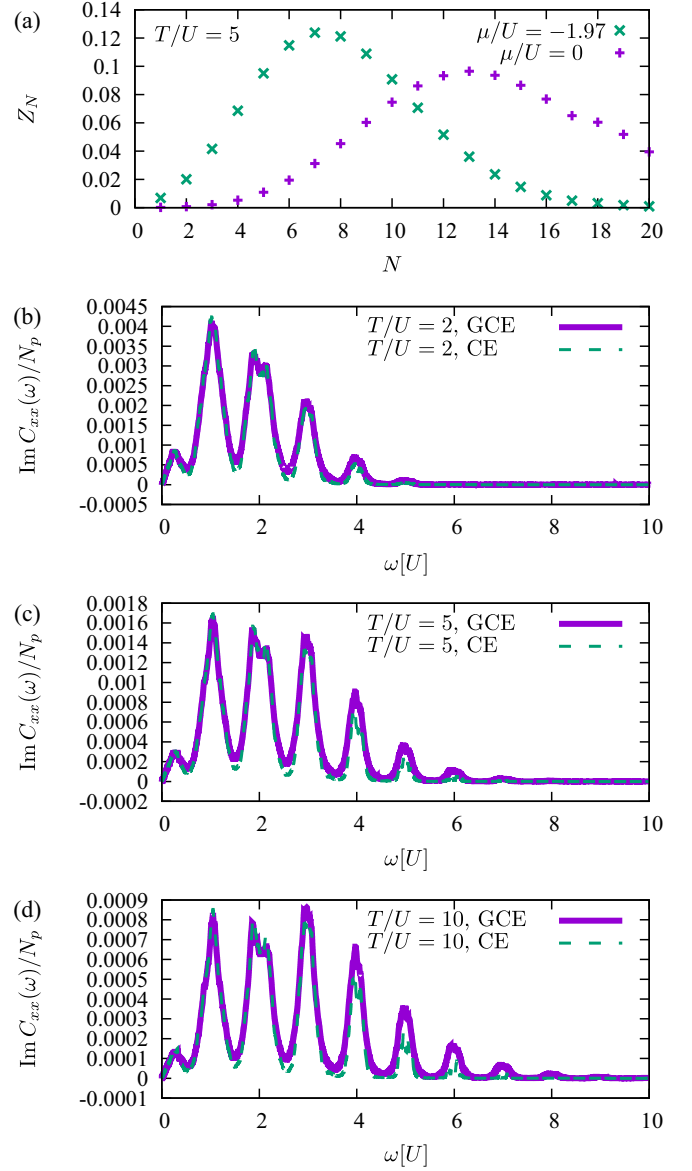


FIG. 13. (a) The partition function in different particle sectors,  $Z_N = \text{Tr} \exp[-\beta(H - \mu N)]$ . The chemical potential is set by the requirement  $\langle N \rangle / (L_x \times L_y) = 1$ . The imaginary part of the current-current correlation function for  $J/U = 0.04$  at (b)  $T/U = 2$ , (c)  $T/U = 5$ , and (d)  $T/U = 10$ . Lattice size  $L_x \times L_y = 4 \times 2$ , with no twisted boundary conditions.

## H. The grand-canonical ensemble

Here we consider the grand-canonical ensemble and introduce chemical potential  $\mu$ ,

$$H_\mu = H - \mu N, \quad (24)$$

where  $N$  is the number of particles. The value of the chemical potential  $\mu$  is set as usual by requiring a certain filling. In Fig. 13 we compare the results obtained in this way with the results within the fixed particle-number sector. We consider a small lattice  $L_x \times L_y = 4 \times 2$  and up to 20 particles. We find that there are some quantitative differences, while the main qualitative features of the correlation function remain unchanged. The contribution of conductivity peaks found at

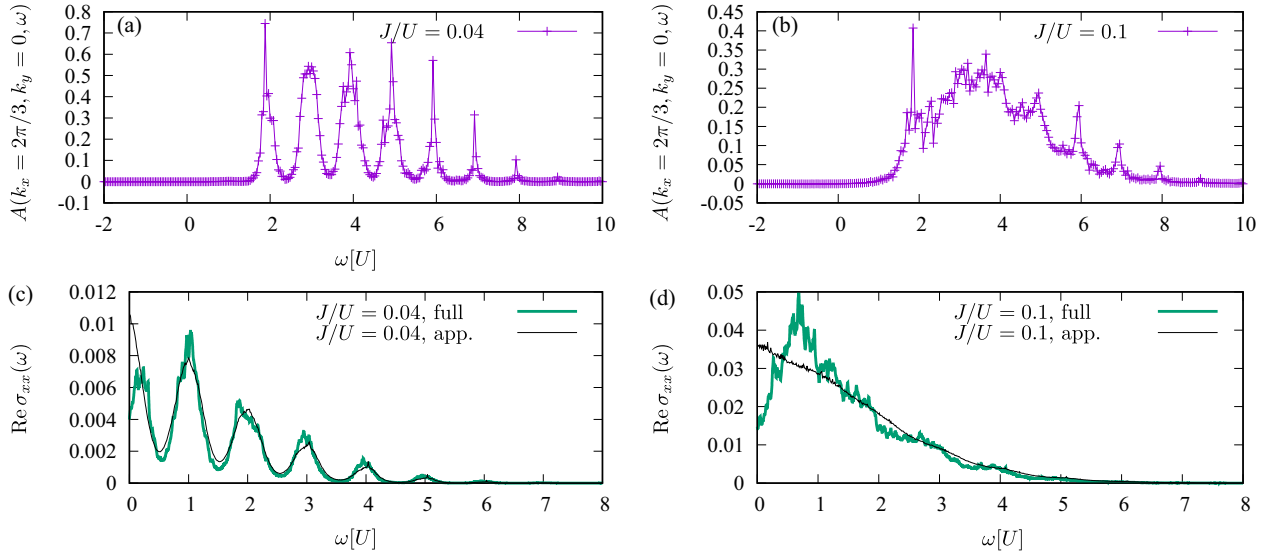


FIG. 14. Spectral functions for (a)  $J/U = 0.04$  and (c)  $J/U = 0.1$ . Optical conductivity  $\text{Re } \sigma_{xx}(\omega)$  as a function of frequency  $\omega$  for (b)  $J/U = 0.04$  and (d)  $J/U = 0.1$ . Parameters are  $L_x \times L_y = 3 \times 2$ ,  $\beta U = 0.2$ , and  $\mu/U \approx -1.97$ , such that  $\langle N \rangle = 1$ .

$\omega = nU$  is stronger at high temperatures when we take into account particle-number fluctuations within the grand-canonical ensemble.

### I. Comparison with the bubble-diagram approximation

Here we use the bubble-diagram approximation, which has been extensively used for the calculation of the conductivity within the Fermi-Hubbard model [11, 12, 14, 15, 17, 47, 51–54]. We find that for small lattices the bubble-diagram approximation works well only at high frequencies. A similar relation between the full result and the bubble-diagram approximation was observed in the fermionic Hubbard model [14] and, more recently, even in the context of the Holstein model [55]. By contrast, however, here vertex corrections appear to reduce conductivity, rather than increase it.

Within the grand-canonical ensemble we first calculate the single-particle Green's function,

$$G_{\mathbf{k}}(\omega + i\delta) = \frac{1}{\text{Tr} e^{-\beta(H - \mu N)}} \sum_{m,n} \frac{e^{-\beta(E_n - \mu N_n)} - e^{-\beta(E_m - \mu N_m)}}{\omega + i\delta + E_n - E_m + \mu} \times \langle n | b_{\mathbf{k}} | m \rangle \langle m | b_{\mathbf{k}}^\dagger | n \rangle, \quad (25)$$

where  $b_{\mathbf{k}} = \frac{1}{\sqrt{L_x L_y}} \sum_{\mathbf{r}} e^{i\mathbf{k}\mathbf{r}} b_{\mathbf{r}}$  and  $\mathbf{r}$  are vectors labeling lattice sites. The eigenenergies  $E_n$  and  $E_m$  and eigenstates  $|n\rangle$  and  $|m\rangle$  are obtained in two different particle sectors with  $N_n$  and  $N_m = N_n + 1$  particles. From here we obtain the spectral function:

$$A_{\mathbf{k}}(\omega) = -\frac{1}{\pi} \text{Im} G_{\mathbf{k}}(\omega + i\delta). \quad (26)$$

The current operator from Eq. (3) is given by  $J_x = \sum_{\mathbf{k}} \partial_{k_x} \varepsilon_{\mathbf{k}} b_{\mathbf{k}}^\dagger b_{\mathbf{k}} / \sqrt{L_x L_y}$ , where  $\varepsilon_{\mathbf{k}} = -2J(\cos k_x + \cos k_y)$  is the noninteracting dispersion relation on a two-dimensional lattice. The current-current correlation function used in Eq. (5) involves four bosonic operators. By using the imaginary time  $\tau$  and Matsubara frequencies  $\omega_n = 2\pi n/\beta$ , where  $n$  is an

integer, we find [43]

$$\sigma_{xx}(i\omega) = \frac{1}{L_x L_y} \frac{1}{\omega} \sum_{\mathbf{k}, \mathbf{q}} \partial_{k_x} \varepsilon_{\mathbf{k}} \partial_{q_x} \varepsilon_{\mathbf{q}} \int_0^\beta d\tau e^{i\omega\tau} \times \langle b_{\mathbf{k}}^\dagger(\tau) b_{\mathbf{k}}(\tau) b_{\mathbf{q}}^\dagger b_{\mathbf{q}} \rangle. \quad (27)$$

To estimate the last expectation value we decouple the four-particle operator by using the Wick theorem. In this way, we obtain an approximate expression for the conductivity:

$$\sigma_{xx}^{\text{bubble}}(i\omega) = \frac{1}{L_x L_y} \frac{1}{\omega \beta} \sum_{\mathbf{k}} (\partial_{k_x} \varepsilon_{\mathbf{k}})^2 \sum_{\omega_n} G_{\mathbf{k}}(i\omega_n) \times G_{\mathbf{k}}(i\omega_n + i\omega). \quad (28)$$

By using the spectral representation  $G_{\mathbf{k}}(i\omega_n) = \int d\omega \frac{1}{i\omega_n - \omega} A_{\mathbf{k}}(\omega)$  and by performing a summation over  $\omega_n$  we arrive at the bubble-diagram approximation for conductivity:

$$\text{Re } \sigma_{xx}^{\text{bubble}}(\omega) = \pi \frac{1}{L_x L_y} \sum_{\mathbf{k}} \int d\omega_1 (\partial_{k_x} \varepsilon_{\mathbf{k}})^2 A_{\mathbf{k}}(\omega_1) \times A_{\mathbf{k}}(\omega_1 + \omega) \frac{n_B(\omega_1) - n_B(\omega_1 + \omega)}{\omega}, \quad (29)$$

where  $n_B(x) = 1/[\exp(\beta x) - 1]$  is the Bose-Einstein distribution. The same approach has often been used in the study of the conductivity of the Fermi-Hubbard model. All the details can be found in Ref. [47]. A closely related calculation for bosons is given in Ref. [30]. In comparison with Ref. [30], here we work at finite temperature and use exact numerical results for the single-particle Green's function in Eq. (29).

We perform a numerical test of the accuracy of this approximation by comparing results obtained from Eq. (29) with the full result from Eq. (5). We find that for small system sizes the approximation works well at higher frequencies  $\omega$ , but it fails to reproduce numerical data in the limit  $\omega \rightarrow 0$ , as shown in Fig. 14. For  $J/U = 0.04$  we find that the spectral function features separate peaks close to  $\omega_n \approx -\mu + nU$ ,  $n = 0, 1, 2, \dots$

From Eq. (29) it follows that the peaks in optical conductivity emerge when the two peaks in  $A(\mathbf{k}, \omega_1)$  and  $A(\mathbf{k}, \omega_1 + \omega)$  overlap, as for  $\omega = 0, U, 2U, \dots$ , as discussed in Sec. III C.

#### IV. CONCLUSION AND DISCUSSION

In this paper we investigated the optical conductivity of the Bose-Hubbard model in the high-temperature regime. Based on the numerically exact calculation for small lattice sizes, we identified multiple peaks in optical conductivity stemming from the Hubbard bands at weak tunneling  $J/U$ . As the tunneling rate gets stronger, these peaks merge, and the conductivity takes a simpler form. We analyzed the regime with resistivity linear in temperature and found that the proportionality constant is inversely proportional to the tunneling rate  $J$  in the limit  $J/U \rightarrow 0$ . Additionally, in some cases we observed two separate linear regimes with different slopes: one at lower temperature corresponding to hard-core-boson behavior and one at high temperature corresponding to the leading order in the  $\beta$  expansion. Finally, we found a striking and unexpected nonmonotonic dependence of  $\sigma_{DC}$  on the coupling constant. At half filling and fixed temperature  $T$ , above some value of  $U$ ,  $\sigma_{DC}$  grows with increasing  $U$ , and eventually, it approaches the hard-core-boson conductivity. Further work is necessary to confirm that this feature of our results survives in the thermodynamic limit.

We expect that these results can be probed in cold-atom experiments, along the lines of Ref. [4]. Because the Bose-Hubbard model is only the low-energy effective description of lattice bosons, the regime of intermediate temperature  $T/U \sim 1$  may be the most realistic for making quantitative comparisons with experiments. For this purpose, it may turn out that additional Hamiltonian terms describing bosons in optical lattices should be taken into account in addition to the Bose-Hubbard model. Moreover, processes beyond the linear-response regime may play a role [42]. In order to extend these calculations to larger system sizes, beyond-mean-field approximations [56–60] could be considered.

#### ACKNOWLEDGMENTS

Numerical computations were performed at the PARADOX-IV supercomputing facility at the Scientific Computing Laboratory, National Center of Excellence for the Study of Complex Systems, Institute of Physics Belgrade. The authors acknowledge funding provided by the Institute of Physics Belgrade through a grant from the Ministry of Science, Technological Development, and Innovation of the Republic of Serbia, as well as by the Science Fund of the Republic of Serbia, under the Key2SM project (PROMIS program, Grant No. 6066160). J.V. acknowledges funding from the European Research Council, Grant No. ERC-2022-StG: 101076100.

- 
- [1] I. Bloch, J. Dalibard, and W. Zwerger, *Rev. Mod. Phys.* **80**, 885 (2008).
  - [2] C.-C. Chien, S. Peotta, and M. di Ventra, *Nat. Phys.* **11**, 998 (2015).
  - [3] S. Krinner, T. Esslinger, and J.-P. Brantut, *J. Phys.: Condens. Matter* **29**, 343003 (2017).
  - [4] P. T. Brown, D. Mitra, E. Guardado-Sanchez, R. Nourafkan, A. Reymbaut, C.-D. Hébert, S. Bergeron, A.-M. S. Tremblay, J. Kokalj, D. A. Huse, P. Schauß, and W. S. Bakr, *Science* **363**, 379 (2019).
  - [5] S. A. Grigera, R. S. Perry, A. J. Schofield, M. Chiao, S. R. Julian, G. G. Lonzarich, S. I. Ikeda, Y. Maeno, A. J. Millis, and A. P. Mackenzie, *Science* **294**, 329 (2001).
  - [6] R. A. Cooper, Y. Wang, B. Vignolle, O. J. Lipscombe, S. M. Hayden, Y. Tanabe, T. Adachi, Y. Koike, M. Nohara, H. Takagi, C. Proust, and N. E. Hussey, *Science* **323**, 603 (2009).
  - [7] Y. Cao, V. Fatemi, A. Demir, S. Fang, S. L. Tomarken, J. Y. Luo, J. D. Sanchez-Yamagishi, K. Watanabe, T. Taniguchi, E. Kaxiras, R. C. Ashoori, and P. Jarillo-Herrero, *Nature (London)* **556**, 80 (2018).
  - [8] A. Legros, S. Benhabib, W. Tabis, F. Laliberté, M. Dion, M. Lizaïre, B. Vignolle, D. Vignolles, H. Raffy, Z. Z. Li, P. Auban-Senzier, N. Doiron-Leyraud, P. Fournier, D. Colson, L. Taillefer, and C. Proust, *Nat. Phys.* **15**, 142 (2019).
  - [9] S. Licciardello, J. Buhot, J. Lu, J. Ayres, S. Kasahara, Y. Matsuda, T. Shibauchi, and N. E. Hussey, *Nature (London)* **567**, 213 (2019).
  - [10] P. Cha, N. Wentzell, O. Parcollet, A. Georges, and E.-A. Kim, *Proc. Natl. Acad. Sci. USA* **117**, 18341 (2020).
  - [11] X. Deng, J. Mravlje, R. Žitko, M. Ferrero, G. Kotliar, and A. Georges, *Phys. Rev. Lett.* **110**, 086401 (2013).
  - [12] J. Vučičević, D. Tanasković, M. J. Rozenberg, and V. Dobrosavljević, *Phys. Rev. Lett.* **114**, 246402 (2015).
  - [13] E. Perepelitsky, A. Galatas, J. Mravlje, R. Žitko, E. Khatami, B. S. Shastri, and A. Georges, *Phys. Rev. B* **94**, 235115 (2016).
  - [14] J. Vučičević, J. Kokalj, R. Žitko, N. Wentzell, D. Tanasković, and J. Mravlje, *Phys. Rev. Lett.* **123**, 036601 (2019).
  - [15] A. Vranić, J. Vučičević, J. Kokalj, J. Skolimowski, R. Žitko, J. Mravlje, and D. Tanasković, *Phys. Rev. B* **102**, 115142 (2020).
  - [16] T. G. Kiely and E. J. Mueller, *Phys. Rev. B* **104**, 165143 (2021).
  - [17] J. Vučičević, S. Predin, and M. Ferrero, *Phys. Rev. B* **107**, 155140 (2023).
  - [18] S. Mukerjee, V. Oganesyan, and D. Huse, *Phys. Rev. B* **73**, 035113 (2006).
  - [19] F. Herman, J. Buhmann, M. H. Fischer, and M. Sigrist, *Phys. Rev. B* **99**, 184107 (2019).
  - [20] A. A. Patel and H. J. Changlani, *Phys. Rev. B* **105**, L201108 (2022).
  - [21] L. Vidmar, S. Langer, I. P. McCulloch, U. Schneider, U. Schollwöck, and F. Heidrich-Meisner, *Phys. Rev. B* **88**, 235117 (2013).
  - [22] J. P. Ronzheimer, M. Schreiber, S. Braun, S. S. Hodgman, S. Langer, I. P. McCulloch, F. Heidrich-Meisner, I. Bloch, and U. Schneider, *Phys. Rev. Lett.* **110**, 205301 (2013).
  - [23] M. Snoek and W. Hofstetter, *Phys. Rev. A* **76**, 051603(R) (2007).

- [24] A. Dhar, C. Baals, B. Santra, A. Müllers, R. Labouvie, T. Mertz, I. Vasić, A. Cichy, H. Ott, and W. Hofstetter, *Phys. Status Solidi B* **256**, 1800752 (2019).
- [25] M. P. A. Fisher, P. B. Weichman, G. Grinstein, and D. S. Fisher, *Phys. Rev. B* **40**, 546 (1989).
- [26] M.-C. Cha, M. P. A. Fisher, S. M. Girvin, M. Wallin, and A. P. Young, *Phys. Rev. B* **44**, 6883 (1991).
- [27] A. P. Kampf and G. T. Zimanyi, *Phys. Rev. B* **47**, 279 (1993).
- [28] N. H. Lindner and A. Auerbach, *Phys. Rev. B* **81**, 054512 (2010).
- [29] S. Bhattacharyya, A. De, S. Gazit, and A. Auerbach, *Phys. Rev. B* **109**, 035117 (2024).
- [30] A. S. Sajna, T. P. Polak, and R. Micnas, *Phys. Rev. A* **89**, 023631 (2014).
- [31] E. O. Rizzatti and E. J. Mueller, *Phys. Rev. A* **109**, 053303 (2024).
- [32] K. Chen, L. Liu, Y. Deng, L. Pollet, and N. Prokof'ev, *Phys. Rev. Lett.* **112**, 030402 (2014).
- [33] A. Lucas, S. Gazit, D. Podolsky, and W. Witczak-Krempa, *Phys. Rev. Lett.* **118**, 056601 (2017).
- [34] T. Zeng, A. Hegg, L. Zou, S. Jiang, and W. Ku, *arXiv:2112.05747*.
- [35] A. Hegg, J. Hou, and W. Ku, *Proc. Natl. Acad. Sci. USA* **118**, e2100545118 (2021).
- [36] X. Yue, A. Hegg, X. Li, and W. Ku, *New J. Phys.* **25**, 053007 (2023).
- [37] C. Yang, H. Liu, Y. Liu, J. Wang, D. Qiu, S. Wang, Y. Wang, Q. He, X. Li, P. Li, Y. Tang, J. Wang, X. C. Xie, J. M. Valles, J. Xiong, and Y. Li, *Nature (London)* **601**, 205 (2022).
- [38] P. Prelovšek and J. Bonča, in *Strongly Correlated Systems: Numerical Methods*, Springer Series in Solid-State Sciences Vol. 176 (Springer, Berlin, 2013), pp. 1–30.
- [39] B. Capogrosso-Sansone, S. G. Söyler, N. Prokof'ev, and B. Svistunov, *Phys. Rev. A* **77**, 015602 (2008).
- [40] N. Prokof'ev, O. Ruebenacker, and B. Svistunov, *Phys. Rev. Lett.* **87**, 270402 (2001).
- [41] N. Goldman, G. Juzeliūnas, P. Öhberg, and I. B. Spielman, *Rep. Prog. Phys.* **77**, 126401 (2014).
- [42] A. Roy, S. Bera, and K. Saha, *Phys. Rev. Res.* **2**, 043133 (2020).
- [43] G. D. Mahan, *Many Particle Physics*, 3rd ed. (Plenum, New York, 2000).
- [44] D. J. Scalapino, S. R. White, and S. C. Zhang, *Phys. Rev. Lett.* **68**, 2830 (1992).
- [45] D. Poilblanc, *Phys. Rev. B* **44**, 9562 (1991).
- [46] C. Gros, *Z. Phys. B* **86**, 359 (1992).
- [47] J. Vučičević and R. Žitko, *Phys. Rev. B* **104**, 205101 (2021).
- [48] P. F. Maldague, *Phys. Rev. B* **16**, 2437 (1977).
- [49] C. Kollath, G. Roux, G. Biroli, and A. M. Läuchli, *J. Stat. Mech.* (2010) P08011.
- [50] J. Bonča and P. Prelovšek, *Phys. Rev. B* **67**, 085103 (2003).
- [51] P. Limelette, P. Wzietek, S. Florens, A. Georges, T. A. Costi, C. Pasquier, D. Jérôme, C. Mézière, and P. Batail, *Phys. Rev. Lett.* **91**, 016401 (2003).
- [52] H. Terletska, J. Vučičević, D. Tanasković, and V. Dobrosavljević, *Phys. Rev. Lett.* **107**, 026401 (2011).
- [53] J. Vučičević, H. Terletska, D. Tanasković, and V. Dobrosavljević, *Phys. Rev. B* **88**, 075143 (2013).
- [54] J. Vučičević and R. Žitko, *Phys. Rev. Lett.* **127**, 196601 (2021).
- [55] V. Janković, P. Mitrić, D. Tanasković, and N. Vukmirović, *Phys. Rev. B* **109**, 214312 (2024).
- [56] M. Snoek and W. Hofstetter, in *Quantum Gases: Finite Temperature and Non-equilibrium Dynamics*, edited by N. Proukakis, S. Gardiner, M. Davis, and M. Szymańska (World Scientific, Singapore, 2013), pp. 355–365.
- [57] L. He and S. Yi, *New J. Phys.* **24**, 023035 (2022).
- [58] U. Pohl, S. Ray, and J. Kroha, *Ann. Phys. (Berlin, Ger.)* **534**, 2100581 (2022).
- [59] F. Caleffi, M. Capone, C. Menotti, I. Carusotto, and A. Recati, *Phys. Rev. Res.* **2**, 033276 (2020).
- [60] V. E. Colussi, F. Caleffi, C. Menotti, and A. Recati, *SciPost Phys.* **12**, 111 (2022).



# Simple predictors of $T_c$ in superconducting cuprates and the role of interactions between effective Wannier orbitals in the $d$ - $p$ three-band model

Jakša Vučičević<sup>1</sup> and Michel Ferrero<sup>2,3</sup>

<sup>1</sup>Scientific Computing Laboratory, Center for the Study of Complex Systems, Institute of Physics Belgrade, University of Belgrade, Pregrevica 118, 11080 Belgrade, Serbia

<sup>2</sup>CPHT, CNRS, Ecole Polytechnique, Institut Polytechnique de Paris, Route de Saclay, 91128 Palaiseau, France

<sup>3</sup>Collège de France, 11 place Marcelin Berthelot, 75005 Paris, France



(Received 18 August 2023; revised 12 December 2023; accepted 1 February 2024; published 26 February 2024)

At optimal doping, different cuprate compounds can exhibit vastly different critical temperatures for superconductivity ( $T_c$ ), ranging from about 20 to about 135 K. The precise properties of the lattice that determine the magnitude of the  $T_c$  are currently unknown. In this paper, we investigate the dependence of the optimal doping  $T_c$  on the parameters of the Emery ( $d$ - $p$ ) model for the  $\text{CuO}_2$  planes in the cuprates. We show that the best scaling is obtained not with the parameters of the model written in the real ( $d/p$ -orbital) space but rather written in the space of effective Wannier orbitals. In this basis, one obtains a model of three sublattices coupled through all possible four-point interactions. We identify multiple predictor variables that fit the experimental  $T_c$  to about  $\pm 4$ – $5$  K and that remarkably depend on the leading attractive coupling constants in the transformed Hamiltonian.

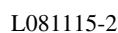
DOI: [10.1103/PhysRevB.109.L081115](https://doi.org/10.1103/PhysRevB.109.L081115)

Finding ways to increase the superconducting critical temperature in cuprate compounds is one of the central goals in condensed matter physics [1–4]. The record  $T_c$  remains at about 135 K for already more than two decades [5,6] (if we only consider systems at atmospheric pressure [7,8]). One of the reasons for the lack of progress is that there is no clear understanding of what to look for in a crystal structure, if one is to identify a high- $T_c$  candidate. Many works focused on how  $T_c$  correlates with the tight-binding parameters [9–26]. The role of phonons [27–31] and disorder [32–34] have been considered as well. In more recent machine learning approaches [35–38], a large number of different quantities was considered systematically. Even though the Coulomb interaction is widely believed to be responsible for superconductivity in the cuprates, no works to our knowledge have attempted to systematically link *ab initio* computed coupling constants to the experimentally measured  $T_c$  for multiple compounds.

Studies so far have mostly looked at correlations between the  $T_c$  and the parameters of two kinds of models: single-band and three-band. In the single-band picture, the main idea was that longer range hopping ( $t'$ ) frustrates the antiferromagnetic (AFM) correlations, which are believed to act as the pairing glue in the cuprates [22,39–44]. However, the experimentally observed trend in  $T_c(t'/t)$  [11,13,18] was not reproduced in single-band calculations [12,14,16,19,24–26,45], thus suggesting that the single-band models (both Hubbard and  $tt'J$ ) do not capture all the mechanisms that determine the  $T_c$  in the cuprates. In the three-band  $d$ - $p$  (Emery) model picture, some works considered the charge-transfer gap (CTG, the difference in energy between copper  $d$  and oxygen  $p$  orbitals [18,44,46], or defined by the gap in the local spectral function [44,47]) as the relevant energy scale that determines the strength of the effective AFM coupling, and thus the  $T_c$ . At least some trends of how the experimental  $T_c$  depends on the tight-binding parameters computed for the Emery model

can be reproduced by many-body calculations (see Ref. [18] and compare to Ref. [15]). More recently, experimentally observed trends of how  $T_c$  depends on the density of holes on the copper and oxygen sites separately [48] was also reproduced in calculations for the  $d$ - $p$  model [47]. These findings seem to indicate that the Emery model is more relevant for the description of the  $T_c$  magnitude in the cuprates. However, the attempt [18] to quantitatively correlate the tight-binding parameters of the Emery model to the experimentally measured  $T_c$  yielded only poor fits, with large standard deviation of about 30 K. This still leaves open the question of the practical relevance of the CTG and the Emery model.

In this paper, we show that the experimentally measured  $T_c$  can indeed be described by a simple function of three Emery-model tight-binding parameters (computed for each compound using *ab initio* methods), with a small standard deviation of about 7 K. Furthermore, we show that the interplay between interaction and geometry plays an essential role, and that even better fits can be obtained if one considers not only the tight-binding parameters, but also the coupling constants. The effective onsite repulsion on copper sites  $U_{dd}$  is unlikely to depend strongly on the specifics of the lattice structure; However, if one transforms the Hamiltonian in such a way that the e-e coupling and the kinetic energy become entangled, the resulting coupling constants can be strongly material dependent. By using one such (exact) transformation, we formally obtain a model of three separate square lattices, coupled through all possible four-point interactions between two electrons. Among the coupling constants, some are positive (repulsive), and some are negative (attractive). We find that the experimentally measured  $T_c$  can be fit to within about 5 K, by using a linear function of only two parameters of our transformed Hamiltonian, one of them being the leading attractive interaction. We explore the correlations of  $T_c$  with the parameters of our transformed model in a systematic and



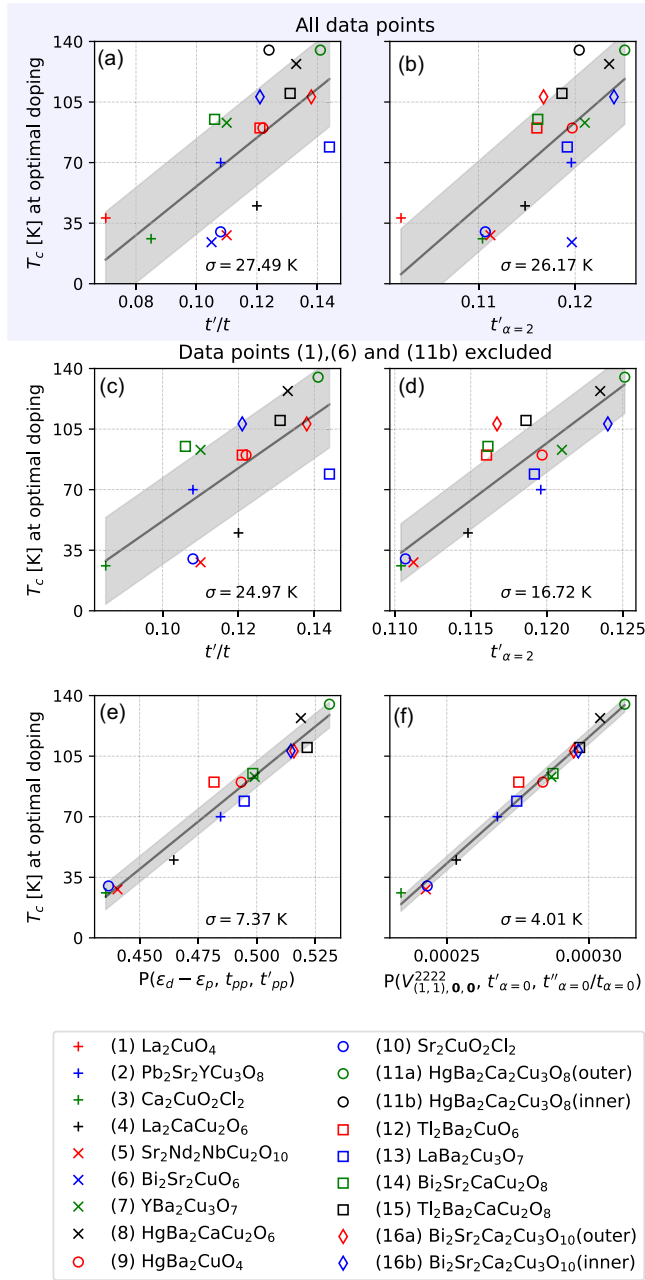


FIG. 2. Test of different predictors of  $T_c$ . The standard deviation of each fit is denoted  $\sigma$ . The black line is the linear fit, the width of the gray shading corresponds to  $\pm\sigma$ .

way, but only weakly. In our opinion, one should not expect that a single Hamiltonian term controls the  $T_c$  in its entirety. One should rather expect a competition (or cooperation) between different processes encoded in the Hamiltonian. Most generally, if the Emery model is correct for the cuprates, the  $T_c$  should in general be a single-valued function of *all* the parameters,  $T_c(\epsilon_d - \epsilon_p, t_{pd}, t_{pp}, t'_{pp})$ . This was not checked in *Weber et al.*, and based on their analyses, one cannot give a clear assessment of the relevance of the Emery model for the cuprates. We provide such a check on Fig. 2(e) (see also Ref. [51]). We demonstrate that a linear combination of three of the Emery model parameters, namely  $\epsilon_d - \epsilon_p$ ,  $t_{pp}$ , and  $t'_{pp}$  is a

solid predictor of  $T_c$ , to within  $\pm 7.4$  K in the whole range of  $T_c$ , except for three apparent outliers (see the explanations in the next section). The remaining variance of our fit could be attributed to  $t_{pd}$ , but we find that adding this parameter to the linear combination does not bring much improvement:  $T_c$  is not a linear function of  $t_{pd}$ . The remaining variance could also be due to parameters not included in the Emery model. However,  $T_c$  does fit linearly and with an even smaller standard deviation to the parameters of our transformed Hamiltonian, as we show in the following: this presents strong evidence that the Emery model indeed captures the mechanisms that dominantly determine the  $T_c$ .

**Strategy and results.** For each entry in the *Weber et al.* dataset (given in Ref. [51]), we evaluate the dispersions and all the parameters of the Hamiltonian in Eq. (4). We then compute from these values about 50 variables that we expect might correlate with  $T_c$  (these include the bandwidths of each band  $D_\alpha$ , short-distance hoppings  $t_\alpha \equiv t_{\alpha,\mathbf{d}=(1,0)}$ ,  $t'_\alpha \equiv t_{\alpha,\mathbf{d}=(1,1)}$ ,  $t''_\alpha \equiv t_{\alpha,\mathbf{d}=(2,0)}$ , as well as various short-distance components and extremal values of  $V_{\mathbf{d}\mathbf{d}'\mathbf{u}}^{\alpha\beta\gamma\delta}$ ).

We first look at the correlation with the  $T_c$  of each individual variable, by doing a linear fit and estimating the standard deviation,  $\sigma$ . We find that the best predictor is  $t'_{\alpha=2}$  (in model B formulation), yielding a fit with  $\sigma = 26.2$  K. This is slightly better than the  $t'/t$  for the effective single band put forward by *Weber et al.*, but  $t'/t$  is, indeed, a close second with  $\sigma = 27.5$  K (see Fig. 2 top row). We readily see that the data points (1), (6), and (11b) are outliers for both of the best predictors. In our other attempts at fitting the  $T_c$ , these three points were consistently presenting a limiting factor in obtaining a small  $\sigma$ . Both points (1) and (6) have a very low  $T_c$ —the point (6) has even the lowest  $T_c$  (it was also found to be an outlier in Ref. [9]), while the point (1) is extreme in terms of many of the model parameters, so we exclude both points from further analysis. The point (11b) represents the parameters for the inner layer of a three-layer material, and it may be that the outer layer parameters, given by the data point (11a), are more relevant, so we exclude the point (11b), as well. In total, we are left with 15 data points, for 14 different compounds. We then redo the fits with respect to individual parameters, and we see that  $\sigma$  for the  $t'/t$  fit has dropped to about 25 K, while the  $\sigma$  for the  $t'_{\alpha=2}$  fit has dropped to 16.7 K. In our subset of data which excludes the apparent outliers,  $t'_{\alpha=2}$  is by far the best single-parameter predictor of  $T_c$ . This holds even in the case of model A.

We now construct all possible linear combinations of any two and three variables,  $P(p_1, p_2, p_3) = c_1 p_1 + c_2 p_2 + c_3 p_3$ , and we keep fixed  $\sum_i c_i^2 = 1$ . For each of the  $\sim 1200$  pairs  $(p_1, p_2)$  and  $\sim 40\,000$  triplets  $(p_1, p_2, p_3)$ , we pinpoint the minimum in  $\sigma(\{p_i\}; \{c_i\})$  using the Nelder-Mead algorithm. We then rank different pairs and triplets according to the minimum standard deviation that we can obtain,  $\min_{\{c_i\}} \sigma(\{p_i\}; \{c_i\})$ . Finally, we count the number of times each variable appears in the top 100 triplets, to gain insight into which parameters might be most relevant. Our results are summarized in Table I (see also Ref. [51]).

We observe a general trend in our results, regardless of the choice of the formulation of the interaction part [Eq. (2) or (3)]—good predictors are the linear combinations of a

TABLE I. Summary of the best predictors of  $T_c$ . In the first column, we restrict to only the original 4 parameters of the model and the  $t'/t$  for the effective single-band model computed in *Weber et al.* In the second and third columns, we include the parameters of models A and B, respectively, and variables computed from those parameters.

category	Original parameters and $t'/t$	$\sigma$ (K)	Model A	$\sigma$ (K)	Model B	$\sigma$ (K)
one-param. best	$t'/t$	24.97	$t'_{\alpha=2}$	21.70	$t'_{\alpha=2}$	16.72
two-param. best	$\varepsilon_d - \varepsilon_p, t_{pp}$	12.67	$t''_{\alpha=1}, \min V_{\mathbf{d}\mathbf{d}'\mathbf{u}}^{\alpha\beta\gamma\delta}$	5.42	$t'_{\alpha=1}, V_{(1,1),(-1,-1),0}^{0000}$	5.74
three-param. best	$\varepsilon_d - \varepsilon_p, t_{pp}, t'_{pp}$	7.37	$D_{\alpha=1}, t''_{\alpha=1}, t'_{\alpha=2}$	4.47	$t'_{\alpha=0}, \frac{t''_{\alpha=0}}{t_{\alpha=0}}, V_{(1,1),0,0}^{2222}$	4.01
tree-param. second best	$\varepsilon_d - \varepsilon_p, t_{pp}, t'/t$	9.74	$D_{\alpha=1}, t''_{\alpha=1}, V_{0,0,0}^{2222}$	4.55	$t'_{\alpha=0}, \min V_{\mathbf{d}\mathbf{d}'\mathbf{u}}^{0000}, V_{(1,1),0,0}^{2222}$	4.03

hopping amplitude and one or two coupling constants, in many cases the attractive ones, and in most cases those acting within or between the bands  $\alpha = 0$  and 2, which are precisely the bands having an appreciable amount of  $d$  character.

The best two-parameter predictor we find is the linear combination of the overall most attractive component of  $V_{\mathbf{d}\mathbf{d}'\mathbf{u}}^{\alpha\beta\gamma\delta}$  and the hopping amplitude  $t''_{\alpha=1}$  (obtained in the model A formulation), yielding  $\sigma = 5.4$  K. The most attractive component in both model A and B formulations is the local density-assisted hybridization from band  $\alpha = 0$  to band  $\alpha = 2$ ,  $V_{0,0,0}^{0020}$ .

The best result that we have obtained in our unbiased search is given in Fig. 2(f). A linear combination of  $V_{(1,1),0,0}^{2222}$ ,  $t'_{\alpha=0}$  and  $t''_{\alpha=0}/t_{\alpha=0}$ , obtained in model B, yields a fit of  $T_c$  with  $\sigma = 4.01$  K. The coupling constant  $V_{(1,1),0,0}^{2222}$  is negative and corresponds to an assisted hopping term in the  $\alpha = 2$  band, say  $n_{\alpha,\uparrow,\mathbf{r}} d_{\alpha,\downarrow,\mathbf{r}}^\dagger d_{\alpha,\downarrow,\mathbf{r}+(1,1)}$  (similar to the terms considered in *Jiang et al.*). The parameters  $V_{(1,1),0,0}^{2222}$ ,  $t'_{\alpha=0}$  appear the most times in the top 100 three-parameter predictors based on model B, in total 65 times. It is interesting that  $t''_{\alpha=0}/t_{\alpha=0}$  correlates closely with  $V_{(2,0),0,0}^{0000}$ , which is, at the same time, the most attractive interaction in the  $\alpha = 0$  band. Indeed, the linear combination of  $V_{(1,1),0,0}^{2222}$ ,  $t'_{\alpha=0}$  and  $\min V_{\mathbf{d}\mathbf{d}'\mathbf{u}}^{0000}$  is our close second best result, with  $\sigma = 4.03$ .

Finally, we find that the local density-density interaction in the  $\alpha = 2$  band,  $V_{000}^{2222}$ , might be very relevant. In model A, it appears the most times in the top 100 three-parameter predictors, and in model B it is in this sense ranked sixth. In all linear combinations in which it appears,  $V_{000}^{2222}$  enters with a negative coefficient. Intuitively, a weaker local repulsion could mean a higher  $T_c$ . The best single-parameter predictor,  $t'_{\alpha=2}$ , indeed, highly (anti)correlates with  $V_{000}^{2222}$  (see Table I and Ref. [51] for details).

*Discussion and prospects for future work.* Our results provide strong evidence that the Emery model well captures the mechanisms that determine the magnitude of  $T_c$  in the cuprates. We identify multiple terms in the Hamiltonian which appear particularly relevant for the  $T_c$ , and propose that these correspond to additional pairing and pair-breaking

mechanisms that are in competition. These processes can be understood only in terms of the spatially extended, effective Wannier orbitals in the Emery model, which were not considered in earlier works.

In addition, we obtain a large set of predictor variables that can be computed cheaply, and thus used practically in high-throughput [54–56] searches for novel high- $T_c$  candidate structures. For practical use, the main question is whether the simple relation between  $T_c$  and our predictor variables holds outside the region of the parameter-space that is covered by the *Weber et al.* data points. The best strategy is then to look at crystal structures inside or close to that region, and focus on points for which multiple predictors agree. We have scanned the parameter space, and we find a case where each of the four parameters of the Emery model is inside the range of values for the existing cuprates, and for which our top 100 predictor variables (based on model B) predict  $T_c \approx 195 \pm 5$  K. Going only slightly away from the range of Emery model parameters covered by the data points, we find cases which correspond to  $T_c$  of even more than 250 K (see Ref. [51] for details).

As was the case with previous similar works, the main limitation of our approach lies in the ambiguity of the DFT calculations [57,58] and the downfolding procedures [49,59], especially when it comes to the choice and computation of Coulomb tensor elements; our work ultimately highlights the necessity of a careful and systematic work in that direction.

*Acknowledgments.* We acknowledge useful discussions with A.-M. S. Tremblay and Antoine Georges. We acknowledge contributions from Bogdan Rajkov and Sidhartha Dash in the early stages of this work. Computations were performed on the PARADOX supercomputing facility (Scientific Computing Laboratory, Center for the Study of Complex Systems, Institute of Physics Belgrade). J.V. acknowledges funding provided by the Institute of Physics Belgrade, through the grant by the Ministry of Science, Technological Development and Innovation of the Republic of Serbia. J.V. acknowledges funding by the European Research Council, Grant No. ERC-2022-StG: 101076100.

- [1] A. P. Malozemoff, J. Mannhart, and D. Scalapino, High-temperature cuprate superconductors get to work, *Phys. Today* **58**, 41 (2005).
- [2] P. A. Lee, N. Nagaosa, and X.-G. Wen, Doping a mott insulator: Physics of high-temperature superconductivity, *Rev. Mod. Phys.* **78**, 17 (2006).

- [3] Z. Guven Ozdemir, O. Aslan Cataltepe, and U. Onbasli, Some contemporary and prospective applications of high temperature superconductors, in *Applications of High-Tc Superconductivity*, edited by A. Moysés Luiz (InTech, Rijeka, Croatia, 2011).
- [4] M. R. Norman, The challenge of unconventional superconductivity, *Science* **332**, 196 (2011).



- [5] A. Schilling, M. Cantoni, J. D. Guo, and H. R. Ott, Superconductivity above 130 K in the Hg-Ba-Ca-Cu-O system, *Nature (London)* **363**, 56 (1993).
- [6] B. Keimer, S. A. Kivelson, M. R. Norman, S. Uchida, and J. Zaanen, From quantum matter to high-temperature superconductivity in copper oxides, *Nature (London)* **518**, 179 (2015).
- [7] I. A. Troyan, D. V. Semenov, A. G. Ivanova, A. G. Kvashnin, D. Zhou, A. V. Sadakov, O. A. Sobolevsky, V. M. Pudalov, I. S. Lyubutin, and A. R. Oganov, High-temperature superconductivity in hydrides, *Phys. Usp.* **65**, 748 (2022).
- [8] A. P. Drozdov, M. I. Erements, I. A. Troyan, V. Ksenofontov, and S. I. Shylin, Conventional superconductivity at 203 Kelvin at high pressures in the sulfur hydride system, *Nature (London)* **525**, 73 (2015).
- [9] Y. Ohta, T. Tohyama, and S. Maekawa, Apex oxygen and critical temperature in copper oxide superconductors: Universal correlation with the stability of local singlets, *Phys. Rev. B* **43**, 2968 (1991).
- [10] L. F. Feiner, M. Grilli, and C. Di Castro, Apical oxygen ions and the electronic structure of the high- $T_c$  cuprates, *Phys. Rev. B* **45**, 10647 (1992).
- [11] R. Raimondi, J. H. Jefferson, and L. F. Feiner, Effective single-band models for the high- $T_c$  cuprates. II. role of apical oxygen, *Phys. Rev. B* **53**, 8774 (1996).
- [12] Th. Maier, M. Jarrell, Th. Pruschke, and J. Keller,  $d$ -wave superconductivity in the Hubbard model, *Phys. Rev. Lett.* **85**, 1524 (2000).
- [13] E. Pavarini, I. Dasgupta, T. Saha-Dasgupta, O. Jepsen, and O. K. Andersen, Band-structure trend in hole-doped cuprates and correlation with  $T_{c,max}$ , *Phys. Rev. Lett.* **87**, 047003 (2001).
- [14] S. R. Hassan, B. Davoudi, B. Kyung, and A.-M. S. Tremblay, Conditions for magnetically induced singlet  $d$ -wave superconductivity on the square lattice, *Phys. Rev. B* **77**, 094501 (2008).
- [15] P. R. C. Kent, T. Saha-Dasgupta, O. Jepsen, O. K. Andersen, A. Macridin, T. A. Maier, M. Jarrell, and T. C. Schulthess, Combined density functional and dynamical cluster quantum Monte Carlo calculations of the three-band Hubbard model for hole-doped cuprate superconductors, *Phys. Rev. B* **78**, 035132 (2008).
- [16] S. S. Kancharla, B. Kyung, D. S  n  chal, M. Civelli, M. Capone, G. Kotliar, and A.-M. S. Tremblay, Anomalous superconductivity and its competition with antiferromagnetism in doped mott insulators, *Phys. Rev. B* **77**, 184516 (2008).
- [17] H. Zhou, Y. Yacoby, V. Y. Butko, G. Logvenov, I. Bo  zovi  , and R. Pindak, Anomalous expansion of the copper-apical-oxygen distance in superconducting cuprate bilayers, *Proc. Natl. Acad. Sci.* **107**, 8103 (2010).
- [18] C. Weber, C. Yee, K. Haule, and G. Kotliar, Scaling of the transition temperature of hole-doped cuprate superconductors with the charge-transfer energy, *Europhys. Lett.* **100**, 37001 (2012).
- [19] K.-S. Chen, Z. Y. Meng, S.-X. Yang, T. Pruschke, J. Moreno, and M. Jarrell, Evolution of the superconductivity dome in the two-dimensional Hubbard model, *Phys. Rev. B* **88**, 245110 (2013).
- [20] A. T. R  mer, A. Kreisel, I. Eremin, M. A. Malakhov, T. A. Maier, P. J. Hirschfeld, and B. M. Andersen, Pairing symmetry of the one-band Hubbard model in the paramagnetic weak-coupling limit: A numerical RPA study, *Phys. Rev. B* **92**, 104505 (2015).
- [21] Xi Chen, J. P. F. LeBlanc, and E. Gull, Superconducting fluctuations in the normal state of the two-dimensional Hubbard model, *Phys. Rev. Lett.* **115**, 116402 (2015).
- [22] J. Vu  i  evi  , T. Ayral, and O. Parcollet, TRILEX and  $GW +$  EDMFT approach to  $d$ -wave superconductivity in the Hubbard model, *Phys. Rev. B* **96**, 104504 (2017).
- [23] Y. Y. Peng, G. Dellea, M. Minola, M. Conni, A. Amorese, D. Di Castro, G. M. De Luca, K. Kummer, M. Salluzzo, X. Sun, X. J. Zhou, G. Balestrino, M. Le Tacon, B. Keimer, L. Braicovich, N. B. Brookes, and G. Ghiringhelli, Influence of apical oxygen on the extent of in-plane exchange interaction in cuprate superconductors, *Nat. Phys.* **13**, 1201 (2017).
- [24] H.-C. Jiang and T. P. Devereaux, Superconductivity in the doped Hubbard model and its interplay with next-nearest hopping  $t'$ , *Science* **365**, 1424 (2019).
- [25] M. Qin, C.-M. Chung, H. Shi, E. Vitali, C. Hubig, U. Schollw  ck, S. R. White, and S. Zhang (Simons Collaboration on the Many-Electron Problem), Absence of superconductivity in the pure two-dimensional Hubbard model, *Phys. Rev. X* **10**, 031016 (2020).
- [26] C. Zhang, J.-W. Li, and J. von Delft, Frustration-induced superconductivity in the  $t$ - $t'$  Hubbard model, *arXiv:2307.14835*.
- [27] T. P. Devereaux, A. Virosztek, and A. Zawadowski, Charge-transfer fluctuation,  $d$ -wave superconductivity, and the  $B_{1g}$  Raman phonon in cuprates, *Phys. Rev. B* **51**, 505 (1995).
- [28] T. P. Devereaux, T. Cuk, Z.-X. Shen, and N. Nagaosa, Anisotropic electron-phonon interaction in the cuprates, *Phys. Rev. Lett.* **93**, 117004 (2004).
- [29] S. Johnston, F. Vernay, B. Moritz, Z.-X. Shen, N. Nagaosa, J. Zaanen, and T. P. Devereaux, Systematic study of electron-phonon coupling to oxygen modes across the cuprates, *Phys. Rev. B* **82**, 064513 (2010).
- [30] Y. Wang, Z. Chen, T. Shi, B. Moritz, Z.-X. Shen, and T. P. Devereaux, Phonon-mediated long-range attractive interaction in one-dimensional cuprates, *Phys. Rev. Lett.* **127**, 197003 (2021).
- [31] B. Rosenstein and B. Y. Shapiro, Apical oxygen vibrations dominant role in  $d$ -wave cuprate superconductivity and its interplay with spin fluctuations, *J. Phys. Commun.* **5**, 055013 (2021).
- [32] Y. Fukuzumi, K. Mizuhashi, K. Takenaka, and S. Uchida, Universal superconductor-insulator transition and  $T_c$  depression in Zn-substituted high- $T_c$  cuprates in the underdoped regime, *Phys. Rev. Lett.* **76**, 684 (1996).
- [33] H. Eisaki, N. Kaneko, D. L. Feng, A. Damascelli, P. K. Mang, K. M. Shen, Z.-X. Shen, and M. Greven, Effect of chemical inhomogeneity in bismuth-based copper oxide superconductors, *Phys. Rev. B* **69**, 064512 (2004).
- [34] H. Hobou, S. Ishida, K. Fujita, M. Ishikado, K. M. Kojima, H. Eisaki, and S. Uchida, Enhancement of the superconducting critical temperature in  $\text{Bi}_2\text{Sr}_2\text{CaCu}_2\text{O}_{8+\delta}$  by controlling disorder outside  $\text{CuO}_2$  planes, *Phys. Rev. B* **79**, 064507 (2009).
- [35] S. Kim, X. Chen, W. Fitzhugh, and X. Li, Apical charge flux-modulated in-plane transport properties of cuprate superconductors, *Phys. Rev. Lett.* **121**, 157001 (2018).
- [36] V. Stanev, C. Oses, A. G. Kusne, E. Rodriguez, J. Paglione, S. Curtarolo, and I. Takeuchi, Machine learning modeling of superconducting critical temperature, *npj Comput. Mater.* **4**, 1 (2018).



- [37] D. Lee, D. You, D. Lee, X. Li, and S. Kim, Machine-learning-guided prediction models of critical temperature of cuprates, *J. Phys. Chem. Lett.* **12**, 6211 (2021).
- [38] Y. Wang, T. Su, Y. Cui, X. Ma, X. Zhou, Y. Wang, S. Hu, and W. Ren, Cuprate superconducting materials above liquid nitrogen temperature from machine learning, *RSC Advances* **13**, 19836 (2023).
- [39] P. Prelovšek and A. Ramšak, Spin-fluctuation mechanism of superconductivity in cuprates, *Phys. Rev. B* **72**, 012510 (2005).
- [40] Y. Wang and A. Chubukov, Charge-density-wave order with momentum  $(2q, 0)$  and  $(0, 2q)$  within the spin-fermion model: Continuous and discrete symmetry breaking, preemptive composite order, and relation to pseudogap in hole-doped cuprates, *Phys. Rev. B* **90**, 035149 (2014).
- [41] M. A. Metlitski and S. Sachdev, Quantum phase transitions of metals in two spatial dimensions. II. spin density wave order, *Phys. Rev. B* **82**, 075128 (2010).
- [42] F. Onufrieva and P. Pfeuty, Superconducting pairing through the spin resonance mode in high-temperature cuprate superconductors, *Phys. Rev. Lett.* **102**, 207003 (2009).
- [43] F. Onufrieva and P. Pfeuty, Low-doping anomalies in high- $T_c$  cuprate superconductors as evidence of a spin-fluctuation-mediated superconducting state, *Phys. Rev. Lett.* **109**, 257001 (2012).
- [44] S. M. O'Mahony, W. Ren, W. Chen, Y. X. Chong, X. Liu, H. Eisaki, S. Uchida, M. H. Hamidian, and J. C. Séamus Davis, On the electron pairing mechanism of copper-oxide high temperature superconductivity, *Proc. Natl. Acad. Sci.* **119**, 37 (2022).
- [45] S. Jiang, D. J. Scalapino, and S. R. White, Ground-state phase diagram of the  $t - t' - J$  model, *Proc. Natl. Acad. Sci. U.S.A.* **118**, e2109978118 (2021).
- [46] C. Weber, T. Giamarchi, and C. M. Varma, Phase diagram of a three-orbital model for high- $T_c$  cuprate superconductors, *Phys. Rev. Lett.* **112**, 117001 (2014).
- [47] N. Kowalski, S. S. Dash, P. Sémon, D. Sénéchal, and A.-M. Tremblay, Oxygen hole content, charge-transfer gap, covalency, and cuprate superconductivity, *Proc. Natl. Acad. Sci. USA* **118**, e2106476118 (2021).
- [48] D. Rybicki, M. Jurkutat, S. Reichardt, C. Kapusta, and J. Haase, Perspective on the phase diagram of cuprate high-temperature superconductors, *Nat. Commun.* **7**, 11413 (2016).
- [49] S. Jiang, D. J. Scalapino, and S. R. White, Density matrix renormalization group based downfolding of the three-band Hubbard model: Importance of density-assisted hopping, *Phys. Rev. B* **108**, L161111 (2023).
- [50] V. J. Emery, Theory of high- $T_c$  superconductivity in oxides, *Phys. Rev. Lett.* **58**, 2794 (1987).
- [51] See Supplemental Material at <http://link.aps.org/supplemental/10.1103/PhysRevB.109.L081115> for detailed definitions of all quantities, derivation of the transformed Hamiltonian that we use, and a comprehensive presentation of results (including illustrative figures and tables summarizing the predictor variables that we study). The Supplemental Material also contains Refs. [18,53].
- [52] N. Marzari, A. A. Mostofi, J. R. Yates, I. Souza, and D. Vanderbilt, Maximally localized wannier functions: Theory and applications, *Rev. Mod. Phys.* **84**, 1419 (2012).
- [53] See Supplemental Material in Ref. [18].
- [54] S. Lebegue, T. Björkman, M. Klintonberg, R. M. Nieminen, and O. Eriksson, Two-dimensional materials from data filtering and *ab initio* calculations, *Phys. Rev. X* **3**, 031002 (2013).
- [55] H. C. Herper, T. Ahmed, J. M. Wills, I. Di Marco, T. Björkman, D. Iuşan, A. V. Balatsky, and O. Eriksson, Combining electronic structure and many-body theory with large databases: A method for predicting the nature of  $4f$  states in Ce compounds, *Phys. Rev. Mater.* **1**, 033802 (2017).
- [56] U. Kumar, H. W. Kim, S. Singh, S. B. Cho, and H. Ko, Designing Pr-based advanced photoluminescent materials using machine learning and density functional theory, *J. Mater. Sci.* **59**, 1433 (2024).
- [57] K. Lejaeghere, G. Bihlmayer, T. Björkman, P. Blaha, S. Blügel, V. Blum, D. Caliste, I. E. Castelli, S. J. Clark, A. D. Corso, S. de Gironcoli, T. Deutsch, J. K. Dewhurst, I. D. Marco, C. Draxl, M. Duřák, O. Eriksson, J. A. Flores-Livas, K. F. Garrity, L. Genovese *et al.*, Reproducibility in density functional theory calculations of solids, *Science* **351**, aad3000 (2016).
- [58] F. Aryasetiawan and F. Nilsson, *Downfolding Methods in Many-Electron Theory* (AIP Publishing LLC Melville, New York, 2022).
- [59] P. Hansmann, N. Parragh, A. Toschi, G. Sangiovanni, and K. Held, Importance of  $d$ - $p$  coulomb interaction for high  $T_c$  cuprates and other oxides, *New J. Phys.* **16**, 033009 (2014).

# Supplemental Material: Simple predictors of $T_c$ in superconducting cuprates and the role of interactions between effective Wannier orbitals in the $d - p$ 3-band model

Jakša Vučičević<sup>1</sup> and Michel Ferrero<sup>2,3</sup>

<sup>1</sup>*Scientific Computing Laboratory, Center for the Study of Complex Systems,*

*Institute of Physics Belgrade, University of Belgrade, Pregrevica 118, 11080 Belgrade, Serbia*

<sup>2</sup>*CPHT, CNRS, Ecole Polytechnique, Institut Polytechnique de Paris, Route de Saclay, 91128 Palaiseau, France*

<sup>3</sup>*Collège de France, 11 place Marcelin Berthelot, 75005 Paris, France*

(Dated: February 2, 2024)

## I. MODEL HAMILTONIAN, TRANSFORMATION TO WANNIER SPACE, AND SYMMETRIES

### A. Non-interacting part

We start from the Hamiltonian written in the basis of  $d, p_x, p_y$ -orbitals (denoted by  $l = 0, 1, 2$ , respectively). For the sake of convenience, we define a row-vector of creation operators

$$\Psi_{\sigma, \mathbf{r}}^\dagger = (c_{l=0, \sigma, \mathbf{r}}^\dagger, c_{l=1, \sigma, \mathbf{r}}^\dagger, c_{l=2, \sigma, \mathbf{r}}^\dagger) \quad (1)$$

where  $\mathbf{r}$  denotes the position of the unit cell (set to the position of the  $d$ -orbital within the unit cell) and  $\sigma$  is the spin projection. The non-interacting part of the Hamiltonian reads

$$\hat{H} = \sum_{\sigma, \mathbf{r}, \mathbf{r}'} \Psi_{\sigma, \mathbf{r}}^\dagger \mathbf{h}_{\mathbf{r}, \mathbf{r}'} \Psi_{\sigma, \mathbf{r}'} \quad (2)$$

where

$$\mathbf{h}_{\mathbf{r}, \mathbf{r}'} = \begin{pmatrix} \varepsilon_d \delta_{\mathbf{r}, \mathbf{r}'} & t_{pd}(\delta_{\mathbf{r}, \mathbf{r}'} - \delta_{\mathbf{r} + \mathbf{e}_x, \mathbf{r}'}) & t_{pd}(\delta_{\mathbf{r}, \mathbf{r}'} - \delta_{\mathbf{r} + \mathbf{e}_y, \mathbf{r}'}) \\ t_{pd}(\delta_{\mathbf{r}, \mathbf{r}'} - \delta_{\mathbf{r} - \mathbf{e}_x, \mathbf{r}'}) & \varepsilon_p \delta_{\mathbf{r}, \mathbf{r}'} + t'_{pp}(\delta_{\mathbf{r} + \mathbf{e}_x, \mathbf{r}'} + \delta_{\mathbf{r} - \mathbf{e}_x, \mathbf{r}'}) & t_{pp}(\delta_{\mathbf{r}, \mathbf{r}'} - \delta_{\mathbf{r} + \mathbf{e}_y, \mathbf{r}'} - \delta_{\mathbf{r} - \mathbf{e}_x, \mathbf{r}'} + \delta_{\mathbf{r} - \mathbf{e}_x + \mathbf{e}_y, \mathbf{r}'}) \\ t_{pd}(\delta_{\mathbf{r}, \mathbf{r}'} - \delta_{\mathbf{r} - \mathbf{e}_y, \mathbf{r}'}) & t_{pp}(\delta_{\mathbf{r}, \mathbf{r}'} - \delta_{\mathbf{r} - \mathbf{e}_y, \mathbf{r}'} - \delta_{\mathbf{r} + \mathbf{e}_x, \mathbf{r}'} + \delta_{\mathbf{r} + \mathbf{e}_x - \mathbf{e}_y, \mathbf{r}'}) & \varepsilon_p \delta_{\mathbf{r}, \mathbf{r}'} + t'_{pp}(\delta_{\mathbf{r} + \mathbf{e}_y, \mathbf{r}'} + \delta_{\mathbf{r} - \mathbf{e}_y, \mathbf{r}'}) \end{pmatrix} \quad (3)$$

and we define the unit vectors  $\mathbf{e}_x = (1, 0)$  and  $\mathbf{e}_y = (0, 1)$ , in units of the lattice spacing (distance between neighboring Cu nuclei). We can now apply the Fourier transform over the unit cells to bring the Hamiltonian into a block-diagonal form. This can be done in multiple ways, as there is a gauge freedom of choosing a  $\mathbf{k}$ -dependent phase in front of  $c_{l, \sigma, \mathbf{k}}^\dagger$  operators. We take the following convention:

$$c_{l, \sigma, \mathbf{k}}^\dagger = \frac{\varphi_{l, \mathbf{k}}}{\sqrt{N}} \sum_{\mathbf{r}} e^{i\mathbf{k} \cdot \mathbf{r}} c_{l, \sigma, \mathbf{r}}^\dagger, \quad c_{l, \sigma, \mathbf{k}} = \frac{\varphi_{l, \mathbf{k}}^*}{\sqrt{N}} \sum_{\mathbf{r}} e^{-i\mathbf{k} \cdot \mathbf{r}} c_{l, \sigma, \mathbf{r}} \quad (4)$$

$$c_{l, \sigma, \mathbf{r}}^\dagger = \frac{1}{\sqrt{N}} \sum_{\mathbf{k}} \varphi_{l, \mathbf{k}}^* e^{-i\mathbf{k} \cdot \mathbf{r}} c_{l, \sigma, \mathbf{k}}^\dagger, \quad c_{l, \sigma, \mathbf{r}} = \frac{1}{\sqrt{N}} \sum_{\mathbf{k}} \varphi_{l, \mathbf{k}} e^{i\mathbf{k} \cdot \mathbf{r}} c_{l, \sigma, \mathbf{k}} \quad (5)$$

with

$$\varphi_{l, \mathbf{k}} = \begin{cases} 1, & l = 0 \\ i \exp\left(-i \frac{k_x}{2}\right), & l = 1 \\ -i \exp\left(-i \frac{k_y}{2}\right), & l = 2 \end{cases} \quad (6)$$

This choice corresponds to doing the sum over the actual real-space positions of the given  $d, p_x$  or  $p_y$  orbitals, which are found at  $\mathbf{r}, \mathbf{r} - \mathbf{e}_x/2$  and  $\mathbf{r} - \mathbf{e}_y/2$ , respectively. The Fourier transformation Eq. 5 of each operator *a priori* leads to the following form

$$\hat{H} = \sum_{\sigma, \mathbf{k}, \mathbf{k}'} \Psi_{\sigma, \mathbf{k}}^\dagger \mathbf{h}_{\mathbf{k}, \mathbf{k}'} \Psi_{\sigma, \mathbf{k}'} \quad (7)$$

Note that the sums over  $\mathbf{r}, \mathbf{r}'$  have been absorbed into the matrix  $\mathbf{h}_{\mathbf{k}\mathbf{k}'}$ , so that it only depends on  $\mathbf{k}, \mathbf{k}'$ , corresponding to the momenta of the creation and annihilation operators to the left and to the right of the matrix. Let's evaluate each of the matrix elements of  $\mathbf{h}_{\mathbf{k}\mathbf{k}'}$ .

$$\begin{aligned} [\mathbf{h}_{\mathbf{k},\mathbf{k}'}]_{l=0,l'=0} &= \frac{\varepsilon_d \varphi_{0,\mathbf{k}} \varphi_{0,\mathbf{k}'}^*}{N} \sum_{\mathbf{r}\mathbf{r}'} \delta_{\mathbf{r}\mathbf{r}'} e^{i\mathbf{k}\cdot\mathbf{r}} e^{-i\mathbf{k}'\cdot\mathbf{r}'} \\ &= \varepsilon_d \frac{1}{N} \sum_{\mathbf{r}} e^{i(\mathbf{k}-\mathbf{k}')\cdot\mathbf{r}} \\ &= \varepsilon_d \delta_{\mathbf{k}\mathbf{k}'} \end{aligned} \quad (8)$$

$$\begin{aligned} [\mathbf{h}_{\mathbf{k},\mathbf{k}'}]_{l=0,l'=1} &= \frac{t_{pd} \varphi_{0,\mathbf{k}} \varphi_{1,\mathbf{k}'}^*}{N} \sum_{\mathbf{r}\mathbf{r}'} e^{i\mathbf{k}\cdot\mathbf{r}} e^{-i\mathbf{k}'\cdot\mathbf{r}'} (\delta_{\mathbf{r}\mathbf{r}'} - \delta_{\mathbf{r}+\mathbf{e}_x,\mathbf{r}'}) \\ &= t_{pd} \varphi_{1,\mathbf{k}'}^* (1 - e^{-ik'_x}) \frac{1}{N} \sum_{\mathbf{r}} e^{i(\mathbf{k}-\mathbf{k}')\cdot\mathbf{r}} \\ &= t_{pd} (-i)(e^{ik_x/2} - e^{-ik_x/2}) \delta_{\mathbf{k}\mathbf{k}'} \\ &= 2t_{pd} \sin \frac{k_x}{2} \delta_{\mathbf{k}\mathbf{k}'} \end{aligned} \quad (9)$$

$$\begin{aligned} [\mathbf{h}_{\mathbf{k},\mathbf{k}'}]_{l=1,l'=1} &= \varepsilon_p \delta_{\mathbf{k}\mathbf{k}'} + t'_{pp} \frac{\varphi_{1,\mathbf{k}} \varphi_{1,\mathbf{k}'}^*}{N} \sum_{\mathbf{r}\mathbf{r}'} e^{i\mathbf{k}\cdot\mathbf{r}} e^{-i\mathbf{k}'\cdot\mathbf{r}'} (\delta_{\mathbf{r}-\mathbf{e}_x,\mathbf{r}'} + \delta_{\mathbf{r}+\mathbf{e}_x,\mathbf{r}'}) \\ &= \varepsilon_p \delta_{\mathbf{k}\mathbf{k}'} + t'_{pp} (e^{ik_x} + e^{-ik'_x}) \frac{\varphi_{1,\mathbf{k}} \varphi_{1,\mathbf{k}'}^*}{N} \sum_{\mathbf{r}} e^{i(\mathbf{k}-\mathbf{k}')\cdot\mathbf{r}} \\ &= (\varepsilon_p + 2t'_{pp} \cos k_x) \delta_{\mathbf{k}\mathbf{k}'} \\ [\mathbf{h}_{\mathbf{k},\mathbf{k}'}]_{l=1,l'=2} &= t_{pp} \frac{\varphi_{1,\mathbf{k}} \varphi_{2,\mathbf{k}'}^*}{N} \sum_{\mathbf{r}\mathbf{r}'} e^{i\mathbf{k}\cdot\mathbf{r}} e^{-i\mathbf{k}'\cdot\mathbf{r}'} (\delta_{\mathbf{r}\mathbf{r}'} - \delta_{\mathbf{r}+\mathbf{e}_y,\mathbf{r}'} - \delta_{\mathbf{r}-\mathbf{e}_x,\mathbf{r}'} + \delta_{\mathbf{r}-\mathbf{e}_x+\mathbf{e}_y,\mathbf{r}'}) \\ &= t_{pp} \varphi_{1,\mathbf{k}} \varphi_{2,\mathbf{k}'}^* (1 - e^{-ik_y} - e^{ik_x} + e^{ik_x-ik_y}) \delta_{\mathbf{k}\mathbf{k}'} \\ &= t_{pp} i e^{-ik_x/2} i e^{ik_y/2} (1 - e^{-ik_y}) (1 - e^{ik_x}) \delta_{\mathbf{k}\mathbf{k}'} \\ &= -4t_{pp} \sin \frac{k_x}{2} \sin \frac{k_y}{2} \delta_{\mathbf{k}\mathbf{k}'} \end{aligned} \quad (10)$$

The rest of the terms can be obtained completely analogously. As all of the terms are proportional to  $\delta_{\mathbf{k}\mathbf{k}'}$ , we can drop the second index in  $\mathbf{h}_{\mathbf{k}\mathbf{k}'}$ , so we get

$$\hat{H}_0 = \sum_{\sigma,\mathbf{k}} \Psi_{\sigma,\mathbf{k}}^\dagger \mathbf{h}_{\mathbf{k}} \Psi_{\sigma,\mathbf{k}} \quad (11)$$

with  $\Psi_{\mathbf{k}}^\dagger = (c_{l=0,\sigma,\mathbf{k}}^\dagger, c_{l=1,\sigma,\mathbf{k}}^\dagger, c_{l=2,\sigma,\mathbf{k}}^\dagger)$ , and we have

$$\mathbf{h}_{\mathbf{k}} = \begin{pmatrix} \varepsilon_d & 2t_{pd} \sin \frac{k_x}{2} & -2t_{pd} \sin \frac{k_y}{2} \\ \text{H.c.} & \varepsilon_p + 2t'_{pp} \cos k_x & -4t_{pp} \sin \frac{k_x}{2} \sin \frac{k_y}{2} \\ \text{H.c.} & \text{H.c.} & \varepsilon_p + 2t'_{pp} \cos k_y \end{pmatrix}. \quad (12)$$

We can now diagonalize each block of the non-interacting Hamiltonian, to arrive at Eq.1 from the main text:

$$\hat{H}_0 = \sum_{\sigma,\alpha,\mathbf{k}} E_{\alpha,\mathbf{k}} d_{\alpha,\sigma,\mathbf{k}}^\dagger d_{\alpha,\sigma,\mathbf{k}} \quad (13)$$

where  $\alpha$  denotes the eigenbands, and the connection with previously defined operators is given in terms of the (transposed) basis-change matrix  $\mathbf{A}_{\mathbf{k}}$

$$d_{\alpha,\sigma,\mathbf{k}}^\dagger = \sum_l [\mathbf{A}_{\mathbf{k}}]_{\alpha,l} c_{l,\sigma,\mathbf{k}}^\dagger, \quad c_{l,\sigma,\mathbf{k}}^\dagger = \sum_\alpha [\mathbf{A}_{\mathbf{k}}^{-1}]_{l,\alpha} d_{\alpha,\sigma,\mathbf{k}}^\dagger \quad (14)$$

Here note that we use the transpose of the basis change matrix  $\mathbf{P}_{\mathbf{k}}^\top \equiv \mathbf{A}_{\mathbf{k}}$  only for the sake of convenience. The basis change is in general performed by  $\Psi_{\sigma,\mathbf{k}}^\dagger \mathbf{h}_{\mathbf{k}} \Psi_{\sigma,\mathbf{k}} \rightarrow (\Psi_{\sigma,\mathbf{k}}^\dagger \mathbf{P}_{\mathbf{k}})(\mathbf{P}_{\mathbf{k}}^{-1} \mathbf{h}_{\mathbf{k}} \mathbf{P}_{\mathbf{k}})(\mathbf{P}_{\mathbf{k}}^{-1} \Psi_{\sigma,\mathbf{k}})$ , but it must hold  $\mathbf{P}_{\mathbf{k}}^{-1} = (\mathbf{P}_{\mathbf{k}}^\top)^*$  because one must have  $d_{\alpha,\sigma,\mathbf{k}} = (d_{\alpha,\sigma,\mathbf{k}}^\dagger)^\dagger$ , and we check that it does.

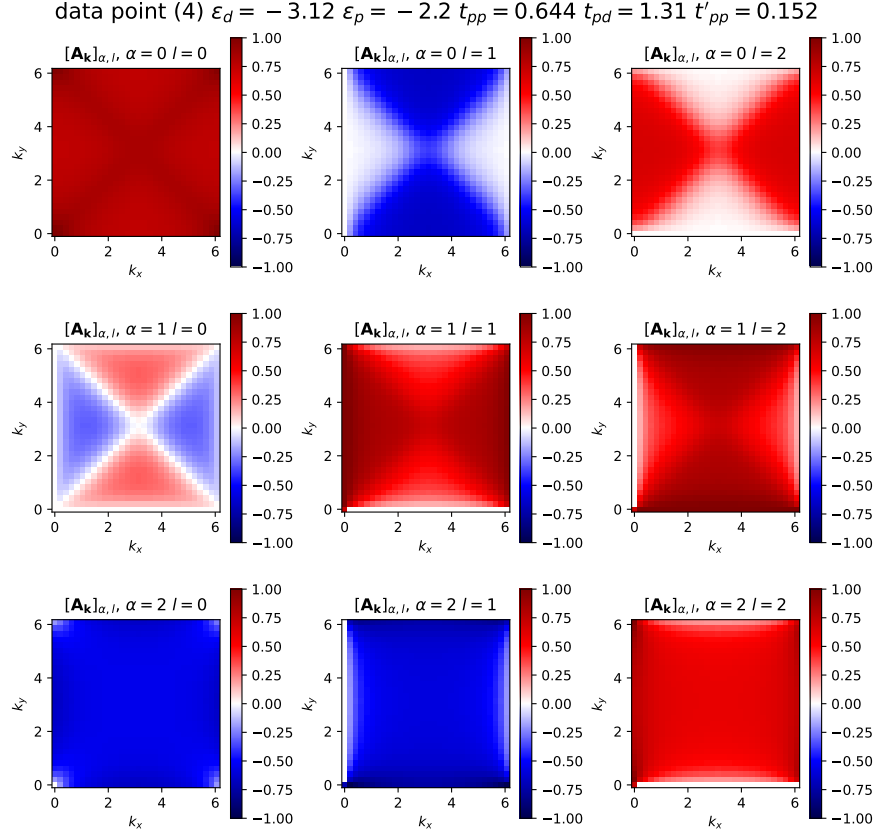


Figure 1. An example of the basis-transformation matrix  $\mathbf{A}_{\mathbf{k}}$ . Note that on this plot we discretize the Brillouin zone with only  $30 \times 30$  points, so that the edge cases are more easily inspected. To compute the hopping amplitudes we have used  $360 \times 360$  points.

There is a gauge freedom associated with the definition of  $d_{\alpha,\sigma,\mathbf{k}}^\dagger$  - eigenstates are defined only up to an overall phase. We make sure that all elements of  $[\mathbf{A}_{\mathbf{k}}]_{\alpha,l}$  are purely real, by subtracting any phase from the result we obtain in the following way:

$$[\mathbf{A}_{\mathbf{k}}]_{\alpha,l} \rightarrow [\mathbf{A}_{\mathbf{k}}]_{\alpha,l} e^{-i \arg[\mathbf{A}_{\mathbf{k}}]_{\alpha,l=\alpha}} \quad (15)$$

where the labelling  $\alpha = 0, 1, 2$  is ordered by increasing  $E_{\alpha,\mathbf{k}}$ . In our implementation, special care to ensure smoothness of  $[\mathbf{A}_{\mathbf{k}}]_{\alpha,l}$  was only needed for  $k_y = 0$  components, where  $[\mathbf{A}_{\mathbf{k}}]_{\alpha,l=\alpha} = 0$  and  $\arg[\mathbf{A}_{\mathbf{k}}]_{\alpha,l=\alpha}$  is undefined. Additionally, the point  $\mathbf{k} = (0, 0)$  is special because the eigenstates  $\alpha = 1$  and  $\alpha = 2$  are degenerate there - then any linear combination of these eigenstates is also an eigenstate. We resolve this by imposing that  $[\mathbf{A}_{\mathbf{k}}]_{\alpha,l}$  is smooth passing through  $\mathbf{k} = (0, 0)$  along the  $k_x = k_y$  direction. This gives us

$$[\mathbf{A}_{\mathbf{k}=(0,0)}]_{\alpha,l} = \frac{(-1)^{\delta_{\alpha,2}\delta_{l,1}}}{\sqrt{2}} \quad (16)$$

Finally, we can Fourier transform the operators acting on the eigenbands, and express the entire Hamiltonian in terms of

$$d_{\alpha,\sigma,\mathbf{r}}^\dagger = \frac{1}{\sqrt{N}} \sum_{\mathbf{k}} e^{-i\mathbf{k}\cdot\mathbf{r}} d_{\alpha,\sigma,\mathbf{k}}^\dagger, \quad d_{\alpha,\sigma,\mathbf{r}} = \frac{1}{\sqrt{N}} \sum_{\mathbf{k}} e^{i\mathbf{k}\cdot\mathbf{r}} d_{\alpha,\sigma,\mathbf{k}} \quad (17)$$

with the inverse transformation being

$$d_{\alpha,\sigma,\mathbf{k}}^\dagger = \frac{1}{\sqrt{N}} \sum_{\mathbf{r}} e^{i\mathbf{k}\cdot\mathbf{r}} d_{\alpha,\sigma,\mathbf{r}}^\dagger, \quad d_{\alpha,\sigma,\mathbf{k}} = \frac{1}{\sqrt{N}} \sum_{\mathbf{r}} e^{-i\mathbf{k}\cdot\mathbf{r}} d_{\alpha,\sigma,\mathbf{r}} \quad (18)$$

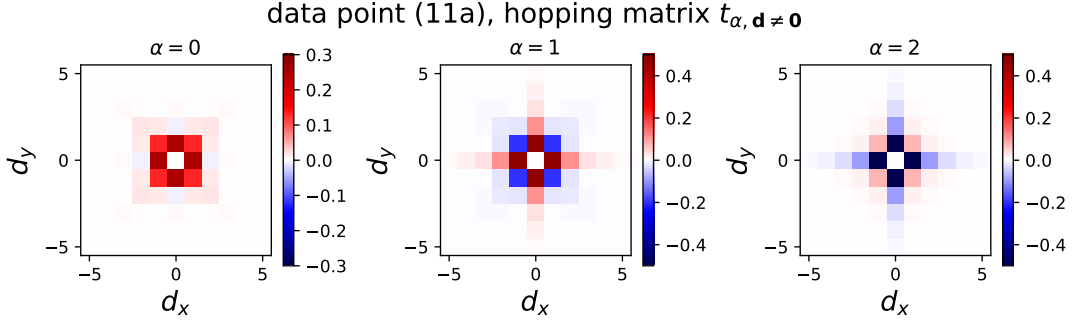


Figure 2. An example of the the hopping amplitudes for the 3 bands, computed with  $360 \times 360$  points in the Brillouin zone (Model A formulation).

The non-interacting part now becomes:

$$\begin{aligned} \hat{H}_0 &= \sum_{\alpha, \sigma, \mathbf{r}, \mathbf{r}'} d_{\alpha, \sigma, \mathbf{r}}^\dagger d_{\alpha, \sigma, \mathbf{r}'} \frac{1}{N} \sum_{\mathbf{k}} e^{-i\mathbf{k} \cdot (\mathbf{r}' - \mathbf{r})} E_{\alpha, \mathbf{k}} \\ &= \sum_{\alpha, \sigma, \mathbf{r}, \mathbf{d}} t_{\alpha, \mathbf{d}} d_{\alpha, \sigma, \mathbf{r}}^\dagger d_{\alpha, \sigma, \mathbf{r} + \mathbf{d}} \end{aligned} \quad (19)$$

where

$$t_{\alpha, \mathbf{d}} = \frac{1}{N} \sum_{\mathbf{k}} e^{-i\mathbf{k} \cdot \mathbf{d}} E_{\alpha, \mathbf{k}} \quad (20)$$

is the hopping matrix corresponding to the band  $\alpha$ . The term  $\mathbf{d} = \mathbf{0}$  has the physical meaning of the onsite energy of the Wannier orbital  $\alpha$ .

The connection between the original  $d, p_x, p_y$  orbitals ( $|l, \sigma, \mathbf{r}\rangle = c_{l, \sigma, \mathbf{r}}^\dagger |0\rangle$ ) and the Wannier orbitals ( $|\alpha, \sigma, \mathbf{r}\rangle = d_{\alpha, \sigma, \mathbf{r}}^\dagger |0\rangle$ ) is the following

$$|\alpha, \sigma, \mathbf{r}\rangle = \frac{1}{\sqrt{N}} \sum_{\mathbf{k}} e^{-i\mathbf{k} \cdot \mathbf{r}} |\alpha, \sigma, \mathbf{k}\rangle \quad (21)$$

$$= \frac{1}{\sqrt{N}} \sum_{\mathbf{k}} e^{-i\mathbf{k} \cdot \mathbf{r}} \sum_l [\mathbf{A}_{\mathbf{k}}]_{\alpha, l} |l, \sigma, \mathbf{k}\rangle \quad (22)$$

$$= \frac{1}{\sqrt{N}} \sum_{\mathbf{k}} e^{-i\mathbf{k} \cdot \mathbf{r}} \sum_l [\mathbf{A}_{\mathbf{k}}]_{\alpha, l} \frac{\varphi_{l, \mathbf{k}}}{\sqrt{N}} \sum_{\mathbf{r}'} e^{i\mathbf{k} \cdot \mathbf{r}'} |l, \sigma, \mathbf{r}'\rangle \quad (23)$$

$$= \sum_{\mathbf{r}', l} \left( \frac{1}{N} \sum_{\mathbf{k}} e^{-i\mathbf{k} \cdot (\mathbf{r} - \mathbf{r}')} [\mathbf{A}_{\mathbf{k}}]_{\alpha, l} \varphi_{l, \mathbf{k}} \right) |l, \sigma, \mathbf{r}'\rangle \quad (24)$$

$$= \sum_{\mathbf{r}', l} F_{\alpha, l, \mathbf{r} - \mathbf{r}'} |l, \sigma, \mathbf{r}'\rangle \quad (25)$$

where  $F_{\alpha, l, \mathbf{r}}$  is the inverse Fourier transform of the quantity  $[\mathbf{A}_{\mathbf{k}}]_{\alpha, l} \varphi_{l, \mathbf{k}}$ .



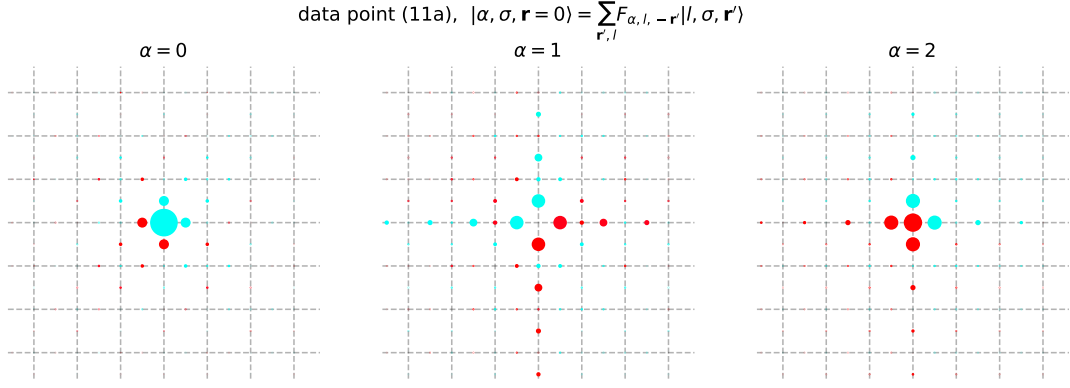


Figure 3. An example of the Wannier orbitals corresponding to the 3 bands, given in terms of the  $d, p_x, p_y$  orbitals (Model A formulation). The area of the point is the amplitude of  $F_{\alpha, l, -\mathbf{r}'}$ , the color is the phase ( $F_{\alpha, l, -\mathbf{r}'}$  is purely real, so the color here denotes the sign).

## B. Interacting part

Let's consider the interacting part (density-density interaction on each orbital  $l$ ):

$$\hat{H}_{\text{int}} = \frac{1}{2} \sum_{l, \sigma, \mathbf{r}} U_l c_{l, \sigma, \mathbf{r}}^\dagger c_{l, \sigma, \mathbf{r}} c_{l, \bar{\sigma}, \mathbf{r}}^\dagger c_{l, \bar{\sigma}, \mathbf{r}} \quad (26)$$

$$= \frac{1}{2} \sum_{l, \sigma} U_l \sum_{\mathbf{k}_1 \dots \mathbf{k}_4} \varphi_{l, \mathbf{k}_1}^* \varphi_{l, \mathbf{k}_2} \varphi_{l, \mathbf{k}_3}^* \varphi_{l, \mathbf{k}_4} c_{l, \sigma, \mathbf{k}_1}^\dagger c_{l, \sigma, \mathbf{k}_2} c_{l, \bar{\sigma}, \mathbf{k}_3}^\dagger c_{l, \bar{\sigma}, \mathbf{k}_4} \frac{1}{N^2} \sum_{\mathbf{r}} e^{-i(\mathbf{k}_1 - \mathbf{k}_2 + \mathbf{k}_3 - \mathbf{k}_4) \cdot \mathbf{r}} \quad (27)$$

$$= \frac{1}{2N} \sum_{l, \sigma} U_l \sum_{\mathbf{k} \mathbf{k}' \mathbf{q}} \varphi_{l, \mathbf{k} + \mathbf{q}}^* \varphi_{l, \mathbf{k}} \varphi_{l, \mathbf{k}'}^* \varphi_{l, \mathbf{k}' + \mathbf{q}} c_{l, \sigma, \mathbf{k} + \mathbf{q}}^\dagger c_{l, \sigma, \mathbf{k}} c_{l, \bar{\sigma}, \mathbf{k}'}^\dagger c_{l, \bar{\sigma}, \mathbf{k}' + \mathbf{q}} \quad (28)$$

We now introduce  $\mathcal{F}_{\mathbf{k} \mathbf{k}' \mathbf{q}, l} \equiv \varphi_{l, \mathbf{k} + \mathbf{q}}^* \varphi_{l, \mathbf{k}} \varphi_{l, \mathbf{k}'}^* \varphi_{l, \mathbf{k}' + \mathbf{q}}$  and transform into the eigenbasis of the non-interacting part:

$$\hat{H}_{\text{int}} = \frac{1}{2N} \sum_{\sigma, \alpha \beta \gamma \delta} \sum_{\mathbf{k} \mathbf{k}' \mathbf{q}} d_{\alpha, \sigma, \mathbf{k} + \mathbf{q}}^\dagger d_{\beta, \sigma, \mathbf{k}} d_{\gamma, \bar{\sigma}, \mathbf{k}'}^\dagger d_{\delta, \bar{\sigma}, \mathbf{k}' + \mathbf{q}} \sum_l U_l [\mathbf{A}_{\mathbf{k} + \mathbf{q}}^{-1}]_{l, \alpha} [\mathbf{A}_{\mathbf{k}}^{-1}]_{l, \beta}^* [\mathbf{A}_{\mathbf{k}'}^{-1}]_{l, \gamma} [\mathbf{A}_{\mathbf{k}' + \mathbf{q}}^{-1}]_{l, \delta}^* \mathcal{F}_{\mathbf{k} \mathbf{k}' \mathbf{q}, l} \quad (29)$$

The above expression is fully general, but we remind the reader that in our case  $[\mathbf{A}_{\mathbf{k}}^{-1}]$  is purely real. Also, in the case that is relevant to us,  $U_l = \delta_{l,0} U$ , and the corresponding  $\mathcal{F}_{\mathbf{k} \mathbf{k}' \mathbf{q}, l=0} = 1$ .

We can now introduce

$$V_{\mathbf{k} \mathbf{k}' \mathbf{q}}^{\alpha \beta \gamma \delta} \equiv \sum_l U_l [\mathbf{A}_{\mathbf{k} + \mathbf{q}}^{-1}]_{l, \alpha} [\mathbf{A}_{\mathbf{k}}^{-1}]_{l, \beta} [\mathbf{A}_{\mathbf{k}'}^{-1}]_{l, \gamma} [\mathbf{A}_{\mathbf{k}' + \mathbf{q}}^{-1}]_{l, \delta} \mathcal{F}_{\mathbf{k} \mathbf{k}' \mathbf{q}, l} \quad (30)$$

and finally we Fourier transform to real (i.e. Wannier) space

$$\hat{H}_{\text{int}} = \frac{1}{2N} \sum_{\sigma, \alpha \beta \gamma \delta} \sum_{\mathbf{k} \mathbf{k}' \mathbf{q}} V_{\mathbf{k} \mathbf{k}' \mathbf{q}}^{\alpha \beta \gamma \delta} d_{\alpha, \sigma, \mathbf{k} + \mathbf{q}}^\dagger d_{\beta, \sigma, \mathbf{k}} d_{\gamma, \bar{\sigma}, \mathbf{k}'}^\dagger d_{\delta, \bar{\sigma}, \mathbf{k}' + \mathbf{q}} \quad (31)$$

$$= \frac{1}{2N^3} \sum_{\sigma, \alpha \beta \gamma \delta} \sum_{\mathbf{r}_1 \dots \mathbf{r}_4} d_{\alpha, \sigma, \mathbf{r}_1}^\dagger d_{\beta, \sigma, \mathbf{r}_2} d_{\gamma, \bar{\sigma}, \mathbf{r}_3}^\dagger d_{\delta, \bar{\sigma}, \mathbf{r}_4} \sum_{\mathbf{k} \mathbf{k}' \mathbf{q}} e^{i(\mathbf{k} + \mathbf{q}) \cdot \mathbf{r}_1} e^{-i\mathbf{k} \cdot \mathbf{r}_2} e^{i\mathbf{k}' \cdot \mathbf{r}_3} e^{-i(\mathbf{k}' + \mathbf{q}) \cdot \mathbf{r}_4} V_{\mathbf{k} \mathbf{k}' \mathbf{q}}^{\alpha \beta \gamma \delta} \quad (32)$$

$$= \frac{1}{2} \sum_{\sigma, \alpha \beta \gamma \delta} \sum_{\mathbf{r}_1 \dots \mathbf{r}_4} d_{\alpha, \sigma, \mathbf{r}_1}^\dagger d_{\beta, \sigma, \mathbf{r}_2} d_{\gamma, \bar{\sigma}, \mathbf{r}_3}^\dagger d_{\delta, \bar{\sigma}, \mathbf{r}_4} \frac{1}{N^3} \sum_{\mathbf{k} \mathbf{k}' \mathbf{q}} e^{-i\mathbf{k} \cdot (\mathbf{r}_2 - \mathbf{r}_1)} e^{-i\mathbf{k}' \cdot (\mathbf{r}_4 - \mathbf{r}_3)} e^{-i\mathbf{q} \cdot (\mathbf{r}_4 - \mathbf{r}_1)} V_{\mathbf{k} \mathbf{k}' \mathbf{q}}^{\alpha \beta \gamma \delta} \quad (33)$$

We introduce the coupling constant in real space

$$V_{\mathbf{d} \mathbf{d}' \mathbf{u}}^{\alpha \beta \gamma \delta} = \frac{1}{N^3} \sum_{\mathbf{k} \mathbf{k}' \mathbf{q}} e^{-i\mathbf{k} \cdot \mathbf{d}} e^{-i\mathbf{k}' \cdot \mathbf{d}'} e^{-i\mathbf{q} \cdot \mathbf{u}} V_{\mathbf{k} \mathbf{k}' \mathbf{q}}^{\alpha \beta \gamma \delta} \quad (34)$$

with the identification  $\mathbf{d} = \mathbf{r}_2 - \mathbf{r}_1$ ,  $\mathbf{d} = \mathbf{r}_4 - \mathbf{r}_3$ , and  $\mathbf{u} = \mathbf{r}_4 - \mathbf{r}_1$  and finally write

$$\hat{H}_{\text{int}} = \frac{1}{2} \sum_{\sigma, \alpha \beta \gamma \delta} \sum_{\mathbf{r} \mathbf{d} \mathbf{d}' \mathbf{u}} V_{\mathbf{d} \mathbf{d}' \mathbf{u}}^{\alpha \beta \gamma \delta} d_{\alpha, \sigma, \mathbf{r}}^\dagger d_{\beta, \sigma, \mathbf{r} + \mathbf{d}} d_{\gamma, \bar{\sigma}, \mathbf{r} + \mathbf{u} - \mathbf{d}'}^\dagger d_{\delta, \bar{\sigma}, \mathbf{r} + \mathbf{u}} \quad (35)$$

The interactions in Eq. 35 are all possible 4-point interactions between two electrons of opposing spins. We list below the physical meaning of some couplings:

- $V_{000}^{\alpha \beta \gamma \delta}$  local coupling.
- $V_{000}^{\alpha \alpha \alpha \alpha}$  local density-density coupling in the band  $\alpha$ .
- $V_{\mathbf{d} \mathbf{d}' \mathbf{u}}^{\alpha \alpha \alpha \alpha}$  intraband coupling.
- $V_{\mathbf{d} \mathbf{d}' \mathbf{u}}^{\alpha \alpha \beta \gamma}$  assisted interband hybridization (assisted by an operator in  $\alpha$ -band; hybridization is from  $\gamma$  to  $\beta$  band).
- $V_{0,0,\mathbf{u}}^{\alpha \alpha \beta \beta}$  density-density coupling
- $V_{\mathbf{d},0,0}^{\alpha \alpha \beta \beta}$  density-assisted hopping in the  $\alpha$  band (assisted by the density in the  $\beta$  band).
- $V_{\mathbf{d},\mathbf{d},\mathbf{d}}^{\alpha \alpha \alpha \alpha}$  (intraband) pair-hopping
- $-V_{\mathbf{d},-\mathbf{d},0}^{\alpha \alpha \alpha \alpha}$   $xy$ -plane spin-spin interaction. This can be understood by commuting the operators  $\sum_{\sigma} d_{\alpha, \sigma, \mathbf{r}}^\dagger d_{\alpha, \sigma, \mathbf{r} + \mathbf{d}} d_{\alpha, \bar{\sigma}, \mathbf{r} + \mathbf{d}}^\dagger d_{\alpha, \bar{\sigma}, \mathbf{r}} = -\sum_{\sigma} d_{\alpha, \sigma, \mathbf{r}}^\dagger d_{\alpha, \bar{\sigma}, \mathbf{r}} d_{\alpha, \bar{\sigma}, \mathbf{r} + \mathbf{d}}^\dagger d_{\alpha, \sigma, \mathbf{r} + \mathbf{d}} = -(S_{\alpha, \mathbf{r}}^+ S_{\alpha, \mathbf{r} + \mathbf{d}}^- + S_{\alpha, \mathbf{r}}^- S_{\alpha, \mathbf{r} + \mathbf{d}}^+) = -2(S_{\alpha, \mathbf{r}}^x S_{\alpha, \mathbf{r} + \mathbf{d}}^x + S_{\alpha, \mathbf{r}}^y S_{\alpha, \mathbf{r} + \mathbf{d}}^y)$ , where  $S^x = \frac{1}{2}(S^+ + S^-)$  and  $S^y = \frac{1}{2i}(S^+ - S^-)$ .

### C. Symmetries

The first sanity check for the coupling constant comes from the requirement that the Hamiltonian is Hermitian. The coupling constant must satisfy:

$$V_{\mathbf{d} \mathbf{d}' \mathbf{u}}^{\alpha \beta \gamma \delta} = V_{-\mathbf{d}', -\mathbf{d}, -\mathbf{u}}^{\delta \gamma \beta \alpha} \quad (36)$$

and we check that it does.

We now restrict to  $U_l = \delta_{l,0} U$ . Under this assumption, with the shift  $\varepsilon_d \rightarrow \varepsilon_d - U/2$ , we can fully equivalently rewrite the interacting term as

$$\hat{H}_{\text{int}} = \frac{1}{2} \sum_{\sigma \sigma', \alpha \beta \gamma \delta} \sum_{\mathbf{r} \mathbf{d} \mathbf{d}' \mathbf{u}} V_{\mathbf{d} \mathbf{d}' \mathbf{u}}^{\alpha \beta \gamma \delta} d_{\alpha, \sigma, \mathbf{r}}^\dagger d_{\beta, \sigma, \mathbf{r} + \mathbf{d}} d_{\gamma, \sigma', \mathbf{r} + \mathbf{u} - \mathbf{d}'}^\dagger d_{\delta, \sigma', \mathbf{r} + \mathbf{u}} \quad (37)$$

Because of the shift in  $\varepsilon_d$ , the coupling constant  $V_{\mathbf{d} \mathbf{d}' \mathbf{u}}^{\alpha \beta \gamma \delta}$  (as well as  $t_{\alpha, \mathbf{d}}$ ) will be different. However, this rewriting of the Hamiltonian is manifestly spin-rotationally invariant. The rotation of the reference frame for the spin projection is in general performed by the following transformation

$$c_{\sigma}^\dagger = \sum_{\sigma'} [e^{\frac{i}{2} \theta \boldsymbol{\sigma}^\eta}]_{\sigma, \sigma'} c_{\sigma'}^\dagger = a_{\sigma \uparrow, \eta \theta} c_{\uparrow}^\dagger + b_{\sigma \downarrow, \eta \theta} c_{\downarrow}^\dagger, \quad c_{\sigma} = a_{\sigma \uparrow, \eta \theta}^* c_{\uparrow} + b_{\sigma \downarrow, \eta \theta}^* c_{\downarrow} \quad (38)$$

where  $\boldsymbol{\sigma}^\eta$  are the Pauli matrices,  $\eta = x, y, z$  is the axis of rotation, and  $\theta$  is the angle of rotation. We have checked numerically that a Hamiltonian term of the form

$$\sum_{\sigma \sigma'} c_{i, \sigma}^\dagger c_{j, \sigma} c_{k, \sigma'}^\dagger c_{l, \sigma'} \quad (39)$$

is invariant under transformations of the form Eq. 38, regardless of the orbital indices  $i, j, k, l$ . Similar can be shown for the hopping terms of the form

$$\sum_{\sigma} c_{i, \sigma}^\dagger c_{j, \sigma} \quad (40)$$

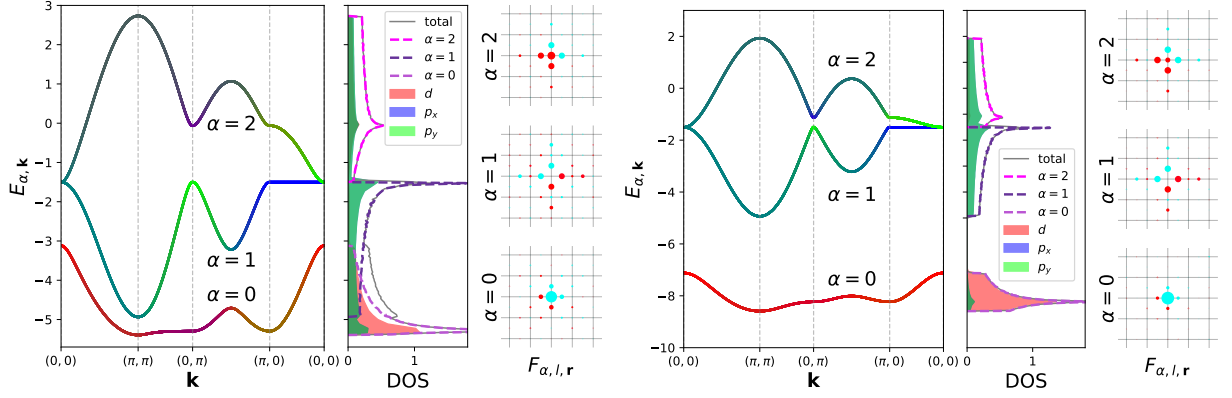


Figure 4. Illustration of the effect of the  $\varepsilon_d \rightarrow \varepsilon_d - U/2$  shift on the non-interacting Hamiltonian and the effective Wannier orbitals, data point (11a). Left: Model A, no shift, corresponding to Eq. 35 formulation of the interacting part; Right: Model B, with the shift, corresponding to Eq. 37 formulation of the interacting part.

Therefore, the Hamiltonian written as Eq. 37 (with the corresponding shift  $\varepsilon_d \rightarrow \varepsilon_d - U/2$  in the non-interacting part) is rotationally invariant, term by term. This cannot be said for the writing in terms of Eq. 35 and the original  $\varepsilon_d$ . The original Hamiltonian is spin-rotationally invariant (when rotation is applied to  $c_{l,\sigma,\mathbf{r}}^\dagger$  and  $c_{l,\sigma,\mathbf{r}}$ ), but, because of the non-local nature of the interaction Eq. 35, when rotations are applied to  $d_{\alpha,\sigma,\mathbf{r}}^\dagger$  and  $d_{\alpha,\sigma,\mathbf{r}}$ , this might yield same-spin interaction terms: the Hamiltonian written as Eq. 35 is not spin-rotationally invariant. We refer to the non-spin-symmetric Hamiltonian as the Model A, and to the spin-symmetric Hamiltonian as the Model B.

We finally look at the spatial symmetries of the coupling constant. We check how the coupling constant  $V_{\mathbf{d}\mathbf{d}'\mathbf{u}}^{\alpha\beta\gamma\delta}$  changes when square-lattice symmetry operations are applied to the arguments  $\mathbf{d}\mathbf{d}'\mathbf{u}$ . There are 8 symmetry operations for the square lattice, that we denote  $R_m(\mathbf{r})$ . The symmetry operations are  $x \rightarrow -x$ ,  $y \rightarrow -y$ ,  $x \leftrightarrow y$  and any combination of these. We find that

$$V_{\mathbf{d}\mathbf{d}'\mathbf{u}}^{\alpha\beta\gamma\delta} = \pm V_{R_m(\mathbf{d}), R_m(\mathbf{d}'), R_m(\mathbf{u})}^{\alpha\beta\gamma\delta}. \quad (41)$$

The minus sign only appears in off-diagonal interactions involving the band  $\alpha = 1$ , more precisely the assisted hybridizations into or from the band  $\alpha = 1$ . It turns out that the coupling constants  $V_{\mathbf{d}\mathbf{d}'\mathbf{u}}^{\alpha\beta\gamma\delta}$  with  $(\delta_{\alpha,1} + \delta_{\beta,1} + \delta_{\gamma,1} + \delta_{\delta,1}) \bmod 2 = 1$  exhibit  $d$ -wave symmetry, i.e. they change sign upon  $\pi/2$  rotation (around the  $z$ -axis) of the spatial indices  $\mathbf{d}, \mathbf{d}', \mathbf{u}$ . The change of sign upon rotation or swapping axes can be formulated as

$$V_{\mathbf{d}\mathbf{d}'\mathbf{u}}^{\alpha\beta\gamma\delta} = (-1)^{\delta_{\alpha,1} + \delta_{\beta,1} + \delta_{\gamma,1} + \delta_{\delta,1}} V_{(\pm d_y, \pm d_x), (\pm d'_y, \pm d'_x), (\pm u_y, \pm u_x)}^{\alpha\beta\gamma\delta}. \quad (42)$$

The absence of full square-lattice symmetry in our coupling constant is not surprising. The original model also does not have full lattice symmetry. This is already clear from the Hamiltonian Eq. 3. This has an effect on correlators of the form  $\rho_{ll',\mathbf{r}-\mathbf{r}'} = \langle c_{l,\sigma,\mathbf{r}}^\dagger c_{l',\sigma,\mathbf{r}'} \rangle$ . Indeed, the single-particle density matrix has full square-lattice symmetry only for  $l = l'$ . With  $l = 1, l' = 2$ ,  $\rho_{ll',\mathbf{r}}$  has  $d$ -wave symmetry. This is reflected in the coupling constants in our rewriting of the Emery model. However, the non-interacting part (i.e.  $t_{\alpha,\mathbf{d}}$ ) in our rewriting has full square-lattice symmetry, and so do all the intraband interactions  $V_{\mathbf{d}\mathbf{d}'\mathbf{u}}^{\alpha\alpha\alpha\alpha}$ . It is only a particular subset of the coupling constants that exhibits  $d$ -wave symmetry.

Finally, we observe numerically that

$$V_{\mathbf{d},-\mathbf{d},\mathbf{0}}^{\alpha\alpha\alpha\alpha} = V_{\mathbf{0},\mathbf{0},\mathbf{d}}^{\alpha\alpha\alpha\alpha} = V_{\mathbf{d},\mathbf{d},\mathbf{d}}^{\alpha\alpha\alpha\alpha}. \quad (43)$$

Some examples of spatial dependence of the interaction are given in Figures 5 and 6.

## II. RESULTS

We start from the Table 1 published in the Supplemental Material of Ref. 1 (i.e. Ref. 2) where Emery model parameters are summarized for 16 different compounds. For two 3-layer compounds, the parameters are given separately for the inner and outer layer. We list the parameters in Table I.

For the diagonalization of the non-interacting part and our rewriting of the Hamiltonian, only the difference  $\varepsilon_d - \varepsilon_p$  matters, not the two parameters independently. However, the values of  $\varepsilon_d$  must be additionally shifted to avoid double counting of

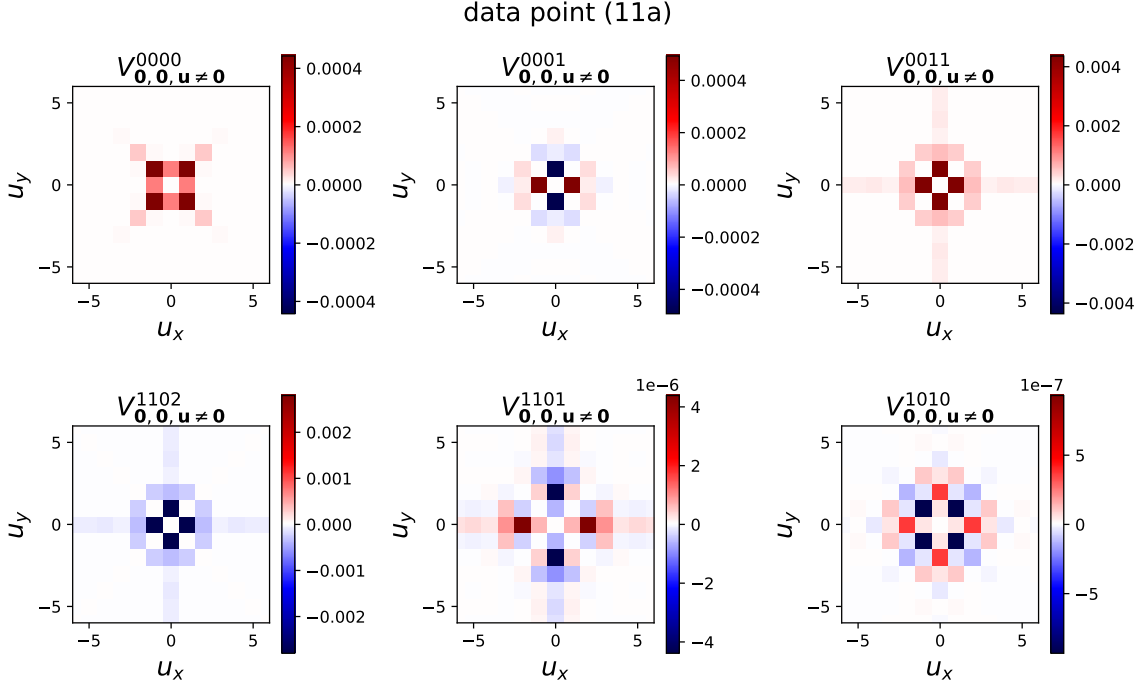


Figure 5. Illustration of the symmetry of  $V_{\mathbf{d}\mathbf{d}'\mathbf{u}}^{\alpha\beta\gamma\delta}$ , in Model A formulation. Most of the components have full square lattice-symmetry. The components representing assisted hybridization into and out of the band  $\alpha = 1$  have  $d$ -wave symmetry. All interactions are computed on a  $12 \times 12$  lattice. Some interactions have a longer range than is the size of the lattice, and in our analyses, we only focus on the short-distance components. Throughout the work,  $V_{\mathbf{d}\mathbf{d}'\mathbf{u}}^{\alpha\beta\gamma\delta}$  is expressed in the units of  $U$ .

Table I. The Table with Emery model parameters for different compounds that is the basis for this work (taken from Ref.2).

index	Compound	$\varepsilon_d - \varepsilon_p$ [eV]	$t_{pd}$ [eV]	$t_{pp}$ [eV]	$t'_{pp}$ [eV]	$T_c$ [K]
(1)	$\text{La}_2\text{CuO}_4$	2.61	1.39	0.64	0.103	38
(2)	$\text{Pb}_2\text{Sr}_2\text{YCu}_3\text{O}_8$	2.32	1.3	0.673	0.16	70
(3)	$\text{Ca}_2\text{CuO}_2\text{Cl}_2$	2.21	1.27	0.623	0.132	26
(4)	$\text{La}_2\text{CaCu}_2\text{O}_6$	2.2	1.31	0.644	0.152	45
(5)	$\text{Sr}_2\text{Nd}_2\text{NbCu}_2\text{O}_{10}$	2.1	1.25	0.612	0.144	28
(6)	$\text{Bi}_2\text{Sr}_2\text{CuO}_6$	2.06	1.36	0.677	0.153	24
(7)	$\text{YBa}_2\text{Cu}_3\text{O}_7$	2.05	1.28	0.673	0.15	93
(8)	$\text{HgBa}_2\text{CaCu}_2\text{O}_6$	1.93	1.28	0.663	0.187	127
(9)	$\text{HgBa}_2\text{CuO}_4$	1.93	1.25	0.649	0.161	90
(10)	$\text{Sr}_2\text{CuO}_2\text{Cl}_2$	1.87	1.15	0.59	0.14	30
(11a)	$\text{HgBa}_2\text{Ca}_2\text{Cu}_3\text{O}_8(\text{outer})$	1.87	1.29	0.674	0.184	135
(11b)	$\text{HgBa}_2\text{Ca}_2\text{Cu}_3\text{O}_8(\text{inner})$	1.94	1.29	0.656	0.167	135
(12)	$\text{Tl}_2\text{Ba}_2\text{CuO}_6$	1.79	1.27	0.63	0.15	90
(13)	$\text{LaBa}_2\text{Cu}_3\text{O}_7$	1.77	1.13	0.62	0.188	79
(14)	$\text{Bi}_2\text{Sr}_2\text{CaCu}_2\text{O}_8$	1.64	1.34	0.647	0.133	95
(15)	$\text{Tl}_2\text{Ba}_2\text{CaCu}_2\text{O}_8$	1.27	1.29	0.638	0.14	110
(16a)	$\text{Bi}_2\text{Sr}_2\text{Ca}_2\text{Cu}_3\text{O}_{10}(\text{outer})$	1.24	1.32	0.617	0.159	108
(16b)	$\text{Bi}_2\text{Sr}_2\text{Ca}_2\text{Cu}_3\text{O}_{10}(\text{inner})$	2.24	1.32	0.678	0.198	108

correlation effects. We follow the prescription from Ref. 1, where a fixed double-counting shift  $E_{dc} = 3.12$  eV was subtracted from  $\varepsilon_d$ , independently of compound (and, in their calculations, independently of doping).

Based on the model parameters from the Table I, we compute the following, for each of the compounds:

- the total bandwidth  $D = \max_{\mathbf{k},\alpha} E_{\alpha,\mathbf{k}} - \min_{\mathbf{k},\alpha} E_{\alpha,\mathbf{k}}$
- the bandwidths of each band  $D_\alpha = \max_{\mathbf{k}} E_{\alpha,\mathbf{k}} - \min_{\mathbf{k}} E_{\alpha,\mathbf{k}}$
- the overlap/gap between the bottom two bands  $O = \max_{\mathbf{k}} E_{\alpha=0,\mathbf{k}} - \min_{\mathbf{k}} E_{\alpha=1,\mathbf{k}}$

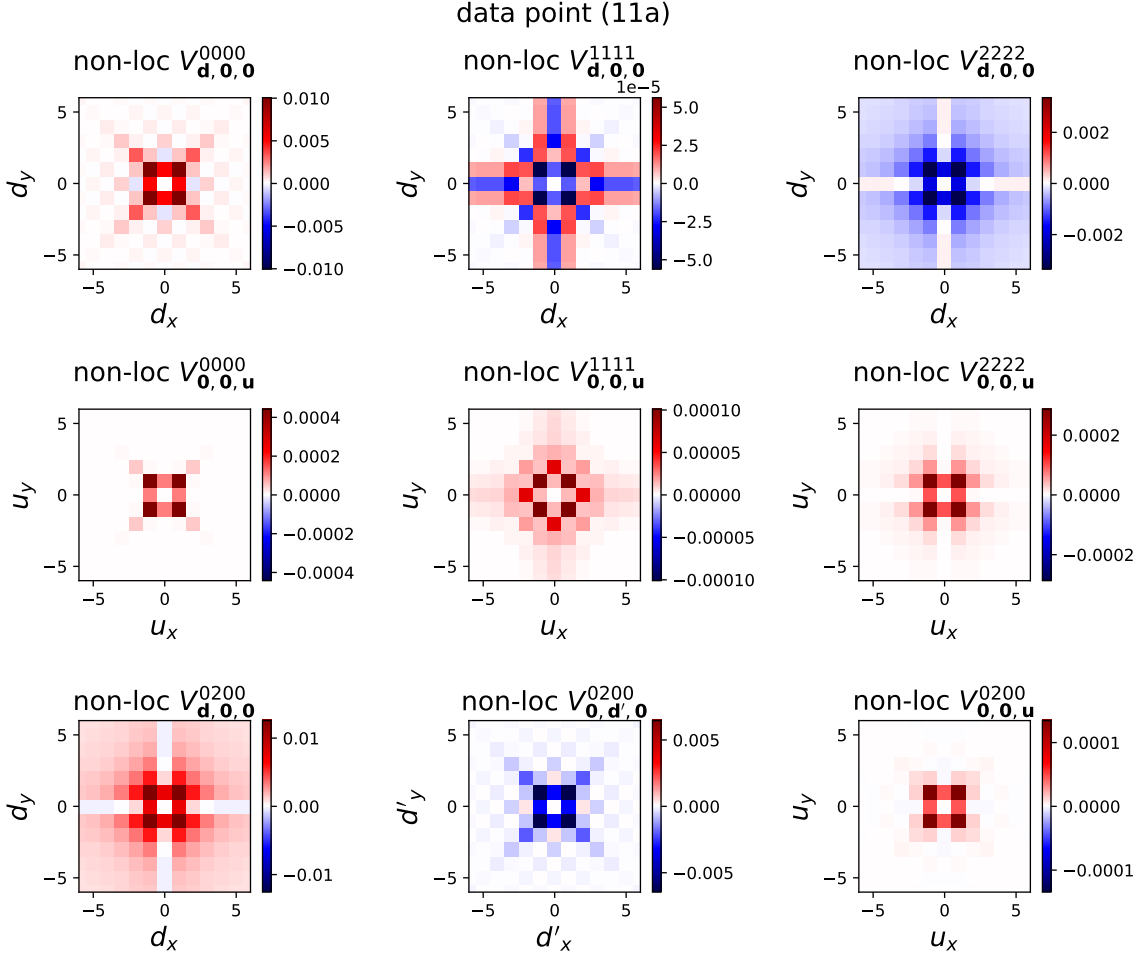


Figure 6. Illustration of the spatial dependence of relevant interaction components (Model A formulation).

- the gap between  $\alpha = 0$  and  $\alpha = 1$  bands at  $\mathbf{k}$ -points  $(0, 0)$  and  $(\pi, \pi)$
- the gap between  $\alpha = 1$  and  $\alpha = 2$  bands at  $\mathbf{k} = (0, \pi)$
- the short-distance hoppings  $t_\alpha \equiv t_{\alpha, \mathbf{d}=(1,0)}$ ,  $t'_\alpha \equiv t_{\alpha, \mathbf{d}=(1,1)}$ ,  $t''_\alpha \equiv t_{\alpha, \mathbf{d}=(2,0)}$
- the ratios  $t'_\alpha/t_\alpha$  and  $t''_\alpha/t_\alpha$
- the total amount of  $d$ -character in the  $\alpha = 2$  band,  $\frac{1}{N} \sum_{\mathbf{k}} |[\mathbf{A}_{\mathbf{k}}]_{\alpha=2, l=0}|^2$
- the total amount of  $p$ -character in the  $\alpha = 0$  band,  $\frac{1}{N} \sum_{l=1,2} \sum_{\mathbf{k}} |[\mathbf{A}_{\mathbf{k}}]_{\alpha=0, l}|^2$
- the maximum and the minimum value in  $V_{\mathbf{d}\mathbf{d}'\mathbf{u}}^{\alpha\beta\gamma\delta}$
- the minimum intraband coupling constant for each band,  $\min_{\mathbf{d}\mathbf{d}'\mathbf{u}} V_{\mathbf{d}\mathbf{d}'\mathbf{u}}^{\alpha\alpha\alpha\alpha}$
- the local density-density interaction in each band  $V_{000}^{\alpha\alpha\alpha\alpha}$
- the nearest ( $\mathbf{d} = (1, 0)$ ) and the next-nearest neighbor ( $\mathbf{d} = (1, 1)$ ) assisted hopping  $V_{\mathbf{d},00}^{\alpha\alpha\alpha\alpha}$  and the spin-spin interaction  $V_{\mathbf{d},-\mathbf{d},0}^{\alpha\alpha\alpha\alpha}$  in each of the bands

Throughout the paper, we give  $V_{\mathbf{d}\mathbf{d}'\mathbf{u}}^{\alpha\beta\gamma\delta}$  in units of  $U$  (the estimate is  $U = 8$  eV for all compounds), while the rest of the parameters are given in units of eV.

After computing the above parameters, we do a linear fit of  $T_c$  to each of the parameters individually, and compute the std. deviation. The results are summarized in Table II. We compare the results for the non-spin-symmetric (Model A, corresponding



to Eq. 35; see Table II.A) and spin-symmetric Hamiltonians (Model B, corresponding to Eq. 37 and a shift  $\varepsilon_d \rightarrow \varepsilon_d - U/2$ ; see Table II.B). We also show the difference in results depending on whether points (1),(6) and (11b) are excluded or not (Table II.A.1 vs. Table II.A.2, and Table II.B.1 vs. Table II.B.2).

Table II. Top list of best single-parameter predictors of  $T_c$ .

Table II.A. Model A (non spin-rotationally symmetric Hamiltonian).

Table II.A.1. All data points included.			Table II.A.2. Points (1),(6) and (11b) excluded.		
rank	parameter	std. dev. $\sigma$	rank	parameter	std. dev. $\sigma$
1	$t'/t$	27.4927	1	$t'_{\alpha=2}$	21.7034
2	$t'_{\alpha=2}$	27.5412	2	$t''_{\alpha=2}$	23.3602
3	$t_{\alpha=1}$	29.5241	3	$t_{\alpha=1}$	23.6241
4	$V_{(1,0),(-1,0),0}^{0000}$	29.6248	4	$t''_{\alpha=1}$	24.0605
5	$t''_{\alpha=1}$	29.9415	5	$D_{\alpha=1}$	24.8676
6	$D_{\alpha=1}$	30.2950	6	$t'/t$	24.9718
7	$t'_{pp}$	30.5228	7	$V_{(1,0),(-1,0),0}^{0000}$	26.9649
8	$V_{(1,0),0,0}^{0000}$	30.8614	8	$t'_{pp}$	27.0259
9	$t'_{\alpha=2}/t_{\alpha=2}$	31.4597	9	$V_{(1,0),0,0}^{0000}$	27.5327
10	$E_{\mathbf{k}=(0,0)}^{\alpha=1} - E_{\mathbf{k}=(0,0)}^{\alpha=0}$	31.7394	10	$t'_{pp}$	28.1611

Table II.B. Model B (spin-rotationally symmetric Hamiltonian).

Table II.B.1. All data points included.			Table II.B.2. Points (1),(6) and (11b) excluded.		
rank	parameter	std. dev. $\sigma$	rank	parameter	std. dev. $\sigma$
1	$t'_{\alpha=2}$	26.1661	1	$t'_{\alpha=2}$	16.7233
2	$t'/t$	27.4927	2	$D_{\alpha=1}$	24.8676
3	$D_{\alpha=1}$	30.2950	3	$t_{\alpha=1}$	24.8911
4	$t_{\alpha=1}$	30.4133	4	$t'/t$	24.9718
5	$t'_{pp}$	30.5228	5	$D$	26.6340
6	$E_{\mathbf{k}=(0,0)}^{\alpha=1} - E_{\mathbf{k}=(0,0)}^{\alpha=0}$	31.7394	6	$t''_{\alpha=2}$	26.7989
7	$t''_{\alpha=2}/t_{\alpha=2}$	32.8284	7	$t''_{\alpha=1}$	26.9456
8	$t''_{\alpha=1}$	33.0235	8	$t'_{pp}$	27.0259
9	$t''_{\alpha=0}$	33.0360	9	$t'_{pp}$	28.1611
10	$\varepsilon_d - \varepsilon_p$	33.1773	10	$t'_{\alpha=1}$	28.2256

Next, we look at all possible linear combinations of two parameters,  $P(p_1, p_2) = c_1 p_1 + c_2 p_2$ , with  $c_1^2 + c_2^2 = 1$ . For each pair  $(p_1, p_2)$  we minimize the std. deviation  $\sigma$  w.r.t.  $c_1$  and  $c_2$ , and sort the pairs according to the minimal  $\sigma$ . The results are given in Table III.

Finally, we look at all possible linear combinations of three parameters,  $P(p_1, p_2, p_3) = c_1 p_1 + c_2 p_2 + c_3 p_3$ , with  $c_1^2 + c_2^2 + c_3^2 = 1$ , and repeat the optimization procedure. The top lists of best 3-parameter predictors, based on the models A and B, are given in Table IV. We note that there are about 30 3-parameter predictors based on model B parameters that are better than the best 3-parameter predictor based on model A parameters. Finally, we identify the parameters which appear the most in the linear combinations which constitute the top 100 predictors. The results for model A and B, separately, are given in the Table V.

The results are illustrated in Fig. 7. We note that the two best 3-parameter predictors (in both Model A and Model B) differ by only one parameter, and yield a very similar  $\sigma$ . The parameters that differ, therefore, must correlate well, which we check in the bottom row.

We now restrict to the original parameters of the Emery model, i.e.  $\varepsilon_d - \varepsilon_p$ ,  $t_{pd}$ ,  $t_{pp}$  and  $t'_{pp}$ , and the  $t'/t$  discussed in Weber *et al.*. We show corresponding fits in Fig. 8. The two best 2-parameter predictors and the best 3-parameter predictor are given in the bottom row. In the panel *g*, we show how the std. deviation depends on the choice of coefficients  $c_{1..3}$ , for the linear combination of  $\varepsilon_d - \varepsilon_p$ ,  $t_{pp}$  and  $t'_{pp}$ , which yields the best fit of  $T_c$ . The collapse of the data points that we can obtain this way is noticeably worse than what we can do with the parameters of the models A or B.

In the end, we want to estimate the probability that the scaling with  $T_c$  we get for some parameters and their linear combinations is due to pure chance. We repeat the entire procedure with all parameters and variables (except  $T_c$ ) replaced by random numbers between 0 and 1. We also exclude the points (1),(6) and (11b). We get the following results:

- best single-parameter predictor:  $\sigma \approx 27K$
- best two-parameter linear-combination:  $\sigma \approx 19K \approx 27/\sqrt{2}$
- best three-parameter linear-combination:  $\sigma \approx 15K \approx 27/\sqrt{3}$

Table III. Best linear combinations of two parameters.

rank	$p_1$	$p_2$	$c_1$	$c_2$	std. dev. $\sigma$
1	$\min_{\mathbf{d}, \mathbf{d}', \mathbf{u}} V_{\mathbf{d}, \mathbf{d}', \mathbf{u}}^{\alpha\beta\gamma\delta} = V_{\mathbf{0}, \mathbf{0}, \mathbf{0}}^{0020}$	$t''_{\alpha=1}$	-0.422894	0.906179	5.4231
2	$\min_{\mathbf{d}, \mathbf{d}', \mathbf{u}} V_{\mathbf{d}, \mathbf{d}', \mathbf{u}}^{\alpha\beta\gamma\delta} = V_{\mathbf{0}, \mathbf{0}, \mathbf{0}}^{0020}$	$t_{\alpha=1}$	-0.894717	0.446634	5.7230
3	$D_{\alpha=1}$	$\min_{\mathbf{d}, \mathbf{d}', \mathbf{u}} V_{\mathbf{d}, \mathbf{d}', \mathbf{u}}^{\alpha\beta\gamma\delta} = V_{\mathbf{0}, \mathbf{0}, \mathbf{0}}^{0020}$	0.060565	-0.998164	5.7304
4	$V_{\mathbf{0}, \mathbf{0}, \mathbf{0}}^{2222}$	$t''_{\alpha=2}$	-0.178606	-0.983921	6.1861
5	$t_{pp}$	$V_{(1,0), \mathbf{0}, \mathbf{0}}^{2222}$	0.012569	-0.999921	6.2400
6	$V_{\mathbf{0}, \mathbf{0}, \mathbf{0}}^{2222}$	$t'_{\alpha=0}$	-0.668412	0.743791	6.5120
7	$\frac{1}{N} \sum_{\mathbf{k}}  [A_{\mathbf{k}}]_{\alpha=2, l=0} ^2$	$t''_{\alpha=2}$	-0.101612	-0.994824	6.8141
8	$\frac{1}{N} \sum_{\mathbf{k}}  [A_{\mathbf{k}}]_{\alpha=2, l=0} ^2$	$t'_{\alpha=0}$	-0.452919	0.891552	7.2931
9	$\min_{\mathbf{d}, \mathbf{d}', \mathbf{u}} V_{\mathbf{d}, \mathbf{d}', \mathbf{u}}^{\alpha\beta\gamma\delta} = V_{\mathbf{0}, \mathbf{0}, \mathbf{0}}^{0020}$	$t'_{\alpha=1}$	-0.774502	-0.632572	7.4161
10	$t'_{\alpha=1}/t_{\alpha=1}$	$t''_{\alpha=2}$	0.346422	-0.938079	7.4191

rank	$p_1$	$p_2$	$c_1$	$c_2$	std. dev. $\sigma$
1	$V_{(1,1), (-1, -1), \mathbf{0}}^{0000}$	$t'_{\alpha=1}$	-0.999998	-0.001861	5.7407
2	$E_{\mathbf{k}=(\pi, \pi)}^{\alpha=1} - E_{\mathbf{k}=(\pi, \pi)}^{\alpha=0}$	$t'_{\alpha=2}$	0.006267	0.999980	6.2854
3	$V_{(1,1), \mathbf{0}, \mathbf{0}}^{0000}$	$t'_{\alpha=1}$	-0.997331	-0.073015	6.4198
4	$V_{(1,1), (-1, -1), \mathbf{0}}^{0000}$	$t''_{\alpha=2}$	-0.999992	-0.004007	6.4207
5	$V_{(1,1), (-1, -1), \mathbf{0}}^{0000}$	$t'_{\alpha=1}$	-0.999994	0.003484	6.8968
6	$V_{(1,1), \mathbf{0}, \mathbf{0}}^{0000}$	$t''_{\alpha=2}$	-0.987743	-0.156088	6.8977
7	$V_{(1,1), \mathbf{0}, \mathbf{0}}^{0000}$	$t''_{\alpha=1}$	-0.990743	0.135753	7.3100
8	$\varepsilon_d - \varepsilon_p$	$\max E_{\mathbf{k}}^{\alpha=0} - \min E_{\mathbf{k}}^{\alpha=1}$	-0.799401	0.600798	7.5377
9	$\varepsilon_d - \varepsilon_p$	$t'_{\alpha=2}$	-0.007130	0.999975	8.0288
10	$\varepsilon_d - \varepsilon_p$	$t_{\alpha=1}$	-0.054257	0.998527	8.1007

Table IV. Top lists of 3-parameter predictors.

rank	$p_1$	$p_2$	$p_3$	$c_1$	$c_2$	$c_3$	std. dev. $\sigma$
1	$D_{\alpha=1}$	$t''_{\alpha=1}$	$t'_{\alpha=2}$	-0.027127	0.997861	0.059480	4.4696
2	$D_{\alpha=1}$	$V_{\mathbf{0}, \mathbf{0}, \mathbf{0}}^{2222}$	$t''_{\alpha=1}$	-0.024756	-0.034964	0.999082	4.5503
3	$D_{\alpha=2}$	$t'_{\alpha=0}$	$t_{\alpha=2}$	-0.103772	0.355220	-0.929005	4.5828
4	$D_{\alpha=2}$	$t''_{\alpha=2}$	$t''_{\alpha=2}/t_{\alpha=2}$	-0.014299	-0.942122	-0.334964	4.6311
5	$D_{\alpha=1}$	$t'_{\alpha=0}$	$t''_{\alpha=1}$	-0.024244	-0.043401	0.998764	4.6446
6	$V_{\mathbf{0}, \mathbf{0}, \mathbf{0}}^{2222}$	$t_{\alpha=1}$	$t''_{\alpha=1}/t_{\alpha=1}$	-0.070622	0.051866	0.996154	4.6573
7	$V_{\mathbf{0}, \mathbf{0}, \mathbf{0}}^{2222}$	$t''_{\alpha=1}$	$t''_{\alpha=1}/t_{\alpha=1}$	-0.076054	0.243175	0.966996	4.6784
8	$\min_{\mathbf{d}, \mathbf{d}', \mathbf{u}} V_{\mathbf{d}, \mathbf{d}', \mathbf{u}}^{2222} = V_{(1,1), \mathbf{0}, \mathbf{0}}^{2222}$	$t''_{\alpha=0}/t_{\alpha=0}$	$t'_{\alpha=2}$	-0.996019	0.031442	0.083417	4.7134
9	$V_{\mathbf{0}, \mathbf{0}, \mathbf{0}}^{2222}$	$\min_{\mathbf{d}, \mathbf{d}', \mathbf{u}} V_{\mathbf{d}, \mathbf{d}', \mathbf{u}}^{0000}$	$t'_{\alpha=1}$	-0.021006	0.999127	-0.036103	4.7267
10	$V_{\mathbf{0}, \mathbf{0}, \mathbf{0}}^{2222}$	$t''_{\alpha=1}$	$t'_{\alpha=2}/t_{\alpha=2}$	-0.335834	0.930401	0.146868	4.7306

rank	$p_1$	$p_2$	$p_3$	$c_1$	$c_2$	$c_3$	std. dev. $\sigma$
1	$V_{(1,1), \mathbf{0}, \mathbf{0}}^{2222}$	$t'_{\alpha=0}$	$t''_{\alpha=0}/t_{\alpha=0}$	0.999856	0.016821	0.002042	4.0065
2	$\min_{\mathbf{d}, \mathbf{d}', \mathbf{u}} V_{\mathbf{d}, \mathbf{d}', \mathbf{u}}^{0000}$	$V_{(1,1), \mathbf{0}, \mathbf{0}}^{2222}$	$t'_{\alpha=0}$	0.115210	0.993193	0.017135	4.0265
3	$V_{(1,0), \mathbf{0}, \mathbf{0}}^{1111}$	$V_{(1,1), \mathbf{0}, \mathbf{0}}^{2222}$	$t'_{\alpha=0}$	0.999946	0.010371	0.000194	4.0770
4	$V_{(1,1), \mathbf{0}, \mathbf{0}}^{2222}$	$V_{(1,1), (-1, -1), \mathbf{0}}^{0000}$	$t'_{\alpha=0}$	0.313155	-0.949673	0.007395	4.0836
5	$V_{(1,1), (-1, -1), \mathbf{0}}^{2222}$	$t'_{\alpha=0}$	$t''_{\alpha=2}/t_{\alpha=2}$	-0.999999	0.001642	-0.000130	4.0942
6	$E_{\mathbf{k}=(0, \pi)}^{\alpha=2} - E_{\mathbf{k}=(0, \pi)}^{\alpha=1}$	$V_{(1,1), (-1, -1), \mathbf{0}}^{2222}$	$t'_{\alpha=0}$	0.000010	-0.999999	0.001553	4.1090
7	$t_{pd}$	$V_{\mathbf{0}, \mathbf{0}, \mathbf{0}}^{2222}$	$V_{(1,1), \mathbf{0}, \mathbf{0}}^{0000}$	0.004709	-0.368569	0.929589	4.1152
8	$D_{\alpha=2}$	$V_{(1,1), (-1, -1), \mathbf{0}}^{2222}$	$t'_{\alpha=0}$	0.000009	-0.999999	0.001444	4.1644
9	$V_{\mathbf{0}, \mathbf{0}, \mathbf{0}}^{2222}$	$t_{\alpha=0}$	$t'_{\alpha=0}/t_{\alpha=0}$	-0.994567	0.093453	0.045869	4.1822
10	$V_{(1,1), (-1, -1), \mathbf{0}}^{2222}$	$t'_{\alpha=0}$	$t_{\alpha=2}$	-0.999999	0.001434	-0.000071	4.2076

Comparing to our best results ( $\sigma = 16K$ ,  $\sigma = 5.4K$  and  $\sigma = 4.0K$  in the three categories, respectively), we conclude that our results are highly unlikely to be obtained by pure chance, and that the quality of scaling we obtain must be indicative of actual

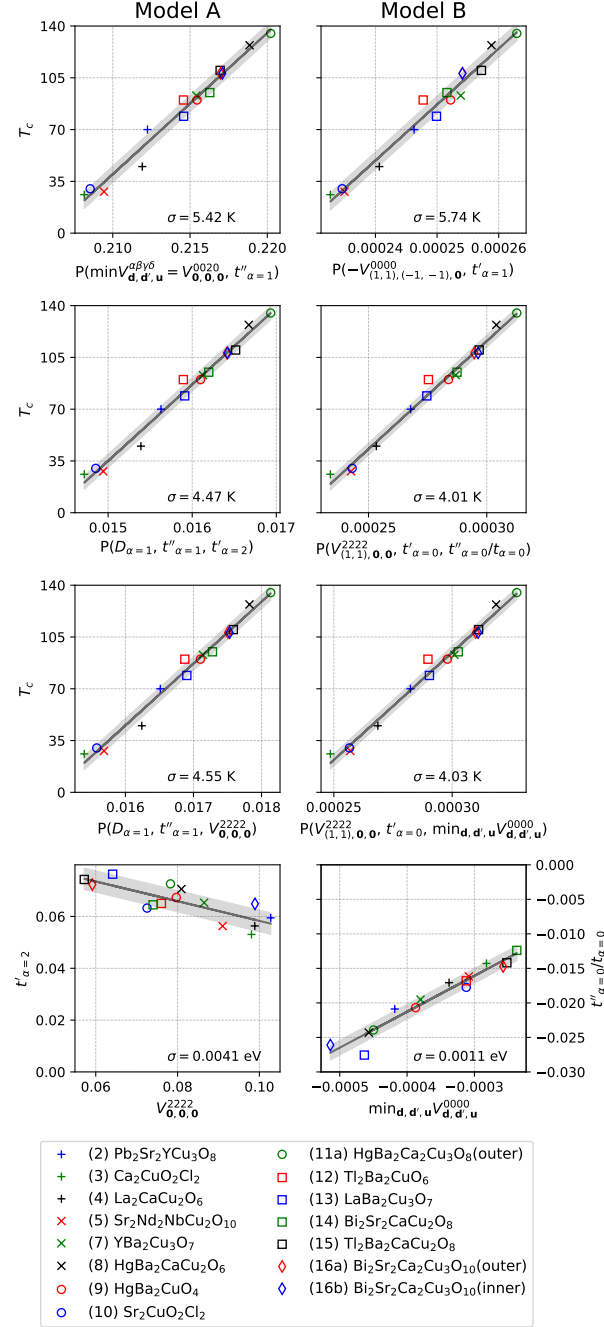


Figure 7. Top row: best 2-parameter predictors. Middle two rows: best and second best 3-parameter predictors. In both cases, only one parameter is different between the best and the second best. We check in the bottom row that these parameters correlate well. The best single parameter predictor  $t'_{\alpha=2}$  correlates closely with  $V_{000}^{2222}$ , which, on the other hand, appears most times in the top 100 best 3-parameter predictors based on Model A. Note that  $V_{dd'u}^{\alpha\beta\gamma\delta}$  is throughout the paper given in units of  $U$ , while the rest of the parameters are given in units of eV.

correlations between  $T_c$  and variables that we study.

### III. SCAN OF THE PARAMETER SPACE - IDENTIFYING HIGH- $T_c$ CANDIDATES

In this section we scan the parameter-space of the Emery model. For each parameter we cover the range of values spanned by the data points (1)-(16b), expanded by 33% in both directions. We discretize each parameter by 6 equidistant points, which gives

Table V. Top list of parameters, ranked by the number of times they appear in the top 100 3-parameter predictors ( $N_{\text{appear.}}$ ).

Table V.A. Model A.			Table V.B. Model B.		
rank	parameter	$N_{\text{appear.}}$	rank	parameter	$N_{\text{appear.}}$
1	$V_{0,0,0}^{2222}$	40	1	$t'_{\alpha=0}$	37
2	$t'_{\alpha=0}$	30	2	$V_{(1,1),0,0}^{2222}$	28
3	$t''_{\alpha=1}$	23	3	$V_{(1,1),(-1,-1),0}^{2222}$	26
4	$t'_{\alpha=1}$	21	4	$V_{(1,1),(-1,-1),0}^{0000}$	25
5	$t''_{\alpha=1}/t_{\alpha=1}$	17	5	$t''_{\alpha=1}$	19
6	$t_{\alpha=1}$	15	6	$V_{0,0,0}^{2222}$	18
7	$\min V_{d,d',u}^{\alpha\beta\gamma\delta} = V_{0,0,0}^{0020}$	15	7	$D_{\alpha=0}$	15
8	$D_{\alpha=1}$	15	8	$t_{pd}$	14
9	$\min_{d,d',u} V_{d,d',u}^{0000}$	12	9	$t''_{\alpha=2}$	11
10	$t''_{\alpha=2}$	11	10	$t_{\alpha=0}$	11

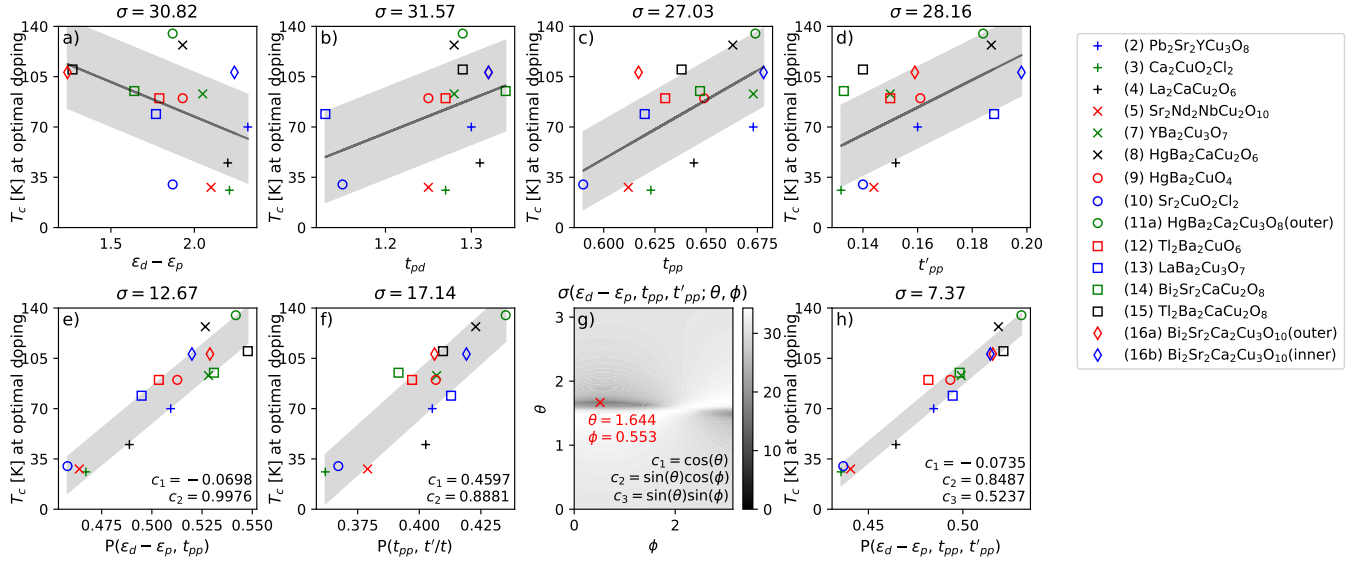


Figure 8. a-d) The fit of  $T_c$  to original parameters of the model. e-f) the two best 2-parameter predictors based on the original parameters and  $t'/t$  from *Weber et al.* g-h) The best 3-parameter fit based on the original parameters and  $t'/t$ . g) shows how the quality of the fit depends on the coefficients of the linear combination.

us in total  $6^4 = 1296$  points to work with. Then, for each point we evaluate the  $T_c$ -prediction, given by the top 100 3-parameter predictors based on parameters of model B (the 100th best has  $\sigma = 5.02$  K). We then compute the average  $T_c$ -prediction,  $\langle T_c \rangle = \sum_P T_c(P)/N_P$ , and the std. deviation,  $\sigma = \sqrt{\sum_P (T_c(P) - \langle T_c \rangle)^2 / N_P}$ , where different predictors are denoted  $P$ , and  $N_P = 100$ .

On Fig. 9 we plot  $\langle T_c \rangle$  vs.  $\sigma$ . We see that, in general, different predictors are correlated in a large portion of the parameter space that we study. There is plenty of cases where different predictors agree to within  $\pm 10$  K. We also see that there are points inside the 4D box spanned by the *Weber et al.* dataset, where  $T_c$  is predicted to be very large. In particular, if we take the minimal  $\epsilon_d - \epsilon_p$  and the maximal  $t_{pd}$ ,  $t_{pp}$  and  $t'_{pp}$  from the *Weber et al.* dataset, the  $T_c$  is predicted to be  $194.9 \pm 4.5$  K. This is in sharp contrast with the analysis presented in *Weber et al.*, where one could only conclude that  $T_c$  for this choice of parameters would be around  $105 \pm 30$  K. In the Table VI we list 10 high- $T_c$  candidates, where  $T_c > 150$  K, and all parameters are inside the range spanned by the data points in the *Weber et al.* dataset.

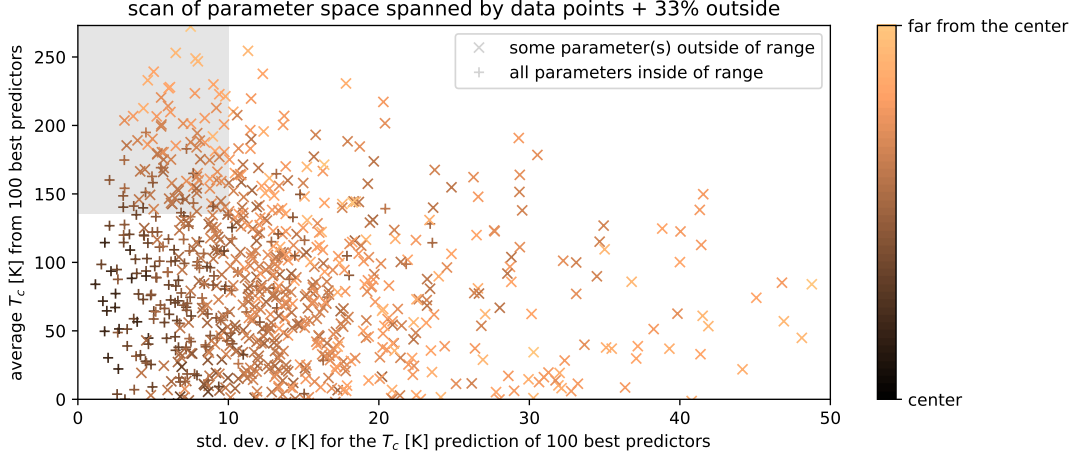


Figure 9. The scan of the parameter space spanned by the data points, enlarged by 33% in both directions, for each parameter. On the plot we show the average  $T_c$  as predicted by the top 100 3-parameter predictors based on Model B, vs. the corresponding standard deviation. The gray rectangle denotes the window of opportunity: where different predictors agree well and the predicted  $T_c$  is high.

Table VI. List of high- $T_c$  candidates in the parameter space spanned by the data points in the *Weber et al.* dataset. The  $T_c$  estimate  $\langle T_c \rangle$  is obtained by averaging predictions of the top 100 3-parameter predictors based on the parameters of the (spin-symmetric) model B, and  $\sigma$  is the corresponding std. deviation. Note that the convention for  $\varepsilon_d - \varepsilon_p$  is the same as in the original table in *Weber et al.*, i.e. we do not include here the  $E_{dc}$  shift of  $\varepsilon_d$  that is, nevertheless, used in our calculation.

$\varepsilon_d - \varepsilon_p$ [eV]	$t_{pd}$ [eV]	$t_{pp}$ [eV]	$t'_{pp}$ [eV]	$\langle T_c \rangle$ [K]	$\sigma$ [K]
1.240	1.390	0.678	0.135	154.1	3.1
1.240	1.390	0.678	0.166	174.7	3.1
1.240	1.390	0.678	0.198	194.9	4.5
1.697	1.217	0.678	0.198	151.1	4.5
1.240	1.303	0.649	0.198	158.2	5.0
1.697	1.390	0.678	0.198	162.8	4.9
1.240	1.303	0.678	0.166	165.0	7.7
1.240	1.303	0.678	0.198	182.9	7.2
1.697	1.303	0.678	0.198	160.2	2.1
1.240	1.390	0.649	0.198	169.2	5.5

#### IV. RELATIONSHIP TO SUPERCONDUCTIVITY IN THE ORIGINAL MODEL

Let us assume a  $d$ -wave superconductivity living on the copper  $d$ -orbitals, and let's assume that the instantaneous anomalous correlator has the following form

$$\langle c_{l,\uparrow,\mathbf{r}}^\dagger c_{l',\downarrow,\mathbf{r}'}^\dagger \rangle = \Delta \delta_{l,0} \delta_{l',0} (\delta_{\mathbf{r}-\mathbf{r}',\mathbf{e}_x} + \delta_{\mathbf{r}-\mathbf{r}',-\mathbf{e}_x} - \delta_{\mathbf{r}-\mathbf{r}',\mathbf{e}_y} - \delta_{\mathbf{r}-\mathbf{r}',-\mathbf{e}_y}) \quad (44)$$

In terms of our Wannier orbitals, the anomalous propagator is then given by

$$\langle d_{\alpha,\uparrow,\mathbf{r}}^\dagger d_{\beta,\downarrow,\mathbf{r}'}^\dagger \rangle = \sum_{l\mathbf{r}'',l'\mathbf{r}'''} F_{\alpha,l,\mathbf{r}-\mathbf{r}''} F_{\beta,l',\mathbf{r}'-\mathbf{r}'''} \langle c_{l,\uparrow,\mathbf{r}''}^\dagger c_{l',\downarrow,\mathbf{r}'''}^\dagger \rangle \quad (45)$$

$$= \sum_{l\mathbf{r}'',l'\mathbf{d} \in \{\pm\mathbf{e}_x, \pm\mathbf{e}_y\}} F_{\alpha,l,\mathbf{r}-\mathbf{r}''} F_{\beta,l',\mathbf{r}'-\mathbf{r}''-\mathbf{d}} \langle c_{l,\uparrow,\mathbf{r}''}^\dagger c_{l',\downarrow,\mathbf{r}''+\mathbf{d}}^\dagger \rangle \quad (46)$$

$$= \sum_{\mathbf{r}'',\mathbf{d} \in \{\pm\mathbf{e}_x, \pm\mathbf{e}_y\}} F_{\alpha,0,\mathbf{r}-\mathbf{r}''} F_{\beta,0,\mathbf{r}'-\mathbf{r}''-\mathbf{d}} (-1)^{\delta_{\mathbf{d},\mathbf{e}_y} + \delta_{\mathbf{d},-\mathbf{e}_y}} \Delta \quad (47)$$

We compute  $\langle d_{\alpha,\uparrow,\mathbf{r}}^\dagger d_{\beta,\downarrow,\mathbf{0}}^\dagger \rangle$  (Figure 10) and see that the dominant values are for  $\alpha, \beta = 0, 2$ ,  $\mathbf{r} = (0, 1)$ , and they have  $d$ -wave symmetry. There is also a weak  $s$ -wave component in the pairing between  $\alpha = 1$  and  $\alpha = 0, 2$  bands. Overall, the superconductivity of  $d$ -orbitals is not very different from the superconductivity in the  $\alpha = 0$  and  $\alpha = 2$  orbitals. This provides



some understanding of why it is mostly the interactions acting inside or between the bands  $\alpha = 0$  and  $\alpha = 2$  that correlate with  $T_c$ .

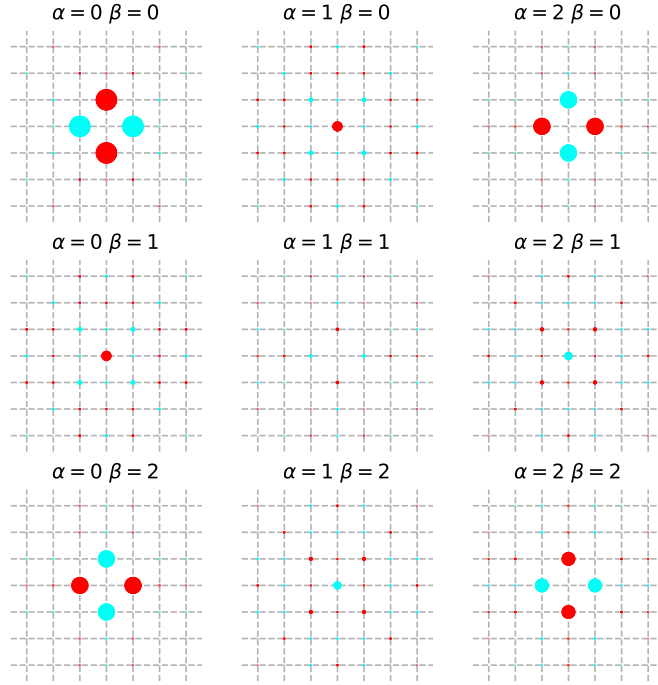


Figure 10. The correlator  $\langle d_{\alpha,\uparrow,\mathbf{r}}^\dagger d_{\beta,\downarrow,\mathbf{0}}^\dagger \rangle$  under the assumption of the standard, nearest-neighbor  $d$ -wave pairing on the  $d$ -orbitals, given by Eq. 44, with  $\Delta = 1$ . The example is data point (4). Area of points is the amplitude, color is the phase.

- 
- <sup>1</sup> C. Weber, C. Yee, K. Haule, and G. Kotliar, [EPL \(Europhysics Letters\) \*\*100\*\*, 37001 \(2012\)](#), [10.1209/0295-5075/100/37001](#), arXiv:1108.3028.
- <sup>2</sup> C. Weber, C.-H. Yee, K. Haule, and G. Kotliar, [\(2011\)](#),

# Charge fluctuations, hydrodynamics, and transport in the square-lattice Hubbard model

J. Vučković,<sup>1</sup> S. Pudin,<sup>1</sup> and M. Ferrero<sup>2,3</sup>

<sup>1</sup>*Scientific Computing Laboratory, Center for the Study of Complex Systems, Institute of Physics Belgrade, University of Belgrade, Pregrevica 118, 11080 Belgrade, Serbia*

<sup>2</sup>*CPHT, CNRS, Ecole Polytechnique, Institut Polytechnique de Paris, Route de Saclay, 91128 Palaiseau, France*

<sup>3</sup>*Collège de France, 11 place Marcelin Berthelot, 75005 Paris, France*



(Received 8 August 2022; revised 31 March 2023; accepted 3 April 2023; published 25 April 2023)

Recent experimental results suggest that a particular hydrodynamic theory describes charge fluctuations at long wavelengths in the square-lattice Hubbard model. Due to the continuity equation, the correlation functions for the charge and the current are directly connected: the parameters of the effective hydrodynamic model thus determine the optical conductivity. Here we investigate the validity of the proposed hydrodynamic theory in the full range of parameters of the Hubbard model. In the noninteracting case, there is no effective hydrodynamics, and the charge fluctuations present a rich variety of nonuniversal behaviors. At weak coupling, the optical conductivity is consistent with the hydrodynamic theory: at low frequency one observes a Lorentzian-shaped Drude peak, but the high-frequency asymptotics is necessarily different; the high-temperature limit for the product of the two hydrodynamic model parameters is also in agreement with numerical data. At strong coupling, we find that a generalization of the proposed hydrodynamic law is consistent with our quantum Monte Carlo, as well as the finite-temperature Lanczos results from literature. Most importantly, the temperature dependence of the hydrodynamic parameters as well as the dc resistivity are found to be very similar in the weak- and the strong-coupling regimes.

DOI: [10.1103/PhysRevB.107.155140](https://doi.org/10.1103/PhysRevB.107.155140)

## I. INTRODUCTION

Strange metallic behavior is one of the central subjects for the theory of strong electronic correlations [1]. It appears to be a universal phenomenon, observed in many different systems, often in close proximity to a superconducting phase [2–5], or quantum critical points [6–8]. In this regime, the dc resistivity is linear in temperature, in a very broad range of temperature. The origin of this behavior is unclear, but numerical investigations converge to the conclusion that the Hubbard model captures the underlying mechanisms [9–15]. Very recently, a variational solution of the semiclassical Boltzmann equation revealed a  $T$ -linear dc resistivity regime at high temperature, extending towards zero temperature as half-filling is approached [16]. This finding of Kiely and Mueller bares an important implication that strange metallicity is not necessarily a strong correlation phenomenon, even in cases when it extends to very low temperature (see also Ref. [17] highlighting the role of van Hove singularities at the Fermi level).

In the high-temperature limit, a simple and quite universal understanding of the linear resistivity was proposed in terms of the effective hydrodynamics that is expected to arise at long wavelengths in interacting systems. Diffusive transport should under very general circumstances lead to  $\sigma_{dc} = \chi_c D$ , where  $\sigma_{dc}$  is the dc conductivity,  $\chi_c$  is the charge compressibility, and  $D$  is the diffusion constant. In Refs. [11,12], it was argued that, at high temperature,  $D$  approaches a constant, while quite generally  $\chi_c \sim 1/T$ , which thus leads to  $\rho_{dc} \sim T$ . In a subsequent optical lattice simulation of the Hubbard model by Brown *et al.* [18], the assumption of hydrodynamic behavior was exploited to extract values for the dc resistivity and the width of the Drude peak. In almost quantitative agreement

with the best available numerical method (finite-temperature Lanczos, FTLN [19,20]), the experiment found linear resistivity in a broad range of temperature. However, the width of the Drude peak  $\Gamma$  was greatly overestimated in the experiment, which brings into question the quality of the  $\rho_{dc}$  estimates and the underlying assumptions. The interpretation of experimental results relied on a specific hydrodynamic ansatz for the charge-charge correlation function, proposed to be valid in the long-wavelength limit. On the other hand, the fits to the direct measurement data were performed at relatively short wavelengths: Any discrepancy between the ansatz and the actual behavior at these wavelengths (and correspondingly higher frequencies) could have led to the apparent bias in the estimates of  $\Gamma$ , but perhaps even in the estimates of  $\rho_{dc}$ .

In this paper we investigate the validity of the hydrodynamic theory proposed in Ref. [18]. We first discuss its analytical properties and find that the high-frequency asymptotics is manifestly nonphysical. We propose a modified hydrodynamic law, which corrects the high-frequency behavior, and ultimately allows for a comparison with Matsubara-axis data we obtain from quantum Monte Carlo. We derive the equation of motion for the current, which must present a microscopic basis for the hydrodynamic theory. We are unable to rigorously connect the hydrodynamic parameters to Hubbard model parameters, but we find evidence that  $D\Gamma \approx 2t^2$  (here  $t$  is the hopping amplitude), which is consistent with numerical results at both weak and strong coupling. Moreover, at weak coupling,  $D\Gamma = 2t^2$  can be derived rigorously as the high-temperature limit of the hydrodynamic theory, only based on the knowledge of the exact asymptotics of the charge-charge correlation function.

We perform numerical calculations for the square-lattice Hubbard model and cover a wide range of parameters. We start with the noninteracting limit where the hydrodynamic theory is not expected to hold and find multiple interesting examples of charge-fluctuation spectra. At weak coupling we use second-order perturbation theory for the self-energy, and compute optical conductivity and the charge-charge correlation function from the bubble approximation. We confirm the recent findings of Kiely and Mueller [16] that the dc resistivity is linear at half-filling and, more generally, at high temperature. At stronger couplings, we use the numerically exact continuous-time quantum Monte Carlo (CTINT [21,22]) on a finite  $10 \times 10$  lattice, and control for the lattice size. We show that a modified hydrodynamic law is consistent with the Matsubara-axis results for the charge-charge and current-current correlation functions, as well as with the FTLM result for optical conductivity. The hydrodynamic model parameters extracted from FTLM at strong coupling display strikingly similar behavior to what we find from the bubble approximation at weak coupling.

The paper is organized as follows. In Sec. II we introduce the two-dimensional (2D) Hubbard model and the hydrodynamic theory proposed to govern its charge and current fluctuations at long wavelengths. In Sec. III we show our numerical results, separated in three subsections based on the coupling strength. In Sec. IV we discuss our findings in the context of existing literature and give concluding remarks in Sec. V. In Appendixes A–E we give detailed derivations of equations used in this paper, and outline the fast algorithm we used for computing the second-order self-energy. In Appendix F we show and discuss static charge susceptibility data in the noninteracting limit.

## II. MODELS

### A. Square-lattice Hubbard model

We solve the Hubbard model given by the Hamiltonian

$$H = -t \sum_{\sigma, \langle i, j \rangle} c_{\sigma, i}^{\dagger} c_{\sigma, j} + U \sum_i n_{\uparrow, i} n_{\downarrow, i} - \mu \sum_{\sigma, i} n_{\sigma, i}, \quad (1)$$

where  $\sigma \in \{\uparrow, \downarrow\}$ ,  $i, j$  enumerate lattice sites,  $t$  is the hopping amplitude between the nearest-neighbor sites  $\langle i, j \rangle$ ,  $U$  is the onsite coupling constant, and  $\mu$  is the chemical potential. We absorb the chemical potential in the bare dispersion, which is thus given by

$$\varepsilon_{\mathbf{k}} = -2t(\cos k_x + \cos k_y) - \mu. \quad (2)$$

We will switch between the site notation and real-space notation whenever convenient ( $A_i \equiv A_{\mathbf{r}}$ , with  $\mathbf{r} = \mathbf{r}_i$ , which is the real-space position of the site  $i$ ). The density operator is denoted  $n_{\sigma, i} = c_{\sigma, i}^{\dagger} c_{\sigma, i}$ . Throughout the paper we use the half-bandwidth  $4t$  as the unit of energy. We only consider paramagnetic solutions. In equilibrium we assume full lattice symmetry.

### B. Hydrodynamic model

In Ref. [18] it was proposed that a hydrodynamic model describes the fluctuations of current and charge at long wave-

lengths in the Hubbard model. The hydrodynamic model reads as

$$\partial_t n = -\nabla \cdot \mathbf{j}, \quad (3)$$

$$\partial_t \mathbf{j} = -\Gamma(D\nabla n + \mathbf{j}), \quad (4)$$

where  $n$  and  $\mathbf{j}$  are scalar and vector fields, respectively, dependent on time and space. The parameters of the model are the momentum-relaxation rate  $\Gamma$  and the diffusion constant  $D$ .

The first equation [Eq. (3)] is the continuity equation, and it is certainly valid in the Hubbard model for the time-dependent operators in the Heisenberg picture. However, on the square lattice, the spatial derivatives must be discretized, and the actual continuity equation reads as

$$\partial_t n_{\mathbf{r}} = - \sum_{\eta \in \{x, y\}} (j_{\mathbf{r}}^{\eta} - j_{\mathbf{r}-\mathbf{e}_{\eta}}^{\eta}) \quad (5)$$

which simply means that any increase in the particle density at a site  $\mathbf{r}$  must be due to a disbalance between the currents entering and exiting the given site. The current operator is given by

$$j_{\mathbf{r}}^{\eta} = it \sum_{\sigma} (c_{\mathbf{r}+\mathbf{e}_{\eta}, \sigma}^{\dagger} c_{\mathbf{r}, \sigma} - c_{\mathbf{r}, \sigma}^{\dagger} c_{\mathbf{r}+\mathbf{e}_{\eta}, \sigma}), \quad (6)$$

where  $\mathbf{e}_{\eta}$  denotes the lattice vector in the direction  $\eta$ . A derivation of Eq. (5) is presented in Appendix A, but can be found elsewhere [23]. Since the operators are connected instantaneously, the charge and current fluctuate synchronously. The corresponding charge-charge and current-current correlation functions must be connected directly, as well. Following the derivation presented in Appendix B, one obtains in the entire complex plane

$$\begin{aligned} z^2 \chi_{\mathbf{q}}(z) &= \sum_{\eta \in \{x, y\}} \sum_{\mathbf{k}} \Phi_{\mathbf{k}, \mathbf{q}}^{\eta} (\langle n_{\mathbf{k}+\mathbf{q}} \rangle - \langle n_{\mathbf{k}} \rangle) \\ &+ \sum_{\eta, \eta' \in \{x, y\}} (1 - e^{iq_{\eta}} - e^{-iq_{\eta'}} + e^{i(q_{\eta} - q_{\eta'})}) \Lambda_{\mathbf{q}}^{\eta, \eta'}(z), \end{aligned} \quad (7)$$

where  $\Phi_{\mathbf{k}, \mathbf{q}}^{\eta} = -2t[\cos(k_{\eta} + q_{\eta}) - \cos k_{\eta}]$ , and  $n_{\mathbf{k}} = \sum_{\sigma} c_{\sigma, \mathbf{k}}^{\dagger} c_{\sigma, \mathbf{k}}$ . We define in imaginary time and site space

$$\chi_{ij}(\tau) = \langle n_i(\tau) n_j(0) \rangle - \langle n \rangle^2 \quad (8)$$

and

$$\Lambda_{ij}^{\eta\eta'}(\tau) = \langle j_i^{\eta}(\tau) j_j^{\eta'}(0) \rangle \quad (9)$$

the charge-charge and current-current correlation functions, respectively, calculated in thermodynamic equilibrium. The standard Fourier transform to Matsubara frequencies gives  $\chi(z)$  and  $\Lambda(z)$  at a discrete set of points along the imaginary axis; a spatial Fourier transform gives the corresponding quantities in reciprocal space. We are ultimately interested in retarded quantities which correspond to taking  $z = \nu + i0^+$  and we denote them as  $\chi_{\mathbf{q}}(\nu)$  and  $\Lambda_{\mathbf{q}}^{\eta\eta'}(\nu)$ . Here,  $\nu$  is real frequency and  $\mathbf{q}$  is momentum. We have checked numerically that Eq. (7) holds in the noninteracting limit, for any  $\mathbf{q}$  and in any parameter regime of the model (data not shown). In general, the transversal components  $\Lambda_{\mathbf{q}}^{\eta, \eta' \neq \eta}$  play a role in Eq. (7). However, the expression greatly simplifies for the

imaginary part on the real axis at small  $\mathbf{q}$  in the  $x$  direction,

$$\lim_{q \rightarrow 0} \text{Im} \chi_{\mathbf{q}=(q,0)}(\nu) = \frac{q^2}{\nu^2} \text{Im} \Lambda_{\mathbf{q}=(q,0)}^{xx}(\nu), \quad (10)$$

which is the same expression one obtains in the continuum limit, directly from Eq. (3).

The second equation [Eq. (4)] is the so-called constitutive equation [24] of a hydrodynamic theory, needed to close the system of equations, as the continuity equation itself does not fully fix  $n$  and  $\mathbf{j}$ . In the stationary regime, Eq. (4) reduces to Fick's law of diffusion  $\mathbf{j} = -D\nabla n$ . Equation (4) is not nec-

essarily satisfied in the Hubbard model, and is an underlying assumption of the work presented in Ref. [18]. It is precisely the aim of this work to investigate whether the hydrodynamics encoded in Eq. (4) truly emerges in the Hubbard model at the longest wavelengths and, if yes, under which conditions.

### 1. Microscopic constitutive equation for the hydrodynamics in the Hubbard model

We start by deriving a microscopic expression for the time derivative of the current operator. The derivation presented in Appendix C yields

$$\begin{aligned} \partial_t j_{\mathbf{r}}^{\eta} = & -t^2 \sum_{\sigma} \left\{ 2n_{\sigma, \mathbf{r}+\mathbf{e}_{\eta}} - 2n_{\sigma, \mathbf{r}} + \sum_{\mathbf{u} \in \{-\mathbf{e}_{\eta}, \mathbf{e}_{\eta}, -\mathbf{e}_{\eta}\}} (c_{\sigma, \mathbf{r}+\mathbf{u}}^{\dagger} c_{\sigma, \mathbf{r}+\mathbf{e}_{\eta}} - c_{\sigma, \mathbf{r}}^{\dagger} c_{\sigma, \mathbf{r}+\mathbf{e}_{\eta}-\mathbf{u}} + \text{H.c.}) \right\} \\ & - tU \sum_{\sigma} (n_{\bar{\sigma}, \mathbf{r}+\mathbf{e}_{\eta}} - n_{\bar{\sigma}, \mathbf{r}}) (c_{\sigma, \mathbf{r}}^{\dagger} c_{\sigma, \mathbf{r}+\mathbf{e}_{\eta}} + c_{\sigma, \mathbf{r}+\mathbf{e}_{\eta}}^{\dagger} c_{\sigma, \mathbf{r}}), \end{aligned} \quad (11)$$

where we used  $\bar{\sigma} = \uparrow$  if  $\sigma = \downarrow$ , and vice versa; similarly  $\bar{\eta} = y$  if  $\eta = x$ , etc. We immediately recognize the lattice version of the local gradient of charge in the direction of the current  $n_{\sigma, \mathbf{r}+\mathbf{e}_{\eta}} - n_{\sigma, \mathbf{r}}$ . If we are interested in the time-dependent averages, we can split the terms in the second row in the disconnected and connected parts  $\langle nc^{\dagger}c \rangle = \langle n \rangle \langle c^{\dagger}c \rangle + \langle nc^{\dagger}c \rangle^{\text{conn}}$ . Assuming that we are close to and approaching equilibrium, one can further split the averages in the equilibrium value and the time-dependent part. Taking into account the lattice symmetries satisfied in equilibrium, the constant appearing in front of the gradient of charge has the terms  $2t^2 + 2tU \langle c_{\sigma, \mathbf{r}+\mathbf{e}_{\eta}}^{\dagger} c_{\sigma, \mathbf{r}} \rangle_{\text{eq}}$ , and will therefore decay towards  $2t^2$  as  $T \rightarrow \infty$  or  $U \rightarrow 0$ . Identifying this with the term  $D\nabla n$  in the hydrodynamic theory [Eq. (4)], one could expect that at high temperature  $D\nabla \approx 2t^2$ . In Sec. III B, we analyze numerical data and indeed find such behavior. However, in Eq. (11) there are also time-dependent factors that multiply the gradient of charge, and other terms which correspond to neither  $\nabla n$  or  $\mathbf{j}$ . It is unclear under which conditions the remaining terms conspire to give rise to the effective Eq. (4), even if only in the long-wavelength, low-frequency, and linear-response limit. In Appendix C, we present Eq. (11) also in momentum space, but find no clear simplifications in the  $\mathbf{q} \rightarrow 0$  limit (the Fourier transform to the frequency domain would be analogous).

### 2. Experimental quench setup and CDW amplitude evolution: The ballistic and diffusive regimes

One can combine Eqs. (3) and (4) to obtain a differential equation governing the time evolution of the amplitude of a charge density wave  $n_{\mathbf{q}}$  (on the lattice, this field corresponds to the operator  $n_{\mathbf{q}} = \sum_{\sigma, \mathbf{k}} c_{\sigma, \mathbf{k}+\mathbf{q}}^{\dagger} c_{\sigma, \mathbf{k}} + \text{H.c.}$ ):

$$\partial_t^2 n_{\mathbf{q}} + \Gamma \partial_t n_{\mathbf{q}} + \Gamma D q^2 n_{\mathbf{q}} = 0. \quad (12)$$

Consider a setup where a charge density wave was first thermalized by applying an external density-modulating field  $V [H \rightarrow H + V \int d\mathbf{r} \sin x n(\mathbf{r})]$  for a long time, and was then let to evolve after abruptly switching off  $V$ . This time evolu-

tion is the solution of Eq. (12) with the boundary condition  $\partial_t n_{\mathbf{q}}(t=0) = 0$ ,  $n_{\mathbf{q}}(t=0) = n_0$ . If  $n_0$  is small, this behavior should also be described by the linear-response theory

$$\begin{aligned} n_{\mathbf{q}}(t) &= \int_{-\infty}^t \chi_{\mathbf{q}}(t-t') \theta(-t') dt' \\ &= \int_t^{\infty} \chi_{\mathbf{q}}(t') dt', \end{aligned} \quad (13)$$

assuming the knowledge of the charge-charge correlation function in real time, obtained as the Fourier transform from the retarded  $\chi_{\mathbf{q}}(\nu)$  as  $\chi_{\mathbf{q}}(t) = \int d\nu e^{-i\nu t} \chi_{\mathbf{q}}(\nu)$ . One can show [18] that the solution of Eq. (12) is equal to Eq. (13) with the retarded charge-charge correlation function of the form

$$\chi_{\mathbf{q}}(\nu) = \frac{\chi_c}{1 - \frac{i\nu}{q^2 D} - \frac{\nu^2}{q^2 D \Gamma}}, \quad (14)$$

where  $\chi_c$  is the charge compressibility, which connects  $n_0$  with the strength of the density modulating field at  $t < 0$ , but does not affect the dynamics of Eq. (12). This correlation function has the important property  $\chi_{\mathbf{q} \rightarrow 0}(\nu \neq 0) = 0$ . This indicates the conservation of the total number of particles, which is a prerequisite for the continuity equation. This is easy to understand as  $n_{\mathbf{q}=0}$  equals the total number of particles  $N_{\text{tot}}$ , and therefore  $\text{Im} \chi_{\mathbf{q} \rightarrow 0}(\nu)$  describes the fluctuations of  $N_{\text{tot}}$ .

At any given  $\mathbf{q}$ , one can rewrite the frequency-dependent part of Eq. (14) in a more revealing way. In the upper half-plane, the dynamic charge susceptibility (14) can be represented as a sum of two poles in the lower half-plane:

$$\chi^{\text{tr}}(z^+) = A \left[ \frac{1}{z^+ - z_1} - \frac{1}{z^+ - z_2} \right] \quad (15)$$

with  $A = -\chi_c/r$ ,  $r = \sqrt{4b - a^2}$ ,  $a = \frac{1}{q^2 D}$ ,  $b = \frac{1}{q^2 D \Gamma}$ ,  $z_1 = \frac{r - ia}{2b}$ ,  $z_2 = \frac{-r - ia}{2b}$ . It is clear that there are two distinct regimes: one where  $r$  is purely real, hence the two poles appear at  $\text{Re} z_1 = -\text{Re} z_2$  and  $\text{Im} z_1 = \text{Im} z_2 = -a$ ; the other one is when  $r$  is purely imaginary, and the two poles appear at  $\text{Re} z_1 = \text{Re} z_2 = 0$ ,  $\text{Im} z_1 = \text{Im} z_2 + 2 \text{Im} r$ . The latter is the “diffusive

regime,” which is realized whenever  $4b < a^2$ , i.e.,

$$q < q_D \equiv \sqrt{\frac{\Gamma}{4D}}. \quad (16)$$

To understand why  $4b < a^2$  represents the diffusive behavior, and  $4b > a^2$  ballistic behavior, we investigate the corresponding solutions of Eq. (12). The linear-response theory (13) can be solved analytically in the case when  $\chi = \chi^{\text{tp}}$ . One has

$$\chi^{\text{tp}}(t) \sim e^{-it z_1} - e^{-it z_2} \quad (17)$$

and, therefore, under the assumption that neither  $z_1$  or  $z_2$  are purely real, one gets

$$n_{\mathbf{q}}(t) \sim \frac{e^{-it z_1}}{z_1} - \frac{e^{-it z_2}}{z_2}. \quad (18)$$

We see that  $n_{\mathbf{q}}(t)$  will be zero whenever

$$\frac{z_2}{z_1} = e^{-it(z_2 - z_1)}. \quad (19)$$

In the ballistic regime,  $z_1 = E - i\eta$  and  $z_2 = -E - i\eta$ , and the condition (19) means

$$t = \frac{1}{2iE} \ln \left( \frac{-E - i\eta}{E - i\eta} \right). \quad (20)$$

At a fixed  $\eta$  and a finite  $E$ , there are infinitely many solutions to the above equation: the amplitude of the CDW presents damped oscillations after turning off the external field  $V$ . In the other case ( $4b < a^2$ ), the poles are placed along the imaginary axis, say  $z_1 = -i\eta_1$ , and  $z_2 = -i\eta_2$ ,  $\eta_2 > \eta_1$  and  $r$  is purely imaginary. One thus has  $n_{\mathbf{q}}(t) \sim \frac{e^{-i\eta_1 t}}{\eta_1} - \frac{e^{-i\eta_2 t}}{\eta_2}$  which can never be zero if  $\eta_1 \neq \eta_2$ . This means that the amplitude of the CDW will “crawl” towards zero, signaling an overdamped, or diffusive, regime. The correlator  $\chi_{\mathbf{q}}(\nu)$  [Eq. (14)] and the corresponding solutions for  $n_{\mathbf{q}}(t)$  [Eq. (12) or, equivalently, Eq. (13)] are illustrated in Fig. 1.

### 3. Asymptotic behavior and the connection between hydrodynamics and transport

The hydrodynamic form for the charge-charge correlation function [Eq. (14)] directly implies the form of the current-current correlation function. Inverting Eq. (10) (which is a direct consequence of the continuity equation) one obtains

$$\text{Im}\Lambda_{\mathbf{q}=(q,0)}^{xx}(\nu) = \frac{\chi_c D}{\frac{q^4 D^2}{\nu^3} + \frac{1}{\nu} \left(1 - 2q^2 \frac{D}{\Gamma}\right) + \frac{\nu}{\Gamma^2}}. \quad (21)$$

At any finite  $q$ , the behavior at small  $\nu$  goes as  $\sim \nu^3$ . At precisely  $q = 0$  one gets

$$\text{Im}\Lambda_{\mathbf{q}=0}^{xx}(\nu) = \frac{\chi_c D}{\frac{1}{\nu} + \frac{\nu}{\Gamma^2}} \quad (22)$$

which at small  $\nu$  goes as  $\sim \nu$ . Having in mind that the conductivity is obtained as [14,25]

$$\sigma_{\mathbf{q}}^{\eta\eta'}(\nu) = \frac{1}{\nu} \text{Im}\Lambda_{\mathbf{q}}^{\eta\eta'}(\nu), \quad (23)$$

this model clearly predicts that  $\sigma_{\text{dc},\mathbf{q}}^{xx} = 0$  for any finite  $\mathbf{q}$  in the  $x$  direction, which is precisely what is expected on physical

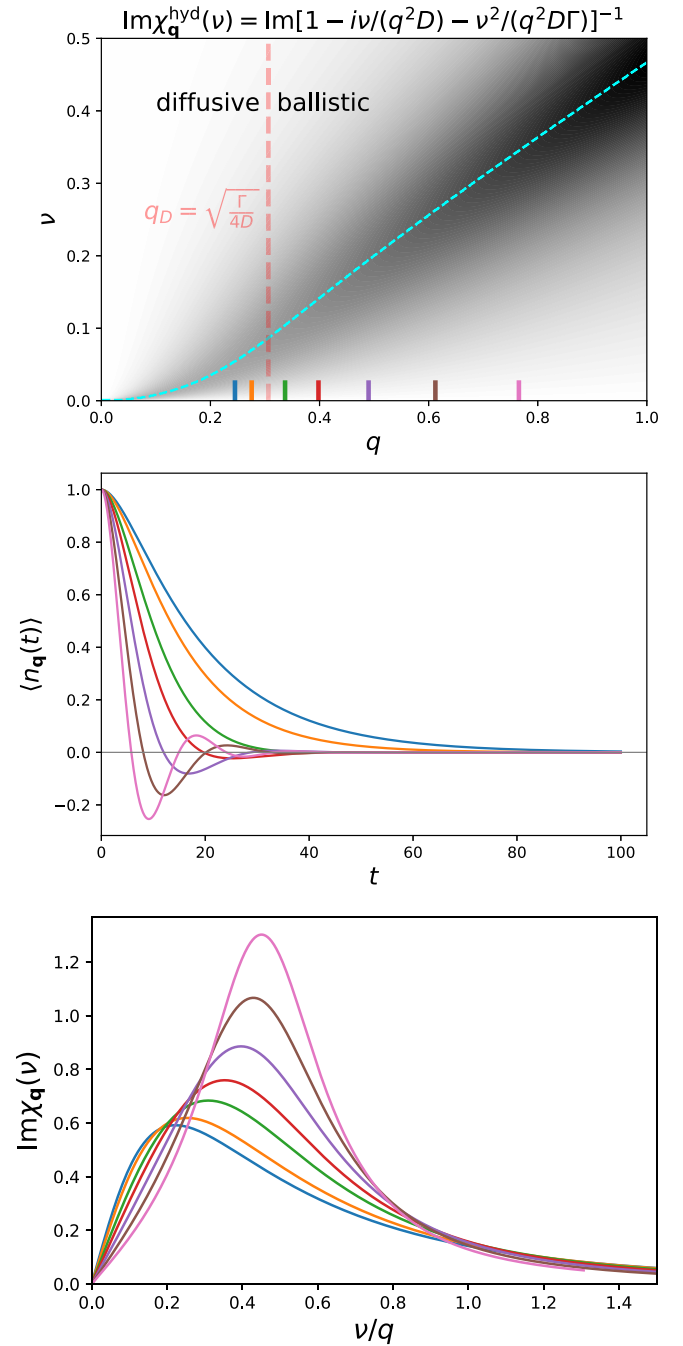


FIG. 1. Illustration of the hydrodynamic theory from Ref. [18], defined by Eqs. (3) and (4), with parameters taken to be  $D = 0.8$ ,  $\Gamma = 0.3$ ,  $\chi_c = 1$ . Top: the imaginary part of the charge-charge correlation function as a function of momentum and frequency [Eq. (14)]. Middle: the time evolution of relaxing charge density waves at wave vectors denoted by matching-color  $x$  ticks in the top panel;  $\langle n_{\mathbf{q}}(t) \rangle$  [computed through Eq. (18)] is normalized to the initial amplitude  $\langle n_{\mathbf{q}}(t=0) \rangle$ . Bottom: frequency dependence of the imaginary part of the charge-charge correlation function at the same wave vectors.

grounds. At  $\mathbf{q} = 0$ , which is the most relevant case, one gets a Lorentzian-shaped Drude peak

$$\sigma_{\mathbf{q}=0}^{xx}(\nu) = \frac{\chi_c D}{1 + \left(\frac{\nu}{\Gamma}\right)^2} \quad (24)$$



indicating  $\sigma_{\text{dc}, \mathbf{q}=0}^{xx} \equiv \sigma_{\mathbf{q}=0}^{xx}(\nu = 0) = \chi_c D$ , which is the well-known Nernst-Einstein equation.

It is important to note that, *a priori*, the forms (21), (22) and (24) of  $\Lambda$  and  $\sigma$  are unphysical. The scaling with high frequency

$$\text{Im} \Lambda_{\mathbf{q}=0}(\nu \rightarrow \infty) \sim \frac{1}{\nu} \quad (25)$$

cannot be obtained from a correlation function in imaginary time  $\Lambda_{\mathbf{q}=0}(\tau)$  that has the correct symmetries. The Lorentzian Drude peak  $\sigma \sim \frac{1}{\nu^2}$  must be restricted to some finite frequency. In general, one expects that at high-frequency,  $\text{Im} \chi(\nu)$  and  $\text{Im} \Lambda(\nu)$  decay exponentially. In the noninteracting case, there is even a sharp cutoff: both charge and current fluctuations are bounded in frequency from above, with a bound that depends on  $\mathbf{q}$  (see Sec. III A). In any case, on the Matsubara axis one must have  $\chi(i\nu \rightarrow i\infty) \sim 1/\nu^2$  and  $\Lambda(i\nu \rightarrow i\infty) \sim 1/\nu^2$ . The hydrodynamic ansatz for the charge fluctuations [Eq. (14)] does not violate this, as on the upper half of the Matsubara axis

$$\chi_{\mathbf{q}}(i\nu) = \frac{\chi_c}{1 + \frac{\nu}{q^2 D} + \frac{\nu^2}{q^2 D^2}}, \quad (26)$$

but, through the continuity equation, it does imply a nonphysical asymptotic behavior  $\Lambda_{\mathbf{q}=0}(i\nu \rightarrow i\infty) \sim \frac{1}{\nu}$ . To be able to compare the hydrodynamic theory with Matsubara-frequency results for the charge-charge and current-current correlation functions, we thus propose a modified hydrodynamic form. The details are given in Sec. III C.

The imaginary-axis form (26) may still be useful in the  $U \rightarrow 0$  limit. The high-frequency asymptotics on the imaginary axis is determined by the entirety of the function on the real axis. As the coupling constant is decreased, the weight of the function  $\chi_{\mathbf{q} \rightarrow 0}$  on the real axis will be contained in an increasingly small range of low frequencies. If we assume that the hydrodynamic theory holds in some low-frequency range, say  $|\omega| < |\omega_{\text{max}}|$ , and that  $\omega_{\text{max}}$  saturates to a finite constant as  $U \rightarrow 0$ , then we can conclude that the imaginary-axis asymptotics of  $\chi_{\mathbf{q} \rightarrow 0}$  will tend to Eq. (26) as  $U \rightarrow 0$ . Clearly, nonuniversal features at high real frequencies will still be there, but they will not contribute significantly to the imaginary-axis asymptotics. Other scenarios are also possible, but in the following we work out the consequences of our expectation that the hydrodynamic law holds in a *finite* range of frequency in the  $U \rightarrow 0$  limit. We start with Eq. (7), which implies the long-wavelength asymptotics of the charge-charge correlation function of the form (see Appendix B for details)

$$\text{Re} \chi_{\mathbf{q} \rightarrow 0}(i\nu \rightarrow i\infty) = -\frac{2t}{\nu^2} \sum_{\eta=\{x,y\}} \sum_{\mathbf{k}} q_{\eta} \sin k_{\eta} \mathbf{q} \cdot \nabla \langle n_{\mathbf{k}} \rangle. \quad (27)$$

This form is not necessarily isotropic. Nevertheless, one can take  $\mathbf{q} = (q, 0)$  and, then, assuming a finite  $\omega_{\text{max}}$  and  $U \rightarrow 0$ , equate the right-hand side of Eq. (27) with the  $i\nu \rightarrow i\infty$  limit of Eq. (26) to obtain

$$D\Gamma = -\frac{1}{\chi_c} \sum_{\mathbf{k}} v_{\mathbf{k}}^x \partial_{k_x} \langle n_{\mathbf{k}} \rangle \quad (28)$$

with  $v_{\mathbf{k}}^x = 2t \sin k_x$ . Under the current assumption of the weak-coupling limit, we can write further

$$D\Gamma = -\frac{1}{\chi_c} \sum_{\mathbf{k}} (v_{\mathbf{k}}^x)^2 [2n'_{\text{F}}(\varepsilon_{\mathbf{k}})]. \quad (29)$$

At high temperature  $T = 1/\beta \rightarrow \infty$ , the first derivative of the Fermi distribution  $n'_{\text{F}}(\omega) \sim -\beta/4$ , and  $\chi_c = \frac{\partial \langle n \rangle}{\partial \mu} = -\int d\varepsilon \rho(\varepsilon) 2n'_{\text{F}}(\varepsilon) \sim \frac{2\beta}{4} \int d\varepsilon \rho(\varepsilon) = \beta/2$ . We also have  $\frac{1}{(2\pi)^2} \int d\mathbf{k} \sin k_x = \frac{1}{2}$ . We conclude that in the weak-coupling limit and high temperature, the effective hydrodynamic theory formulated by Eqs. (3) and (4) for the square-lattice Hubbard model [Eq. (1)], if valid in a finite range of real frequency, must satisfy

$$\lim_{\substack{U \rightarrow 0 \\ T \rightarrow \infty}} D\Gamma = 2t^2. \quad (30)$$

Thus, the equation of motion (11) provides some microscopic support for the effective hydrodynamic theory. As already mentioned, Eq. (30) indeed coincides with numerical results, and is roughly satisfied in a broad range of temperatures, even at strong coupling (see Sec. III B). Finally, we note that the imaginary-axis asymptotics [Eq. (27)] combined with  $\sigma_{\text{dc}} = \chi_c D$  [Eq. (24)] reveals that the hydrodynamic theory [Eq. (26)], taken to be valid at any frequency, is consistent with the Boltzmann expression for the dc conductivity

$$\sigma_{\text{dc}} = -\frac{1}{\Gamma} \sum_{\mathbf{k}} v_{\mathbf{k}}^x \partial_{k_x} \langle n_{\mathbf{k}} \rangle. \quad (31)$$

### III. RESULTS

#### A. Noninteracting limit

We are interested in calculating two-particle correlation functions, in particular for the charge and current. In the noninteracting limit, these can be obtained numerically exactly, to a high accuracy, from the general (Kubo) bubble formula

$$Q_{\mathbf{q}}[\varphi, \phi](\tau) = 2 \sum_{\mathbf{k}} \varphi_{\mathbf{k}, \mathbf{q}} G_{0, \mathbf{k}}(\tau) G_{0, \mathbf{k}+\mathbf{q}}(-\tau) \phi_{\mathbf{k}+\mathbf{q}, -\mathbf{q}}. \quad (32)$$

The factor 2 in front is due to summation over  $\sigma$ . We denote  $G_0$  the bare propagator, which is, at a finite temperature  $T = \frac{1}{\beta}$ , defined in the imaginary-time window  $\tau \in [-\beta, \beta]$  as

$$G_{0, \mathbf{k}}(\tau) = -\text{sign}(\tau) e^{-\varepsilon_{\mathbf{k}} \tau} n_{\text{F}}[-\text{sign}(\tau) \varepsilon_{\mathbf{k}}] \quad (33)$$

with  $n_{\text{F}}(\omega) = \frac{1}{e^{\beta\omega} + 1}$  the Fermi-Dirac distribution function.

The “vertex factors”  $\varphi$  and  $\phi$  correspond to the operators for which the correlation function is calculated (in general,  $\mathcal{O}_{\mathbf{q}} = \sum_{\sigma, \mathbf{k}} \varphi_{\mathbf{k}, \mathbf{q}} c_{\sigma, \mathbf{k}+\mathbf{q}}^{\dagger} c_{\sigma, \mathbf{k}}$ ). We then simply have  $\chi_{\mathbf{q}} = Q_{\mathbf{q}}[\varphi = 1, \phi = 1]$ , and  $\Lambda_{\mathbf{q}}^{\eta, \eta'} = Q_{\mathbf{q}}[\varphi = v^{\eta}, \phi = v^{\eta'}]$ , with  $v_{\mathbf{k}, \mathbf{q}}^{\eta} = it(e^{-i(k_{\eta} + q_{\eta})} - e^{ik_{\eta}})$ . In the entire complex frequency plane, one can then write

$$Q_{\mathbf{q}}[\varphi, \phi](z) = 2 \sum_{\mathbf{k}} \varphi_{\mathbf{k}, \mathbf{q}} \phi_{\mathbf{k}+\mathbf{q}, -\mathbf{q}} \frac{n_{\text{F}}(\varepsilon_{\mathbf{k}+\mathbf{q}}) - n_{\text{F}}(\varepsilon_{\mathbf{k}})}{z - (\varepsilon_{\mathbf{k}} - \varepsilon_{\mathbf{k}+\mathbf{q}})}. \quad (34)$$

We now consider the long-wavelength limit for the charge-charge correlation function  $\chi$ . At small enough  $\mathbf{q}$ , one can write further:  $\varepsilon_{\mathbf{k}+\mathbf{q}} = \varepsilon_{\mathbf{k}} + \mathbf{q} \cdot \nabla \varepsilon_{\mathbf{k}}$  and  $n_{\text{F}}(\varepsilon_{\mathbf{k}+\mathbf{q}}) = n_{\text{F}}(\varepsilon_{\mathbf{k}}) +$

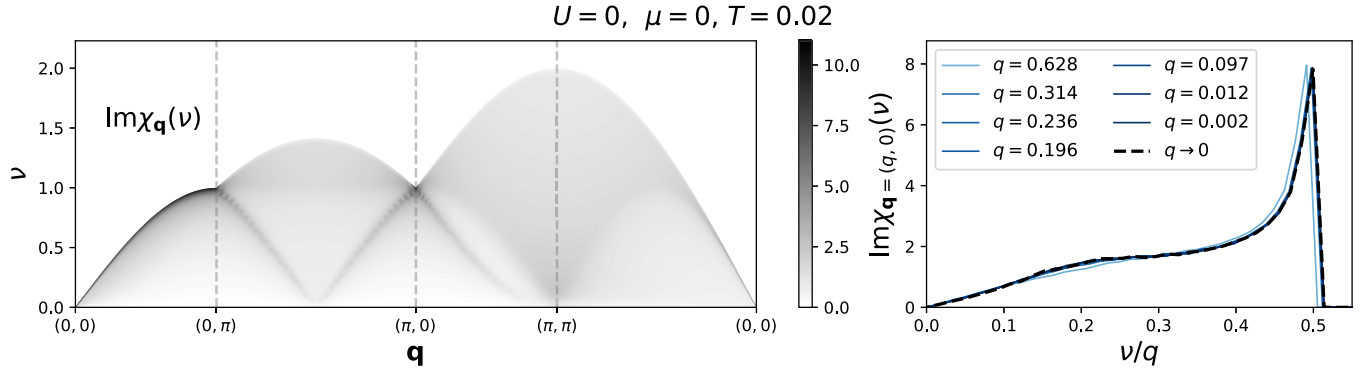


FIG. 2. Noninteracting case, half-filling. Left: imaginary part of the charge-charge correlation function along a high-symmetry path in the BZ. Right: frequency dependence in the long-wavelength limit, for waves in the  $x$  direction. The spectral weight drops off abruptly at  $\nu/q = \frac{1}{2}$ ; the apparent finite slope comes from the finite-frequency resolution in our numerics.

$(\mathbf{q} \cdot \nabla \varepsilon_{\mathbf{k}}) n'_F(\varepsilon_{\mathbf{k}})$ . These yield

$$\chi_{\mathbf{q} \rightarrow 0}(z) = 2 \sum_{\mathbf{k}} \frac{(\mathbf{q} \cdot \nabla \varepsilon_{\mathbf{k}}) n'_F(\varepsilon_{\mathbf{k}})}{z + \mathbf{q} \cdot \nabla \varepsilon_{\mathbf{k}}}. \quad (35)$$

We see that at small  $q \equiv |\mathbf{q}|$ , the frequency dependence no longer depends on  $q$ . In the denominator,  $q$  multiplies the number which determines the position of a pole on the energy axis. Therefore,  $q$  sets the energy scale, which means that with a proper rescaling of the  $\nu$  axis,  $\chi$  results for different small  $\mathbf{q}$  along a given direction can be collapsed onto a single curve. In the special case  $\mathbf{q} = (q, 0)$ , the gradient of the dispersion will simply yield the velocity  $v_{\mathbf{k}}^x \equiv v_{\mathbf{k}, \mathbf{q}=0}^x = 2t \sin k_x$ , and one arrives at

$$\lim_{q \rightarrow 0} \chi_{\mathbf{q}=(q,0)}(z) = 2 \sum_{\mathbf{k}} \frac{v_{\mathbf{k}}^x n'_F(\varepsilon_{\mathbf{k}})}{z/q + v_{\mathbf{k}}^x}. \quad (36)$$

On the most general physical grounds, it is not expected that in the noninteracting limit an effective hydrodynamics governs the charge fluctuations at however long the wavelengths. The diffusive motion of carriers at length scales  $\lambda > 2\pi/q_D$  ultimately comes from a finite-lasting memory the electrons have of momentum; in the noninteracting case, the momentum eigenstates are infinitely long lived. It is clear that no identification between Eqs. (36) and (14) is possible. In fact, the noninteracting case presents strongly nonuniversal, parameter-dependent, and even anisotropic behavior that we illustrate in the following.

We obtain the  $\chi_{\mathbf{q}}(\nu)$  along a high-symmetry path in the Brillouin zone (BZ) using a  $6000 \times 6000$  site lattice, and adaptive frequency grids to ensure sufficient frequency resolution at all  $\mathbf{q}$  vectors. We color plot  $\text{Im}\chi_{\mathbf{q}}(\nu)$  and show the frequency-dependent part at small  $\mathbf{q}$  in Figs. 2–5.

In Fig. 2 we show results for the half-filled case  $\mu = 0$ ,  $T = 0.02$ . In the long-wavelength limit, we observe a sharp peak at the edge of the spectrum, at  $\nu \sim q$ . The peak is highly asymmetric, as the spectral weight drops off abruptly on the higher-frequency side. The single-peak structure at  $\nu \sim q$  is the expected linear zero-sound mode [23].

As the system is doped away from half-filling, we start to observe a two-peak structure at long wavelengths (Fig. 3). This can be understood by analyzing Eq. (36). In Fig. 3 we illustrate how the contributions to  $\text{Im}\chi_{\mathbf{q}=(q,0)}(\nu)$  at a given

energy  $\nu$  comes from a line in the Brillouin zone (BZ) where  $-v_{\mathbf{k}}^x = \nu/q$ . The amplitude of a contribution at a given  $\mathbf{k}$  is given by  $v_{\mathbf{k}}^x n'_F(\varepsilon_{\mathbf{k}})$ , which roughly selects the Fermi surface. Therefore, one gets a peak at frequencies where  $v_{\mathbf{k}}^x$  is maximal, but also where the Fermi surface is parallel to the  $k_y$  axis. This calculation resembles a histogram of a one-dimensional (1D) function, and thus the spectrum resembles a typical density of states of a 1D tight-binding chain.

On Fig. 4 we illustrate the great level of anisotropy, by comparing the  $q \rightarrow 0$  limit for  $\mathbf{q} = (q, 0)$  and  $\mathbf{q} = \frac{1}{\sqrt{2}}(q, q)$ . It is interesting that, as the temperature is increased, the anisotropy at low frequency becomes somewhat reduced.

Doping all the way to the near-empty limit, one observes a completely different behavior (see Fig. 5). The charge fluctuation spectrum closely resembles the electron dispersion. This indicates that in the single-particle limit, due to the irrelevance of the Fermi-Dirac statistics, the charge and the electron become the same.

### 1. CDW amplitude evolution

It is of interest to understand these  $\chi_{\mathbf{q}}(\nu)$  results in the context of the quench setup studied in Ref. [18] and already mentioned in Sec. II B. Namely, we wish to investigate the time evolution of the amplitude of a relaxing charge density wave (CDW). If the initial CDW is weak, we can work within the linear-response theory, which can be solved numerically, by plugging Eq. (34) with  $\varphi, \phi = 1$  in Eq. (13). The Fourier transform needed for this step is performed analogously to Eq. (17). Then, to perform the integral in Eq. (13) analytically, it is necessary to regularize the integrand function, first. As is always done when working with retarded quantities, we take that the poles are located slightly below the real axis. We obtain

$$\langle n_{\mathbf{q}}(t) \rangle \sim \sum_{\mathbf{k}} \frac{n_F(\varepsilon_{\mathbf{k}+\mathbf{q}}) - n_F(\varepsilon_{\mathbf{k}})}{\varepsilon_{\mathbf{k}} - \varepsilon_{\mathbf{k}+\mathbf{q}}} e^{-it(\varepsilon_{\mathbf{k}} - \varepsilon_{\mathbf{k}+\mathbf{q}})}. \quad (37)$$

We show several examples of this calculation in Fig. 6. We find numerous categories of solutions, and we illustrate some of them on the panels of Fig. 6, left to right:

- (i) power-law damped oscillations,
- (ii) power-law damped oscillations with a breathing amplitude,

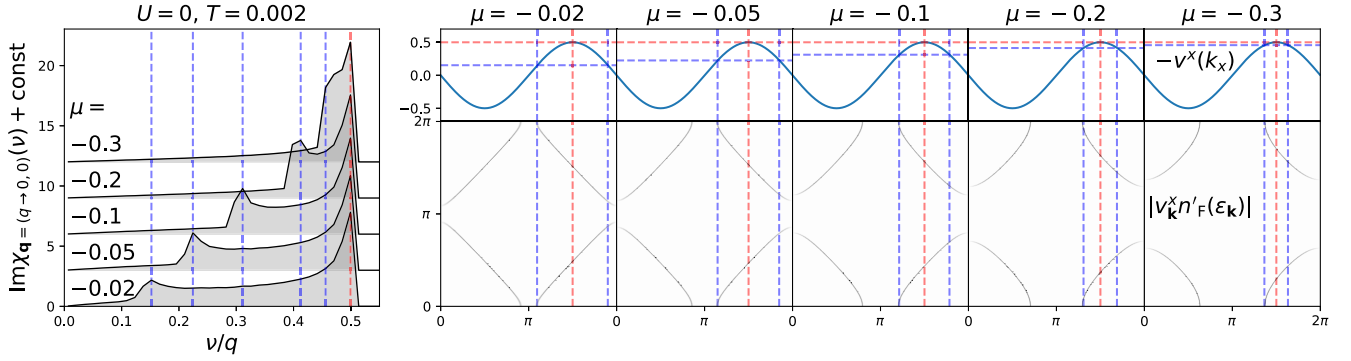


FIG. 3. Noninteracting case, various moderate dopings. Left: frequency dependence of the imaginary part of the charge-charge correlation function in the long-wavelength limit, for waves in the  $x$  direction. Vertical blue and red dashed lines denote frequencies of two apparent peaks. Right: explanation for the appearance of two peaks. Top row: the electron velocity. Blue and red dashed lines denote the momenta where  $v_k^x = -v/q$ , where  $v$  is the frequency of the two peaks in the spectra on the left. Bottom row: the intensity plots (black and white scale) of the amplitude of the contribution to the charge-charge correlation function coming from different  $\mathbf{k}$  vectors in the BZ. The blue and red dashed lines denote the contributions to the two peaks in the spectra on the left.

(iii) power-law damped oscillations with a decaying nonoscillatory component,

(iv) power-law decaying nonoscillatory behavior.

The behavior at  $\mathbf{q} = (\pi, \pi)$  is drastically different from the behavior at long wavelengths. At  $(\pi, \pi)$  there is no clear peak in the spectrum, i.e., no characteristic frequency to produce oscillatory behavior. In particular, as  $T \rightarrow 0$ , the

charge-charge correlation function (which is in the noninteracting limit equal to the spin-spin correlation function) approaches the form of a second-order pole  $\sim 1/z^2$ , which signals the instability towards order. One therefore finds only a nonoscillatory decay of the initial CDW amplitude, somewhat reminiscent of the diffusive regime of the hydrodynamic theory.

## 2. Beyond linear response

To cross-check these results and to be able to access the regime beyond the linear response (corresponding to initial density wave of a bigger amplitude) we perform the corresponding Kadanoff-Baym three-piece contour calculation [26].

The external field couples to the density wave at the wave vector  $\mathbf{q} = (q, 0)$ ,

$$\begin{aligned} H[V] &= H_0 - V \sum_{\sigma, \mathbf{r}} \cos(\mathbf{q} \cdot \mathbf{r}) n_{\sigma, \mathbf{r}} \\ &= H_0 - \frac{V}{2} \sum_{\sigma, \mathbf{k}} (c_{\sigma, \mathbf{k}+\mathbf{q}}^\dagger c_{\sigma, \mathbf{k}} + \text{H.c.}) \end{aligned} \quad (38)$$

$$= H_0 - \frac{V}{2} (n_{\mathbf{q}} + n_{-\mathbf{q}}), \quad (39)$$

where  $V$  is the strength of the field. We assume the field was turned on slowly at  $t = -\infty$ , and that by the time  $t = 0$ , the system is already thermalized. Then, at  $t = 0$ , the field is turned off abruptly. Therefore,

$$H(t < 0) = H[V], \quad H(t > 0) = H_0. \quad (40)$$

In general, the expectation value of an operator  $\mathcal{O}$  at time  $t$  following the quench of the field  $V$  is given by

$$\langle \mathcal{O}(t) \rangle = \frac{\text{Tr}[e^{-\beta H[V]} e^{iH_0 t} \mathcal{O} e^{-iH_0 t}]}{\text{Tr}[e^{-\beta H[V]}]}. \quad (41)$$

After the quench, the Hamiltonian has the diagonal form

$$H_0 = \sum_{\mathbf{k}\sigma} \epsilon_{\mathbf{k}} c_{\sigma, \mathbf{k}}^\dagger c_{\sigma, \mathbf{k}}, \quad (42)$$

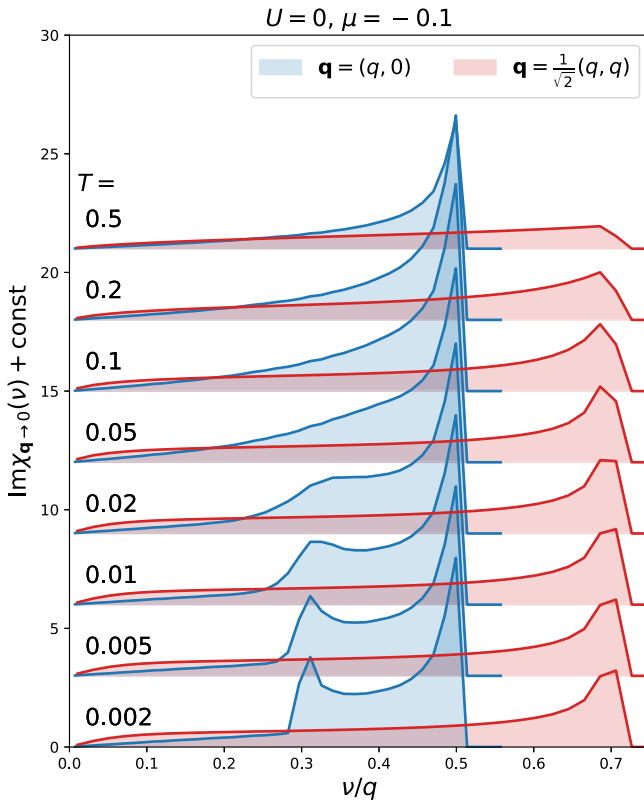


FIG. 4. Noninteracting case, moderate doping, various temperatures. Blue and red curves correspond to the long-wavelength limit of the imaginary part of the charge-charge correlation function for waves in the  $x$  and  $x = y$  directions.

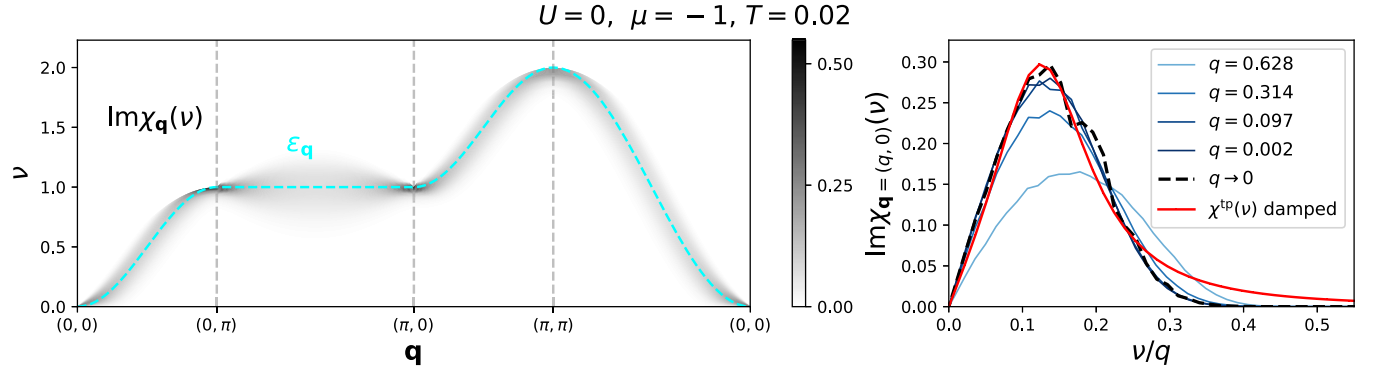


FIG. 5. Noninteracting case, nearly empty limit. Left and right: same as Fig. 2. Cyan line on the left: electron dispersion. Red line on the right: fit to the frequency-dependent part of the hydrodynamic theory  $\chi^{\text{tp}}$  as defined in Eq. (15); best fit corresponds to the damped oscillations (or ballistic) regime ( $r$  purely real).

whereas before the quench, the diagonal form is

$$H[V] = \sum_{\tilde{k}_x \mathcal{V} k_y} \sum_{\sigma} \varepsilon_{(\tilde{k}_x \mathcal{V} k_y) \sigma} c_{(\tilde{k}_x \mathcal{V} k_y) \sigma}^{\dagger} c_{(\tilde{k}_x \mathcal{V} k_y) \sigma}. \quad (43)$$

Because of the symmetry-breaking field, there is a reduction of the Brillouin zone, i.e.,  $\tilde{k}_x \in [0, 2\pi/\lambda)$ , where  $\lambda = 2\pi/q$  is the wavelength, or the number of sites in the unit cell; the additional quantum number arising due to the reduction of the BZ is  $\mathcal{V}$ .

The time evolution of density at a given point in space  $\mathbf{r} = (x, 0)$  [the translational symmetry is not broken along the  $y$  axis: nothing changes if we take a more general  $\mathbf{r} = (x, y)$ ] is given by

$$\langle n_{\mathbf{r}}(t) \rangle \equiv \left\langle \sum_{\sigma} c_{\mathbf{r}\sigma}^{\dagger}(t) c_{\mathbf{r}\sigma}(t) \right\rangle$$

$$= \frac{2}{N} \sum_{\tilde{k}_x, k_y \in \text{RBZ}} \sum_{c, c' \in [0, \lambda)} \sum_{\mathcal{V}} e^{ix(c-c')q} e^{-i(\epsilon_{\tilde{k}} - \epsilon_{\tilde{k}'})t} \times \langle \tilde{k}_x \mathcal{V} k_y | k'_x k_y \rangle \langle k_x k_y | \tilde{k}_x \mathcal{V} k_y \rangle n_{\text{F}}(\varepsilon_{\tilde{k}_x \mathcal{V} k_y}), \quad (44)$$

where we take  $k_x = \tilde{k}_x + cq$ ,  $k'_x = \tilde{k}_x + c'q$ . The eigenstates of  $H_0$  are denoted  $|k_x k_y\rangle$ , and the eigenstates of  $H[V]$  are denoted  $|\tilde{k}_x \mathcal{V} k_y\rangle$ . The amplitude of the charge density wave  $n_{\mathbf{q}}$  is given by the deviation of  $n_{\mathbf{r}}$  from the lattice-averaged density, at the antinode of the wave, say  $\mathbf{r} = (0, 0)$ .

We find perfect agreement between the results of Eq. (44) with  $V$  taken small and Eq. (37) which is in the strict  $V \rightarrow 0$  limit. The full Kadanoff-Baym calculation is clearly more computationally expensive, but it allows us to set  $V$  to stronger values and investigate the behavior starting from CDWs of finite amplitude. This is shown in Fig. 7. In the two panels on the right, we see that regular damped oscillations are replaced by a superposition of multiple waves as  $V \rightarrow \infty$ . This can

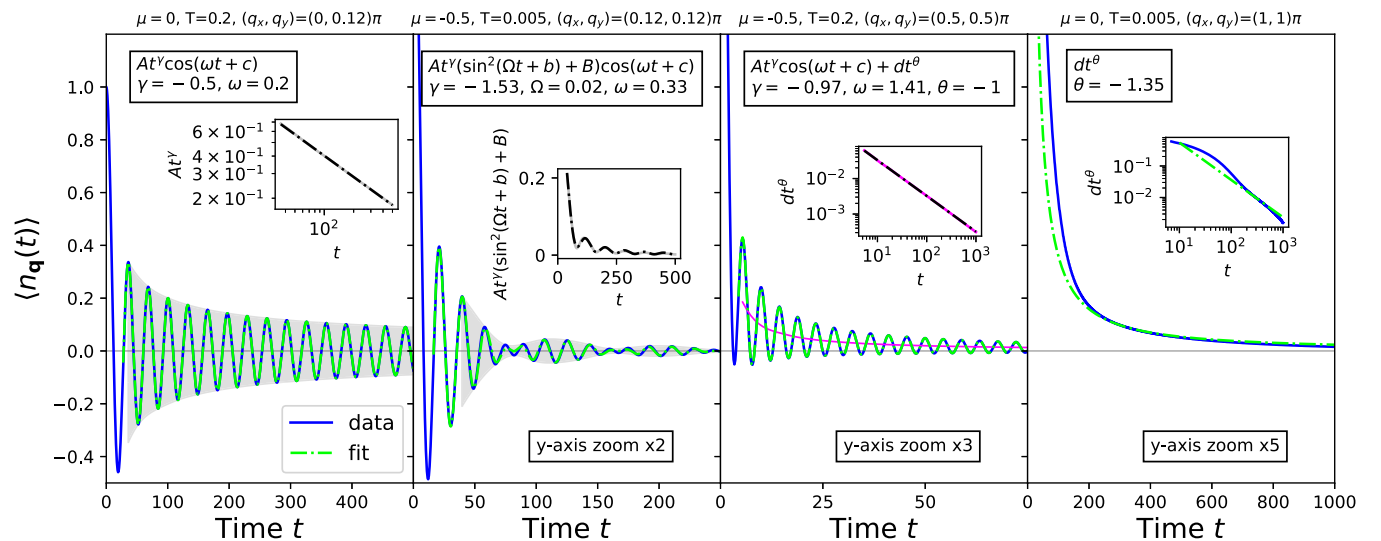


FIG. 6. Noninteracting case, various dopings, and temperatures. CDW amplitude vs time at various wave vectors, calculated within linear-response theory, normalized to the initial amplitude of the CDW. Text boxes show the fitting function and its main parameters. The insets in the two plots on the left show the amplitude of damped oscillations vs time, and the corresponding fit. The insets in the two plots on the right show the background, i.e., nonoscillatory components and the corresponding fits. Full lines are data, dotted-dashed lines are fits.

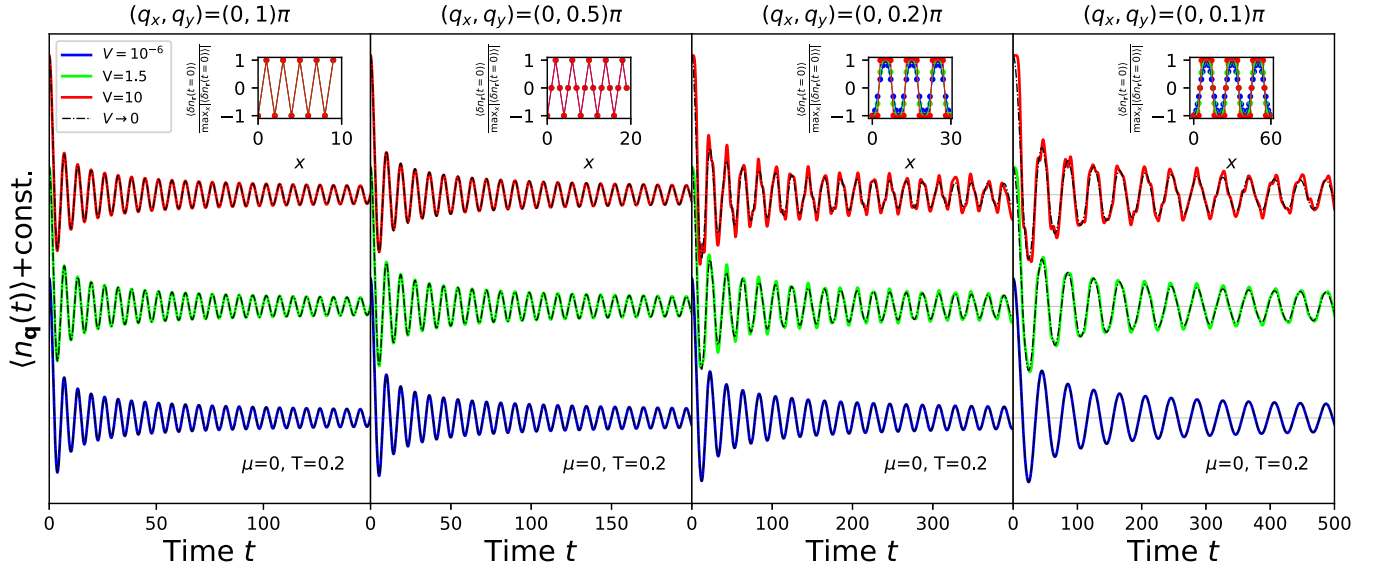


FIG. 7. Noninteracting case, half-filling, moderate temperature. CDW amplitude vs time at various wave vectors along the  $x$  axis, calculated within linear-response theory and from the full Kadanoff-Baym three-piece contour formalism, assuming different amplitudes of the density-modulating field  $V$  at  $t < 0$ . CDW amplitude is normalized to the initial amplitude of the CDW. Insets: density profile of the initial CDW at different strengths of the field  $V$ . See text for details.

be understood by looking at the density profile  $n_r$  at  $t < 0$  (shown in the insets of Fig. 7). One cannot place more than two electrons on a single site, which means that at strong values of  $V$ , the CDW is no longer harmonic; as  $V \rightarrow \infty$  it becomes similar to the step function. This density profile corresponds to having multiple CDWs at the same time, at  $q, 3q, 5q$ , etc. All these CDWs will oscillate at different frequencies, but one also expects interactions between the waves. It is not easy to explain the detailed structure of  $n_q(t)$  beyond the linear-response regime. However, in the long-wavelength limit, the characteristic frequency of CDWs is proportional to  $q$ , and we are able to roughly fit the resulting  $\langle n_q(t) \rangle$  to a superposition of waves  $\sim \sum_{l=1,3,5,\dots} t^{a_l} \cos(\omega t + c_l)$ . This is shown in Fig. 8. However, the two panels on the left in Fig. 7

show that at shortest wavelengths, one observes no change in behavior as  $V$  is increased. This is because the density profile  $n_r(t < 0)$  cannot change: there are no shorter waves to be excited by the increasing field.

## B. Weak-coupling theory

### 1. Self-energy

We start by calculating the self-energy up to the second order in the coupling constant:

$$\Sigma_{\mathbf{k}}(z) = U \langle n_{\bar{\sigma}} \rangle + U^2 \tilde{\Sigma}_{\mathbf{k}}(z), \quad (45)$$

$$\tilde{\Sigma}_{\mathbf{k}}(z) = \sum_{\mathbf{k}', \mathbf{q}} \frac{\sum_{s=\pm 1} n_F(-s\varepsilon_{\mathbf{k}'} ) n_F(s\varepsilon_{\mathbf{k}'+\mathbf{q}}) n_F(s\varepsilon_{\mathbf{k}-\mathbf{q}})}{z - \varepsilon_{\mathbf{k}-\mathbf{q}} - \varepsilon_{\mathbf{k}'+\mathbf{q}} + \varepsilon_{\mathbf{k}'}}. \quad (46)$$

The first term is the instantaneous Hartree shift, and the second term is the dynamic part, described by the second-order Feynman diagram illustrated in Fig. 9. The calculation of  $\tilde{\Sigma}$  is expensive. In Appendix E we describe a fast algorithm we used for this calculation, which allowed us to scan the phase diagram in considerable detail.

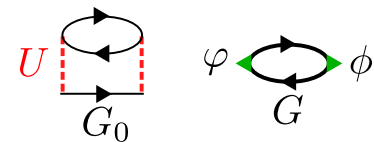


FIG. 9. Illustration of our weak-coupling theory. Left: second-order self-energy diagram comprising the dynamical part of the self-energy, formulated in terms of the bare fermionic propagator [Eq. (33)]. Right: generalized (Kubo) bubble approximation for two-particle correlation functions, formulated in terms of the “dressed” Green’s function [Eq. (47)].

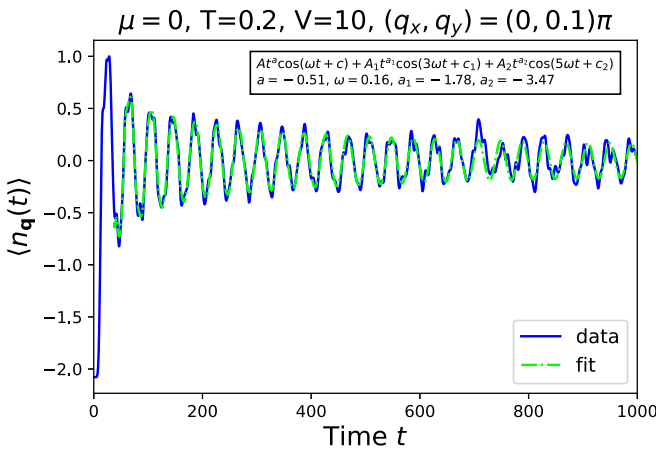


FIG. 8. Noninteracting case, half-filling, moderate temperature. Fit to the CDW amplitude vs time, starting from a saturated CDW with a short wave vector.



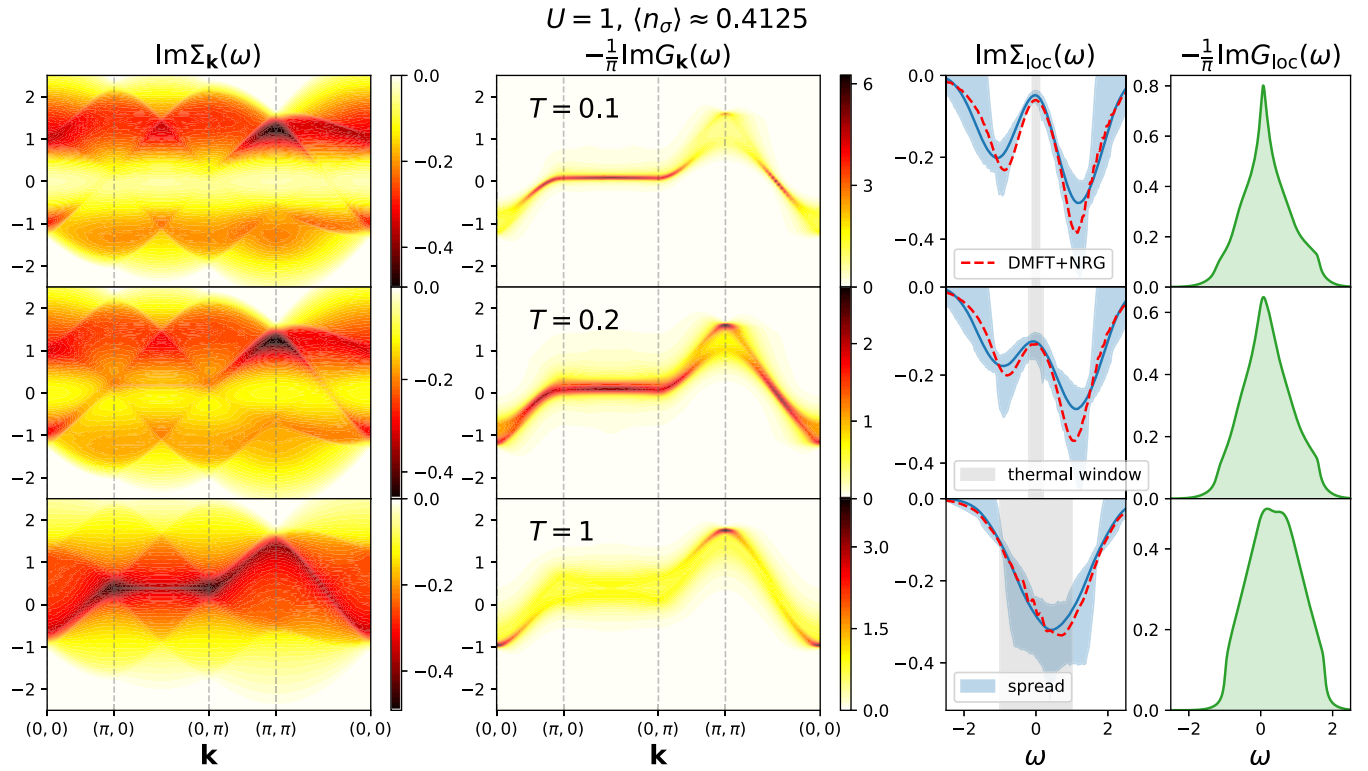


FIG. 10. Moderate coupling, moderate doping, various temperatures. Self-energy at the level of second-order perturbation theory, and the corresponding Green's functions. Third column: blue line is the local self-energy; blue shading is the  $\mathbf{k}$  spread, i.e., the range of values of  $\text{Im}\Sigma_{\mathbf{k}}$  at the given real frequency  $\omega$ ; red line DMFT (NRG) result for local self-energy; gray shading is the thermal window, denoting  $\omega \in [-T, T]$ . Rightmost column: the local density of states.

As we will see, for the practical calculations of conductivity in the limit  $U \rightarrow 0$ , the Hartree shift vanishes. At a finite  $U$ , we absorb the Hartree shift in the chemical potential, i.e.,  $\mu \rightarrow \mu - U\langle n_\sigma \rangle$ . This means that at a finite  $U$ , we compute the second-order self-energy diagram with Hartree-shifted propagators. Therefore, the frequency dependence of the dynamical part of the self-energy does not change with increasing  $U$ , if  $\tilde{\mu} = \mu - U\langle n_\sigma \rangle$  is kept fixed. In practice, we compute the occupancy *a posteriori*, and infer  $\mu$  from  $U\langle n_\sigma \rangle$  and  $\tilde{\mu}$ . The other possibility is to compute the self-energy diagram using bare propagators. The difference between the two approaches disappears when higher-order diagrams are also computed (under the condition that both series converge), as well as in the  $U \rightarrow 0$  limit.

We show examples of the self-energy results in Fig. 10. It is interesting that at low temperature, the frequency dependence of the self-energy generally features two peaks, while at high temperature, it features a single peak. At the highest temperatures, the peak follows the shape of the electron dispersion.

In Fig. 11 we zoom in on the low-frequency part, along a high-symmetry path in the BZ. We see that the scaling with  $\omega$  around  $\omega = 0$  takes different forms depending on  $\mathbf{k}$  and parameters of the model. The most interesting is the half-filling case, where we see that  $\mathbf{k} = (\pi, 0)$  and  $\mathbf{k} = (\frac{\pi}{2}, \frac{\pi}{2})$  are special points where in the  $T \rightarrow 0$  limit one approaches  $\text{Im}\tilde{\Sigma}(\omega \rightarrow 0) \sim |\omega|^\alpha$  with  $\alpha \approx \frac{4}{5}$  and  $\alpha = 1$ , respectively. More precisely, the linear scaling  $\alpha = 1$  is observed along the path connecting  $(0, \pi)$  and  $(\pi, 0)$ , but is modified abruptly to  $\alpha \approx \frac{4}{5}$  at those points. The linear scaling has been noted

before [27]. However, the apparent  $T \rightarrow 0$  limit of our second-order self-energy should only apply in the strict  $U \rightarrow 0$  limit. At any finite coupling and low enough temperature, higher perturbation orders will play a role, and produce an insulating state [28–31].

We also note a large number of kinks in the frequency dependence of  $\text{Im}\tilde{\Sigma}$ . The prominent peaks that appear at high temperature are not smooth: at the maximum no derivatives appear to be well defined.

## 2. Green's function and compressibility

Once we have the self-energy, we can plug it in the expression for the Green's function

$$G_{\mathbf{k}}(\omega) = \frac{1}{\omega - \varepsilon_{\mathbf{k}} - \Sigma_{\mathbf{k}}(\omega)}. \quad (47)$$

Examples of the Green's function are shown in Fig. 10, as well as for the local density of states  $-\frac{1}{\pi} \sum_{\mathbf{k}} \text{Im}G_{\mathbf{k}}(\omega)$ . We observe that the sharp structures in the self-energy at intermediate temperature lead to a splitting of the peak in the single-particle spectrum at  $\mathbf{k} \approx (\pi, \pi)$ .

Ultimately, from the Green's function we get the average density  $\langle n \rangle = -\frac{2}{\pi} \int d\omega \sum_{\mathbf{k}} \text{Im}G_{\mathbf{k}}(\omega) n_F(\omega)$ , and from it, the charge compressibility  $\chi_c = \frac{\partial \langle n \rangle}{\partial \mu}$ , which will be needed to estimate the diffusion constant. At finite  $U$ , in practice, what enters the calculation is  $\tilde{\mu} = \mu - U\langle n_\sigma \rangle$ . It is then easiest to compute the quantity  $\tilde{\chi}_c = \frac{\partial \langle n \rangle}{\partial \tilde{\mu}}$ . To get to the physical charge compressibility, one uses  $\chi_c = (\tilde{\chi}_c^{-1} + U/2)^{-1}$ .

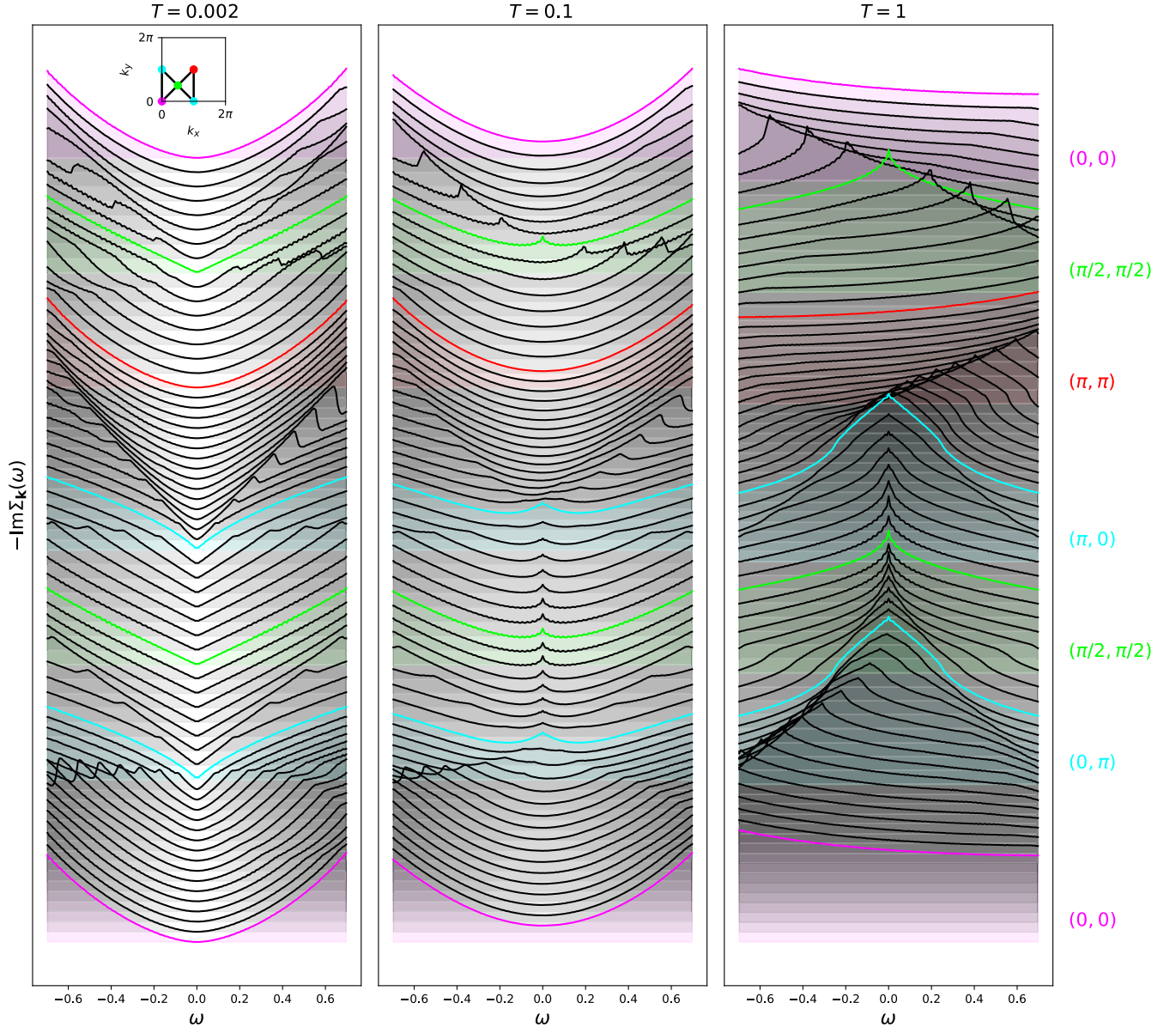


FIG. 11. Half-filling, various temperatures. Second-order self-energy along a high-symmetry path in the BZ; zoom in on low frequencies.

### 3. Bubble approximation for two-particle correlation functions

It is of great interest to see how the long-wavelength behavior of the charge-charge (or equivalently the current-current) correlation functions changes due to weak interactions. The simplest approach is to just calculate the bubble approximation for  $\chi$  or  $\Lambda$  (illustrated in Fig. 9). The bubble expression is simply the real-frequency formulation of Eq. (34), with the replacement  $G_0 \rightarrow G$ . One obtains (under assumption that  $\varphi_{\mathbf{k},\mathbf{q}}\phi_{\mathbf{k}+\mathbf{q},-\mathbf{q}}$  is purely real)

$$\begin{aligned} \text{Im}Q_{\mathbf{q}}[\varphi, \phi](\nu) &= \frac{2}{\pi} \sum_{\mathbf{k}} \varphi_{\mathbf{k},\mathbf{q}}\phi_{\mathbf{k}+\mathbf{q},-\mathbf{q}} \int d\omega \\ &\times \text{Im}G_{\mathbf{k}}(\omega)\text{Im}G_{\mathbf{k}+\mathbf{q}}(\omega+\nu)[n_{\text{F}}(\omega)-n_{\text{F}}(\omega+\nu)], \end{aligned} \quad (48)$$

where 2 in front comes from the summation over spin, and  $\frac{1}{\pi} = \frac{1}{\pi^2}\pi$  comes from the double Hilbert transform, and taking the delta-peak part of the integral (for detailed derivation in a more general case see Ref. [32]). We have implemented this calculation and show results below.

However, the bubble approximation is not sufficient to properly address the question of whether the hydrodynamic form for  $\chi$  [Eq. (14)] or  $\Lambda$  [Eq. (21)] is valid at small  $\mathbf{q}$ . By construction, the bubble does *not* satisfy the continuity equation. The reason for this is simple: the bubble expression is *formally* an exact solution for a noninteracting system coupled to an external fermionic bath, the hybridization being the dynamical part of the self-energy. The bubble approximation for  $\chi_{\mathbf{q}}(\nu)$  will therefore be manifestly wrong at  $\mathbf{q} = 0$ , as one will get  $\chi_{\mathbf{q}=0}(\nu \neq 0) \neq 0$ . Similarly, the bubble approximation for  $\text{Im}\Lambda_{\mathbf{q}}(\nu)$  will be manifestly wrong at  $\mathbf{q} \neq 0, \nu \rightarrow 0$ , as it will scale as  $\sim \nu$ , and thus signal a finite conductivity.

Clearly, if the system is open, a static wave of the electric field will scatter the incoming particles and maintain a current wave. The bubble approximations for  $\chi$  and  $\Lambda$  do not satisfy Eq. (7), and are not connected in a simple way. To restore physical properties, one needs to include vertex corrections, even at tiny couplings.

On the other hand, the bubble approximation for  $\text{Im}\Lambda_{\mathbf{q}=0}^{xx}(\nu)$  will not be *a priori* unphysical, and can be considered a reasonable approximation for this object at low couplings. The parameters of the hydrodynamic model are encoded in  $\text{Im}\Lambda_{\mathbf{q}=0}^{xx}(\nu)$  or, equivalently, in  $\sigma_{\mathbf{q}=0}^{xx}(\nu)$ . One can check whether  $\text{Im}\Lambda_{\mathbf{q}=0}^{xx}(\nu)$  satisfies Eq. (22). However, one has to keep in mind that different theories may reduce to the same form of  $\Lambda^{xx}$  at  $\mathbf{q} = 0$ . Even if  $\text{Im}\Lambda_{\mathbf{q}=0}^{xx}(\nu)$  satisfies Eq. (22) to a good degree, this cannot serve as proof that the hydrodynamic theory is valid. Nevertheless, assuming that the hydrodynamic theory is valid, one could use  $\text{Im}\Lambda_{\mathbf{q}=0}^{xx}(\nu)$  [or  $\sigma_{\mathbf{q}=0}^{xx}(\nu)$ ] to extract the parameters for the hydrodynamic model, and investigate how they change with the microscopic parameters, which is what we will present in the following.

#### 4. Optical conductivity in the weak-coupling limit

We distinguish here between the general weak-coupling regime (say  $U < 1$ ) and the strict  $U \rightarrow 0$  regime, i.e., the *weak-coupling limit*. To have a finite conductivity it is necessary to have scattering, so one cannot simply take  $U = 0$ , but must rather consider an infinitesimal  $U$ . In the weak-coupling limit, the bubble calculation for  $\sigma_{\mathbf{q}=0}^{xx}(\nu)$  simplifies. In this way, one obtains the scaling of quantities in terms of  $U$  in the  $U \rightarrow 0$  limit. In the following, we will distinguish between the simplified, *weak-coupling bubble*, and the *full bubble* calculations. The latter is computed for a finite  $U$ , using Eq. (48). The weak-coupling bubble is inexpensive and we use it to cover the entire phase diagram. We also perform some full bubble calculations at  $U = 0.75$  and  $1.0$  and show results below.

The weak-coupling limit simplification of the bubble can be understood as follows. If  $U$  is sufficiently small, then the peaks in the spectral function start to resemble Lorentzians centered at  $\omega = \varepsilon_{\mathbf{k}}$ :

$$G_{\mathbf{k}}(\omega \approx \varepsilon_{\mathbf{k}}; U \rightarrow 0) = \frac{1}{\omega - \varepsilon_{\mathbf{k}} - i \text{Im}\Sigma_{\mathbf{k}}(\varepsilon_{\mathbf{k}})}. \quad (49)$$

The shifts coming from  $\text{Re}\Sigma_{\mathbf{k}}(\omega)$  can be neglected, and  $\text{Im}\Sigma_{\mathbf{k}}(\omega)$  can be considered to be constant at the scale of the width of the peak. Away from  $\omega \approx \varepsilon_{\mathbf{k}}$ ,  $\text{Im}G(\omega)$  can be considered zero. Furthermore, the optical conductivity is expected to be nonzero only at tiny frequencies, which also simplifies the Fermi-Dirac factor. We are ultimately able to employ the integral

$$\int dx \text{Im} \frac{1}{x \pm iy} \text{Im} \frac{1}{x \pm \Delta \pm iy} = \frac{\pi}{2y} \frac{1}{\left(\frac{\Delta}{2y}\right)^2 + 1} \quad (50)$$

which in the limit  $\Delta = 0$  reduces to  $\frac{\pi}{2y}$ . In total we obtain

$$\sigma_{\mathbf{q}=0}^{xx}(\nu) = \sum_{\mathbf{k}} \frac{(v_{\mathbf{k}}^x)^2 n_F'(\varepsilon_{\mathbf{k}})}{\text{Im}\Sigma_{\mathbf{k}}(\varepsilon_{\mathbf{k}})} \left[ \left( \frac{\nu}{2 \text{Im}\Sigma_{\mathbf{k}}(\varepsilon_{\mathbf{k}})} \right)^2 + 1 \right]^{-1}. \quad (51)$$

It is important to compare this expression to the Boltzmann expression for the dc conductivity (31). The two expressions do coincide, but only under the assumption that  $\text{Im}\Sigma_{\mathbf{k}}(\varepsilon_{\mathbf{k}})$  does *not* depend on  $\mathbf{k}$ , in which case one would have  $\Gamma = -2 \text{Im}\Sigma_{\mathbf{k}}(\varepsilon_{\mathbf{k}})$ . However,  $\text{Im}\Sigma_{\mathbf{k}}(\varepsilon_{\mathbf{k}})$  retains considerable  $\mathbf{k}$  dependence even at infinite temperature as  $\lim_{T \rightarrow \infty} \text{Im}\tilde{\Sigma}_{\mathbf{k}}(\varepsilon_{\mathbf{k}}) = -\frac{\pi}{4} \sum_{\mathbf{k}'\mathbf{q}} \delta(\varepsilon_{\mathbf{k}} - \varepsilon_{\mathbf{k}+\mathbf{q}} - \varepsilon_{\mathbf{k}'+\mathbf{q}} + \varepsilon_{\mathbf{k}'})$ . The expression (51) presents a sum of Lorentzians of different heights and widths, and the end result might not fit well to the Lorentzian shape. Our weak-coupling theory does not *a priori* reduce to Eq. (31) or the hydrodynamic equation (24). At infinite temperature, the  $D$  and  $\Gamma$  we might extract from our results are *a priori* separate objects: their product  $D\Gamma$  will depend on the precise form of the self-energy.

We now pull the  $U^2$  factor out of the self-energy to obtain

$$\tilde{\sigma}_{\mathbf{q}=0}^{xx}(\tilde{\nu}) \equiv \sum_{\mathbf{k}} \frac{(v_{\mathbf{k}}^x)^2 n_F'(\varepsilon_{\mathbf{k}})}{\text{Im}\tilde{\Sigma}_{\mathbf{k}}(\varepsilon_{\mathbf{k}})} \left[ \left( \frac{\tilde{\nu}}{2 \text{Im}\tilde{\Sigma}_{\mathbf{k}}(\varepsilon_{\mathbf{k}})} \right)^2 + 1 \right]^{-1} \quad (52)$$

with the definitions

$$\sigma(\nu = \tilde{\nu}U^2) = \frac{\tilde{\sigma}(\tilde{\nu})}{U^2}. \quad (53)$$

At low frequency, we can now equate the hydrodynamic form (24) with the above equation, to reach the following:

$$\tilde{D} = \frac{\tilde{\sigma}_{\mathbf{q}=0}^{xx}(\tilde{\nu} = 0)}{\chi_c}, \quad D = \frac{\tilde{D}}{U^2}, \quad (54)$$

$$\tilde{\Gamma} = \delta \left( 1 - \frac{\tilde{\sigma}_{\mathbf{q}=0}^{xx}(\tilde{\nu} = 0)}{\tilde{\sigma}_{\mathbf{q}=0}^{xx}(\tilde{\nu} = \delta)} \right)^{-\frac{1}{2}}, \quad \Gamma = \tilde{\Gamma}U^2, \quad (55)$$

where we take  $\delta$  small.

This result gives us the estimate of how  $\Gamma$  and  $D$  behave as functions of  $U^2$ , at low coupling. Additionally, one can conclude that the diffusive regime extends to shorter wavelengths as coupling is increased, i.e.,

$$q_D = \sqrt{\frac{\Gamma}{4D}} = U^2 \sqrt{\frac{\tilde{\Gamma}}{4\tilde{D}}} \equiv U^2 \tilde{q}_D. \quad (56)$$

The coefficients  $\tilde{D}$  and  $\tilde{\Gamma}$  depend on the microscopic parameters, and we extract them from  $\tilde{\sigma}_{\mathbf{q}=0}^{xx}(\tilde{\nu})$ , calculated by Eq. (52).

Even though  $\tilde{\sigma}(\tilde{\nu})$  might not have the shape of a Lorentzian, the property  $\tilde{\sigma}(\tilde{\nu} \rightarrow 0) \sim \tilde{\sigma}_{\text{dc}}(1 - \tilde{\nu}^2)$  is guaranteed. Therefore, the form (24) is bound to hold at least at the lowest frequencies, and one can certainly extract the effective  $\tilde{\Gamma}$  via Eq. (55). It is interesting to see in what range of frequencies will the hydrodynamic equation (24) be valid.

#### 5. Results for dc resistivity

We first focus on the  $\tilde{\rho}_{\text{dc}} = 1/\tilde{\sigma}_{\text{dc}}$  results. The color plot of  $\tilde{\rho}_{\text{dc}}$  as a function of doping and temperature is given in Fig. 12. We show the  $T$  dependence at different dopings in the upper part of Fig. 13. We see the following trends. At half-filling one observes  $\tilde{\rho}_{\text{dc}} \sim T$  in the full range of accessible temperatures. The high-temperature limit of Eq. (52) can be easily computed for the half-filled case based on the high-temperature asymptotic form of  $\tilde{\Sigma}_{\mathbf{k}}(\varepsilon_{\mathbf{k}})$ . One obtains  $\tilde{\rho}_{\text{dc}}(T) = 13.08T$ . This appears to be the high-temperature asymptotic behavior at least at moderate dopings, as well. As one dopes away from

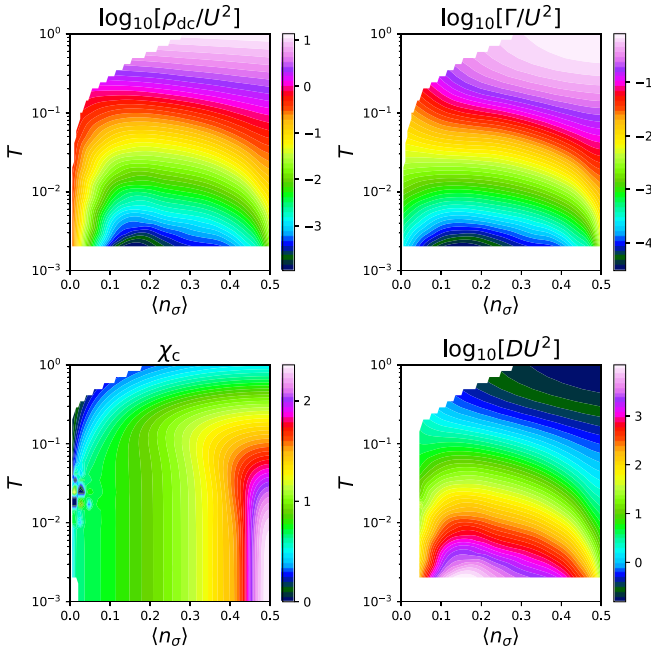


FIG. 12. Summary of weak-coupling results: doping-temperature phase diagram. Color plots of dc resistivity, diffusion constant, momentum-relaxation rate in the  $U \rightarrow 0$  limit, extracted from the weak-coupling bubble calculation (52), and the corresponding noninteracting compressibility.

half-filling, a  $\tilde{\rho}_{dc} \sim T^2$  (Fermi liquid, FL) regime emerges at ever higher temperatures, while the  $\tilde{\rho}_{dc} \sim T$  is pushed to higher  $T$ . Starting from around  $\langle n_\sigma \rangle = 0.3$ , the low- $T$  regime transforms into  $\tilde{\rho}_{dc} \sim T^{1.9}$ . At  $\langle n_\sigma \rangle = 0.15$  we no longer observe  $\tilde{\rho}_{dc} \sim T$  in the accessible range of temperature, but further doping continuously reduces the exponent in the FL-like regime. At very low fillings, we again see  $\tilde{\rho}_{dc} \sim T$  in the full range of  $T$ . The effective exponent  $\alpha$  of the  $T$  dependence of resistivity can be obtained as  $\alpha = \frac{\partial \ln \rho_{dc}(T)}{\partial \ln T}|_{\langle n \rangle}$  [33] and is color coded in the bottom part of Fig. 13.

It is interesting to inspect the case of fixed  $\mu = -1$ : this means that strictly  $k_F = 0$  and all occupancy comes from thermal excitations. There we observe roughly  $\tilde{\rho}_{dc} \rightarrow 0.4$  as  $T \rightarrow 0$  (see Fig. 14). This can be understood as follows: at low temperature, the contribution will come from an increasingly small vicinity of  $\mathbf{k} = 0$ . We observe that  $\text{Im} \Sigma_{\mathbf{k}=0}(\omega = 0) \sim T$ . On the other hand, the velocity of electrons will decrease as temperature is lower. Ultimately, the amplitude of contributions will reduce to the integral  $\int d\mathbf{k} k_x^2 e^{-\beta k^2} \sim \int_0^\infty dk k^3 e^{-\beta k^2} \sim T$ . This means that the increased coherence of the electrons will be canceled exactly by their decreasing velocity, and the resistivity will converge to a constant as  $T \rightarrow 0$ . At  $\mu$  slightly above  $-1$  one expects the resistivity to go to 0, whereas for  $\mu$  slightly below, one expects it to go to infinity.

### 6. Results for hydrodynamic parameters

The results for  $\tilde{D}$  and  $\tilde{\Gamma}$  are summarized on Fig. 12. It is apparent that roughly  $\tilde{D} \sim 1/\tilde{\Gamma}$ . This can be understood intuitively: the more coherent the quasiparticles, the bigger the

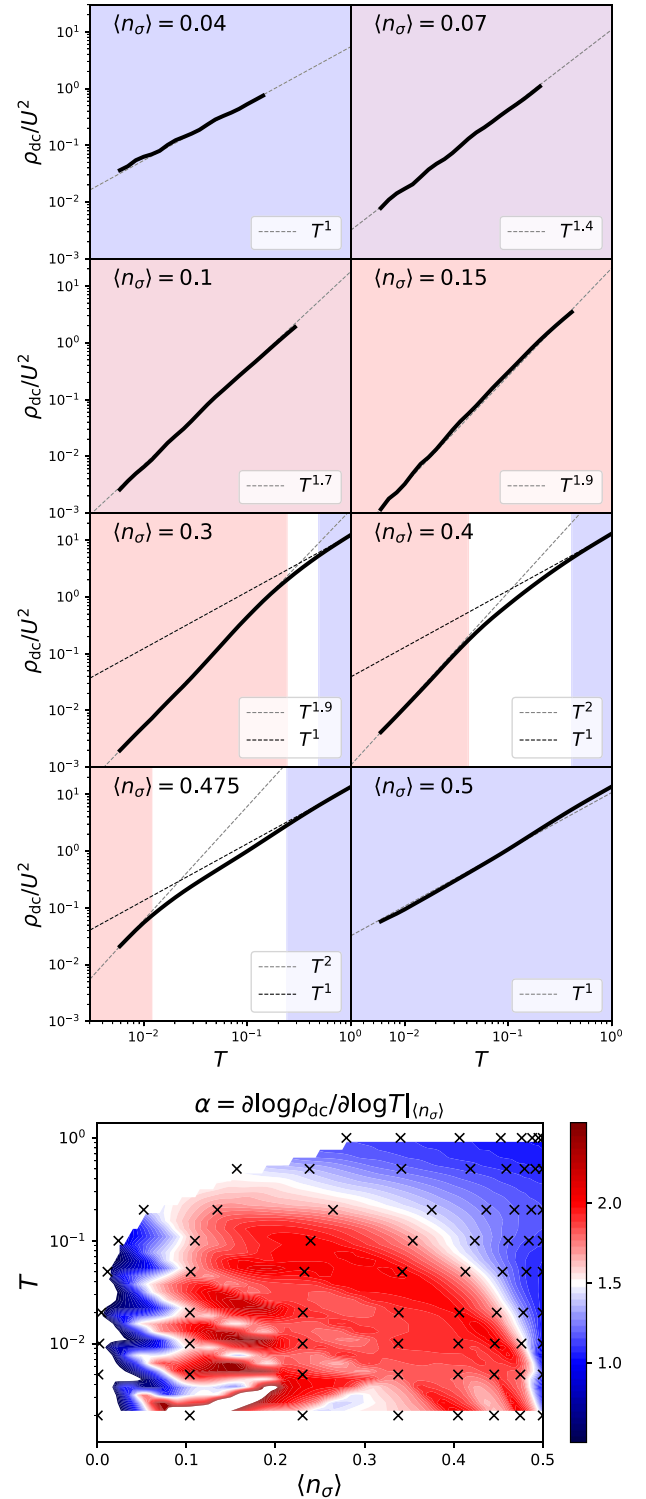


FIG. 13. Weak-coupling bubble dc resistivity results. Upper panels: temperature dependence at different dopings. Lower panel: effective exponent of the temperature dependence, color plotted in the doping-temperature plane; black crosses are actual data points; the rest are obtained by interpolation.

dc conductivity and the narrower the Drude peak. However, the inverse proportionality coefficient, i.e.,  $D\Gamma$  value is *a priori* unclear. We plot  $D\Gamma$  in Fig. 15 and find that results approach  $2t^2$  at high temperature. This is in agreement with



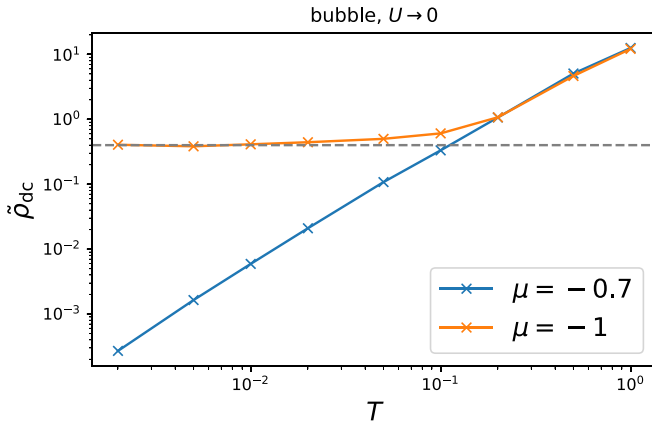


FIG. 14. Weak-coupling bubble ( $U \rightarrow 0$  limit) dc resistivity results at a fixed chemical potential. Horizontal line denotes 0.4, which is the value  $\rho_{dc}$  apparently converges to at  $\mu = -1$  and  $T \rightarrow 0$ .

the loose expectation based on Eq. (11), but also in agreement with the hydrodynamic theory [Eq. (30)]. We also plot the corresponding result from FTLM computed at a moderate and a strong value of coupling (strong-coupling data were reconstructed from Ref. [18]), and find a similar result. It is striking that  $D\Gamma$  is within  $\approx 20\%$  of  $2t^2$  in a large range of temperature and even at strong coupling.

In Fig. 16 we cross-check our weak-coupling  $\rho_{dc}$  result based on Eq. (51) with the corresponding full bubble calculation [Eq. (48)] at  $U = 1$ . As expected, the agreement is better at lower temperature and lower coupling (for the latter, the data are not shown), i.e., in cases where scattering rates  $\text{Im}\tilde{\Sigma}_k(\varepsilon_k)$  are smaller. We also compare our full bubble result to dynamical mean field theory (DMFT) [34] calculation at  $U = 1$  (implemented with the numerical renormalization group, NRG, real-frequency impurity solver [14,15,32,35–38]) and surprisingly, find excellent agreement. Our second-order self-energy  $\tilde{\Sigma}$  is clearly nonlocal (and remains nonlocal up to infinite temperature; see Fig. 10), yet the nonlocal part does not seem to play a big role in the value of dc resistivity. We check this explicitly by computing the bubble with only the local part of our self-energy: we find a very similar result. Moreover, the agreement with DMFT suggests that the local part of our second-order self-energy agrees well with DMFT. We confirm this in Fig. 10, especially in the thermal window  $\omega \in [-T, T]$ , which is the range of frequencies relevant for the conductivity calculation. We also compute the full bubble on a small  $4 \times 4$  lattice. In the previous work of some of us [14], it was shown that finite-size effects subside at high temperature, and that the  $(4 \times 4)$ -lattice FTLM calculation was correct at  $T \gtrsim 0.3$ . However, this was at the value of coupling  $U = 2.5$ ; we now see similar lack of finite-size effects even at  $U = 1$ , which is somewhat unexpected (at a lower  $U$  the relevant correlation lengths should be greater, and the systematic errors due to finite system size more pronounced). Comparing our full bubble result for  $\rho_{dc}$  at  $U = 1$  with the FTLM result at  $U = 1.25$  we can conclude that the vertex corrections are still sizable, and affect the result in a similar fashion as at  $U = 2.5$ , i.e., the vertex corrections present a roughly constant shift towards lower resistivity.

We compare  $D$  and  $\Gamma$  obtained from the weak-coupling bubble at  $U = 0.65$  [Eqs. (54) and (55)] to the FTLM result at  $U = 1.875$  and  $1.25$  and find surprising similarity (see Fig. 17). As was already apparent from Refs. [14,18], the bubble approximation tends to overestimate  $\rho_{dc}$  (i.e., underestimate  $D$ ) and overestimate  $\Gamma$ . This explains the apparent agreement between the weak-coupling bubble approximation and the numerically exact result at strong coupling. However, up to a prefactor, even our weak-coupling bubble results for  $\tilde{D}(T)$  and  $\tilde{\Gamma}(T)$  display a shape very similar to the FTLM result at  $U = 1.875$ . The behavior of the hydrodynamic parameters does not seem to change drastically going from weak to rather strong coupling. At a fixed temperature  $T = 0.5$ , the weak-coupling  $\Gamma \sim U^2$  and  $D \sim 1/U^2$  trends slow down at stronger coupling, so that the difference in  $\Gamma$  and  $D$  between  $U = 1.25$  and  $1.875$  results is rather small. The full bubble computed at  $U = 0.75$  improves the result of the weak-coupling bubble. It appears that in the strong-coupling limit,  $D \rightarrow 2t$ , and roughly  $\Gamma \rightarrow t$ , which is consistent with  $\lim_{U \rightarrow \infty} D\Gamma \approx 2t^2$ .

### 7. Deviations from the Lorentzian Drude peak

As for the frequency range of the validity of Eq. (24), i.e., the hydrodynamic form for the current-current correlation function (22): it strongly depends on the microscopic parameters. At high temperature the agreement is excellent up to the peak of  $\text{Im}\Lambda(\nu)$ , but, as expected, the high-frequency tail has a different scaling. This is shown in Fig. 18 where we compare a fitted equation (22) with the result of the full bubble calculation (48).

### 8. Critical wavelength for diffusive behavior

Finally, we go back to the simple prediction (56) that the characteristic wavelength for diffusive behavior will become shorter with increasing coupling. We check this directly in our  $\chi_q(\nu)$  results. As already mentioned, the bubble approximation is unsuitable for the investigation of  $\chi$  at very long wavelengths, but one might still want to inspect the results at somewhat bigger  $\mathbf{q}$ . In Fig. 19 we show the  $\text{Im}\chi_q(\nu)$  results at a fixed  $\mathbf{q} = (0.159, 0)\pi$ , and vary the coupling. The corresponding  $\langle n_q(t) \rangle$  results calculated via Eq. (13) are presented on the panel on the right. For the occupancy  $\langle n_\sigma \rangle \approx 0.4125$  and  $T = 0.2$ , our weak-coupling bubble calculation yields  $\tilde{q}_D = \sqrt{\frac{T}{4D}} \approx 0.15\pi$ , which means that the behavior should become diffusive at wave vector  $\mathbf{q} \approx (0.15\pi, 0)$  at around  $U = 1$ . This is in excellent agreement with the result we obtain directly from the full bubble approximation for  $\chi$ , as evidenced by Fig. 19, panel on the right. Here we have plugged the full bubble result for  $\chi_q(\nu)$  in the linear-response theory expression for the CDW amplitude  $n_q(t)$  [Eq. (13)].

### C. Strong coupling

We focus now on quantum Monte Carlo (QMC) results for the charge-charge and current-current correlation functions. We make use of the continuous-time interaction-expansion QMC, CTINT [21]. This method is numerically exact for a given lattice size. We calculate the intersite  $\chi_{ij}(i\nu)$  on the Matsubara frequency axis for a cyclic lattice of size  $L \times L$  and



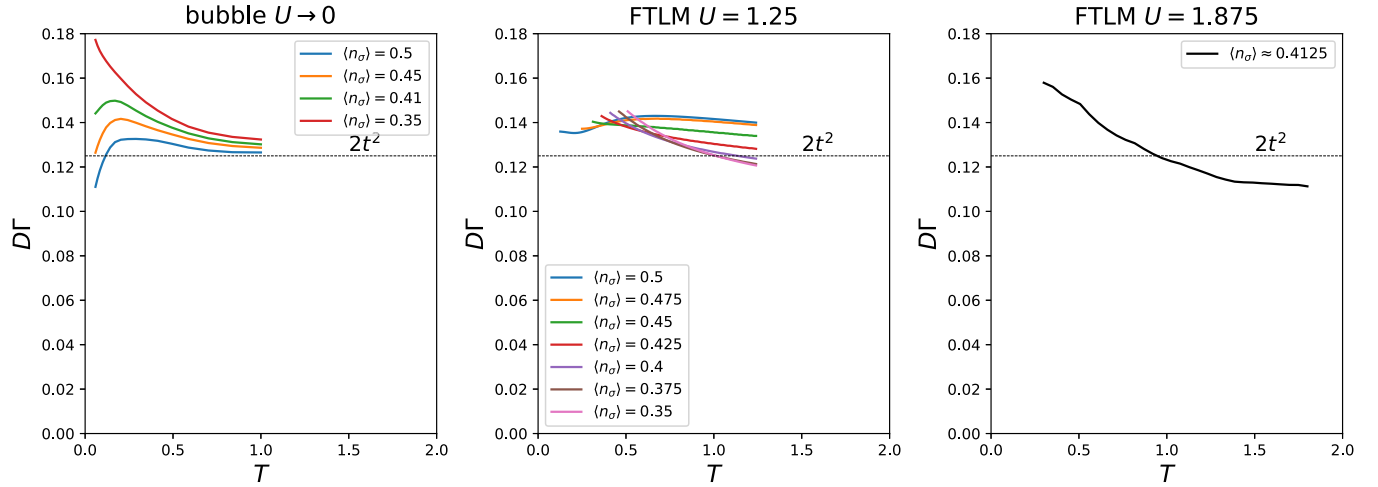


FIG. 15. Weak-coupling bubble ( $U \rightarrow 0$  limit) in comparison with moderate and strong coupling. At weak coupling,  $D$  and  $\Gamma$  are computed using Eqs. (55) and (54) at various dopings. At moderate and strong coupling, FTLM result is the best available result. At strong coupling, data are reconstructed from Ref. [18], but only for a single doping.

then perform a periodization procedure, where we promote the intersite components to the real-space components of an infinite lattice, and thus obtain  $\chi_{\mathbf{r}}(iv)$  of a finite range (components at  $\mathbf{r} : r_\eta > L/2$  are considered 0). We then Fourier transform to obtain  $\chi_{\mathbf{q}}(iv)$  with arbitrary resolution in the BZ. However, very short  $\mathbf{q}$  vectors corresponding to wavelengths much greater than  $L$  remain inaccessible. Nevertheless, we are able to obtain solid results for wavelengths up to 20 lattice spacings and that way cover the range of wavelengths studied in the cold-atom experiment by Brown *et al.* [18]. We perform the exact same procedure for  $\Lambda^{xx}$  as well.

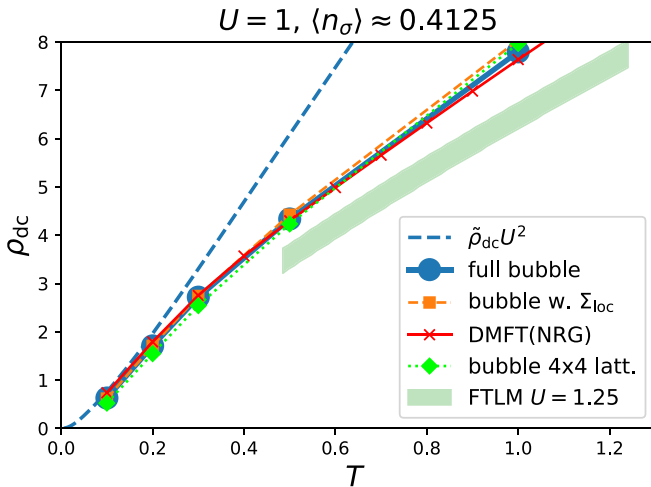


FIG. 16. Moderate coupling  $U = 1$ , moderate doping, results for dc resistivity. Dashed blue: weak coupling bubble. Blue line and dots: full bubble calculation. Orange dashed and squares: full bubble calculated with only the local component of self-energy. Red with crosses: full bubble with the local DMFT(NRG) self-energy result. Lime dotted with diamonds: full bubble computed on a  $4 \times 4$  lattice with the full  $\mathbf{k}$ -dependent second-order self-energy. Green stripe: FTLM  $4 \times 4$  result at a larger coupling  $U = 1.25$  (including the vertex corrections).

We perform a finite-size scaling analysis and observe that no obvious trends with  $L$  are apparent in the results already between  $L = 4$  and 10 (data not shown). This is consistent with the estimates from the recent Ref. [39] where it was shown in a thermodynamic limit DiagMC calculation that the charge correlations are short ranged, with values becoming very small already at distances of about 5 lattice spacings. In our calculations, we consider the statistical errors to be the leading uncertainty, and use the  $L = 10$  results to perform analyses.

As already mentioned, it would make no sense to compare the hydrodynamic law to imaginary-axis data because the hydrodynamic law predicts an unphysical asymptotic behavior of the current-current correlation function. To be able to compare the hydrodynamic theory with our Matsubara-frequency results, we propose a modified hydrodynamic form

$$\text{Im} \chi_{\mathbf{q}}^{\text{mh}}(\nu) = \text{Im} \chi_{\mathbf{q}}^{\text{hyd}}(\nu) [1 + L(\nu; a, b, c)] n_F(\nu - C; \beta_{\text{art}}), \quad (57)$$

where  $\chi^{\text{hyd}}$  denotes the form in Eq. (14),  $L(\nu; a, b, c) = a \exp[-(\ln \nu - b)^2/c^2]$  is the log-normal distribution, and  $n_F(\omega; \beta) = \frac{1}{e^{\beta\omega} + 1}$  is the Fermi-Dirac distribution function. The  $1 + L$  part here is necessary to introduce high-frequency excitations to and from the upper Hubbard band, which are expected in the doped Mott insulator regime. The Fermi-Dirac distribution function facilitates the exponential cutoff at high frequency. This modified hydrodynamic form thus has five additional parameters:  $a, b, c$  are the amplitude, position, and width of the Hubbard peak, respectively, and  $C$  and  $\beta_{\text{art}}$  are the cutoff frequency and the artificial temperature determining the rate at which the spectral weight is exponentially suppressed at cutoff. We make sure that  $\beta_{\text{art}}$  is small enough so that  $n_F(-C, \beta_{\text{art}}) \approx 1$ . Our choice of  $\text{Im} \chi_{\mathbf{q}}^{\text{mh}}(\nu)$  ensures  $\sim 1/\nu^2$  Matsubara-axis asymptotic behavior for  $\Lambda^{xx}$ . The prefactor of the asymptotic behavior will in general depend on the parameters  $a, b, c, C, \beta_{\text{art}}$ .

We now check whether the modified hydrodynamic form (57) is consistent with the available CTINT and FTLM data.

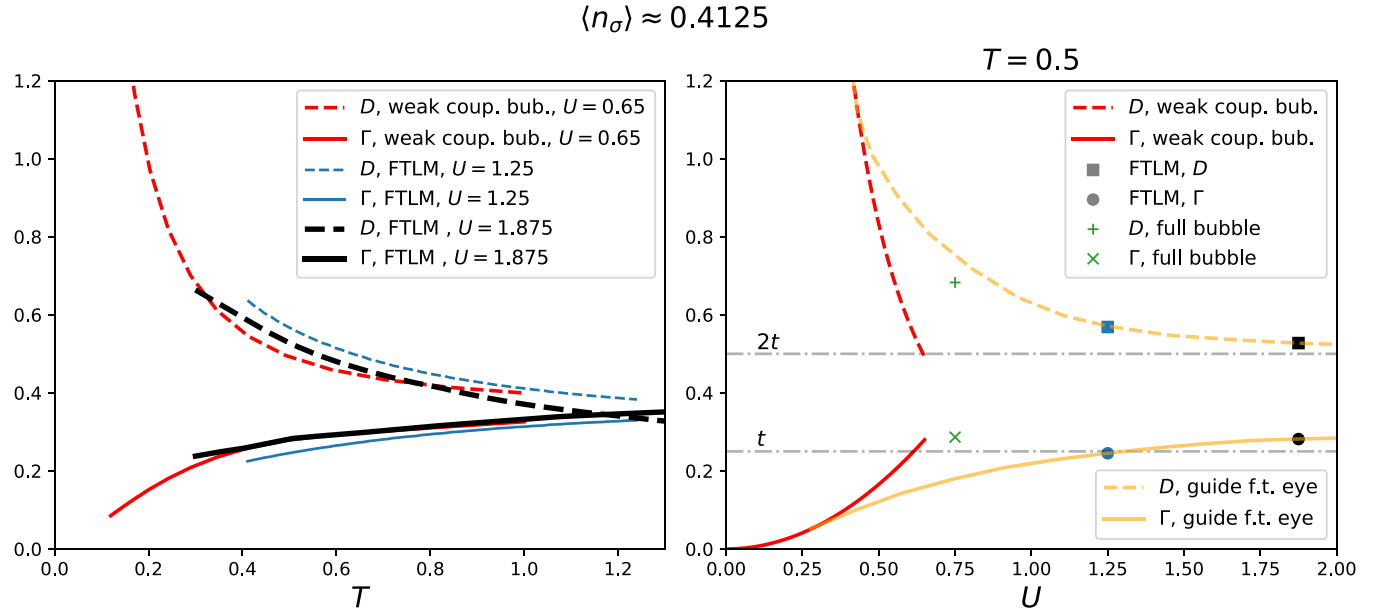


FIG. 17. Left panel: Temperature dependence of  $D$  and  $\Gamma$  in the weak-, moderate-, and strong-coupling regimes. Right panel: Coupling dependence of  $\Gamma$  and  $D$ , as obtained from the weak-coupling bubble, full bubble, and FTLM. The orange lines are guides for the eye, a possible scenario connecting results in the weak- and moderate- to strong-coupling regimes.

We first hand-pick the parameters so that the FTLM result for the optical conductivity is reproduced. It is noteworthy that we can get a very good fit to FTLM data, and that the shape of the high-frequency peak is roughly a log-normal distribution. We then compare the resulting  $\chi_q^{\text{mh}}(i\nu)$  and the corresponding  $\Lambda^{\text{xx,mh}}$  [obtained via Eq. (10)] to CTINT data. We find solid agreement, as shown in the upper part of Fig. 20.

In the lower part of Fig. 20 we illustrate how fitting the Matsubara data to a hydrodynamic law without the high-frequency peak will yield wrong results for  $D$  and  $\Gamma$ , even if a

proper high-frequency cutoff is used. We do a fully unbiased fit of  $\chi_q^{\text{mh}}(i\nu)$  (with  $a, b, c = 0$  and  $\beta_{\text{art}}$  fixed to 0.3,  $D, \Gamma, \chi_c, C$  free), to reproduce at the same time  $\chi$  and  $\Lambda$  CTINT results at five small  $\mathbf{q}$  vectors. We get an excellent fit, but we get completely wrong values for  $D$  and  $\Gamma$ . The optical conductivity contains two peaks, and fitting with only a single peak will compensate by making this one peak wider and shorter, thus underestimating  $D$  and overestimating  $\Gamma$ . Figure 20 nicely illustrates the difficulty of analytical continuation: the fit function on the imaginary axis is almost indistinguishable between the top and bottom rows, yet corresponds to drastically different optical conductivity.

In Fig. 21 we show the  $\langle n_q(t) \rangle$  curves, corresponding to  $\chi^{\text{mh}}$  parameters from the upper part of Fig. 20. Comparing to the corresponding pure hydrodynamic law  $\chi^{\text{hyd}}$  [Eq. (21)], we find no visible difference: the inability of the hydrodynamic law to describe high-frequency features of  $\chi$  are unlikely to have affected the fitting procedure in Ref. [18].

#### IV. DISCUSSION AND PROSPECTS

Our work builds on the milestone study of charge fluctuations in the Hubbard model by Hafermann *et al.* [23]. In that work, the noninteracting charge-charge correlation function was calculated, but only at half-filling, and with a relatively low resolution: the striking two-linear-modes feature that we observe at finite doping was, therefore, overlooked. More importantly, the Matsubara data were fitted to a law which only allows for a linear mode at long wavelengths, which may not be appropriate. In light of more recent experimental evidence, and on general physical grounds, the emergence of diffusive behavior and a quadratic mode around  $\mathbf{q} = 0$  is expected. Furthermore, in the work by Hafermann *et al.*, vertex corrections had unlimited range, but were calculated as a diagrammatic extension of DMFT [40], which introduces

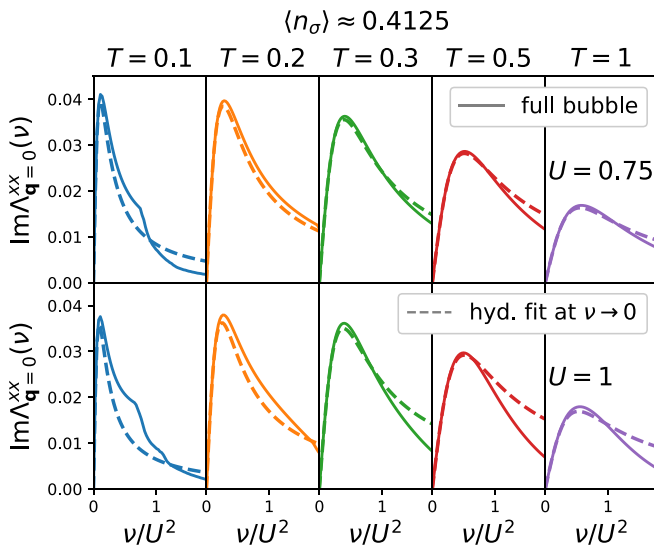


FIG. 18. Moderate coupling, moderate doping. Full lines: full bubble result [Eq. (48)] for the uniform ( $\mathbf{q} = 0$ ) longitudinal current-current correlation function. Dashed lines: hydrodynamic form (22) fitted at  $\nu \rightarrow 0$ .

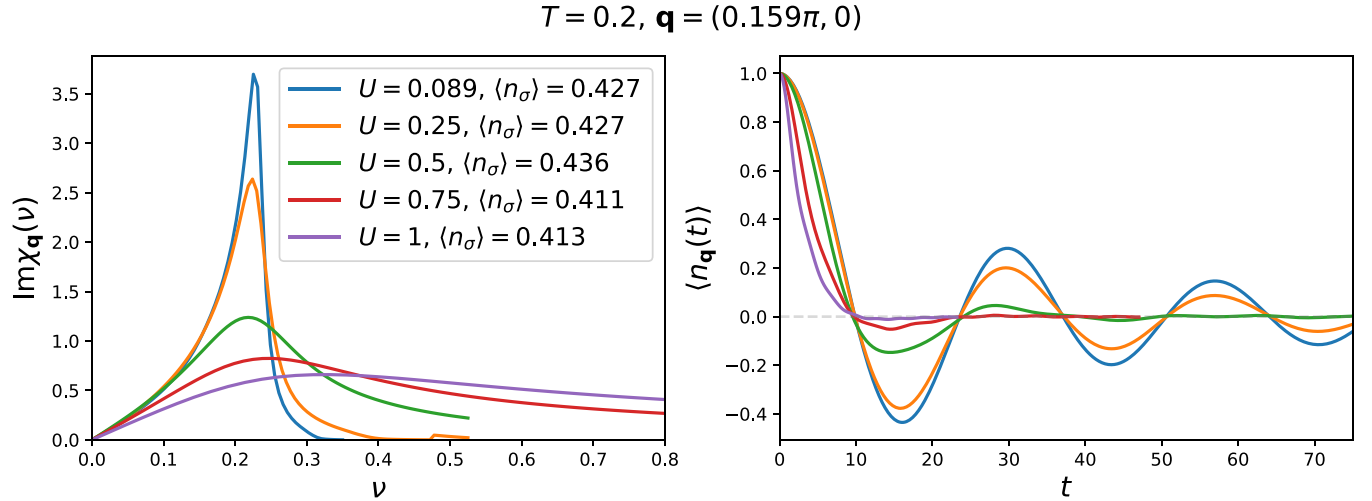


FIG. 19. Weak to moderate coupling, moderate doping, moderate temperature. Left: full bubble calculation [Eq. (48)] for the charge-charge correlation function at a fixed wave vector at different values of coupling. Right: corresponding CDW amplitude vs time curves [Eq. (13)]. Prediction based on Eq. (56) for this doping and temperature is that  $q_D(U=1) \approx 0.15\pi$ , in agreement with the data in the plot on the right.

systematic errors. By using CTINT at  $10 \times 10$  lattice size, we capture complete vertex corrections up to a medium range, yet the finite-size effects in our theory are unlikely to have introduced significant systematic error. Finally, Hafermann *et al.* have derived numerous useful identities relevant for charge-charge and current-current correlation function. However, the fully general equation (7) may have been overlooked so far.

Our weak-coupling calculation is complementary to the semiclassical Boltzmann equation approach of Kiely and Mueller [16]. It is not clear that either of the two approaches yield exact results, even in the  $U \rightarrow 0$  limit, thus it is important to cross-check the results and look for robust, shared features. Indeed, our results at low dopings are in excellent qualitative agreement with the Boltzmann equation: we observe linear resistivity at half-filling and an emerging  $T^2$  at low temperature as one dopes away from half-filling. However, there is a significant quantitative difference in the values of  $\tilde{\rho}_{\text{dc}}$ . The Boltzmann equation predicts the high-temperature asymptotic behavior  $\tilde{\rho}_{\text{dc}} = 0.076(T/t) = 0.304(T/4t)$  while our Kubo bubble theory yields  $\tilde{\rho}_{\text{dc}} = 13.08(T/4t)$ . The difference is nearly two orders of magnitude. Comparing to numerically exact FTLM result at  $U = 1.25$ , it is clear that our extrapolated  $U \rightarrow 0$  theory strongly overestimates  $\rho_{\text{dc}}$  at high temperature (see Fig. 16). However, the coefficient for the linear high- $T$  asymptotics is overestimated by a factor of 2–3, at most. Furthermore, we can compute the bubble result at a finite coupling to obtain much better results, the relative error unlikely being more than 30%–40% in the relevant range of temperature. The Boltzmann theory result extrapolated to  $U = 1.25$ , on the other hand, would be barely visible on the scale of Fig. 16. Our bubble theory appears to give results in significantly better agreement with the reference FTLM solution. There is also a striking qualitative difference in the  $\rho_{\text{dc}}(T)$  at large doping. At  $\langle n_{\sigma} \rangle = 0.1$  Kiely and Mueller observe an exponential drop of resistivity at low temperature, in sharp contrast to our observations. Their finding was argued to be due to frustration of umklapp scattering. It is possible

that, in our approach, vertex corrections are needed to observe this phenomenon. Further work is necessary to fully resolve the origin of this discrepancy. Finally, our approach allows us to compute the full optical conductivity, and estimate  $D$  and  $\Gamma$  as separate objects, which, to the best of our understanding, could not have been done in their work. To our understanding,  $\Gamma$  was extracted from  $D$ , assuming the validity of the Boltzmann expression for conductivity [Eq. (31)]. The analysis based on the asymptotic behavior of  $\chi_{\mathbf{q} \rightarrow 0}(i\nu)$  that shows that the hydrodynamic theory [Eqs. (3) and (4)] is consistent with Eq. (31) may have been previously overlooked.

Our analysis of the equation of motion for the current [Eq. (11)], as well as our numerical results displaying  $D\Gamma = 2\tau^2$  at weak coupling and high temperature (Fig. 15) provide some microscopic evidence for the validity of the hydrodynamic theory proposed in Ref. [18]. Also, our Fig. 19 provides some support for  $q_D = \sqrt{\Gamma/4D}$  which is a specific property of the hydrodynamic theory [Eqs. (3) and (4)]. However, the definite answer to the questions raised in this paper will have to come from more sophisticated methods. It is essential to formulate the theory in real frequency and at the same time treat the thermodynamic limit and the vertex corrections. The recently developed real-frequency diagrammatic Monte Carlo (RFDiagMC) [41–45] is a clear candidate, and our Kubo bubble and second-order self-energy theory is the first step in this approach. Very recently, RFDiagMC was used to calculate the charge-charge correlation function in a slightly different model, at very weak coupling [46]. Pushing RFDiagMC to stronger coupling [45,47–50] and higher resolution necessary to investigate the hydrodynamic behavior in the regime relevant for cold-atom experiments is a difficult task that we leave for future work.

Finally, it is important to view our  $T$ -linear-resistivity result in the  $U \rightarrow 0$  limit in light of the very recent work by Xu *et al.* [51]. In this work, a quantum critical line is observed to pass through  $U = 0, \langle n_{\sigma} \rangle = 0.5$ , separating two distinct ordered phases in the ground-state  $(\delta, U)$  phase diagram of the Hubbard model. This is in line with our observation that

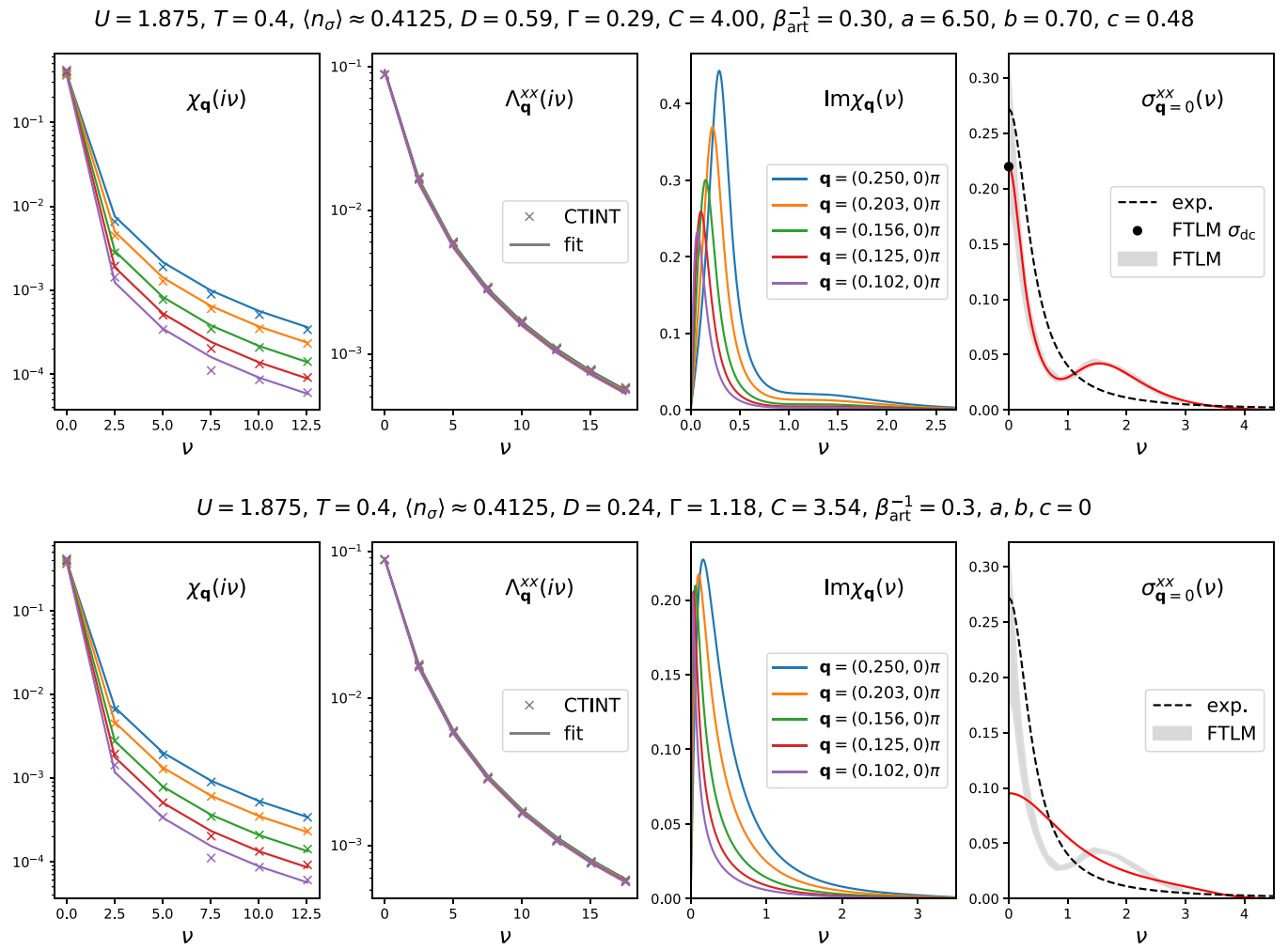


FIG. 20. Strong coupling, moderate doping, and temperature. Upper panels: modified hydrodynamic law with parameters hand-picked to reproduce FTLM result for optical conductivity (rightmost panel, gray stripe, and black dot); two panels on the left: comparison of the modified hydrodynamic law the with corresponding CTINT results for the Matsubara-axis charge-charge and current-current correlation functions; third panel: corresponding real-frequency charge-charge correlation function. Lower panels: unbiased fit of the modified hydrodynamic law without the high-frequency peak to the CTINT charge-charge and current-current correlation functions, simultaneously. The result has a strong bias for the values of  $D$  and  $\Gamma$ .

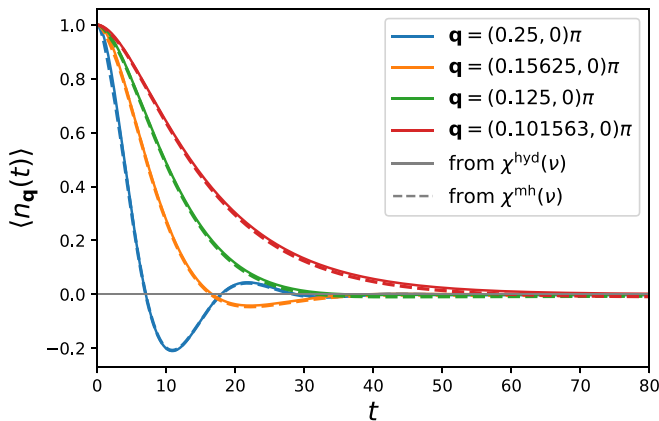


FIG. 21. CDW amplitude vs time curves, corresponding to the modified hydrodynamic law from the upper panels of Fig. 20, compared to the original hydrodynamic law [Eq. (14)] with the same  $D$  and  $\Gamma$ .

the charge-charge and spin-spin susceptibilities diverge at  $\mathbf{q} = (\pi, \pi)$  as  $T \rightarrow 0$  at  $U = 0, \mu = 0$  (see Appendix F). The hypothesis considered in many works [8] is that linear resistivity is expected above quantum critical points. The linear resistivity that we observe may, indeed, be intimately linked to instability towards order, i.e., a degeneracy of the ground state at  $U \rightarrow 0$  at half-filling. The van Hove singularity at the Fermi level perhaps does not play the essential role here, in contrast to the conclusions in Ref. [17]. Whether resistivity remains linear all the way down to zero temperature when Fermi level is at a van Hove singularity in the density of states, regardless of any ordering instabilities, is currently unclear.

## V. CONCLUSIONS

We have studied charge fluctuations and transport in the Hubbard model. In the noninteracting limit, charge fluctuations are anisotropic, and can have multiple linear modes at long wavelengths. Near the empty limit, the charge spectral

function resembles that of the electron. At weak coupling, the self-energy presents several peculiar behaviors, including an abundance of kinks in the frequency dependence. At low temperature we generally find two peaks in  $\text{Im}\Sigma_{\mathbf{k}}(\omega)$  at any  $\mathbf{k}$ . At half-filling and  $T \rightarrow 0$ , we find  $\text{Im}\Sigma_{\mathbf{k}=(0,\pi)}(\omega) \sim |\omega|^{4/5}$  and, along the Fermi surface,  $\text{Im}\Sigma_{\mathbf{k}=(0,\pi) \leftrightarrow (\pi,0)}(\omega) \sim |\omega|$ , the latter being in agreement with previous work [27]. As temperature is raised, a sharp peak in  $\text{Im}\Sigma_{\mathbf{k}}(\omega)$  rises at low frequency, splitting the quasiparticle peak in  $\text{Im}G_{\mathbf{k}}(\omega)$  at around  $\mathbf{k} = (\pi, \pi)$ . At high temperature, we find that self-energy has a single peak as a function of frequency at around  $\omega = \varepsilon_{\mathbf{k}}$ , and it is not smooth. We observe that the dc resistivity is linear at half-filling and at high temperature, in agreement with recent findings [16]. Surprisingly, nonlocal self-energy components are found to have little effect on dc resistivity. Precisely at the band insulator transition, our bubble approximation predicts a finite resistivity at  $T \rightarrow 0$ , coming as a consequence of perfect cancellation of the reducing velocity and scattering rate, both scaling as  $T$ . We observe that the hydrodynamic parameters (diffusion constant and momentum relaxation rate) are roughly inversely proportional, in the bubble approximation at weak coupling, as well as in the numerically exact FTLT result at strong coupling. Their product appears to be  $D\Gamma \approx 2t^2$ , which coincides with one term in the microscopic equation of motion for the current, indicating that other terms might play less of a role. This supports the hydrodynamic theory, for which we show that it must satisfy  $D\Gamma = 2t^2$  at weak coupling and high temperature. Finally, we propose a modified hydrodynamic law that has correct behavior at high frequency, and find that it is consistent with both the numerically exact FTLT and the numerically exact CTINT. Our results provide some evidence that the hydrodynamic theory is correct, but further work with better methods is needed to fully resolve this issue.

### ACKNOWLEDGMENTS

We acknowledge useful discussions with (in no particular order) M. Čubrović, W. Bakr, R. Žitko, J. Mravlje, J. Kokalj, and A. Georges. We acknowledge contributions from P. Stipsić in the early stages of the work. The FTLT  $U = 1.25 \rho_{\text{dc}}(T)$  data were provided by M. Ulaga and J. Kokalj.

The DMFT data were provided by J. Mravlje, using the NRG code by R. Žitko. R. Žitko communicated to us Eq. (B1) and its derivation, and contributed to the derivation of Eq. (7). The CTINT method was implemented using the TRIQS library [52]. Computations were performed on the PARADOX supercomputing facility (Scientific Computing Laboratory, Center for the Study of Complex Systems, Institute of Physics Belgrade). J.V. and S.P. acknowledge funding provided by the Institute of Physics Belgrade, through the grant by the Ministry of Education, Science, and Technological Development of the Republic of Serbia, as well as by the Science Fund of the Republic of Serbia, under the Key2SM project (PROMIS program, Grant No. 6066160). J.V. acknowledges funding by the European Research Council, Grant No. ERC-2022-StG: 101076100. S.P. acknowledges funding by the Deutsche Gesellschaft für Internationale Zusammenarbeit (GIZ) on behalf of the German Federal Ministry for Economic Cooperation and Development (BMZ), within the Support for Returning Experts program. This work was granted access to the HPC resources of TGCC and IDRIS under the allocation A0110510609 attributed by GENCI (Grand Equipement National de Calcul Intensif).

### APPENDIX A: CONTINUITY EQUATION ON THE LATTICE

We start by noting the general expression for the time derivative of a bosonic operator  $\mathcal{O}$  in the Heisenberg picture

$$\partial_t \mathcal{O}(t) = \partial_t e^{iH} \mathcal{O} e^{-iH} = i[H, \mathcal{O}]. \quad (\text{A1})$$

We will also need the general expression for commutators of the following general form, with  $a^\dagger, b, c^\dagger, d$  fermionic creation and annihilation operators

$$[a^\dagger b, c^\dagger d] = \delta_{bc} a^\dagger d - \delta_{ad} c^\dagger b. \quad (\text{A2})$$

This can be proven simply by using  $[AB, C] = A[B, C] + [A, C]B$ ,  $[A, BC] = B[A, C] + [A, B]C$ , and therefore  $[AB, CD] = A(C[B, D] + [B, C]D) + (C[A, D] + [A, C]D)B$ .

Using these we can then show

$$\begin{aligned} \partial_t n_{\mathbf{r}}(t) &= i[H_{\text{kin}}, n_{\mathbf{r}}] = -it \left[ \sum_{\sigma', \mathbf{r}', s \in \{1, -1\}, \eta \in \{x, y\}} c_{\sigma', \mathbf{r}'}^\dagger c_{\sigma', \mathbf{r}' + s\mathbf{e}_\eta}, \sum_{\sigma} c_{\sigma, \mathbf{r}}^\dagger c_{\sigma, \mathbf{r}} \right] \\ &= -it \sum_{\sigma, s \in \{1, -1\}, \eta \in \{x, y\}} ([c_{\sigma, \mathbf{r}}^\dagger c_{\sigma, \mathbf{r} + s\mathbf{e}_\eta}, c_{\sigma, \mathbf{r}}^\dagger c_{\sigma, \mathbf{r}}] + [c_{\sigma, \mathbf{r} - s\mathbf{e}_\eta}^\dagger c_{\sigma, \mathbf{r}}, c_{\sigma, \mathbf{r}}^\dagger c_{\sigma, \mathbf{r}}]) \\ &= -it \sum_{\sigma, s \in \{1, -1\}, \eta \in \{x, y\}} (-c_{\sigma, \mathbf{r}}^\dagger c_{\sigma, \mathbf{r} + s\mathbf{e}_\eta} + c_{\sigma, \mathbf{r} - s\mathbf{e}_\eta}^\dagger c_{\sigma, \mathbf{r}}) = - \sum_{\eta \in \{x, y\}} (j_{\mathbf{r}}^\eta - j_{\mathbf{r} - \mathbf{e}_\eta}^\eta) \end{aligned} \quad (\text{A3})$$

with the definition  $j_{\mathbf{r}}^\eta = it \sum_{\sigma} (c_{\sigma, \mathbf{r} + \mathbf{e}_\eta}^\dagger c_{\sigma, \mathbf{r}} - c_{\sigma, \mathbf{r}}^\dagger c_{\sigma, \mathbf{r} + \mathbf{e}_\eta})$ . The expression  $\sum_{\eta \in \{x, y\}} (j_{\mathbf{r}}^\eta - j_{\mathbf{r} - \mathbf{e}_\eta}^\eta)$  is the lattice version of the divergence of current.

We can express the continuity equation in momentum space by Fourier transform of both sides

$$\partial_t n_{\mathbf{q}} = i[H, n_{\mathbf{q}}] = - \sum_{\eta \in \{x, y\}} (1 - e^{iq_\eta}) j_{\mathbf{q}}^\eta, \quad (\text{A4})$$

where  $n_{\mathbf{q}} = \sum_{\mathbf{r}} e^{iq \cdot \mathbf{r}} n_{\mathbf{r}} = \sum_{\mathbf{k}} c_{\mathbf{k} + \mathbf{q}}^\dagger c_{\mathbf{k}}$ . Notice that we distinguish between  $n_{\mathbf{k}} = c_{\mathbf{k}}^\dagger c_{\mathbf{k}}$  and  $n_{\mathbf{q}}$  solely by the choice of the symbol in the subscript.



## APPENDIX B: CONNECTION BETWEEN THE CHARGE-CHARGE AND CURRENT-CURRENT CORRELATION FUNCTIONS

Here we make use of the general equation of motion

$$z^2 \langle \langle A; B \rangle \rangle_z = -z \langle [A, B] \rangle - \langle [[A, H], B] \rangle + \langle \langle [A, H]; [B, H] \rangle \rangle_z, \quad (\text{B1})$$

where we denote with  $\langle \langle A; B \rangle \rangle_z$  the correlator of operators  $A$  and  $B$  as a function of complex frequency  $z$ . The full derivation of Eq. (B1) is given in Appendix D.

If we replace  $A = n_{\mathbf{q}}$  and  $B = n_{-\mathbf{q}}$ , and using  $[A, H] = -[H, A]$  and  $1/i = -i$  we get

$$\begin{aligned} z^2 \langle \langle n_{\mathbf{q}}; n_{-\mathbf{q}} \rangle \rangle_z &= -z \langle [n_{\mathbf{q}}, n_{-\mathbf{q}}] \rangle + i \sum_{\eta \in \{x, y\}} (1 - e^{iq_{\eta}}) \langle [j_{\mathbf{q}}^{\eta}, n_{-\mathbf{q}}] \rangle \\ &+ \sum_{\eta, \eta' \in \{x, y\}} (1 - e^{iq_{\eta}} - e^{-iq_{\eta'}} + e^{i(q_{\eta} - q_{\eta'})}) \\ &\times \langle \langle j_{\mathbf{q}}^{\eta}; j_{-\mathbf{q}}^{\eta'} \rangle \rangle_z. \end{aligned} \quad (\text{B2})$$

Let us work out the two commutators

$$\begin{aligned} [n_{\mathbf{q}}, n_{-\mathbf{q}}] &= \sum_{\sigma} \left[ \sum_{\mathbf{k}} c_{\sigma, \mathbf{k}+\mathbf{q}}^{\dagger} c_{\sigma, \mathbf{k}}, \sum_{\mathbf{k}'} c_{\sigma, \mathbf{k}'}^{\dagger} c_{\sigma, \mathbf{k}'+\mathbf{q}} \right] \\ &= \sum_{\sigma} \sum_{\mathbf{k}} [c_{\sigma, \mathbf{k}+\mathbf{q}}^{\dagger} c_{\sigma, \mathbf{k}}, c_{\sigma, \mathbf{k}}^{\dagger} c_{\sigma, \mathbf{k}+\mathbf{q}}] \\ &= \sum_{\sigma} \sum_{\mathbf{k}} (n_{\sigma, \mathbf{k}+\mathbf{q}} - n_{\sigma, \mathbf{k}}) \\ &= \sum_{\sigma} (n_{\sigma, \mathbf{r}=0} - n_{\sigma, \mathbf{r}=0}) \\ &= 0. \end{aligned} \quad (\text{B3})$$

Therefore, the first term drops out.

For the second term one gets

$$[j_{\mathbf{q}}^{\eta}, n_{-\mathbf{q}}] = \left[ \sum_{\mathbf{k}} v_{\mathbf{k}, \mathbf{q}}^{\eta} c_{\sigma, \mathbf{k}+\mathbf{q}}^{\dagger} c_{\sigma, \mathbf{k}}, \sum_{\mathbf{k}'} c_{\sigma, \mathbf{k}'}^{\dagger} c_{\sigma, \mathbf{k}'+\mathbf{q}} \right]$$

$$= \sum_{\sigma} \sum_{\mathbf{k}} v_{\mathbf{k}, \mathbf{q}}^{\eta} (n_{\sigma, \mathbf{k}+\mathbf{q}} - n_{\sigma, \mathbf{k}}), \quad (\text{B4})$$

where  $v_{\mathbf{k}, \mathbf{q}}^{\eta} = it(e^{-i(k_{\eta}+q_{\eta})} - e^{ik_{\eta}})$ . The overall prefactor is purely real for each  $\mathbf{k}$ :

$$\begin{aligned} i^2 t (1 - e^{iq_{\eta}}) (e^{-i(k_{\eta}+q_{\eta})} - e^{ik_{\eta}}) \\ = -t (e^{-i(k_{\eta}+q_{\eta})} - e^{ik_{\eta}} - e^{-ik_{\eta}} + e^{i(k_{\eta}+q_{\eta})}) \\ = -2t [\cos(k_{\eta} + q_{\eta}) - \cos k_{\eta}] \\ \equiv \Phi_{\mathbf{k}, \mathbf{q}}^{\eta}. \end{aligned} \quad (\text{B5})$$

This leads us to the fully general expression (7), and here we write it separately for the real and imaginary parts:

$$z^2 \text{Re} \chi_{\mathbf{q}}(z) \quad (\text{B6})$$

$$\begin{aligned} &= \sum_{\eta \in \{x, y\}} \sum_{\mathbf{k}} \Phi_{\mathbf{k}, \mathbf{q}}^{\eta} (\langle n_{\mathbf{k}+\mathbf{q}} \rangle - \langle n_{\mathbf{k}} \rangle) \\ &+ \text{Re} \sum_{\eta, \eta' \in \{x, y\}} (1 - e^{iq_{\eta}} - e^{-iq_{\eta'}} + e^{i(q_{\eta} - q_{\eta'})}) \Lambda_{\mathbf{q}}^{\eta, \eta'}(z), \end{aligned}$$

$$\begin{aligned} z^2 \text{Im} \chi_{\mathbf{q}}(z) \\ = \text{Im} \sum_{\eta, \eta' \in \{x, y\}} (1 - e^{iq_{\eta}} - e^{-iq_{\eta'}} + e^{i(q_{\eta} - q_{\eta'})}) \Lambda_{\mathbf{q}}^{\eta, \eta'}(z). \end{aligned} \quad (\text{B7})$$

Notice that the constant shift in Eq. (B6) is crucial to allow that both  $\chi$  and  $\Lambda$  scale as  $1/\nu^2$  at high Matsubara frequency, which is expected on grounds of symmetry of these correlators in imaginary time. At large  $\nu$  we get for the real part  $\nu^2 \frac{\text{const}}{\nu^2} = \text{const} + 1/\nu^2$  which reduces to  $\text{const} = \text{const}$  as  $\nu$  goes to infinity. This expression also reveals the high-frequency scaling which must hold in general:

$$\text{Re} \chi_{\mathbf{q}}(i\nu \rightarrow i\infty) = -\frac{1}{\nu^2} \sum_{\eta \in \{x, y\}} \sum_{\mathbf{k}} \Phi_{\mathbf{k}, \mathbf{q}}^{\eta} (\langle n_{\mathbf{k}+\mathbf{q}} \rangle - \langle n_{\mathbf{k}} \rangle). \quad (\text{B8})$$

## APPENDIX C: CONSTITUTIVE EQUATION

In the following we derive the time derivative of current operator in the Heisenberg picture. The derivation boils down to working out the following commutators:

$$\partial_t j_{\mathbf{r}}^{\eta} = i[H, j_{\mathbf{r}}^{\eta}] = i([H_{\text{kin}}, j_{\mathbf{r}}^{\eta}] + [H_{\text{int}}, j_{\mathbf{r}}^{\eta}] + [H_{\text{chem}}, j_{\mathbf{r}}^{\eta}]). \quad (\text{C1})$$

The commutator with kinetic energy reads as

$$\begin{aligned} i[H_{\text{kin}}, j_{\mathbf{r}}^{\eta}] &= i \left[ -t \sum_{\mathbf{r}', \sigma', s \in \{1, -1\}, \eta' \in \{x, y\}} c_{\sigma', \mathbf{r}'}^{\dagger} c_{\sigma', \mathbf{r}'+s\mathbf{e}_{\eta'}}, it \sum_{\sigma} (c_{\sigma, \mathbf{r}+\mathbf{e}_{\eta}}^{\dagger} c_{\sigma, \mathbf{r}} - c_{\sigma, \mathbf{r}}^{\dagger} c_{\sigma, \mathbf{r}+\mathbf{e}_{\eta}}) \right] \\ &= -t^2 \sum_{\sigma} \left\{ [c_{\sigma, \mathbf{r}+\mathbf{e}_{\eta}}^{\dagger} c_{\sigma, \mathbf{r}}, c_{\sigma, \mathbf{r}}^{\dagger} c_{\sigma, \mathbf{r}+\mathbf{e}_{\eta}}] - [c_{\sigma, \mathbf{r}}^{\dagger} c_{\sigma, \mathbf{r}+\mathbf{e}_{\eta}}, c_{\sigma, \mathbf{r}+\mathbf{e}_{\eta}}^{\dagger} c_{\sigma, \mathbf{r}}] \right. \\ &+ \sum_{\mathbf{u} \in \{-\mathbf{e}_{\eta}, \mathbf{e}_{\eta}, -\mathbf{e}_{\eta}\}} ([c_{\sigma, \mathbf{r}+\mathbf{u}}^{\dagger} c_{\sigma, \mathbf{r}}, c_{\sigma, \mathbf{r}}^{\dagger} c_{\sigma, \mathbf{r}+\mathbf{e}_{\eta}}] + [c_{\sigma, \mathbf{r}+\mathbf{e}_{\eta}}^{\dagger} c_{\sigma, \mathbf{r}+\mathbf{e}_{\eta}-\mathbf{u}}, c_{\sigma, \mathbf{r}}^{\dagger} c_{\sigma, \mathbf{r}+\mathbf{e}_{\eta}}] \\ &\left. - [c_{\sigma, \mathbf{r}}^{\dagger} c_{\sigma, \mathbf{r}+\mathbf{u}}, c_{\sigma, \mathbf{r}+\mathbf{e}_{\eta}}^{\dagger} c_{\sigma, \mathbf{r}}] - [c_{\sigma, \mathbf{r}+\mathbf{e}_{\eta}-\mathbf{u}}^{\dagger} c_{\sigma, \mathbf{r}+\mathbf{e}_{\eta}}, c_{\sigma, \mathbf{r}+\mathbf{e}_{\eta}}^{\dagger} c_{\sigma, \mathbf{r}}] \right\} \end{aligned}$$



$$= -t^2 \sum_{\sigma} \left\{ 2c_{\sigma, \mathbf{r}+\mathbf{e}_{\eta}}^{\dagger} c_{\sigma, \mathbf{r}+\mathbf{e}_{\eta}} - 2c_{\sigma, \mathbf{r}}^{\dagger} c_{\sigma, \mathbf{r}} + \sum_{\mathbf{u} \in \{-\mathbf{e}_{\eta}, \mathbf{e}_{\eta}, -\mathbf{e}_{\bar{\eta}}\}} (c_{\sigma, \mathbf{r}+\mathbf{u}}^{\dagger} c_{\sigma, \mathbf{r}+\mathbf{e}_{\eta}} - c_{\sigma, \mathbf{r}}^{\dagger} c_{\sigma, \mathbf{r}+\mathbf{e}_{\eta}-\mathbf{u}} + \text{H.c.}) \right\}. \quad (\text{C2})$$

The first two terms comprise the lattice version of the gradient of charge in the direction of current. The other terms are longer-range hoppings.

The commutator of the current with the total number of particles has to be zero, and we leave out the explicit derivation of  $[H_{\text{chem}}, j_{\mathbf{r}}^{\eta}]$ . The commutator with the local Hubbard interaction, on the other hand, is nontrivial:

$$\begin{aligned} i[H_{\text{int}}, j_{\mathbf{r}}^{\eta}] &= i \left[ U \sum_{\mathbf{r}'} c_{\uparrow, \mathbf{r}'}^{\dagger} c_{\uparrow, \mathbf{r}'} c_{\downarrow, \mathbf{r}'}^{\dagger} c_{\downarrow, \mathbf{r}'} - it \sum_{\sigma} (c_{\sigma, \mathbf{r}}^{\dagger} c_{\sigma, \mathbf{r}+\mathbf{e}_{\eta}} - c_{\sigma, \mathbf{r}+\mathbf{e}_{\eta}}^{\dagger} c_{\sigma, \mathbf{r}}) \right] \\ &= tU \sum_{\sigma} \{ n_{\bar{\sigma}, \mathbf{r}} [c_{\sigma, \mathbf{r}}^{\dagger} c_{\sigma, \mathbf{r}} c_{\sigma, \mathbf{r}+\mathbf{e}_{\eta}}^{\dagger} - [c_{\sigma, \mathbf{r}}^{\dagger} c_{\sigma, \mathbf{r}}, c_{\sigma, \mathbf{r}+\mathbf{e}_{\eta}}^{\dagger} c_{\sigma, \mathbf{r}}]] \\ &\quad + n_{\bar{\sigma}, \mathbf{r}+\mathbf{e}_{\eta}} [c_{\sigma, \mathbf{r}+\mathbf{e}_{\eta}}^{\dagger} c_{\sigma, \mathbf{r}+\mathbf{e}_{\eta}} c_{\sigma, \mathbf{r}}^{\dagger} - [c_{\sigma, \mathbf{r}+\mathbf{e}_{\eta}}^{\dagger} c_{\sigma, \mathbf{r}+\mathbf{e}_{\eta}}, c_{\sigma, \mathbf{r}}^{\dagger} c_{\sigma, \mathbf{r}}]] \} \\ &= tU \sum_{\sigma} \{ n_{\bar{\sigma}, \mathbf{r}} (c_{\sigma, \mathbf{r}}^{\dagger} c_{\sigma, \mathbf{r}+\mathbf{e}_{\eta}} + c_{\sigma, \mathbf{r}+\mathbf{e}_{\eta}}^{\dagger} c_{\sigma, \mathbf{r}}) - n_{\bar{\sigma}, \mathbf{r}+\mathbf{e}_{\eta}} (c_{\sigma, \mathbf{r}}^{\dagger} c_{\sigma, \mathbf{r}+\mathbf{e}_{\eta}} + c_{\sigma, \mathbf{r}+\mathbf{e}_{\eta}}^{\dagger} c_{\sigma, \mathbf{r}}) \} \\ &= -tU \sum_{\sigma} (n_{\bar{\sigma}, \mathbf{r}+\mathbf{e}_{\eta}} - n_{\bar{\sigma}, \mathbf{r}}) (c_{\sigma, \mathbf{r}}^{\dagger} c_{\sigma, \mathbf{r}+\mathbf{e}_{\eta}} + c_{\sigma, \mathbf{r}+\mathbf{e}_{\eta}}^{\dagger} c_{\sigma, \mathbf{r}}). \end{aligned} \quad (\text{C3})$$

The terms we get are all assisted hopping terms.

The final expression reads as

$$\begin{aligned} \partial_t j_{\mathbf{r}}^{\eta} &= -t^2 \sum_{\sigma} \left\{ 2n_{\sigma, \mathbf{r}+\mathbf{e}_{\eta}} - 2n_{\sigma, \mathbf{r}} + \sum_{\mathbf{u} \in \{-\mathbf{e}_{\eta}, \mathbf{e}_{\eta}, -\mathbf{e}_{\bar{\eta}}\}} (c_{\sigma, \mathbf{r}+\mathbf{u}}^{\dagger} c_{\sigma, \mathbf{r}+\mathbf{e}_{\eta}} - c_{\sigma, \mathbf{r}}^{\dagger} c_{\sigma, \mathbf{r}+\mathbf{e}_{\eta}-\mathbf{u}} + \text{H.c.}) \right\} \\ &\quad - tU \sum_{\sigma} (n_{\bar{\sigma}, \mathbf{r}+\mathbf{e}_{\eta}} - n_{\bar{\sigma}, \mathbf{r}}) (c_{\sigma, \mathbf{r}}^{\dagger} c_{\sigma, \mathbf{r}+\mathbf{e}_{\eta}} + c_{\sigma, \mathbf{r}+\mathbf{e}_{\eta}}^{\dagger} c_{\sigma, \mathbf{r}}). \end{aligned} \quad (\text{C4})$$

A straightforward Fourier transformation of both sides yields

$$\begin{aligned} \partial_t j_{\mathbf{q}}^{\eta} &= -t^2 \sum_{\sigma} \left\{ 2(e^{iq_{\eta}} - 1)n_{\sigma, \mathbf{q}} + \sum_{\mathbf{u} \in \{-\mathbf{e}_{\eta}, \mathbf{e}_{\eta}, -\mathbf{e}_{\bar{\eta}}\}} \left( (e^{-i\mathbf{q} \cdot \mathbf{u}} - 1) \sum_{\mathbf{k}} e^{i\mathbf{k} \cdot (\mathbf{e}_{\eta} - \mathbf{u})} c_{\sigma, \mathbf{k}+\mathbf{q}}^{\dagger} c_{\sigma, \mathbf{k}} + \text{H.c.} \right) \right\} \\ &\quad + tU \sum_{\sigma} \sum_{\mathbf{k}, \mathbf{q}'} (e^{-ik_{\eta}} + e^{i(k_{\eta}+q_{\eta}-q'_{\eta})})(1 - e^{iq'_{\eta}}) n_{\bar{\sigma}, \mathbf{q}'} c_{\sigma, \mathbf{k}+\mathbf{q}-\mathbf{q}'}^{\dagger} c_{\sigma, \mathbf{k}}. \end{aligned} \quad (\text{C5})$$

It is interesting to consider the limit  $\mathbf{q} = 0$ ,

$$\begin{aligned} \partial_t j_{\mathbf{q}=0}^{\eta} &= tU \sum_{\sigma} \sum_{\mathbf{k}, \mathbf{q}'} (e^{-ik_{\eta}} + e^{i(k_{\eta}-q'_{\eta})})(1 - e^{iq'_{\eta}}) n_{\bar{\sigma}, \mathbf{q}'} c_{\sigma, \mathbf{k}-\mathbf{q}'}^{\dagger} c_{\sigma, \mathbf{k}} \\ &= iU \sum_{\sigma} \sum_{\mathbf{k}, \mathbf{q}'} (v_{\mathbf{k}-\mathbf{q}'}^{\eta} - v_{\mathbf{k}}^{\eta}) n_{\bar{\sigma}, \mathbf{q}'} c_{\sigma, \mathbf{k}-\mathbf{q}'}^{\dagger} c_{\sigma, \mathbf{k}}, \end{aligned} \quad (\text{C6})$$

which clearly shows that scattering events that do not transfer momentum do not contribute to the decay of current; more precisely, only the scattering events that change the velocity of an electron in the direction of the current contribute to the decay of the current. In principle, this expression can be used to express the optical conductivity via higher-order correlation functions using Eq. (B1).

#### APPENDIX D: EQUATION OF MOTION

Here we derive Eq. (B1). We start with the standard definition of the correlator in real time

$$\langle\langle A; B \rangle\rangle_t = i\theta(t) \langle[A(t), B(0)]\rangle, \quad (\text{D1})$$

where  $A$  and  $B$  are bosonic operators, thus we adopt the definition without the minus sign in front.

The equations of motion are obtained by taking time derivatives. The first derivative yields

$$\frac{d}{dt} \langle\langle A; B \rangle\rangle_t = i\theta(t) \langle[\dot{A}(t), B(0)]\rangle + i\delta(t) \langle[A, B]\rangle. \quad (\text{D2})$$

We now perform the Laplace transform with respect to  $t$ :

$$\langle\langle A; B \rangle\rangle_z = \int_0^{\infty} dt e^{izt} \langle\langle A; B \rangle\rangle_t. \quad (\text{D3})$$

Now for  $f(t) = \langle \langle A; B \rangle \rangle_t$ , we integrate per parts

$$\begin{aligned} \int_{0+}^{\infty} dt e^{izt} \frac{d}{dt} f(t) &= e^{izt} f(t) \Big|_{0+}^{+\infty} - iz \int_{0+}^{\infty} dt e^{izt} f(t) \\ &= -i \langle [A, B] \rangle - iz \langle \langle A; B \rangle \rangle_z. \end{aligned} \quad (\text{D4})$$

Note that the  $\delta$  is not included in the integration domain. The second term comes directly from the definition of the Laplace transform (D3). Equating this result with the Laplace transform of the right-hand side of Eq. (D8) we get

$$-i \langle [A, B] \rangle - iz \langle \langle A; B \rangle \rangle_z = \langle \langle i[H, A]; B \rangle \rangle_z \quad (\text{D5})$$

which, up to the factor  $i$ , is the equation of motion in its usual form.

We will want the second derivative to apply to the operator  $B$ , thus, we first perform a time shift

$$\frac{d}{dt} \langle \langle A; B \rangle \rangle_t = i\theta(t) \langle [\dot{A}(0), B(-t)] \rangle + i\delta(t) \langle [A, B] \rangle \quad (\text{D6})$$

and only then apply the second time derivative

$$\begin{aligned} \frac{d^2}{dt^2} \langle \langle A; B \rangle \rangle_t &= i\theta(t) \langle [\dot{A}(0), -\dot{B}(-t)] \rangle \\ &\quad + i\delta(t) \langle [\dot{A}, B] \rangle + i\delta'(t) \langle [A, B] \rangle. \end{aligned} \quad (\text{D7})$$

For convenience, we shift back in time

$$\begin{aligned} \frac{d^2}{dt^2} \langle \langle A; B \rangle \rangle_t &= -i\theta(t) \langle [\dot{A}(t), \dot{B}(0)] \rangle \\ &\quad + i\delta(t) \langle [\dot{A}, B] \rangle + i\delta'(t) \langle [A, B] \rangle. \end{aligned} \quad (\text{D8})$$

The integration by parts once more leads to

$$\begin{aligned} \int_{0+}^{\infty} dt e^{izt} \frac{d^2}{dt^2} f(t) &= \frac{d}{dt} (e^{izt} \dot{f}(t)) \Big|_{0+}^{+\infty} - iz \int_{0+}^{\infty} dt e^{izt} \frac{d}{dt} f(t) \\ &= -i \langle [\dot{A}, B] \rangle - iz \langle -i \langle [A, B] \rangle - iz \langle \langle A; B \rangle \rangle_z \rangle \\ &= -i \langle [\dot{A}, B] \rangle - z \langle [A, B] \rangle - z^2 \langle \langle A; B \rangle \rangle_z, \end{aligned} \quad (\text{D9})$$

where the second and third terms come directly from Eq. (D5). Equating this result with the Laplace transform of the right-hand side of Eq. (D8) (there note the minus sign in front of the first term, and note that  $\dot{A}\dot{B} = -[H, A][H, B]$ ):

$$-i \langle [\dot{A}, B] \rangle - z \langle [A, B] \rangle - z^2 \langle \langle A; B \rangle \rangle_z = \langle \langle [H, A]; [H, B] \rangle \rangle_z. \quad (\text{D10})$$

We rearrange the result

$$z^2 \langle \langle A; B \rangle \rangle_z = -i \langle [\dot{A}, B] \rangle - z \langle [A, B] \rangle - \langle \langle [H, A]; [H, B] \rangle \rangle_z \quad (\text{D11})$$

and finally obtain

$$\begin{aligned} z^2 \langle \langle A; B \rangle \rangle_z &= -\langle [A, H], B \rangle - z \langle [A, B] \rangle + \langle \langle [A, H]; [H, B] \rangle \rangle_z \\ &= -\langle [A, H], B \rangle - z \langle [A, B] \rangle + \langle \langle [A, H]; [H, B] \rangle \rangle_z \end{aligned} \quad (\text{D12})$$

which is the expression used in the derivation in Appendix B.

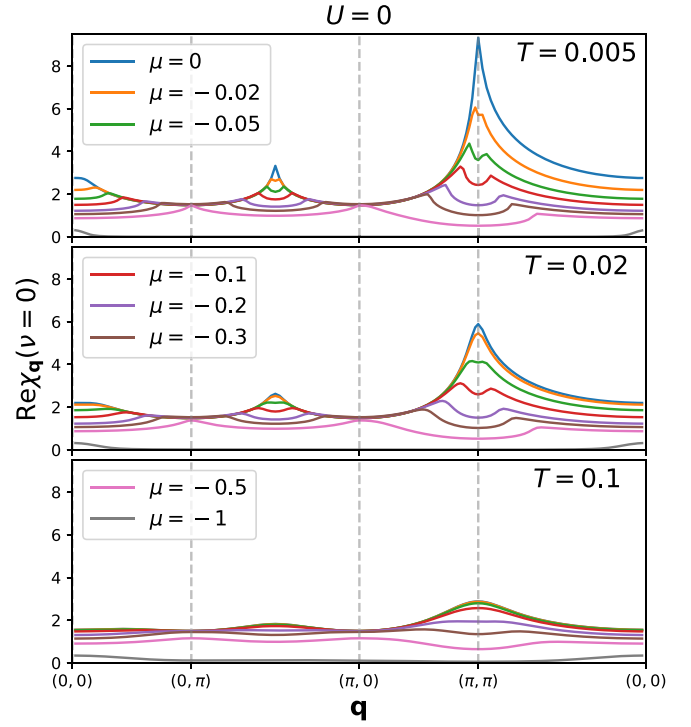


FIG. 22. Static susceptibility in the noninteracting limit as a function of momentum, at different fillings and temperatures.

## APPENDIX E: CALCULATION OF SECOND-ORDER SELF-ENERGY

The optimal way to compute the second-order self-energy (46) it is to first evaluate the “triple density of states” by a three-dimensional (3D) histogram on a dense energy grid

$$\rho_{3,\mathbf{k}}(\varepsilon_1, \varepsilon_2, \varepsilon_3) = \frac{1}{N^2 \Delta\omega^3} \sum_{\mathbf{k}', \mathbf{q}} \delta_{\varepsilon_1, \varepsilon_{\mathbf{k}-\mathbf{q}}} \delta_{\varepsilon_2, \varepsilon_{\mathbf{k}'+\mathbf{q}}} \delta_{\varepsilon_3, \varepsilon_{\mathbf{k}'}} \quad (\text{E1})$$

where  $\Delta\omega$  is the step in the energy grid. This calculation only needs to be performed once, for  $\mu = 0$ , and it does not depend

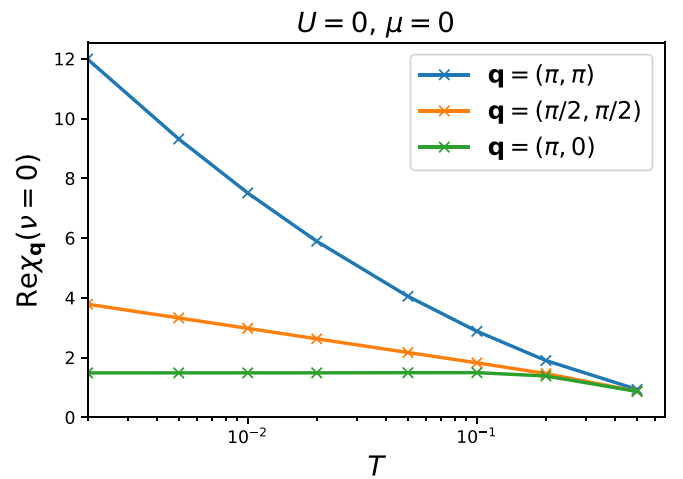


FIG. 23. Static susceptibilities in the noninteracting limit, at half-filling, as a function of temperature. The values at  $\mathbf{q} = (\pi, \pi)$  and  $\mathbf{q} = (\pi/2, \pi/2)$  appear to diverge as  $T \rightarrow 0$ .

on  $T$ . Then for a given  $(\mu, T)$  we accumulate pole amplitudes for the self-energy on the same energy grid as

$$\begin{aligned} \text{Im} \tilde{\Sigma}_{\mathbf{k}}(\omega) &= -\frac{\pi}{\Delta\omega} \int d\varepsilon_1 d\varepsilon_2 d\varepsilon_3 \rho_{3,\mathbf{k}}(\varepsilon_1, \varepsilon_2, \varepsilon_3) \delta_{\omega+\mu-\varepsilon_1-\varepsilon_2+\varepsilon_3} \\ &\times \sum_{s=\pm 1} n_F[s(\varepsilon_1 - \mu)] n_F[s(\varepsilon_2 - \mu)] n_F[-s(\varepsilon_3 - \mu)]. \end{aligned} \quad (\text{E2})$$

The real part of the self-energy can then be obtained via the standard Kramers-Kronig relation.

In our calculations we consider lattices  $L \times L$ , up to  $L = 256$ . When calculating histograms, the optimal number of bins is the square root of the number of the data points. Therefore, in Eq. (E1) the number of energy bins per axis should be equal to  $\sqrt{N^{2/3}} = L^{2/3}$ , but for the sake of numerical simplicity, we take the number of energy bins (per axis) to be  $L$ . This means that, up to the overhead of evaluating Eq. (E1) once, we have reduced the complexity of the calculation from  $L^4$  [Eq. (46)] to  $L^3$  [Eq. (E2)], which is a huge speedup.

## APPENDIX F: DIVERGENCE OF STATIC SUSCEPTIBILITY AT $U = 0, T \rightarrow 0$

In this Appendix we show results for the static susceptibility  $\text{Re} \chi_{\mathbf{q}}(v = 0)$ , in the noninteracting limit. The results are obtained by setting  $\phi, \varphi = 1, z = 0$  in Eq. (34) and using a  $6000 \times 6000$  lattice. In Fig. 22 we observe that there are peaks at  $\mathbf{q} = (0, 0)$ ,  $\mathbf{q} = (\pi, \pi)$ , and  $\mathbf{q} = (\pi/2, \pi/2)$ , but the highest peak is at  $\mathbf{q} = (\pi, \pi)$ . As one dopes away from half-filling, the peaks split. At  $\mu = -0.5$ , the peaks are at  $\mathbf{q} = (0, \pi)$  and the symmetry related  $\mathbf{q} = (\pi, 0)$ . In the nearly empty limit, the only peak is at  $\mathbf{q} = (0, 0)$ . As expected, the peaks become less pronounced as one increases temperature. In Fig. 23 we further observe that the value at  $\mathbf{q} = (\pi, \pi)$  and  $\mathbf{q} = (\pi/2, \pi/2)$  appears to diverge as  $T \rightarrow 0$ , indicating competing instabilities towards charge order. It is important to note that in the noninteracting limit, spin and charge susceptibilities are equal. Therefore, any instability towards charge order is accompanied by instability towards spin order. As soon as interaction is turned on, the degeneracy between charge and spin order is lifted.

- 
- [1] B. Keimer, S. A. Kivelson, M. R. Norman, S. Uchida, and J. Zaanen, *Nature (London)* **518**, 179 (2015).
  - [2] R. A. Cooper, Y. Wang, B. Vignolle, O. J. Lipscombe, S. M. Hayden, Y. Tanabe, T. Adachi, Y. Koike, M. Nohara, H. Takagi, C. Proust, and N. E. Hussey, *Science* **323**, 603 (2009).
  - [3] A. Legros, S. Benhabib, W. Tabis, F. Laliberté, M. Dion, M. Lizaïre, B. Vignolle, D. Vignolles, H. Raffy, Z. Z. Li, P. Auban-Senzier, N. Doiron-Leyraud, P. Fournier, D. Colson, L. Taillefer, and C. Proust, *Nat. Phys.* **15**, 142 (2018).
  - [4] Y. Cao, D. Chowdhury, D. Rodan-Legrain, O. Rubies-Bigorda, K. Watanabe, T. Taniguchi, T. Senthil, and P. Jarillo-Herrero, *Phys. Rev. Lett.* **124**, 076801 (2020).
  - [5] J. Ayres, M. Berben, M. Čulo, Y.-T. Hsu, E. van Heumen, Y. Huang, J. Zaanen, T. Kondo, T. Takeuchi, J. R. Cooper, C. Putzke, S. Friedemann, A. Carrington, and N. E. Hussey, *Nature (London)* **595**, 661 (2021).
  - [6] S. A. Grigera, R. S. Perry, A. J. Schofield, M. Chiao, S. R. Julian, G. G. Lonzarich, S. I. Ikeda, Y. Maeno, A. J. Millis, and A. P. Mackenzie, *Science* **294**, 329 (2001).
  - [7] S. Licciardello, J. Buhot, J. Lu, J. Ayres, S. Kasahara, Y. Matsuda, T. Shibauchi, and N. E. Hussey, *Nature (London)* **567**, 213 (2019).
  - [8] P. Cha, N. Wentzell, O. Parcollet, A. Georges, and E.-A. Kim, *Proc. Natl. Acad. Sci. USA* **117**, 18341 (2020).
  - [9] X. Deng, J. Mravlje, R. Žitko, M. Ferrero, G. Kotliar, and A. Georges, *Phys. Rev. Lett.* **110**, 086401 (2013).
  - [10] J. Vučković, D. Tanasković, M. J. Rozenberg, and V. Dobrosavljević, *Phys. Rev. Lett.* **114**, 246402 (2015).
  - [11] E. Perepelitsky, A. Galatas, J. Mravlje, R. Žitko, E. Khatami, B. S. Shastry, and A. Georges, *Phys. Rev. B* **94**, 235115 (2016).
  - [12] J. Kokalj, *Phys. Rev. B* **95**, 041110(R) (2017).
  - [13] E. W. Huang, R. Sheppard, B. Moritz, and T. P. Devereaux, *Science* **366**, 987 (2019).
  - [14] J. Vučković, J. Kokalj, R. Žitko, N. Wentzell, D. Tanasković, and J. Mravlje, *Phys. Rev. Lett.* **123**, 036601 (2019).
  - [15] A. Vranić, J. Vučković, J. Kokalj, J. Skolimowski, R. Žitko, J. Mravlje, and D. Tanasković, *Phys. Rev. B* **102**, 115142 (2020).
  - [16] T. G. Kiely and E. J. Mueller, *Phys. Rev. B* **104**, 165143 (2021).
  - [17] F. Herman, J. Buhmann, M. H. Fischer, and M. Sigrist, *Phys. Rev. B* **99**, 184107 (2019).
  - [18] P. T. Brown, D. Mitra, E. Guardado-Sanchez, R. Nourafkan, A. Reymbaut, C.-D. Hébert, S. Bergeron, A.-M. S. Tremblay, J. Kokalj, D. A. Huse, P. Schauf, and W. S. Bakr, *Science* **363**, 379 (2019).
  - [19] J. Jaklič and P. Prelovšek, *Adv. Phys.* **49**, 1 (2000).
  - [20] J. Kokalj and R. H. McKenzie, *Phys. Rev. Lett.* **110**, 206402 (2013).
  - [21] A. N. Rubtsov, V. V. Savkin, and A. I. Lichtenstein, *Phys. Rev. B* **72**, 035122 (2005).
  - [22] E. Gull, A. J. Millis, A. I. Lichtenstein, A. N. Rubtsov, M. Troyer, and P. Werner, *Rev. Mod. Phys.* **83**, 349 (2011).
  - [23] H. Hafermann, E. G. C. P. van Loon, M. I. Katsnelson, A. I. Lichtenstein, and O. Parcollet, *Phys. Rev. B* **90**, 235105 (2014).
  - [24] D. Forster, *Hydrodynamic Fluctuations, Broken Symmetry, and Correlation Functions* (CRC Press, Boca Raton, FL, 2018).
  - [25] P. Coleman, *Introduction to Many-body Physics* (Cambridge University Press, Cambridge, England, 2015).
  - [26] H. Aoki, N. Tsuji, M. Eckstein, M. Kollar, T. Oka, and P. Werner, *Rev. Mod. Phys.* **86**, 779 (2014).
  - [27] D. Rohe and C. Honerkamp, *SciPost Phys.* **9**, 084 (2020).
  - [28] F. Šimković, J. P. F. LeBlanc, A. J. Kim, Y. Deng, N. V. Prokof'ev, B. V. Svistunov, and E. Kozik, *Phys. Rev. Lett.* **124**, 017003 (2020).
  - [29] A. J. Kim, F. Šimković, and E. Kozik, *Phys. Rev. Lett.* **124**, 117602 (2020).
  - [30] M. Klett, N. Wentzell, T. Schäfer, F. Šimković, O. Parcollet, S. Andergassen, and P. Hansmann, *Phys. Rev. Res.* **2**, 033476 (2020).
  - [31] T. Schäfer, N. Wentzell, F. Šimković, Y.-Y. He, C. Hille, M. Klett, C. J. Eckhardt, B. Arzhang, V. Harkov, F.-M. Le Régent,

- A. Kirsch, Y. Wang, A. J. Kim, E. Kozik, E. A. Stepanov, A. Kauch, S. Andergassen, P. Hansmann, D. Rohe, Y. M. Vilk *et al.* *Phys. Rev. X* **11**, 011058 (2021).
- [32] J. Vučičević and R. Žitko, *Phys. Rev. B* **104**, 205101 (2021).
- [33] J. Vučičević, H. Terletska, D. Tanasković, and V. Dobrosavljević, *Phys. Rev. B* **88**, 075143 (2013).
- [34] A. Georges, G. Kotliar, W. Krauth, and M. J. Rozenberg, *Rev. Mod. Phys.* **68**, 13 (1996).
- [35] K. G. Wilson, *Rev. Mod. Phys.* **47**, 773 (1975).
- [36] H. R. Krishna-murthy, J. W. Wilkins, and K. G. Wilson, *Phys. Rev. B* **21**, 1003 (1980).
- [37] R. Bulla, T. A. Costi, and T. Pruschke, *Rev. Mod. Phys.* **80**, 395 (2008).
- [38] R. Žitko and T. Pruschke, *Phys. Rev. B* **79**, 085106 (2009).
- [39] F. Šimković IV, R. Rossi, and M. Ferrero, *Phys. Rev. Res.* **4**, 043201 (2022).
- [40] G. Rohringer, H. Hafermann, A. Toschi, A. A. Katanin, A. E. Antipov, M. I. Katsnelson, A. I. Lichtenstein, A. N. Rubtsov, and K. Held, *Rev. Mod. Phys.* **90**, 025003 (2018).
- [41] A. Taheridehkordi, S. H. Curnoe, and J. P. F. LeBlanc, *Phys. Rev. B* **99**, 035120 (2019).
- [42] J. Vučičević and M. Ferrero, *Phys. Rev. B* **101**, 075113 (2020).
- [43] A. Taheridehkordi, S. H. Curnoe, and J. P. F. LeBlanc, *Phys. Rev. B* **101**, 125109 (2020).
- [44] A. Taheridehkordi, S. H. Curnoe, and J. P. F. LeBlanc, *Phys. Rev. B* **102**, 045115 (2020).
- [45] J. Vučičević, P. Stipsić, and M. Ferrero, *Phys. Rev. Res.* **3**, 023082 (2021).
- [46] B. D. E. McNiven, H. Terletska, G. T. Andrews, and J. P. F. LeBlanc, *Phys. Rev. B* **106**, 035145 (2022).
- [47] W. Wu, M. Ferrero, A. Georges, and E. Kozik, *Phys. Rev. B* **96**, 041105(R) (2017).
- [48] F. Šimković and E. Kozik, *Phys. Rev. B* **100**, 121102(R) (2019).
- [49] R. Rossi, F. Šimković, and M. Ferrero, *Europhys. Lett.* **132**, 11001 (2020).
- [50] A. J. Kim, N. V. Prokof'ev, B. V. Svistunov, and E. Kozik, *Phys. Rev. Lett.* **126**, 257001 (2021).
- [51] H. Xu, H. Shi, E. Vitali, M. Qin, and S. Zhang, *Phys. Rev. Res.* **4**, 013239 (2022).
- [52] O. Parcollet, M. Ferrero, T. Ayral, H. Hafermann, I. Krivenko, L. Messio, and P. Seth, *Comput. Phys. Commun.* **196**, 398 (2015).

# **Erratum: Charge fluctuations, hydrodynamics, and transport in the square-lattice Hubbard model [Phys. Rev. B **107**, 155140 (2023)]**

J. Vučičević , S. Predin, and M. Ferrero



(Received 31 January 2025; published 20 February 2025)

DOI: [10.1103/PhysRevB.111.079903](https://doi.org/10.1103/PhysRevB.111.079903)

We have identified two bugs in the code that affected some of the results shown in Figs. 12–18 of the original publication. The results affected were the  $U \rightarrow 0$  bubble  $\rho_{dc}$  and the quantities extracted from it, as well as the frequency-dependent current-current correlation function at high frequency. We have corrected the code and reproduced the results. The changes in the results are only quantitative, and do not affect any conclusions in the paper. On the contrary, the corrected Fig. 15 better confirms that at weak coupling,  $D\Gamma \approx 2t^2$ , which is one of the main results of our paper. The correct versions of the original Figs. 12–18 are shown in Figs. 1–7 of this Erratum.

A quantitative difference is present in Fig. 14, where  $\rho_{dc}$  saturates to 0.65 (instead of 0.4) as  $T \rightarrow 0$ , but the overall behavior is not qualitatively different.

Also, the high-temperature asymptotic behavior in Fig. 13 is  $\rho_{dc} \sim 13.8 U^2 T$  (rather than  $\rho_{dc} \sim 13.08 U^2 T$ ). We also note that in the corrected results, there is a more pronounced “knee” in the  $\rho_{dc}(T)$  curve at half-filling, leading to two separate linear regimes—one at low and one at high temperature, with slightly different prefactors.

In addition, we have made a mistake in converting the units when comparing our results to the Boltzmann theory results from Ref. [1]. The correct conversion is  $\rho_{dc} = 0.076(T/t)(U/t)^2 = 4.864(T/D)(U/D)^2$ . Our conclusion that there is a significant difference between Boltzmann theory and the Kubo bubble results remains correct, but the difference is half an order of magnitude, rather than two orders of magnitude as stated in the original publication.

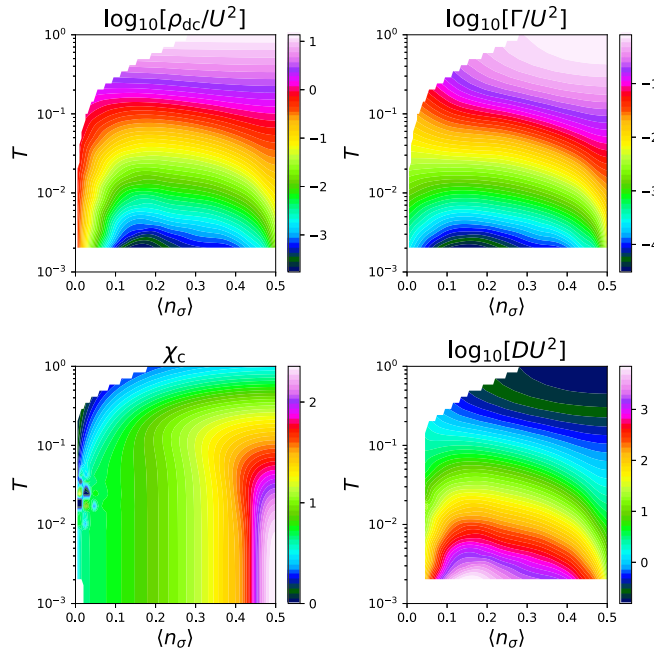


FIG. 1. Correct version of Fig. 12 in original publication. The  $\chi_c$  results were not affected.



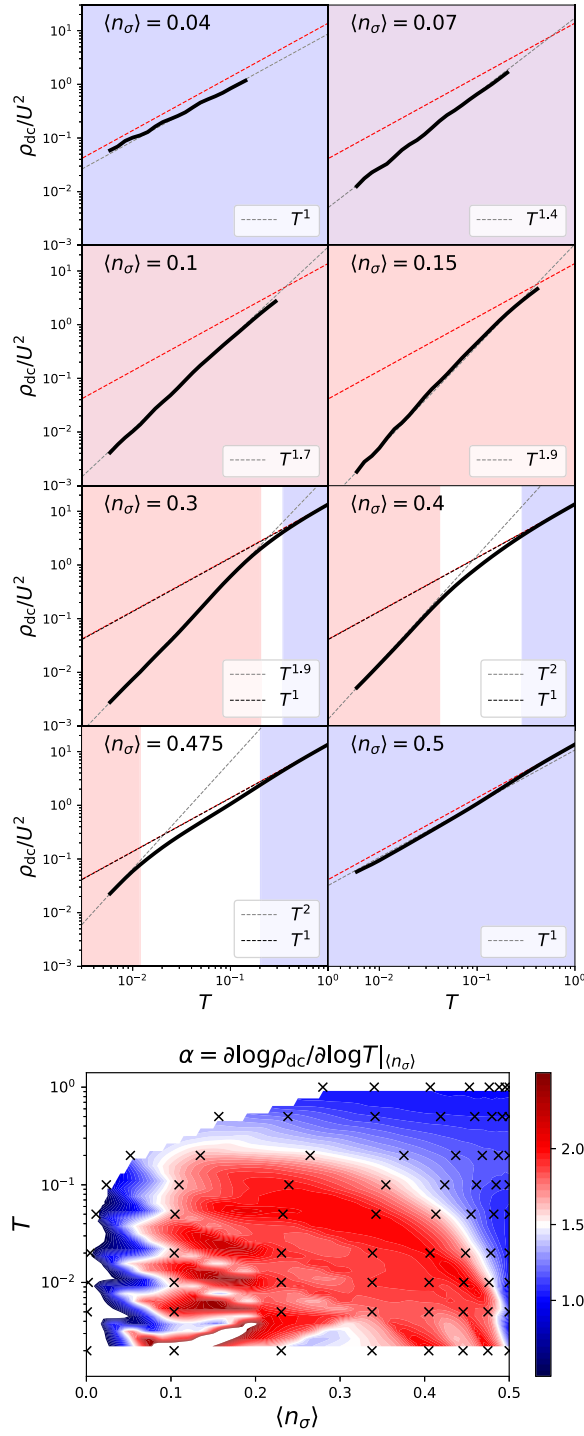


FIG. 2. Correct version of Fig. 13 in the original publication. The red dashed line in the upper panels is the high-temperature asymptotic behavior at half-filling,  $\rho_{dc} \sim 13.8U^2T$ , not shown in the original publication.

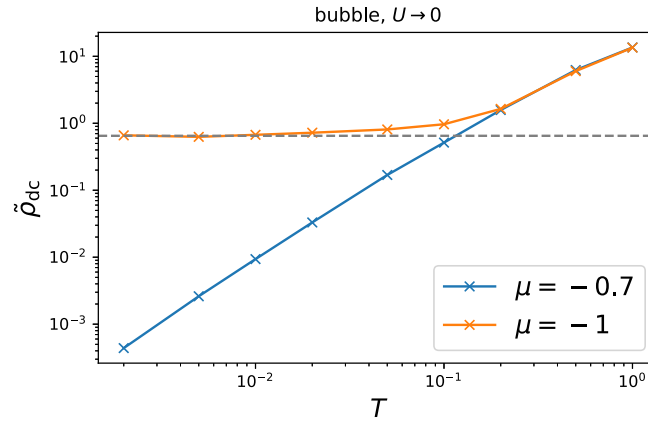


FIG. 3. Correct version of Fig. 14 in the original publication. As  $T \rightarrow 0$ ,  $\rho_{dc}$  saturates at around 0.65 (rather than 0.4, as was stated in the original publication).

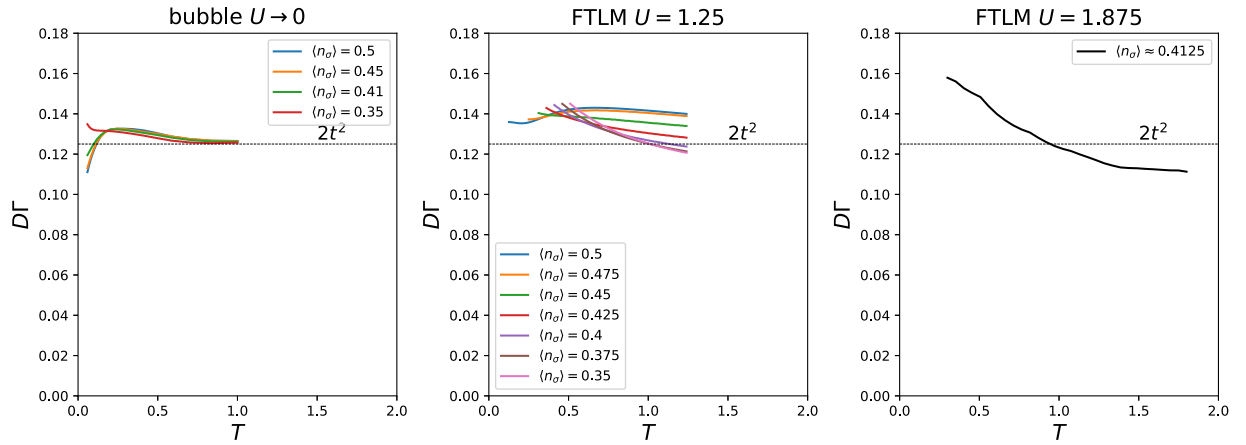


FIG. 4. Correct version of Fig. 15 in the original publication. Only the first panel was affected. The correct results better confirm our expectation that  $D\Gamma \approx 2t^2$ .

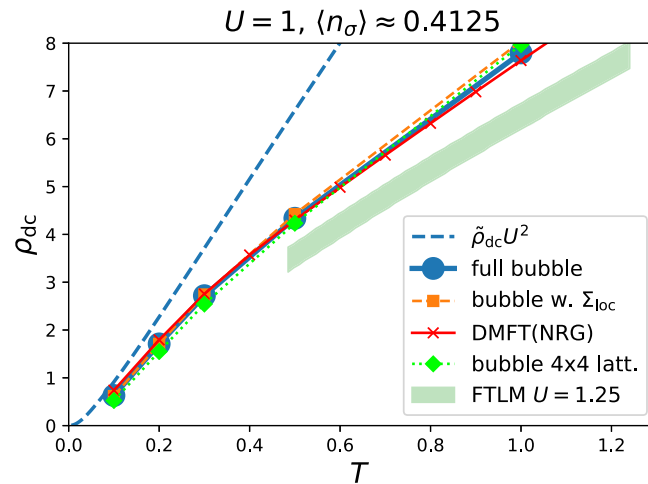


FIG. 5. Correct version of Fig. 16 in the original publication. Only the  $U \rightarrow 0$  bubble results (blue dashed) were affected.

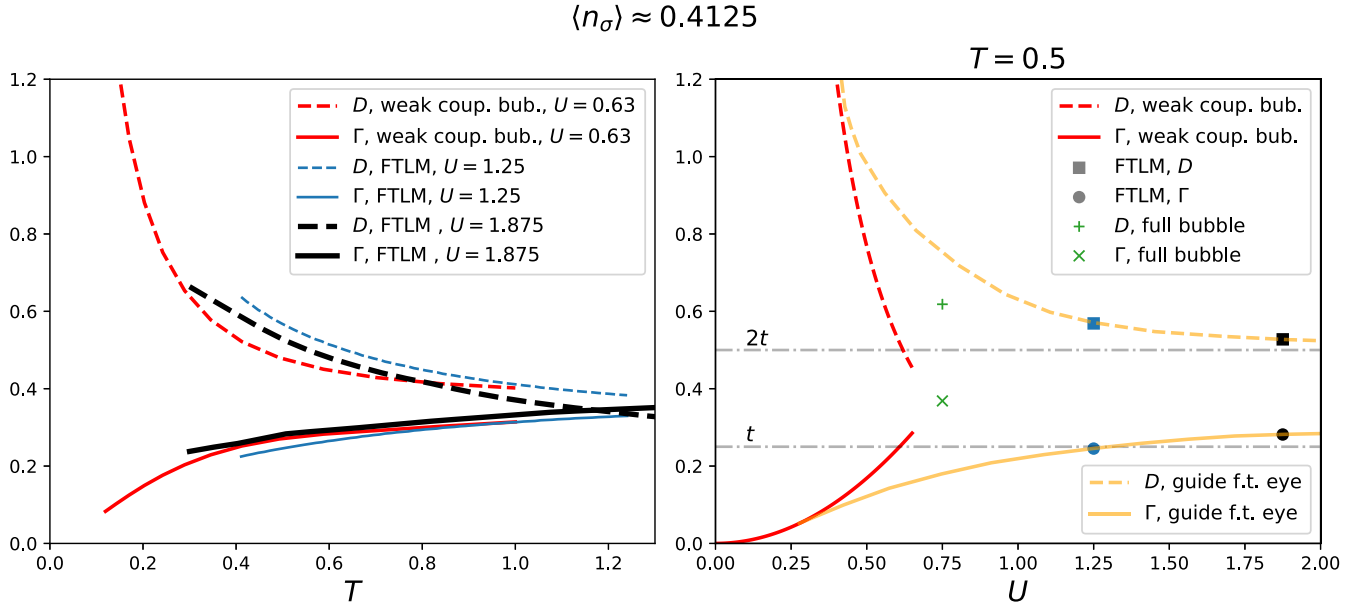


FIG. 6. Correct version of Fig. 17 in the original publication. Only the red curves were affected, and we have slightly changed the choice of parameters for those curves. The qualitative picture remains the same.

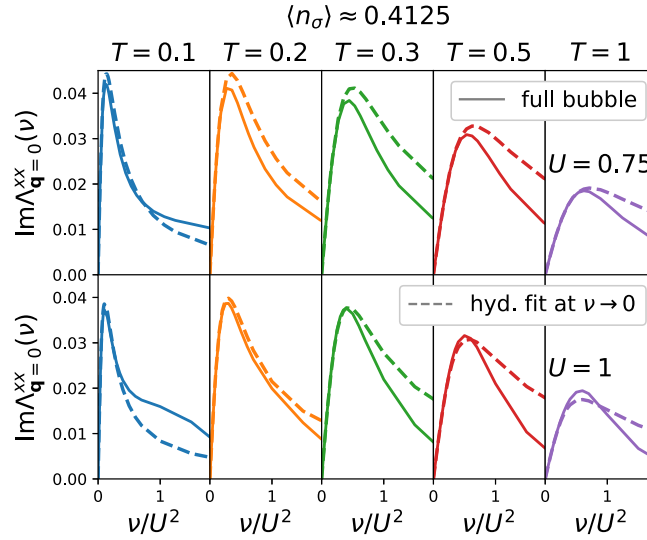


FIG. 7. Correct version of Fig. 18 in the original publication. A small difference is visible at high frequency in the leftmost panels ( $T = 0.1$ ).

[1] T. G. Kiely and E. J. Mueller, *Phys. Rev. B* **104**, 165143 (2021).

# Fermionic-propagator and alternating-basis quantum Monte Carlo methods for correlated electrons on a lattice

Cite as: J. Chem. Phys. 158, 044108 (2023); doi: 10.1063/5.0133597

Submitted: 4 November 2022 • Accepted: 2 January 2023 •

Published Online: 24 January 2023



Veljko Janković<sup>a)</sup>  and Jakša Vučičević<sup>b)</sup> 

## AFFILIATIONS

Institute of Physics Belgrade, University of Belgrade, Pregrevica 118, 11080 Belgrade, Serbia

<sup>a)</sup> Author to whom correspondence should be addressed: [veljko.jankovic@ipb.ac.rs](mailto:veljko.jankovic@ipb.ac.rs)

<sup>b)</sup> [jaksa.vucicevic@ipb.ac.rs](mailto:jaksa.vucicevic@ipb.ac.rs)

## ABSTRACT

Ultracold-atom simulations of the Hubbard model provide insights into the character of charge and spin correlations in and out of equilibrium. The corresponding numerical simulations, on the other hand, remain a significant challenge. We build on recent progress in the quantum Monte Carlo (QMC) simulation of electrons in continuous space and apply similar ideas to the square-lattice Hubbard model. We devise and benchmark two discrete-time QMC methods, namely the fermionic-propagator QMC (FPQMC) and the alternating-basis QMC (ABQMC). In FPQMC, the time evolution is represented by snapshots in real space, whereas the snapshots in ABQMC alternate between real and reciprocal space. The methods may be applied to study equilibrium properties within the grand-canonical or canonical ensemble, external field quenches, and even the evolution of pure states. Various real-space/reciprocal-space correlation functions are also within their reach. Both methods deal with matrices of size equal to the number of particles (thus independent of the number of orbitals or time slices), which allows for cheap updates. We benchmark the methods in relevant setups. In equilibrium, the FPQMC method is found to have an excellent average sign and, in some cases, yields correct results even with poor imaginary-time discretization. ABQMC has a significantly worse average sign, but also produces good results. Out of equilibrium, FPQMC suffers from a strong dynamical sign problem. On the contrary, in ABQMC, the sign problem is not time-dependent. Using ABQMC, we compute survival probabilities for several experimentally relevant pure states.

Published under an exclusive license by AIP Publishing. <https://doi.org/10.1063/5.0133597>

## I. INTRODUCTION

The last two decades have witnessed remarkable developments in laser and ultracold-atom technologies that have enabled experimental studies of strongly correlated electrons in and out of equilibrium.<sup>1,2</sup> Ultracold atoms in optical lattices<sup>2,3</sup> and optical tweezers arrays<sup>4–6</sup> have been used as quantum simulators for paradigmatic models of condensed-matter physics, such as the Hubbard model.<sup>7,8</sup> Recent experiments with fermionic ultracold atoms have probed the equation of state,<sup>9</sup> charge, and spin correlation functions,<sup>10–13</sup> as well as transport properties (by monitoring charge and spin diffusion<sup>14–17</sup>).

These experimental achievements pose a significant challenge for the theory. The level of difficulty, however, greatly depends on whether one computes instantaneous (equal-time) correlations

or the full time/frequency dependence of dynamical correlators. The other factor is whether one considers thermal equilibrium or out-of-equilibrium setups.

Instantaneous correlators in equilibrium are the best-case scenario. The average density, double occupancy, and correlations between particle or spin densities on adjacent sites are still very important. They serve as a thermometer: the temperature in cold-atom experiments cannot be measured directly and is often gauged in comparison with numerical simulations.<sup>11,14</sup> For this kind of application, current state-of-the-art methods<sup>18–43</sup> are often sufficient. Equal-time multipoint density correlations are also of interest, as they hold information, e.g., about the emergence of string patterns<sup>13,44,45</sup> or the effect of holes on antiferromagnetic correlations.<sup>46–48</sup> However, measuring density at a larger number of points simultaneously is more difficult in many algorithms. For

example, in the Hirsch–Fye (HF) algorithm,<sup>24,49</sup> one cannot do this straight-forwardly, as the auxiliary Ising spins only distinguish between singly occupied and doubly occupied/empty sites.

Of even greater interest and much greater difficulty are the time-dependent correlations in equilibrium. These pertain to studies of transport and hydrodynamics at the level of linear response theory.<sup>50–52</sup> The limitations of current state-of-the-art methods here become starkly apparent. If one is interested in long-wavelength behavior (as is precisely the case in the study of hydrodynamic properties<sup>52</sup>), the lattices treated in the simulation need to be sufficiently large. The finite-temperature Lanczos method<sup>53,54</sup> can only treat up to 20 lattice sites<sup>50,55</sup> and is unsuitable for such applications. Quantum Monte Carlo (QMC) methods can treat up to 300 sites,<sup>29,30</sup> but only under certain conditions: doping away from half-filling leads to a significant sign problem, which becomes more severe as the lattice size, inverse temperature, and coupling constant are increased. Moreover, QMC methods are formulated in imaginary time and require ill-defined analytical continuation to reconstruct optical conductivity or any other real-frequency spectrum.<sup>51</sup>

Direct real-time calculations, regardless of proximity to the equilibrium, are the most difficult.<sup>31,56–69</sup> These present an alternative to analytical continuation in equilibrium calculations but are necessary to describe non-equilibrium regimes, e.g., in external field quenches.<sup>16</sup> In the corresponding Kadanoff–Baym–Keldysh three- or two-piece contour formalism, QMC computations are plagued by the dynamical sign problem, which has so far been overcome in only the smallest systems.<sup>61</sup> The time-dependent density matrix renormalization group<sup>70–72</sup> produces practically exact results, however, only in one-dimensional<sup>63,64</sup> or ladder systems.<sup>73</sup> Simulations based on the nonequilibrium Green’s functions formalism<sup>74</sup> are also possible but not numerically exact. They can, however, treat much larger systems over much longer time scales than other real-time approaches.<sup>64,75–77</sup>

The main goal of this work is to construct a numerically exact way to compute spatially resolved densities in setups relevant for optical lattice experiments. This includes general multipoint correlators in real space and momentum space, and we focus on densities of charge and spin. We are interested in both the equilibrium expectation values and their time dependence in transient regimes. (The latter can formally be used to access temporal correlations in equilibrium as well.)

We take a largely unexplored QMC route<sup>78–80</sup> toward the computation of correlation functions in the square-lattice Hubbard model. Current state-of-the-art methods, such as the continuous-time interaction-expansion (CT-INT),<sup>31–33</sup> the continuous-time auxiliary field (CT-AUX),<sup>31,34</sup> and HF,<sup>24,49</sup> rely on the computation of large matrix determinants, which, in many cases, presents the bottleneck of the algorithm. In CT-INT and CT-AUX, the size of the matrices generally grows with coupling, inverse temperature, and lattice size. In the HF, which is based on the Suzuki–Trotter decomposition (STD), the matrix size is fixed, yet presents a measure of the systematic error: the size of the matrix scales with both the number of time slices and the number of lattice sites. A rather separate approach is possible, where the size of the matrices scales only with the total number of electrons. This approach builds on the path-integral MC (PIMC).<sup>81,82</sup> In PIMC, the trajectories of individual electrons are tracked. In continuous-space models,

PIMC was used successfully even in the calculation of dynamical response functions.<sup>83,84</sup> The downside is that the antisymmetry of electrons feeds into the overall sign of a given configuration, thus contributing to the sign problem. A more sophisticated idea was put forward in Refs. 85–87. Namely, the propagation between two time slices can be described by a single many-fermion propagator, which groups (blocks) all possible ways the electrons can go from one set of positions to another—including all possible exchanges. The many-fermion propagator is evaluated as a determinant of a matrix of size equal to the total number of electrons. This scheme automatically eliminates one important source of the sign problem and improves the average sign drastically. Such *permutation blocking* algorithms have been utilized with great success to compute thermodynamic quantities in continuous-space fermionic models.<sup>88–96</sup> Here, we investigate and test analogous formulations in the *lattice models* of interest and try generalizing the approach to real-time dynamics.

We develop and test two slightly different QMC methods. The Fermionic-propagator QMC (FPQMC) is a real-space method similar to the permutation-blocking and fermionic-propagator PIMC, respectively, developed by Dornheim *et al.*<sup>90</sup> and Filinov *et al.*<sup>96</sup> for continuous models. On the other hand, the alternating-basis QMC (ABQMC) method is formulated simultaneously in both real and reciprocal space, which makes measuring distance- and momentum-resolved quantities equally simple. The motion of electrons and their interactions are treated on an equal footing. Both methods are based on the STD and are straight-forwardly formulated along any part of or the entire Kadanoff–Baym–Keldysh three-piece contour. This allows access to both real- and imaginary-time correlation functions in and out of equilibrium. Unlike CT-INT, CT-AUX, and HF, our methods can also be used to treat canonical ensembles as well as the time evolution of pure states. Our formulation ensures that the measurement of an arbitrary multipoint charge or spin correlation function is algorithmically trivial and cheap.

We perform benchmarks on several examples where numerically exact results are available.

In calculations of instantaneous correlators for the 2D Hubbard model in equilibrium, our main finding is that the FPQMC method has a rather manageable sign problem. The average sign is anti-correlated with coupling strength, which is in sharp contrast with some of the standard QMC methods. More importantly, we find that the average sign drops off relatively slowly with the lattice size and the number of time slices—we have been able to converge results with as many as eight time slices, or as many as 80 lattice sites. At strong coupling and at half-filling, we find the average sign to be very close to 1. In the temperature range relevant for optical-lattice experiments, we find that the average occupancy can be computed to a high accuracy with as few as two time slices; the double occupancy and the instantaneous spin–spin correlations require somewhat finer time discretization, but often not more than six time-slices in total. We also document that FPQMC appears to be sign-problem-free for Hubbard chains.

However, in calculations of the time-evolving and spatially resolved density, we find that the FPQMC sign problem is mostly prohibitive of obtaining results. Nevertheless, employing the ABQMC algorithm, we are able to compute survival probabilities of various pure states on  $4 \times 4$  clusters—in the ABQMC formulation, the sign-problem is manifestly independent of time and interaction



strength, and one can scan the entire time evolution for multiple strengths of interaction in a single run. The numerical results reveal several interesting trends. Similarly to observations made in Ref. 97, we find in general that the survival probability decays over longer times when interactions are stronger. At shorter times, we observe that the behavior depends strongly on the type of the initial state, likely related to the average density.

The paper is organized as follows: The FPQMC and ABQMC methods are developed in Sec. II and applied to equilibrium and out-of-equilibrium setups in Sec. III. Section IV discusses the FPQMC and ABQMC methods in light of other widely used QMC algorithms. Section V summarizes our main findings and their implications, and discusses prospects for further work.

## II. MODEL AND METHOD

### A. Hubbard Hamiltonian

We study the Hubbard model on a square-lattice cluster containing  $N_c = N_x N_y$  sites under periodic boundary conditions (PBC). The Hamiltonian reads as

$$H = H_0 + H_{\text{int}}. \quad (1)$$

The noninteracting (single-particle) part  $H_0$  of the Hamiltonian describes a band of itinerant electrons

$$H_0 = -J \sum_{\langle \mathbf{r}, \mathbf{r}' \rangle \sigma} c_{\mathbf{r}\sigma}^\dagger c_{\mathbf{r}'\sigma} = \sum_{\mathbf{k}\sigma} \varepsilon_{\mathbf{k}} n_{\mathbf{k}\sigma}, \quad (2)$$

where  $J$  is the hopping amplitude between the nearest-neighbor lattice sites  $\mathbf{r}$  and  $\mathbf{r}'$ , while the operators  $c_{\mathbf{r}\sigma}^\dagger$  ( $c_{\mathbf{r}\sigma}$ ) create (destroy) an electron of spin  $\sigma$  on lattice site  $\mathbf{r}$ . Under PBC,  $H_0$  is diagonal in the momentum representation; the wave vector  $\mathbf{k}$  may assume any of the  $N_c$  allowed values in the first Brillouin zone of the lattice. The free-electron dispersion is given by  $\varepsilon_{\mathbf{k}} = -2J(\cos k_x + \cos k_y)$ . The density operator is  $n_{\mathbf{k}\sigma} = c_{\mathbf{k}\sigma}^\dagger c_{\mathbf{k}\sigma}$  with  $c_{\mathbf{k}\sigma} = \sum_{\mathbf{r}} (\mathbf{k}|\mathbf{r}) c_{\mathbf{r}\sigma}$ . The Hamiltonian of the on-site Hubbard interaction (two-particle part) reads as

$$H_{\text{int}} = U \sum_{\mathbf{r}} n_{\mathbf{r}\uparrow} n_{\mathbf{r}\downarrow}, \quad (3)$$

where  $U$  is the interaction strength, while  $n_{\mathbf{r}\sigma} = c_{\mathbf{r}\sigma}^\dagger c_{\mathbf{r}\sigma}$ .

If the number of particles is not fixed, Eq. (1) additionally features the chemical-potential term  $-\mu \sum_{\mathbf{r}\sigma} n_{\mathbf{r}\sigma} = -\mu \sum_{\mathbf{k}\sigma} n_{\mathbf{k}\sigma}$  that can be added to either  $H_0$  or  $H_{\text{int}}$ . Here, since we develop a coordinate-space QMC method, we add it to  $H_{\text{int}}$ .

### B. FPQMC method

Finding viable approximations to the exponential of the form  $e^{-\alpha H}$  is crucial to many QMC methods. With  $\alpha = 1/T$  ( $T$  denotes temperature), this is the Boltzmann operator, which will play a role whenever the system is in thermal equilibrium. In the formulation of dynamical responses, the time-evolution operator will also have this form, with  $\alpha = it$ , where  $t$  is the (real) time. One possible way to deal with these is the lowest-order STD<sup>98</sup>

$$e^{-\alpha H} \approx \left( e^{-\Delta\alpha H_0} e^{-\Delta\alpha H_{\text{int}}} \right)^{N_\alpha}, \quad (4)$$

where the interval of length  $|\alpha|$  is divided into  $N_\alpha$  subintervals of length  $|\Delta\alpha|$  each, where  $\Delta\alpha = \alpha/N_\alpha$ . The error of the approximation is of the order of  $|\Delta\alpha|^2 \| [H_0, H_{\text{int}}] \|$ , where the norm  $\| [H_0, H_{\text{int}}] \|$  may be defined as the largest (in modulus) eigenvalue of the commutator  $[H_0, H_{\text{int}}]$ .<sup>80</sup> The error can in principle be made arbitrarily small by choosing  $N_\alpha$  large enough. However, the situation is complicated by the fact that the RHS of Eq. (4) contains both single-particle and two-particle contributions. The latter are diagonal in the coordinate representation, so that the spectral decomposition of  $e^{-\Delta\alpha H_{\text{int}}}$  is performed in terms of totally antisymmetric states in the coordinate representation, aka the Fock states,

$$|\Psi_i\rangle = \prod_{\sigma} \prod_{j=1}^{N_\sigma} c_{\mathbf{r}_j^\sigma \sigma}^\dagger |\emptyset\rangle \quad (5)$$

that contain  $N_\sigma$  electrons of spin  $\sigma$  whose positions  $\mathbf{r}_1^\sigma, \dots, \mathbf{r}_{N_\sigma}^\sigma$  are ordered according to a certain rule. We define  $\varepsilon_{\text{int}}(\Psi_i) \equiv \langle \Psi_i | H_{\text{int}} | \Psi_i \rangle$ . On the other hand, the matrix element of  $e^{-\Delta\alpha H_0}$  between many-body states  $|\Psi_i'\rangle$  and  $|\Psi_i\rangle$  can be expressed in terms of determinants of single-electron propagators

$$\langle \Psi_i' | e^{-\Delta\alpha H_0} | \Psi_i \rangle = \prod_{\sigma} \det S(\Psi_i', \Psi_i, \Delta\alpha, \sigma), \quad (6)$$

$$[S(\Psi_i', \Psi_i, \Delta\alpha, \sigma)]_{j_1 j_2} = \langle \mathbf{r}_{j_1}^{\sigma'} | e^{-\Delta\alpha H_0} | \mathbf{r}_{j_2}^\sigma \rangle. \quad (7)$$

We provide a formal proof of Eqs. (6) and (7) in Appendix A. The same equations lie at the crux of conceptually similar permutation-blocking<sup>90</sup> and fermionic-propagator<sup>96</sup> PIMC methods, which are formulated for continuous-space models. When  $\Delta\alpha$  is purely real (purely imaginary), the quantity on the right-hand side of Eq. (7) is the imaginary-time (real-time) lattice propagator of a free particle in the coordinate representation.<sup>80</sup> Its explicit expressions are given in Appendix B.

Further developments of the method somewhat depend on the physical situation of interest. We formulate the method first in equilibrium and then in out-of-equilibrium situations. To facilitate discussion, in Figs. 1(a)–1(d), we summarize the contours appropriate for the different situations we consider.

#### 1. FPQMC method for thermodynamic quantities

The equilibrium properties at temperature  $T = \beta^{-1}$  follow from the partition function  $Z \equiv \text{Tr } e^{-\beta H}$ , which may be computed by dividing the imaginary-time interval  $[0, \beta]$  into  $N_\tau$  slices of length  $\Delta\tau \equiv \beta/N_\tau$ , employing Eq. (4), and inserting the spectral decompositions of  $e^{-\Delta\tau H_{\text{int}}}$ . The corresponding approximant for  $Z$  reads as

$$Z \approx \sum_{\mathcal{C}} \mathcal{D}_{\beta}(\mathcal{C}, \Delta\tau) e^{-\Delta\tau \varepsilon_{\text{int}}(\mathcal{C})}. \quad (8)$$

The configuration

$$\mathcal{C} = \{ |\Psi_{i_1}\rangle, \dots, |\Psi_{i_{N_\tau}}\rangle \} \quad (9)$$

resides on the contour depicted in Fig. 1(a) and consists of  $N_\tau$  Fock states  $|\Psi_{i,l}\rangle$  in the coordinate representation.  $\mathcal{D}_{\beta}(\mathcal{C}, \Delta\tau)$  depends

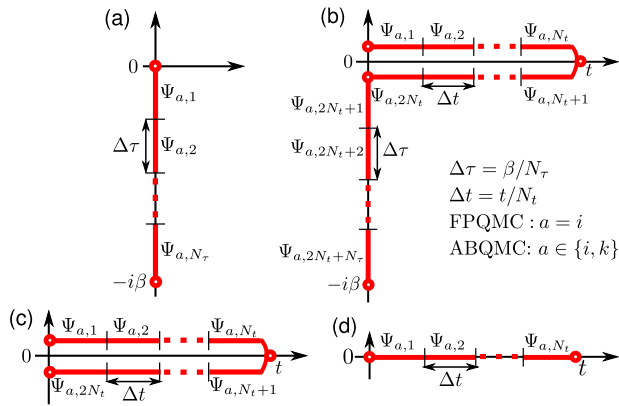


**FIG. 1.** Contours appropriate for computing (a) thermodynamic quantities at temperature  $T = 1/\beta$ , (b) time-dependent quantities after quantum quench in which the Hamiltonian is suddenly changed from  $H(0)$  at  $t < 0$  to  $H$  at  $t > 0$ , (c) time-dependent quantities during evolution from a pure state  $|\psi(0)\rangle \equiv |\Psi_{i,1}\rangle$ , (d) the survival probability of the initial pure state  $|\psi(0)\rangle \equiv |\Psi_{i,1}\rangle$ . In (a) and (b), the vertical part is divided into  $N_\tau$  identical slices of length  $\Delta\tau$ . In (b)–(d), each horizontal line is divided into  $N_t$  identical slices of length  $\Delta t$ . Within the FPQMC method, a many-body state in the coordinate representation  $|\Psi_{i,l}\rangle$  [Eq. (5)] is associated with each slice  $l$ . Within the ABQMC method, in addition to  $|\Psi_{i,l}\rangle$ , each slice  $l$  features a many-body state in the momentum representation  $|\Psi_{k,l}\rangle$  [Eq. (29)].

on the temperature and imaginary-time discretization through the imaginary-time step  $\Delta\tau$

$$\begin{aligned} \mathcal{D}_\beta(C, \Delta\tau) &\equiv \prod_{l=1}^{N_\tau} \langle \Psi_{i,l \oplus 1} | e^{-\Delta\tau H_0} | \Psi_{i,l} \rangle \\ &= \prod_{l=1}^{N_\tau} \prod_{\sigma} \det S(\Psi_{i,l \oplus 1}, \Psi_{i,l}, \Delta\tau, \sigma) \end{aligned} \quad (10)$$

and is a product of  $2N_\tau$  determinants of imaginary-time single-particle propagators on a lattice (this is emphasized by adding the subscript  $\beta$ ). The cyclic addition in Eq. (10) is the standard addition for  $l = 1, \dots, N_\tau - 1$ , while  $N_\tau \oplus 1 = 1$ . The symbol  $\epsilon_{\text{int}}(C)$  stands for

$$\epsilon_{\text{int}}(C) \equiv \sum_{l=1}^{N_\tau} \epsilon_{\text{int}}(\Psi_{i,l}). \quad (11)$$

By virtue of the cyclic invariance under trace, the thermodynamic expectation value of an observable  $A$  can be expressed as

$$\langle A \rangle = \frac{1}{N_\tau} \sum_{l=0}^{N_\tau-1} \frac{1}{Z} \text{Tr} \left\{ (e^{-\Delta\tau H})^l A (e^{-\Delta\tau H})^{N_\tau-l} \right\}. \quad (12)$$

The FPQMC method is particularly suitable for observables diagonal in the coordinate representation (e.g., the interaction energy  $H_{\text{int}}$  or the real-space charge density  $n_{\text{rs}}$ ). Such observables will be distinguished by adding the subscript  $i$ . Equation (12), combined with the lowest-order STD [Eq. (4)], produces the following approximant for  $\langle A_i \rangle$ :

$$\langle A_i \rangle \approx \frac{\sum_C \mathcal{D}_\beta(C, \Delta\tau) e^{-\Delta\tau \epsilon_{\text{int}}(C)} \frac{1}{N_\tau} \sum_{l=1}^{N_\tau} \mathcal{A}_i(\Psi_{i,l})}{\sum_C \mathcal{D}_\beta(C, \Delta\tau) e^{-\Delta\tau \epsilon_{\text{int}}(C)}}, \quad (13)$$

where

$$\mathcal{A}_i(\Psi_{i,l}) \equiv \langle \Psi_{i,l} | A_i | \Psi_{i,l} \rangle. \quad (14)$$

Defining the weight  $w(C, \Delta\tau)$  of configuration  $C$  as

$$w(C, \Delta\tau) \equiv |\mathcal{D}_\beta(C, \Delta\tau)| e^{-\Delta\tau \epsilon_{\text{int}}(C)}, \quad (15)$$

Eq. (13) is rewritten as

$$\langle A_i \rangle \approx \frac{\langle \text{sgn}(C) \frac{1}{N_\tau} \sum_{l=1}^{N_\tau} \mathcal{A}_i(\Psi_{i,l}) \rangle_w}{\langle \text{sgn}(C) \rangle_w}, \quad (16)$$

where  $\langle \dots \rangle_w$  denotes the weighted average over all  $C$  with respect to the weight  $w(C)$ ;  $\text{sgn}(C) \equiv \mathcal{D}_\beta(C, \Delta\tau) / |\mathcal{D}_\beta(C, \Delta\tau)|$  is the sign of configuration  $C$ , while  $|\langle \text{sgn} \rangle| \equiv |\langle \text{sgn}(C) \rangle_w|$  is the average sign of the QMC simulation.

By construction, our FPQMC approach yields exact results for the noninteracting electrons (ideal gas,  $U = 0$ ) and in the atomic limit ( $J = 0$ ). In both limits, due to  $[H_0, H_{\text{int}}] = 0$ , the FPQMC method with arbitrary  $N_\tau$  should recover the exact results. However, the performance of the method, quantified through the average sign of the simulation, deteriorates with increasing  $N_\tau$ . For  $N_\tau = 1$ , the FPQMC algorithm is sign-problem-free because it sums only diagonal elements  $\langle \Psi_{i,1} | e^{-\beta H_0} | \Psi_{i,1} \rangle$  of the positive operator  $e^{-\beta H_0}$ . The sign problem is absent also for  $N_\tau = 2$  because  $\mathcal{D}_\beta(C, \beta/2)$  is a square of a real number.

An important feature of the above-presented methodology is its direct applicability in both the grand-canonical and canonical ensemble. The grand-canonical formulation is essential to current state-of-the-art approaches<sup>31</sup> (e.g., CT-INT or CT-AUX) relying on the thermal Wick's theorem, which is not valid in the canonical ensemble.<sup>99</sup> In the auxiliary-field QMC,<sup>22,23,25,27,28</sup> the Hubbard–Stratonovich transformation<sup>100</sup> decouples many-body propagators into sums (or integrals) over one-body operators whether the particle number is fixed or not. Working in the grand-canonical ensemble is then analytically and computationally more convenient because the traces over *all possible* fermion occupations result in determinants.<sup>23,101</sup> In the canonical ensemble, the computation of traces over constrained fermion occupations is facilitated by observing that the Hubbard–Stratonovich decoupling produces an ensemble of noninteracting systems<sup>101</sup> to which theories developed for noninteracting systems in the canonical ensemble, such as particle projection<sup>102,103</sup> or recursive methods,<sup>104,105</sup> can be applied. While such procedures may be numerically costly and/or unstable,<sup>101</sup> a very recent combination of the auxiliary-field QMC with the recursive auxiliary partition function formalism<sup>105</sup> is reported to be stable and scale favorably with the numbers of particles and available orbitals.<sup>106</sup> In contrast to all these approaches, the formulation of the FPQMC method does not depend on whether the electron number is fixed or not. However, the selection of MC updates does depend on the ensemble we work with. In the canonical ensemble, the updates should conserve the number of electrons; in the grand-canonical ensemble, we also need to include the updates that insert/remove electrons. Our MC updates, together with the

procedure used to extract MC results and estimate their statistical error, are presented in great detail in Sec. SI of the [supplementary material](#).

## 2. FPQMC method for time-dependent quantities

Ideally, numerical simulations of quench experiments such as those from Refs. 14, 16, and 17 should provide the time-dependent expectation value  $\langle A(t) \rangle$  of an observable  $A$  at times  $t > 0$  after the Hamiltonian undergoes a sudden change from  $H(0)$  for  $t < 0$  to  $H$  for  $t > 0$ . Again, in many instances,<sup>14,17</sup> the experimentally measurable observable  $A$  is diagonal in the coordinate representation, which will be emphasized by the subscript  $i$ . The computation proceeds along the three-piece Kadanoff–Baym–Keldysh contour<sup>1</sup>

$$\langle A_i(t) \rangle = \frac{\text{Tr}(e^{-\beta H(0)} e^{iHt} A_i e^{-iHt})}{\text{Tr}(e^{-\beta H(0)} e^{iHt} e^{-iHt})}, \quad (17)$$

where one may employ the above-outlined fermionic-propagator approach after dividing the whole contour into a number of slices, see Fig. 1(b). While  $H$  is the Hubbard Hamiltonian given in Eqs. (1)–(3),  $H(0)$  describes correlated electrons whose charge (or spin) density is spatially modulated by external fields.

The immediate complication (compared to the equilibrium case) is that there are now three operators (instead of one) that need to be decomposed via the STD. A preset accuracy determined by the size of both  $\Delta\tau$  and  $\Delta t$  will, therefore, require a larger number of time-slices. In turn, this will enlarge the configuration space to be sampled and potentially worsen the sign problem in the MC summation. Even worse, the individual terms in the denominator depend on time, so that the sign problem becomes time-dependent (dynamical). The problem is expected to become worse at long times  $t$ , yet vanishes in the  $t \rightarrow 0$  limit.

To simplify the task and yet keep it relevant, we consider the evolution from a pure state  $|\psi(0)\rangle$  that is an eigenstate of real-space density operators  $n_{r\sigma}$ , so that its most general form is given by Eq. (5). Such a setup has been experimentally realized.<sup>5,6,14,17</sup> Replacing  $e^{-\beta H(0)} \rightarrow |\psi(0)\rangle\langle\psi(0)|$  in Eq. (17) leads to the expression for the time-dependent expectation value of the observable  $A_i$

$$\langle A_i(t) \rangle = \frac{\langle \psi(0) | e^{iHt} A_i e^{-iHt} | \psi(0) \rangle}{\langle \psi(0) | e^{iHt} e^{-iHt} | \psi(0) \rangle}. \quad (18)$$

Here, the STD should be applied to both the forward and backward evolution operators, see Fig. 1(c), which requires a larger number of time-slices to reach the desired accuracy (in terms of the systematic error). Nevertheless, Eq. (18) is the simplest example in which the applicability of the real-time FPQMC method to follow the evolution of real-space observables may be examined.

Generally speaking, the symmetries of the model should be exploited to enable as efficient as possible MC evaluation of Eq. (18). Recent experimental<sup>15</sup> and theoretical<sup>107</sup> studies have discussed the dynamical symmetry of the Hubbard model, according to which the temporal evolution of certain observables is identical for repulsive and attractive interactions of the same magnitude. The symmetry relies on specific transformation laws of the Hamiltonian  $H$ , the

initial state  $|\psi(0)\rangle$ , and the observable of interest  $A_i$  under the combined action of two symmetry operations. The first is the bipartite lattice symmetry, or the  $\pi$ -boost<sup>15</sup> operation, which exploits the symmetry  $\epsilon_{\mathbf{k}} = -\epsilon_{\mathbf{k}+(\pi,\pi)}$  of the free-electron dispersion and is represented by the unitary operator  $B$ . The second is the time reversal symmetry represented by the antiunitary operator  $T$  ( $TiT = -i$ ) that reverses electron spin and momentum according to  $Tc_{r\sigma}^{(\dagger)}T = (-1)^{\delta_{r,i}}c_{r\bar{\sigma}}^{(\dagger)}$  and  $Tc_{k\sigma}^{(\dagger)}T = (-1)^{\delta_{k,i}}c_{-k,\bar{\sigma}}^{(\dagger)}$ . In Appendix C, we formulate our FPQMC method to evaluate Eq. (18) in a way that manifestly respects the dynamical symmetry of the model (each contribution to the MC sums respects the symmetry). Here, we only cite the final expression for the time-dependent expectation value of an observable  $A_i$  that satisfies  $TBA_iBT = A_i$  when the evolution starts from a state  $|\psi(0)\rangle$  satisfying  $TB|\psi(0)\rangle = e^{i\chi}|\psi(0)\rangle$

$$\langle A_i(t) \rangle \approx \frac{\sum_C \mathcal{A}_i(\Psi_{i,N_t+1}) \text{Re}\{\mathcal{D}_{2t}(C, \Delta t)\} \cos[\Delta\epsilon_{\text{int}}(C)\Delta t]}{\sum_C \text{Re}\{\mathcal{D}_{2t}(C, \Delta t)\} \cos[\Delta\epsilon_{\text{int}}(C)\Delta t]}. \quad (19)$$

Here, the configuration resides on the contour depicted in Fig. 1(c), which is divided into  $2N_t$  slices in total, and contains  $2N_t - 1$  independent states. We assume that states  $|\Psi_{i,l}\rangle$  for  $l = 1, \dots, N_t$  ( $l = N_t + 1, \dots, 2N_t$ ) lie on the forward (backward) branch of the contour, while  $|\Psi_{i,1}\rangle \equiv |\psi(0)\rangle$ .  $\mathcal{A}_i(\Psi_{i,N_t+1})$  is defined as in Eq. (14), while

$$\Delta\epsilon_{\text{int}}(C) \equiv \sum_{l=1}^{N_t} [\epsilon_{\text{int}}(\Psi_{i,l+N_t}) - \epsilon_{\text{int}}(\Psi_{i,l})]. \quad (20)$$

The symbol  $\mathcal{D}_{2t}(C, \Delta t)$  stands for the following combination of forward and backward fermionic propagators (which is also emphasized by the subscript  $2t$ ):

$$\mathcal{D}_{2t}(C, \Delta t) = \prod_{l=N_t+1}^{2N_t} \langle \Psi_{i,l} | e^{iH_0\Delta t} | \Psi_{i,l} \rangle \prod_{l=1}^{N_t} \langle \Psi_{i,l} | e^{-iH_0\Delta t} | \Psi_{i,l} \rangle. \quad (21)$$

The bipartite lattice symmetry guarantees that  $\mathcal{D}_{2t}(C, \Delta t) = \mathcal{D}_{2t}(C, -\Delta t)$ , see Eq. (C9). The numerator and denominator of the RHS of Eq. (19) are term-by-term invariant under the transformations  $\Delta t \rightarrow -\Delta t$  and  $\Delta\epsilon_{\text{int}}(C) \rightarrow -\Delta\epsilon_{\text{int}}(C)$  that respectively reflect the transformation properties under the time reversal symmetry and the fact that the dynamics of  $\langle A_i(t) \rangle$  are identical in the repulsive and the attractive model. Defining  $w(C) \equiv |\text{Re}\{\mathcal{D}_{2t}(C, \Delta t)\}|$  and  $\text{sgn}(C) \equiv \text{Re}\{\mathcal{D}_{2t}(C, \Delta t)\}/|\text{Re}\{\mathcal{D}_{2t}(C, \Delta t)\}|$ , Eq. (19) is recast as

$$\langle A_i(t) \rangle \approx \frac{\mathcal{A}_i(\Psi_{i,N_t+1}) \text{sgn}(C) \cos[\Delta\epsilon_{\text{int}}(C)\Delta t]}{\langle \text{sgn}(C) \cos[\Delta\epsilon_{\text{int}}(C)\Delta t] \rangle_w}. \quad (22)$$

The sign problem in the MC evaluation of Eq. (22) is dynamical. It generally becomes more serious with increasing time  $t$  and interaction strength  $|U|$ . Moreover,  $w(C)$  also depends on both  $t$  and  $U$ , meaning that MC evaluations for different  $t$ s and  $U$ s should be performed separately, using different Markov chains. It is thus highly desirable to employ further symmetries in order to improve the performance of the method. Particularly relevant initial states

$|\psi(0)\rangle$ , from both an experimental<sup>14,17</sup> and theoretical<sup>108</sup> viewpoint, are pure density-wave-like states. Such states correspond to extreme spin-density wave (SDW) and charge-density wave (CDW) patterns, which one obtains by applying strong external density-modulating fields. The SDW-like state can be written as

$$|\psi_{\text{SDW}}(\mathcal{G})\rangle = \prod_{\mathbf{r}_1 \in \mathcal{G}} c_{\mathbf{r}_1 \uparrow}^\dagger \prod_{\mathbf{r}_2 \in \mathcal{U} \setminus \mathcal{G}} c_{\mathbf{r}_2 \downarrow}^\dagger |\emptyset\rangle, \quad (23)$$

where  $\mathcal{G}$  denotes the multitude of sites on which the electron spins are polarized up, while set  $\mathcal{U}$  contains all sites of the cluster studied. The electron spins on sites belonging to  $\mathcal{U} \setminus \mathcal{G}$  are thus polarized down. Such states have been experimentally realized in Ref. 17. The CDW-like states have also been realized in experiment,<sup>14</sup> and they read as

$$|\psi_{\text{CDW}}(\mathcal{G})\rangle = \prod_{\mathbf{r} \in \mathcal{G}} c_{\mathbf{r} \uparrow}^\dagger c_{\mathbf{r} \downarrow}^\dagger |\emptyset\rangle. \quad (24)$$

The sites belonging to  $\mathcal{G}$  are doubly occupied, while the remaining sites are empty. The state  $|\psi_{\text{CDW}}(\mathcal{G})\rangle$  can be obtained from the corresponding  $|\psi_{\text{SDW}}(\mathcal{G})\rangle$  state by applying the partial particle-hole transformation that acts on spin-down electrons only

$$|\psi_{\text{SDW}}(\mathcal{G})\rangle = \prod_{\mathbf{r} \in \mathcal{U}} (c_{\mathbf{r} \downarrow}^\dagger (1 - n_{\mathbf{r} \downarrow}) + c_{\mathbf{r} \downarrow} n_{\mathbf{r} \downarrow}) |\psi_{\text{CDW}}(\mathcal{G})\rangle, \quad (25)$$

see also Refs. 109 and 110. By combining the partial particle-hole, time-reversal, and bipartite lattice symmetries, the authors of Ref. 108 have shown that the time evolution of spatially resolved charge and spin densities starting from states  $|\psi_{\text{CDW}}(\mathcal{G})\rangle$  and  $|\psi_{\text{SDW}}(\mathcal{G})\rangle$ , respectively, obey

$$\begin{aligned} & \langle \psi_{\text{CDW}}(\mathcal{G}) | e^{iHt} (n_{\mathbf{r} \uparrow} + n_{\mathbf{r} \downarrow} - 1) e^{-iHt} | \psi_{\text{CDW}}(\mathcal{G}) \rangle \\ &= \langle \psi_{\text{SDW}}(\mathcal{G}) | e^{iHt} (n_{\mathbf{r} \uparrow} - n_{\mathbf{r} \downarrow}) e^{-iHt} | \psi_{\text{SDW}}(\mathcal{G}) \rangle. \end{aligned} \quad (26)$$

Equation (26) may be used to acquire additional statistics by combining the Markov chains for the two symmetry-related evolutions. The procedure is briefly described in Appendix C and applied to all corresponding computations presented in Sec. III B.

### 3. ABQMC method for time-dependent quantities

In this section, we develop the so-called alternating-basis QMC method, which is aimed at removing the dynamical character of the sign problem in real-time FPQMC simulations. Moreover, using the ABQMC method, the results for different real times  $t$  and different interactions  $U$  may be obtained using just a single Markov chain, in contrast to the FPQMC method, which employs separate chains for each  $t$  and  $U$ .

Possible advantages of the ABQMC over the FPQMC method are most easily appreciated on the example of the survival probability of the initial state  $|\psi(0)\rangle$

$$P(t) = |\langle \psi(0) | e^{-iHt} | \psi(0) \rangle|^2, \quad (27)$$

which is the probability of finding the system in its initial state after a time  $t$  has passed. Evaluating Eq. (27) by any discrete-time QMC

method necessitates only one STD, see Fig. 1(d). The survival probability is thus the simplest example on which the applicability of any QMC method to out-of-equilibrium setups can be systematically studied.

The FPQMC computation of  $P(t)$  may proceed via the ratio

$$\mathcal{R}(t) = \frac{\langle \psi(0) | e^{-iHt} | \psi(0) \rangle}{\langle \psi(0) | e^{-iH_0 t} | \psi(0) \rangle} \quad (28)$$

of the survival-probability amplitudes in the presence and absence of electron-electron interactions. However, the average sign of the MC simulation of Eq. (28) is proportional to the survival-probability amplitude of the noninteracting system, which generally decays very quickly to zero, especially for large clusters.<sup>62</sup> This means that the dynamical sign problem in the FPQMC evaluation of Eq. (28) may become very severe already at relatively short times  $t$ .

Instead of expressing the many-body free propagator  $\langle \Psi_i' | e^{-iH_0 \Delta t} | \Psi_i \rangle$  as a determinant of single-particle free propagators [Eqs. (6) and (7)], we could have introduced the spectral decomposition of  $e^{-iH_0 \Delta t}$  in terms of Fock states  $|\Psi_k\rangle$  in the momentum representation. In analogy with Eq. (5), such states are defined as

$$|\Psi_k\rangle = \prod_{\sigma} \prod_{j=1}^{N_{\sigma}} c_{\mathbf{k}_{j\sigma}}^\dagger |\emptyset\rangle. \quad (29)$$

The state  $|\Psi_k\rangle$  contains  $N_{\sigma}$  electrons of spin  $\sigma$  whose momenta  $\mathbf{k}_1^{\sigma}, \dots, \mathbf{k}_{N_{\sigma}}^{\sigma}$  are ordered according to a certain rule and we define  $\varepsilon_0(\Psi_k) \equiv \langle \Psi_k | H_0 | \Psi_k \rangle$ . In this case, the final expression for the survival probability of state  $|\psi(0)\rangle$  that satisfies  $TB|\psi(0)\rangle = e^{iX}|\psi(0)\rangle$  reads as

$$P(t) \approx \left| \frac{\sum_{\mathcal{C}} \text{Re}\{\mathcal{D}(\mathcal{C})\} \cos[\varepsilon_0(\mathcal{C})\Delta t] \cos[\varepsilon_{\text{int}}(\mathcal{C})\Delta t]}{\sum_{\mathcal{C}} \text{Re}\{\mathcal{D}(\mathcal{C})\}} \right|^2. \quad (30)$$

A derivation of Eq. (30) is provided in Appendix D. The MC evaluation of Eq. (30) should sample a much larger configuration space than the MC evaluation of Eq. (28). The configuration  $\mathcal{C}$  in Eq. (30) also resides on the contour depicted in Fig. 1(d), but comprises  $2N_t - 1$  states in total:  $N_t$  Fock states  $|\Psi_{k,l}\rangle$  ( $l = 1, \dots, N_t$ ) and  $N_t - 1$  Fock states  $|\Psi_{i,l}\rangle$  ( $l = 2, \dots, N_t$ ) (again,  $|\Psi_{i,1}\rangle \equiv |\psi(0)\rangle$ ).  $\mathcal{D}(\mathcal{C})$  is the product of  $2N_t$  Slater determinants

$$\mathcal{D}(\mathcal{C}) = \prod_{l=1}^{N_t} \langle \Psi_{i,l} | \Psi_{k,l} \rangle \langle \Psi_{k,l} | \Psi_{i,l} \rangle \quad (31)$$

that stem from the sequence of basis alternations between the momentum and coordinate eigenbasis. Using the notation of Eqs. (5) and (29), the most general Slater determinant  $\langle \Psi_i | \Psi_k \rangle$  entering Eq. (10) is given as

$$\langle \Psi_i | \Psi_k \rangle = \prod_{\sigma} \det \tilde{\mathcal{S}}(\Psi_i, \Psi_k, \sigma), \quad (32)$$

$$[\tilde{\mathcal{S}}(\Psi_i, \Psi_k, \sigma)]_{j_1 j_2} = \langle \mathbf{r}_{j_1}^{\sigma} | \mathbf{k}_{j_2}^{\sigma} \rangle = \frac{\exp(i\mathbf{k}_{j_2}^{\sigma} \cdot \mathbf{r}_{j_1}^{\sigma})}{\sqrt{N_c}}, \quad (33)$$

where  $1 \leq j_1, j_2 \leq N_{\sigma}$ . The symbol  $\varepsilon_0(\mathcal{C})$  stands for [cf. Eq. (11)]



$$\varepsilon_0(C) \equiv \sum_{l=1}^{N_t} \varepsilon_0(\Psi_{k,l}). \quad (34)$$

We note that each term in Eq. (30) is invariant under transformations  $\varepsilon_0(C) \rightarrow -\varepsilon_0(C)$  and  $\Delta t \rightarrow -\Delta t$ , which reflect the action of the bipartite lattice symmetry and the time reversal symmetry, respectively. Being term-by-term invariant under the transformation  $\varepsilon_{\text{int}}(C) \rightarrow -\varepsilon_{\text{int}}(C)$ , Eq. (30) explicitly satisfies the requirement that the dynamics of  $P(t)$  for repulsive and attractive interactions of the same magnitude are identical. Defining  $w(C) \equiv |\text{Re}\{\mathcal{D}(C)\}|$  and  $\text{sgn}(C) \equiv \text{Re}\{\mathcal{D}(C)\}/|\text{Re}\{\mathcal{D}(C)\}|$ , Eq. (30) is recast as

$$P(t) \approx \left| \frac{\langle \text{sgn}(C) \cos[\varepsilon_0(C)\Delta t] \cos[\varepsilon_{\text{int}}(C)\Delta t] \rangle_w}{\langle \text{sgn}(C) \rangle_w} \right|^2. \quad (35)$$

This choice for  $w$  is optimal in the sense that it minimizes the variance of  $\langle \text{sgn}(C) \rangle_w$ ,<sup>111</sup> whose modulus is the average sign of the ABQMC simulation. The sign problem encountered in the MC evaluation of Eq. (35) does not depend on either time  $t$  or interaction strength  $U$ , i.e., it is not dynamical. The weight  $w(C)$  in Eq. (35) does not depend on either  $\Delta t$  or any other property of configuration  $C$  ( $\varepsilon_0, \varepsilon_{\text{int}}$ ). Therefore, the MC evaluation of Eq. (35) may be performed simultaneously (using a single Markov chain) for any  $U$  and any  $t$ . This presents a technical advantage over the FPQMC method, which may be outweighed by the huge increase in configuration space when going from FPQMC to ABQMC. To somewhat reduce the dimension of the ABQMC configuration space and improve the sampling efficiency, we design the MC updates so as to respect the momentum conservation law throughout the real-time evolution. The momentum conservation poses the restriction that all the momentum-space states  $|\Psi_{k,l}\rangle$  have the same total electron momentum  $\mathbf{K} \equiv \sum_{\mathbf{k}\sigma} \mathbf{k} \langle \Psi_{k,l} | n_{\mathbf{k}\sigma} | \Psi_{k,l} \rangle$  [modulo  $(2\pi, 2\pi)$ ]. The MC updates in the ABQMC method for the evaluation of the survival probability are presented in great detail in Sec. SII of the [supplementary material](#).

By relying on the partial particle-hole and bipartite lattice symmetries, in [Appendix D](#) we demonstrate that the dynamics of the survival probabilities of states  $|\psi_{\text{SDW}}(\mathcal{G})\rangle$  and  $|\psi_{\text{CDW}}(\mathcal{G})\rangle$  are identical, i.e.,

$$|\langle \psi_{\text{SDW}}(\mathcal{G}) | e^{-iHt} | \psi_{\text{SDW}}(\mathcal{G}) \rangle|^2 = |\langle \psi_{\text{CDW}}(\mathcal{G}) | e^{-iHt} | \psi_{\text{CDW}}(\mathcal{G}) \rangle|^2. \quad (36)$$

Evaluating Eq. (35), additional statistics can be acquired by combining the Markov chains for the  $P(t)$  calculations starting from the two symmetry-related states  $|\psi_{\text{CDW}}(\mathcal{G})\rangle$  and  $|\psi_{\text{SDW}}(\mathcal{G})\rangle$ . The procedure is similar to that described in [Appendix C](#), and we apply it to all corresponding computations presented in Sec. III C.

### III. NUMERICAL RESULTS

We first apply the FPQMC method to equilibrium situations (the particle number is not fixed), see Sec. III A, and then to time-dependent local densities during the evolution of pure states, see Sec. III B. Section III C presents our ABQMC results for the survival probability of pure states. Our implementation of the ABQMC method on the full Kadanoff-Baym-Keldysh contour [Eq. (17)] is benchmarked in Sec. SVII of the [supplementary material](#).

#### A. Equilibrium results: Equation of state

We start by considering the Hubbard dimer, the minimal model capturing the subtle interplay between electron delocalization and electron-electron interaction.<sup>112</sup> We opt for moderate temperature  $T/J = 1$  and interaction  $U/J = 4$ , so that the expected number of imaginary-time slices needed to obtain convergent FPQMC results is not very large. [Figure 2](#) presents the equation of state (i.e., the dependence of the electron density  $\rho_e = \langle \hat{N}_\uparrow + \hat{N}_\downarrow \rangle / N_c$  on the chemical potential  $\mu$ ) for a range of  $\mu$  below the half-filling. Here,  $\hat{N}_\uparrow$  and  $\hat{N}_\downarrow$  are the operators of the total number of spin-up and spin-down electrons, respectively. [Figure 2](#) suggests that already  $N_\tau = 2$  imaginary-time slices suffice to obtain very good results in the considered range of  $\mu$ , while increasing  $N_\tau$  from 2 to 4 somewhat improves the accuracy of the FPQMC results. It is interesting that, irrespective of the value of  $N_\tau$ , FPQMC simulations on the dimer are manifestly sign-problem-free. First, the one-dimensional imaginary-time propagator defined in Eq. (B2) is positive,  $\mathcal{I}(J\Delta\tau, l) = [e^{J\Delta\tau} + (-1)^l e^{-J\Delta\tau}]/2$  for both  $l = 0$  and 1. Second, the configuration containing two electrons of the same spin is of weight  $\cosh^2(J\Delta\tau) - \sinh^2(J\Delta\tau) \equiv 1$ , implying that the weights of all configurations are positive. Furthermore, our results on longer chains suggest that FPQMC simulations of one-dimensional lattice fermions do not display a sign problem. While similar statements have been repeated for continuum one-dimensional models of both noninteracting<sup>85,86</sup> and interacting fermions,<sup>87</sup> there is, to the best of our knowledge, no rigorous proof that the sign problem is absent from coordinate-space QMC simulations of one-dimensional fermionic systems. While we do not provide such a proof either, [Fig. 3](#) is an illustrative example showing how the FPQMC results for the double occupancy  $\sum_{\mathbf{r}} \langle n_{\mathbf{r}\uparrow} n_{\mathbf{r}\downarrow} \rangle / N_c$  of the Hubbard chain at half-filling approach the reference result (taken from Ref. 113) as the imaginary-time discretization becomes finer. For all  $N_\tau$ s considered, the average sign of FPQMC simulations is  $|\langle \text{sgn} \rangle| = 1$ .

We now apply the FPQMC method to evaluate the equation of state on larger clusters. We focus on a  $4 \times 4$  cluster, which may already be representative of the thermodynamic limit at  $T/J \gtrsim 1$ .<sup>50</sup> We compare our  $\rho_e(\mu)$  results with the results of the numerical linked-cluster expansion (NLCE) method.<sup>40–42</sup> The NLCE results are numerically exact and converged with respect to the control parameter, i.e., the maximal cluster-size used. NLCE is commonly

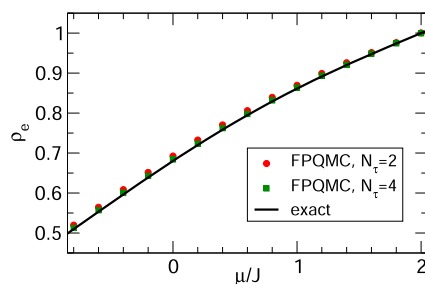


**FIG. 2.** Equation of state  $\rho_e(\mu)$  for the Hubbard dimer with  $T/J = 1$ ,  $U/J = 4$ . Full red circles (green squares) are the results of FPQMC simulations employing  $N_\tau = 2$  ( $N_\tau = 4$ ) imaginary-time slices, while the solid black line is computed using the exact diagonalization. The estimated statistical error of the FPQMC data is in all cases smaller than the symbol size.



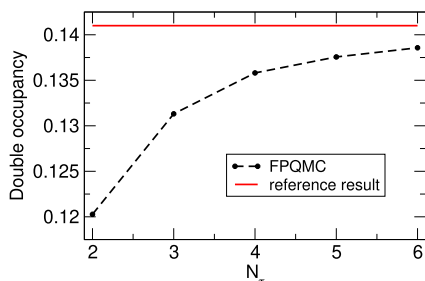


**FIG. 3.** Double occupancy of the  $N_c = 20$ -site Hubbard chain at half-filling ( $\mu = U/2$ ,  $\rho_e = 1$ ) as a function of the number  $N_\tau$  of imaginary-time slices. The remaining parameters are  $U/J = 3$  and  $T/J = 1$ . The dotted line connecting full symbols (FPQMC results) serves as a guide to the eye. The reference result is taken from Ref. 113. The relative deviation of the FPQMC result with  $N_\tau = 6$  from the reference result is around 2%. The statistical error bars of the FPQMC results are smaller than the symbol size.

used to benchmark methods and understand experimental data.<sup>9,10</sup> Again, we keep  $U/J = 4$ , but we take  $T/J = 1.0408$  to be able to compare results to the data of Ref. 41. Figure 4(a) reveals that the FPQMC results with only  $N_\tau = 2$  imaginary-time slices agree very well (within a couple of percent) with the NLCE results over a wide range of chemical potentials. This is a highly striking observation, especially keeping in mind that the FPQMC method with  $N_\tau = 2$  is sign-problem-free, see Fig. 4(b). It is unclear whether other STD-based methods would reach here the same level of accuracy with only two imaginary-time slices (and without the sign problem). This may be a specific property of the FPQMC method. Finer imaginary-time discretization introduces the sign problem, see Fig. 4(b), which becomes more pronounced as the density is increased and reaches a plateau for  $\rho_e \gtrsim 0.8$ . Still, the sign problem remains manageable. Increasing  $N_\tau$  for 2 to 6 somewhat improves the agreement of the density  $\rho_e$  [the inset of Fig. 4(a)] and considerably improves the agreement of the double occupancy [Fig. 4(c)] with the referent NLCE results. Still, comparing the insets of Figs. 4(a) and 4(c), we observe that the agreement between FPQMC ( $N_\tau = 6$ ) and NLCE results for  $\rho_e$  is significantly better than for the double occupancy. The systematic error in FPQMC comes from the time-discretization and the finite size of the system. At  $N_\tau = 6$ , it is not *a priori* clear which error contributes more, but it appears most likely that the time-discretization error is dominant. In any case, the reason why systematic error is greater for the double occupancy than for the average density could be that the double occupancy contains more detailed information about the correlations in the system. This might be an indication that measurement of multipoint density correlations will generally be more difficult—it may require a finer time resolution and/or greater lattice size.

The average sign above the half-filling,  $\rho_e = 1$ , mirrors that below the half-filling. The particle-hole symmetry ensures that  $\rho_e(\mu) = 2 - \rho_e(U - \mu)$ , but that it also governs the average sign is not immediately obvious from the construction of the method. A formal demonstration of the electron-doping-hole-doping symmetry of the average sign is, however, possible (see Appendix E). Note that we restrict our density calculations to  $\rho_e < 1$  because, in this case, the numerical effort to manipulate the determinants [Eqs. (7) and (10)]

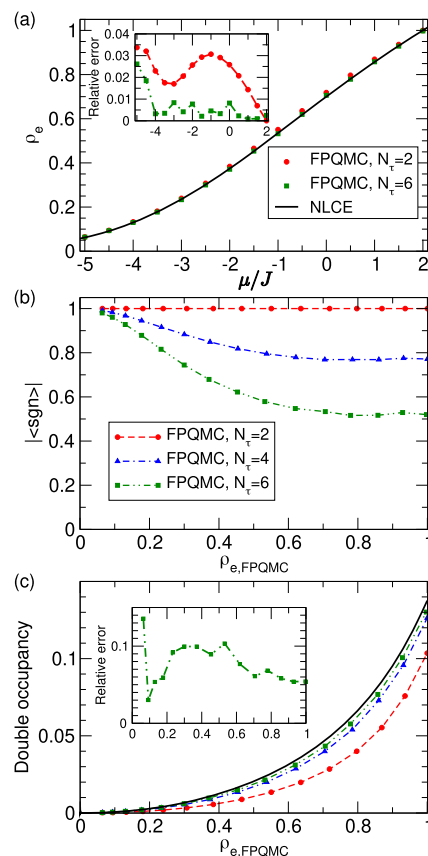


**FIG. 4.** (a) Equation of state  $\rho_e(\mu)$  for the Hubbard model on a  $4 \times 4$  cluster with the following values of model parameters:  $U/J = 4$ ,  $T/J = 1.0408$ . (b) The average sign as a function of the FPQMC estimate  $\rho_{e,\text{FPQMC}}$  of the electron density for different values of  $N_\tau$ . The dashed lines are guides for the eye. (c) The double occupancy  $\sum_\tau \langle n_{\tau\uparrow} n_{\tau\downarrow} \rangle / N_c$  as a function of the FPQMC estimate  $\rho_{e,\text{FPQMC}}$  of the electron density for different values of  $N_\tau$ . In (a) and (c), full symbols represent FPQMC results, the solid line shows the NLCE data taken from Ref. 41, while the insets show the relative deviation of FPQMC results from the reference NLCE results. The estimated statistical error of the FPQMC data is in all cases smaller than the symbol size.

is lower (size of the corresponding matrices is given by the number of particles of a given spin). The performance of the FPQMC algorithm to compute  $\rho_e(\mu)$  (average time needed to propose/accept an MC update and acceptance rates of individual MC updates) is discussed in Sec. SIII of the [supplementary material](#).

We further benchmark our method in the case of very strong coupling,  $U/J = 24$  and, again,  $T/J = 1.0408$ . Figure 5(a) compares the FPQMC results on a  $4 \times 4$  cluster using  $N_\tau = 2, 4$ , and 6 imaginary-time slices with the NLCE results. At extremely low fillings  $\rho_e \lesssim 0.1$ , the relative importance of the interaction term with respect to the kinetic term is quite small, and taking only  $N_\tau = 2$  suffices to reach a very good agreement between the FPQMC and NLCE results, see the inset of Fig. 5(a). As the filling is increased, the interaction effects become increasingly important, and it is necessary to increase  $N_\tau$  in order to accurately describe the competition between

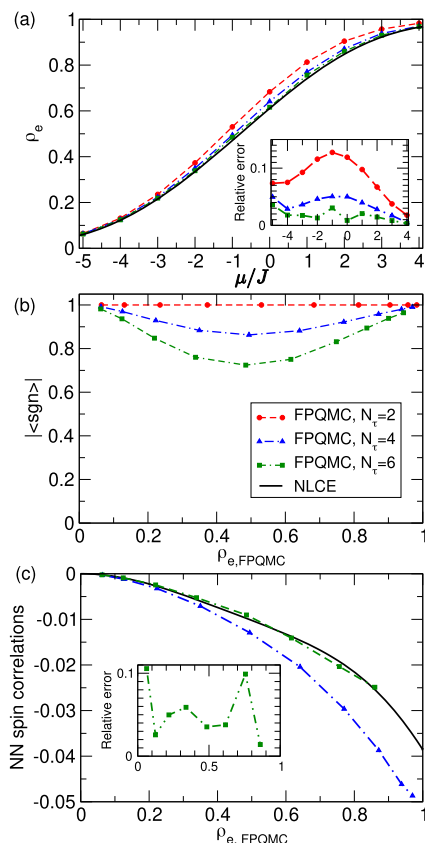


**FIG. 5.** (a) Equation of state  $\rho_e(\mu)$  for the Hubbard model on a  $4 \times 4$  cluster with the following values of model parameters:  $U/J = 24$ ,  $T/J = 1.0408$ . (b) The average sign as a function of the FPQMC estimate  $\rho_{e, \text{FPQMC}}$  of the electron density for different values of  $N_\tau$ . (c) Nearest-neighbor spin correlations  $\sum_{\mathbf{r}\delta} \langle S_{\mathbf{r}}^z S_{\mathbf{r}+\delta}^z \rangle / N_c$  as a function of the FPQMC estimate  $\rho_{e, \text{FPQMC}}$  of the electron density for  $N_\tau = 4$  and 6. In (a) and (c), full symbols represent FPQMC results, the solid line shows the NLCE data taken from Ref. 41, while the insets show the relative deviation of FPQMC results from the reference NLCE results. The dashed or dashed-dotted lines connecting the symbols serve as guides to the eye. The estimated statistical error of the FPQMC data are in all cases smaller than the symbol size.

the kinetic and interaction terms. In the inset of Fig. 5(a), we see that  $N_\tau = 6$  is sufficient to reach an excellent (within a couple of percent) agreement between FPQMC and NLCE results over a broad range of fillings. At very high fillings  $\rho_e \gtrsim 0.9$  and for  $N_\tau = 6$ , our MC updates that insert/remove particles have very low acceptance rates, which may lead to a slow sampling of the configuration space. It is for this reason that FPQMC results with  $N_\tau = 6$  do not significantly improve over  $N_\tau = 4$  in this parameter regime. For  $N_\tau = 6$ , an inefficient sampling near the half-filling also renders the corresponding results for the nearest-neighbor spin correlations  $\sum_{\mathbf{r}\delta} \langle S_{\mathbf{r}}^z S_{\mathbf{r}+\delta}^z \rangle / N_c$  inaccurate, so that they are not displayed in Fig. 5(c). Here, vector  $\delta$  connects nearest-neighboring sites, while  $S_r^z = (n_{r\uparrow} - n_{r\downarrow})/2$  is the operator of  $z$  projection of the local spin. At lower fillings,  $\rho_e \lesssim 0.8$ , the agreement between our FPQMC results with  $N_\tau = 6$  and the NLCE results is good, while decreasing  $N_\tau$  from 6 to 4 severely deteriorates the quality of the FPQMC results.

At this strong coupling, the dependence of the average sign on the density is somewhat modified, see Fig. 5(b). The minimal sign is no longer reached around half-filling but at quarter-filling,  $\rho_e \sim 0.5$ , around which  $|\langle \text{sgn} \rangle|$  appears to be symmetric. Comparing Fig. 5(b) to Fig. 4(b), we see that the average sign does not become smaller with increasing interaction, in sharp contrast with interaction-expansion-based methods, such as CT-INT<sup>32,33</sup> or configuration PIMC.<sup>89</sup>

To better understand the relation between the average sign and the interaction, in Fig. 6(a) we plot  $|\langle \text{sgn} \rangle|$  as a function of the ratio  $U/(4J)$  of the typical interaction and kinetic energy. We take  $N_\tau = 6$  and adjust the chemical potential using the data from Ref. 41 so that  $\rho_e \approx 0.5$ . We see that  $|\langle \text{sgn} \rangle|$  monotonically increases with the interaction and reaches a plateau at very strong interactions. This is different from interaction-expansion-based QMC methods, whose sign problem becomes more pronounced as the interaction is

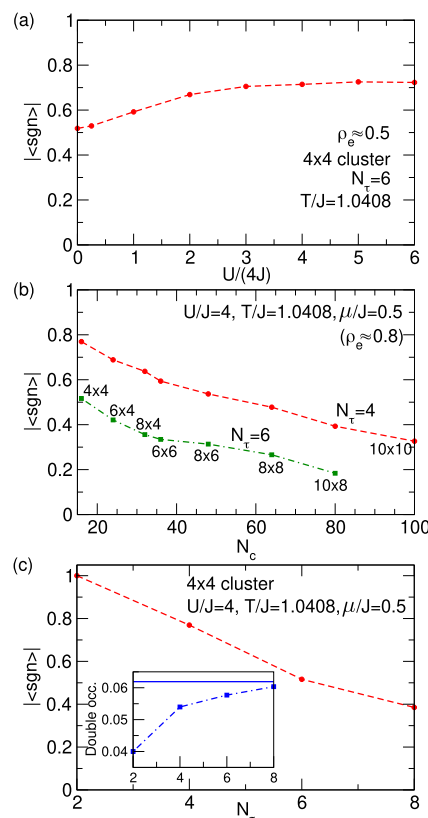


**FIG. 6.** (a) The average sign as a function of the ratio between the typical interaction and kinetic energies. Full symbols are results of FPQMC computations on a  $4 \times 4$  cluster with  $N_\tau = 6$ , the temperature is fixed to  $T/J = 1.0408$ , and the chemical potential at each  $U$  is chosen such that  $\rho_e \approx 0.5$ . (b) The average sign as a function of the cluster size  $N_c$  for the values of model parameters summarized in the figure. The FPQMC results (full symbols) are obtained using  $N_\tau = 4$  and 6. (c) Average sign as a function of  $N_\tau$ . The FPQMC results (full symbols) are obtained on a  $4 \times 4$  cluster for the values of model parameters summarized in the main part of the figure. The inset shows how the FPQMC result for double occupancy approaches the referent NLCE result as the imaginary-time discretization becomes finer.

increased. Moreover, for weak interactions, the performance of the FPQMC method deteriorates at high densities, see Fig. 4(b), while methods such as CT-INT become problematic at low densities. The FPQMC method could thus become a method of choice to study the regimes of moderate coupling and temperature, which are highly relevant for optical lattice experiments. Figure 6(b) shows the decrease of the average sign with the cluster size  $N_c$  in the weak-coupling and moderate-temperature regime at filling  $\rho_e \approx 0.8$ . We observe that for both  $N_\tau = 4$  and  $N_\tau = 6$ , the average sign decreases linearly with  $N_c$ . For  $N_\tau = 6$ , we observe that the decrease for  $N_c \lesssim 40$  is somewhat faster than the decrease for  $N_c \gtrsim 40$ . We, however, note that the acceptance rates of our MC updates strongly decrease with  $N_c$  and that this decrease is more pronounced for finer imaginary-time discretizations. That is why we were not able to obtain any meaningful result for the  $10 \times 10$  cluster with  $N_\tau = 6$ . At fixed cluster size and filling, the average sign decreases linearly with  $N_\tau$ , see the main part of Fig. 6(c), while the double occupancy tends to the referent NLCE value, see the inset of Fig. 6(c).

In Sec. SIV of the [supplementary material](#), we provide an implementation of the ABQMC method in the equilibrium setup. Figures 7(a) and 7(b), which deal with the same parameter regimes as Figs. 4 and 5, respectively, clearly illustrate the advantages of the fermionic-propagator approach with respect to the alternating-basis approach in equilibrium. The average sign of ABQMC simulations with only two imaginary-time slices is orders of magnitude smaller than the sign of FPQMC simulations with three times finer imaginary-time discretization. Since the FPQMC and ABQMC methods are related by an exact transformation, they should produce

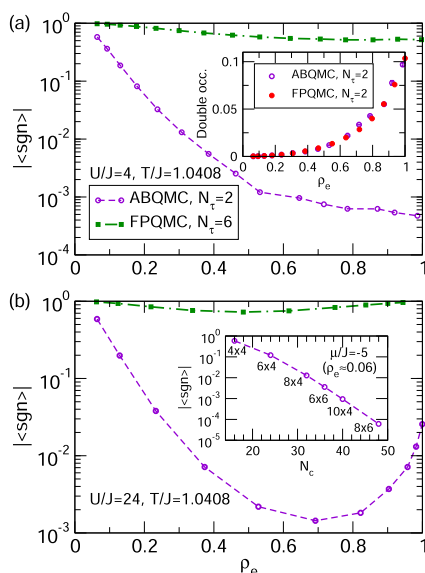


**FIG. 7.** Average sign as a function of the electron density in ABQMC simulations with  $N_\tau = 2$  (open circles) and FPQMC simulations with  $N_\tau = 6$  (full squares) for  $T/J = 1.0408$  and (a)  $U/J = 4$  and (b)  $U/J = 24$ . The inset in panel (a) compares ABQMC (open circles) and FPQMC (full circles) results for the double occupancy as a function of  $\rho_e$  (both methods employ  $N_\tau = 2$ ). The inset in panel (b) shows the average sign of ABQMC simulations with  $N_\tau = 2$  as a function of cluster size  $N_c$  at low density ( $\rho_e \approx 0.06$ ,  $\mu/J = -5$ ).

the same results for thermodynamic quantities (assuming that  $N_\tau$  is the same in both methods). This is shown in the inset of Fig. 7(a) on the example of the double occupancy. The inset of Fig. 7(b) suggests that the average sign decreases exponentially with the cluster size  $N_c$ . Overall, our current implementation of the ABQMC method in equilibrium cannot be used to simulate larger clusters with a finer imaginary-time discretization.

## B. Time-dependent results using FPQMC method: Local charge and spin densities

### 1. Benchmarks on small clusters

In Figs. 8(a) and 8(b), we benchmark our FPQMC method for time-dependent local densities on the example of the CDW state of the Hubbard tetramer, see the inset of Fig. 8(b). We follow the evolution of local charge densities on initially occupied sites for different ratios  $U/D$ , where  $D$  is the half-bandwidth of the free-electron band ( $D = 2J$  for the tetramer). For all the interaction strengths considered, taking  $N_t = 2$  real-time slices on each branch (four slices in total) is sufficient to accurately describe the evolution of local densities up to times  $Dt \sim 2$ , see full symbols in Fig. 8(a). At longer times,  $2 < Dt \leq 4$ , taking  $N_t = 3$  improves results obtained using  $N_t = 2$ , compare empty to full symbols in Fig. 8(a). Nevertheless, for the strongest interaction considered ( $U/D = 1$ ), 6 real-time slices are not sufficient to bring the FPQMC result closer to the exact result at times  $3 \leq Dt \leq 4$ . The average sign strongly depends on time, and it drops by an order of magnitude upon increasing  $N_t$  from 2 to 3, see Fig. 8(b). Despite this, the discrepancy between the  $N_t = 3$  result

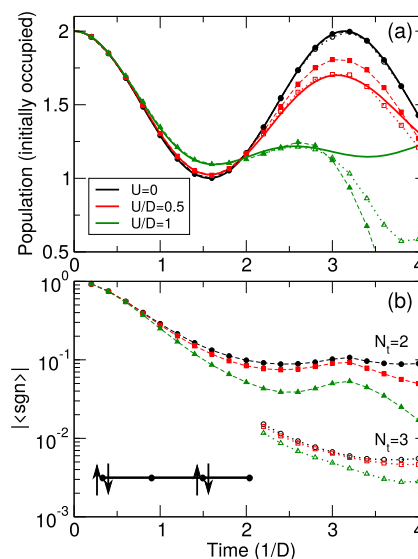


**FIG. 8.** (a) Time-dependent population of sites occupied in the initial CDW state of a tetramer for different interaction strengths. Solid lines represent exact results, full symbols connected by dashed lines are FPQMC results using  $N_t = 2$  real-time slices, while empty symbols connected by dotted lines are FPQMC results using  $N_t = 3$  real-time slices. The initial CDW state is schematically depicted in panel (b). (b) Time-dependent average sign of the FPQMC simulation using  $N_t = 2$  (full symbols connected by dashed lines) and  $N_t = 3$  (empty symbols connected by dotted lines) for different interaction strengths. In (a) and (b), FPQMC simulations using  $N_t = 3$  real-time slices are carried out only for  $2 < Dt \leq 4$ .





and the exact result for  $U/D = 1$  cannot be ascribed to statistical errors but rather to the systematic error of the FPQMC method (the minimum  $N_t$  needed to obtain results with certain systematic error increases with both time and interaction strength).

## 2. Results on larger clusters

Figure 9(a) summarizes the evolution of local charge densities on initially occupied sites of a half-filled  $4 \times 4$  cluster, on which the electrons are initially arranged as depicted in the inset of Fig. 9(b). This state is representative of a CDW pattern formed by applying strong external density-modulating fields with wave vector  $\mathbf{q} = (\pi, 0)$ . The FPQMC method employs four real-time slices in total, i.e., the forward and backward branches are divided into  $N_t = 2$  identical slices each. On the basis of the  $N_t = 2$  results in Fig. 8(a), we present the FPQMC dynamics up to the maximum time  $Dt_{\max} = 2$ . The extent of the dynamical sign problem is shown in Fig. 9(b).

At the shortest times,  $Dt \lesssim 1$ , the results for all the interactions considered do not significantly differ from the noninteracting result. The same also holds for the average sign. As expected, the decrease of  $|\langle \text{sgn} \rangle|$  with time becomes more rapid as the interaction  $U$  and time discretization  $\Delta t = t/N_t$  are increased. The oscillatory nature of  $\langle \text{sgn} \rangle$  as a function of time [see Eq. (22)] is correlated with the discontinuities in time-dependent populations observed in Fig. 9(a) for  $U/D \geq 0.5$ . Namely, at the shortest times and for all the interactions considered,  $\langle \text{sgn} \rangle$  is positive, while for sufficiently strong interactions, it becomes negative at longer times. This change is indicated in Fig. 9(b) by placing the symbols “+” and “−” next to each relevant point. We now see that the discontinuities in populations occur precisely around instants at which  $\langle \text{sgn} \rangle$  turns from positive to negative values. Focusing on  $U/D = 1$ , in Figs. 9(c1)–9(c3) we show the MC series for the population of initially occupied sites at instants before

**TABLE I.** Schematic representations of the initial states of small systems on which the ABQMC method for  $P(t)$  is benchmarked.

system	$ \psi_{\text{CDW}}\rangle$	$ \psi_{\text{SDW}}\rangle$
Dimer		
Tetramer		

[(c1)] and after [(c2), (c3)]  $\langle \text{sgn} \rangle$  passes through zero. The corresponding series for  $\langle \text{sgn} \rangle$  are presented in Figs. 9(d1)–9(d3). Well before [Figs. 9(c1) and 9(d1)] and after [Figs. 9(c3) and 9(d3)]  $\langle \text{sgn} \rangle$  changes sign, the convergence with the number of MC steps is excellent, while it is somewhat slower close to the positive-to-negative transition point, see Figs. 9(c2) and 9(d2). Still, the convergence at  $Dt = 1.4$  cannot be denied, albeit the statistical error of the population is larger than at  $Dt = 1.2$  and 1.6. At longer times  $Dt \geq 1.5$ , when  $\langle \text{sgn} \rangle$  is negative and of appreciable magnitude, the population again falls in the physical range  $[0, 2]$ . Nevertheless, at such long times, the systematic error may be large due to the coarse real-time discretization.

In Sec. SV of the [supplementary material](#), we discuss FPQMC results for the dynamics of local charge densities starting from some other initial states.

## C. Time-dependent results using ABQMC method: Survival probability

### 1. Benchmarks on small clusters

We first benchmark our ABQMC method for the survival probability on Hubbard dimers and tetramers. The initial states

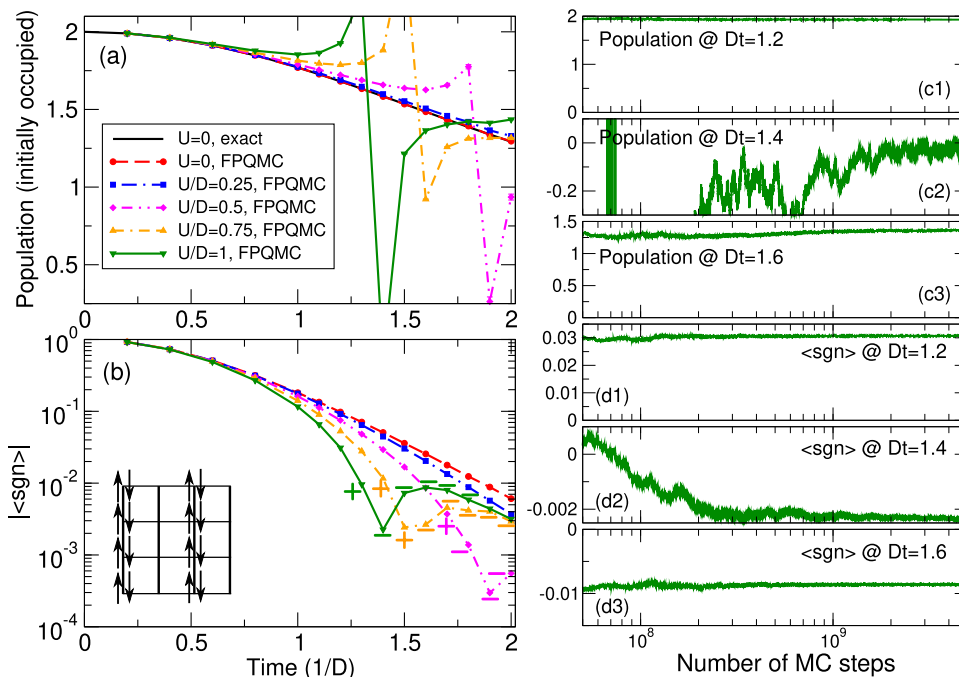


**FIG. 9.** (a) Time-dependent population of sites occupied in the initial CDW state of a  $4 \times 4$  cluster, which is schematically depicted in the inset of panel (b). FPQMC results using  $N_t = 2$  real-time slices (four slices in total) are shown for five different interaction strengths (symbols) and compared with the noninteracting result (solid line). (b) Magnitude of the average sign as a function of time for different interaction strengths. The color code is the same as in panel (a). For  $U/D = 0.5, 0.75$ , and 1 and  $Dt \geq 1.2$ , symbols “+” and “−” next to each point specify whether  $\langle \text{sgn} \rangle$  is positive or negative. (c) MC series for the population of initially occupied sites for  $U/D = 1$  and (c1)  $Dt = 1.2$ , (c2)  $Dt = 1.4$ , and (c3)  $Dt = 1.6$ . (d) MC series for  $\langle \text{sgn} \rangle$  for  $U/D = 1$  and (d1)  $Dt = 1.2$ , (d2)  $Dt = 1.4$ , and (d3)  $Dt = 1.6$ . Note the logarithmic scale on the abscissa in (c) and (d).



are schematically summarized in Table I. In both cases, we are at half-filling.

Figures 10(a1)–10(e2) present the time evolution of the survival probability of the initial CDW-like and SDW-like states depicted in Table I for the dimer (left panels,  $D = J$ ) and tetramer (right panels,  $D = 2J$ ) for different values of  $U/D$  starting from the limit of a weakly nonideal gas ( $U/D = 0.05$ ) and approaching the atomic limit ( $U/D = 20$ ). The results are obtained using  $N_t = 2$  (full red circles) and  $N_t = 4$  (blue stars) real-time slices and contrasted with the exact result (solid black lines). The ABQMC results with  $N_t = 2$  agree both qualitatively (oscillatory behavior) and quantitatively with the exact result up to  $t_{\max} \sim 1/U$ . Increasing  $N_t$  from 2 to 4 may help decrease the deviation of the ABQMC data from the exact result at later times. Even when finer real-time discretization does not lead to better quantitative agreement, it may still help the ABQMC method qualitatively reproduce the gross features of the exact result. The converged values of  $|\langle \text{sgn} \rangle|$  for the dimer and tetramer

**TABLE II.** Modulus of the average sign for ABQMC simulations of  $P(t)$  on dimer and tetramer with  $N_t = 2, 3$ , and 4.

System	$N_t = 2$	$N_t = 3$	$N_t = 4$
Dimer	1/2	1/4	1/8
Tetramer	1/8	$2.4 \times 10^{-2}$	$3 \times 10^{-3}$

for  $N_t = 2, 3$ , and 4 are summarized in Table II. For the dimer, increasing  $N_t$  by one reduces  $|\langle \text{sgn} \rangle|$  by a factor of 2. In contrast, in the case of the tetramer, increasing  $N_t$  by one reduces  $|\langle \text{sgn} \rangle|$  by almost an order of magnitude.

## 2. Results on larger clusters

We move on to discuss the survival probability dynamics of different 16-electron and eight-electron states on a  $4 \times 4$

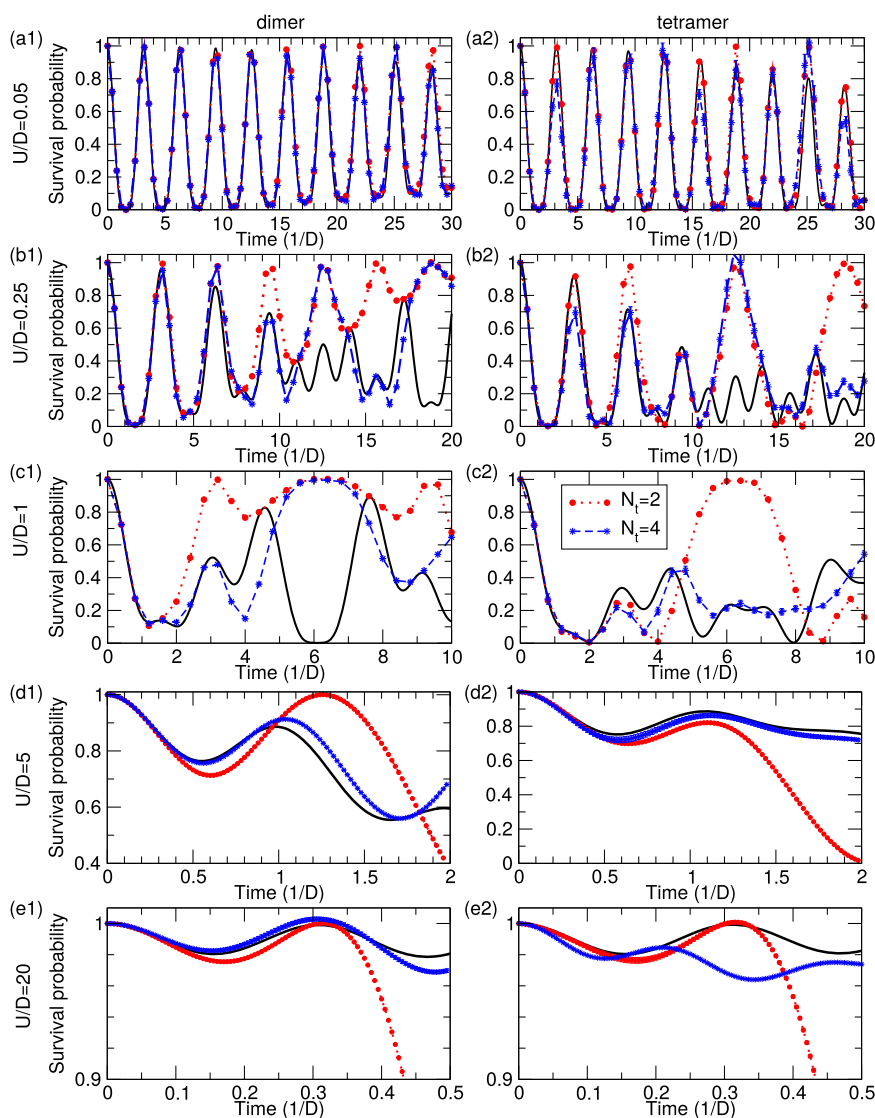


**FIG. 10.** Time dependence of the survival probability of the initial state  $|\psi_{\text{CDW}}\rangle$  or  $|\psi_{\text{SDW}}\rangle$  (see Table I) for the dimer [(a1)–(e1)] and tetramer [(a2)–(e2)] for five different interaction strengths starting from the noninteracting limit and approaching the atomic limit:  $U/D = 0.05$  [(a1) and (a2)],  $U/D = 0.25$  [(b1) and (b2)],  $U/D = 1$  [(c1) and (c2)],  $U/D = 5$  [(d1) and (d2)], and  $U/D = 20$  [(e1) and (e2)]. The ABQMC results with  $N_t = 2$  (red full circles) and  $N_t = 4$  (blue stars) are compared with the exact result (black solid lines). The dotted/dashed lines connecting subsequent circles/stars are guides to the eye. In most cases, the MC error bars are smaller than the linear size of the symbols.



cluster. Figures 11(a) and 11(b) present  $P(t)$  for 16-electron states schematically depicted in their respective insets. These states are representative of CDW patterns formed by applying strong external density-modulating fields with wave vectors  $\mathbf{q} = (\pi, 0)$  in Figs. 11(a) and  $\mathbf{q} = (\pi, \pi)$  in Fig. 11(b). Figures 11(c) and 11(d) present  $P(t)$  for eight-electron states schematically depicted in their respective insets. The ABQMC method employs  $N_t = 2$  real-time slices. The results are shown up to the maximum time  $Dt_{\max} = 2.5$ , which we chose on the basis of the results presented in Fig. 10(c2).

As a sensibility check of our ABQMC results, we first compare the exact result in the noninteracting limit, see solid lines in Figs. 11(a)–11(d), with the corresponding ABQMC prediction, see full circles in Figs. 11(a)–11(d). While the exact and ABQMC results agree quite well in Figs. 11(b) and 11(c), the agreement in Figs. 11(a) and 11(d) is not perfect. Since no systematic errors are expected in ABQMC at  $U = 0$ , the discrepancy must be due to statistical error. We confirm this expectation in Fig. 12 where we see that the obtained curve tends to the exact one with the increasing number of MC steps. The average sign cited in Fig. 11(d) suggests that more MC steps are needed to obtain fully converged results. Even though the converged average sign in Figs. 11(a)–11(c) is of the same order of magnitude, we find that the rate of convergence depends on both the number and the initial configuration of electrons.

In Figs. 11(a)–11(d), we observe that weak interactions ( $U/D \lesssim 0.5$ ) do not cause any significant departure of  $P(t)$  from the corresponding noninteracting result. On the other hand, the effect of somewhat stronger interactions on  $P(t)$  depends crucially on the filling. In the 16-electron case, the increasing interactions speed up the initial decay of  $P$ , see Figs. 11(a) and 11(b), while in the eight-electron case interactions have little effect at  $Dt < 1$ , see Figs. 11(c) and 11(d). This we attribute to the essential difference in the overall electron density and the relative role of the interaction term in the Hamiltonian. In the 16-electron case, starting from the moderate coupling  $U/D \sim 1$ , there is a clear revival of the initial

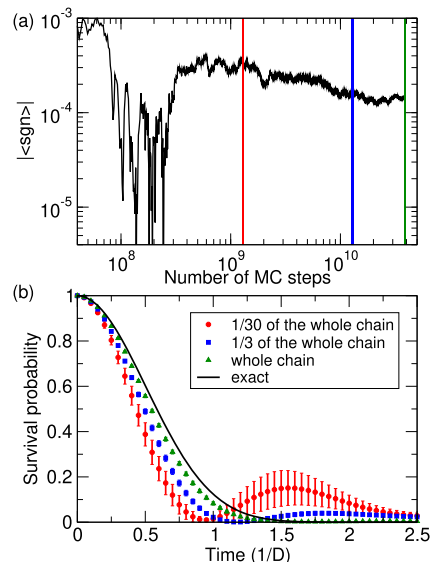


**FIG. 12.** (a) Average sign as a function of the number of MC steps in the ABQMC simulation of  $P(t)$  for the 16-electron initial state schematically depicted in Fig. 11(a). (b) Time dependence of the survival probability for  $U = 0$  extracted using the first 1/30 of the total number of MC steps completed ( $1.29 \times 10^9$  steps, full red circles), the first 1/3 of the total number of MC steps completed ( $1.29 \times 10^{10}$  steps, full blue squares), and all the MC steps completed ( $3.87 \times 10^{10}$  steps, full green up-triangles). These results are compared to the exact result in the noninteracting limit, which is represented by the solid line. The vertical lines in (a), whose colors match the colors of the symbols in (b), denote the ending points of the simulations.

state in Fig. 11(a), while no such a revival is observed in Fig. 11(b). Furthermore, the memory loss of the initial density-wave pattern is more rapid in Fig. 11(a) than in Fig. 11(b), even at  $U = 0$ . The revival of the initial state is observed in the eight-electron case as well: at

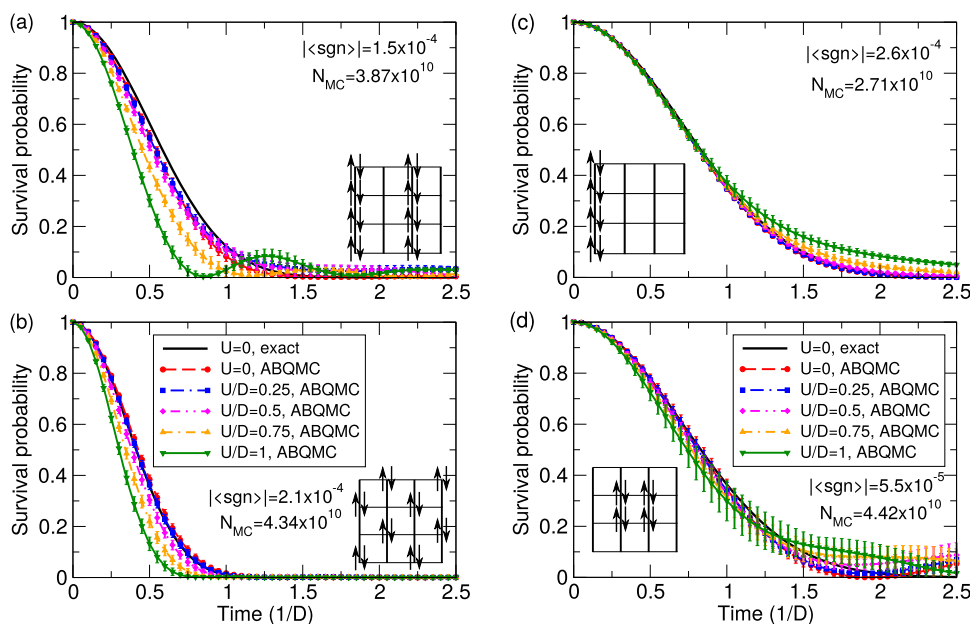


**FIG. 11.** Survival-probability dynamics of the 16-electron states [in (a) and (b)] and 8-electron states [in (c) and (d)] that are schematically depicted in the respective insets. The ABQMC results are shown for five different interaction strengths (symbols) and compared with the noninteracting result (solid line). We cite the converged value of the average sign  $|\langle \text{sgn} \rangle|$ , as well as the total number  $N_{MC}$  of MC steps completed.

$t < 1/D$  there is barely any effect of the interaction, yet at longer times it boosts  $P$ . However, in contrast to the 16-electron case, the results in Figs. 11(c) and 11(d) exhibit a weaker dependence of the survival-probability dynamics on the initial density-wave pattern. Indeed, the exact results in the noninteracting case are identical for both patterns in Figs. 11(c) and 11(d). Except in the case of the  $(\pi, \pi)$  wave, the interactions lead to a persistence of the initial pattern at longer times,  $t > 1/D$ . The precise form of temporal correlations that develop due to interactions apparently depends on the initial spatial arrangement of the electrons.

Section SVI of the [supplementary material](#) presents additional ABQMC results for the time-dependent survival probability.

#### IV. RELATION TO OTHER ALGORITHMS

As mentioned in the introduction, a variant of the FPQMC method was first proposed by De Raedt and Lagendijk in the 1980s.<sup>78–80</sup> They, however, explicitly retain permutation operators appearing in Eq. (A5) in their final expression for  $Z$ , see, e.g., Eq. (3) in Ref. 78 or Eqs. (4.13) and (4.14) in Ref. 80. On the other hand, we analytically perform summation over permutation operators, thus grouping individual contributions into determinants. This is much more efficient [as the factorial number of terms is captured in only  $O(N^3)$  steps, or even faster] and greatly improves the average sign (cancellations between different permutations are already contained in the determinant, see Fig. 7). The approach followed by De Raedt and Lagendijk later became known as permutation-sampling QMC, and the route followed by us is known as antisymmetric-propagator QMC,<sup>85,86</sup> permutation-blocking QMC,<sup>90</sup> or fermionic-propagator QMC.<sup>96</sup> The analytical summation over permutation operators entering Eq. (A5) was first performed by Takahashi and Imada.<sup>85</sup>

Our FPQMC method employs the lowest-order STD [Eq. (4)], which was also used in the permutation-sampling QMC method of De Raedt and Lagendijk.<sup>78–80</sup> The maximum number of imaginary-time slices  $N_\tau$  they could use was limited by the acceptance rates of MC updates, which decrease quickly with increasing  $N_\tau$  and the cluster size  $N_c$ . In our present implementation of FPQMC, we encounter the same issue, and our sampling becomes prohibitively inefficient when the total number of time slices is greater than 6–8, depending on the cluster size. To circumvent this issue, the fermionic-propagator idea was combined with higher-order STDs<sup>98,114–116</sup> and more advanced sampling techniques<sup>117,118</sup> to simulate the equilibrium properties of continuum models of interacting fermions in the canonical<sup>90,92</sup> and grand-canonical<sup>96</sup> ensembles. More recent algorithmic developments enabled simulations with as much as 2000 imaginary-time slices,<sup>119</sup> which is a great improvement. Whether similar ideas can be applied to lattice systems to improve the efficiency of sampling is currently unclear. Generally, more sophisticated STD schemes have been regarded as not useful in lattice-model applications.<sup>120</sup> It is important to note that the success of the antisymmetric-propagator algorithms in continuous systems relies on weak degeneracy. This corresponds to an extremely low occupancy regime in lattice models, and it is precisely in this regime that our FPQMC method has an average sign close to 1 [see Figs. 4(b) and 5(b)], and the sampling is most efficient [see Sec. SIII of the [supplementary material](#)]. Near half-filling, lattice models present a fundamentally different physics,

which may ultimately require a substantially different algorithmic approach.

We further emphasize that the low acceptance rates and the resulting inefficiency of sampling that we encounter are directly related to the discrete nature of space in our model. Some strategies for treating the analogous problem in continuous-space models may not be applicable here. For example, in continuous-space models, acceptance rates of individual updates can be adjusted by moving electrons over shorter distances, so that the new configuration weight is less likely to be substantially different from the old one. In contrast, in lattice models, electronic coordinates are discrete, and the minimum distance the electrons may cover is set by the lattice constant; in most cases, moving a single electron by a single lattice spacing in a single time slice is sufficient to drastically reduce the configuration weight. There is no general rule on how electrons should be moved to ensure that the new configuration weight is close to the original one. This is particularly true for the updates that insert/remove a particle, and the problem becomes more pronounced with increasing  $N_\tau$ . When each of the  $N_\tau$  states  $|\Psi_{i,l}\rangle$  [see Eq. (9)] is changed to  $|\Psi'_{i,l}\rangle$ , the chances that at least one of  $\langle \Psi'_{i,l} | e^{-\Delta\tau H_0} | \Psi_{i,l} \rangle$  is much smaller than  $\langle \Psi_{i,l} | e^{-\Delta\tau H_0} | \Psi_{i,l} \rangle$  [see Eq. (10)] increase with  $N_\tau$ . Our configuration weight is appreciable only in small, mutually disconnected regions of the configuration space, the movement between which is difficult. In Sec. V, we touch upon possible strategies to improve sampling of such a structured configuration space.

It is also important to compare our methods to the HF QMC method,<sup>24,49</sup> which is a well-established STD-based method for the treatment of the Hubbard model. The HF method is manifestly sign-problem-free but only at particle-hole symmetry. The sign problem can become severe away from half-filling, or on lattices other than the simple square lattice with no longer-range hoppings. On the other hand, our FPQMC method is nearly sign-problem-free at low occupancy, but also near half-filling, albeit only at strong coupling [see Figs. 4(b) and 5(b)]. The other important difference is that matrices manipulated in HF are of the size  $N_c N_\tau$ , while in FPQMC, the matrices are of the size  $< 2N_c$ , i.e., given by the number of particles. Algorithmic complexity of the individual MC step in FPQMC scales only linearly with  $N_\tau$ , while in HF, the MC step may go as  $O(N_\tau^2)$  [determinant is  $O(N^3)$ , but fast updates  $O(N^2)$  are possible when the determinant is not calculated from scratch<sup>49</sup>]. Low cost of individual steps in FPQMC has allowed us to perform as many as  $\sim 10^{10}$  MC steps in some calculations. This advantage, however, weighs against an increased configuration space to be sampled. In HF the number of possible configurations is  $2^{N_c N_\tau}$  (space is spanned by  $N_c N_\tau$  auxiliary Ising spins), while in FPQMC it is  $4^{N_c N_\tau}$  (although, symmetries can be used to significantly reduce the number of possible configurations). The ABQMC method manipulates matrices of the same size as does FPQMC, but with twice the number, and the configuration space is *a priori* even bigger ( $16^{N_c N_\tau}$ ). Our methods also have the technical advantage that the measurements of multipoint charge and spin correlation functions are algorithmically trivial and cheap. Especially in ABQMC, the densities in both coordinate and momentum space can be simply read off the configuration. This is not possible in HF, where the auxiliary Ising spin only distinguishes between singly occupied and doubly-occupied/empty sites. Most importantly, the ABQMC/FPQMC methods can be readily applied to canonical ensembles and pure states, which may

not be possible with the HF method. However, the HF is commonly used with tens of time slices for lattice sizes of order  $N_c = 100$ – $200$ ; in FPQMC, algorithmic developments related to configuration updates are necessary before it can become a viable alternative to the HF in a wide range of applications.

Finally, we are unaware of any numerically exact method for large lattice systems, which can treat the full Kadanoff–Baym–Keldysh contour, and yield real-time correlation functions. Our ABQMC method represents an interesting example of a real-time QMC method with manifestly no dynamical sign problem. However, the average sign is generally poor. To push ABQMC to larger number of time slices (as needed for calculation of the time-dependence of observables) and lattices larger than  $4 \times 4$  will require further work, and most likely, conceptually new ideas.

## V. SUMMARY AND OUTLOOK

We revisit one of the earliest proposals for a QMC treatment of the Hubbard model, namely the permutation-sampling QMC method developed in Refs. 78–80. Motivated by recent progress in the analogous approach to continuous space models, we group all permutations into a determinant, which is known as the antisymmetric-propagator,<sup>85</sup> permutation-blocking,<sup>90</sup> or fermionic-propagator<sup>96</sup> idea. We devise and implement two slightly different QMC methods. Depending on the details of the STD scheme, we distinguish between (1) the FPQMC method, where snapshots are given by real-space Fock states and determinants represent antisymmetric propagators between those states, and (2) the ABQMC method, where slices alternate between real and reciprocal space representation and determinants are simple Slater determinants. We thoroughly benchmark both methods against the available numerically exact data and then use ABQMC to obtain some new results in the real-time domain.

The FPQMC method exhibits several promising properties. The average sign can be close to 1 and does not drop off rapidly with either the size of the system or the number of time slices. In 1D, the method appears to be sign-problem-free. At present, the limiting factor is not the average sign but rather the ability to sample the large configuration space. At discretizations finer than  $N_\tau = 6$ – $8$ , further algorithmic developments are necessary. Nevertheless, our calculations show that excellent results for instantaneous correlators can be obtained with very few time slices and efficiently. Average density, double occupancy, and antiferromagnetic correlations can already be computed with high accuracy at temperatures and coupling strengths relevant for optical-lattice experiments. The FPQMC method is promising for further applications in equilibrium setups. In real-time applications, however, the sign problem in FPQMC is severe.

On the other hand, the ABQMC method has a significant sign problem in equilibrium applications but has some advantages in real-time applications. In ABQMC, the sign problem is manifestly time-independent, and calculations can be performed for multiple times and coupling strengths with a single Markov chain. We use this method to compute time-dependent survival probabilities of different density-modulated states and identify several trends. The relevant transient regime is short, and based on benchmarks, we estimate the systematic error due to the time discretization here to be small. Our results reveal that interactions speed up the initial decay

of the survival probability but facilitate the persistence of the initial charge pattern at longer times. Additionally, we observe a characteristic value of the coupling constant,  $U \sim 0.5D$ , below which the interaction has no visible effect on time evolution. These findings bare qualitative predictions for future ultracold-atom experiments, but are limited to dynamics at the shortest wave-lengths, as dictated by the maximal size of the lattice that we can treat. We finally note that, within the ABQMC method, uniform currents, which are diagonal in the momentum representation, may be straightforwardly treated.

There is room for improvement in both the ABQMC and FPQMC methods. We already utilize several symmetries of the Hubbard model to improve efficiency and enforce some physical properties of solutions, but more symmetries can certainly be uncovered in the configuration spaces. Further grouping of configurations connected by symmetries can be used to alleviate some of the sign problem or improve efficiency. Also, sampling schemes may be improved along the lines of the recently proposed many-configuration Markov chain MC, which visits an arbitrary number of configurations at every MC step.<sup>121</sup> Moreover, a better insight into the symmetries of the configuration space may make deterministic, structured sampling (along the lines of quasi-MC methods<sup>122–124</sup>) superior to the standard pseudo-random sampling.

## SUPPLEMENTARY MATERIAL

See the [supplementary material](#) for (i) a detailed description of MC updates within the FPQMC method, (ii) a detailed description of MC updates within the ABQMC method for time-dependent survival probability, (iii) details on the performance of the FPQMC method in equilibrium calculations, (iv) discussion on the applicability of the ABQMC method in equilibrium calculations, (v) additional FPQMC calculations of time-dependent local densities, (vi) additional ABQMC calculations of time-dependent survival probability, and (vii) formulation and benchmarks of ABQMC method in quench setups (on the full three-piece Kadanoff–Baym–Keldysh contour).

## ACKNOWLEDGMENTS

We acknowledge funding provided by the Institute of Physics Belgrade through a grant from the Ministry of Education, Science, and Technological Development of the Republic of Serbia as well as by the Science Fund of the Republic of Serbia under the Key2SM project (PROMIS program, Grant No. 6066160). Numerical simulations were performed on the PARADOX-IV supercomputing facility at the Scientific Computing Laboratory, National Center of Excellence for the Study of Complex Systems, Institute of Physics Belgrade.

## AUTHOR DECLARATIONS

### Conflict of Interest

The authors have no conflicts to disclose.

### Author Contributions

J.V. conceived the research. V.J. developed the formalism and computational codes under the guidance of J.V., conducted all numerical

simulations, analyzed their results, and prepared the initial version of the manuscript. Both authors contributed to the submitted version of the manuscript.

**Veljko Janković:** Conceptualization (supporting); Data curation (lead); Formal analysis (lead); Investigation (lead); Methodology (lead); Software (lead); Validation (lead); Visualization (lead); Writing – original draft (lead); Writing – review & editing (equal). **Jakša Vučičević:** Conceptualization (lead); Funding acquisition (lead); Project administration (lead); Resources (lead); Software (supporting); Supervision (lead); Writing – review & editing (equal).

## DATA AVAILABILITY

The data that support the findings of this study are available from the corresponding author upon reasonable request.

## APPENDIX A: MANY-BODY PROPAGATOR AS A DETERMINANT OF SINGLE-PARTICLE PROPAGATORS

The demonstration of Eqs. (6) and (7) can be conducted for each spin component separately. We thus fix the spin index  $\sigma$  and further omit it from the definition of the many-fermion state  $|\Psi_i\rangle$  [Eq. (5)]. Since  $H_0$  is diagonal in the momentum representation, we express the state  $|\Psi_i\rangle$  in the momentum representation

$$|\Psi_i\rangle = \sum_{\{\mathbf{k}_j\}} \left( \prod_{l=1}^N \langle \mathbf{k}_l | \mathbf{r}_l \rangle c_{\mathbf{k}_l}^\dagger \right) |\emptyset\rangle \quad (\text{A1})$$

and similarly for  $|\Psi'_i\rangle$ . While the positions  $\mathbf{r}_1, \dots, \mathbf{r}_N$  are ordered according to a certain rule, the wave vectors  $\mathbf{k}_1, \dots, \mathbf{k}_N$  entering Eq. (A1) are not ordered, and there is no restriction on the sum over them. We have

$$\begin{aligned} \langle \Psi'_i | e^{-\Delta\alpha H_0} | \Psi_i \rangle &= \sum_{\{\mathbf{k}'_j\}} \sum_{\{\mathbf{k}_j\}} e^{-\Delta\alpha \varepsilon_{\mathbf{k}_1}} \dots e^{-\Delta\alpha \varepsilon_{\mathbf{k}_N}} \\ &\times \langle \mathbf{r}'_1 | \mathbf{k}'_1 \rangle \dots \langle \mathbf{r}'_N | \mathbf{k}'_N \rangle \langle \mathbf{k}_1 | \mathbf{r}_1 \rangle \dots \langle \mathbf{k}_N | \mathbf{r}_N \rangle \\ &\times \langle \emptyset | c_{\mathbf{k}'_N} \dots c_{\mathbf{k}'_1} c_{\mathbf{k}_1}^\dagger \dots c_{\mathbf{k}_N}^\dagger | \emptyset \rangle. \end{aligned} \quad (\text{A2})$$

The sums over  $\{\mathbf{k}'_j\}$  are eliminated by employing the identity<sup>80</sup>

$$\begin{aligned} \langle \emptyset | c_{\mathbf{k}'_N} \dots c_{\mathbf{k}'_1} c_{\mathbf{k}_1}^\dagger \dots c_{\mathbf{k}_N}^\dagger | \emptyset \rangle \\ = \sum_{\mathcal{P}} \text{sgn}(\mathcal{P}) \delta(\mathbf{k}'_1, \mathbf{k}_{\mathcal{P}(1)}) \dots \delta(\mathbf{k}'_N, \mathbf{k}_{\mathcal{P}(N)}), \end{aligned} \quad (\text{A3})$$

where the permutation operator  $\mathcal{P}$  acts on the set of indices  $\{1, \dots, N\}$ , while  $\text{sgn}(\mathcal{P}) = \pm 1$  is the permutation parity. We then observe that

$$\prod_{l=1}^N \langle \mathbf{r}'_l | \mathbf{k}_{\mathcal{P}(l)} \rangle = \prod_{l=1}^N \langle \mathbf{r}'_{\mathcal{P}^{-1}(l)} | \mathbf{k}_l \rangle, \quad (\text{A4})$$

which permits us to perform the sums over individual  $\mathbf{k}_j$ s independently. Combining Eqs. (A2)–(A4) and changing the permutation variable  $\mathcal{P}' = \mathcal{P}^{-1}$  we eventually obtain

$$\begin{aligned} \langle \Psi'_i | e^{-\Delta\alpha H_0} | \Psi_i \rangle &= \sum_{\mathcal{P}'} \text{sgn}(\mathcal{P}') \prod_{l=1}^N \langle \mathbf{r}'_{\mathcal{P}'(l)} | \mathbf{k}_l \rangle e^{-\Delta\alpha H_0} | \mathbf{r}_l \rangle \\ &= \det S(\Psi'_i, \Psi_i, \Delta\alpha), \end{aligned} \quad (\text{A5})$$

where matrix  $S(\Psi'_i, \Psi_i, \Delta\alpha)$  (here without the spin index) is defined in Eq. (7).

## APPENDIX B: PROPAGATOR OF A FREE PARTICLE ON THE SQUARE LATTICE

Here, we provide the expressions for the propagator of a free particle on the square lattice in imaginary [ $\Delta\alpha = \Delta\tau$  in Eq. (7)] and real [ $\Delta\alpha = i\Delta t$  in Eq. (7)] time. In imaginary time,

$$\langle \mathbf{r}' | e^{-\Delta\tau H_0} | \mathbf{r} \rangle = \mathcal{I}(2J\Delta\tau, \mathbf{r}'_x - \mathbf{r}_x) \mathcal{I}(2J\Delta\tau, \mathbf{r}'_y - \mathbf{r}_y), \quad (\text{B1})$$

where the one-dimensional imaginary-time propagator ( $l$  is an integer)

$$\mathcal{I}(z, l) = \frac{1}{N} \sum_{j=0}^{N-1} \cos\left(\frac{2\pi j l}{N}\right) \exp\left(z \cos\left(\frac{2\pi j}{N}\right)\right) \quad (\text{B2})$$

is related to the modified Bessel function of the first kind  $I_l(z)$  via

$$\lim_{N \rightarrow \infty} \mathcal{I}(z, l) = \frac{1}{\pi} \int_0^\pi d\theta \cos(l\theta) e^{z \cos \theta} = I_l(z). \quad (\text{B3})$$

In real time,

$$\langle \mathbf{r}' | e^{-i\Delta t H_0} | \mathbf{r} \rangle = \mathcal{J}(2J\Delta t, \mathbf{r}'_x - \mathbf{r}_x) \mathcal{J}(2J\Delta t, \mathbf{r}'_y - \mathbf{r}_y), \quad (\text{B4})$$

where the one-dimensional real-time propagator ( $l$  is an integer)

$$\mathcal{J}(z, l) = \frac{1}{N} \sum_{j=0}^{N-1} \cos\left(\frac{2\pi j l}{N}\right) \exp\left(iz \cos\left(\frac{2\pi j}{N}\right)\right) \quad (\text{B5})$$

is related to the Bessel function of the first kind  $J_l(z)$  via

$$\lim_{N \rightarrow \infty} \mathcal{J}(z, l) = \frac{1}{\pi} \int_0^\pi d\theta \cos(l\theta) e^{iz \cos \theta} = i^l J_l(z). \quad (\text{B6})$$

For finite  $N$ ,  $\mathcal{J}(z, 2l)$  is purely real, while  $\mathcal{J}(z, 2l+1)$  is purely imaginary.

## APPENDIX C: DERIVATION OF THE FPQMC FORMULAE THAT MANIFESTLY RESPECT THE DYNAMICAL SYMMETRY OF THE HUBBARD MODEL

Here, we derive the FPQMC expression for the time-dependent expectation value of a local observable [Eq. (18)] that manifestly respects the dynamical symmetry of the Hubbard model.

We start by defining the operation of the bipartite lattice symmetry, which is represented by a unitary, hermitean, and involutive operator  $B$  ( $B^\dagger = B = B^{-1}$ ) whose action on electron creation and annihilation operators in the real space is given as



$$Bc_{\mathbf{r}\sigma}^{(\dagger)}B = (-1)^{r_x+r_y}c_{\mathbf{r}\sigma}^{(\dagger)}. \quad (\text{C1})$$

In the momentum space,  $B$  is actually the so-called  $\pi$ -boost<sup>15</sup>

$$Bc_{\mathbf{k}\sigma}^{(\dagger)}B = c_{\mathbf{k}+\mathbf{Q},\sigma}^{(\dagger)} \quad (\text{C2})$$

that increases the electronic momentum by  $\mathbf{Q} = (\pi, \pi)$ . The time reversal operator  $T$  is an antiunitary (unitary and antilinear), involutive, and hermitean operator whose action on electron creation and annihilation operators in the real space is given as

$$Tc_{\mathbf{r}\uparrow}^{(\dagger)}T = c_{\mathbf{r}\downarrow}^{(\dagger)}, \quad Tc_{\mathbf{r}\downarrow}^{(\dagger)}T = -c_{\mathbf{r}\uparrow}^{(\dagger)}, \quad (\text{C3})$$

while the corresponding relations in the momentum space read as

$$Tc_{\mathbf{k}\uparrow}^{(\dagger)}T = c_{-\mathbf{k}\uparrow}^{(\dagger)}, \quad Tc_{\mathbf{k}\downarrow}^{(\dagger)}T = -c_{-\mathbf{k}\downarrow}^{(\dagger)}. \quad (\text{C4})$$

Using Eqs. (C1)–(C4), consequently

$$BH_0B = -H_0, \quad BH_{\text{int}}B = H_{\text{int}}, \quad TH_0T = H_0, \quad TH_{\text{int}}T = H_{\text{int}}. \quad (\text{C5})$$

In Sec. II B 2, we assumed that the initial state  $|\psi(0)\rangle$  is an eigenstate of local density operators  $n_{\mathbf{r}\sigma}$ , which means that  $B|\psi(0)\rangle = e^{i\chi_{\mathbf{r}}}|\psi(0)\rangle$ , see Eq. (C1).

The denominator of Eq. (18)

$$A_{\text{den}}(t) = \langle \psi(0) | e^{iHt} e^{-iHt} | \psi(0) \rangle \quad (\text{C6})$$

is purely real,  $A_{\text{den}}(t) = A_{\text{den}}(t)^*$ , so that

$$A_{\text{den}}(t) \approx \frac{1}{2} \left\langle \psi(0) \left| \left( e^{iH_0\Delta t} e^{iH_{\text{int}}\Delta t} \right)^{N_t} \left( e^{-iH_0\Delta t} e^{-iH_{\text{int}}\Delta t} \right)^{N_t} \right| \psi(0) \right\rangle + \frac{1}{2} \left\langle \psi(0) \left| \left( e^{iH_{\text{int}}\Delta t} e^{iH_0\Delta t} \right)^{N_t} \left( e^{-iH_{\text{int}}\Delta t} e^{-iH_0\Delta t} \right)^{N_t} \right| \psi(0) \right\rangle. \quad (\text{C7})$$

We thus obtain

$$A_{\text{den}}(t) \approx \sum_C \{ \text{Re}\{\mathcal{D}_{2t}(C, \Delta t)\} \cos[\Delta\varepsilon_{\text{int}}(C)\Delta t] - \text{Im}\{\mathcal{D}_{2t}(C, \Delta t)\} \sin[\Delta\varepsilon_{\text{int}}(C)\Delta t] \}, \quad (\text{C8})$$

where configuration  $C$  consists of  $2N_t - 1$  independent states  $|\Psi_{i,2}\rangle, \dots, |\Psi_{i,2N_t}\rangle, |\Psi_{i,1}\rangle \equiv |\psi(0)\rangle$ , while  $\mathcal{D}_{2t}(C, \Delta t)$  and  $\Delta\varepsilon_{\text{int}}(C)$  are defined in Eqs. (21) and (20), respectively. The denominator is also invariant under time reversal,  $A_{\text{den}}(t) = A_{\text{den}}(-t)$ , which is not a consequence of a specific behavior of the initial state under time reversal but rather follows from  $A_{\text{den}}(t) \equiv \langle \psi(0) | \psi(0) \rangle$ . In other words, Eq. (C8) should contain only contributions invariant under the transformation  $\Delta t \rightarrow -\Delta t$ . Using the bipartite lattice symmetry, under which  $B|\Psi_{i,l}\rangle = e^{i\chi_l}|\Psi_{i,l}\rangle$ , we obtain

$$\begin{aligned} \mathcal{D}_{2t}(C, -\Delta t) &= \prod_{l=N_t+1}^{2N_t} \langle \Psi_{i,l\oplus 1} | B B e^{-iH_0\Delta t} B B | \Psi_{i,l} \rangle \\ &\quad \times \prod_{l=1}^{N_t} \langle \Psi_{i,l\oplus 1} | B B e^{iH_0\Delta t} B B | \Psi_{i,l} \rangle \\ &= \prod_{l=N_t+1}^{2N_t} \langle \Psi_{i,l\oplus 1} | e^{iH_0\Delta t} | \Psi_{i,l} \rangle \prod_{l=1}^{N_t} \langle \Psi_{i,l\oplus 1} | e^{-iH_0\Delta t} | \Psi_{i,l} \rangle \\ &= \mathcal{D}_{2t}(C, \Delta t). \end{aligned} \quad (\text{C9})$$

Equation (C8) then reduces to

$$A_{\text{den}}(t) = \sum_C \text{Re}\{\mathcal{D}_{2t}(C, \Delta t)\} \cos[\Delta\varepsilon_{\text{int}}(C)\Delta t]. \quad (\text{C10})$$

We now turn to the numerator of Eq. (18)

$$A_{\text{num}}(t) = \langle \psi(0) | e^{iHt} A_i e^{-iHt} | \psi(0) \rangle, \quad (\text{C11})$$

which is also purely real,  $A_{\text{num}}(t) = A_{\text{num}}(t)^*$ , so that

$$\begin{aligned} A_{\text{num}}(t) &\approx \sum_C \mathcal{A}_i(\Psi_{i,N_t+1}) \{ \text{Re}\{\mathcal{D}_{2t}(C, \Delta t)\} \cos[\Delta\varepsilon_{\text{int}}(C)\Delta t] \\ &\quad - \text{Im}\{\mathcal{D}_{2t}(C, \Delta t)\} \sin[\Delta\varepsilon_{\text{int}}(C)\Delta t] \}. \end{aligned} \quad (\text{C12})$$

In the following discussion, we assume that the time reversal operation changes  $|\psi(0)\rangle$  by a phase factor,  $T|\psi(0)\rangle = e^{i\chi_{\mathbf{r}}}|\psi(0)\rangle$ . This, combined with  $B|\psi(0)\rangle = e^{i\chi_{\mathbf{r}}}|\psi(0)\rangle$ , gives the assumption on  $|\psi(0)\rangle$  that is mentioned before Eq. (19). We further assume that  $TBA_iBT = A_i$ . Under these assumptions, the numerator is invariant under time reversal,  $A_{\text{num}}(-t) = A_{\text{num}}(t)$ , meaning that Eq. (C12) should contain only contributions invariant under the transformation  $\Delta t \rightarrow -\Delta t$ . Using Eq. (C9), Eq. (C12) reduces to

$$A_{\text{num}}(t) \approx \sum_C \mathcal{A}_i(\Psi_{i,N_t+1}) \text{Re}\{\mathcal{D}_{2t}(C, \Delta t)\} \cos[\Delta\varepsilon_{\text{int}}(C)\Delta t], \quad (\text{C13})$$

and Eq. (22) follows immediately.

An example of the initial state  $|\psi(0)\rangle$  and the observable  $A_i$  that satisfy  $TB|\psi(0)\rangle = e^{i\chi}|\psi(0)\rangle$  and  $TBA_iBT = A_i$  are the CDW state  $|\psi_{\text{CDW}}\rangle$  [Eq. (24)] and the local charge density  $A_i = \sum_{\sigma} n_{\mathbf{r}\sigma}$ . While the time-reversal operation may change a general SDW state [Eq. (23)] by more than a phase factor, Eq. (C13) is still applicable when the observable of interest is the local spin density  $A_i = n_{\mathbf{r}\uparrow} - n_{\mathbf{r}\downarrow}$ . This follows from the transformation law  $T(n_{\mathbf{r}\uparrow} - n_{\mathbf{r}\downarrow})T = n_{\mathbf{r}\downarrow} - n_{\mathbf{r}\uparrow}$  and the fact that the roles of spin-up and spin-down electrons in the state  $T|\psi_{\text{SDW}}\rangle$  are exchanged with respect to the state  $|\psi_{\text{SDW}}\rangle$ .

We now explain how we use Eq. (26) to enlarge statistics in computations of time-dependent local spin (charge) densities when the evolution starts from state  $|\psi_{\text{SDW}}\rangle$  in Eq. (23) [ $|\psi_{\text{CDW}}\rangle$  in Eq. (24)]. Let us limit the discussion to the spin (charge) density at fixed position  $\mathbf{r}$ . Suppose that we obtained Markov chains (of length  $N_{\text{CDW}}$ )  $\{\mathcal{N}_1^{\text{CDW}}(t), \dots, \mathcal{N}_{N_{\text{CDW}}}^{\text{CDW}}(t)\}$  and  $\{\mathcal{D}_1^{\text{CDW}}, \dots, \mathcal{D}_{N_{\text{CDW}}}^{\text{CDW}}\}$  for the numerator and denominator. Suppose also that we obtained Markov chains (of length  $N_{\text{SDW}}$ )  $\{\mathcal{N}_1^{\text{SDW}}(t), \dots, \mathcal{N}_{N_{\text{SDW}}}^{\text{SDW}}(t)\}$  and  $\{\mathcal{D}_1^{\text{SDW}}, \dots, \mathcal{D}_{N_{\text{SDW}}}^{\text{SDW}}\}$  for the numerator and denominator. Using these Markov chains, we found that the best result for the time-dependent local spin (charge) density is obtained by joining them into one Markov chain  $\{\mathcal{N}_1^{\text{SDW}}(t), \dots, \mathcal{N}_{N_{\text{SDW}}}^{\text{SDW}}(t), \mathcal{N}_1^{\text{CDW}}(t), \dots, \mathcal{N}_{N_{\text{CDW}}}^{\text{CDW}}(t)\}$  of length  $N_{\text{SDW}} + N_{\text{CDW}}$  for the numerator, and another Markov chain



$\{\mathcal{D}_1^{\text{SDW}}, \dots, \mathcal{D}_{N_{\text{SDW}}}^{\text{SDW}}, \mathcal{D}_1^{\text{CDW}}, \dots, \mathcal{D}_{N_{\text{CDW}}}^{\text{CDW}}\}$  of length  $N_{\text{SDW}} + N_{\text{CDW}}$  for the denominator. If individual chain lengths  $N_{\text{CDW}}$  and  $N_{\text{SDW}}$  are sufficiently large, the manner in which the chains are joined is immaterial; here, we append the CDW chain to the SDW chain, and we note that other joining possibilities lead to the same final result (within the statistical error bars). To further reduce statistical error bars, we also combine SDW + CDW chains at all positions  $\mathbf{r}$  that have the same spin (charge) density by the symmetry of the initial state.

## APPENDIX D: DERIVATION OF THE ABQMC FORMULA FOR THE SURVIVAL PROBABILITY

We start from the survival-probability amplitude

$$A_P(t) = \frac{\langle \psi(0) | e^{-iHt} | \psi(0) \rangle}{\langle \psi(0) | \psi(0) \rangle}, \quad (\text{D1})$$

whose numerator can be expressed as

$$\begin{aligned} \langle \psi(0) | e^{-iHt} | \psi(0) \rangle &\approx \frac{1}{2} \left\langle \psi(0) \left| \left( e^{-iH_0 \Delta t} e^{-iH_{\text{int}} \Delta t} \right)^{N_t} \right| \psi(0) \right\rangle + \frac{1}{2} \left\langle \psi(0) \left| \left( e^{-iH_{\text{int}} \Delta t} e^{-iH_0 \Delta t} \right)^{N_t} \right| \psi(0) \right\rangle \\ &= \sum_{\Psi_{i,2} \dots \Psi_{i,N_t}} \text{Re} \left\{ \prod_{l=1}^{N_t} \langle \Psi_{i,l \oplus 1} | e^{-iH_0 \Delta t} | \Psi_{i,l} \rangle \right\} e^{-i\varepsilon_{\text{int}}(C) \Delta t} \\ &= \sum_{\Psi_{i,2} \dots \Psi_{i,N_t}} \sum_{\Psi_{k,1} \dots \Psi_{k,N_t}} \text{Re} \left\{ \prod_{l=1}^{N_t} \langle \Psi_{i,l \oplus 1} | \Psi_{k,l} \rangle \langle \Psi_{k,l} | \Psi_{i,l} \rangle e^{-i\varepsilon_0(C) \Delta t} \right\} e^{-i\varepsilon_{\text{int}}(C) \Delta t} \\ &= \sum_C \{ \text{Re}\{\mathcal{D}(C)\} \cos[\varepsilon_0(C) \Delta t] + \text{Im}\{\mathcal{D}(C)\} \sin[\varepsilon_0(C) \Delta t] \} e^{-i\varepsilon_{\text{int}}(C) \Delta t}. \end{aligned} \quad (\text{D2})$$

In going from the second to the third line of Eq. (D2), we introduced spectral decompositions of  $N_t$  factors  $e^{-iH_0 \Delta t}$ . The configuration  $C$  entering the last line of Eq. (D2) consists of  $N_t - 1$  independent states  $|\Psi_{i,2}\rangle, \dots, |\Psi_{i,N_t}\rangle$  in the coordinate representation and  $N_t$  independent states  $|\Psi_{k,1}\rangle, \dots, |\Psi_{k,N_t}\rangle$  in the momentum representation, while  $|\Psi_{i,1}\rangle \equiv |\psi(0)\rangle$ .  $\mathcal{D}(C)$  and  $\varepsilon_0(C)$  are defined in Eqs. (31) and (34), respectively. By virtue of the bipartite lattice symmetry, under which  $\mathcal{D}(C)$  remains invariant, while  $\varepsilon_0(C)$  changes sign, the summand containing  $\sin[\varepsilon_0(C) \Delta t]$  in Eq. (D2) vanishes, so that

$$\langle \psi(0) | e^{-iHt} | \psi(0) \rangle \approx \sum_C \text{Re}\{\mathcal{D}(C)\} \cos[\varepsilon_0(C) \Delta t] e^{-i\varepsilon_{\text{int}}(C) \Delta t}. \quad (\text{D3})$$

This form should be used, e.g., when  $|\psi(0)\rangle$  is the SDW state defined in Eq. (23). When the initial state is the CDW state defined in Eq. (24),  $T|\psi(0)\rangle = e^{i\chi_r} |\psi(0)\rangle$ ,  $\langle \psi(0) | e^{-iHt} | \psi(0) \rangle$  is purely real, so that

$$\langle \psi(0) | e^{-iHt} | \psi(0) \rangle \approx \sum_C \text{Re}\{\mathcal{D}(C)\} \cos[\varepsilon_0(C) \Delta t] \cos[\varepsilon_{\text{int}}(C) \Delta t]. \quad (\text{D4})$$

Equation (30) then follows by combining Eq. (D4) with  $\langle \psi(0) | \psi(0) \rangle = \sum_C \text{Re}\{\mathcal{D}(C)\}$ .

We now provide a formal demonstration of Eq. (36). The partial particle-hole transformation is represented by a unitary, hermitean, and involutive operator  $P$  ( $P^\dagger = P = P^{-1}$ ), whose action on electron creation and annihilation operators in real space is given as<sup>109,110</sup>

$$P c_{\mathbf{r}\uparrow} P = c_{\mathbf{r}\uparrow}, \quad P c_{\mathbf{r}\uparrow}^\dagger P = c_{\mathbf{r}\uparrow}^\dagger, \quad (\text{D5})$$

$$P c_{\mathbf{r}\downarrow} P = (-1)^{r_x+r_y} c_{\mathbf{r}\downarrow}^\dagger, \quad P c_{\mathbf{r}\downarrow}^\dagger P = (-1)^{r_x+r_y} c_{\mathbf{r}\downarrow}. \quad (\text{D6})$$

The interaction Hamiltonian  $H_{\text{int}}$  thus transforms under the partial particle-hole transformation as  $PH_{\text{int}}P = U\hat{N}_\uparrow - H_{\text{int}}$ . The action of the partial particle-hole transformation in the momentum space reads as [ $\mathbf{Q} = (\pi, \pi)$ ]

$$P c_{\mathbf{k}\uparrow} P = c_{\mathbf{k}\uparrow}, \quad P c_{\mathbf{k}\uparrow}^\dagger P = c_{\mathbf{k}\uparrow}^\dagger, \quad (\text{D7})$$

$$P c_{\mathbf{k}\downarrow} P = c_{\mathbf{Q}-\mathbf{k},\downarrow}^\dagger, \quad P c_{\mathbf{k}\downarrow}^\dagger P = c_{\mathbf{Q}-\mathbf{k},\downarrow}. \quad (\text{D8})$$

The kinetic energy, therefore, remains invariant under the partial particle-hole transformation, i.e.,  $PH_0P = H_0$ . Equations (D5) and (D6) imply that  $P|\emptyset\rangle = \prod_{\mathbf{r} \in \mathcal{U}} c_{\mathbf{r}\uparrow}^\dagger |\emptyset\rangle$ . We then find that  $P|\psi_{\text{CDW}}\rangle = |\psi_{\text{SDW}}\rangle$ , i.e., the partial particle-hole transformation transforms the CDW state defined in Eq. (24) into the SDW state defined in Eq. (23) and vice versa.<sup>108</sup> The states  $|\psi_{\text{CDW}}\rangle$  and  $|\psi_{\text{SDW}}\rangle$  have the same number of spin-up electrons, while their numbers of spin-down electrons add to  $N_c$ . Using the combination of the partial particle-hole transformation  $P$  and the bipartite lattice transformation  $B$  defined in Appendix C, one obtains

$$\langle \psi_{\text{CDW}} | e^{-iHt} | \psi_{\text{CDW}} \rangle = e^{-iN_\uparrow(\psi)Ut} \langle \psi_{\text{SDW}} | e^{-iHt} | \psi_{\text{SDW}} \rangle^*, \quad (\text{D9})$$

where  $N_\uparrow(\psi) = \langle \psi_{\text{CDW}} | \hat{N}_\uparrow | \psi_{\text{CDW}} \rangle = \langle \psi_{\text{SDW}} | \hat{N}_\uparrow | \psi_{\text{SDW}} \rangle$  is the total number of spin-up electrons in CDW and SDW states. Equation (36) then follows immediately from Eq. (D9).

A similar procedure to that described in Appendix C is used to combine Markov chains for the survival probabilities of the CDW and SDW states related by the dynamical symmetry in Eq. (D9).

## APPENDIX E: USING THE PARTICLE-HOLE SYMMETRY TO DISCUSS THE AVERAGE SIGN OF THE FPQMC METHOD FOR CHEMICAL POTENTIALS $\mu$ AND $U - \mu$

The (full) particle-hole transformation is represented by a unitary, hermitean, and involutive operator  $P_f$  ( $P_f^\dagger = P_f = P_f^{-1}$ ) whose action on electron creation and annihilation operators in real space is defined as<sup>109,110</sup>

$$P_f c_{r\sigma} P_f = (-1)^{r_x+r_y} c_{r\sigma}^\dagger. \quad (\text{E1})$$

The corresponding formula in the momentum space reads as

$$P_f c_{\mathbf{k}\sigma} P_f = c_{\mathbf{Q}-\mathbf{k},\sigma}^\dagger. \quad (\text{E2})$$

Let us fix  $J, U, T$ , and  $N_\tau$  and compute the equation of state  $\rho_e(\mu)$  using Eq. (13) in which  $A_i(\Psi_{i,l}) = [N_\uparrow(C) + N_\downarrow(C)]/N_c$ . It is convenient to make the  $\mu$ -dependence in  $\varepsilon_{\text{int}}(C, \mu)$  explicit. In the sums entering Eq. (13) we make the substitution

$$C \rightarrow C' = \{|\Phi_{i,l}\rangle = P_f |\Psi_{i,l}\rangle | l = 1, \dots, N_\tau\} \quad (\text{E3})$$

under which

$$\mathcal{D}_\beta(C, \Delta\tau) = \mathcal{D}_\beta(C', \Delta\tau), \quad (\text{E4})$$

$$\varepsilon_{\text{int}}(C, \mu) = \varepsilon_{\text{int}}(C', U - \mu) + (U - 2\mu)N_\tau N_c, \quad (\text{E5})$$

$$N_\sigma(C') = N_c - N_\sigma(C). \quad (\text{E6})$$

It then follows that

$$\begin{aligned} & \frac{\sum_C \mathcal{D}_\beta(C, \Delta\tau) e^{-\Delta\tau \varepsilon_{\text{int}}(C, \mu)} [N_\uparrow(C) + N_\downarrow(C)]/N_c}{\sum_C \mathcal{D}_\beta(C, \Delta\tau) e^{-\Delta\tau \varepsilon_{\text{int}}(C, \mu)}} \\ &= 2 - \frac{\sum_{C'} \mathcal{D}_\beta(C', \Delta\tau) e^{-\Delta\tau \varepsilon_{\text{int}}(C', U - \mu)} [N_\uparrow(C') + N_\downarrow(C')]/N_c}{\sum_{C'} \mathcal{D}_\beta(C', \Delta\tau) e^{-\Delta\tau \varepsilon_{\text{int}}(C', U - \mu)}}. \end{aligned} \quad (\text{E7})$$

The FPQMC simulations of the ratios in the last equation are performed for chemical potentials  $\mu$  and  $U - \mu$ , which are symmetric with respect to the chemical potential  $U/2$  at the half-filling. Since  $\varepsilon_{\text{int}}(C, \mu)$  and  $\varepsilon_{\text{int}}(C', U - \mu)$  differ by a constant additive factor, the corresponding configuration weights differ by a constant multiplicative factor, and the average signs of the two FPQMC simulations are thus mutually equal.

## REFERENCES

- <sup>1</sup>H. Aoki, N. Tsuji, M. Eckstein, M. Kollar, T. Oka, and P. Werner, "Nonequilibrium dynamical mean-field theory and its applications," *Rev. Mod. Phys.* **86**, 779–837 (2014).
- <sup>2</sup>L. Tarruell and L. Sanchez-Palencia, "Quantum simulation of the Hubbard model with ultracold fermions in optical lattices," *C. R. Phys.* **19**, 365–393 (2018).
- <sup>3</sup>I. Bloch, J. Dalibard, and W. Zwerger, "Many-body physics with ultracold gases," *Rev. Mod. Phys.* **80**, 885–964 (2008).
- <sup>4</sup>S. Murmann, A. Bergschneider, V. M. Klinkhamer, G. Zürn, T. Lompe, and S. Jochim, "Two fermions in a double well: Exploring a fundamental building block of the Hubbard model," *Phys. Rev. Lett.* **114**, 080402 (2015).

- <sup>5</sup>B. M. Spar, E. Guardado-Sanchez, S. Chi, Z. Z. Yan, and W. S. Bakr, "Realization of a Fermi-Hubbard optical tweezer array," *Phys. Rev. Lett.* **128**, 223202 (2022).
- <sup>6</sup>Z. Z. Yan, B. M. Spar, M. L. Prichard, S. Chi, H.-T. Wei, E. Ibarra-García-Padilla, K. R. A. Hazzard, and W. S. Bakr, "Two-dimensional programmable tweezer arrays of fermions," *Phys. Rev. Lett.* **129**, 123201 (2022).
- <sup>7</sup>J. Hubbard, "Electron correlations in narrow energy bands," *Proc. R. Soc. London, Ser. A* **276**, 238–257 (1963).
- <sup>8</sup>"The Hubbard model at half a century," *Nat. Phys.* **9**, 523 (2013).
- <sup>9</sup>E. Cocchi, L. A. Miller, J. H. Drewes, M. Koschorreck, D. Pertot, F. Brennecke, and M. Köhl, "Equation of state of the two-dimensional Hubbard model," *Phys. Rev. Lett.* **116**, 175301 (2016).
- <sup>10</sup>E. Cocchi, L. A. Miller, J. H. Drewes, C. F. Chan, D. Pertot, F. Brennecke, and M. Köhl, "Measuring entropy and short-range correlations in the two-dimensional Hubbard model," *Phys. Rev. X* **7**, 031025 (2017).
- <sup>11</sup>M. F. Parsons, A. Mazurenko, C. S. Chiu, G. Ji, D. Greif, and M. Greiner, "Site-resolved measurement of the spin-correlation function in the Fermi-Hubbard model," *Science* **353**, 1253–1256 (2016).
- <sup>12</sup>L. W. Cheuk, M. A. Nichols, K. R. Lawrence, M. Okan, H. Zhang, E. Khatami, N. Trivedi, T. Paiva, M. Rigol, and M. W. Zwierlein, "Observation of spatial charge and spin correlations in the 2D Fermi-Hubbard model," *Science* **353**, 1260–1264 (2016).
- <sup>13</sup>C. S. Chiu, G. Ji, A. Bohrdt, M. Xu, M. Knap, E. Demler, F. Grusdt, M. Greiner, and D. Greif, "String patterns in the doped Hubbard model," *Science* **365**, 251–256 (2019).
- <sup>14</sup>P. T. Brown, D. Mitra, E. Guardado-Sanchez, R. Nourafkan, A. Reymbaut, C.-D. Hébert, S. Bergeron, A.-M. S. Tremblay, J. Kokalj, D. A. Huse, P. Schauss, and W. S. Bakr, "Bad metallic transport in a cold atom Fermi-Hubbard system," *Science* **363**, 379–382 (2019).
- <sup>15</sup>U. Schneider, L. Hackermüller, J. P. Ronzheimer, S. Will, S. Braun, T. Best, I. Bloch, E. Demler, S. Mandt, D. Rasch, and A. Rosch, "Fermionic transport and out-of-equilibrium dynamics in a homogeneous Hubbard model with ultracold atoms," *Nat. Phys.* **8**, 213–218 (2012).
- <sup>16</sup>W. Xu, W. R. McGehee, W. N. Morong, and B. DeMarco, "Bad-metal relaxation dynamics in a Fermi lattice gas," *Nat. Commun.* **10**, 1588 (2019).
- <sup>17</sup>M. A. Nichols, L. W. Cheuk, M. Okan, T. R. Hartke, E. Mendez, T. Senthil, E. Khatami, H. Zhang, and M. W. Zwierlein, "Spin transport in a Mott insulator of ultracold fermions," *Science* **363**, 383–387 (2019).
- <sup>18</sup>J. E. Hirsch, D. J. Scalapino, R. L. Sugar, and R. Blankenbecler, "Efficient Monte Carlo procedure for systems with fermions," *Phys. Rev. Lett.* **47**, 1628–1631 (1981).
- <sup>19</sup>J. E. Hirsch, R. L. Sugar, D. J. Scalapino, and R. Blankenbecler, "Monte Carlo simulations of one-dimensional fermion systems," *Phys. Rev. B* **26**, 5033–5055 (1982).
- <sup>20</sup>R. Blankenbecler, D. J. Scalapino, and R. L. Sugar, "Monte Carlo calculations of coupled boson-fermion systems. I," *Phys. Rev. D* **24**, 2278–2286 (1981).
- <sup>21</sup>D. J. Scalapino and R. L. Sugar, "Monte Carlo calculations of coupled Boson-Fermion systems. II," *Phys. Rev. B* **24**, 4295–4308 (1981).
- <sup>22</sup>J. E. Hirsch, "Monte Carlo study of the two-dimensional Hubbard model," *Phys. Rev. Lett.* **51**, 1900–1903 (1983).
- <sup>23</sup>J. E. Hirsch, "Two-dimensional Hubbard model: Numerical simulation study," *Phys. Rev. B* **31**, 4403–4419 (1985).
- <sup>24</sup>J. E. Hirsch and R. M. Fye, "Monte Carlo method for magnetic impurities in metals," *Phys. Rev. Lett.* **56**, 2521–2524 (1986).
- <sup>25</sup>S. R. White, D. J. Scalapino, R. L. Sugar, E. Y. Loh, J. E. Gubernatis, and R. T. Scalettar, "Numerical study of the two-dimensional Hubbard model," *Phys. Rev. B* **40**, 506–516 (1989).
- <sup>26</sup>S. Zhang, J. Carlson, and J. E. Gubernatis, "Constrained path quantum Monte Carlo method for fermion ground states," *Phys. Rev. Lett.* **74**, 3652–3655 (1995).
- <sup>27</sup>S. Zhang, "Finite-temperature Monte Carlo calculations for systems with fermions," *Phys. Rev. Lett.* **83**, 2777–2780 (1999).
- <sup>28</sup>S. Zhang and H. Krakauer, "Quantum Monte Carlo method using phase-free random walks with Slater determinants," *Phys. Rev. Lett.* **90**, 136401 (2003).
- <sup>29</sup>C. N. Varney, C.-R. Lee, Z. J. Bai, S. Chiesa, M. Jarrell, and R. T. Scalettar, "Quantum Monte Carlo study of the two-dimensional fermion Hubbard model," *Phys. Rev. B* **80**, 075116 (2009).

- <sup>30</sup>J. P. F. LeBlanc, A. E. Antipov, F. Becca, I. W. Bulik, G. K.-L. Chan, C.-M. Chung, Y. Deng, M. Ferrero, T. M. Henderson, C. A. Jiménez-Hoyos, E. Kozik, X.-W. Liu, A. J. Millis, N. V. Prokof'ev, M. Qin, G. E. Scuseria, H. Shi, B. V. Svistunov, L. F. Tocchio, I. S. Tupitsyn, S. R. White, S. Zhang, B.-X. Zheng, Z. Zhu, E. Gull Simons Collaboration on the Many-Electron Problem, "Solutions of the two-dimensional Hubbard model: Benchmarks and results from a wide range of numerical algorithms," *Phys. Rev. X* **5**, 041041 (2015).
- <sup>31</sup>E. Gull, A. J. Millis, A. I. Lichtenstein, A. N. Rubtsov, M. Troyer, and P. Werner, "Continuous-time Monte Carlo methods for quantum impurity models," *Rev. Mod. Phys.* **83**, 349–404 (2011).
- <sup>32</sup>A. N. Rubtsov and A. I. Lichtenstein, "Continuous-time quantum Monte Carlo method for fermions: Beyond auxiliary field framework," *JETP Lett.* **80**, 61–65 (2004).
- <sup>33</sup>A. N. Rubtsov, V. V. Savkin, and A. I. Lichtenstein, "Continuous-time quantum Monte Carlo method for fermions," *Phys. Rev. B* **72**, 035122 (2005).
- <sup>34</sup>E. Gull, P. Werner, O. Parcollet, and M. Troyer, "Continuous-time auxiliary-field Monte Carlo for quantum impurity models," *Europhys. Lett.* **82**, 57003 (2008).
- <sup>35</sup>N. V. Prokof'ev and B. V. Svistunov, "Polaron problem by diagrammatic quantum Monte Carlo," *Phys. Rev. Lett.* **81**, 2514–2517 (1998).
- <sup>36</sup>N. Prokof'ev and B. Svistunov, "Bold diagrammatic Monte Carlo technique: When the sign problem is welcome," *Phys. Rev. Lett.* **99**, 250201 (2007).
- <sup>37</sup>E. Kozik, K. Van Houcke, E. Gull, L. Pollet, N. Prokof'ev, B. Svistunov, and M. Troyer, "Diagrammatic Monte Carlo for correlated fermions," *Europhys. Lett.* **90**, 10004 (2010).
- <sup>38</sup>K. Van Houcke, E. Kozik, N. Prokof'ev, and B. Svistunov, "Diagrammatic Monte Carlo," *Phys. Procedia* **6**, 95–105 (2010).
- <sup>39</sup>W. Wu, M. Ferrero, A. Georges, and E. Kozik, "Controlling Feynman diagrammatic expansions: Physical nature of the pseudogap in the two-dimensional Hubbard model," *Phys. Rev. B* **96**, 041105 (2017).
- <sup>40</sup>M. Rigol, T. Bryant, and R. R. P. Singh, "Numerical linked-cluster approach to quantum lattice models," *Phys. Rev. Lett.* **97**, 187202 (2006).
- <sup>41</sup>E. Khatami and M. Rigol, "Thermodynamics of strongly interacting fermions in two-dimensional optical lattices," *Phys. Rev. A* **84**, 053611 (2011).
- <sup>42</sup>B. Tang, E. Khatami, and M. Rigol, "A short introduction to numerical linked-cluster expansions," *Comput. Phys. Commun.* **184**, 557–564 (2013).
- <sup>43</sup>F. Šimković IV, R. Rossi, and M. Ferrero, "Two-dimensional Hubbard model at finite temperature: Weak, strong, and long correlation regimes," *Phys. Rev. Res.* **4**, 043201 (2022).
- <sup>44</sup>J. Yang, L. Liu, J. Mongkolkeha, and P. Schauss, "Site-resolved imaging of ultracold fermions in a triangular-lattice quantum gas microscope," *PRX Quantum* **2**, 020344 (2021).
- <sup>45</sup>S. Humeniuk and Y. Wan, "Numerically exact mimicking of quantum gas microscopy for interacting lattice fermions," *Phys. Rev. B* **104**, 075155 (2021).
- <sup>46</sup>J. Koepsell, D. Bourund, P. Sompet, S. Hirthe, A. Bohrdt, Y. Wang, F. Grusdt, E. Demler, G. Salomon, C. Gross, and I. Bloch, "Microscopic evolution of doped Mott insulators from polaronic metal to Fermi liquid," *Science* **374**, 82–86 (2021).
- <sup>47</sup>Y. Wang, A. Bohrdt, S. Ding, J. Koepsell, E. Demler, and F. Grusdt, "Higher-order spin-hole correlations around a localized charge impurity," *Phys. Rev. Res.* **3**, 033204 (2021).
- <sup>48</sup>D. Garwood, J. Mongkolkeha, L. Liu, J. Yang, and P. Schauss, "Site-resolved observables in the doped spin-imbalanced triangular Hubbard model," *Phys. Rev. A* **106**, 013310 (2022).
- <sup>49</sup>K. Mikelson, "Extensions of numerical methods for strongly correlated electron systems," Ph.D. thesis, University of Cincinnati, 2009.
- <sup>50</sup>J. Vučković, J. Kokalj, R. Žitko, N. Wentzell, D. Tanasković, and J. Mravlje, "Conductivity in the square lattice Hubbard model at high temperatures: Importance of vertex corrections," *Phys. Rev. Lett.* **123**, 036601 (2019).
- <sup>51</sup>E. W. Huang, R. Sheppard, B. Moritz, and T. P. Devereaux, "Strange metallicity in the doped Hubbard model," *Science* **366**, 987–990 (2019).
- <sup>52</sup>J. Vučković, S. Predin, and M. Ferrero, "Charge fluctuations, hydrodynamics and transport in the square-lattice Hubbard model," *arXiv:2208.04047* (2022).
- <sup>53</sup>J. Jaklič and P. Prelovšek, "Finite-temperature properties of doped antiferromagnets," *Adv. Phys.* **49**, 1–92 (2000).
- <sup>54</sup>P. Prelovšek and J. Bonča, "Ground state and finite temperature Lanczos methods," in *Strongly Correlated Systems: Numerical Methods*, edited by A. Avella and F. Mancini (Springer, Berlin, Heidelberg, 2013), pp. 1–30.
- <sup>55</sup>A. Vranić, J. Vučković, J. Kokalj, J. Skolimowski, R. Žitko, J. Mravlje, and D. Tanasković, "Charge transport in the Hubbard model at high temperatures: Triangular versus square lattice," *Phys. Rev. B* **102**, 115142 (2020).
- <sup>56</sup>P. Werner, T. Oka, and A. J. Millis, "Diagrammatic Monte Carlo simulation of nonequilibrium systems," *Phys. Rev. B* **79**, 035320 (2009).
- <sup>57</sup>M. Schiró and M. Fabrizio, "Real-time diagrammatic Monte Carlo for nonequilibrium quantum transport," *Phys. Rev. B* **79**, 153302 (2009).
- <sup>58</sup>M. Schiró, "Real-time dynamics in quantum impurity models with diagrammatic Monte Carlo," *Phys. Rev. B* **81**, 085126 (2010).
- <sup>59</sup>E. Gull, D. R. Reichman, and A. J. Millis, "Numerically exact long-time behavior of nonequilibrium quantum impurity models," *Phys. Rev. B* **84**, 085134 (2011).
- <sup>60</sup>G. Cohen, D. R. Reichman, A. J. Millis, and E. Gull, "Green's functions from real-time bold-line Monte Carlo," *Phys. Rev. B* **89**, 115139 (2014).
- <sup>61</sup>G. Cohen, E. Gull, D. R. Reichman, and A. J. Millis, "Taming the dynamical sign problem in real-time evolution of quantum many-body problems," *Phys. Rev. Lett.* **115**, 266802 (2015).
- <sup>62</sup>M. S. Church and B. M. Rubenstein, "Real-time dynamics of strongly correlated fermions using auxiliary field quantum Monte Carlo," *J. Chem. Phys.* **154**, 184103 (2021).
- <sup>63</sup>C. Karrasch, D. M. Kennes, and J. E. Moore, "Transport properties of the one-dimensional Hubbard model at finite temperature," *Phys. Rev. B* **90**, 155104 (2014).
- <sup>64</sup>N. Schlünzen, J.-P. Joost, F. Heidrich-Meisner, and M. Bonitz, "Nonequilibrium dynamics in the one-dimensional Fermi-Hubbard model: Comparison of the nonequilibrium Green-functions approach and the density matrix renormalization group method," *Phys. Rev. B* **95**, 165139 (2017).
- <sup>65</sup>A. Akbari, M. J. Hashemi, A. Rubio, R. M. Nieminen, and R. van Leeuwen, "Challenges in truncating the hierarchy of time-dependent reduced density matrices equations," *Phys. Rev. B* **85**, 235121 (2012).
- <sup>66</sup>D. Lacroix, S. Hermanns, C. M. Hinz, and M. Bonitz, "Ultrafast dynamics of finite Hubbard clusters: A stochastic mean-field approach," *Phys. Rev. B* **90**, 125112 (2014).
- <sup>67</sup>Z. Li, N. Tong, X. Zheng, D. Hou, J. Wei, J. Hu, and Y. Yan, "Hierarchical Liouville-space approach for accurate and universal characterization of quantum impurity systems," *Phys. Rev. Lett.* **109**, 266403 (2012).
- <sup>68</sup>S. Wang, X. Zheng, J. Jin, and Y. J. Yan, "Hierarchical Liouville-space approach to nonequilibrium dynamical properties of quantum impurity systems," *Phys. Rev. B* **88**, 035129 (2013).
- <sup>69</sup>R. E. V. Profumo, C. Groth, L. Messio, O. Parcollet, and X. Waintal, "Quantum Monte Carlo for correlated out-of-equilibrium nanoelectronic devices," *Phys. Rev. B* **91**, 245154 (2015).
- <sup>70</sup>M. A. Cazalilla and J. B. Marston, "Time-dependent density-matrix renormalization group: A systematic method for the study of quantum many-body out-of-equilibrium systems," *Phys. Rev. Lett.* **88**, 256403 (2002).
- <sup>71</sup>S. R. White and A. E. Feiguin, "Real-time evolution using the density matrix renormalization group," *Phys. Rev. Lett.* **93**, 076401 (2004).
- <sup>72</sup>U. Schollwöck, "Time-dependent density-matrix renormalization-group methods," *J. Phys. Soc. Jpn.* **74**, 246–255 (2005).
- <sup>73</sup>C. Yang and A. E. Feiguin, "Spectral function of the two-dimensional Hubbard model: A density matrix renormalization group plus cluster perturbation theory study," *Phys. Rev. B* **93**, 081107 (2016).
- <sup>74</sup>G. Stefanucci and R. van Leeuwen, *Nonequilibrium Many-Body Theory of Quantum Systems: A Modern Introduction* (Cambridge University Press, New York, 2013).
- <sup>75</sup>N. Schlünzen, S. Hermanns, M. Scharnke, and M. Bonitz, "Ultrafast dynamics of strongly correlated fermions—Nonequilibrium Green functions and selfenergy approximations," *J. Phys.: Condens. Matter* **32**, 103001 (2019).
- <sup>76</sup>N. Schlünzen, J. P. Joost, and M. Bonitz, "Achieving the scaling limit for nonequilibrium Green functions simulations," *Phys. Rev. Lett.* **124**, 076601 (2020).

- <sup>77</sup>J.-P. Joost, N. Schlünzen, H. Ohldag, M. Bonitz, F. Lackner, and I. Březinová, "Dynamically screened ladder approximation: Simultaneous treatment of strong electronic correlations and dynamical screening out of equilibrium," *Phys. Rev. B* **105**, 165155 (2022).
- <sup>78</sup>H. De Raedt and A. Lagendijk, "Monte Carlo calculation of the thermodynamic properties of a quantum model: A one-dimensional fermion lattice model," *Phys. Rev. Lett.* **46**, 77–80 (1981).
- <sup>79</sup>H. De Raedt and A. Lagendijk, "Monte Carlo calculation of the thermodynamic properties of a one-dimensional fermion lattice model," *J. Stat. Phys.* **27**, 731–744 (1982).
- <sup>80</sup>H. De Raedt and A. Lagendijk, "Monte Carlo simulation of quantum statistical lattice models," *Phys. Rep.* **127**, 233–307 (1985).
- <sup>81</sup>D. M. Ceperley, "Path integrals in the theory of condensed helium," *Rev. Mod. Phys.* **67**, 279–355 (1995).
- <sup>82</sup>D. Thirumalai and B. J. Berne, "Methods for simulating time correlation functions in quantum systems," *Comput. Phys. Commun.* **63**, 415–426 (1991).
- <sup>83</sup>T. Dornheim, S. Groth, J. Vorberger, and M. Bonitz, "*Ab initio* path integral Monte Carlo results for the dynamic structure factor of correlated electrons: From the electron liquid to warm dense matter," *Phys. Rev. Lett.* **121**, 255001 (2018).
- <sup>84</sup>P. Hamann, T. Dornheim, J. Vorberger, Z. A. Moldabekov, and M. Bonitz, "Dynamic properties of the warm dense electron gas based on *ab initio* path integral Monte Carlo simulations," *Phys. Rev. B* **102**, 125150 (2020).
- <sup>85</sup>M. Takahashi and M. Imada, "Monte Carlo calculation of quantum systems," *J. Phys. Soc. Jpn.* **53**, 963–974 (1984).
- <sup>86</sup>A. P. Lyubartsev, "Simulation of excited states and the sign problem in the path integral Monte Carlo method," *J. Phys. A: Math. Gen.* **38**, 6659–6674 (2005).
- <sup>87</sup>A. P. Lyubartsev, "Interacting electrons in one dimension: A path integral Monte Carlo study," *J. Phys. A: Math. Theor.* **40**, 7151–7157 (2007).
- <sup>88</sup>V. S. Filinov, M. Bonitz, W. Ebeling, and V. E. Fortov, "Thermodynamics of hot dense H-plasmas: Path integral Monte Carlo simulations and analytical approximations," *Plasma Phys. Control. Fusion* **43**, 743–759 (2001).
- <sup>89</sup>T. Schoof, M. Bonitz, A. Filinov, D. Hochstuhl, and J. W. Dufty, "Configuration path integral Monte Carlo," *Contrib. Plasma Phys.* **51**, 687–697 (2011).
- <sup>90</sup>T. Dornheim, S. Groth, A. Filinov, and M. Bonitz, "Permutation blocking path integral Monte Carlo: A highly efficient approach to the simulation of strongly degenerate non-ideal fermions," *New J. Phys.* **17**, 073017 (2015).
- <sup>91</sup>T. Dornheim, T. Schoof, S. Groth, A. Filinov, and M. Bonitz, "Permutation blocking path integral Monte Carlo approach to the uniform electron gas at finite temperature," *J. Chem. Phys.* **143**, 204101 (2015).
- <sup>92</sup>S. Groth, T. Schoof, T. Dornheim, and M. Bonitz, "*Ab initio* quantum Monte Carlo simulations of the uniform electron gas without fixed nodes," *Phys. Rev. B* **93**, 085102 (2016).
- <sup>93</sup>T. Dornheim, S. Groth, and M. Bonitz, "The uniform electron gas at warm dense matter conditions," *Phys. Rep.* **744**, 1–86 (2018).
- <sup>94</sup>T. Dornheim, "Fermion sign problem in path integral Monte Carlo simulations: Quantum dots, ultracold atoms, and warm dense matter," *Phys. Rev. E* **100**, 023307 (2019).
- <sup>95</sup>T. Dornheim, "Fermion sign problem in path integral Monte Carlo simulations: Grand-canonical ensemble," *J. Phys. A: Math. Theor.* **54**, 335001 (2021).
- <sup>96</sup>A. Filinov, P. R. Levashov, and M. Bonitz, "Thermodynamics of the uniform electron gas: Fermionic path integral Monte Carlo simulations in the restricted grand canonical ensemble," *Contrib. Plasma Phys.* **61**, e202100112 (2021).
- <sup>97</sup>C. Watzböck, M. Feller, K. Held, and A. Toschi, "Long-term memory magnetic correlations in the Hubbard model: A dynamical mean-field theory analysis," *SciPost Phys.* **12**, 184 (2022).
- <sup>98</sup>M. Suzuki, "Generalized Trotter's formula and systematic approximants of exponential operators and inner derivations with applications to many-body problems," *Commun. Math. Phys.* **51**, 183–190 (1976).
- <sup>99</sup>A. L. Fetter and J. D. Walecka, *Quantum Theory of Many-Particle Systems* (McGraw-Hill, Boston, 1971).
- <sup>100</sup>J. E. Hirsch, "Discrete Hubbard-Stratonovich transformation for Fermion lattice models," *Phys. Rev. B* **28**, 4059–4061 (1983).
- <sup>101</sup>T. Shen, Y. Liu, Y. Yu, and B. M. Rubenstein, "Finite temperature auxiliary field quantum Monte Carlo in the canonical ensemble," *J. Chem. Phys.* **153**, 204108 (2020).
- <sup>102</sup>R. D. Sedgewick, D. J. Scalapino, R. L. Sugar, and L. Capriotti, "Canonical and grand canonical ensemble expectation values from quantum Monte Carlo simulations," *Phys. Rev. B* **68**, 045120 (2003).
- <sup>103</sup>C. N. Gilbreth, S. Jensen, and Y. Alhassid, "Reducing the complexity of finite-temperature auxiliary-field quantum Monte Carlo," *Comput. Phys. Commun.* **264**, 107952 (2021).
- <sup>104</sup>P. Borrmann and G. Franke, "Recursion formulas for quantum statistical partition functions," *J. Chem. Phys.* **98**, 2484–2485 (1993).
- <sup>105</sup>H. Barghathi, J. Yu, and A. Del Maestro, "Theory of noninteracting fermions and bosons in the canonical ensemble," *Phys. Rev. Res.* **2**, 043206 (2020).
- <sup>106</sup>T. Shen, H. Barghathi, J. Yu, A. Del Maestro, and B. Rubenstein, "A stable, recursive auxiliary field quantum Monte Carlo algorithm in the canonical ensemble: Applications to thermometry and the Hubbard model," *arXiv:2212.08654* (2022).
- <sup>107</sup>J. Yu, N. Sun, and H. Zhai, "Symmetry protected dynamical symmetry in the generalized Hubbard models," *Phys. Rev. Lett.* **119**, 225302 (2017).
- <sup>108</sup>H. Zhai, N. Sun, J. Yu, and P. Zhang, "New relations between spin and charge dynamics of the Fermi Hubbard model," *New J. Phys.* **21**, 015003 (2019).
- <sup>109</sup>C. N. Yang and S. C. Zhang, "SO<sub>4</sub> symmetry in a Hubbard model," *Mod. Phys. Lett. B* **04**, 759–766 (1990).
- <sup>110</sup>G.-S. Tian, "Particle-hole transformations and sum rules for the Hubbard model," *Phys. Lett. A* **228**, 383–390 (1997).
- <sup>111</sup>T. D. Kieu and C. J. Griffin, "Monte Carlo simulations with indefinite and complex-valued measures," *Phys. Rev. E* **49**, 3855–3859 (1994).
- <sup>112</sup>A. Avella, F. Mancini, and T. Saikawa, "The 2-site Hubbard and *t*-*J* models," *Eur. Phys. J. B* **36**, 445–473 (2003).
- <sup>113</sup>O. I. Pătu, A. Klümper, and A. Foerster, "Quantum critical behavior and thermodynamics of the repulsive one-dimensional Hubbard model in a magnetic field," *Phys. Rev. B* **101**, 035149 (2020).
- <sup>114</sup>M. Takahashi and M. Imada, "Monte Carlo calculation of quantum systems. II. Higher order correction," *J. Phys. Soc. Jpn.* **53**, 3765–3769 (1984).
- <sup>115</sup>M. Suzuki, "Fractal decomposition of exponential operators with applications to many-body theories and Monte Carlo simulations," *Phys. Lett. A* **146**, 319–323 (1990).
- <sup>116</sup>K. Sakko, J. Casulleras, and J. Boronat, "High order Chin actions in path integral Monte Carlo," *J. Chem. Phys.* **130**, 204109 (2009).
- <sup>117</sup>N. Prokofev, B. Svistunov, and I. Tupitsyn, "'Worm' algorithm in quantum Monte Carlo simulations," *Phys. Lett. A* **238**, 253–257 (1998).
- <sup>118</sup>M. Boninsegni, N. Prokofev, and B. V. Svistunov, "Worm algorithm for continuous-space path integral Monte Carlo simulations," *Phys. Rev. Lett.* **96**, 070601 (2006).
- <sup>119</sup>T. Dornheim, S. Groth, and M. Bonitz, "Permutation blocking path integral Monte Carlo simulations of degenerate electrons at finite temperature," *Contrib. Plasma Phys.* **59**, e201800157 (2019).
- <sup>120</sup>W. von der Linden, "A quantum Monte Carlo approach to many-body physics," *Phys. Rep.* **220**, 53–162 (1992).
- <sup>121</sup>F. Šimković and R. Rossi, "Many-configuration Markov-chain Monte Carlo," *arXiv:2102.05613* [physics.comp-ph] (2021).
- <sup>122</sup>H. Niederreiter, "Quasi-Monte Carlo methods and pseudo-random numbers," *Bull. Am. Math. Soc.* **84**, 957–1041 (1978).
- <sup>123</sup>M. Maček, P. T. Dumitrescu, C. Bertrand, B. Triggs, O. Parcollet, and X. Waintal, "Quantum quasi-Monte Carlo technique for many-body perturbative expansions," *Phys. Rev. Lett.* **125**, 047702 (2020).
- <sup>124</sup>C. Bertrand, D. Bauernfeind, P. T. Dumitrescu, M. Maček, X. Waintal, and O. Parcollet, "Quantum quasi Monte Carlo algorithm for out-of-equilibrium Green functions at long times," *Phys. Rev. B* **103**, 155104 (2021).

# Supplementary Material for: Fermionic-propagator and alternating-basis quantum Monte Carlo methods for correlated electrons on a lattice

Veljko Janković<sup>1, a)</sup> and Jakša Vučičević<sup>1, b)</sup>

*Institute of Physics Belgrade, University of Belgrade, Pregrevica 118, 11080 Belgrade, Serbia*

## SI. FPQMC METHOD: MONTE CARLO UPDATES

Here, we present the Monte Carlo updates we use to move through the configuration space of our FPQMC method.

The configuration space is sampled through Markov chains starting from an, in principle arbitrary, configuration  $\mathcal{C}_0$ . The Metropolis–Hastings algorithm is used to determine the probability of transferring from configuration  $\mathcal{C}_n$  at Monte Carlo step  $n$  to configuration  $\mathcal{C}_{n+1}$  at the subsequent Monte Carlo step  $n + 1$ . The transition probability  $W_{n \rightarrow n+1}$  is

$$W_{n \rightarrow n+1} = W_{n \rightarrow n+1}^{\text{prop}} W_{n \rightarrow n+1}^{\text{acc}} \quad (\text{S1})$$

where  $W_{n \rightarrow n+1}^{\text{prop}}$  is the probability of proposing the update from configuration  $\mathcal{C}_n$  to configuration  $\mathcal{C}_{n+1}$ , while  $W_{n \rightarrow n+1}^{\text{acc}}$  determines the probability with which such a proposal is accepted. The Metropolis–Hastings acceptance rate reads as

$$W_{n \rightarrow n+1}^{\text{acc}} = \min\{1, R_{n \rightarrow n+1}\} \quad (\text{S2})$$

where the acceptance ratio  $R_{n \rightarrow n+1} = 1/R_{n+1 \rightarrow n}$  depends on the weights of the configurations involved, as well as on the proposal probabilities in both directions  $\mathcal{C}_n \leftrightarrow \mathcal{C}_{n+1}$  in the following manner

$$R_{n \rightarrow n+1} = \frac{w(\mathcal{C}_{n+1})W_{n+1 \rightarrow n}^{\text{prop}}}{w(\mathcal{C}_n)W_{n \rightarrow n+1}^{\text{prop}}}. \quad (\text{S3})$$

### A. Updates that conserve the number of particles

#### 1. `change_r_local`

We randomly choose one real-space state  $|\Psi_{i,l_0}^n\rangle$  [in all the time-dependent computations we perform,  $l_0 \neq 1$  due to  $|\Psi_{i,1}^n\rangle \equiv |\psi(0)\rangle$  at each Monte Carlo step  $n$ ] and move an arbitrarily chosen electron (spin  $\sigma$ , position  $\mathbf{r}_j^\sigma$ ) to a new position  $\mathbf{s}_j^\sigma$  under the condition that the state  $(\sigma, \mathbf{s}_j^\sigma)$  is unoccupied in  $|\Psi_{i,l_0}^n\rangle$ .

The inverse move proceeds in the same manner as described above. The ratio of proposal weights is  $\frac{W_{n+1 \rightarrow n}^{\text{prop}}}{W_{n \rightarrow n+1}^{\text{prop}}} = 1$ .

This move ensures that we sample configurations with different real-space electron patterns.

#### 2. `change_r_global`

We randomly choose one real-space state  $|\Psi_{i,l_0}^n\rangle$  [in all the time-dependent computations we perform,  $l_0 \neq 1$  due to  $|\Psi_{i,1}^n\rangle \equiv |\psi(0)\rangle$  at each Monte Carlo step  $n$ ] and replace it by a new state  $|\Psi_{i,l_0}^{n+1}\rangle \neq |\Psi_{i,l_0}^n\rangle$ . While the effects of this “global” move can be mimicked by multiple applications of its “local” version `change_r_local`, we found this move very useful in evenly sampling the configuration space, especially in time-dependent FPQMC simulations.

#### 3. `spin_flip`—used only in equilibrium FPQMC simulations because it does not separately conserve the number of spin-up and spin-down electrons, yet it conserves the total electron number

We randomly choose spin  $\sigma$  and attempt to increase/decrease the number of electrons of spin  $\sigma/\bar{\sigma}$  by one.

---

<sup>a)</sup> veljko.jankovic@ipb.ac.rs

<sup>b)</sup> jaksa.vucicevic@ipb.ac.rs



In each imaginary-time slice  $l = 1, \dots, N_\tau$ , we choose an electron of spin  $\sigma$  at position  $\mathbf{r}$  from the real-space state  $|\Psi_{i,l}^n\rangle$  and construct the real-space state  $|\Psi_{i,l}^{n+1}\rangle$  by changing the electron's position  $\mathbf{r} \rightarrow \mathbf{s}$  and spin  $\sigma \rightarrow \bar{\sigma}$ . The ratio of the proposal probabilities in the real space can be directly computed as  $\left(\frac{W_{n+1 \rightarrow n}^{\text{prop}}}{W_{n \rightarrow n+1}^{\text{prop}}}\right)_{i,l} = \frac{N_\sigma(N_c - N_{\bar{\sigma}})}{(1 + N_{\bar{\sigma}})(N_c - N_\sigma + 1)}$ , where  $N_\sigma$  and  $N_{\bar{\sigma}}$  are numbers of electrons of spin  $\sigma$  and  $\bar{\sigma}$  in  $|\Psi_{i,l}^n\rangle$ .

This move is very useful once the FPQMC starts sampling configurations whose total electron number (the sum of the numbers of spin-up and spin-down electrons) fluctuates around the value predicted by the fixed temperature and chemical potential. One value of the total electron number may be realized via many different combinations of numbers of spin-up and spin-down electrons, and it is precisely this move that enables efficient sampling through all these combinations.

## B. Updates that do not conserve the number of particles

The updates `add_particle` and `remove_particle` are used only in equilibrium FPQMC simulations, when the number of particles fluctuates according to the fixed chemical potential and temperature.

The move `add_particle/remove_particle` adds/removes one electron from the configuration. These two moves are inverses of one another and their acceptance rates are mutually equal. The spin  $\sigma$  of the electron added to/removed from the imaginary-time slice  $l = 1$  fixes that an electron added to/removed from the remaining imaginary-time slices  $l = 2, \dots, N_\tau$  must have the same spin  $\sigma$ .

Let  $N_\sigma$  denote the number of electrons of spin  $\sigma$  in state  $|\Psi_{i,l}^n\rangle$  (before the update). In the first imaginary-time slice  $l = 1$ , an electron can be added to any of  $N_c - N_\uparrow + N_c - N_\downarrow$  empty single-particle states, while an electron can be removed from any of  $N_\uparrow + N_\downarrow$  occupied single-particle states. Concerning the inverse move, an electron can be removed from any of  $N_\uparrow + N_\downarrow + 1$  occupied single-particle states, while an electron can be added to any of  $2N_c - N_\uparrow - N_\downarrow + 1$  empty single-particle states. We thus have

$$\left(\frac{W_{n+1 \rightarrow n}^{\text{prop}}}{W_{n \rightarrow n+1}^{\text{prop}}}\right)_{i,l=1}^{\text{add}} = \frac{2N_c - N_\uparrow - N_\downarrow}{N_\uparrow + N_\downarrow + 1}, \quad \left(\frac{W_{n+1 \rightarrow n}^{\text{prop}}}{W_{n \rightarrow n+1}^{\text{prop}}}\right)_{i,l=1}^{\text{rmv}} = \frac{N_\uparrow + N_\downarrow}{2N_c - N_\uparrow - N_\downarrow + 1}. \quad (\text{S4})$$

In all other imaginary-time slices  $l = 2, \dots, N_\tau$ , we have

$$\left(\frac{W_{n+1 \rightarrow n}^{\text{prop}}}{W_{n \rightarrow n+1}^{\text{prop}}}\right)_{i,l \geq 2}^{\text{add}} = \frac{N_c - N_\sigma}{N_\sigma + 1}, \quad \left(\frac{W_{n+1 \rightarrow n}^{\text{prop}}}{W_{n \rightarrow n+1}^{\text{prop}}}\right)_{i,l \geq 2}^{\text{rmv}} = \frac{N_\sigma}{N_c - N_\sigma + 1}. \quad (\text{S5})$$

## C. Fast determinant updates

The determinant  $\mathcal{D}_\beta(\mathcal{C}, \Delta\tau)$  is a product of  $2N_\tau$  determinants of imaginary-time single-particle propagators on a lattice. Since all the updates can be seen as a single row/column change or addition/removal of a single row/column, changes in individual determinants may be efficiently computed using the formulae for fast determinant updates. These formulae, which provide the determinant ratio before and after the update, deal with the inverses of the corresponding matrices. We store these inverses in memory and recompute them from scratch each time a Monte Carlo update is accepted.

## D. Extraction of Monte Carlo results

The average sign of FPQMC simulations is relatively large, so that, after the initial equilibration phase, the physical quantities we compute depend quite weakly on the number of Monte Carlo steps completed. All relevant quantities are measured at every Monte Carlo step, and the individual-step data are grouped into bins of length  $L_b$ , where  $L_b \sim 10^4 - 10^5$ , depending on the total number of steps completed. To provide the best possible estimate of a quantity, we discard the first 80% of the simulation. The average of the binned data in the last 20% of the simulation is taken as the Monte Carlo estimate of the quantity of interest. The statistical error is estimated as the root-mean-square deviation of the binned data in the final 20% of the simulation from the above-computed average value. Such an estimate of the error is appropriate for statistically independent data. While we have not performed a systematic binning analysis, we may expect that the bin length we chose is sufficiently large that the data from different bins may be considered as statistically independent.

## SII. ABQMC METHOD IN REAL TIME: MONTE CARLO UPDATES

Here, we present the Monte Carlo updates we use to move through the configuration space of our real-time ABQMC method to compute the survival probability of an initial (pure) state. We only need updates that conserve the number of particles of each spin orientation.

Within the alternating-basis method, which employs both coordinate-space and momentum-space many-body states, we perform individual Monte Carlo updates on one of the two sets of states. The updates changing coordinate-space states are the updates `change_r_local` and `change_r_global` that we present in Sec. SI. The updates that change momentum-space states are designed so as to respect the momentum-conservation law. While the proposal probabilities  $W_{n \rightarrow n+1}^{\text{prop}}$  for coordinate-space updates can be determined relatively straightforwardly (even analytically), see Sec. SI, their determination for the momentum-space updates may be quite challenging due to the explicit momentum conservation. For all such moves, we can give no analytical expression for  $W_{n \rightarrow n+1}^{\text{prop}}$ , and we have to devise computer algorithms capable of precisely enumerating all possible propositions that comply with the momentum (and also particle-number) conservation.

### 1. add\_q

The momentum  $\mathbf{K}$  of each of the states  $|\Psi_{k,l}^n\rangle$ ,  $l = 1, \dots, N_{\tau/t}$ , is increased by a randomly chosen momentum  $\mathbf{q} \neq 0$ , thereby obtaining new states  $|\Psi_{k,l}^{n+1}\rangle$ ,  $l = 1, \dots, N_{\tau/t}$ , with momentum  $\mathbf{K} + \mathbf{q}$ . The real-space states are not changed, i.e.,  $|\Psi_{i,l}^n\rangle = |\Psi_{i,l}^{n+1}\rangle$ . In each momentum-space state, momentum  $\mathbf{q}$  is added to an electron of spin  $\sigma$  that carries momentum  $\mathbf{k}_{j,l}^\sigma$  under the condition that the state  $(\sigma, \mathbf{k}_{j,l}^\sigma + \mathbf{q})$  is unoccupied in  $|\Psi_{k,l}^n\rangle$ . All possible momentum-accepting states  $(\sigma, \mathbf{k}_{j,l}^\sigma)$  have to be explicitly enumerated and their number is denoted as  $p_l^{+\mathbf{q}}$ .

The inverse move starts from states  $|\Psi_{k,l}^{n+1}\rangle$ ,  $l = 1, \dots, N_{\tau/t}$ , with momentum  $\mathbf{K} + \mathbf{q}$ , and adds momentum  $-\mathbf{q}$  to each of them. All possible momentum-accepting states in  $|\Psi_{k,l}^{n+1}\rangle$  have to be explicitly enumerated and their number is denoted as  $p_l^{-\mathbf{q}}$ .

The ratio of the proposal probabilities is then  $\frac{W_{n+1 \rightarrow n}^{\text{prop}}}{W_{n \rightarrow n+1}^{\text{prop}}} = \prod_l \frac{p_l^{+\mathbf{q}}}{p_l^{-\mathbf{q}}}$ .

This move ensures that we sample configurations from sectors featuring different electronic momenta.

### 2. exchange\_q

We randomly choose one momentum-space state  $|\Psi_{k,l_0}^n\rangle$  in which we select two electrons of spins  $\sigma_1$  and  $\sigma_2$  and momenta  $\mathbf{k}_{j_1}^{\sigma_1}$  and  $\mathbf{k}_{j_2}^{\sigma_2}$ , which are ordered so that  $k_{j_1,y} + N_y k_{j_1,x} > k_{j_2,y} + N_y k_{j_2,x}$ . The momenta are subsequently changed using  $\mathbf{k}_{j_1}^{\sigma_1} \rightarrow \mathbf{k}_{j_1}^{\sigma_1} + \mathbf{q}$ ,  $\mathbf{k}_{j_2}^{\sigma_2} \rightarrow \mathbf{k}_{j_2}^{\sigma_2} - \mathbf{q}$  ( $\mathbf{q} \neq 0$ ). As a consequence, the net momentum of  $|\Psi_{k,l_0}^n\rangle$  remains unchanged. Obviously, the move may be realized only when the states  $(\sigma_1, \mathbf{k}_{j_1}^{\sigma_1} + \mathbf{q})$  and  $(\sigma_2, \mathbf{k}_{j_2}^{\sigma_2} - \mathbf{q})$  are both unoccupied in  $|\Psi_{k,l_0}^n\rangle$ .

We note that enumerating all possible momenta  $\mathbf{q} \neq 0$  that may be transferred between the electrons is relatively simple for  $\sigma_1 \neq \sigma_2$  ( $\sigma_2 = \bar{\sigma}_1$ ), when the two electrons can be distinguished by their spins. It is then enough to go through all empty states  $(\sigma_1, \mathbf{k}')$  to which the electron  $(\sigma_1, \mathbf{k}_{j_1}^{\sigma_1})$  can be moved and to determine the corresponding momentum transfer  $\mathbf{q} = \mathbf{k}' - \mathbf{k}_{j_1}^{\sigma_1}$ . We then ask if the state  $(\bar{\sigma}_1, \mathbf{k}_{j_2}^{\bar{\sigma}_1} - \mathbf{q})$  is empty; in the affirmative case, we memorize the current  $\mathbf{q}$  as one possible momentum transfer. The inverse move proceeds in a completely analogous manner by explicitly enumerating possible back-transfers.

On the other hand, two electrons of the same spin are indistinguishable, and special care should be exercised to avoid double counting. For given  $\mathbf{k}_{j_1}$  and  $\mathbf{k}_{j_2}$  (we now omit  $\sigma_1 = \sigma_2$ ), possible values of  $\mathbf{q}$  follow from the construction that is schematically summarized in Fig. S1. We make use of the periodic boundary conditions to construct a new unit cell (in the momentum space) such that the electron of momentum  $\mathbf{k}_{j_1}$  is in its “center”, while its vertices are at  $\mathbf{k}_{j_2}$  and its periodic copies  $\mathbf{k}_{j_2} + 2\pi(1, 0)$ ,  $\mathbf{k}_{j_2} + 2\pi(0, 1)$ , and  $\mathbf{k}_{j_2} + 2\pi(1, 1)$ . The “central point” and the four vertices partition the unit cell into four rectangular regions that are colored yellow (bottom left), green (top left), cyan (top right), and magenta (bottom right). The vectors  $\mathbf{q}$  that may be added to  $\mathbf{k}_{j_1}$  and subtracted from  $\mathbf{k}_{j_2}$  are to be selected so that the final states  $\mathbf{k}_{j_1} + \mathbf{q}$  and  $\mathbf{k}_{j_2} - \mathbf{q}$  belong to just one half of each of the regions, the two halves being separated by the line connecting the “central” point and the vertices. The halves from which possible final states  $\mathbf{k}_{j_1} + \mathbf{q}$ , and thus possible momentum transfers  $\mathbf{q}$ , are selected is shaded. Choosing the momentum transfer such that the final state  $\mathbf{k}_{j_1} + \mathbf{q}$  belongs to the other (unshaded) half is equivalent to assigning momentum  $\mathbf{k}_{j_1}$  to the blue electron and  $\mathbf{k}_{j_2}$  to the red electron, i.e., to exchanging momentum labels  $\mathbf{k}_{j_1}$  and  $\mathbf{k}_{j_2}$ , which produces the setup equivalent to that presented in Fig. S1. The momentum transfer  $\mathbf{q}$

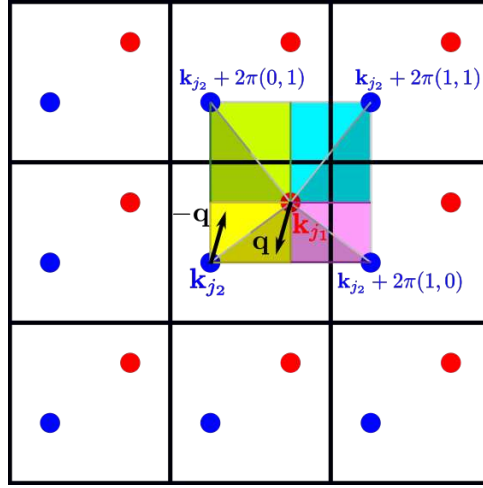


Figure S1. Construction used to correctly enumerate all possible momenta  $\mathbf{q} \neq 0$  that can be exchanged between two electrons of equal spins that carry momenta  $\mathbf{k}_{j_1}$  and  $\mathbf{k}_{j_2}$ . The momenta  $\mathbf{q}$  that may be added to  $\mathbf{k}_{j_1}$  (and subtracted from  $\mathbf{k}_{j_2}$ ) are such that the final state  $\mathbf{k}_{j_1} + \mathbf{q}$  is found in one of the four shaded triangles, while  $\mathbf{k}_{j_2} - \mathbf{q}$  is found in one of the four unshaded triangles.

along the edges of the four shaded triangles should be counted only once because of the periodic boundary conditions. For example, if we enumerate possible  $\mathbf{q}$ s along the vertical edge of the green shaded triangle, then we should not enumerate possible  $\mathbf{q}$ s along the vertical edge of the cyan shaded triangle. Moreover, if any of the lines connecting the “center” and the four edges contains any other lattice point, possible  $\mathbf{q}$ s along that line are subjected to the condition  $|\mathbf{q}| \leq |\mathbf{k}_{j_1} - \mathbf{k}_{j_2} - 2\pi(a_x, a_y)|/2$ , where  $(a_x, a_y) \in \{(0, 0), (1, 0), (0, 1), (1, 1)\}$ . While this construction is appropriate for  $k_{j_1, x} \neq k_{j_2, x}$  and  $k_{j_1, y} \neq k_{j_2, y}$ , further discussion is needed when either  $k_{j_1, x} = k_{j_2, x}$  or  $k_{j_1, y} = k_{j_2, y}$ . In the inverse move, we start from the two electrons carrying momenta  $\mathbf{k}'_{j_1} = \mathbf{k}_{j_1} + \mathbf{q}$  and  $\mathbf{k}'_{j_2} = \mathbf{k}_{j_2} - \mathbf{q}$ , we order them so that  $k'_{j_1, y} + N_y k'_{j_1, x} > k'_{j_2, y} + N_y k'_{j_2, x}$ , and repeat the above-described procedure.

This move ensures that we sample configurations belonging to the sector of the chosen total electron momentum.

### SIII. DETAILED PERFORMANCE OF THE FPQMC METHOD APPLIED TO EVALUATE THE EQUATION OF STATE

A.  $U/J = 4$ ,  $T/J = 1.0408$

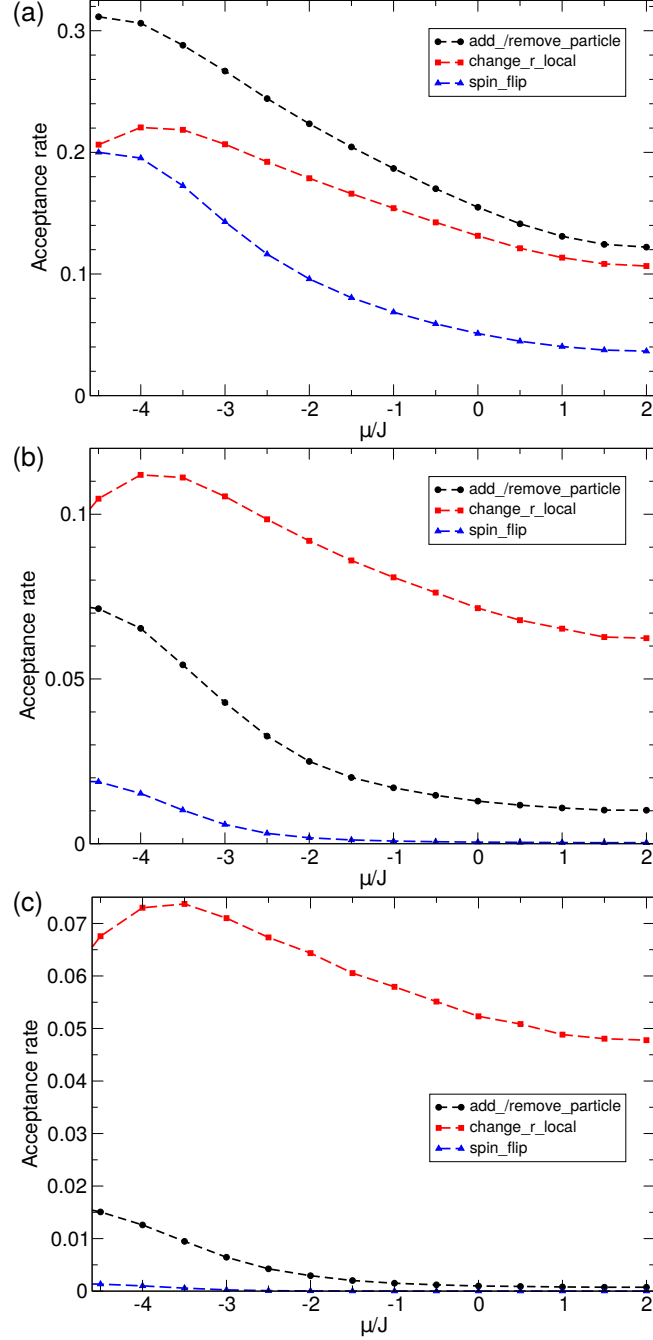


Figure S2. Acceptance rates of individual moves as a function of the chemical potential. FPQMC simulations are performed on a  $4 \times 4$  square-lattice cluster using (a)  $N_\tau = 2$ , (b)  $N_\tau = 4$ , and (c)  $N_\tau = 6$  imaginary-time slices. The remaining parameters are:  $U/J = 4$ ,  $T/J = 1.0408$ . Acceptance rates generally decrease with  $N_\tau$  and with the filling (chemical potential).

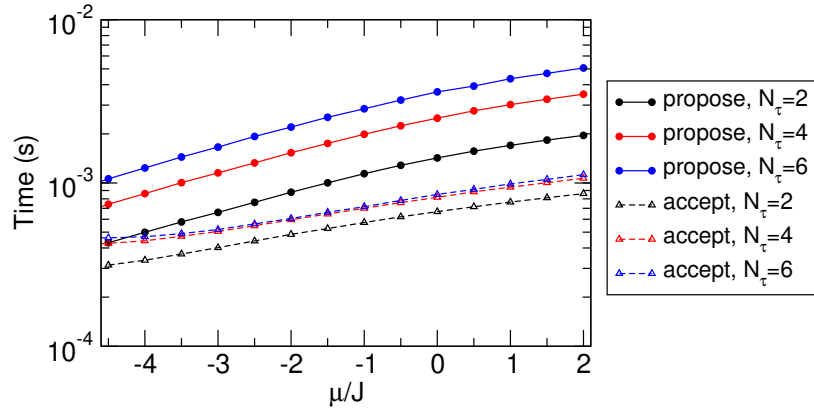


Figure S3. Average time needed to propose (full symbols connected by solid lines) and accept (empty symbols connected by dashed lines) a Monte Carlo update as a function of the chemical potential. FPQMC simulations are performed on a  $4 \times 4$  square-lattice cluster with different numbers of imaginary-time slices  $N_\tau$ . The remaining parameters are:  $U/J = 4$ ,  $T/J = 1.0408$ .



B.  $U/J = 24$ ,  $T/J = 1.0408$

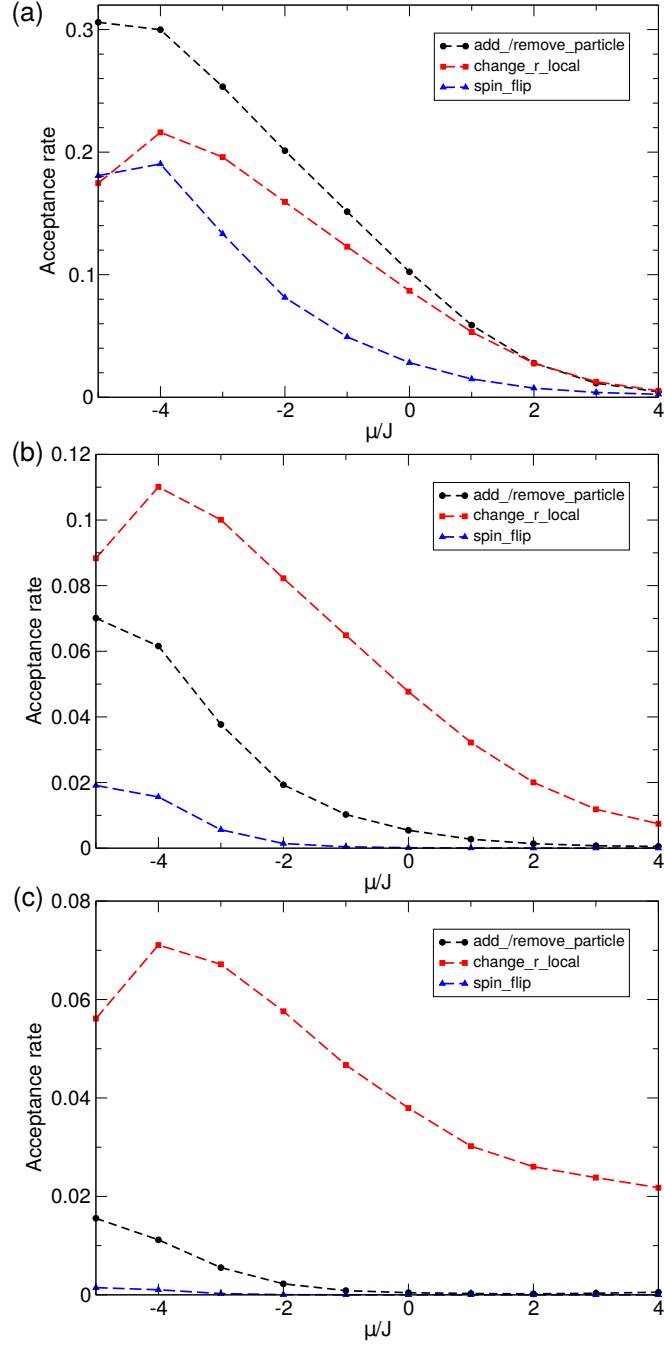


Figure S4. Acceptance rates of individual moves as a function of the chemical potential. FPQMC simulations are performed on a  $4 \times 4$  square-lattice cluster using (a)  $N_\tau = 2$ , (b)  $N_\tau = 4$ , and (c)  $N_\tau = 6$  imaginary-time slices. The remaining parameters are:  $U/J = 24$ ,  $T/J = 1.0408$ . Acceptance rates generally decrease with  $N_\tau$  and with the filling (chemical potential).

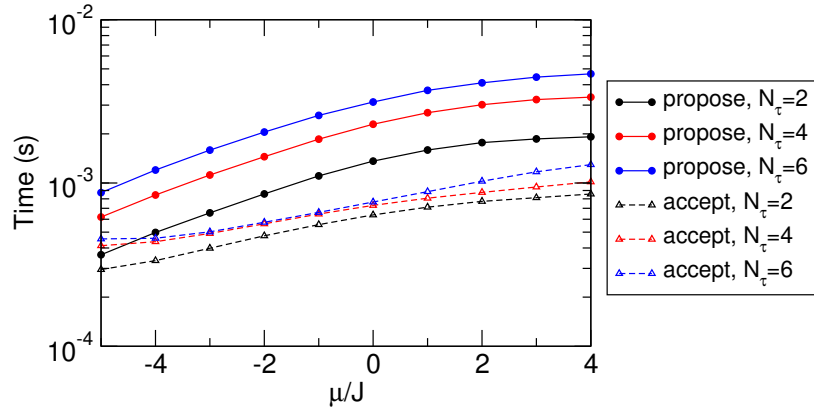


Figure S5. Average time needed to propose (full symbols connected by solid lines) and accept (empty symbols connected by dashed lines) an MC update as a function of the chemical potential. FPQMC simulations are performed on a  $4 \times 4$  square-lattice cluster with different numbers of imaginary-time slices  $N_\tau$ . The remaining parameters are:  $U/J = 24$ ,  $T/J = 1.0408$ .

#### SIV. ABQMC METHOD APPLIED TO EQUILIBRIUM SITUATIONS

Here, we derive the ABQMC method in equilibrium situations (Sec. SIV A) and present our implementation of the method (Sec. SIV B). Since the ABQMC method is equally adept at calculating quantities in real and momentum space, we complement the results presented in Fig. 7 of the main text by presenting the momentum distribution at different fillings (Sec. SIV C). We conclude in Sec. SIV D by discussing acceptance rates and proposal/acceptance times of MC updates introduced in Sec. SIV B.

##### A. ABQMC method in equilibrium: Basic equations

Dividing the imaginary-time interval  $[0, \beta]$  into  $N_\tau$  slices of length  $\Delta\tau \equiv \beta/N_\tau$ , employing the lowest-order STD, and inserting the spectral decompositions of  $H_0$  and  $H_{\text{int}}$ , we find the following ABQMC approximant for the partition function at temperature  $T = 1/\beta$ :

$$Z \approx \sum_{\mathcal{C}} \mathcal{D}(\mathcal{C}) e^{-\Delta\tau \varepsilon(\mathcal{C})}. \quad (\text{S6})$$

The configuration

$$\mathcal{C} = \{|\Psi_{k,1}\rangle, \dots, |\Psi_{k,N_\tau}\rangle, |\Psi_{i,1}\rangle, \dots, |\Psi_{i,N_\tau}\rangle\} \quad (\text{S7})$$

resides on the contour depicted in Fig. 1(a) of the main text and consists of  $N_\tau$  Fock states  $|\Psi_{k,l}\rangle$  ( $l = 1, \dots, N_\tau$ ) in the momentum representation and  $N_\tau$  Fock states  $|\Psi_{i,l}\rangle$  in the coordinate representation.  $\mathcal{D}(\mathcal{C})$  is the product of  $2N_\tau$  Slater determinants

$$\mathcal{D}(\mathcal{C}) \equiv \prod_{l=1}^{N_\tau} \langle \Psi_{i \oplus 1, l} | \Psi_{k, l} \rangle \langle \Psi_{k, l} | \Psi_{i, l \ominus 1} \rangle \quad (\text{S8})$$

that stem from the sequence of basis alternations between the momentum and coordinate eigenbasis. The symbol  $\varepsilon(\mathcal{C})$  stands for

$$\varepsilon(\mathcal{C}) \equiv \sum_{l=1}^{N_\tau} [\varepsilon_0(\Psi_{k,l}) + \varepsilon_{\text{int}}(\Psi_{i,l})]. \quad (\text{S9})$$

The equilibrium expectation value an observable  $A_a$  diagonal in either coordinate ( $a = i$ ) or momentum ( $a = k$ ) representation reads as

$$\langle A_a \rangle \approx \frac{1}{Z} \sum_{\mathcal{C}} \mathcal{D}(\mathcal{C}) e^{-\Delta\tau \varepsilon(\mathcal{C})} \frac{1}{N_\tau} \sum_{l=1}^{N_\tau} \mathcal{A}_a(\Psi_{a,l}), \quad (\text{S10})$$

where

$$\mathcal{A}_a(\Psi_{a,l}) \equiv \langle \Psi_{a,l} | A_a | \Psi_{a,l} \rangle. \quad (\text{S11})$$

The evaluation of Eq. (S10) using the importance-sampling MC procedure is complicated by the fact that  $\mathcal{D}(\mathcal{C})$  is a complex number defined by its modulus and phase. While the modulus can be included in the weight of configuration  $\mathcal{C}$ , the phase gives rise to the so-called phase problem, which is generally much harder to curb than the ordinary sign problem. However, since the STD preserves the equality  $Z = Z^*$ ,<sup>1</sup> Eq. (S6) can be replaced by

$$Z \approx \sum_{\mathcal{C}} \text{Re}\{\mathcal{D}(\mathcal{C})\} e^{-\Delta\tau \varepsilon(\mathcal{C})}, \quad (\text{S12})$$

and we remain with the ordinary sign problem. Equation (S10) should then be replaced by

$$\langle A_a \rangle \approx \frac{\sum_{\mathcal{C}} \text{Re}\{\mathcal{D}(\mathcal{C})\} e^{-\Delta\tau \varepsilon(\mathcal{C})} \frac{1}{N_\tau} \sum_{l=1}^{N_\tau} \mathcal{A}_a(\Psi_{a,l})}{\sum_{\mathcal{C}} \text{Re}\{\mathcal{D}(\mathcal{C})\} e^{-\Delta\tau \varepsilon(\mathcal{C})}}. \quad (\text{S13})$$

Defining the weight  $w(\mathcal{C})$  of configuration  $\mathcal{C}$  as

$$w(\mathcal{C}) \equiv |\text{Re}\{\mathcal{D}(\mathcal{C})\}|e^{-\Delta\tau\varepsilon(\mathcal{C})}, \quad (\text{S14})$$

Eq. (S13) is rewritten as

$$\langle A_a \rangle \approx \frac{\left\langle \text{sgn}(\mathcal{C}) \frac{1}{N_\tau} \sum_{l=1}^{N_\tau} \mathcal{A}_a(\Psi_{a,l}) \right\rangle_w}{\langle \text{sgn}(\mathcal{C}) \rangle_w} \quad (\text{S15})$$

where  $\langle \dots \rangle_w$  denotes the weighted average over all  $\mathcal{C}$  with respect to the weight  $w(\mathcal{C})$ ;  $\text{sgn}(\mathcal{C}) \equiv \text{Re}\{\mathcal{D}(\mathcal{C})\}/|\text{Re}\{\mathcal{D}(\mathcal{C})\}|$  is the sign of configuration  $\mathcal{C}$ , while  $|\langle \text{sgn} \rangle| \equiv |\langle \text{sgn}(\mathcal{C}) \rangle_w|$  is the average sign of the ABQMC simulation.

## B. ABQMC method in equilibrium: Monte Carlo updates

Apart from previously introduced updates `change_r_local` and `change_r_global` in real space (Sec. SI) and `add_q` and `exchange_q` in momentum space (Sec. SII), we need updates that insert/remove a particle, which are different from their counterparts in Sec. SI.

The ABQMC move `add_particle/remove_particle` adds/removes one electron from the configuration. These two moves are inverses of one another. While analogous moves are relatively simply implemented in the FPQMC algorithm, here, special care is to be exercised because of the particle-number and momentum conservation. In more detail, the spin  $\sigma$  of the electron added to/removed from the imaginary-time slice  $l = 1$  fixes that an electron added to/removed from the remaining imaginary-time slices  $l = 2, \dots, N_\tau$  must have the same spin  $\sigma$ . Furthermore, the momentum  $\mathbf{q}$  of the electron added to/removed from the imaginary-time slice  $l = 1$  fixes that momentum change upon addition/removal of an electron in the remaining imaginary-time slices  $l = 2, \dots, N_\tau$  must be precisely  $\mathbf{q}$ . This requirement may be realized in many different ways. One trivial possibility is to add/remove the electron to/from the state  $(\sigma, \mathbf{q})$  if this state is empty/occupied. On the other hand, we may add/remove the electron to/from state  $(\sigma, \mathbf{k})$ , in which case we should find another electron  $(\sigma_{\text{comp}}, \mathbf{k}_{\text{comp}})$  (of arbitrary spin  $\sigma_{\text{comp}}$ ) to compensate for the difference in the momentum change from  $\pm \mathbf{q}$ , where  $+/-$  sign is for electron addition/removal. The electron in the state  $(\sigma_{\text{comp}}, \mathbf{k}_{\text{comp}})$  that may receive the momentum difference  $\pm(\mathbf{q} - \mathbf{k})$  will be termed the compensating electron. The situation is relatively simple when the spin of the compensating electron is  $\bar{\sigma}$  because the added electron and the compensating electron may be distinguished by their spins. When the spins of the added and compensating electrons are both equal to  $\sigma$ , these two electrons cannot be distinguished in the sense that their roles (added/compensating) may be reverted. Special care should thus be taken to avoid double counting. An elaborate analysis reveals that the double counting is avoided by ordering the momenta of:

(add) the added electron  $\mathbf{k}$  and the compensating electron  $\mathbf{k}_{\text{comp}} + \mathbf{q} - \mathbf{k}$  after the compensation;

(rmv) the removed electron  $\mathbf{k}$  and the compensating electron  $\mathbf{k}_{\text{comp}}$  before the compensation.

The ordering is the same as in the update `exchange_q`.

While the above discussion regards the momentum-space states  $|\Psi_{k,l}^n\rangle \rightarrow |\Psi_{k,l}^{n+1}\rangle$ , the situation with the real-space states  $|\Psi_{i,l}^n\rangle \rightarrow |\Psi_{i,l}^{n+1}\rangle$  is far less complicated because only the particle-number conservation should be satisfied. The spin of the electron to be added to/removed from each  $|\Psi_{i,l}^n\rangle$  is determined by the spin of the electron added to/removed from  $|\Psi_{k,0}^n\rangle$ . The ratio of the backward and forward proposal probabilities for the real-space parts of the configuration may be directly computed as:

$$\begin{aligned} (\text{add}) \quad \left( \frac{W_{n+1 \rightarrow n}^{\text{prop}}}{W_{n \rightarrow n+1}^{\text{prop}}} \right)_{i,l} &= \frac{N_c - N_\sigma}{1 + N_\sigma}, \\ (\text{rmv}) \quad \left( \frac{W_{n+1 \rightarrow n}^{\text{prop}}}{W_{n \rightarrow n+1}^{\text{prop}}} \right)_{i,l} &= \frac{N_\sigma}{N_c - N_\sigma + 1}, \end{aligned}$$

where  $N_\sigma$  is the number of electrons of spin  $\sigma$  in all the states  $|\Psi_{i/k,l}^n\rangle$  (before the update).

There are also some differences in the move `spin_flip`, in which we randomly choose spin  $\sigma$  and attempt to increase/decrease the number of electrons of spin  $\sigma/\bar{\sigma}$  by one.

In each imaginary-time slice  $l = 1, \dots, N_\tau$ , we explicitly enumerate the momentum states  $(\sigma, \mathbf{k}) \in |\Psi_{k,l}^n\rangle$  such that  $(\bar{\sigma}, \mathbf{k}) \notin |\Psi_{k,l}^n\rangle$ . This is the simplest possible update that changes the spin of an electron and yet keeps the

total momentum of the configuration fixed. The state  $|\Psi_{k,l}^{n+1}\rangle$  is then obtained from the state  $|\Psi_{k,l}^n\rangle$  by removing the electron in the state  $(\sigma, \mathbf{k})$  and adding the electron in the state  $(\bar{\sigma}, \mathbf{k})$ . The inverse move proceeds in an analogous manner: we explicitly enumerate momentum the states  $(\bar{\sigma}, \mathbf{k}') \in |\Psi_{k,l}^{n+1}\rangle$  such that  $(\sigma, \mathbf{k}') \notin |\Psi_{k,l}^{n+1}\rangle$ .

In each imaginary-time slice  $l = 1, \dots, N_\tau$ , we choose an electron of spin  $\sigma$  at position  $\mathbf{r}$  from the real-space state  $|\Psi_{i,l}^n\rangle$  and construct the real-space state  $|\Psi_{i,l}^{n+1}\rangle$  by changing the electron's position  $\mathbf{r} \rightarrow \mathbf{s}$  and spin  $\sigma \rightarrow \bar{\sigma}$ . The ratio of the proposal probabilities in the real space can be directly computed as  $\left(\frac{W_{n+1 \rightarrow n}^{\text{prop}}}{W_{n \rightarrow n+1}^{\text{prop}}}\right)_{i,l} = \frac{N_\sigma(N_c - N_{\bar{\sigma}})}{(1 + N_{\bar{\sigma}})(N_c - N_\sigma + 1)}$ , where  $N_\sigma$  and  $N_{\bar{\sigma}}$  are numbers of electrons of spin  $\sigma$  and  $\bar{\sigma}$  in  $|\Psi_{i,l}^n\rangle$ .

### C. ABQMC method in equilibrium: Numerical results

Within the ABQMC method, coordinate and momentum bases are treated symmetrically, meaning that the method should be equally adept at calculating quantities diagonal in these two bases. As an example applications in the momentum space, in Fig. S6 we show the momentum distribution,  $\frac{1}{2} \sum_\sigma \langle n_{\mathbf{k}\sigma} \rangle$ , in the same setup as in Fig. 4 of the main text ( $U/J = 4$ ,  $T/J = 1.0408$ ).

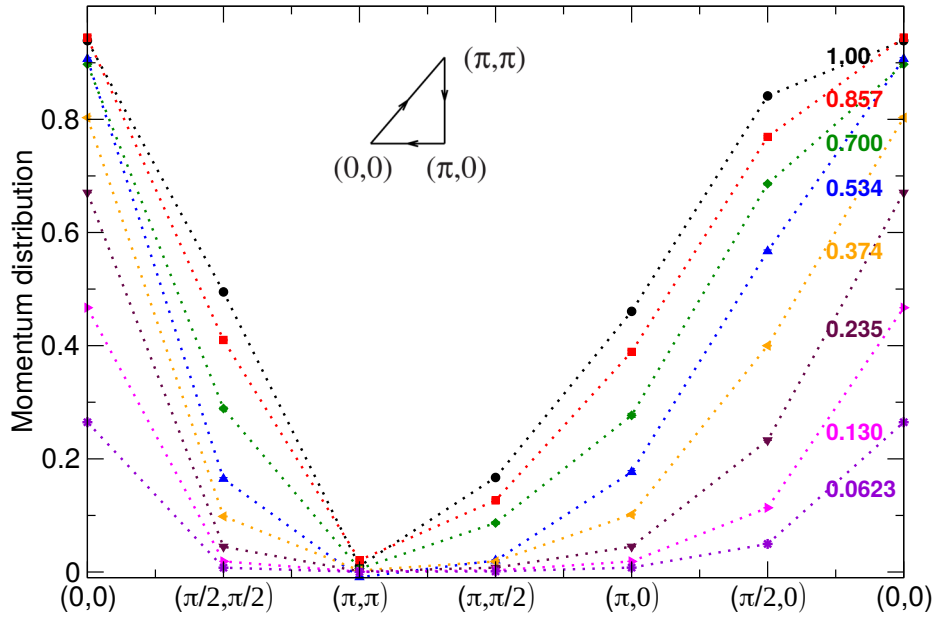


Figure S6. Momentum distribution,  $\frac{1}{2} \sum_\sigma \langle n_{\mathbf{k}\sigma} \rangle$ , for different fillings  $\rho_e$  (half filling is  $\rho_e = 1$ ) computed using the equilibrium ABQMC approach on a  $4 \times 4$  square-lattice cluster. Model parameters are  $U/J = 4$ ,  $T/J = 1.0408$ , while  $\mu/J$  is varied from 2 to  $-5$ . The pathway through the irreducible Brillouin zone is summarized in the inset. Cited values of  $\rho_e$  are from Ref. 2. Dotted lines serve as guides to the eye. Statistical error bars are generally smaller than symbol size.



### D. ABQMC method in equilibrium: Acceptance rates and proposal/acceptance times

1.  $U/J = 4$ ,  $T/J = 1.0408$

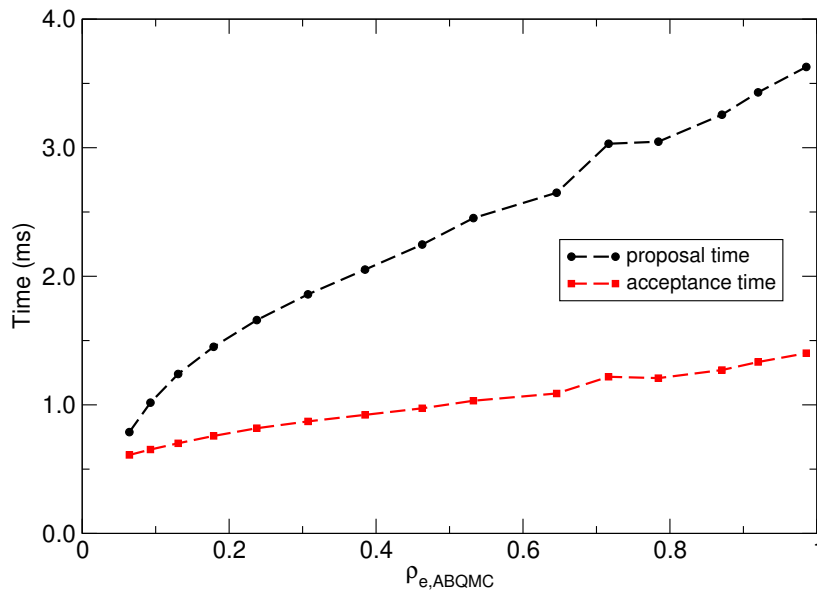


Figure S7. Average time needed to propose (black circles) and accept (red squares) one Monte Carlo update as a function of the ABQMC electron density. The averaging is performed over all updates used in ABQMC simulations to evaluate the equation of state: `add_particle`, `remove_particle`, `spin_flip`, `add_q`, `exchange_q`, `change_r_local`, and `change_r_global`.

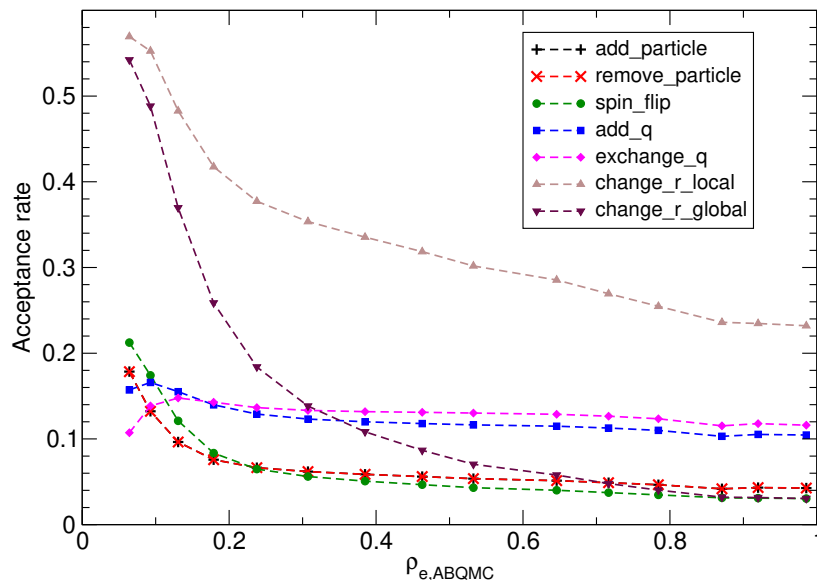


Figure S8. Acceptance rates of individual Monte Carlo updates as a function of the ABQMC electron density. Being inverses of one another, the acceptance rates of moves `add_particle` and `remove_particle` are mutually equal. The acceptance rates of moves `add_particle`, `remove_particle`, `spin_flip`, `add_q`, and `exchange_q` exhibit weak dependence on the filling, while moves involving changes in the real-space part of configurations tend to be accepted less frequently as the filling is increased.

2.  $U/J = 24$ ,  $T/J = 1.0408$

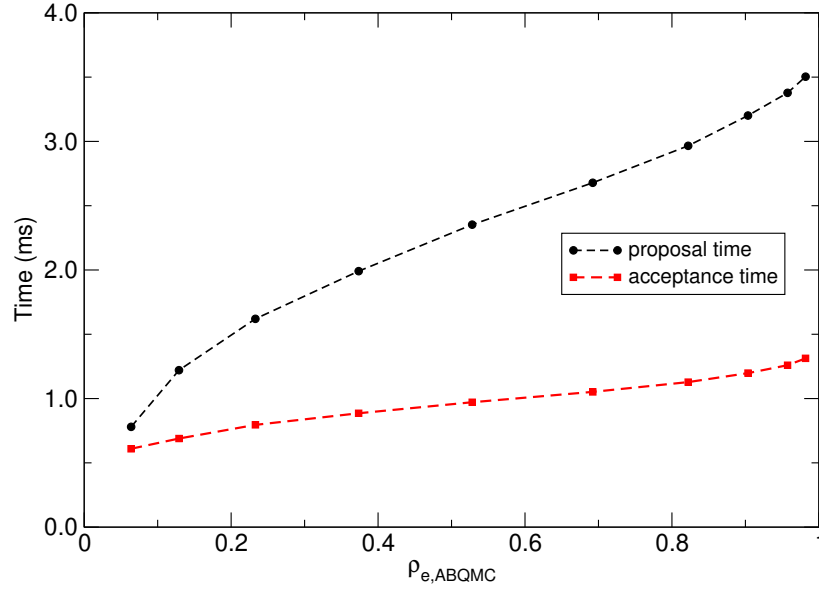


Figure S9. Average time needed to propose (black circles) and accept (red squares) one Monte Carlo update as a function of the ABQMC electron density. The averaging is performed over all updates used in ABQMC simulations to evaluate the equation of state: `add_particle`, `remove_particle`, `spin_flip`, `add_q`, `exchange_q`, `change_r_local`, and `change_r_global`.

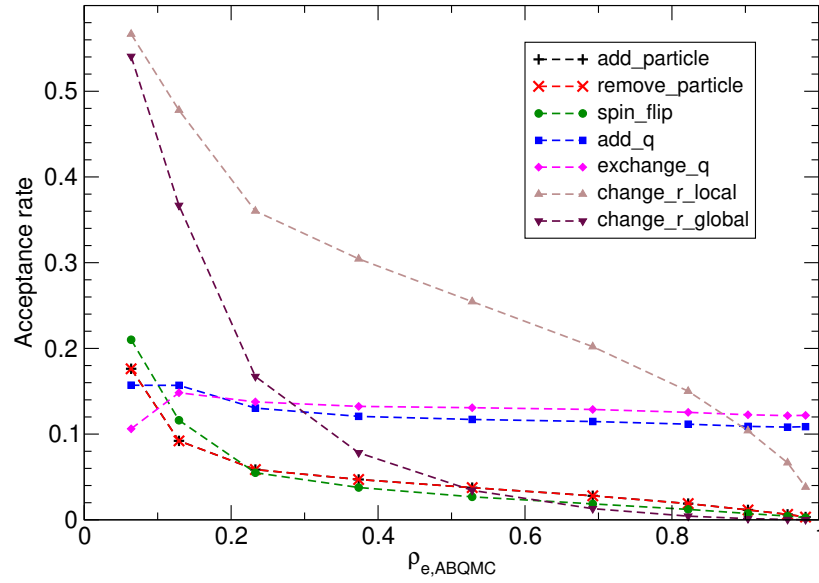


Figure S10. Acceptance rates of individual Monte Carlo updates as a function of the ABQMC electron density. Being inverses of one another, the acceptance rates of moves `add_particle` and `remove_particle` are mutually equal. The acceptance rates of moves `add_q` and `exchange_q` exhibit weak dependence on the filling, while moves `add_particle`, `remove_particle`, `spin_flip`, `change_r_local`, and `change_r_global` tend to be accepted less frequently as the filling is increased.

# SV. FPQMC METHOD FOR TIME-DEPENDENT DENSITIES: ADDITIONAL RESULTS

Figure S11(a) summarizes the evolution of charge densities on initially unoccupied sites of a half-filled  $4 \times 4$  cluster, on which the electrons are initially arranged as summarized in the inset of Fig. S11(b) [the so-called  $(\pi, \pi)$  density wave]. Figure S11(b) summarizes the extent of the dynamical sign problem, which appears to be somewhat more severe than in the case of the  $(\pi, 0)$  density wave discussed in Figs. 8(a) and 8(b) of the main text.

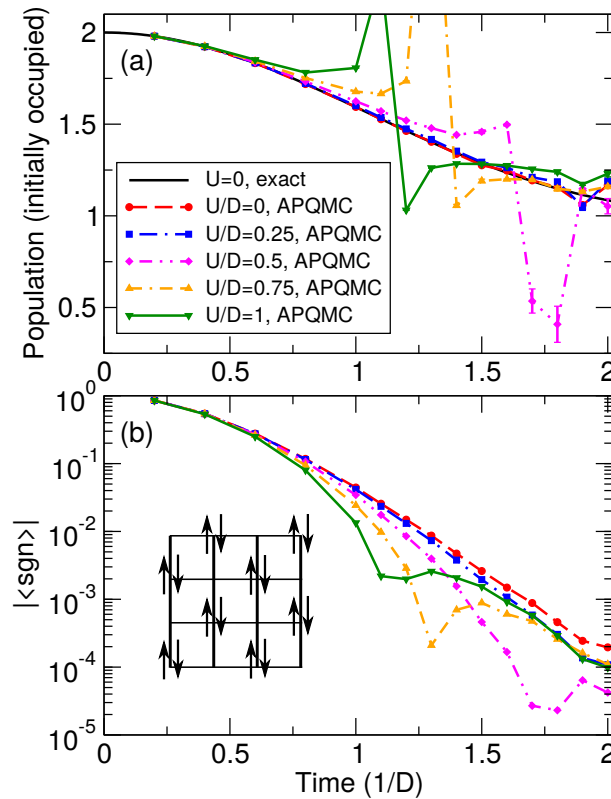


Figure S11. (a) Time-dependent population of sites occupied in the initial CDW state of a  $4 \times 4$  cluster, which is schematically depicted in the inset of panel (b). FPQMC results using  $N_t = 2$  real-time slices (4 slices in total) are shown for five different interaction strengths (symbols) and compared with the noninteracting result (solid line). (b) Magnitude of the average sign as a function of time for different interaction strengths. Color code is the same as in panel (a).

In equilibrium and in the weak-interaction regime, we concluded that the sign problem becomes more pronounced with the filling, see Fig. 4(b) of the main text. Motivated by this finding, we finally study the dynamics of local densities at a smaller filling, see Figs. S12(a1)–S12(b2), which permits us to perform FPQMC simulations on an  $8 \times 4$  cluster. While the average sign displayed in Fig. S12(a2) is somewhat enhanced with respect to the values reported in Fig. S11(b) and Fig. 8(b) of the main text, the simulated dynamics retains the above-described problems. The average sign decreases with the cluster size, compare the average signs for the noninteracting electrons in Figs. S12(a2) and S12(b2).

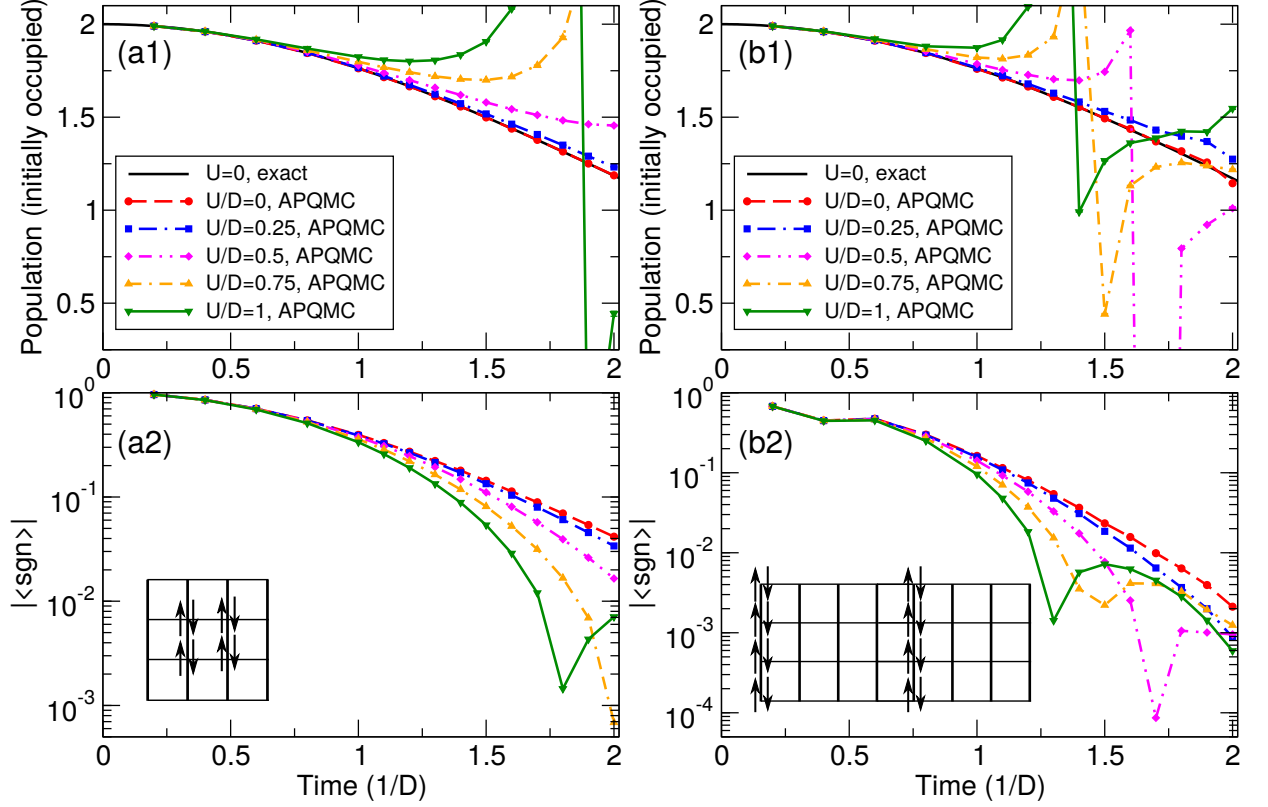


Figure S12. (a1) and (b1) Time-dependent population of sites occupied in the initial state of a  $4 \times 4$  (a1) and  $8 \times 4$  (b1) cluster, which is schematically depicted in the inset of panels (a2) and (b2), respectively. FPQMC results using  $N_t = 2$  real-time slices (4 slices in total) are shown for five different interaction strengths (symbols) and compared with the noninteracting result (solid line). (a2) and (b2) Time-dependent average sign of the FPQMC simulation for different interaction strengths. Color code is the same as in (a1) and (b1), respectively. Statistical errors are generally smaller than the symbol size.

## SVI. ABQMC METHOD FOR TIME-DEPENDENT SURVIVAL PROBABILITY: ADDITIONAL RESULTS

### A. Applicability of the ABQMC method to a $4 \times 4$ cluster with $N_t = 4$ real-time slices

This section addresses the applicability of the ABQMC method to compute the survival probability of the 16-electron CDW-like/SDW-like state depicted in Fig. 10(a) of the main text when the number of real-time slices is increased from  $N_t = 2$  to  $N_t = 4$ . In Fig. S13 we compare the behavior of the average sign for  $N_t = 2$ , when we make  $3.87 \times 10^{10}$  steps, and  $N_t = 4$ , when we make  $1.16 \times 10^{10}$  steps. Increasing the number of real-time slices from 2 to 4 decreases  $|\langle \text{sgn} \rangle|$  after  $10^{10}$  MC steps by an order of magnitude. With  $N_t = 4$ , the stabilization of the average sign takes much more than  $10^{10}$  MC steps, and its overall decrease as the simulation proceeds may be very well described by a power law with the exponent of  $-1/2$ , see the dashed line in Fig. S13.

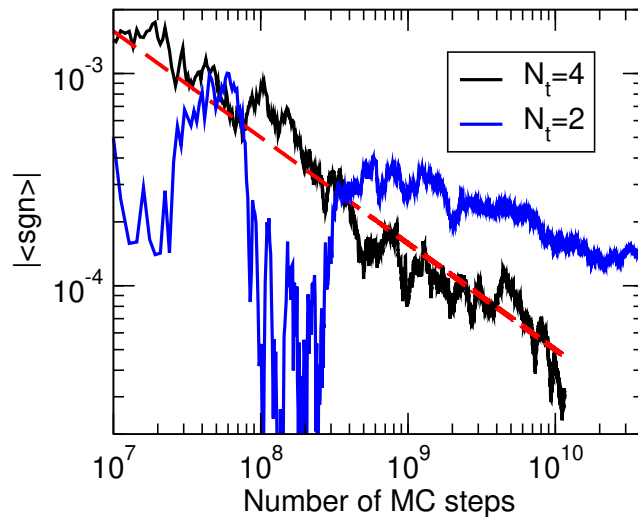


Figure S13. Magnitude of the average sign as a function of the number of MC steps during the ABQMC simulation of the survival probability of the 16-electron CDW/SDW state on a  $4 \times 4$  square-lattice cluster using  $N_t = 2$  and  $N_t = 4$  real-time slices. The overall behavior of  $|\langle \text{sgn} \rangle|$  for  $N_t = 4$  may be fitted very well by the function  $5/\sqrt{N_{\text{MC}}}$  that is shown by the dashed line.



### B. Applicability of the ABQMC method to an $8 \times 4$ cluster with $N_t = 2$ real-time slices

This section addresses the applicability of the ABQMC method to compute the survival probability of a 16-electron initial state on an  $8 \times 4$  cluster with  $N_t = 2$  real-time slices. The initial CDW-like state is schematically depicted in Fig. S14(a), while Fig. S14(b) shows the evolution of the average sign during the MC simulation. We perform  $10^{10}$  MC steps, during which the magnitude of the average sign shows no signals of stabilization, but steadily decreases in a power-law fashion with the exponent  $-1/2$ , see the dashed line in Fig. S14(b). Even though the final stages of our MC simulation may suggest that  $|\langle \text{sgn} \rangle|$  stabilizes on the level of  $\sim 4 \times 10^{-5}$ , a very noisy behavior of  $|\langle \text{sgn} \rangle|$  throughout the simulation casts doubts on such a conclusion. We observe in Fig. S14(b) that  $|\langle \text{sgn} \rangle|$  displays pronounced dips whose duration may be as long as a couple of billions of steps, which is in stark contrast with the rather smooth decrease of  $|\langle \text{sgn} \rangle|$  observed, e.g., in Fig. S13. These dips suggest that there may be problems with the configuration-space sampling. The dimension of the configuration space of our ABQMC method is much larger than the dimension of the Hilbert space of the model, which is astronomically large for the Hubbard model on an  $8 \times 4$  cluster. To further illustrate the last point, in Fig. S14(c) we present the survival probability of the initial state in the noninteracting case. In contrast to the  $4 \times 4$  cluster, for which perfect collapses and revivals in  $P(t)$  are observed already on relatively short time scales, there is no such a regular behavior on the  $8 \times 4$  cluster, see Fig. S14(c). On general grounds, the noninteracting system is bound to display perfect collapses and revivals in  $P(t)$ , while the time scale on which the pattern in  $P(t)$  repeats itself is inversely proportional to the dimension of the system's Hilbert space.

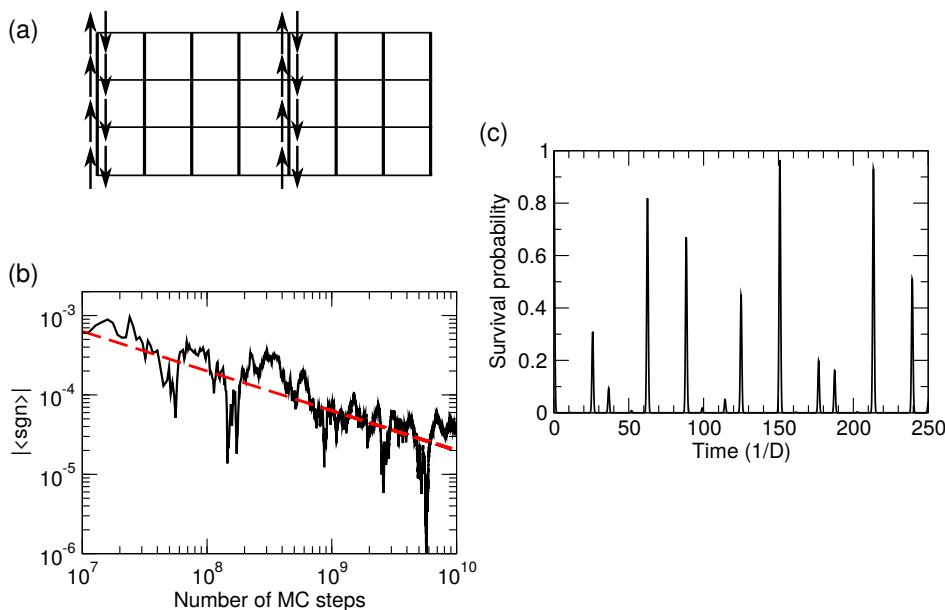


Figure S14. (a) Schematic view of the 16-electron initial state on an  $8 \times 4$  square-lattice cluster whose survival probability is computed. (b) Magnitude of the average sign as a function of the number of MC steps during the ABQMC simulation of the survival probability of the initial state depicted in (a).  $N_t = 2$  real-time slices are used. The overall behavior of  $|\langle \text{sgn} \rangle|$  may be fitted very well by the function  $2/\sqrt{N_{\text{MC}}}$  that is shown by the dashed line. (c) Time dependence of the survival probability of the initial state depicted in (a) in the noninteracting case  $U = 0$ . The dimensionality of the system's Hilbert space is so large that no perfect revival in  $P(t)$  (which is bound to occur since  $U = 0$ ) is observed up to  $Dt = 250$ .

### C. ABQMC results for the survival probability near the atomic limit

Figure S15 shows  $P(t)$  for the 16-electron initial state schematically depicted in Fig. 10(a) of the main text in regimes that are close to the atomic limit. In these regimes, the natural energy unit is  $U$ , so that the time is measured in units  $1/U$ . The time range is chosen on the basis of the results in Figs. (d1)–(e2), which suggest that the ABQMC method with  $N_t = 2$  real-time slices produces a qualitatively correct behavior of  $P(t)$  up to times  $Ut \approx 6$ .  $P(t)$  exhibits oscillations whose amplitude decreases in time. There is almost no difference between  $P(t)$  for  $D/U = 0.05$  and  $0.1$  during the first oscillation, while  $P(t)$  for  $D/U = 0.2$  is at all times below  $P(t)$  for stronger  $U$ . While for the strongest  $U$  the maxima reached by  $P(t)$  are always close to 1, the maxima for weaker  $U$  are smaller than 1 and decrease with time. All these observations can be rationalized by an increased importance of the kinetic over the interaction term as  $U/D$  is decreased.

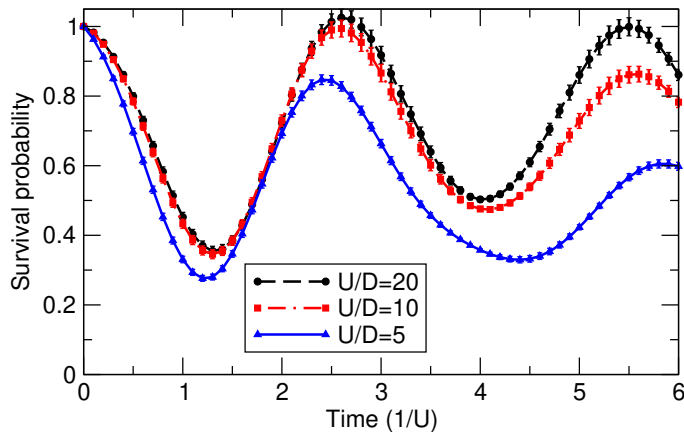


Figure S15. (Color online) Survival-probability dynamics of the 16-electron initial state schematically depicted in Fig. (a) for three values of the interaction strength that are close to the atomic limit.

## SVII. ABQMC METHOD TO EVALUATE TIME-DEPENDENT EXPECTATION VALUES ALONG THE KELDysh-KADANOFF-BAYM CONTOUR

We start from

$$\langle A_a(t) \rangle = \frac{\text{Tr} (e^{-\beta H(0)} e^{iHt} A_a e^{-iHt})}{\text{Tr} (e^{-\beta H(0)})} \quad (\text{S16})$$

where  $H$  is the Hubbard Hamiltonian, while  $H(0)$  additionally contains terms that modulate charge or spin density. For example, to simulate the response recorded in Ref. 3, the following  $H(0)$  may be appropriate:

$$H(0) = \underbrace{\sum_{\mathbf{k}\sigma} \tilde{\varepsilon}_{\mathbf{k}} n_{\mathbf{k}\sigma}}_H + U \sum_{\mathbf{r}} n_{\mathbf{r}\uparrow} n_{\mathbf{r}\downarrow} - \sum_{\mathbf{r}\sigma} v_{\mathbf{r}} n_{\mathbf{r}\sigma} \quad (\text{S17})$$

where  $v_{\mathbf{r}}$  is the external harmonic potential that modulates electron density, e.g.,

$$v_{\mathbf{r}} = V_0 \cos(\mathbf{q} \cdot \mathbf{r}). \quad (\text{S18})$$

Inspired by Ref. 3, we assume that  $\mathbf{q} = q\mathbf{e}_x$ , i.e., we assume that the electron density is modulated along one direction with the wavelength  $\lambda = 2\pi/q$ . We also assume that  $\lambda \leq N_x$  and that  $N_x \bmod \lambda = 0$ , i.e., the cluster's linear dimension along  $x$  axis is spanned by an integer number of wavelengths.

There are at least two manners in which the ABQMC method in the presence of external density-modulating potential (at  $t < 0$ ) can be formulated. They differ by the choice of the contributions that are diagonal in the coordinate and momentum representations.

1. The part diagonal in the momentum representation is

$$[H(0)]_{\text{mom}} = \sum_{\mathbf{k}} \varepsilon_{\mathbf{k}} n_{\mathbf{k}\sigma},$$

while the part diagonal in the coordinate representation

$$[H(0)]_{\text{coord}} = U \sum_{\mathbf{r}} n_{\mathbf{r}\uparrow} n_{\mathbf{r}\downarrow} - \sum_{\mathbf{r}\sigma} \mu_{\mathbf{r}} n_{\mathbf{r}\sigma}$$

contains position-dependent chemical potential  $\mu_{\mathbf{r}} = \mu + v_{\mathbf{r}}$ . Such a decomposition provides exact results in the atomic limit ( $J = 0$ ) and is expected to provide reasonable results when the electron–electron interaction dominates over the electronic hopping.

2. The part diagonal in some momentum representation is

$$[H(0)]_{\text{mom}} = \sum_{\mathbf{k}\sigma} \tilde{\varepsilon}_{\mathbf{k}} n_{\mathbf{k}\sigma} - \frac{V_0}{2} \sum_{\mathbf{k}\sigma} \left( c_{(k_x+q, k_y)\sigma}^\dagger c_{(k_x, k_y)\sigma} + c_{(k_x-q, k_y)\sigma}^\dagger c_{(k_x, k_y)\sigma} \right)$$

while the part diagonal in the coordinate representation is

$$[H(0)]_{\text{coord}} = U \sum_{\mathbf{r}} n_{\mathbf{r}\uparrow} n_{\mathbf{r}\downarrow}.$$

Such a decomposition provides exact results in the noninteracting limit ( $U = 0$ ) and is expected to provide reasonable results when the electronic hopping dominates over the electron–electron interaction. Our further developments will be focused on this decomposition.

The external harmonic potential introduces the coupling between different  $\mathbf{k}$  states which results in a reduction of the Brillouin zone along  $x$  axis by a factor of  $\lambda$ . The wave vector  $\mathbf{k}$  in the full Brillouin zone  $[0, 2\pi) \times [0, 2\pi)$  is not a good quantum number anymore. Its role is taken by the wave vector  $\tilde{\mathbf{k}}$  in the reduced Brillouin zone  $[0, 2\pi/\lambda) \times [0, 2\pi)$ , whose  $x$  projection  $\tilde{k}_x$  may assume any of the  $n_q = N_x \text{div } \lambda$  allowed values in the interval  $[0, 2\pi/\lambda)$  ( $p \times 2\pi/N_x$ , where  $p = 0, \dots, n_q - 1$ ) and whose  $y$  projection  $\tilde{k}_y$  may assume any of the  $N_y$  allowed values in the interval  $[0, 2\pi)$  ( $p \times 2\pi/N_y$ , where  $p = 0, \dots, N_y - 1$ ). In addition to  $\tilde{\mathbf{k}}$ , there is another degree of freedom that will be denoted by

$\nu_x$  and that may assume values  $0, \dots, \lambda - 1$ . The Hamiltonian  $H_{\text{mom}}$  has a block-diagonal structure and the blocks defined by the wave vector  $\mathbf{k}$  can be diagonalized separately. There are  $n_q N_y$  such blocks and the dimension of each of them is  $\lambda \times \lambda$ .

The Hubbard Hamiltonian  $H$  appears in combination  $e^{iHt} \dots e^{-iHt}$ , meaning that the chemical-potential term  $-\mu \sum_{\mathbf{r}\sigma} n_{\mathbf{r}\sigma} = -\mu \sum_{\mathbf{k}\sigma} n_{\mathbf{k}\sigma}$  is not effective (we assume that  $A_a$  conserves the total particle number, which is a reasonable assumption) and there is no ambiguity regarding the part  $H_{\text{mom}}$  or  $H_{\text{coord}}$  to which it should be associated. Therefore, the partition of the Hubbard Hamiltonian in parts that are diagonal in the momentum and coordinate representation is the same as in the main body of the paper

$$H_{\text{mom}} = \sum_{\mathbf{k}\sigma} \varepsilon_{\mathbf{k}} n_{\mathbf{k}\sigma}, \quad H_{\text{coord}} = U \sum_{\mathbf{r}} n_{\mathbf{r}\uparrow} n_{\mathbf{r}\downarrow}.$$

Let us now exploit symmetries to develop as efficient as possible ABQMC algorithm to evaluate Eq. (S16). Since  $H(0)$  is not invariant under the bipartite lattice symmetry, we use only the time-reversal symmetry, according to which  $\langle A_a(-t) \rangle = \langle A_a(t) \rangle$ . Furthermore, we note that both the numerator and the denominator of Eq. (S16) are purely real. Using the strategy described in the main text, one may derive the ABQMC counterpart of Eq. (S16)

$$\langle A_a(t) \rangle = \frac{\sum_{\mathcal{C}} \text{Re}\{\mathcal{D}(\mathcal{C})\} e^{-\Delta\tau\varepsilon_{\text{M}}(\mathcal{C})} \cos\{[\Delta\varepsilon_0(\mathcal{C}) + \Delta\varepsilon_{\text{int}}(\mathcal{C})]\Delta t\} \mathcal{A}_a(\Psi_{a,l_a})}{\sum_{\mathcal{C}} \text{Re}\{\mathcal{D}(\mathcal{C})\} e^{-\Delta\tau\varepsilon_{\text{M}}(\mathcal{C})}} \quad (\text{S19})$$

The configuration  $\mathcal{C}$  consists of  $2N_t + N_\tau$  many-body states  $|\Psi_{k,l}\rangle$  ( $l = 1, \dots, 2N_t + N_\tau$ ) composed of single-particle momentum eigenstates and  $2N_t + N_\tau$  many-body states  $|\Psi_{i,l}\rangle$  composed of single-particle coordinate eigenstates. While momenta of states  $|\Psi_{k,1}\rangle, \dots, |\Psi_{k,2N_t}\rangle$  are defined in the full Brillouin zone, states  $|\Psi_{k,2N_t+1}\rangle, \dots, |\Psi_{k,2N_t+N_\tau}\rangle$  have their momenta defined in the reduced Brillouin zone. The symbols  $\mathcal{D}(\mathcal{C})$ ,  $\Delta\varepsilon_0(\mathcal{C})$ , and  $\Delta\varepsilon_{\text{int}}(\mathcal{C})$  are defined as in the main text, while  $\varepsilon_{\text{M}}(\mathcal{C})$  is the sum of energies of  $2N_\tau$  states along the Matsubara part of the contour, i.e.,

$$\varepsilon_{\text{M}}(\mathcal{C}) = \sum_{l=2N_t+1}^{2N_t+N_\tau} [\varepsilon_0(\Psi_{k,l}) + \varepsilon_{\text{int}}(\Psi_{i,l})]. \quad (\text{S20})$$

The slice on which the expectation value  $\mathcal{A}_a(\Psi_{a,l_a}) = \langle \Psi_{a,l_a} | A_a | \Psi_{a,l_a} \rangle$  is evaluated depends on the representation  $a = i, k$  in which the observable  $A_a$  is diagonal, so that  $l_i = N_t + 1$  and  $l_k = N_t$ .

The structure of Eq. (S19) is intuitively clear as it is a combination of the ABQMC formula for thermodynamic quantities [Eq. (17) of the main text] and the ABQMC formula for the time-dependent expectation value along the Keldysh contour [Eq. (26) of the main text]. However, since we cannot exploit the bipartite lattice symmetry in this setup, the time-dependent part of the numerator in Eq. (S19) is  $\cos\{[\Delta\varepsilon_0(\mathcal{C}) + \Delta\varepsilon_{\text{int}}(\mathcal{C})]\Delta t\}$  instead of  $\cos[\Delta\varepsilon_0(\mathcal{C})\Delta t] \cos[\Delta\varepsilon_{\text{int}}(\mathcal{C})\Delta t]$ . Configuration weight may be chosen as  $w(\mathcal{C}) = |\text{Re}\{\mathcal{D}(\mathcal{C})\}| e^{-\Delta\tau\varepsilon_{\text{M}}(\mathcal{C})}$  and Eq. (S19) is recast as

$$\langle A_a(t) \rangle = \frac{\langle \text{sgn}(\mathcal{C}) \cos\{[\Delta\varepsilon_0(\mathcal{C}) + \Delta\varepsilon_{\text{int}}(\mathcal{C})]\Delta t\} \mathcal{A}_a(\Psi_{a,l_a}) \rangle_w}{\langle \text{sgn}(\mathcal{C}) \rangle_w}. \quad (\text{S21})$$

Markov-chain MC evaluation of Eq. (S21) suffers from the sign problem that does not depend on time  $t$  (it is not dynamical). Still, it becomes more pronounced when the cluster size  $N_c$  or the number of slices ( $N_t$  and  $N_\tau$ ) are increased. Similarly to equilibrium ABQMC calculations, the weight  $w(\mathcal{C})$  depends on all model parameters ( $U, T, \mu, V_0, t$ ). Therefore, the calculations for different values of these parameters have to be performed using different Markov chains, which is different from the computation of  $P(t)$  or  $\langle A_a(t) \rangle$  starting from a pure state  $|\psi(0)\rangle$ .

The application of conservation laws on the Kadanoff–Baym contour is somewhat more involved than on simpler contours studied in the main body of the paper. The particle-number conservation demands that all the many-body states constituting configuration  $\mathcal{C}$  have the same number of spin-up and spin-down electrons. We discuss the momentum conservation under the assumption that the observable  $A_a$  is diagonal in the coordinate representation (e.g.,  $A_i = \sum_{\sigma} n_{\mathbf{r}\sigma}$ ). From the main text, we know that the momentum conservation along the horizontal parts of the contour (Keldysh branch) is broken into two conservation laws that are satisfied separately on the forward and backward branch. In other words, the momenta (in the full Brillouin zone!) of  $N_t$  momentum-space states  $|\Psi_{k,1}\rangle, \dots, |\Psi_{k,N_t}\rangle$  on the forward branch are all equal to  $\mathbf{K}_{\text{fwd}}$ , while the momenta of  $N_t$  momentum-space states  $|\Psi_{k,N_t+1}\rangle, \dots, |\Psi_{k,2N_t}\rangle$  on the backward branch are all equal to  $\mathbf{K}_{\text{bwd}}$ . In contrast to the situation encountered in the main text,  $\mathbf{K}_{\text{fwd}}$  and  $\mathbf{K}_{\text{bwd}}$  are not completely independent because states  $|\Psi_{k,1}\rangle$  and  $|\Psi_{k,2N_t}\rangle$  are “in contact” with states  $|\Psi_{k,2N_t+N_\tau}\rangle$  and  $|\Psi_{k,2N_t+1}\rangle$  on the Matsubara branch. Therefore, the relation between  $\mathbf{K}_{\text{fwd}}$  and  $\mathbf{K}_{\text{bwd}}$  is determined by the momentum-conservation law along the Matsubara branch, which is formulated in the reduced Brillouin zone. Namely,

the momenta (in the reduced Brillouin zone!) of  $N_\tau$  momentum-space states  $|\Psi_{k,2N_t+1}\rangle, \dots, |\Psi_{k,2N_t+N_\tau}\rangle$  are all equal to  $\tilde{\mathbf{K}}_M$ . The momenta  $\mathbf{K}_{\text{fwd}}$ ,  $\mathbf{K}_{\text{bwd}}$ , and  $\tilde{\mathbf{K}}_M$  are related as follows:

$$\mathbf{K}_{\text{fwd}} \cdot \mathbf{e}_y = \mathbf{K}_{\text{bwd}} \cdot \mathbf{e}_y = \tilde{\mathbf{K}}_M \cdot \mathbf{e}_y,$$

$$\frac{\mathbf{K}_{\text{fwd}} \cdot \mathbf{e}_x}{2\pi/N_x} \bmod \frac{N_x}{\lambda} = \frac{\tilde{\mathbf{K}}_M \cdot \mathbf{e}_x}{2\pi/N_x}, \quad \frac{\mathbf{K}_{\text{bwd}} \cdot \mathbf{e}_x}{2\pi/N_x} \bmod \frac{N_x}{\lambda} = \frac{\tilde{\mathbf{K}}_M \cdot \mathbf{e}_x}{2\pi/N_x}$$

Due to the more complicated momentum-conservation law, MC updates presented in Sec. SI have to be amply modified. Instead of describing modified MC updates in detail, we demonstrate the correctness of our implementation by benchmarking it on small clusters. Motivated by Ref. 3, we limit the discussion to the electron occupation dynamics on individual sites.

We start from the noninteracting electrons, where already  $N_\tau = 1$  imaginary-time slice and  $2N_t = 2$  real-time slices ( $2N_t + N_\tau = 3$  slices in total) are expected to reproduce the exact result. Trivial as they may seem, the benchmarks on the noninteracting case are quite important, because densities of individual sites are expected to display nontrivial oscillatory behavior. The fact that our ABQMC results reproduce these oscillations quite accurately strongly suggests that our implementation is correct. In Fig. S16 we present results for the Hubbard dimer initially subjected to the external density-modulating field  $v_{r_x} = V_0 \cos(\pi r_x)$  with  $r_x = 0, 1$ . Figure S17 displays results for the Hubbard tetramer initially subjected to the external density-modulating field of wavelength  $\lambda = 4$ ,  $v_{r_x} = V_0 \cos(\pi r_x/2)$ , with  $r_x = 0, 1, 2, 3$ . Figure S18 displays results for the Hubbard tetramer initially subjected to the external density-modulating field of wavelength  $\lambda = 2$ ,  $v_{r_x} = V_0 \cos(\pi r_x)$ , with  $r_x = 0, 1, 2, 3$ .

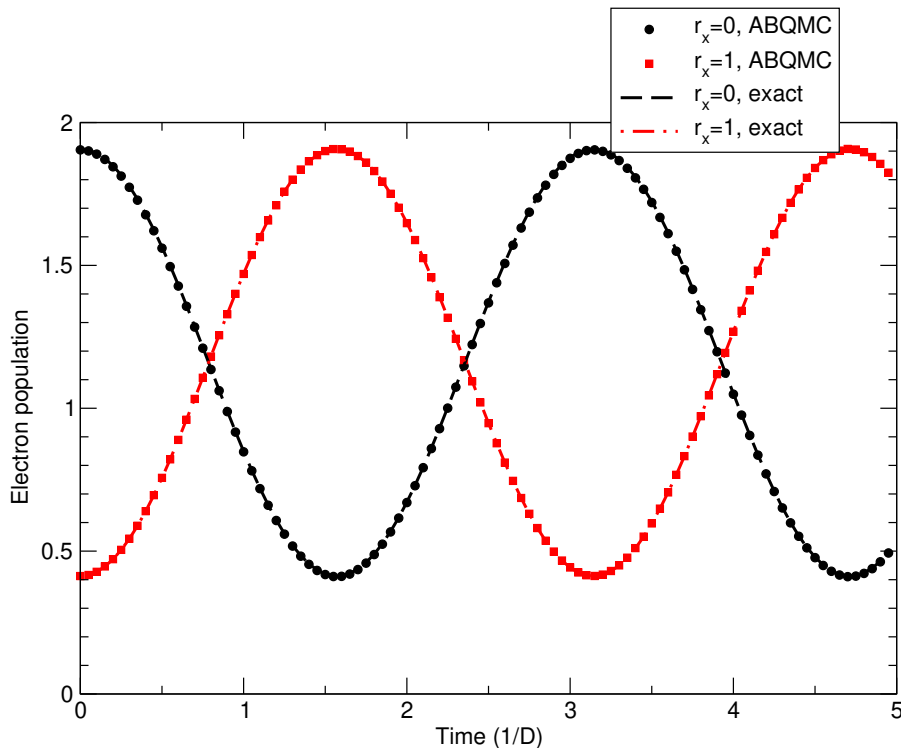


Figure S16. Time-dependent site populations of the Hubbard dimer with the following values of model parameters:  $\mu/D = 1.3$ ,  $V_0/D = 2$ ,  $U = 0$ ,  $T/D = 0.57$ . The external potential at  $t < 0$  is  $v_{r_x} = V_0 \cos(\pi r_x)$  with  $r_x = 0, 1$ .

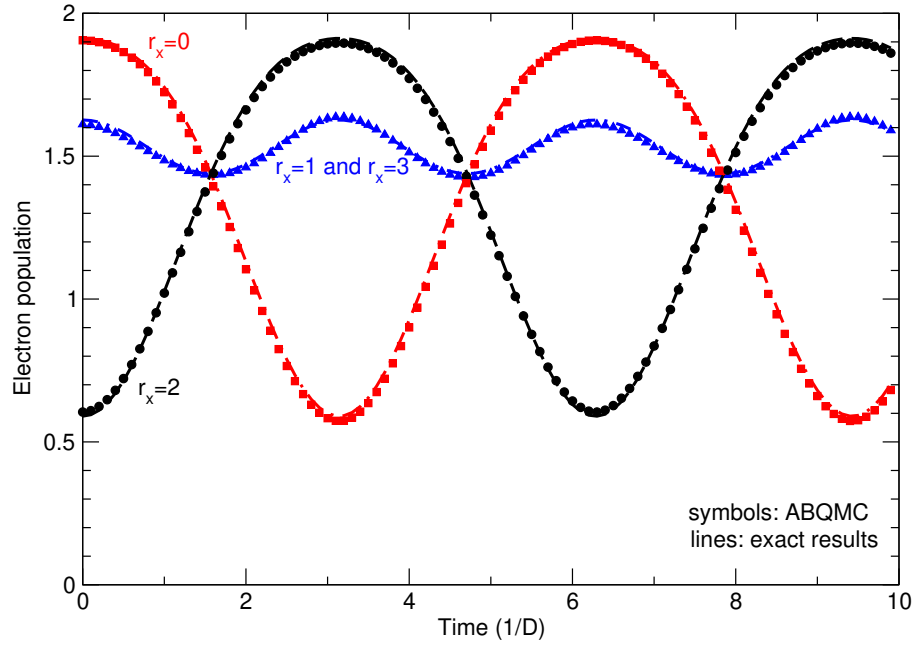


Figure S17. Time-dependent site populations of the Hubbard tetramer with the following values of model parameters:  $\mu/D = 0.65$ ,  $V_0/D = 1$ ,  $U = 0$ ,  $T/D = 0.285$ . The external potential at  $t < 0$  is  $v_{r_x} = V_0 \cos(\pi r_x/2)$  with  $r_x = 0, 1, 2, 3$ .

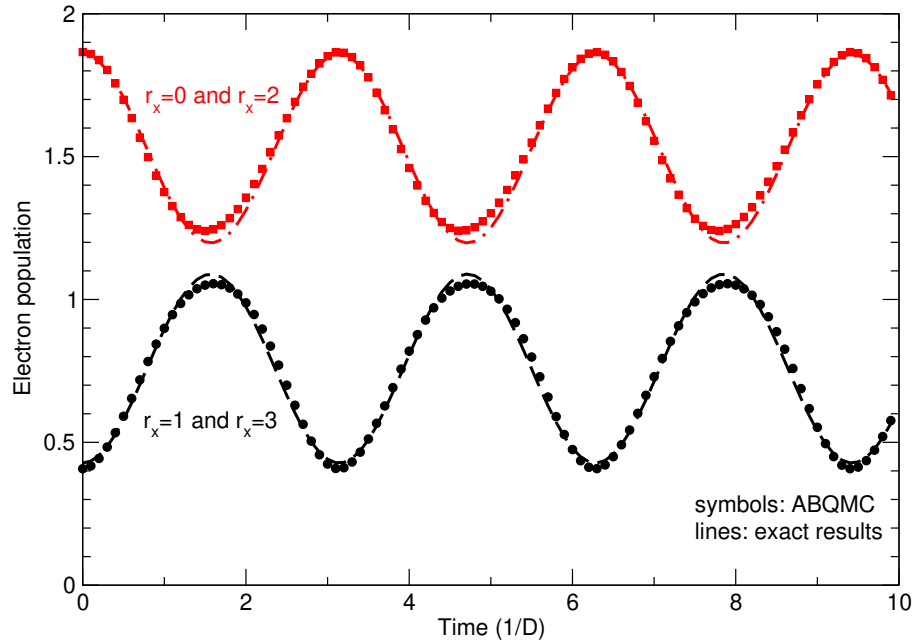


Figure S18. Time-dependent site populations of the Hubbard tetramer with the following values of model parameters:  $\mu/D = 0.65$ ,  $V_0/D = 1$ ,  $U = 0$ ,  $T/D = 0.285$ . The external potential at  $t < 0$  is  $v_{r_x} = V_0 \cos(\pi r_x)$  with  $r_x = 0, 1, 2, 3$ .

We conclude this section by applying the ABQMC algorithm to interacting electrons. We first discuss the Hubbard dimer in the canonical ensemble, where we can obtain converged results with as many as  $2N_t + N_\tau = 12$  slices in total at half-filling ( $N_\uparrow = N_\downarrow = 1$ ). The results are presented in Fig. S19. We observe that ABQMC results qualitatively reproduce the exact result in the whole time window considered. The quantitative agreement is reasonable up to  $Dt \approx 2$ . Figure S20 presents results for the Hubbard tetramer in the grand-canonical ensemble, where we obtain converged results using only  $N_t = 1$  and  $N_\tau = 2$ . Further increase in  $N_t$  reduces the average sign by orders of magnitude: for  $N_t = 1$ ,  $N_\tau = 2$  we obtain  $|\langle \text{sgn} \rangle| = 1.2 \times 10^{-2}$ , while for  $N_t = 2$ ,  $N_\tau = 2$  we find  $|\langle \text{sgn} \rangle| \sim 10^{-4}$ .



While  $N_\tau = 2$  is enough to reproduce equilibrium populations in the external field at  $t = 0$ , a single real-time slice leads to the quantitative agreement between the ABQMC and exact results only at shortest times.

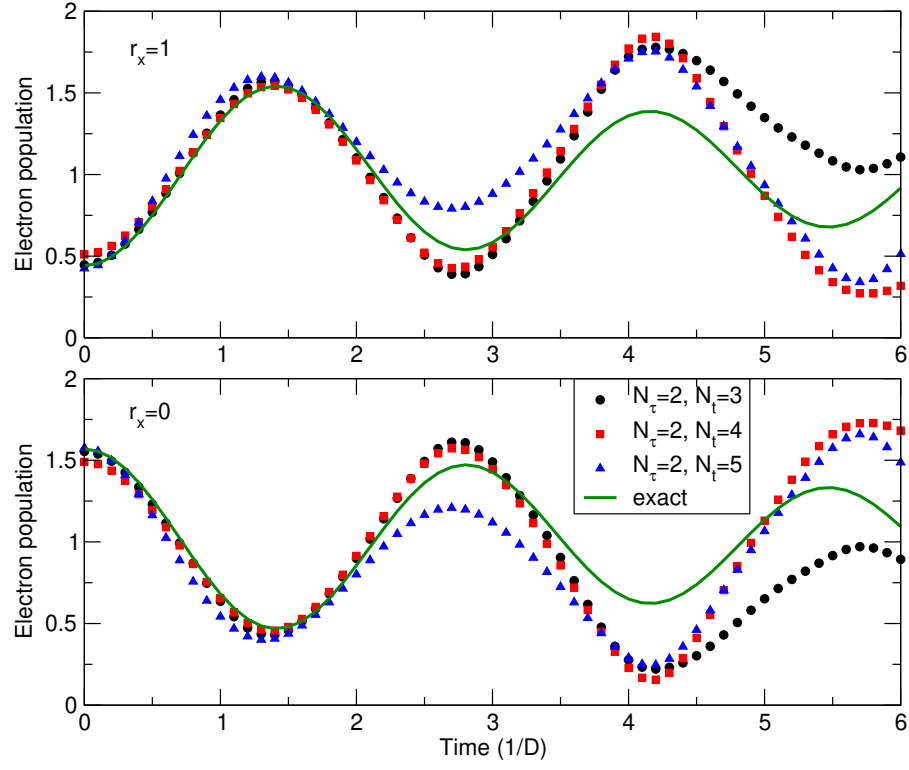


Figure S19. Dynamics of electron populations on individual sites of the Hubbard dimer that at  $t < 0$  is subjected to the density-modulating potential  $v_{r_x} = V_0 \cos(\pi r_x)$  with  $r_x = 0, 1$ . We work in the canonical ensemble with  $N_\uparrow = N_\downarrow = 1$ . The model parameters assume the following values:  $V_0/D = 1$ ,  $U/D = 0.6$ ,  $T/D = 0.45$ .

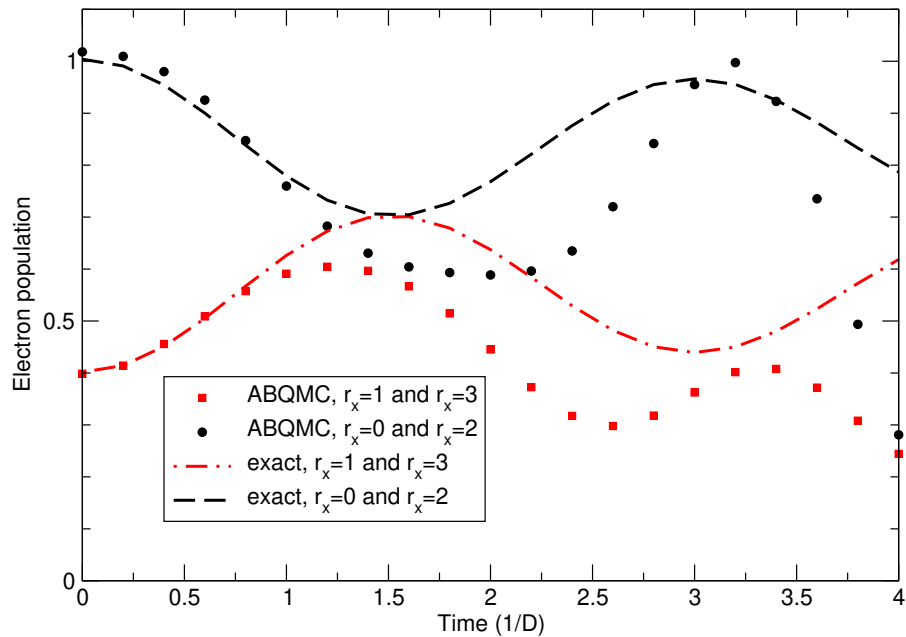


Figure S20. Dynamics of electron populations on individual sites of the Hubbard tetramer that at  $t < 0$  is subjected to the density-modulating potential  $v_{r_x} = V_0 \cos(\pi r_x)$  with  $r_x = 0, 1, 2, 3$ . We work in the grand-canonical ensemble with  $N_t = 1$ ,  $N_\tau = 2$  ( $2N_t + N_\tau = 4$  slices in total), and the following values of model parameters:  $\mu/D = -0.325$ ,  $V_0/D = 0.5$ ,  $U/D = 0.5$ ,  $T/D = 0.5$ .

## REFERENCES

<sup>1</sup>This follows from the cyclic invariance under the trace.

<sup>2</sup>E. Khatami and M. Rigol, “Thermodynamics of strongly interacting fermions in two-dimensional optical lattices,” *Phys. Rev. A* **84**, 053611 (2011).

<sup>3</sup>P. T. Brown, D. Mitra, E. Guardado-Sanchez, R. Nourafkan, A. Reymbaut, C.-D. Hébert, S. Bergeron, A.-M. S. Tremblay, J. Kokalj, D. A. Huse, P. Schauss, and W. S. Bakr, “Bad metallic transport in a cold atom Fermi-Hubbard system,” *Science* **363**, 379–382 (2019).

**Mott domain walls: A (strongly) non-Fermi liquid state of matter**Tsung-Han Lee<sup>1,2</sup>, J. Vučičević,<sup>3</sup> D. Tanasković,<sup>3</sup> E. Miranda<sup>4</sup>, and V. Dobrosavljević<sup>1</sup><sup>1</sup>*Department of Physics and National High Magnetic Field Laboratory, Florida State University, Tallahassee, Florida 32306, USA*<sup>2</sup>*Physics and Astronomy Department, Rutgers University, Piscataway, New Jersey 08854, USA*<sup>3</sup>*Institute of Physics Belgrade, University of Belgrade, Pregrevica 118, 11080 Belgrade, Serbia*<sup>4</sup>*Gleb Wataghin Physics Institute, The University of Campinas, Rua Sérgio Buarque de Holanda, 777, CEP 13083-859, Campinas, Brazil*

(Received 24 November 2021; revised 19 September 2022; accepted 20 September 2022; published 3 October 2022)

Most Mott systems display a low-temperature phase coexistence region around the metal-insulator transition. The domain walls separating the respective phases have very recently been observed displaying unusual properties both in simulations and in experiments. First, they often cover a significant volume fraction, thus cannot be neglected. Second, they resemble neither a typical metal nor a standard insulator, displaying unfamiliar temperature dependence of (local) transport properties. Here we take a closer look at such domain wall matter by examining an appropriate unstable solution of the Hubbard model. We show that transport in this regime is dominated by the emergence of “resilient quasiparticles” displaying strong non-Fermi liquid features, reflecting the quantum-critical fluctuations in the vicinity of the Mott point.

DOI: [10.1103/PhysRevB.106.L161102](https://doi.org/10.1103/PhysRevB.106.L161102)

**Introduction.** The Mott metal-insulator transition [1,2] remains a subject of much controversy and debate, with disagreement even concerning the physical mechanism [3] that dominates its vicinity. One popular viewpoint [4] regards it as a (strictly) second-order phase transition at  $T = 0$ , where the dominant degrees of freedom are the intersite spin singlets (e.g. the “spinon” excitations) arising in the vicinity of the Mott insulating state. A complementary dynamical mean-field theory (DMFT) perspective [5] builds on the seminal ideas of Hubbard and Mott, focusing on local Kondo-like processes that govern the condensation [6] of the strongly correlated Fermi liquid on the metallic side. The latter viewpoint predicts that the “evaporation” of the electron liquid at the transition bears some analogy to conventional liquid-gas transitions, with a phase coexistence region arising at low temperatures [5]. While many experiments [7,8] indeed reported the predicted first-order transition within the paramagnetic phase, other experiments [9,10] reported behavior consistent with quantum criticality, which sometimes has been interpreted in terms of the former picture [4].

Resolving this important issue in the context of real materials is further complicated by the emergence of various magnetic, charge, or orbital orders in the vicinity of the Mott point [2], which can often mask the basic underlying mechanism. Recent experimental work, however, has successfully identified [11] a simpler class of model systems, where no broken symmetry phases have been observed anywhere in the phase diagram. This situation is best documented in “spin-liquid” organic materials [12], where careful and precise experiments are starting to paint a clearer picture of the genuine Mott point. Most remarkably, experiments here provided [13] clear evidence for quantum critical scaling [14] of the resistivity curves at intermediate temperatures, with some evidence for a resistivity jump at  $T < T_c \sim 30\text{K}$ , consistent with

the DMFT prediction of a weakly first-order transition [15]. Still, direct evidence of the phase coexistence has emerged only in the recent reports of a colossal enhancement of the dielectric response [16] and the previous near-field infrared imaging [17].

In parallel with the experimental progress, recent theoretical work provided complementary insight into the nature of the metal-insulator coexistence region [18]. Surprisingly “thick” domain walls were observed [19], which are likely to play a central role in governing the observable response in experiments. Indeed, the local transport properties of such domain walls were found [18,19] to display a variety of unusual features, with properties not akin to either those of the conventional metal nor of the insulator. To obtain clear and precise insight into the physical nature of such domain wall matter (DWM), we present in this paper model calculations within the framework of the DMFT picture. We argue that, similarly to conventional Landau theories for domain walls, the *central region* of a domain wall corresponds to a “saddle point” (unstable solution) of the spatially uniform DMFT equations, at the top of the free-energy barrier separating the two competing phases [20,21]. In dramatic contrast to the conventional Landau theory (e.g., for the Ising model), here the two solutions are *not* related by symmetry and display very different physical behavior [22–24]. One is a Fermi liquid metal with coherent quasiparticles (QP) and  $T^2$  resistivity, whereas the other is a Mott insulator with completely incoherent activated transport. What, then, should be the physical properties of the unstable solution separating them? Should it resemble more closely a metal or a Mott insulator? What are the thermal properties of transport in this unfamiliar regime? As a matter of fact, it is almost impossible to guess. Previous studies of the unstable solution were restricted only to the near vicinity of the critical end point ( $T \sim T_c$ ) [25–27], but they did

not provide clear insight as to what happens through the phase coexistence region.

In this paper we present a clear and yet somewhat surprising answer to all these important questions, in a setup which can be considered as a (numerically) exact solution of one of the simplest toy models of strong correlations. Based on a reliable numerical solution of the corresponding DMFT equations we establish that (1) transport in DWM assumes resilient quasiparticle (RQP) character [28,29] throughout the coexistence region; and (2) the relevant RQPs display surprising non-Fermi liquid  $T$ -dependence of the QP parameters (see below). These results firmly establish that DWM is a qualitatively different form of matter, which we associate with quantum critical fluctuations around the Mott point.

*Model calculations.* To describe the Mott metal-insulator transition (MIT), while suppressing all forms of magnetic orders, we focus on the maximally frustrated Hubbard model [5,14,30], given by the Hamiltonian,

$$H = - \sum_{\langle i,j \rangle \sigma} t_{ij} (c_{i\sigma}^\dagger c_{j\sigma} + \text{H.c.}) + U \sum_i n_{i\uparrow} n_{i\downarrow}, \quad (1)$$

where  $c_{i\sigma}^\dagger$  and  $c_{i\sigma}$  are the electron creation and annihilation operators,  $n_{i\sigma} = c_{i\sigma}^\dagger c_{i\sigma}$ ,  $t_{ij}$  are the hopping elements with zero average and variance  $\langle t_{ij}^2 \rangle = t^2 / \sqrt{N}$ , and  $U$  is the onsite Coulomb potential. The energy unit is set to the half band width,  $D = 2t$ . Similarly to the popular Sachdev-Ye-Kitaev (SYK) model [31], such an infinite-range model can be exactly solved in the limit where the number of sites  $N \rightarrow \infty$ . In this case, this is performed through self-consistently solving an Anderson impurity model using the DMFT framework [5]. To solve the impurity problem, we utilize well-known continuous time quantum Monte Carlo (CTQMC) methods as well as iterative perturbation theory (IPT) as impurity solvers [32,33]. The analytical continuation to the real-frequency axis is done using the maximum entropy method (MEM), the fifth-order polynomial fitting for CTQMC, and the Padé approximant for IPT [34,35]. The use of an appropriate  $N$ -dimensional optimizer [26] is essential for the convergence to the local saddle point of the free-energy functional (the unstable solution). In addition, an appropriate free-energy analysis [23,36] allows us to identify the first-order transition line, as well as the location of the unstable solution.

The DMFT phase diagram (obtained from IPT), Fig. 1(a), features a second-order critical end point at  $T = T_c \sim 0.045$ . Below  $T_c$ , there emerges a phase coexistence region confined by two spinodal lines  $U_{c1}(T)$  and  $U_{c2}(T)$ , marking the respective instabilities of the Mott insulator and the metallic solutions. At  $T = 0$ , the first-order transition line merges with the spinodal line  $U_{c2}(T)$ , and the insulating solution becomes marginally unstable exactly at  $T = 0$  [36]. Above  $T_c$ ,  $U_{c1}(T)$  and  $U_{c2}(T)$  merge to form a single Widom line, determined from the minimum of the Landau free energy [14].

*Finding the unstable solution.* In order to understand the behavior of all three solutions of our DMFT theory (metal, insulator, and unstable), we employ the Landau free-energy functional method [23,36], which provides information about the form of the free-energy landscape. Within DMFT, the free energy can be considered as a functional of the local Green function,  $G(i\omega_n)$ , which for our model assumes the

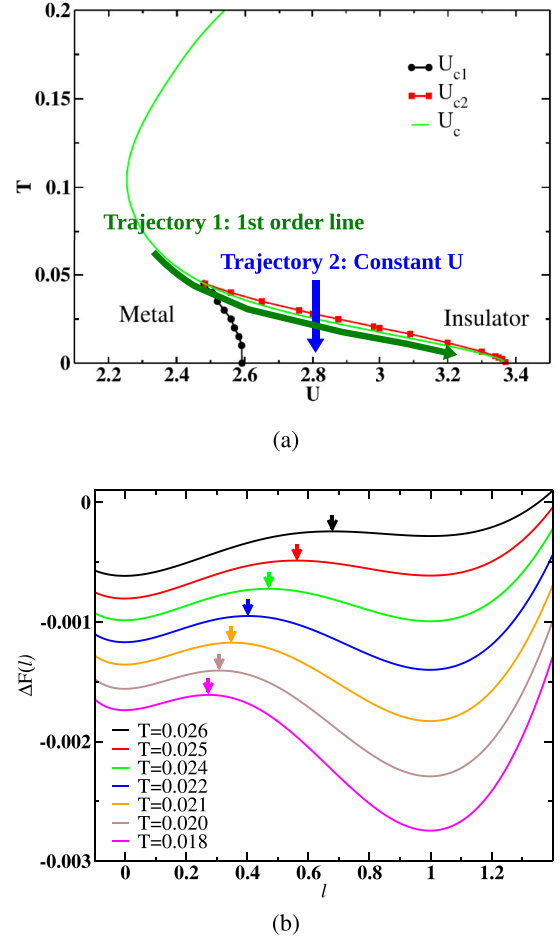


FIG. 1. (a) DMFT phase diagram for the half-filled Hubbard model and the trajectories studied (see text). (b) Evolution of the free-energy functional [36] as  $T$  varies for the fixed- $U$  trajectory ( $U = 2.83$ ). Here  $l = 0$  and  $l = 1$  correspond to the insulating and metallic solutions, respectively. The arrows mark the position of the unstable solutions.

form  $F[G] = F_{\text{imp}}[G] - t^2 T \sum_n G^2(i\omega_n)$ , where  $F_{\text{imp}}[G]$  is the free-energy functional of the associated impurity problem. When solving the DMFT equations by the standard iteration method, one finds convergence [36] to a given local minimum of the free-energy functional, depending on the initial guess for  $G(i\omega_n)$ . Within the coexistence region, two stable solutions separated by the unstable solution (saddle point) are found. To illustrate this, we follow a “phase space path” [36] connecting the two solutions, which can be parameterized as  $G(l) = (1-l)G_{\text{ins}}(i\omega) + lG_{\text{metal}}(i\omega)$  with a parameter  $l \in [0, 1]$ . The corresponding variation of the free energy can be calculated [36] by evaluating the line integral  $\Delta F(l) = t^2 T \int_0^l dl' e_l \cdot \delta G[G(l')]$ , where  $e_l = (G_{\text{ins}} - G_{\text{metal}}) / |G_{\text{ins}} - G_{\text{metal}}|$  and  $\delta G = G_{\text{imp}}(G) - G$ . Here, the dot product denotes a trace over Matsubara frequencies and  $G_{\text{imp}}$  is the impurity Green function dependent on the initial condition of  $G$ .

The unstable solution we seek exists anywhere within the phase coexistence region. To be concrete, however, we examine its evolution following two specific trajectories: (1) along the first-order transition line (where the two stable solutions

have the same free energy); and (2) a trajectory where we vary  $T$  at constant  $U$ , Fig. 1(a). For illustration, in Fig. 1(b) we follow Ref. [36] and plot the free energy along trajectory (2) (constant  $U$ ). Here we observe how the unstable solution shifts towards the insulating solution as we lower the temperature and finally merges with the insulating solution at  $T = 0$ . This confirms that the insulating solution becomes unstable precisely at  $T = 0$  throughout the phase coexistence region.

To be able to precisely converge to the desired unstable solution, we should keep in mind that the standard iterative method (essentially a “steepest descent” method) can only find local minima of the free energy, i.e., only the stable solutions. Instead, we use the Broyden method, which can converge to any *extremum* of a given functional (including saddle points) [26], if the initial guess is sufficiently close to the given extremum. Indeed, we find that this method can efficiently converge even to the unstable solution within only a moderate number of iterations. We should stress that the unstable solution found in this way is generally not restricted to lie exactly on the phase space path connecting the two stable solutions, except very close to  $T = T_c$ . Still, Broyden-converging to the proper unstable solution is greatly facilitated by using the phase space path to estimate an appropriate initial guess for the root search.

*Resistivity calculations and quasiparticle transport.* To study the transport properties, we utilize the Kubo formula [29] for the DMFT-based DC conductivity,

$$\sigma = \sigma_0 \int d\epsilon \Phi(\omega) \int d\omega \left( -\frac{\partial f(\omega)}{\partial \omega} \right) A(\epsilon, \omega)^2, \quad (2)$$

where the spectral function  $A(\epsilon, \omega) = -(1/\pi) \text{Im}[\omega + \mu - \epsilon - \Sigma(\omega)]^{-1}$ ,  $\Phi(\omega) = \Phi(0)[1 - (\omega/D)^2]^{3/2}$ ,  $\sigma_0 = 2\pi e^2/\hbar$ , and  $f(\omega)$  is the Fermi distribution function. Here  $\Sigma(\omega)$  is obtained on the real axis using standard MEM for CTQMC and the Padé approximant for IPT. The resistivity is  $\rho = 1/\sigma$ . To normalize the resistivity, we use the Mott-Ioffe-Regel (MIR) limit  $\rho_{\text{MIR}} = \hbar D/e^2 \Phi(0)$ , which represents the scale where the scattering process becomes incoherent and the mean free path is comparable to the Fermi wavelength.

The resistivity calculation, based on Eq. (2), dramatically simplifies in the quasiparticle regime [28], where transport is dominated by only the leading low-energy excitations. Here the Green function can be approximated as  $G(\omega, \epsilon) \simeq \frac{Z}{\omega - Z\epsilon + i\Gamma_{QP}}$ , with the quasiparticle weight  $Z = (1 - \frac{\partial \text{Re}\Sigma(\omega)}{\partial \omega})_{\omega=0}^{-1}$  and scattering rate  $\Gamma_{QP} = -Z \text{Im}\Sigma(\omega=0)$ . A further Sommerfeld approximation can be performed in situations where  $\Gamma_{QP} < T$  and  $T < ZD$ , and the conductivity can be expressed in terms of only two parameters:  $Z$  and  $\Gamma = \Gamma_{QP}/Z$ , viz.,

$$\frac{\sigma}{\sigma_{\text{MIR}}} \approx \frac{1}{\Gamma} \tanh\left(\frac{Z}{2T}\right). \quad (3)$$

We explicitly checked that these conditions are indeed obeyed throughout the coexistence region, not only by our metallic solution, but also by the unstable solution. As we explicitly show below, the results obtained from numerically evaluating the conductivity using our full DMFT solution and Eq. (2) demonstrate remarkable qualitative and even semiquantitative agreement with our QP approximation. This important

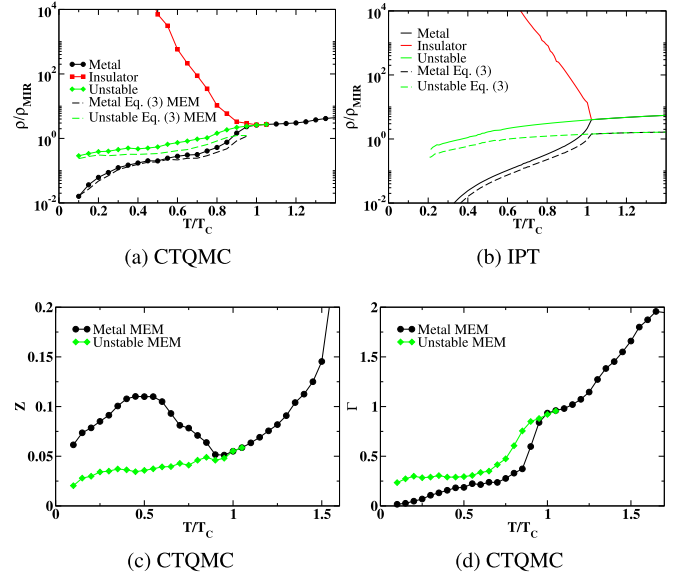


FIG. 2. The resistivity for the metallic (black circles), insulating (red squares), and unstable (green squares) solutions along the first-order transition line in a logarithmic  $\rho$  scale for (a) CTQMC and (b) IPT. The Sommerfeld approximations to the resistivities [Eq. (3)] are shown in the corresponding dashed and dotted lines with different analytic continuation methods (MEM for CTQMC and Padé approximant for IPT). (c) The quasiparticle weight  $Z$  for the metallic and unstable solutions analytic continued by MEM (black and green symbols). (d) The scattering rate  $\Gamma$ , for the metallic and the unstable solutions, obtained from MEM (black and green symbols).

result demonstrates the resilient quasiparticle character [29] of transport even for our unstable solution, despite the very unusual behavior of the QP parameters in question.

*Following the first-order transition line.* To investigate how our three solutions evolve when approaching the zero-temperature critical point  $U_{c2}(T=0)$ , we study the transport properties along the first-order transition line connecting the two critical points,  $U_c(T=T_c)$  and  $U_{c2}(T=0)$ . In Figs. 2(a) and 2(b) we show the results obtained from CTQMC and IPT, respectively. At the critical end point  $T = T_c$ , the three solutions merge as expected, and the resistivity is of the order of the MIR limit. Below  $T_c$ , the three solutions trifurcate into different trajectories. The unstable solution (green diamonds) displays higher resistivity than the metallic solution (black circles), with values of the order of the MIR limit,  $\rho \sim \rho_{\text{MIR}}$ , indicating bad metal behavior [37]. The insulating solution has much higher resistivity due to standard activated transport.

Close to the zero-temperature critical point  $U_{c2}(T=0)$  the three solutions do not merge, in contrast to the situation around the critical end point ( $T \sim T_c$ ). Instead, while the resistivity of the metallic solution drops at low temperatures, that of the unstable solution remains comparable to the MIR limit, suggesting incoherent transport, despite these trends being well captured by the QP approximation [see Figs. 2(a) and 2(b)]. To better understand this behavior, in Fig. 2(c) we show the quasiparticle weight  $Z$  for the unstable (green diamonds) and metallic (black circles) solutions. The unstable solution has significantly lower  $Z$  than the metal, displaying



a more pronounced decrease at low temperatures, reminiscent of resilient quasiparticles [29]. Note that the increase followed by the decrease of  $Z$  in the metallic solution may be attributed to the position of the first-order transition line in the coexistence region, which shifts towards the insulating phase with lowering the temperature. Similar behavior is seen in Fig. 2(d), where we display the behavior of the scattering rate  $\Gamma$ , which for the unstable solution (green diamonds) remains appreciable down to the lowest temperatures, again signaling poorly developed (resilient) quasiparticles. Remarkably, such non-Fermi Liquid (NFL) behavior here persists down to the lowest temperatures, in contrast to previously identified examples of RQPs [29], which emerged only at temperatures intermediate between the conventional Fermi liquid metal at the lowest  $T$  and a fully incoherent conductor at high  $T$ .

**Constant  $U$  trajectory.** In order to further understand the behavior of the unstable solution in the entire coexistence regime, we also study the resistivity as a function of  $T$  along a constant  $U$  trajectory. From the free-energy analysis, Fig. 1(b), we anticipate that the unstable solution gradually shifts towards the insulator as  $T$  is reduced at fixed  $U$ , eventually merging with it at  $T = 0$ . In contrast, in Figs. 3(a) and 3(b), we observe the metallic and insulating solutions displaying conventional Fermi liquid and activated behaviors, respectively. On the other hand, for the unstable solution, we find that the resistivity (green diamonds) increases as the temperature decreases, reaching values as much as two orders of magnitude larger than the MIR limit. Nevertheless, as shown in Figs. 3(c) and 3(d), we observe that the unstable solution's density of states (DOS) at the lowest temperature still features a very small quasiparticle peak at the Fermi level. This suggests that the unstable solution still retains some metallic character, even though the resistivity is much larger than the MIR limit. In some sense, this situation could be characterized as an extreme example of bad metal (BM) behavior [37], albeit in a setup which is dramatically different than the familiar high- $T$  BM behavior in correlated matter. And indeed, the standard RQP-Sommerfeld approximation again captures remarkably well all the transport trends, even in this extreme high-resistivity regime.

To even more precisely characterize such RQP-NFL behavior, we next examine the corresponding QP parameters and their evolution as a function of  $T$ . In Fig. 3(e) we show the quasiparticle weight for  $Z$  for metallic (black circles) and unstable (green diamonds) solutions. The metal has a normal behavior with  $Z$  saturating at low temperatures, consistent with the expected FL behavior. In dramatic contrast,  $Z$  corresponding to the unstable solution decreases rapidly with temperature, displaying power-law behavior  $Z \sim T^2$ . Remarkably, a similar but much weaker decrease of the form  $Z \sim 1/|\log T|$ , dubbed a ‘marginal Fermi liquid’ (MFL) [38], was proposed as the key signature of the breakdown of Fermi liquid theory in optimally doped cuprates. The behavior found here is not even marginal. By analogy, it can be described as ‘fully developed NFL’ behavior, the like of which is seldom seen in correlated matter. Analogously, the unstable solution's scattering rate *increases* at low temperatures [Fig. 3(f)], again in power-law fashion  $\Gamma \sim 1/T^2$ , well exceeding the MIR limit and consistent with transport.

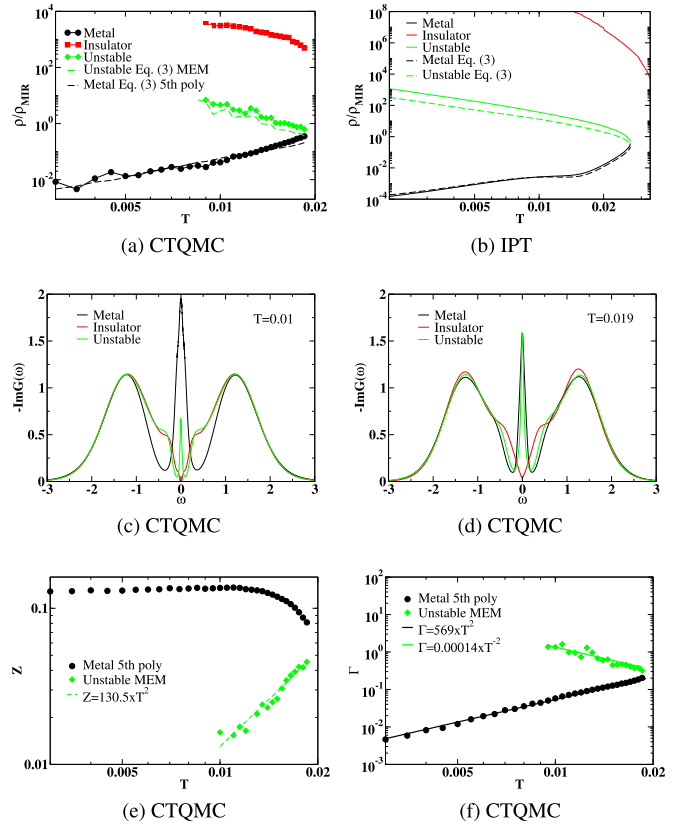


FIG. 3. The resistivity for the metallic (black circles), insulating (red squares), and unstable (green diamonds) solutions along the constant  $U$  trajectory in logarithmic  $\rho$  scale for (a) CTQMC and (b) IPT. The Sommerfeld approximations to the resistivities [Eq. (3)] are shown in the corresponding dashed and dotted lines with different analytic continuation methods (MEM and polynomial fitting for CTQMC and Padé approximant for IPT). The density of states at low temperatures (c)  $T = 0.01$  and (d)  $T = 0.019$  near the spinodal line  $U_{c2}$  computed from the CTQMC impurity solver and MEM analytic continuation. (e) The quasiparticle weight  $Z$  for the metallic and the unstable solutions. (f) The scattering rate  $\Gamma$  for the metallic and the unstable solutions.

**Conclusions.** In this paper, we identified what may be a new state of correlated electronic matter, characterizing the domain walls within the metal-insulator coexistence region around the Mott point. We showed that its low-energy excitations display a number of unusual properties which qualitatively differ from either a conventional metal or an insulator. This paints a physical picture of exotic quasiparticles barely persisting at the brink of an insulating state. Conceptually, such non-Fermi liquid behavior can be viewed as reflecting the quantum critical fluctuations associated with the metal-insulator transition region.

Our solution was obtained within the framework of single-site DMFT theory, which physically represents the limit of large frustration, where all possible symmetry-breaking fluctuations are suppressed. The MIT coexistence region, however, is presently known [16] to persist in real physical systems such as quasi-two-dimensional Mott organics, where intersite spin correlations could also play a role [39]. The



effects of such perturbations can be systematically studied within cluster-DMFT theories [36,40], with indications that the phase coexistence region can be significantly influenced. Nevertheless, we expect the short-range correlation effects will only modify quantitatively the behavior of the unstable solutions revealed in this work. Interesting modifications can also arise by introducing extrinsic disorder due to impurities and defects, which in some cases can significantly reduce the size of the entire coexistence region [41,42]. How these perturbations will affect the stability and the relevance of the domain wall matter we discussed here is a fascinating open problem which remains a challenge for future experiments as well as theory.

*Acknowledgments.* The work was supported in Brazil by CNPq through Grant No. 307041/2017-4 and Capes through Grant No. 0899/2018 (E.M.). Work in Florida (V.D. and T.-H.L.) was supported by NSF Grant No. 1822258, and the National High Magnetic Field Laboratory through NSF Cooperative Agreement No. 1157490 and the State of Florida. J.V. and D.T. acknowledge funding provided by the Institute of Physics Belgrade through a grant by the Ministry of Education, Science, and Technological Development of the Republic of Serbia. Numerical simulations were performed on the PARADOX supercomputing facility at the Scientific Computing Laboratory, National Center of Excellence for the Study of Complex Systems, Institute of Physics Belgrade.

- [1] N. F. Mott, *Metal-Insulator Transition* (Taylor and Francis, London, 1990).
- [2] M. Imada, A. Fujimori, and Y. Tokura, *Rev. Mod. Phys.* **70**, 1039 (1998).
- [3] V. Dobrosavljević, N. Trivedi, and J. M. Valles, Jr., *Conductor Insulator Quantum Phase Transitions* (Oxford University Press, 2012).
- [4] T. Senthil, *Phys. Rev. B* **78**, 045109 (2008).
- [5] A. Georges, G. Kotliar, W. Krauth, and M. J. Rozenberg, *Rev. Mod. Phys.* **68**, 13 (1996).
- [6] A. Pustogow, Y. Saito, A. Löhle, M. S. Alonso, A. Kawamoto, V. Dobrosavljević, M. Dressel, and S. Fratini, *Nat. Commun.* **12**, 1571 (2021).
- [7] P. Limelette, A. Georges, D. Jerome, P. Wzietek, P. Metcalf, and J. M. Honig, *Science* **302**, 89 (2003).
- [8] F. Kagawa, K. Miyagawa, and K. Kanoda, *Nature (London)* **436**, 534 (2005).
- [9] T. Furukawa, K. Kobashi, Y. Kurosaki, K. Miyagawa, and K. Kanoda, *Nat. Commun.* **9**, 307 (2018).
- [10] T. Li, S. Jiang, L. Li, Y. Zhang, K. Kang, J. Zhu, K. Watanabe, T. Taniguchi, D. Chowdhury, L. Fu *et al.*, *Nature (London)* **597**, 350 (2021).
- [11] Y. Kurosaki, Y. Shimizu, K. Miyagawa, K. Kanoda, and G. Saito, *Phys. Rev. Lett.* **95**, 177001 (2005).
- [12] M. Dressel and S. Tomic, *Adv. Phys.* **69**, 1 (2020).
- [13] T. Furukawa, K. Miyagawa, H. Taniguchi, R. Kato, and K. Kanoda, *Nat. Phys.* **11**, 221 (2015).
- [14] H. Terletska, J. Vučičević, D. Tanasković, and V. Dobrosavljević, *Phys. Rev. Lett.* **107**, 026401 (2011).
- [15] J. Vučičević, H. Terletska, D. Tanasković, and V. Dobrosavljević, *Phys. Rev. B* **88**, 075143 (2013).
- [16] A. Pustogow, R. Rösslhuber, Y. Tan, E. Uykur, A. Böhme, M. Wenzel, Y. Saito, A. Löhle, R. Hübner, A. Kawamoto *et al.*, *npj Quantum Mater.* **6**, 9 (2021).
- [17] M. M. Qazilbash, M. Brehm, B.-G. Chae, P.-C. Ho, G. O. Andreev, B.-J. Kim, S. J. Yun, A. V. Balatsky, M. B. Maple, F. Keilmann *et al.*, *Science* **318**, 1750 (2007).
- [18] M. Y. Suárez-Villagrán, N. Mitsakos, T.-H. Lee, V. Dobrosavljević, J. H. Miller, and E. Miranda, *Phys. Rev. B* **101**, 235112 (2020).
- [19] M. Y. Suárez-Villagrán, N. Mitsakos, T.-H. Lee, J. H. Miller, E. Miranda, and V. Dobrosavljević, *Phys. Rev. B* **104**, 155114 (2021).
- [20] P. M. Chaikin and T. C. Lubensky, *Principles of Condensed Matter Physics* (Cambridge University, Cambridge, 1995).
- [21] See Supplemental Material at <http://link.aps.org/supplemental/10.1103/PhysRevB.106.L161102> for Ginzburg-Landau theory of domain-wall in dynamical mean-field theory.
- [22] G. Kotliar, *Eur. Phys. J. B* **11**, 27 (1999).
- [23] G. Kotliar, E. Lange, and M. J. Rozenberg, *Phys. Rev. Lett.* **84**, 5180 (2000).
- [24] S. Onoda, *arXiv:cond-mat/0408207* (2004).
- [25] N.-H. Tong, S.-Q. Shen, and F.-C. Pu, *Phys. Rev. B* **64**, 235109 (2001).
- [26] H. U. R. Strand, A. Sabashvili, M. Granath, B. Hellsing, and S. Östlund, *Phys. Rev. B* **83**, 205136 (2011).
- [27] M. J. Rozenberg, R. Chitra, and G. Kotliar, *Phys. Rev. Lett.* **83**, 3498 (1999).
- [28] W. Xu, K. Haule, and G. Kotliar, *Phys. Rev. Lett.* **111**, 036401 (2013).
- [29] X. Deng, J. Mravlje, R. Žitko, M. Ferrero, G. Kotliar, and A. Georges, *Phys. Rev. Lett.* **110**, 086401 (2013).
- [30] V. Dobrosavljević and G. Kotliar, *Phys. Rev. Lett.* **71**, 3218 (1993).
- [31] D. Chowdhury, A. Georges, O. Parcollet, and S. Sachdev, *Rev. Mod. Phys.* **94**, 035004 (2022).
- [32] E. Gull, A. J. Millis, A. I. Lichtenstein, A. N. Rubtsov, M. Troyer, and P. Werner, *Rev. Mod. Phys.* **83**, 349 (2011).
- [33] H. Kajuter and G. Kotliar, *Phys. Rev. Lett.* **77**, 131 (1996).
- [34] H. J. Vidberg and J. W. Serene, *J. Low Temp. Phys.* **29**, 179 (1977).
- [35] M. Jarrell and J. Gubernatis, *Phys. Rep.* **269**, 133 (1996).
- [36] G. Moeller, V. Dobrosavljević, and A. E. Ruckenstein, *Phys. Rev. B* **59**, 6846 (1999).
- [37] N. E. Hussey, K. Takenaka, and H. Takagi, *Philos. Mag.* **84**, 2847 (2004).
- [38] C. M. Varma, P. B. Littlewood, S. Schmitt-Rink, E. Abrahams, and A. E. Ruckenstein, *Phys. Rev. Lett.* **63**, 1996 (1989).
- [39] B. Miksch, A. Pustogow, M. J. Rahim, A. A. Bardin, K. Kanoda, J. A. Schlueter, R. Hübner, M. Scheffler, and M. Dressel, *Science* **372**, 276 (2021).
- [40] M. Balzer, B. Kyung, D. Sénéchal, A.-M. S. Tremblay, and M. Potthoff, *Europhys. Lett.* **85**, 17002 (2009).
- [41] M. Urai, T. Furukawa, Y. Seki, K. Miyagawa, T. Sasaki, H. Taniguchi, and K. Kanoda, *Phys. Rev. B* **99**, 245139 (2019).
- [42] R. Yamamoto, T. Furukawa, K. Miyagawa, T. Sasaki, K. Kanoda, and T. Itou, *Phys. Rev. Lett.* **124**, 046404 (2020).

# Supplemental Material: Mott domain walls: a (strongly) non-Fermi liquid state of matter

Tsung-Han Lee,<sup>1,2</sup> J. Vučičević,<sup>3</sup> D. Tanasković,<sup>3</sup> E. Miranda,<sup>4</sup> and V. Dobrosavljević<sup>1</sup>

<sup>1</sup>*Department of Physics and National High Magnetic Field Laboratory,  
Florida State University, Tallahassee, Florida 32306, USA*

<sup>2</sup>*Physics and Astronomy Department, Rutgers University, Piscataway, New Jersey 08854, USA*

<sup>3</sup>*Institute of Physics Belgrade, University of Belgrade, Pregrevica 118, 11080 Belgrade, Serbia*

<sup>4</sup>*Gleb Wataghin Physics Institute, The University of Campinas,  
Rua Sérgio Buarque de Holanda, 777, CEP 13083-859, Campinas, Brazil*

In this Supplemental Material, we review, in Sec. I, the Ginzburg-Landau theory and the  $\phi^4$  theory for dynamical mean-field theory (DMFT) following Refs. [1–3] and the domain-wall solutions in the inhomogeneous Ginzburg-Landau theory. In Sec. II, we provide a detailed comparison of different analytic continuation results for the quasiparticle parameters and transport properties.

## I. GINZBURG-LANDAU THEORY FOR DYNAMICAL MEAN-FIELD THEORY

We start from the Ginzburg-Landau free energy functional for DMFT [1]

$$F_{\text{GL}}[G] = F_{\text{imp}}[G] - \frac{t^2 T}{2} \sum_n G^2(i\omega_n). \quad (1)$$

Then, we expand the free energy functional around the critical point  $\delta G = G - G_{\text{cr}}$  leading to

$$F_{\text{GL}} = F_{\text{GL}}^{(0)} + F_{\text{GL}}^{(1)} + F_{\text{GL}}^{(2)} + F_{\text{GL}}^{(3)} + F_{\text{GL}}^{(4)}, \quad (2)$$

where

$$F_{\text{GL}}^{(0)} = F_{\text{GL}}[G_{\text{cr}}], \quad (3)$$

$$F_{\text{GL}}^{(l)} = \frac{T}{l} \sum_{k_1, \dots, k_l} \Gamma_{k_1, \dots, k_l}^{(l)}[G_{\text{cr}}] \prod_{j=1}^l \delta G_{k_j}, \quad (4)$$

$$\Gamma_{k_1, \dots, k_l}^{(l)}[G] = \frac{1}{T} \frac{l}{l!} \left( \prod_{j=1}^l \frac{\delta}{\delta G_{k_j}} \right) F_{\text{GL}}[G], \quad (5)$$

$k \equiv (\mathbf{k}, i\omega_n)$  is the momentum and frequency index, and  $F_{\text{GL}}^{(1)} = 0$  from the DMFT self-consistency condition.

### A. $\phi^4$ -model for dynamical mean-field theory

The DMFT Ginzburg-Landau functional can be mapped to a  $\phi^4$ -model around the critical point [2, 3]. We write

$$\sum_{k_2} \Gamma_{k_1 k_2}^{(2)}[G_{\text{cr}}] \Psi_{\lambda, k_2 p} = \Psi_{\lambda, p k_1} \gamma_{\lambda, p}^{(2)}, \quad (6)$$

where  $\Psi_{\lambda, k_1 p}$  and  $\gamma_{\lambda, p}^{(2)}$  is the eigenbasis and the eigenvalues of  $\Gamma_{k_1 k_2}^{(2)}$ , respectively, and  $\lambda$  labels the eigenmodes. We then introduce the  $\phi_{\lambda, p}$  defined by

$$\delta G_k = \sum_{\lambda, p} \Psi_{\lambda, k p} \phi_{\lambda, p}, \quad (7)$$

such that the Ginzburg-Landau free energy can be written in the eigenbasis as

$$F_{\text{GL}}^{(2)} = \frac{T}{2} \sum_P \gamma_P^{(2)} |\phi_P|^2 \quad (8)$$

$$F_{\text{GL}}^{(3)} = \frac{T}{3} \sum_{P_1 P_2 P_3} \gamma_{P_1 P_2 P_3}^{(3)} \phi_{P_1} \phi_{P_2} \phi_{P_3} \quad (9)$$

$$F_{\text{GL}}^{(4)} = \frac{T}{4} \sum_{P_1 \dots P_4} \gamma_{P_1 P_2 P_3 P_4}^{(4)} \phi_{P_1} \phi_{P_2} \phi_{P_3} \phi_{P_4}, \quad (10)$$

where  $P \equiv (\lambda, p)$  and

$$\gamma_{P_1 \dots P_l}^{(l)} = \sum_{k_1 \dots k_l} \Gamma_{k_1 \dots k_l}^{(l)} [G_{\text{cr}}] \prod_{j=1}^l \Psi_{\lambda_j, k_j P_j}. \quad (11)$$

As pointed out in Refs. [1–3], the critical behavior is dominated by the soft eigenmode so we can project the free energy functional to this specific eigenbasis. Focusing on the static and uniform part of the free energy function, we can write down the  $\phi^4$ -model for DMFT

$$\frac{F_{\text{GL}}}{T} = \frac{1}{2} \sum_p \gamma_p^{(2)} \phi_p^2 + \frac{1}{3} \sum_{p_1 p_2 p_3} \gamma_{p_1 p_2 p_3}^{(3)} \phi_{p_1} \phi_{p_2} \phi_{p_3} + \frac{1}{4} \sum_{p_1 p_2 p_3 p_4} \gamma_{p_1 p_2 p_3 p_4}^{(4)} \phi_{p_1} \phi_{p_2} \phi_{p_3} \phi_{p_4}. \quad (12)$$

### B. Domain-wall solution

To interpret the domain-wall solution, we write the Ginzburg-Landau free energy in the real space

$$\frac{F_{\text{GL}}[\phi]}{T} = \int d\mathbf{x} \left\{ \frac{\kappa}{2} (\nabla \phi(\mathbf{x}))^2 + \frac{1}{2} \gamma^{(2)} \phi(\mathbf{x})^2 + \frac{\gamma^{(4)}}{4} \phi(\mathbf{x})^4 \right\}, \quad (13)$$

where the cubic term in Eq. 12 can be eliminated by properly shifting the field  $\phi$  [2, 3]. The Euler-Lagrange equation of  $F_{\text{GL}}$  is

$$\gamma^{(2)} \phi(\mathbf{x}) + \gamma^{(4)} \phi(\mathbf{x})^3 - \kappa \nabla^2 \phi(\mathbf{x}) = 0. \quad (14)$$

For simplicity we consider the domain-wall forms along the x-direction, so the Euler-Lagrange equation becomes

$$\gamma^{(2)} \phi(x) + \gamma^{(4)} \phi(x)^3 - \kappa \phi''(x) = 0. \quad (15)$$

with the boundary condition  $\phi(x \rightarrow -\infty) = -\phi_0$  and  $\phi(x \rightarrow \infty) = \phi_0$  and  $\phi_0 = \sqrt{-\gamma^{(2)}/\gamma^{(4)}}$ . Note that the uniform saddle-point solution  $\phi_0$  can be related to the double occupancy or the density of states at the Fermi level, where the positive and negative values of  $\phi_0$  correspond to the metallic and the insulating solutions, respectively [2]. One can show that the inhomogeneous domain-wall solution is [4]

$$\phi(x) = \phi_0 \tanh\left[\frac{x}{\sqrt{2}\xi}\right], \quad (16)$$

where  $\xi = \sqrt{-\kappa/\gamma^{(2)}}$  is the correlation length. We can see that the domain-wall solution at  $\phi(x) = 0$  corresponds to the local maximum of the uniform Landau free energy

$$f[\phi] = \frac{1}{2} \gamma^{(2)} \phi^2 + \frac{\gamma^{(4)}}{4} \phi^4 \quad (17)$$

shown schematically in Fig. 1.

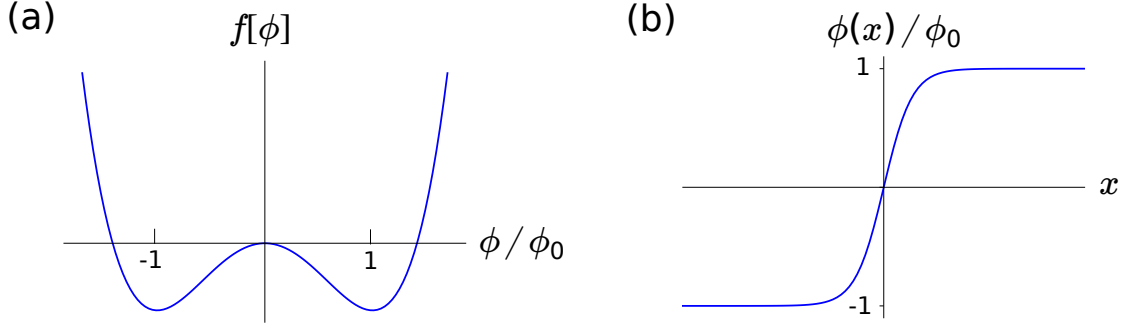


FIG. 1. (a) Schematic Landau free energy  $f[\phi]$  as a function of  $\phi$ . (b) Schematic domain-wall solution profile  $\phi(x)$  as a function of  $x$ .

## II. COMPARISON OF MAXIMUM ENTROPY METHOD AND POLYNOMIAL FITTING ANALYTIC CONTINUATION

In this section, we compare the quasiparticle and transport properties obtained from two analytic continuation approaches: maximum entropy method (MEM) and fifth-order polynomial fitting.

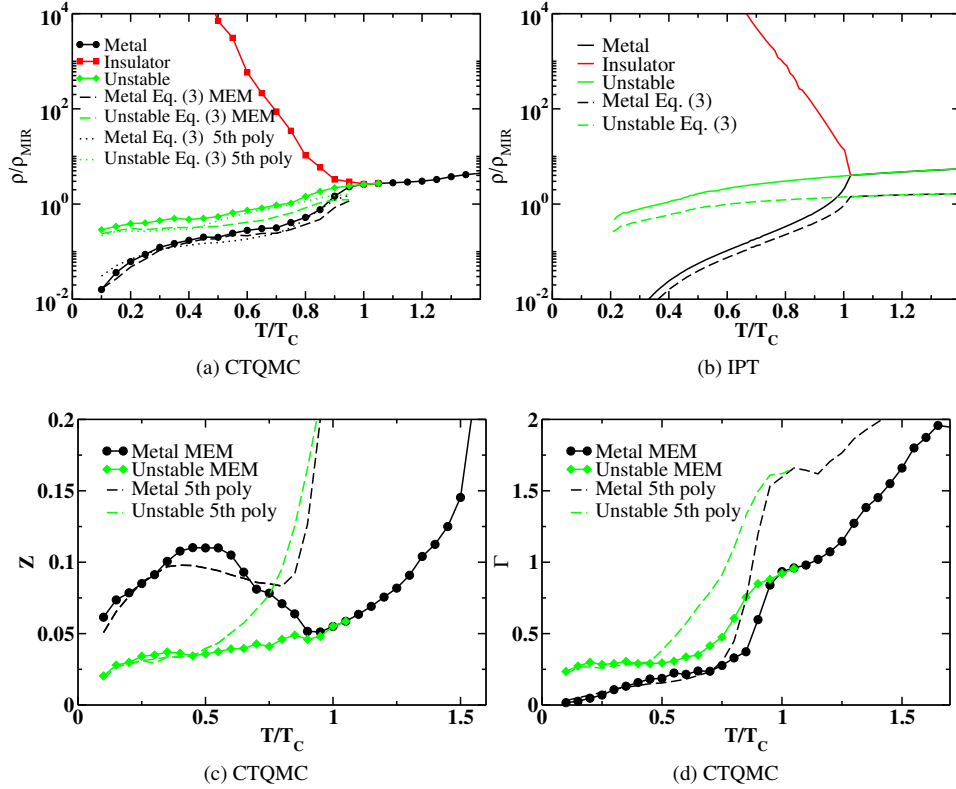


FIG. 2. The resistivity for the metallic (black circles), insulating (red squares), and unstable (green squares) solutions along the first-order transition line in a logarithmic  $\rho$  scale for (a) CTQMC and (b) IPT. The Sommerfeld approximations to the resistivities (Eq. (3)) are shown in the corresponding dashed and dotted lines with different analytic continuation methods (MEM and polynomial fitting for CTQMC and Padé approximation for IPT). (c) The quasiparticle weight,  $Z$ , for the metallic and unstable solutions analytic continued by MEM (black and green symbols) and by polynomial fitting (black and green dashed lines). (d) The scattering rate  $\Gamma$ , for the metallic and the unstable solutions, obtained from MEM (black and green symbols) and from polynomial fitting (black and green dashed lines).

First, we discuss the results along the first-order transition line. Figure 2(a) shows the resistivities computed from the Som-

merfeld approximation (Eq. (3) in the main text) using MEM and polynomial fitting analytic continuations. We see that the two analytic continuations agree at low temperatures. However, around  $T_c$ , the two methods show significant differences. This behavior is also observed in the quasiparticle weight  $Z$  (Fig. 2(c)) and the scattering rate  $\Gamma$  (Fig. 2(d)). The difference between the two analytic continuation methods stems from the breakdown of the polynomial fitting around  $T_c$ , where the polynomial fitting of the first few Matsubara points of the self-energy does not yield reliable quasiparticle parameters  $Z$  and  $\Gamma$ . Therefore, around  $T_c$ , one should trust the MEM results. On the other hand, the polynomial fitting should be more reliable at low temperatures, where the first few Matsubara points are enough to determine the quasiparticle parameters, whereas the MEM is noisier.

We now discuss the results of different analytic continuation approaches along a constant  $U$  trajectory. In Fig. 3(a), we show the resistivity calculated from the Sommerfeld approximation (Eq. (3) in the main text) using MEM and polynomial fitting analytic continuation. We observe that the two analytic continuation approaches give semi-quantitatively similar behavior. In Fig. 3(c), we show the quasiparticle weight  $Z$  calculated from the two analytic continuation approaches. We observe that the two analytic continuations give the same behavior for the metallic solutions quantitatively. Note that the polynomial fitting is expected to give a more reliable analytic continued  $Z$  at low temperature. On the other hand, for the unstable solutions, we see that the two analytic continuation approaches yield different powers where the polynomial fitting gives  $Z \sim T^{1.5}$  and MEM gives  $Z \sim T^2$ . Both differ significantly from the Fermi-liquid saturation behavior shown in the metallic solutions. Finally, in Fig. 3(d), we show the scattering rate  $\Gamma$  calculated from the two analytic continuation approaches. We observed that the two approaches give semi-quantitatively the same behavior with similar power,  $\Gamma \sim T^2$  for the metallic solutions and  $\Gamma \sim T^{-2}$  for the unstable solutions. We note that the polynomial fitting is expected to yield more reliable analytic continued  $\Gamma$  for the metallic solutions at low temperatures.

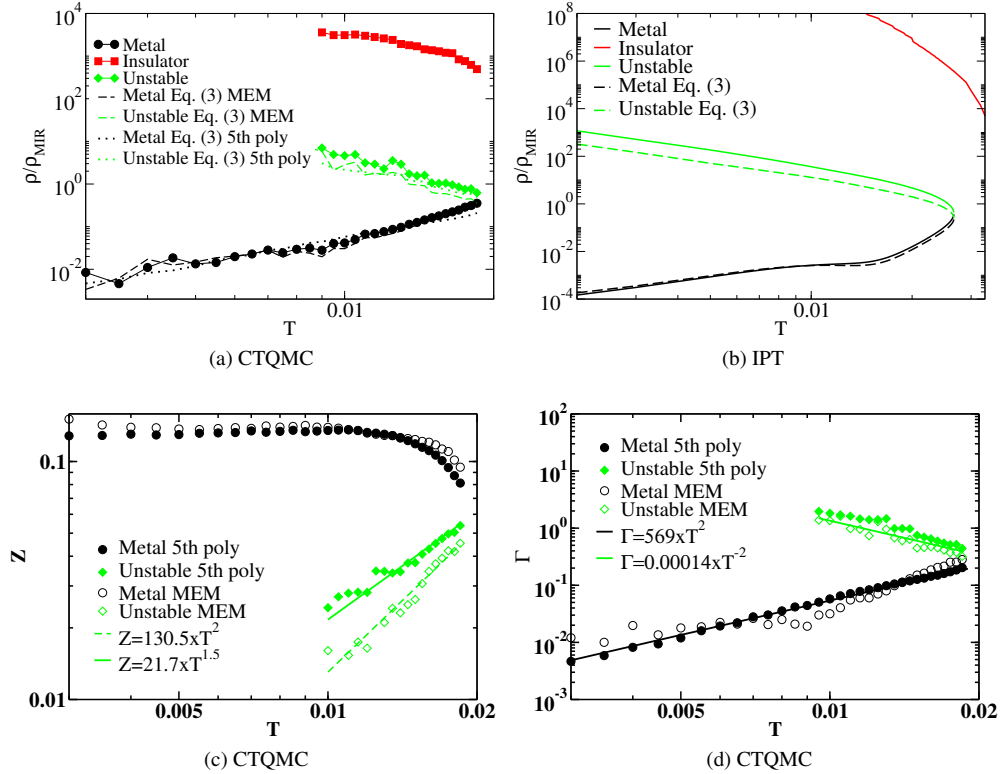


FIG. 3. The resistivity for the metallic (black circles), insulating (red squares), and unstable (green diamonds) solutions along the constant  $U$  trajectory in logarithmic  $\rho$  scale for (a) CTQMC and (b) IPT. The Sommerfeld approximations to the resistivities are shown in the corresponding dashed and dotted lines with different analytic continuation methods (MEM and polynomial fitting for CTQMC and Padé approximation for IPT). (c) The quasiparticle weight,  $Z$ , for the metallic and the unstable solutions. (d) The scattering rate  $\Gamma$  for the metallic and the unstable solutions.

## REFERENCES

---

- [1] Kotliar, G., Eur. Phys. J. B **11**, 27 (1999), URL <https://doi.org/10.1007/s100510050914>.
- [2] G. Kotliar, E. Lange, and M. J. Rozenberg, Phys. Rev. Lett. **84**, 5180 (2000), URL <https://link.aps.org/doi/10.1103/PhysRevLett.84.5180>.
- [3] S. Onoda (2004), URL <https://arxiv.org/abs/cond-mat/0408207>.
- [4] P. M. Chaikin and T. C. Lubensky, *Principles of Condensed Matter Physics* (Cambridge University Press, 1995).



# Universal Magnetic Oscillations of dc Conductivity in the Incoherent Regime of Correlated Systems

Jakša Vučičević<sup>1</sup> and Rok Žitko<sup>2,3</sup>

<sup>1</sup>*Scientific Computing Laboratory, Center for the Study of Complex Systems, Institute of Physics Belgrade, University of Belgrade, Pregrevica 118, 11080 Belgrade, Serbia*

<sup>2</sup>*Jožef Stefan Institute, Jamova 39, SI-1000 Ljubljana, Slovenia*

<sup>3</sup>*Faculty of Mathematics and Physics, University of Ljubljana, Jadranska 19, SI-1000 Ljubljana, Slovenia*



(Received 19 May 2021; revised 13 August 2021; accepted 21 September 2021; published 2 November 2021)

Using the dynamical mean field theory we investigate the magnetic field dependence of dc conductivity in the Hubbard model on the square lattice, fully taking into account the orbital effects of the field introduced via the Peierls substitution. In addition to the conventional Shubnikov–de Haas quantum oscillations, associated with the coherent cyclotron motion of quasiparticles and the presence of a well-defined Fermi surface, we find an additional oscillatory component with a higher frequency that corresponds to the total area of the Brillouin zone. These paradigm-breaking oscillations appear at elevated temperature. This finding is in excellent qualitative agreement with the recent experiments on graphene superlattices. We elucidate the key roles of the off-diagonal elements of the current vertex and the incoherence of electronic states, and explain the trends with respect to temperature and doping.

DOI: 10.1103/PhysRevLett.127.196601

Quantum oscillations (QOs) are a fundamental phenomenon in solid state physics. The Lorentz force affects electrons in such a way that all the system properties vary periodically with the inverse of the magnetic field [1]. Conventionally, QOs are observable at low temperatures  $T$  and in absence of strong incoherence, and provide detailed information about the topology and shape of the Fermi surface [1,2]. Yet, QOs are surprisingly ubiquitous. They also appear in non-Fermi liquids [3–5] and even in gapped systems such as Kondo insulators [6]. They were observed in graphite [7,8], graphene [9,10], organics [11], cuprates [12–14], perovskite heterostructures [15,16], iron-pnictide superconductors [17], and moiré systems [18].

In moiré systems, huge superlattice spacing allows access to regime of large flux per unit cell  $\Phi$ . Precisely in this regime, recent experiments [19–22] have uncovered a new, peculiar type of QOs of conductivity: peaks at  $\Phi$  equal to simple fractions of the flux quantum, i.e.,  $\Phi = \Phi_0 p/q$  with  $p, q$  coprime integers, and  $p$  and  $q$  small [21]. These Brown-Zak (BZ) oscillations are clearly distinct from the conventional Shubnikov–de Haas (SdH) oscillations: BZ QOs appear at elevated temperatures [20], and their frequency does not depend on the electron density  $n$  (in 2D, SdH QOs have a frequency proportional to  $n$ ). Some understanding of this phenomenon was reached by noting that the conductivity is high whenever the non-interacting density of states consists of a small number ( $q$ ) of wide energy bands (magnetic “minibands”) [20,21]. States in wider bands should have a higher velocity, and therefore conduct better. However, this heuristic picture cannot explain the totality of experimental observations. In

this Letter we present a microscopic theory of conductivity in the Hubbard model and unexpectedly recover a phenomenology strikingly similar to that observed in the experiments of Refs. [20] and [21]. Our analysis elucidates the essential role of incoherence for the BZ oscillations, and explains the temperature, doping and interaction trends in a systematic manner.

We employ the recently developed extension of the dynamical mean field theory (DMFT) [23] to finite magnetic fields [24–26]. In absence of the magnetic field, the DMFT solution of the Hubbard model was previously shown to describe the transport properties of various materials [27–31] and cold atoms in optical lattices [32,33]. The DMFT approximates the self-energy by a local quantity, and becomes exact in the limit of infinite coordination number. In a separate accompanying publication Ref. [26], we prove that the vertex corrections for the longitudinal conductivity cancel at the level of DMFT, regardless of the magnetic field (see also Refs. [34] and [25]); this makes it possible to calculate conductivity by the Kubo bubble without any additional approximations. Our approach fully takes into account local correlations due to electron-electron ( $e$ - $e$ ) interaction, and is formally applicable at any  $T$ , coupling strength  $U$  and field  $B$ .

Our conductivity results exhibit oscillations that clearly correspond to the BZ QOs observed in experiment. The oscillations have a frequency  $p/q = 1$  (corresponding to maxima at  $p/q = 1/q$ ) and appear at relatively high  $T$  where the SdH oscillations are getting thermally washed out. BZ either coexist with the SdH oscillations or appear as the sole oscillatory component. As  $T$  is lowered, higher

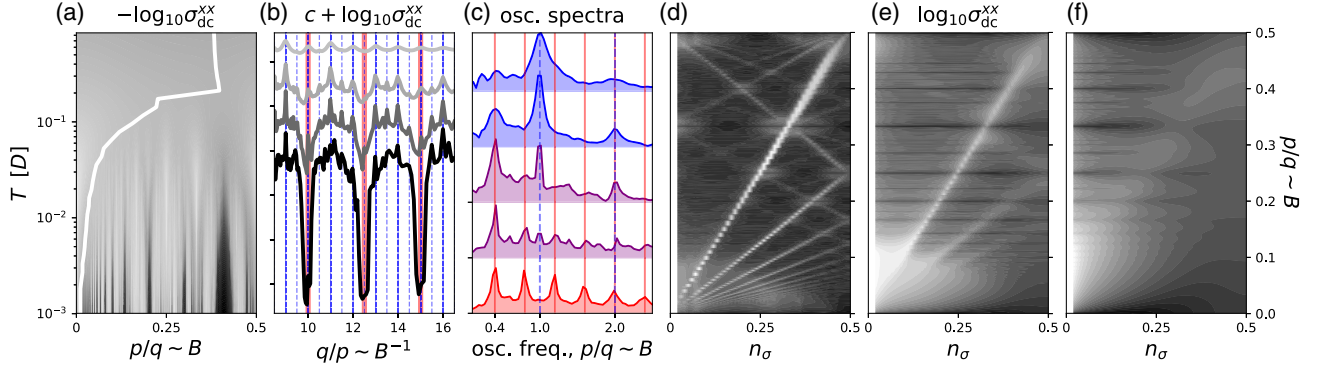


FIG. 1. DMFT results for conductivity in the Hubbard model for  $U = 1D$ . (a) Conductivity as a function of temperature and field at band filling  $n_\sigma = 0.4$ . Color code is logarithmic; black means  $\log_{10} \sigma_{dc}^{xx} \approx -7.95$ , white means  $\log_{10} \sigma_{dc}^{xx} \approx 2.12$ . White line: onset points of the nonmonotonic behavior of  $\sigma_{dc}^{xx}(B)|_T$ . (b) Conductivity as a function of inverse magnetic field. Bottom to top:  $T = 0.0012, 0.0049, 0.0109, 0.024D$ ; lines are plotted on the log scale, and offset for the sake of clarity. (c) Frequency spectrum of conductivity in the range  $p/q \in [0.03, 0.15]$  at different temperatures. Bottom to top:  $T = 0.001, 0.009, 0.016, 0.029, 0.064D$ . Each spectrum is normalized to 1 and shifted for the sake of clarity. (b),(c) Vertical lines: peaks due to SdH oscillations (red), and BZ oscillations (blue). (d)–(f) Conductivity with respect to band filling and field at  $T = 0.005, 0.03, 0.1D$ , respectively. Color code: white means  $-8.22, -3.57, -3.12$ , black means  $2.14, 1.77, 1.03$ , respectively.

harmonics of BZ oscillations become more pronounced (peaks become sharper, and additional maxima at  $p/q = 2/q, 3/q, \dots$  appear). Ultimately, at very low  $T$ , regular BZ oscillations give way to fractal behavior which does not yield any pronounced peaks in the Fourier spectrum. It turns out that the essential ingredient for the regular (sinusoidal) BZ oscillations are the incoherent electronic states. Incoherence allows for conduction processes that involve tunneling between two eigenstates of the Hamiltonian, and it is precisely the contribution of those processes that oscillates at frequency  $p/q = 1$ . Our numerical data suggest that in strongly correlated regimes, regular BZ oscillations should appear at very low temperature.

**Model and method.**—We consider the Hubbard model on the square lattice with nearest-neighbor hopping  $t$ , coupling  $U$ , and band filling per spin  $n_\sigma$ , with  $n = \sum_\sigma n_\sigma$ . We use  $D = 4t$  as the unit of energy. The field is included through Peierls phases for rational flux values  $\Phi/\Phi_0 = p/q$  to obtain commensurate magnetic cell [35]. We do not include the Zeeman term [36,37], as it does not affect the QO frequencies, only their amplitudes [1]. We solve the problem within the DMFT with numerical renormalization group solver. Full details of our calculations are given in Ref. [26].

**Results.**—Figure 1(a) shows the conductivity for moderate doping and interaction ( $n_\sigma = 0.4$ ,  $U = 1$ ) over a broad range of temperature and field (flux). At low  $T$ , we clearly see prominent oscillations. The onset of nonmonotonic behavior is marked with the white line: it indicates the value of  $B$  where the first extremum in  $\sigma_{dc}^{xx}$  is encountered for a given  $T$ . In Fig. 1(b) we close in on a narrow field range and plot  $\sigma_{dc}^{xx}$  as a function of  $1/B$  at several  $T$ . At low  $T$ , we see large dips in conductivity for  $p/q = n_\sigma/i$  (red lines;  $i$  is integer), corresponding to occurrences of a large

gap in the density of states at the Fermi level. These are the SdH oscillations with a frequency related to the area of the Fermi sea  $A_{FS}$  by the Onsager relation  $F = \Phi_0/(2\pi)^2 A_{FS}$ ,  $A_{FS} = (2\pi)^2 n_\sigma$ . In between the sharp SdH dips, one can observe a weak but highly nonmonotonic behavior of  $\sigma_{dc}^{xx}$  with high-frequency oscillatory features exceeding the resolution of our calculations. With increasing  $T$ , the amplitude of the SdH oscillations is reduced in line with the Lifshitz-Kosevich theory [2,26], and the behavior in between the SdH dips becomes simpler: one gets spikes coinciding with small- $p$  moderate- $q$  values of flux (denoted with blue lines: full line is  $p = 1$ , dashed line is  $p = 2$ ). Ultimately, only regular sinusoidal oscillations of period 1 remain, with maxima at  $p/q = 1/q$ . Increasing  $T$  further erases all nonmonotonic behavior.

Figure 1(c) shows the oscillation spectra obtained by Fourier transforming  $\sigma_{dc}^{xx}(B^{-1} \sim q/p)$  on the range  $p/q \in [0.03, 0.15]$ . At the lowest temperature we see strong peaks at  $p/q = n_\sigma$  and its higher harmonics, corresponding to (sharp) SdH oscillations. The fractal behavior in between the SdH dips seen in Fig. 1(b) does not produce a clear oscillatory signal [26]. As  $T$  is increased, the peaks at  $p/q = 1$  and  $p/q = 2$  appear, while at the highest  $T$  one is left only with the peak at  $p/q = 1$ .

In Figs. 1(d)–1(f) we plot the conductivity in the  $(n_\sigma, B)$  plane. At low  $T$ , the SdH oscillation fans out from the  $(0,0)$  point, clearly indicating the  $n_\sigma$  dependence of the oscillation frequency. At a higher  $T$ , SdH oscillations become weaker; horizontal (i.e.,  $n_\sigma$ -independent) stripes corresponding to fractal BZ oscillations become visible, and are particularly pronounced at small  $p$  values. At the highest  $T$  shown, only the BZ oscillations remain.

We summarize our observations by presenting in Figs. 2(a) and 2(b) the two relevant Hubbard model phase

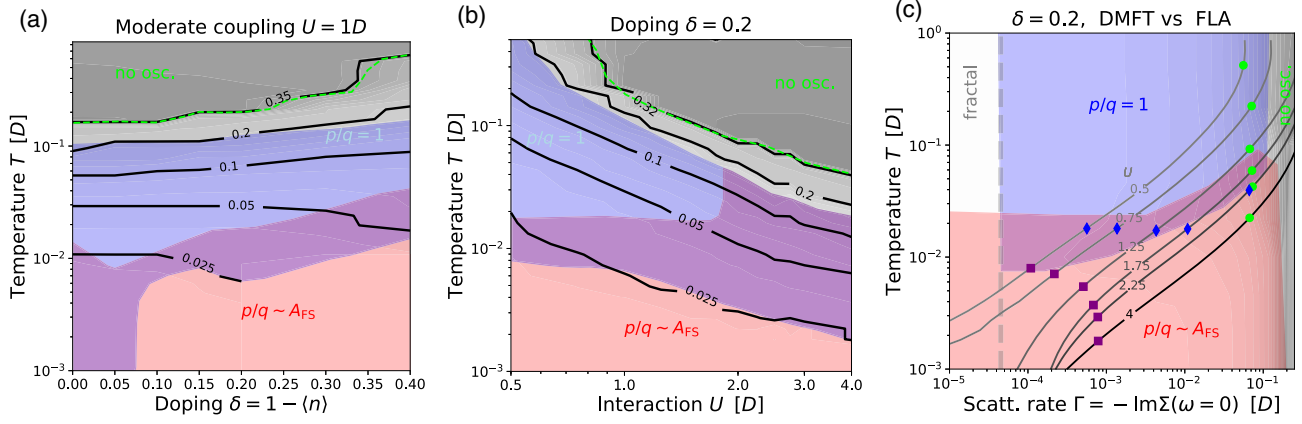


FIG. 2. Phase diagrams showing the type of QOs observed in the range of field  $p/q \in [0.03, 0.15]$ . (a) DMFT results in  $(\delta, T)$  plane, (b) DMFT results in  $(U, T)$  plane, (c) FLA results in  $(\Gamma, T)$  plane. Red: SdH only. Purple: both SdH and BZ, but SdH dominant. Blue: BZ dominant ( $p/q = 1$  peak stronger than  $p/q \approx n_\sigma$  peak). Black shading and contours in (a),(b) denote the value of the field where nonmonotonic behavior starts in  $1/\sigma_{dc}^{\text{xx}}(B)|_T$  (analogous to the white line in Fig. 1). Above the lime dashed line, no oscillations are detectable at any field strength. In (c), lines and symbols correspond to DMFT results, shading to FLA results. Lines are  $\Gamma(T)$  for various values of  $U$ . Purple squares indicate where the BZ oscillations start with increasing  $T$ , blue diamonds where the BZ becomes dominant, and lime circles where all QOs cease [corresponding to the top edge of blue and purple regions in (b)].

diagrams, showing the dominant type of (regular) oscillations, based on the Fourier spectrum of  $\sigma_{dc}^{\text{xx}}(q/p)$  in the field range  $p/q \in [0.03, 0.15]$ . We also indicate the onset field for the nonmonotonic behavior (gray scale color coding and the black contours). Clearly, the onset field depends strongly on  $U$  and  $n$ ; the nonmonotonic behavior is stronger and requires less strong fields in more coherent regimes (lower  $U$  and/or higher doping away from half-filling  $\delta = 1 - n$ ). Another notable trend is that the BZ oscillations start at a lower temperature in less coherent regimes (lower  $\delta$  at fixed  $U$ ; stronger  $U$  at fixed  $\delta$ ).

To elucidate the role of incoherence we perform calculations within the finite-lifetime approximation (FLA) [26], where a lifetime of electronic states is set by hand by fixing the (local) self-energy to  $\Sigma(\omega) = -i\Gamma$ . We determine the phase diagram of FLA with respect to the two parameters of this toy model, the scattering rate  $\Gamma$ , and temperature  $T$  [Fig. 2(c)]. There appears to be a well-defined upper cutoff value of  $\Gamma$  for the observation of any QOs. For the observation of SdH oscillations, there is a relatively well-defined upper cutoff  $T$ . The region of dominant regular BZ oscillations is additionally limited by lower cutoff  $\Gamma$  and  $T$ . Below  $\Gamma \approx 5 \times 10^{-5}$ , fractal behavior is observed, with or without the SdH oscillations, depending on temperature. At moderate  $\Gamma$ , increasing the temperature alone does not wash out the BZ oscillations, and they persist up to infinite temperature.

We superimpose on the FLA phase diagram the DMFT results by identifying  $\Gamma = -\text{Im}\Sigma(\omega = 0)$ . In DMFT the self-energy has frequency dependence and depends on both  $U$  and  $T$ . The gray scale lines represent the DMFT result for  $\Gamma(T)$  for different  $U$  values. The upper cutoff  $\Gamma$  for QOs (lime points) holds in good agreement with FLA results, as

well as the upper cutoff  $T$  for SdH oscillations (blue diamonds). At low  $U$ , the lower cutoff  $T$  for BZ oscillations is also in agreement with FLA. However, at high  $U$ , the discrepancy from FLA is significant: the sinusoidal BZ oscillations appear at much lower  $T$  than one would expect based on a simple FLA toy model where  $\Sigma$  has no frequency dependence. At very strong  $U$ , there rather seems to be a well-defined lower cutoff  $\Gamma$  for regular BZ QOs extending to very low  $T$  (this lower  $\Gamma$  cutoff being a bit higher than the one at high  $T$ ). The observation of BZ oscillations at very low  $T$  is therefore a clear indication of strong electronic correlations that go beyond simple incoherence effects.

*Discussion.*—The trends related to incoherence and temperature can be understood from the linear-response transport theory underlying our calculations. The Kubo bubble for conductivity is illustrated in Fig. 3(a). At the level of the DMFT where the self-energy does not depend on the momentum, the product of two velocities  $v_{\mathbf{k},m,m'} v_{\mathbf{k}',m',m}$  can be rewritten as a single factor with two kinetic-energy arguments,  $v(\epsilon, \epsilon')$ . Depending on temperature, effective scattering rate, and chemical potential, different  $(\epsilon, \epsilon')$  domains play a role [26]. In particular, only  $(\epsilon, \epsilon')$  such that  $|\epsilon - \epsilon'| < \Gamma$  and  $\epsilon^{(n)} - \mu < T$  give significant contributions. At low  $T$ , we observe that the SdH effect is already contained in  $v(\epsilon, \epsilon')$ . The oscillation spectrum for  $v(\epsilon, \epsilon' \approx \epsilon \approx \mu)$ , exhibits a peak that moves with  $\mu$  and coincides with  $n_\sigma$ . As the thermal window becomes larger, a wider range of  $v(\epsilon, \epsilon' \approx \epsilon)$  enter the calculation, yet oscillate with different frequencies, depending on  $\epsilon$ . This leads to dephasing and washing out of the SdH oscillations. By contrast, the BZ oscillation is mild at any given  $\epsilon$ , but it *always* has the same frequency



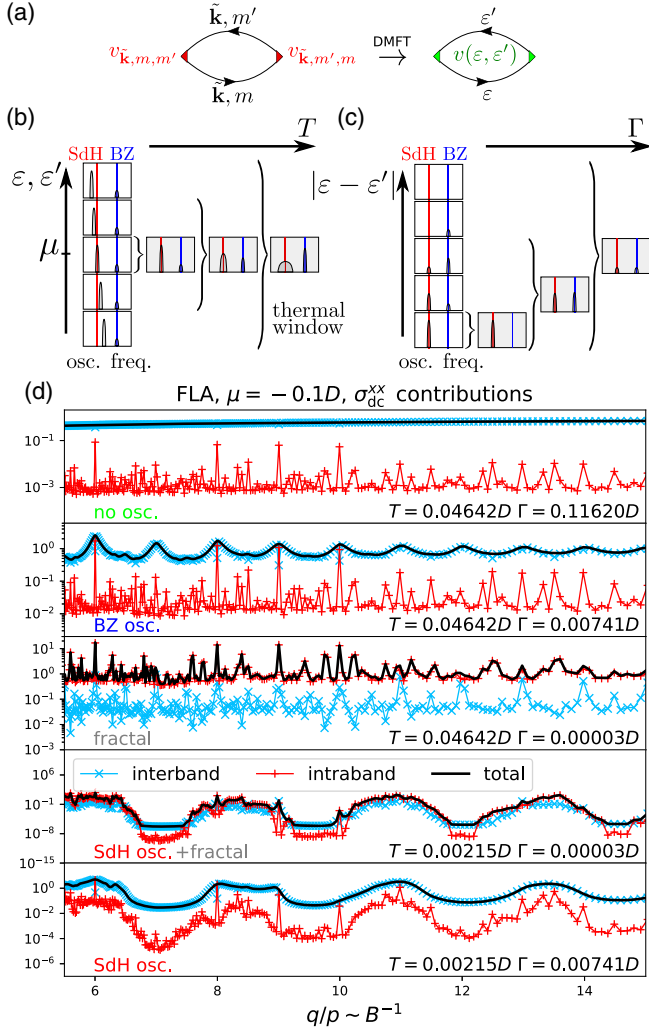


FIG. 3. (a) Diagrammatic representation of the Kubo bubble. Left: in general; right: at the level of the DMFT.  $(\vec{k}, m)$  denotes eigenstates of the noninteracting Hamiltonian (see [26] for details). Red or lime triangles are the velocity vertices, in DMFT rewritten as a single factor depending on two kinetic energies,  $v(\epsilon, \epsilon')$ . (b), (c) White panels: oscillation spectra of  $v(\epsilon, \epsilon')$  at a given  $(\epsilon, \epsilon')$ . Gray panels: oscillation spectra of  $v$  integrated over the relevant  $(\epsilon, \epsilon')$  domain, depending on model parameters  $(T$  and  $\Gamma)$ , as indicated by the large curly bracket; (b) trend with respect to temperature. (c) Trend with respect to the scattering rate. (d) Field dependence of conductivity and the contributions of interband ( $\epsilon \neq \epsilon'$ ) and intraband ( $\epsilon \approx \epsilon'$ ) processes in FLA in four different parameter regimes.

( $p/q = 1$ ), thus its contribution accumulates with increasing  $T$  and can become the dominant effect, as illustrated in Fig. 3(b). The domain of  $v$  that turns out to oscillate with the BZ frequency is found at moderate  $|\epsilon - \epsilon'|$ . Therefore, as the scattering rate  $\Gamma$  is increased, those values enter the calculation and the BZ oscillations become visible in  $\sigma_{dc}^{xx}(q/p)$ . The values of  $v(\epsilon, \epsilon')$  at large  $|\epsilon - \epsilon'|$  do not oscillate with any particular frequency. As those get included at large  $\Gamma$ , all oscillations are ultimately overcome

by the nonoscillatory contributions, as illustrated in Fig. 3(c). The velocity  $v$  is the only source of BZ oscillations in the Kubo bubble, as Green's function and the self-energy do not have an oscillatory component at the frequency of BZ oscillations [26].

In previous works [20,21], the BZ oscillations were connected with the velocity of the magnetic minibands, calculated as  $v = \partial \epsilon_{\vec{k}, m} / \partial \vec{k}_x$ . Nevertheless, it is important to note that the eigenstates of the noninteracting Hamiltonian do not have a well-defined velocity in the presence of the field. Rather, the velocity  $v_{\vec{k}, m, m'}$  is a matrix in the miniband space  $m, m'$ . In previous works this was not taken into account and the results were interpreted in terms of only the *intraband* processes (diagonal elements of  $v$ ). This would be well justified only in the limit of coherent, long-lived quasiparticle states. However, increasing  $T$  even at weak coupling leads to decoherence of electron states, which activates the contribution of off-diagonal velocity components and even makes them fully dominant [26]. This corresponds to  $m \neq m'$  (or  $\epsilon \neq \epsilon'$ ) terms in the Kubo bubble in Fig. 3(a). For these *interband* processes, the amplitude is determined by the probability of *tunneling* between two minibands upon measurement of velocity. We illustrate the relative contributions of interband and intraband processes to overall dc conductivity in Fig. 3(d) in five different regions of parameters of the FLA toy model. These plots reveal that the diagonal components of the velocity cannot account for the regular sinusoidal BZ oscillations, but only for the fractal behavior that is observed at low  $\Gamma$ . It is interesting to note that even at very high  $\Gamma$ , the intraband processes still exhibit strong fractal behavior, while the overall conductivity is already devoid of any apparent QOs. This indicates that the regular BZ oscillations are not a simple “smoothing” of the fractal behavior due to widened peaks in the (fractal) spectral function. Rather, this is a separate phenomenon, ultimately due to oscillations in the tunneling amplitudes  $v_{\vec{k}, m, m' \neq m}$ .

**Relation to experiment.**—Both the fractal behavior (peaks in  $\sigma_{dc}^{xx}$  up to  $p/q = 4/q$ ) and the regular BZ oscillations have been observed in experiment [20,21]. The  $T$ -trend observed in Figs. 1(d)–1(f) is in qualitative agreement with the experimental findings of Ref. [20]. Note that the lattice in this moiré system is different from that in our model, and that the dominant interaction in graphene at high  $T$  is likely of the electron-phonon ( $e$ -ph) type, while our Hamiltonian only includes  $e$ - $e$  repulsion. The agreement despite such differences indicates a significant level of universality in these phenomena. Notwithstanding, the doping trend at the highest temperature is in apparent contrast to the measurements in Ref. [20]. In our Fig. 1(f), BZ oscillations are regular (sinusoidal) close to half-filling; closer to the empty band limit a stronger fractal behavior remains in place. In the corresponding high- $T$  experimental result in Ref. [20] [Figs. 2(b) and 2(c)], only the regular oscillations are

observed, and no oscillations at all are observed close to the “neutrality point” (corresponding to the empty band limit in our calculations). This discrepancy appears to be due to the difference in the scattering mechanism: the  $e$ - $e$  scattering rate goes to zero as the band empties, but the  $e$ -ph scattering rate does not. The FLA calculation [26] where  $\Gamma$  is fixed regardless of the doping clearly reproduces the doping trend observed in the experiment. Similarly, at low temperature in the Hubbard model, one observes both the SdH oscillations and fractal behavior [Fig. 1(b)]. In experiment, there are cases where only SdH oscillations are observed at low temperature. This discrepancy is, again, likely due to the difference in scattering mechanisms. In the Hubbard model the scattering rate goes down with temperature [Fig. 2(c)]. If the scattering rate is kept fixed at a moderate value (as in FLA), at low  $T$  one only observes the SdH effect [see bottom panel in Fig. 3(d)].

**Conclusion.**—We have studied the magnetic quantum oscillations of longitudinal dc conductivity in the 2D Hubbard model. We observe three types of nonmonotonic behavior in  $\sigma_{dc}^{xx}$ : (1) Shubnikov–de Haas oscillations with frequency  $p/q = n_\sigma$  (and higher harmonics), at low temperature; (2) fractal behavior of conductivity with peaks at  $\Phi/\Phi_0 = 1/q, 2/q, 3/q, \dots$ , in the coherent regimes; (3) sinusoidal  $p/q = 1$ -frequency oscillations, in moderately incoherent regimes (the Brown-Zak oscillations, BZ). Our findings are in striking agreement with recent experiments on graphene superlattices. The discrepancies from experiment can be traced back to a difference in interactions present in the system. The oscillation phenomenology crucially depends on the scattering rate, and can thus be used in experiment as a characterization tool for scattering mechanisms. The fractal behavior is ultimately a manifestation of the Hofstadter butterfly, and is an indication of a low scattering rate; in contrast, the BZ oscillations indicate a higher scattering rate, and when observed at very low temperature are an indication of a strong  $e$ - $e$  coupling. Our results present clear predictions for future experiments where the dependence on coupling strength and doping might be investigated.

Computations were performed on the PARADOX supercomputing facility (Scientific Computing Laboratory, Center for the Study of Complex Systems, Institute of Physics Belgrade). J. V. acknowledges funding provided by the Institute of Physics Belgrade, through the grant by the Ministry of Education, Science, and Technological Development of the Republic of Serbia, as well as by the Science Fund of the Republic of Serbia, under the Key2SM project (PROMIS program, Grant No. 6066160). R. Ž. is supported by the Slovenian Research Agency (ARRS) under Program P1-0044 and Projects No. J1-1696 and No. J1-2458.

- [1] D. Schoenberg, *Magnetic Oscillations in Metals* (Cambridge University Press, Cambridge, England, 1984).
- [2] I. M. Lifshitz and A. M. Kosevich, Zh. Éksp. Teor. Fiz. **29**, 730 (1956) [Sov. Phys. JETP **2**, 636 (1956)].
- [3] F. Denef, S. A. Hartnoll, and S. Sachdev, Phys. Rev. D **80**, 126016 (2009).
- [4] S. A. Hartnoll and D. M. Hofman, Phys. Rev. B **81**, 155125 (2010).
- [5] D. V. Else, R. Thorngren, and T. Senthil, Phys. Rev. X **11**, 021005 (2021).
- [6] J. Knolle and N. R. Cooper, Phys. Rev. Lett. **115**, 146401 (2015).
- [7] D. E. Soule, J. W. McClure, and L. B. Smith, Phys. Rev. **134**, A453 (1964).
- [8] S. B. Hubbard, T. J. Kershaw, A. Usher, A. K. Savchenko, and A. Shytov, Phys. Rev. B **83**, 035122 (2011).
- [9] K. S. Novoselov, A. K. Geim, S. V. Morozov, D. Jiang, M. I. Katsnelson, I. V. Grigorieva, S. V. Dubonos, and A. A. Firsov, Nature (London) **438**, 197 (2005).
- [10] Y. Zhang, Y.-W. Tan, H. L. Stormer, and P. Kim, Nature (London) **438**, 201 (2005).
- [11] M. V. Kartsovniuk and V. G. Peschansky, Low Temp. Phys. **31**, 185 (2005).
- [12] N. Doiron-Leyraud, C. Proust, D. LeBoeuf, J. Levallois, J.-B. Bonnemaison, R. Liang, D. A. Bonn, W. N. Hardy, and L. Taillefer, Nature (London) **447**, 565 (2007).
- [13] S. E. Sebastian, N. Harrison, E. Palm, T. P. Murphy, C. H. Mielke, R. Liang, D. A. Bonn, W. N. Hardy, and G. G. Lonzarich, Nature (London) **454**, 200 (2008).
- [14] S. E. Sebastian and C. Proust, Annu. Rev. Condens. Matter Phys. **6**, 411 (2015).
- [15] A. D. Caviglia, S. Gariglio, C. Cancellieri, B. Sacépé, A. Fête, N. Reyren, M. Gabay, A. F. Morpurgo, and J.-M. Triscone, Phys. Rev. Lett. **105**, 236802 (2010).
- [16] P. Moetakef, D. G. Ouellette, J. R. Williams, S. J. Allen, L. Balents, D. Goldhaber-Gordon, and S. Stemmer, Appl. Phys. Lett. **101**, 151604 (2012).
- [17] A. Carrington, Rep. Prog. Phys. **74**, 124507 (2011).
- [18] Y. Cao, J. Y. Luo, V. Fatemi, S. Fang, J. D. Sanchez-Yamagishi, K. Watanabe, T. Taniguchi, E. Kaxiras, and P. Jarillo-Herrero, Phys. Rev. Lett. **117**, 116804 (2016).
- [19] B. Hunt, J. D. Sanchez-Yamagishi, A. F. Young, M. Yankowitz, B. J. LeRoy, K. Watanabe, T. Taniguchi, P. Moon, M. Koshino, P. Jarillo-Herrero, and R. C. Ashoori, Science **340**, 1427 (2013).
- [20] R. K. Kumar, X. Chen, G. H. Auton, A. Mishchenko, D. A. Bandurin, S. V. Morozov, Y. Cao, E. Khestanova, M. B. Shalom, A. V. Kretinin, K. S. Novoselov, L. Eaves, I. V. Grigorieva, L. A. Ponomarenko, V. I. Fal’ko, and A. K. Geim, Science **357**, 181 (2017).
- [21] R. K. Kumar, A. Mishchenko, X. Chen, S. Pezzini, G. H. Auton, L. A. Ponomarenko, U. Zeitler, L. Eaves, V. I. Fal’ko, and A. K. Geim, Proc. Natl. Acad. Sci. U.S.A. **115**, 5135 (2018).
- [22] J. Barrier, P. Kumaravadivel, R. K. Kumar, L. A. Ponomarenko, N. Xin, M. Holwill, C. Mullan, M. Kim, R. V. Gorbachev, M. D. Thompson, J. R. Prance, T. Taniguchi, K. Watanabe, I. V. Grigorieva, K. S. Novoselov,

- A. Mishchenko, V.I. Fal'ko, A.K. Geim, and A.I. Berdyugin, *Nat. Commun.* **11**, 5756 (2020).
- [23] A. Georges, G. Kotliar, W. Krauth, and M.J. Rozenberg, *Rev. Mod. Phys.* **68**, 13 (1996).
- [24] S. Acheche, L.-F. Arsenault, and A.-M. S. Tremblay, *Phys. Rev. B* **96**, 235135 (2017).
- [25] A. A. Markov, G. Rohringer, and A. N. Rubtsov, *Phys. Rev. B* **100**, 115102 (2019).
- [26] J. Vučičević and R. Žitko, companion paper, *Phys. Rev. B* **104**, 205101 (2021).
- [27] P. Limelette, P. Wzietek, S. Florens, A. Georges, T. A. Costi, C. Pasquier, D. Jérôme, C. Mézière, and P. Batail, *Phys. Rev. Lett.* **91**, 016401 (2003).
- [28] H. Terletska, J. Vučičević, D. Tanasković, and V. Dobrosavljević, *Phys. Rev. Lett.* **107**, 026401 (2011).
- [29] J. Vučičević, H. Terletska, D. Tanasković, and V. Dobrosavljević, *Phys. Rev. B* **88**, 075143 (2013).
- [30] T. Furukawa, K. Miyagawa, H. Taniguchi, R. Kato, and K. Kanoda, *Nat. Phys.* **11**, 221 (2015).
- [31] J. Vučičević, D. Tanasković, M.J. Rozenberg, and V. Dobrosavljević, *Phys. Rev. Lett.* **114**, 246402 (2015).
- [32] J. Vučičević, J. Kokalj, R. Žitko, N. Wentzell, D. Tanasković, and J. Mravlje, *Phys. Rev. Lett.* **123**, 036601 (2019).
- [33] P. T. Brown, D. Mitra, E. Guardado-Sanchez, R. Nourafkan, A. Reymbaut, C.-D. Hébert, S. Bergeron, A.-M. S. Tremblay, J. Kokalj, D.A. Huse, P. Schauß, and W. S. Bakr, *Science* **363**, 379 (2019).
- [34] A. Khurana, *Phys. Rev. Lett.* **64**, 1990 (1990).
- [35] D. R. Hofstadter, *Phys. Rev. B* **14**, 2239 (1976).
- [36] L. Laloux, A. Georges, and W. Krauth, *Phys. Rev. B* **50**, 3092 (1994).
- [37] J. Bauer and A.C. Hewson, *Phys. Rev. B* **76**, 035118 (2007).



**Electrical conductivity in the Hubbard model: Orbital effects of magnetic field**J. Vučičević<sup>1</sup> and R. Žitko<sup>2,3</sup><sup>1</sup>*Scientific Computing Laboratory, Center for the Study of Complex Systems, Institute of Physics Belgrade, University of Belgrade, Pregrevica 118, 11080 Belgrade, Serbia*<sup>2</sup>*Jožef Stefan Institute, Jamova 39, SI-1000 Ljubljana, Slovenia*<sup>3</sup>*Faculty of Mathematics and Physics, University of Ljubljana, Jadranska 19, SI-1000 Ljubljana, Slovenia*

(Received 19 May 2021; revised 13 August 2021; accepted 17 August 2021; published 2 November 2021)

Calculation of conductivity in the Hubbard model is a challenging task. Recent years have seen much progress in this respect and numerically exact solutions are now possible in certain regimes. In this paper we discuss the calculation of conductivity for the square-lattice Hubbard model in the presence of a perpendicular magnetic field, focusing on orbital effects. We present the relevant formalism in all detail and in full generality, and then discuss the simplifications that arise at the level of the dynamical mean field theory (DMFT). We prove that the Kubo bubble preserves gauge and translational invariance, and that in the DMFT the vertex corrections cancel regardless of the magnetic field. We present the DMFT results for the spectral function and both the longitudinal and Hall conductivities in several regimes of parameters. We analyze thoroughly the quantum oscillations of the longitudinal conductivity and identify a high-frequency oscillation component, arising as a combined effect of scattering and temperature, in line with recent experimental observations in moiré systems.

DOI: [10.1103/PhysRevB.104.205101](https://doi.org/10.1103/PhysRevB.104.205101)**I. INTRODUCTION**

Strong correlations in electronic systems have a profound effect on conductivity, and lead to a range of unconventional behaviors which are at the center of interest in condensed matter theory. One such behavior is the linear temperature dependence of resistivity, observed in the cuprate superconductors [1–3]. The linear resistivity has been reproduced by numerical simulation of the Hubbard model [4–13], as well as with ultra-cold-atom simulations [14]. It is viewed as an effect of proximity to the Mott transition [8,15,16] or quantum critical points [6,17–19], as well as a generic high-temperature feature of correlated materials which are well approximated by a single-band model [9].

External magnetic fields are also known to affect the transport properties of electronic systems [20], sometimes drastically: in the context of the two-dimensional electron gas, magnetic field leads to the well-known quantum Hall effect (QHE), where conductivity displays intricate dependence on the magnetic field [21–24]. The effect of the Coulomb interaction is here essential for the understanding of the fractional QHE [25,26]. In conventional metals, resistivity is an oscillatory function of the magnetic field, which is the well-known Shubnikov–de Haas effect (SdH) [27,28]. However, the SdH effect is often observed even in states which are assumed to be correlated and are not yet fully understood [29–31]. In such cases, an effective Fermi-liquid description of the material is often invoked to analyze the experimental data, and to map out the geometry of the Fermi surface. It is, therefore, of great importance to understand the interplay of strong coupling and magnetic fields in lattice systems. The study of magnetoresistance in correlated lattice models has been so far limited

to perturbative approaches, either for weak fields [32–34] or weak interactions [22,35,36]. To the best of our knowledge, the only nonperturbative calculations of magnetotransport were limited to the transversal conductivity [37–39]. Nonperturbative calculations were also performed for the effective Fermi-liquid parameters (quasiparticle weight, scattering rate, and density of states at the Fermi level) [38,40,41], which can be considered relevant for longitudinal conductivity.

In this paper we study the effect of magnetic field on both the longitudinal and transversal conductivity in the square-lattice Hubbard model in several parameter regimes: from weak to strong coupling, low to high temperature, and in the full range of the magnetic field.

We first lay out the general formalism for the calculation of conductivity in the presence of the magnetic field and then describe the simplifications that arise at the level of the dynamical mean field theory (DMFT), as previously implemented in Refs. [38,41]. Most importantly, we show that the Kubo bubble is gauge invariant and that the vertex corrections to the current-current correlation function cancel, analogously to the zero-field case. The latter is done by rederiving the well-known zero-field proof from Ref. [42] in real space, and then generalizing it to the case of external magnetic fields. Cancellation of vertex corrections at the level of DMFT was previously shown only for the transversal conductivity [38], and here we give a different, fully general proof.

We perform extensive DMFT calculations to cover a large part of the phase diagram. Our numerical results show that the oscillatory behavior of conductivity is restricted to a finite range of temperature which is mainly determined by the amount of dynamic correlations (which are promoted by interactions, yet hindered by doping). The amplitude of

oscillations decays exponentially with temperature, as expected from the Lifshitz-Kosevich theory [43]. Above a certain characteristic temperature, no nonmonotonic behavior can be induced no matter how strong the magnetic field is. We also observe that in a big range of magnetic fields and interaction strengths, the conductivity follows a scaling law, with the temperature scale set by the coupling strength. Most importantly, the  $T$ -linear dependence of resistivity in the high-temperature regime is not qualitatively modified by the magnetic field.

We investigate transverse conductivity in the noninteracting limit, and observe exponential decay of  $\sigma^{xy}$  with temperature, and a power-law divergence as  $B_z \rightarrow 0$ . The analytic behavior at  $B_z = 0$  is restored by interactions, which led to a smooth decay of  $\sigma^{xy}$  as the magnetic field is gradually turned off.

Finally, we investigate the oscillatory behavior of conductivity in weak-to-moderate magnetic fields. In all the cases we studied, the longitudinal conductivity turns out to be dominated by the current-vertex factors, rather than the local density of states at the Fermi level or the effective scattering rate. This leads to an important simplification: one can reliably calculate conductivity at an arbitrary field by using the zero-field DMFT calculation for the self-energy. We further observe that at high temperature, moderate-to-high interactions, and moderate fields, the oscillation occurs at two separate frequencies: one that corresponds to the area of the Fermi sea, as in the Shubnikov-de Haas effect, and the other which corresponds to the full area of the two-dimensional Brillouin zone (BZ), and is therefore of higher frequency and independent of the doping level. This finding is in excellent qualitative agreement with the recent experimental observations in graphene superlattices [44–47]. The full discussion of the observed phenomenology of quantum oscillations of conductivity in the Hubbard model is presented in a separate publication, Ref. [48], while here we present the raw data and describe the basic mechanism behind the onset of the high-frequency oscillations.

The paper is organized as follows. We first describe the formalism: the Hamiltonian, the gauge choice, reciprocal-space formulation, gauge-invariant Green's function, current operators and the correlation function, DMFT approach, calculation of the conductivity tensor, and vertex factors. We then present and discuss the results. For the benefit of the reader and for easy rederivation and validation of the results presented in this work, we provide very detailed proofs of all steps in the derivations in the Appendices. For reasons of clarity and to facilitate dimensional analysis we maintain all constants ( $e$ ,  $\hbar$ ,  $k_B$ , and lattice constants  $a$  in  $c$ ) in the equations.

## II. FORMALISM

### A. Model

We study the Hubbard model on the square lattice with lattice constant  $a$ , defined by the Hamiltonian

$$H = H_0 + H_{\text{int}}, \quad (1)$$

where the noninteracting part  $H_0$  is the tight-binding (TB) model that we discuss in the following sections, while the interacting part  $H_{\text{int}}$  is the local density-density coupling, i.e.,

the Hubbard interaction

$$H_{\text{int}} = U \sum_i n_{i,\uparrow} n_{i,\downarrow}, \quad (2)$$

where  $i$  indexes the lattice sites,  $n_{i,\sigma}$  are the density operators, and  $U$  is the coupling constant. The electron spin is denoted  $\sigma = \uparrow, \downarrow$ .

### 1. Orbital space

The lattice sites are assumed to lie in the  $z = 0$  plane; where convenient, we will treat the system as a three-dimensional stack of such planes separated by the lattice constant  $c$  in the perpendicular direction.

The effect of the external magnetic field  $\mathbf{B}$  in the TB model is twofold: it couples to the electrons' spin degree of freedom (Zeeman term), as well as the momentum. The latter is approximated on the lattice by means of the Peierls substitution [49,50]. The resulting Hamiltonian is

$$H_0 = -\mu \sum_{i,\sigma} n_{i,\sigma} + g\mu_B \sum_i \mathbf{B}(\mathbf{r}_i) \cdot \mathbf{S}_i - \sum_{i,j,\sigma} t_{ij} e^{if_{ij}} c_{i,\sigma}^\dagger c_{j,\sigma}, \quad (3)$$

where  $\mu$  is the chemical potential,  $g$  is the gyromagnetic factor,  $\mu_B$  is the Bohr magneton, the position vector of site  $i$  is  $\mathbf{r}_i$ , and the operator of the electron SU(2) spin is

$$S_i^\eta = \frac{1}{2} (c_{i,\uparrow}^\dagger, c_{i,\downarrow}^\dagger) \hat{\sigma}^\eta \begin{pmatrix} c_{i,\uparrow} \\ c_{i,\downarrow} \end{pmatrix}, \quad (4)$$

where  $\hat{\sigma}^\eta$  are the Pauli matrices, and  $\eta$  enumerates the spatial directions  $x, y, z$ . The  $t_{ij}$  is the hopping amplitude between the sites  $i$  and  $j$ . The Peierls substitution introduces a phase shift  $f_{ij}$  that is picked up by an electron on the path from site  $i$  to site  $j$ :

$$f_{ij} = \frac{e}{\hbar} \int_{\mathbf{r}_i}^{\mathbf{r}_j} \mathbf{A}(\mathbf{r}) \cdot d\mathbf{r}. \quad (5)$$

Here  $\mathbf{A}$  is the vector potential,  $e$  the elementary charge, and  $\hbar$  the reduced Planck's constant. In matrix notation in site space, the effect of the gauge field corresponds to element-wise multiplication of the bare Hamiltonian:

$$\mathbf{H}_0[\mathbf{A}] = \mathbf{H}_0[\mathbf{A} = 0] \circ e^{i\mathbf{f}}, \quad (6)$$

where  $e^{i\mathbf{f}}$  is simply a matrix constructed out of  $e^{if_{ij}}$  elements.

We are interested in the effects of a uniform magnetic field perpendicular to the two-dimensional (2D) lattice:  $\mathbf{B} = (0, 0, B_z)$ . The vector potential  $\mathbf{A}$  is not uniquely determined by  $\mathbf{B}$ . There are two obvious choices: the Landau gauge

$$\mathbf{A}(\mathbf{r}) = (0, xB_z, 0), \quad (7)$$

and the symmetric gauge

$$\mathbf{A}(\mathbf{r}) = \left( -\frac{y}{2} B_z, \frac{x}{2} B_z, 0 \right). \quad (8)$$

Throughout this paper, we work in the Landau gauge.

In the rest of the paper, we define lattice site coordinates  $x_i$  and  $y_i$  as integers, and define  $\mathbf{r}_i = (x_i, y_i, 0)$ . The physical position vector of the lattice site  $i$  is then  $a\mathbf{r}_i$  and we give spatial indices in terms of  $\mathbf{r}$  as, e.g.,  $\mathbf{A}_{\mathbf{r}} \equiv \mathbf{A}(a\mathbf{r})$ .

Plugging the Landau gauge field  $\mathbf{A}$  [Eq. (7)] in the expression for the Peierls phase [Eq. (5)] one obtains [41,48] (see Appendix A for proof)

$$\begin{aligned} f_{ij} &\equiv f_{\mathbf{r}_i, \mathbf{r}_j} \\ &= \frac{e}{\hbar} (B_z a^2) \frac{(y_j - y_i)(x_i + x_j)}{2} \\ &= 2\pi \frac{\Phi}{\Phi_0} \frac{(y_j - y_i)(x_i + x_j)}{2}, \end{aligned} \quad (9)$$

where  $\Phi_0 = h/e$  is the unit flux, and  $\Phi = B_z a^2$  is the flux per lattice plaquette.

To be able to define a finite-sized (commensurate) magnetic unit cell, the values of  $B_z$  must satisfy

$$\frac{e}{\hbar} (B_z a^2) = 2\pi \frac{p}{q}, \quad (10)$$

where  $p$  and  $q$  are coprime integers.  $q$  is then the size of the unit cell in the  $x$  direction (for proof see Appendix B). In the other direction the size of the unit cell is 1, as the translational invariance is not broken along the  $y$  axis; this is obvious as  $f_{ij}$  depends only on the difference  $y_i - y_j$ .

The effect of  $B_z$  on the kinetic energy term is periodic. As  $B_z$  enters the kinetic energy through  $e^{2\pi i \frac{p}{q} (y_j - y_i)(x_i + x_j)/2}$ , if  $(y_j - y_i)(x_i + x_j)/2$  is an integer for all  $(i, j)$  connected by hopping (as is the case with nearest-neighbor hopping), increasing  $p/q$  by an integer makes no difference. Therefore, the effect of  $\frac{p}{q}$  is the same as that of  $\frac{p+m}{q}$ , with  $m$  integer. The inversion symmetry of the lattice implies that the effect of  $\frac{p}{q}$  is the same as that of  $\frac{q-p}{q}$ . When it comes to the kinetic energy term, all physically discernible magnetic fields [that satisfy Eq. (10)] can be mapped onto the range  $0 \leq p/q \leq \frac{1}{2}$ . The field  $p/q = 1$  is then a characteristic value of the field, the lowest one (other than zero) that does not couple with electron motion.

In numerics, we will consider a finite  $L \times L$  cyclic lattice, which must fit an integer number of magnetic unit cells of size  $q \times 1$ . We can rewrite the condition (10) as

$$\frac{e}{\hbar} (B_z a^2) = 2\pi \frac{p}{q} = 2\pi \frac{n}{L} \quad (11)$$

with the size of magnetic unit cell being  $L$  or smaller, as given by  $L/\text{gcd}(L, n)$ , where “gcd” denotes the greatest common divisor, and  $n$  is an arbitrary integer. In fact, the relation between the finite and infinite lattice is simply

$$q = L/\text{gcd}(L, n), \quad p = n/\text{gcd}(L, n).$$

The size of the lattice  $L$  determines the resolution of  $p/q$  that one can achieve in scanning the strength of the field in the model.

Under the assumption of only the nearest-neighbor hopping, we now rewrite the full Hamiltonian as

$$\begin{aligned} H_0 &= -\mu \sum_{i,\sigma} n_{i,\sigma} + \frac{1}{2} g \mu_B B_z \sum_{i,\sigma=\uparrow,\downarrow} (-1)^{\delta_{\sigma,\downarrow}} n_{i,\sigma} \\ &\quad - t \sum_{i,\mathbf{u} \in \{\mathbf{e}_x, \mathbf{e}_y\}, \sigma} e^{i \frac{e a^2}{\hbar} B_z \mathbf{u} \cdot \mathbf{e}_y} c_{\mathbf{r}_i, \sigma}^\dagger c_{\mathbf{r}_i + \mathbf{u}, \sigma} + \text{H.c.} \end{aligned} \quad (12)$$

*Numeric scales.* The importance of the Zeeman splitting depends on the ratio of the Zeeman energy over the bandwidth. Both  $g$  and the bandwidth are material specific. A quick

estimate for cuprate compounds, under the assumption of  $g = 2$  and half-bandwidth of around  $10^5$  K, gives that  $B_z$  of about 50 T corresponds to a Zeeman energy of about  $\approx 3 \times 10^{-3} D$ , where  $D = 4t$  is the half-bandwidth. While the effect of Zeeman splitting is interesting to study on its own, throughout this paper we restrict to only the gauge-field effects and set  $g = 0$ .

The effect of the gauge field is determined by the lattice spacing. Assuming  $a \sim 5 \times 10^{-10}$  m which is relevant for cuprates, we see that the characteristic  $p/q = \frac{1}{2}$  field corresponds to  $B_z = \frac{\pi \hbar}{e a^2} \approx 8 \times 10^3$  T. At  $B_z = 50$  T, we therefore have  $p/q \approx \frac{1}{300}$ , and we need at least the lattice size  $L = 300$  to describe this regime. Clearly, the bigger the lattice spacing, the bigger the phase picked up upon traveling between the lattice sites, and the bigger the effect of the coupling to the gauge field. The regime of large  $p/q$  is therefore relevant for systems with a larger lattice spacing (as in moiré heterostructures [51]), or where high gauge fields can be introduced artificially (as in optical lattices [52,53]).

## 2. Momentum space

Rewriting the kinetic energy in momentum space leads to the Harper equation [54,55]. By applying to the kinetic energy term the Fourier transformation of the creation and annihilation operators,

$$c_i^\dagger = \frac{1}{\sqrt{N}} \sum_{\mathbf{k}} e^{-i\mathbf{k} \cdot \mathbf{r}_i} c_{\mathbf{k}}^\dagger, \quad c_i = \frac{1}{\sqrt{N}} \sum_{\mathbf{k}} e^{i\mathbf{k} \cdot \mathbf{r}_i} c_{\mathbf{k}}, \quad (13)$$

where  $N = L^2$  is the number of sites in the lattice, one obtains

$$\begin{aligned} H_{\text{kin}} &= -t \sum_{i, \mathbf{u} \in \{\mathbf{e}_x, \mathbf{e}_y\}, \sigma} e^{i 2\pi \frac{n}{L} x_i \mathbf{u} \cdot \mathbf{e}_y} c_{\mathbf{r}_i, \sigma}^\dagger c_{\mathbf{r}_i + \mathbf{u}, \sigma} + \text{H.c.} \\ &= -2t \sum_{\mathbf{k}, \sigma} \cos k_x n_{\mathbf{k}, \sigma} - t \sum_{\mathbf{k}, \sigma} e^{i k_y} c_{\mathbf{k}, \sigma}^\dagger c_{\mathbf{k} - 2\pi \frac{n}{L} \mathbf{e}_x, \sigma} + \text{H.c.} \end{aligned} \quad (14)$$

For a detailed proof see Appendix C.

There is a coupling between the different  $\mathbf{k}$  states which results in a reduction of the Brillouin zone (BZ) by a factor of  $q = L/\text{gcd}(L, n)$ , where  $q$  is the size of the magnetic unit cell. We define  $\tilde{\mathbf{k}}$  as  $\mathbf{k}$  within the reduced BZ (RBZ). Now,  $\tilde{k}_x \in [0, 2\pi/q)$ , while  $\tilde{k}_y \in [0, 2\pi)$ .  $\tilde{\mathbf{k}}$  is a good quantum number, but there is now an additional degree of freedom that we denote  $l$  such that  $l \in [0, q)$ . A single-particle state is fully determined by a triplet  $(\tilde{\mathbf{k}}, l, \sigma)$ , with  $c_{\tilde{\mathbf{k}}, l, \sigma} \equiv c_{\mathbf{k} = \tilde{\mathbf{k}} + l \frac{2\pi}{q} \mathbf{e}_x, \sigma}$ .

On a finite cyclic lattice, the momentum space is discrete, with a step of the size  $2\pi/L$ . If  $\text{gcd}(L, n) = 1$  there is only one  $\tilde{k}_x$  value in the RBZ (equal to 0), and for each momentum there are  $q = L$  different values of  $l$ .

The Hamiltonian has a block-diagonal structure. For a given  $(\tilde{\mathbf{k}}, \sigma)$ , the Hamiltonian in the space of  $l$  is given by the Harper equation

$$\begin{aligned} [H_{0, \tilde{\mathbf{k}}, \sigma}]_{l, l'} &= \left( -\mu_\sigma - 2t \cos \left( \tilde{k}_x + l \frac{2\pi}{q} \right) \right) \delta_{l, l'} \\ &\quad - t (e^{i \tilde{k}_y} \delta_{l, l' \oplus p} + e^{-i \tilde{k}_y} \delta_{l', l \oplus p}), \end{aligned} \quad (15)$$

where  $\oplus$  denotes the cyclic addition modulo  $q$  defined as

$$l \oplus l' \equiv l + l' - q \text{div}(l + l', q), \quad (16)$$

and  $p = n/\text{gcd}(L, n)$ . We also introduced  $\mu_\sigma = \mu - (-1)^{\delta_{\sigma,\downarrow}} g\mu_B B_z/2$ .

Each block of the Hamiltonian can be diagonalized to yield the eigenenergies  $\varepsilon_{\tilde{\mathbf{k}},\sigma,m}$ , with  $m \in [0, q)$ . The basis change matrix elements are defined by

$$c_{\tilde{\mathbf{k}},l,\sigma}^\dagger = \sum_m [\alpha_{\tilde{\mathbf{k}},\sigma}]_{l,m} c_{\tilde{\mathbf{k}},m,\sigma}^\dagger. \quad (17)$$

Note that throughout this work, we distinguish between different operators ( $c_{i,\sigma} \equiv c_{\mathbf{r}_i,\sigma}$ ,  $c_{\mathbf{k},\sigma}$ ,  $c_{\tilde{\mathbf{k}},l,\sigma}$ ,  $c_{\tilde{\mathbf{k}},m,\sigma}$ , etc.) only by the choice of the symbols in the subscript (e.g.,  $c_{\tilde{\mathbf{k}},l,\sigma}$  is not equal  $c_{\tilde{\mathbf{k}},m,\sigma}$  even if  $l = m$ ), and similarly for other functions.

The blocks of the Hamiltonian have several symmetries. One can invert the  $x$  axis

$$[H_{0,(\tilde{k}_x,\tilde{k}_y),\sigma}]_{l,l'} = [H_{0,(-\tilde{k}_x,\tilde{k}_y),\sigma}]_{q-l,q-l'}^*, \quad (18)$$

which means that

$$[\alpha_{(\tilde{k}_x,\tilde{k}_y),\sigma}]_{l,m} = [\alpha_{(-\tilde{k}_x,\tilde{k}_y),\sigma}]_{q-l,m}^* \quad (19)$$

and that the eigenenergies remain the same upon inverting the  $x$  axis.

One can also invert the  $y$  axis

$$[H_{0,(\tilde{k}_x,\tilde{k}_y),\sigma}]_{l,l'} = [H_{0,(\tilde{k}_x,-\tilde{k}_y),\sigma}]_{l,l'}^*. \quad (20)$$

Again, inverting  $k_y$  does not affect the eigenenergies, but merely flips the chirality of the eigenstates

$$[\alpha_{(\tilde{k}_x,\tilde{k}_y),\sigma}]_{l,m} = [\alpha_{(\tilde{k}_x,-\tilde{k}_y),\sigma}]_{l,m}^*. \quad (21)$$

Inverting both axes at the same time therefore means

$$[H_{0,(\tilde{k}_x,\tilde{k}_y),\sigma}]_{l,l'} = [H_{0,(-\tilde{k}_x,-\tilde{k}_y),\sigma}]_{q-l,q-l'} \quad (22)$$

and

$$[\alpha_{\tilde{\mathbf{k}},\sigma}]_{l,m} = [\alpha_{-\tilde{\mathbf{k}},\sigma}]_{q-l,m}. \quad (23)$$

There is an additional periodicity along the  $y$  axis

$$\varepsilon_{\tilde{\mathbf{k}},\sigma,m} = \varepsilon_{\tilde{\mathbf{k}}+(2\pi C/q)\mathbf{e}_y,\sigma,m} \quad (24)$$

and

$$[\alpha_{\tilde{\mathbf{k}},\sigma}]_{lp \bmod q, m} = e^{iC\frac{2\pi}{q}l} [\alpha_{\tilde{\mathbf{k}}+(2\pi C/q)\mathbf{e}_y,\sigma}]_{lp \bmod q, m} \quad (25)$$

with  $C$  integer. This symmetry is important on a finite lattice, where  $k_y$  takes values of the form  $C2\pi/L$ . If  $L = q$  [i.e.,  $\text{gcd}(n, L) = 1$ ], this means that the density of states and other relevant quantities can be obtained by considering only the block  $\tilde{\mathbf{k}} = (0, 0)$ . Otherwise,  $k_y$  values up to  $2\pi/q$  need to be considered. For a proof see Appendix D.

## B. Gauge-invariant Green's function

A uniform magnetic field does not break physical translational invariance. However, at the formal level, the inclusion of the appropriate vector potential means that all correlators connecting two or more points in space depend not only on the relative positions, but also on the absolute positions. The spatial dependence of correlators can depend on the gauge choice. Nevertheless, physical observables preserve both translational and gauge invariance.

The quantity of primary interest is the Green's function. It is defined as a function of imaginary time

$$G_{ij,\sigma}(\tau) = -\langle T_\tau c_{i,\sigma}(\tau) c_{j,\sigma}^\dagger(0) \rangle. \quad (26)$$

As a function of complex frequency  $z$ , and as a matrix in the site space, one can always write

$$\mathbf{G}_\sigma(z) = [\hbar z \mathbf{I} - \mathbf{H}_0 - \boldsymbol{\Sigma}(z)]^{-1}, \quad (27)$$

where  $\boldsymbol{\Sigma}(z)$  is the self-energy. The diagonal elements of the Green's function with  $z = \omega + i0^+$  determine the local spectral function which is a physical observable. As such, the local Green's function is uniform in space. Nevertheless, the off-diagonal elements do not exhibit translational invariance  $G_{ij} = G_{\mathbf{r}_i - \mathbf{r}_j}$ , but rather this equality is satisfied only up to a phase.

It can be shown that the quantity

$$\tilde{G}_{ij,\sigma}(z) \equiv e^{-if_{ij}} G_{ij,\sigma}(z) \quad (28)$$

is gauge invariant, and *preserves the full symmetry of the lattice*. We reproduce here a proof from Ref. [56] which is valid in the noninteracting case, but is completely analogous in the case of a fully local and spatially uniform self-energy. In orbital space we have

$$\begin{aligned} \mathbf{G} &= [\mathbf{I}\hbar z - \mathbf{H}_0[\mathbf{A}] - \mathbf{I}\boldsymbol{\Sigma}(z)]^{-1}, \\ \mathbf{G}^{-1} &= [\mathbf{I}\hbar z - \mathbf{H}_0 \circ e^{i\mathbf{f}} - \mathbf{I}\boldsymbol{\Sigma}(z)], \\ \mathbf{I} &= [\mathbf{I}\hbar z - \mathbf{H}_0 \circ e^{i\mathbf{f}} - \mathbf{I}\boldsymbol{\Sigma}(z)]\mathbf{G}. \end{aligned} \quad (29)$$

It is also easy to verify that  $\mathbf{I} \circ e^{i\mathbf{f}} = \mathbf{I}$  so we can further write

$$\begin{aligned} \mathbf{I} \circ e^{i\mathbf{f}} &= ([\mathbf{I}\hbar z - \mathbf{H}_0 - \mathbf{I}\boldsymbol{\Sigma}(z)] \circ e^{i\mathbf{f}})\mathbf{G}, \\ \mathbf{I} \circ e^{i\mathbf{f}} &= ([\mathbf{I}\hbar z - \mathbf{H}_0 - \mathbf{I}\boldsymbol{\Sigma}(z)] \circ e^{i\mathbf{f}})(\tilde{\mathbf{G}} \circ e^{i\mathbf{f}}). \end{aligned} \quad (30)$$

We now write the scalar form

$$\begin{aligned} \delta_{ij} e^{if_{ij}} &= \sum_k [\mathbf{I}\hbar z - \mathbf{H}_0 - \mathbf{I}\boldsymbol{\Sigma}(z)]_{ik} e^{if_{ik}} \tilde{G}_{kj} e^{if_{kj}}, \\ \delta_{ij} &= \sum_k [\mathbf{I}\hbar z - \mathbf{H}_0 - \mathbf{I}\boldsymbol{\Sigma}(z)]_{ik} \tilde{G}_{kj} e^{if_{ik}} e^{if_{kj}} e^{-if_{ij}}, \\ \delta_{ij} &= \sum_k [\mathbf{I}\hbar z - \mathbf{H}_0 - \mathbf{I}\boldsymbol{\Sigma}(z)]_{ik} \tilde{G}_{kj} e^{if_{ik}} e^{if_{kj}} e^{if_{ji}}. \end{aligned} \quad (31)$$

The expression  $e^{if_{ik}} e^{if_{kj}} e^{if_{ji}}$  is simply the magnetic flux passing through the triangle defined by the lattice sites  $i$ ,  $j$ , and  $k$ . This quantity is gauge invariant. As Eq. (31) is a defining relation for  $\tilde{G}_{ij}$ , it means that  $\tilde{G}_{ij}$  is gauge invariant. Furthermore, the quantity  $[\mathbf{I}\hbar z - \mathbf{H}_0 - \mathbf{I}\boldsymbol{\Sigma}(z)]_{ik}$  has full lattice symmetry, thus  $\tilde{G}_{ij}$  does as well.

However, it is interesting to consider the case of a general (possibly nonlocal and nonuniform) self-energy  $\boldsymbol{\Sigma}$ . In that case, the step performed between Eqs. (29) and (30) reads as

$$[\mathbf{I}\hbar z - \mathbf{H}_0 \circ e^{i\mathbf{f}} - \boldsymbol{\Sigma}(z)] = [\mathbf{I}\hbar z - \mathbf{H}_0 - \boldsymbol{\Sigma}(z) \circ e^{-i\mathbf{f}}] \circ e^{i\mathbf{f}}. \quad (32)$$

The proof can proceed from there completely analogously, but only if the quantity  $\tilde{\boldsymbol{\Sigma}}(z) \equiv \boldsymbol{\Sigma}(z) \circ e^{-i\mathbf{f}}$  is gauge invariant and preserves the full lattice symmetry.

A proof for the gauge invariance and lattice symmetry of  $\tilde{\boldsymbol{\Sigma}}$  can be given in terms of Feynman diagrams for a special case of local density-density interactions, as follows.



Each diagram's contribution is a product of a certain number of fermionic loops. In case of local density-density interactions, a single Green's function loop is just the density, and this quantity is gauge invariant. Then, we have a loop of arbitrary size  $N$ :

$$G_{0,i_1 i_2} G_{0,i_2 i_3} \dots G_{0,i_N i_1} = \tilde{G}_{0,i_1 i_2} \tilde{G}_{0,i_2 i_3} \dots \tilde{G}_{0,i_N i_1} \times e^{if_{i_1 i_2}} e^{if_{i_2 i_3}} \dots e^{if_{i_N i_1}}, \quad (33)$$

which is gauge invariant for the same reason as we had above [note that for the bare propagator  $\tilde{G}_0$ , gauge invariance and symmetries have already been proven by Eq. (31)]. The closed fermionic loops are multiplied with the fermionic line connecting the terminals of the self-energy. Say, in case of  $\Sigma_{i_1, i_N}$ ,

$$G_{0,i_1 i_2} G_{0,i_2 i_3} \dots G_{0,i_N i_1} = \tilde{G}_{0,i_1 i_2} \tilde{G}_{0,i_2 i_3} \dots \tilde{G}_{0,i_N i_1} \times e^{if_{i_1 i_2}} e^{if_{i_2 i_3}} \dots e^{if_{i_N i_1}}. \quad (34)$$

Clearly, if we multiply now both sides with  $e^{-if_{i_1, i_N}}$ , we get on one side  $\tilde{\Sigma}_{i_1, i_N}$ , and on the other

$$\begin{aligned} \tilde{G}_{0,i_1 i_2} \tilde{G}_{0,i_2 i_3} \dots \tilde{G}_{0,i_N i_1} e^{if_{i_1 i_2}} e^{if_{i_2 i_3}} \dots e^{if_{i_N i_1}} e^{-if_{i_1, i_N}} \\ = \tilde{G}_{0,i_1 i_2} \tilde{G}_{0,i_2 i_3} \dots \tilde{G}_{0,i_N i_1} e^{if_{i_1 i_2}} e^{if_{i_2 i_3}} \dots e^{if_{i_N i_1}} e^{if_{i_N i_1}} \end{aligned} \quad (35)$$

and again the right-hand side is gauge invariant. This proves that the contribution to  $\tilde{\Sigma}_{ij}$  of each Feynman diagram individually is gauge invariant. Moreover,  $\tilde{\Sigma}$  is expressed solely in terms of objects with full lattice symmetry, thus, it must itself exhibit full lattice symmetry.

### Efficient calculation of $\tilde{G}$

A straightforward calculation of  $\tilde{G}$  performed in site space would involve an inverse of the  $N \times N$  matrix

$$\tilde{G}(z) = e^{-if} \circ [\hbar z \mathbf{I} - \mathbf{H}_0[\mathbf{A}] - \Sigma(z)]^{-1}. \quad (36)$$

[Note that here the Peierls phase needs to be taken as Eq. (A2), see Appendix A]. This operation scales as  $O(N^3)$  and the size of the lattice one can treat this way is limited to  $N \sim 1000$ . A more efficient approach can be formulated, and especially so in the noninteracting case, and the case when the self-energy is fully local, i.e., whenever the Green's function is fully diagonal in the eigenbasis of  $\mathbf{H}_0$ , i.e.,  $G_{(\tilde{\mathbf{k}}, m), (\tilde{\mathbf{k}}', m')} = \delta_{\tilde{\mathbf{k}}, \tilde{\mathbf{k}}} \delta_{mm'} G_{\tilde{\mathbf{k}}, m}$ . This is precisely the case relevant for our DMFT calculations. We will make use of the basis change matrix elements to go from eigenbasis  $|\tilde{\mathbf{k}}, m, \sigma\rangle$  to orbital basis  $|i, \sigma\rangle$ :

$$\begin{aligned} |i, \sigma\rangle &= \frac{1}{\sqrt{N}} \sum_{\mathbf{k}} e^{-i\mathbf{k} \cdot \mathbf{r}_i} |\mathbf{k}, \sigma\rangle \\ &= \frac{1}{\sqrt{N}} \sum_{\tilde{\mathbf{k}}, l} e^{-i(\tilde{\mathbf{k}} + l \frac{2\pi}{q} \mathbf{e}_x) \cdot \mathbf{r}_i} |\tilde{\mathbf{k}}, l, \sigma\rangle \\ &= \frac{1}{\sqrt{N}} \sum_{\tilde{\mathbf{k}}, l} e^{-i(\tilde{\mathbf{k}} + l \frac{2\pi}{q} \mathbf{e}_x) \cdot \mathbf{r}_i} \sum_m [\alpha_{\tilde{\mathbf{k}}, \sigma}]_{l, m} |\tilde{\mathbf{k}}, m, \sigma\rangle. \end{aligned} \quad (37)$$

Therefore,

$$G_{\mathbf{r}, \mathbf{r}', \sigma}(z) = \frac{1}{N} \sum_{\tilde{\mathbf{k}}, m} W_{\tilde{\mathbf{k}}, m, \mathbf{r}, \sigma}^* W_{\tilde{\mathbf{k}}, m, \mathbf{r}', \sigma} G_{\tilde{\mathbf{k}}, m, \sigma}(z) \quad (38)$$

with

$$W_{\tilde{\mathbf{k}}, m, \mathbf{r}, \sigma} = \sum_l e^{-i(\tilde{\mathbf{k}} + l \frac{2\pi}{q} \mathbf{e}_x) \cdot \mathbf{r}} [\alpha_{\tilde{\mathbf{k}}, \sigma}]_{l, m}. \quad (39)$$

Calculation of  $[\alpha_{\tilde{\mathbf{k}}, \sigma}]$  scales as  $O(q^3)$ . As there is  $N/q$  different  $\tilde{\mathbf{k}}$  to consider, the first step scales as  $O(Nq^2)$ , with  $q \leq L$ , i.e., at most  $O(N^2)$ . Then the calculation of  $W_{\tilde{\mathbf{k}}, m, \mathbf{r}, \sigma}$  scales as  $O(q)$  but there is  $N$  different  $\tilde{\mathbf{k}}$ ,  $m$  to consider, and we need  $N$  different  $\mathbf{r}$ , which is in total  $O(N^2 q)$ , i.e., at most  $O(N^2 L)$ , which is the bottleneck in the calculation. The calculation of each  $G_{\mathbf{r}, \mathbf{r}', \sigma}(z)$  then scales as  $O(N)$ , but only if  $G$  is diagonal in  $\tilde{\mathbf{k}}, m$ ; if it is only diagonal in  $\tilde{\mathbf{k}}$  but not in  $m$ , this scales as  $O(Nq)$ . As  $\tilde{G}_{\mathbf{r}, \mathbf{r}'} = \tilde{G}_{\mathbf{r}-\mathbf{r}'}$ , we only need to calculate  $N$  different elements of the  $\mathbf{G}$  matrix rather than all  $N^2$  of them:

$$\tilde{G}_{\mathbf{r}} = e^{-if_{\mathbf{r}, \mathbf{r}'=0}} G_{\mathbf{r}, \mathbf{r}'=0}. \quad (40)$$

In total, this scales as  $O(N^2)$ . Again, if  $G$  is diagonal in  $\tilde{\mathbf{k}}$  (as we expect it to be in the absence of translational symmetry breaking), but not in  $m$ , then the scaling is  $O(N^2 q)$ , which is still better than the direct matrix inverse. When there is no translational symmetry (e.g., there is disorder), then the scaling is  $O(N^4)$ , which is worse than the direct matrix inverse. In that case  $\tilde{G}$  is still gauge invariant, but is not translationally invariant, and all  $N^2$   $\mathbf{r}, \mathbf{r}'$  components need to be calculated.

Finally, we are interested in the spatial Fourier transform

$$\tilde{G}_{\mathbf{k}} = \sum_{\mathbf{r}} e^{i\mathbf{k} \cdot \mathbf{r}} \tilde{G}_{\mathbf{r}}, \quad (41)$$

which will be discussed in Sec. III A 2.

We note that other approaches might be possible for the efficient calculation of  $\tilde{G}$ , e.g., the recursive scheme from Ref. [57].

## C. Current density operator and the current-current correlation function

### 1. Orbital space

We will be interested in the direct current conductivity with respect to an infinitesimal uniform electric field. Such electric field  $\mathbf{E} = \partial_t \mathbf{A}^{\text{ext}}$  can be introduced with an additional vector potential  $\mathbf{A}^{\text{ext}}$  pointing uniformly in a given direction, and growing linearly with time. For the purposes of a linear-response calculation, the current couples to such vector potential instantaneously through  $-\int \mathbf{j}(\mathbf{r}) \cdot \mathbf{A}^{\text{ext}}(\mathbf{r}) d^3 \mathbf{r} = -v_{\text{cell}} \sum_i \mathbf{j}_{\mathbf{r}_i} \cdot \mathbf{A}_{\mathbf{r}_i}^{\text{ext}}$ , where  $v_{\text{cell}} = a^2 c$  is the volume of the unit cell. The additional Peierls phase coming from a  $\mathbf{A}^{\text{ext}}$  can therefore be safely rewritten within the slowly varying field approximation

$$\frac{e}{\hbar} \int_{\mathbf{r}_i}^{\mathbf{r}_j} \mathbf{A}^{\text{ext}}(\mathbf{r}) \cdot d\mathbf{r} \approx \frac{ea}{\hbar} \mathbf{A}^{\text{ext}} \cdot (\mathbf{r}_j - \mathbf{r}_i). \quad (42)$$

In the case when we have just the nearest-neighbor hoppings [as in Eq. (12)], the kinetic term in the Hamiltonian can be rewritten as

$$H_{\text{kin}} = -t \sum_{i, \mathbf{u} \in \{\mathbf{e}_x, \mathbf{e}_y\}, \sigma} e^{i(f_{\mathbf{r}_i, \mathbf{r}_i + \mathbf{u}} + \frac{ea}{\hbar} \mathbf{A}_{\mathbf{r}_i}^{\text{ext}} \cdot \mathbf{u})} c_{\mathbf{r}_i, \sigma}^\dagger c_{\mathbf{r}_i + \mathbf{u}, \sigma} + \text{H.c.} \quad (43)$$

without any additional approximation.

We can now derive the expression for the current *density* operator (with units of A/m<sup>2</sup>) in the absence of electric field, by employing

$$\mathbf{j}_r = -\frac{1}{v_{\text{cell}}} \frac{\partial H}{\partial \mathbf{A}_r^{\text{ext}}} \Big|_{\mathbf{A}^{\text{ext}} \rightarrow 0} \quad (44)$$

$$= it \frac{1}{ac} \frac{e}{\hbar} \sum_{\mathbf{u} \in \{\mathbf{e}_x, \mathbf{e}_y\}, \sigma} \mathbf{u} e^{i f_{r_i, r_i + \mathbf{u}}} c_{r_i, \sigma}^\dagger c_{r_i + \mathbf{u}, \sigma} + \text{H.c.} \quad (45)$$

The vector component  $\eta$  can be written as

$$j_r^\eta = it \frac{1}{ac} \frac{e}{\hbar} \sum_{\sigma} \gamma^\eta(\mathbf{r}) c_{r_i, \sigma}^\dagger c_{r_i + \mathbf{e}_\eta, \sigma} + \text{H.c.} \quad (46)$$

with  $\gamma(\mathbf{r}) = (1, e^{i \frac{ea^2}{\hbar} B_z x})$ .

The current is an observable and it should be zero even in the presence of a magnetic field. Commonly, one separates the current into the paramagnetic and diamagnetic parts. In magnetic field they may be nonzero even in thermal equilibrium, but they must cancel. See Appendix E for details.

For the sake of generality, we define the current-current correlation function without assuming zero persistent currents:

$$\begin{aligned} \Lambda_{\mathbf{r}, \mathbf{r}'}^{\eta \eta'}(\tau) &= \langle j_r^\eta(\tau) j_{r'}^{\eta'}(0) \rangle - \langle j_r^\eta \rangle \langle j_{r'}^{\eta'} \rangle \\ &= -t^2 \frac{1}{a^2 c^2} \frac{e^2}{\hbar^2} \sum_{\sigma, \sigma'} \sum_{b, b' \in \{0, 1\}} (-1)^{b+b'} C^b[\gamma_\eta(\mathbf{r})] C^{b'}[\gamma_{\eta'}(\mathbf{r}')] \\ &\quad \times \langle c_{\mathbf{r}+b\mathbf{e}_\eta, \sigma}^\dagger(\tau^+) c_{\mathbf{r}+(1-b)\mathbf{e}_\eta, \sigma}(\tau) c_{\mathbf{r}'+b'\mathbf{e}_{\eta'}, \sigma'}^\dagger(0^+) c_{\mathbf{r}'+(1-b')\mathbf{e}_{\eta'}, \sigma'}(0) \rangle - \langle j_r^\eta \rangle \langle j_{r'}^{\eta'} \rangle, \end{aligned} \quad (47)$$

where  $C[\dots]$  is the operator of complex conjugation, and  $C^0 = 1$ .

We are interested in calculating the Kubo bubble, i.e., the disconnected part. The disconnected part will have a static and a dynamic term. The static one cancels the persistent current part, and the dynamic term can be expressed in terms of the Green's function as

$$\begin{aligned} \Lambda_{\mathbf{r}, \mathbf{r}'}^{\eta \eta', \text{disc}}(\tau) &= t^2 \frac{1}{a^2 c^2} \frac{e^2}{\hbar^2} \sum_{\sigma} \sum_{b, b' \in \{0, 1\}} (-1)^{b+b'} C^b[\gamma_\eta(\mathbf{r})] C^{b'}[\gamma_{\eta'}(\mathbf{r}')] \\ &\quad \times G_{\mathbf{r}'+(1-b')\mathbf{e}_{\eta'}, \mathbf{r}+b\mathbf{e}_\eta, \sigma}(-\tau) G_{\mathbf{r}+(1-b)\mathbf{e}_\eta, \mathbf{r}'+b'\mathbf{e}_{\eta'}, \sigma}(\tau). \end{aligned} \quad (48)$$

We can now rewrite this expression in terms of  $\tilde{G}$ . In the case of the longitudinal component

$$\begin{aligned} \Lambda_{\mathbf{r}, \mathbf{r}'}^{xx, \text{disc}}(\tau) &= t^2 \frac{1}{a^2 c^2} \frac{e^2}{\hbar^2} \sum_{\sigma} \left[ \tilde{G}_{\mathbf{r}'-\mathbf{r}+\mathbf{e}_x, \sigma}(-\tau) \tilde{G}_{\mathbf{r}-\mathbf{r}'+\mathbf{e}_x, \sigma}(\tau) \right. \\ &\quad + \tilde{G}_{\mathbf{r}'-\mathbf{r}-\mathbf{e}_x, \sigma}(-\tau) \tilde{G}_{\mathbf{r}-\mathbf{r}'+\mathbf{e}_x, \sigma}(\tau) \\ &\quad \left. - 2 \cos\left(\frac{ea^2 B_z}{\hbar}(y-y')\right) \tilde{G}_{\mathbf{r}'-\mathbf{r}, \sigma}(-\tau) \tilde{G}_{\mathbf{r}-\mathbf{r}', \sigma}(\tau) \right]. \end{aligned} \quad (49)$$

We see that the expression only depends on the distance which means that it preserves translational symmetry, and is only expressed in terms of gauge-invariant quantities. We have checked explicitly that exactly the same expression is also obtained in the symmetric gauge. Furthermore, this expression has all the expected spatial symmetries. A completely

analogous calculation for  $\Lambda_{\mathbf{r}, \mathbf{r}'}^{yy, \text{disc}}(\tau)$  yields the expression with  $x, y \rightarrow y, x$ . A general proof of the gauge invariance of  $\Lambda_{\mathbf{r}, \mathbf{r}'}^{\eta, \eta', \text{disc}}(\tau)$  is given in Appendix F.

## 2. Momentum space

As we have shown that the current-current correlation function satisfies all the desired spatial symmetries, we can proceed to discuss the uniform current-current correlation function in a straightforward manner by performing the spatial Fourier transform. We have

$$\Lambda_{\mathbf{q}=0}^{\eta \eta'}(\tau) = v_{\text{cell}} \sum_{\mathbf{r}} \Lambda_{\mathbf{r}, \mathbf{r}=0}(\tau). \quad (50)$$

This is followed by the Fourier transform in imaginary time to finally obtain

$$\Lambda_{\mathbf{q}=0}^{\eta \eta'}(i\nu) = v_{\text{cell}} \sum_{\mathbf{r}} \frac{1}{2\hbar} \int_{-\beta\hbar}^{\beta\hbar} d\tau e^{i\nu\tau} \Lambda_{\mathbf{r}, \mathbf{r}=0}(\tau). \quad (51)$$

We can rewrite this expression more conveniently using the uniform current operator as

$$\Lambda_{\mathbf{q}=0}^{\eta \eta'}(i\nu) = \frac{V}{2\hbar} \int_{-\beta\hbar}^{\beta\hbar} d\tau \langle j_{\mathbf{q}=0}^\eta(\tau) j_{\mathbf{q}=0}^{\eta'}(0) \rangle, \quad (52)$$

where  $V$  is the total volume  $V = N v_{\text{cell}}$  and

$$j_{\mathbf{q}=0}^\eta = \frac{1}{N} \sum_{\mathbf{r}} j_{\mathbf{r}}^\eta. \quad (53)$$

Note that we have here defined the uniform current operator as the average current (density) operator, rather than the spatial Fourier transform of the current operator. Using the creation



and annihilation operators in the eigenbasis of the noninteracting Hamiltonian, we can write

$$j_{\mathbf{q}=0}^{\eta} = \frac{it}{N} \frac{1}{ac} \frac{e}{\hbar} \sum_{\sigma} \sum_{\tilde{\mathbf{k}}, m, m'} v_{\tilde{\mathbf{k}}, m, m', \sigma}^{\eta} c_{\tilde{\mathbf{k}}, m, \sigma}^{\dagger} c_{\tilde{\mathbf{k}}, m', \sigma} \quad (54)$$

with

$$v_{\tilde{\mathbf{k}}, m, m', \sigma}^x = \sum_l [\alpha_{\tilde{\mathbf{k}}, \sigma}]_{l, m} [\alpha_{\tilde{\mathbf{k}}, \sigma}]_{l, m'}^* [e^{i\tilde{\mathbf{k}}_x} e^{il\frac{2\pi}{q}} - e^{-i\tilde{\mathbf{k}}_x} e^{-il\frac{2\pi}{q}}] \quad (55)$$

and

$$v_{\tilde{\mathbf{k}}, m, m', \sigma}^y = \sum_l [\alpha_{\tilde{\mathbf{k}}, \sigma}]_{l, m} [e^{i\tilde{\mathbf{k}}_y} [\alpha_{\tilde{\mathbf{k}}, \sigma}]_{l \ominus p, m'}^* - e^{-i\tilde{\mathbf{k}}_y} [\alpha_{\tilde{\mathbf{k}}, \sigma}]_{l \oplus p, m'}^*]. \quad (56)$$

The proof for the above expressions is given in Appendix G. Assuming no persistent currents, the uniform current-current correlation function is therefore

$$\begin{aligned} \Lambda_{\mathbf{q}=0}^{\eta\eta'}(i\nu) &= -\frac{t^2 e^2}{c\hbar^2} \frac{1}{N} \sum_{\sigma_1, \sigma_2} \frac{1}{2\hbar} \int_{-\beta\hbar}^{\beta\hbar} d\tau e^{i\nu\tau} \\ &\times \sum_{\tilde{\mathbf{k}}_1, m_1, m'_1} \sum_{\tilde{\mathbf{k}}_2, m_2, m'_2} v_{\tilde{\mathbf{k}}_1, m_1, m'_1, \sigma_1}^{\eta} v_{\tilde{\mathbf{k}}_2, m_2, m'_2, \sigma_2}^{\eta'} \\ &\times \langle c_{\tilde{\mathbf{k}}_1, m_1, \sigma_1}^{\dagger}(\tau^+) c_{\tilde{\mathbf{k}}_1, m'_1, \sigma_1}(\tau) c_{\tilde{\mathbf{k}}_2, m_2, \sigma_2}^{\dagger}(0^+) c_{\tilde{\mathbf{k}}_2, m'_2, \sigma_2}(0) \rangle. \end{aligned} \quad (57)$$

The disconnected part written as a function of bosonic Matsubara frequency reads as (see Appendix H for proof)

$$\begin{aligned} \Lambda_{\mathbf{q}=0}^{\eta\eta', \text{disc}}(i\nu) &= \frac{t^2 e^2}{c\hbar^2} \frac{1}{N} \sum_{\sigma} \sum_{\tilde{\mathbf{k}}, m_1, m'_1, m_2, m'_2} \\ &\times v_{\tilde{\mathbf{k}}, m_1, m'_1, \sigma}^{\eta} v_{\tilde{\mathbf{k}}, m_2, m'_2, \sigma}^{\eta'} \\ &\times \frac{1}{\beta} \sum_{i\omega} G_{\tilde{\mathbf{k}}, m'_2, m_1 \sigma}(i\omega) G_{\tilde{\mathbf{k}}, m'_1, m_2, \sigma}(i\omega + i\nu). \end{aligned} \quad (58)$$

## D. Method

### 1. DMFT

In dynamical mean field theory (DMFT), the lattice problem is mapped onto a set of self-consistent local impurity problems on each lattice site  $i$ , defined by the action [58–61]

$$\begin{aligned} S_i^{\text{imp}} &= \sum_{\sigma} \int d\tau d\tau' c_{i, \sigma}^{\dagger}(\tau) [-\mathcal{G}_{0, i}^{-1}](\tau - \tau') c_{i, \sigma}(\tau') \\ &+ U \int d\tau c_{i, \uparrow}^{\dagger}(\tau) c_{i, \uparrow}(\tau) c_{i, \downarrow}^{\dagger}(\tau) c_{i, \downarrow}(\tau). \end{aligned} \quad (59)$$

The bare propagator  $\mathcal{G}_{0, i}$  in the impurity problem  $i$  is determined self-consistently, so that the Green's function in each impurity problem is equal to the local Green's function on the site of the impurity problem, assuming that the self-energy on the lattice is local and on each site equal to the self-energy

of the corresponding impurity problem. This self-consistency condition can be written as

$$\mathcal{G}_{0, i}(z) = 1/([G^{-1}]_{ii}(z) + \Sigma_i^{\text{imp}}(z)), \quad (60)$$

where  $\Sigma_i^{\text{imp}}(z)$  is the self-energy calculated in the impurity problem at site  $i$ , and the lattice Green's function is calculated as a matrix in the site space as

$$\mathbf{G}(z) = [\mathbf{I}\hbar z - \mathbf{H}_0[\mathbf{A}] - \text{diag}(\Sigma^{\text{imp}}(z))]^{-1}, \quad (61)$$

where  $\text{diag}(\Sigma^{\text{imp}})$  is a diagonal matrix, with  $\Sigma_i^{\text{imp}}(z)$  entries on the diagonal. This construction is general and can be used in the presence of translational symmetry breaking fields, disorder, and even used to probe spatially ordered phases. The DMFT approximation notably becomes exact in the limit of infinite coordination number, where the self-energy can be shown to be fully local [58], at least in the absence of magnetic fields.

We see that in the calculation of the bare propagator for the impurity problems, only the local Green's function plays a role, and this quantity is gauge invariant and spatially uniform. Therefore, even in the presence of the uniform magnetic field, all impurity problems are equivalent, and we may solve only one impurity problem and calculate the lattice Green's function as

$$\mathbf{G}(z) = [\mathbf{I}\hbar z - \mathbf{H}_0[\mathbf{A}] - \mathbf{I}\Sigma^{\text{imp}}(z)]^{-1}. \quad (62)$$

This leads to further simplifications. First, a local and spatially uniform self-energy is diagonal in the noninteracting eigenbasis ( $\Sigma_{\sigma, ij} = \delta_{ij} \Sigma_{\sigma} \implies \langle \mathbf{k}, \sigma, m | \Sigma | \mathbf{k}', \sigma, m' \rangle = \delta_{\mathbf{k}, \mathbf{k}'} \delta_{m, m'} \Sigma_{\sigma}$ , see Appendix I for proof) which means that the lattice Green's function is diagonal as well:

$$G_{\tilde{\mathbf{k}}, m, m', \sigma}(z) = \delta_{mm'} G_{\tilde{\mathbf{k}}, mm, \sigma}(z), \quad (63)$$

thus, we can drop the second eigenstate index and simply calculate the lattice Green's function as

$$G_{\tilde{\mathbf{k}}, m, \sigma}(z) = \frac{1}{\hbar z - \varepsilon_{\tilde{\mathbf{k}}, m, \sigma} - \Sigma_{\sigma}(z)}. \quad (64)$$

The local Green's function can then be obtained at low numerical cost from the knowledge of the local density of states  $\rho_0(\varepsilon)$  as (see Appendix J for proof)

$$G_{ii, \sigma}(z) = \int d\varepsilon \frac{\rho_0(\varepsilon)}{\hbar z - \varepsilon - \Sigma_{\sigma}(z)}. \quad (65)$$

Therefore, the DMFT calculation for the Hubbard model in the magnetic field proceeds as the standard DMFT, and all the effects of the gauge field are contained in the noninteracting density of states [41]. In all our calculations we employ the numerical renormalization group (NRG) impurity solver [62–65] which works directly in real-frequency space, so no analytical continuation is needed to perform calculations of conductivity. The NRG solver has been previously thoroughly cross checked in Refs. [7, 11, 13].

### 2. Calculation of conductivity in DMFT

The fact that the Green's function is diagonal in the noninteracting eigenbasis leads to a simplification in the Kubo bubble [Eq. (57)]. One is left with only two summations over

eigenstates  $m$ :

$$\Lambda_{\mathbf{q}=0}^{\eta\eta',\text{disc}}(i\nu) = \frac{t^2 e^2}{c\hbar^2} \frac{1}{N} \sum_{\sigma} \sum_{\mathbf{k},m,m'} \frac{1}{\beta} \sum_{i\omega} v_{\mathbf{k},m,m',\sigma}^{\eta} v_{\mathbf{k},m',m,\sigma}^{\eta'} G_{\mathbf{k},m,\sigma}(i\omega + i\nu) G_{\mathbf{k},m',\sigma}(i\omega). \quad (66)$$

Furthermore, because the self-energy is local, the Green's function only depends on the energy of the eigenstate, so we can define  $G(\varepsilon_{\mathbf{k},m,\sigma}, i\omega) \equiv G_{\mathbf{k},m,\sigma}(i\omega)$  and rewrite

$$\Lambda_{\mathbf{q}=0}^{\eta\eta',\text{disc}}(i\nu) = \frac{t^2 e^2}{c\hbar^2} \sum_{\sigma} \frac{1}{\beta} \sum_{i\omega} \int d\varepsilon \int d\varepsilon' \times v_{\sigma}^{\eta,\eta'}(\varepsilon, \varepsilon') G(\varepsilon, i\omega + i\nu) G(\varepsilon', i\omega) \quad (67)$$

with

$$v_{\sigma}^{\eta,\eta'}(\varepsilon, \varepsilon') \equiv \frac{1}{N} \sum_{\mathbf{k},m,m'} \delta(\varepsilon - \varepsilon_{\mathbf{k},m,\sigma}) \times \delta(\varepsilon' - \varepsilon_{\mathbf{k},m',\sigma}) v_{\mathbf{k},m,m',\sigma}^{\eta} v_{\mathbf{k},m',m,\sigma}^{\eta'}. \quad (68)$$

In Landau gauge, one has the symmetry  $v_{\mathbf{k},m,m',\sigma}^x = -(v_{\mathbf{k},m',m,\sigma}^x)^*$  (see Appendix G), and therefore  $v_{\mathbf{k},m,m',\sigma}^x v_{\mathbf{k},m',m,\sigma}^x = -|v_{\mathbf{k},m',m,\sigma}^x|^2$ , which means  $v_{\sigma}^{xx}(\varepsilon, \varepsilon')$  is purely real. On the contrary, as already noted in Ref. [38],  $v_{\sigma}^{xy}(\varepsilon, \varepsilon')$  is purely imaginary.

The *sheet conductance* is related to the current-current correlation function through

$$\sigma^{\eta\eta'}(\nu) = c \frac{\Lambda^{\eta\eta'}(\nu) - \Lambda^{\eta\eta'}(\nu=0)}{i\nu}. \quad (69)$$

The  $z$ -axis lattice constant  $c$  cancels out  $c$  from  $v_{\text{cell}} = a^2 c$  and its value is irrelevant. In the following we will discard the difference between the sheet conductance and the conductivity, and refer to  $\sigma$  as conductivity, even though it is actually sheet conductance and the units of the two quantities are different  $[(\Omega m)^{-1} \text{ vs } \Omega^{-1}]$ ; this is common practice in the field.

After several lines of algebra aimed at the analytical continuation to the real-axis frequency (see Appendix K), we obtain

$$\text{Re}\sigma_{\mathbf{q}=0}^{xx,\text{disc}}(\nu=0) = t^2 \frac{e^2}{\hbar} \frac{1}{\pi} \sum_{\sigma} \int d\varepsilon \int d\varepsilon' v_{\sigma}^{xx}(\varepsilon, \varepsilon') \int d\omega \times \text{Im}G(\varepsilon, \omega) \text{Im}G(\varepsilon', \omega) n'_{\text{F}}(\omega), \quad (70)$$

where  $n'_{\text{F}}(\omega) = -\beta\hbar e^{\beta\hbar\omega} / (1 + e^{\beta\hbar\omega})^2$  is the derivative of the Fermi function.

For Hall conductivity one obtains [38]

$$\begin{aligned} \text{Re}\sigma_{\mathbf{q}=0}^{xy,\text{disc}}(\nu=0) &= -t^2 \frac{e^2}{\hbar} \frac{1}{\pi^2} \sum_{\sigma} \int d\varepsilon \int d\varepsilon' \text{Im}v_{\sigma}^{xy}(\varepsilon, \varepsilon') \int d\omega \int d\omega' \\ &\times \text{Im}G(\varepsilon, \omega) \text{Im}G(\varepsilon', \omega') \frac{n_{\text{F}}(\omega) - n_{\text{F}}(\omega')}{(\omega - \omega')^2}. \end{aligned} \quad (71)$$

An additional simplification is possible in the case of Hall conductivity when  $U = 0$ . In that case we have [22]

$$\begin{aligned} \text{Re}\sigma_{\mathbf{q}=0}^{xy,\text{disc}}(\nu=0; U=0) &= -t^2 \frac{e^2}{\hbar} \sum_{\sigma} \int d\varepsilon \int d\varepsilon' \text{Im}v_{\sigma}^{xy}(\varepsilon, \varepsilon') \frac{n_{\text{F}}(\varepsilon) - n_{\text{F}}(\varepsilon')}{(\varepsilon - \varepsilon')^2}. \end{aligned} \quad (72)$$

Finally, the resistivity is obtained as a matrix inverse

$$\begin{pmatrix} \rho^{xx} & \rho^{xy} \\ \rho^{yx} & \rho^{yy} \end{pmatrix} = \begin{pmatrix} \sigma^{xx} & \sigma^{xy} \\ \sigma^{yx} & \sigma^{yy} \end{pmatrix}^{-1}. \quad (73)$$

### 3. Vertex corrections in DMFT

Finally, to calculate the full current-current correlation function, one should in principle also compute the vertex corrections. At the level of the DMFT, in the absence of an external magnetic field, the vertex corrections cancel due to the well-known argument due to Khurana [42]. As we show in the following, a generalized Khurana argument holds even in the presence of the magnetic field. In the following we first derive the Khurana argument in real space, and then generalize it to the case of nonzero magnetic fields.

We start first by writing the vertex corrections in orbital space, in the most general way:

$$\begin{aligned} \Lambda_{\mathbf{q}=0}^{\eta\eta',\text{conn}}(\tau - \tau') &= t^2 \frac{e^2}{a^2 c^2 \hbar^2} \sum_{\sigma,\sigma'} \sum_{b,b' \in \{0,1\}} (-1)^{b+b'} \\ &\times \frac{1}{N^2} \sum_{\mathbf{r},\mathbf{r}'} C^b[\gamma_{\eta}(\mathbf{r})] C^{b'}[\gamma_{\eta'}(\mathbf{r}')] \\ &\times \sum_{\mathbf{r}_1,\mathbf{r}_2,\mathbf{r}_3,\mathbf{r}_4} \int d\tau_1 d\tau_2 d\tau_3 d\tau_4 \\ &\times G_{\mathbf{r}_1,\mathbf{r}+b\mathbf{e}_{\eta},\sigma}(\tau_1 - \tau) G_{\mathbf{r}+(1-b)\mathbf{e}_{\eta},\mathbf{r}_2,\sigma}(\tau - \tau_2) \\ &\times F((\mathbf{r}_1, \tau_1), (\mathbf{r}_2, \tau_2), (\mathbf{r}_3, \tau_3), (\mathbf{r}_4, \tau_4)) \\ &\times G_{\mathbf{r}'+(1-b')\mathbf{e}_{\eta'},\mathbf{r}_3,\sigma'}(\tau' - \tau_3) G_{\mathbf{r}_4,\mathbf{r}'+b'\mathbf{e}_{\eta'},\sigma'}(\tau_4 - \tau'), \end{aligned} \quad (74)$$

as illustrated in Fig. 1(a). In the absence of external magnetic field or spontaneous symmetry breaking,  $G_{\mathbf{r},\mathbf{r}'}$  has full lattice symmetry and depends only on the difference  $G_{\mathbf{r}-\mathbf{r}'}$ . However, there is no symmetry operation which guarantees cancellation of all terms. There is only one symmetry operation that leaves the Green's functions intact and flips the overall sign, but it does change the full vertex. It can be formulated either for internal variables  $\mathbf{r}_1, \mathbf{r}_2, b$  or for  $\mathbf{r}_3, \mathbf{r}_4, b'$ , and we illustrate the latter case in Fig. 1(b). The transformation can be formulated as follows:

$$\begin{aligned} \mathbf{r}' &\rightarrow -\mathbf{r}' + \mathbf{r}_3 + \mathbf{r}_4 - \mathbf{e}_{\eta'}, & b' &\rightarrow 1 - b', \\ (\mathbf{r}_3, \tau_3) &\leftrightarrow (\mathbf{r}_4, \tau_4). \end{aligned} \quad (75)$$

The flip of  $b'$  changes the overall sign, but the exchange of terminals of the full vertex function changes its value in no obvious way, and there is no cancellation in the general case.

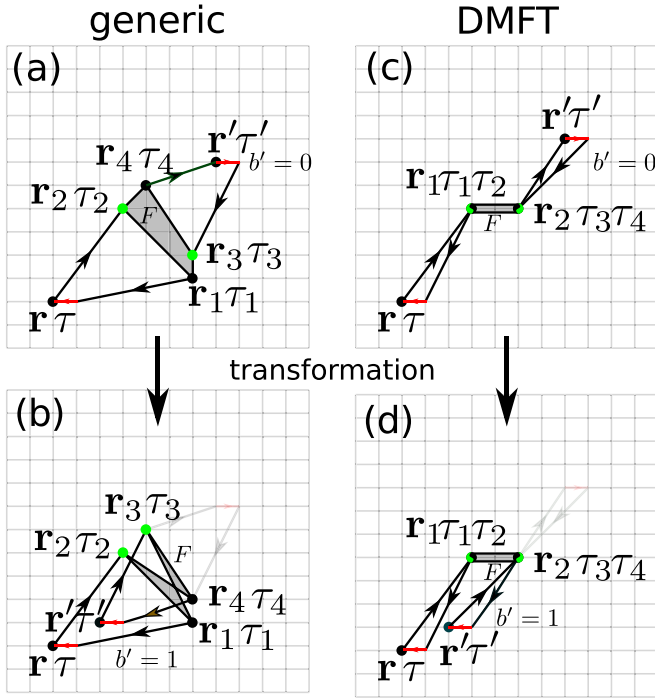


FIG. 1. Real-space diagrammatic representation of a contribution to the connected part of the current-current correlation function.  $F$  is the full vertex, red segments indicate a term in the current operator connecting two nearest-neighbor sites in the  $x$  direction; swapping the direction of the red arrow changes its sign. Top panels: for generic case [left, Eq. (74)] and DMFT [right, Eq. (76)]. Bottom panels: after the transformation in Eqs. (75) (left) and (77) (right).

However, in DMFT there is an additional simplification that the full vertex  $F$  depends on only two spatial indices:

$$\begin{aligned} \Lambda_{\mathbf{q}=0}^{\eta\eta',\text{conn}}(\tau - \tau') &= t^2 \frac{e^2}{a^2 c^2 \hbar^2} \sum_{\sigma, \sigma'} \sum_{b, b' \in \{0, 1\}} (-1)^{b+b'} \\ &\times \frac{1}{N^2} \sum_{\mathbf{r}, \mathbf{r}'} C^b[\gamma_\eta(\mathbf{r})] C^{b'}[\gamma_{\eta'}(\mathbf{r}')] \sum_{\mathbf{r}_1, \mathbf{r}_2} \int d\tau_1 d\tau_2 d\tau_3 d\tau_4 \\ &\times G_{\mathbf{r}_1, \mathbf{r}+b\mathbf{e}_\eta, \sigma}(\tau_1 - \tau) G_{\mathbf{r}+(1-b)\mathbf{e}_\eta, \mathbf{r}_1, \sigma}(\tau - \tau_2) \\ &\times F((\mathbf{r}_1, \tau_1), (\mathbf{r}_1, \tau_2), (\mathbf{r}_2, \tau_3), (\mathbf{r}_2, \tau_4)) \\ &\times G_{\mathbf{r}'+(1-b')\mathbf{e}_{\eta'}, \mathbf{r}_2, \sigma'}(\tau' - \tau_3) G_{\mathbf{r}_2, \mathbf{r}'+b'\mathbf{e}_{\eta'}, \sigma'}(\tau_4 - \tau'). \end{aligned} \quad (76)$$

In that case, a transformation

$$\mathbf{r}' \rightarrow -\mathbf{r}' - \mathbf{e}_{\eta'} + 2\mathbf{r}_2, \quad b' \rightarrow 1 - b' \quad (77)$$

keeps both the Green's functions and the full vertex intact, while changing the overall sign. Then the two symmetry-connected terms together read as (up to a prefactor)

$$\begin{aligned} &G_{\mathbf{r}'+(1-b')\mathbf{e}_{\eta'}, \mathbf{r}_2, \sigma'}(\tau' - \tau_3) G_{\mathbf{r}_2, \mathbf{r}'+b'\mathbf{e}_{\eta'}, \sigma'}(\tau_4 - \tau') \\ &- G_{-\mathbf{r}'+2\mathbf{r}_2-(1-b')\mathbf{e}_{\eta'}, \mathbf{r}_2, \sigma'}(\tau' - \tau_3) \\ &\times G_{\mathbf{r}_2, -\mathbf{r}'+2\mathbf{r}_2-b'\mathbf{e}_{\eta'}, \sigma'}(\tau_4 - \tau'). \end{aligned} \quad (78)$$

When the lattice preserves inversion symmetry, one has  $G_{\mathbf{r}, \mathbf{r}'} = G_{\mathbf{r}-\mathbf{r}'} = G_{\mathbf{r}'-\mathbf{r}}$ , and the above two terms always cancel. This is the real-space version of the Khurana argument.

However, when there is magnetic field, there are additional complications. Nevertheless, the full vertex is a gauge-invariant quantity, as the irreducible vertex in the particle-hole channel  $\Gamma^{\text{ph}}$  is fully local and therefore gauge invariant and spatially uniform  $\Gamma_{ijkl}^{\text{ph}} = \delta_{ij} \delta_{jk} \delta_{kl} \Gamma^{\text{ph}}$ . This comes as DMFT is the local approximation of the Luttinger-Ward functional [58,66], and  $\Gamma_{ijkl}^{\text{ph}} = \frac{\partial^2 \Phi[\mathbf{G}]}{\partial G_{ij} \partial G_{kl}}|_{\mathbf{G}=\mathbf{G}_{\text{exact}}} \approx \frac{\partial^2 \Phi^{\text{DMFT}}[\{G_{ii}\}_i]}{\partial G_{ij} \partial G_{kl}}|_{\mathbf{G}=\mathbf{G}_{\text{DMFT}}}$ . Therefore, we have

$$\begin{aligned} F_{ii, jj} &= \delta_{ij} \Gamma^{\text{ph}} + \Gamma^{\text{ph}} G_{ij} G_{ji} \Gamma^{\text{ph}} \\ &+ \sum_l \Gamma^{\text{ph}} G_{il} G_{li} \Gamma^{\text{ph}} G_{lj} G_{jl} \Gamma^{\text{ph}} + \dots \\ &= \delta_{ij} \Gamma^{\text{ph}} + \Gamma^{\text{ph}} \tilde{G}_{ij} \tilde{G}_{ji} \Gamma^{\text{ph}} \\ &+ \sum_l \Gamma^{\text{ph}} \tilde{G}_{il} \tilde{G}_{li} \Gamma^{\text{ph}} \tilde{G}_{lj} \tilde{G}_{jl} \Gamma^{\text{ph}} + \dots \end{aligned} \quad (79)$$

and  $F$  is clearly expressed entirely with gauge-invariant quantities. Here we have omitted spin and temporal arguments and the corresponding sums and integrals for the sake of brevity, as they do not play a role in the proof.

In the presence of the magnetic field, the Green's function does not satisfy  $G_{\mathbf{r}, \mathbf{r}'} = G_{\mathbf{r}-\mathbf{r}'} = G_{\mathbf{r}'-\mathbf{r}}$  and it is not *a priori* clear that the terms in Eq. (78) cancel. We can, however, rewrite them in terms of  $\bar{G}$ :

$$\begin{aligned} &e^{i f_{\mathbf{r}'+(1-b')\mathbf{e}_{\eta'}, \mathbf{r}_2}} \bar{G}_{\mathbf{r}'+(1-b')\mathbf{e}_{\eta'}, \mathbf{r}_2, \sigma'}(\tau' - \tau_3) \\ &\times e^{i f_{\mathbf{r}_2, \mathbf{r}'+b'\mathbf{e}_{\eta'}}} \bar{G}_{\mathbf{r}_2, \mathbf{r}'+b'\mathbf{e}_{\eta'}, \sigma'}(\tau_4 - \tau') \\ &- e^{i f_{-\mathbf{r}'+2\mathbf{r}_2-(1-b')\mathbf{e}_{\eta'}, \mathbf{r}_2}} \bar{G}_{-\mathbf{r}'+2\mathbf{r}_2-(1-b')\mathbf{e}_{\eta'}, \mathbf{r}_2, \sigma'}(\tau' - \tau_3) \\ &\times e^{i f_{\mathbf{r}_2, -\mathbf{r}'+2\mathbf{r}_2-b'\mathbf{e}_{\eta'}}} \bar{G}_{\mathbf{r}_2, -\mathbf{r}'+2\mathbf{r}_2-b'\mathbf{e}_{\eta'}, \sigma'}(\tau_4 - \tau'). \end{aligned} \quad (80)$$

As  $\bar{G}$  satisfies  $\bar{G}_{\mathbf{r}, \mathbf{r}'} = \bar{G}_{\mathbf{r}-\mathbf{r}'} = \bar{G}_{\mathbf{r}'-\mathbf{r}}$ , the products of  $\bar{G}$  are the same in both terms, thus, what determines whether there is cancellation or not is

$$e^{i f_{\mathbf{r}'+(1-b')\mathbf{e}_{\eta'}, \mathbf{r}_2}} e^{i f_{\mathbf{r}_2, \mathbf{r}'+b'\mathbf{e}_{\eta'}}} - e^{i f_{-\mathbf{r}'+2\mathbf{r}_2-(1-b')\mathbf{e}_{\eta'}, \mathbf{r}_2}} e^{i f_{\mathbf{r}_2, -\mathbf{r}'+2\mathbf{r}_2-b'\mathbf{e}_{\eta'}}}. \quad (81)$$

In Landau gauge and for, say,  $\eta' = x$ , we get

$$\begin{aligned} &e^{i \frac{ea^2 B_z}{2\hbar} (y_2 - y') [x' + x_2 + (1-b')]} e^{i \frac{ea^2 B_z}{2\hbar} (y' - y_2) (x' + x_2 + b')} \\ &- e^{i \frac{ea^2 B_z}{2\hbar} (-y_2 + y') [3x_2 - x' - (1-b')]} e^{i \frac{ea^2 B_z}{2\hbar} (-y' + y_2) (-x' - b' + 3x_2)} \\ &= e^{i \frac{ea^2 B_z}{2\hbar} (y_2 - y') (1-2b')} - e^{i \frac{ea^2 B_z}{2\hbar} B_z (-y_2 + y') (-1+2b')} \\ &= 0. \end{aligned} \quad (82)$$

This means that the vertex corrections cancel. This proof is immediately valid for both  $\Lambda^{xx}$  and  $\Lambda^{yx}$ . Having in mind a completely analogous transformation of  $\mathbf{r}$  and  $b$ , this proof holds also for  $\Lambda^{xy}$  (a different proof was given for  $\Lambda^{xy}$  in Ref. [38]). However, we also want to check what happens with  $\eta' = y$ , which is relevant for  $\Lambda^{yy}$ . In that case, the

transformation affects also  $C^{b'}[\gamma_y(\mathbf{r}')]$  so we need to take that into account:

$$\begin{aligned}
 & e^{i(1-2b')\frac{ea^2}{h}B_zx'} e^{if_{r'}+(1-b')e_{\eta'}r_2} e^{if_{r_2,r'}+b'e_{\eta'}r_2} - e^{-i(1-2b')\frac{ea^2}{h}B_z(-x'+2x_2)} e^{if_{-r'}+2r_2-(1-b')e_{\eta'}r_2} e^{if_{r_2,-r'}+2r_2-b'e_{\eta'}r_2} \\
 &= e^{i(1-2b')\frac{ea^2}{h}B_zx'} e^{i\frac{ea^2}{2h}B_z[y_2-y'-(1-b')(x_2+x')]} e^{i\frac{ea^2}{2h}B_z(y'+b'-y_2)(x_2+x')} - e^{-i(1-2b')\frac{ea^2}{h}B_z(-x'+2x_2)} \\
 &\quad \times e^{i\frac{ea^2}{2h}B_z[y'-y_2+(1-b')(3x_2-x')]} e^{i\frac{ea^2}{2h}B_z(-y'+y_2-b')(-x'+3x_2)} \\
 &= e^{i(1-2b')\frac{ea^2}{h}B_zx'} e^{i\frac{ea^2}{2h}B_z(-1+2b')(x_2+x')} - e^{-i(1-2b')\frac{ea^2}{h}B_z(-x'+2x_2)} e^{i\frac{ea^2}{2h}B_z[(1-2b')(3x_2-x')]} \\
 &= e^{i\frac{ea^2}{2h}B_z[2(1-2b')x'-(1-2b')(x_2+x')]} - e^{i\frac{ea^2}{2h}B_z[2(1-2b')x'-4(1-2b')x_2+(1-2b')(3x_2-x')]} \\
 &= e^{i\frac{ea^2}{2h}B_z(x'-2b'x'-x_2+2b'x_2)} - e^{i\frac{ea^2}{2h}B_z(x'-2b'x'-x_2+2b'x_2)} \\
 &= 0.
 \end{aligned} \tag{83}$$

Indeed, the vertex corrections for  $\Lambda^{yy}$  cancel as well. As we have shown that the Kubo bubble is gauge invariant (see Appendix F), and having that the full correlation function needs to be gauge invariant as it relates to observables, the proof given here is fully general, even though it is formulated in Landau gauge. The proof also does not depend on whether there is Zeeman term in the Hamiltonian or not.

### III. RESULTS

#### A. Density of states and spectral function

##### 1. Noninteracting density of states

In the DMFT, the magnetic field enters through the noninteracting density of states  $\rho_0(\omega)$ . The magnetic field dependence of  $\rho_0(\omega)$  (the famous Hofstadter butterfly [55]) is shown in Fig. 2. This result was obtained with lattice size  $L = 1999$ , and about 4000 energy bins, which sets the resolution and the minimal size of an energy gap that one can observe.

##### 2. Translation-invariant spectral function

As we have already proven, on a finite lattice  $L \times L$  and  $L = q$ , there is no dependence of the Hamiltonian on

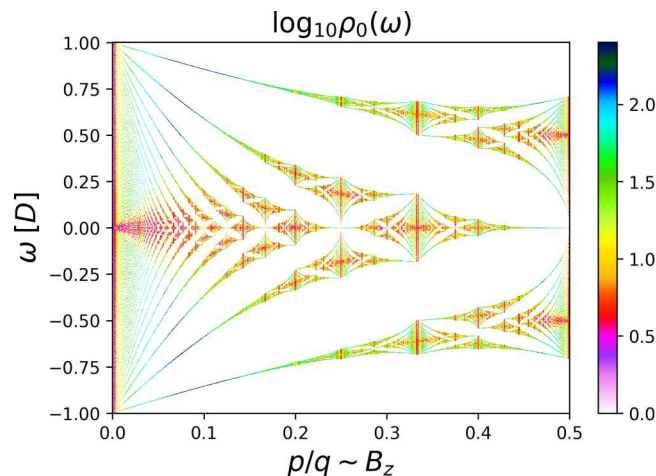


FIG. 2. Noninteracting density of states, as a function of frequency and magnetic field (the Hofstadter butterfly [55]).

$k_y$ . A straightforward basis change of the Green's function to the original  $\mathbf{k}$  states in the full BZ yields a meaningless result for the spectral function with no  $k_y$  dependence whatsoever. Moreover, this result is gauge dependent, as the choice of a slightly different gauge  $\mathbf{A} \sim (-y, 0)$  would yield a spectral function result with no  $k_x$  dependence instead.

One is therefore interested in the translationally invariant  $\bar{G}$ , as it has all the lattice symmetries, and can ultimately be Fourier transformed into momentum space. We show this result in the noninteracting case in Fig. 3. We have used a small broadening  $\Sigma(z) = -i \text{sgn}(\text{Im}z)\eta$ ,  $\eta = 0.02$ , to regularize the results. We observe that the result for the imaginary part of  $\bar{G}$  is not necessarily negative, which is a signature of a breaking of causality, and thus the result is not a proper physical spectral function. As expected, the nonphysical features subside as the magnetic field is taken to zero. Note also that  $\bar{G}_{\text{loc}} = G_{\text{loc}}$ , so the causality of the resulting local Green's function is restored upon the summation over momenta.

##### 3. Local spectra from DMFT

In Fig. 4 we present the DMFT(NRG) results for  $\text{Im}G_{\text{loc}}(\omega)$ , at different values of magnetic field, and fixed  $U = 2.5D$ ,  $n = 0.85$ , and  $T = 0.025D$ , which corresponds to the regime of the doped Mott insulator. On the left panel we show the full frequency range, while on the right panel we focus on the quasiparticle part of the spectrum. Increasing the magnetic field appears to affect an ever growing range of frequencies around  $\omega = 0$ , but up to the highest fields the effect is restricted to the quasiparticle peak and no significant change is observed in the Hubbard bands, apart from the lower Hubbard band getting flatter. No apparent change at all is observed below  $p/q = 0.1$  for these values of model parameters.

#### B. Conductivity

##### 1. Longitudinal dc conductivity $\sigma^{xx}(\nu = 0)$

We start by inspecting the effect of the magnetic-field dependence of the self-energy on the conductivity. In the upper panel of Fig. 5 we show  $1/\sigma^{xx}(\nu = 0)$  calculated with the self-energy obtained from the DMFT(NRG) calculation for



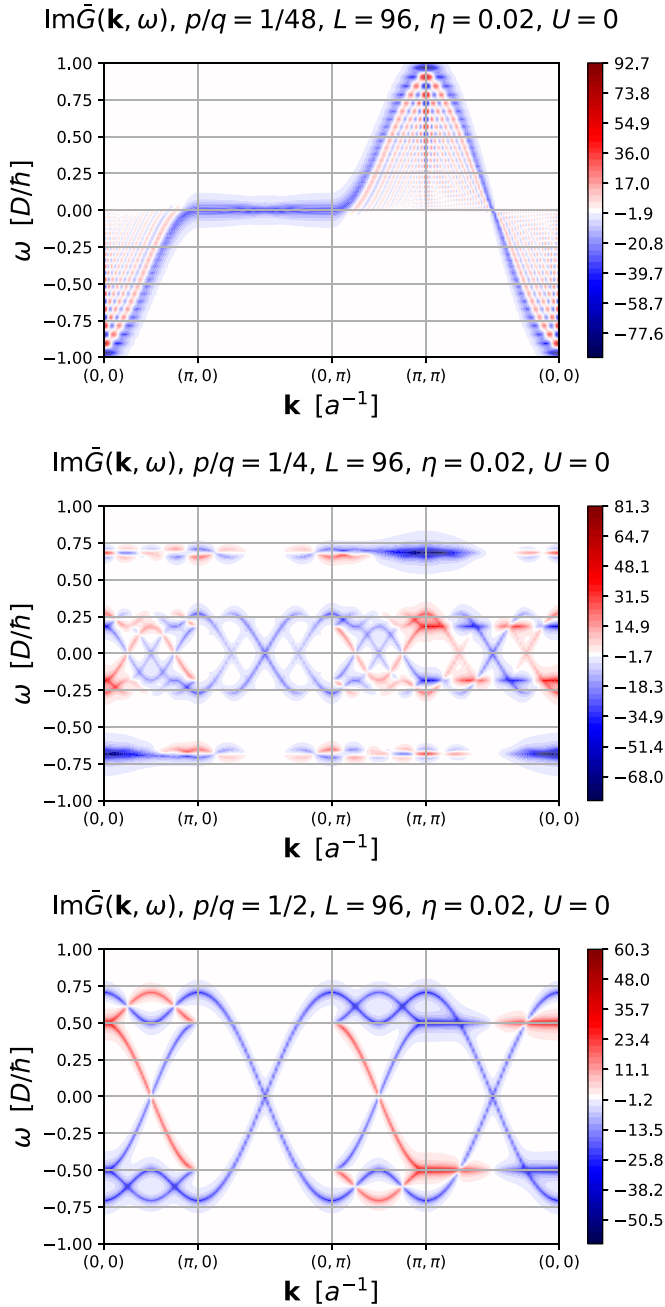


FIG. 3. Spectrum of the translation-invariant Green's function  $\text{Im}\tilde{G}_{\mathbf{k}}(\omega)$ . The examples are given for  $U = 0$  with a broadening  $\eta = 0.02D$ , and at three different values of  $p/q$ , as indicated in panel titles. The spectrum is not negative definite, and is therefore not indicative of the physical spectral function.

the given  $B_z$  (black curve), and compare it to the one obtained with the self-energy obtained in the  $B_z = 0$  calculation; in that case the magnetic-field enters the calculation only through the current vertex  $v_{\mathbf{k},m,m',\sigma}^{xx}$ . Here, we can choose to fix the chemical potential to the one corresponding to the  $B_z = 0$  calculation, which will lead to some density variation as the magnetic field is increased (red curve); otherwise, we can correct the chemical potential for each given  $B_z$  so that the overall occupancy is fixed (lime curve).

We see that there is excellent agreement between all three curves. The parts of the black curve that are missing are due to our inability to properly converge the DMFT(NRG) calculation at those values of  $B_z$ . As finite- $B_z$  DMFT(NRG) calculations are difficult and require significant computational time, it is a very important observation that we can obtain solid finite  $B_z$  results by using the self-energy from the  $B_z = 0$  calculation. This way, the bottleneck of our calculation becomes the calculation of the conductivity, rather than the DMFT solver. In the regime of the main interest, this does not present a significant additional approximation. Therefore, in the remainder of the paper we fix  $\Sigma = \Sigma(B_z = 0)$  and correct  $\mu$  at each  $B_z$  so that the overall density is fixed, unless stated otherwise.

In the bottom panel of Fig. 5 we present the density of states at the Fermi level [ $\sim \text{Im}G(\omega = 0)$ ], as well as the effective scattering rate [ $\sim \text{Im}\Sigma(\omega = 0)$ ]. The oscillations in these two quantities as functions of the magnetic field appear synchronous. However, the oscillations in the conductivity follow a completely different pattern. The oscillations in the density of states and the scattering rate can be readily connected with the Shubnikov-de Haas effect, where the period of oscillations in the space of inverse magnetic field is inversely proportional to the surface area of the Fermi sea (roughly the density  $\langle n_\sigma \rangle$ ), while the oscillations of the conductivity appear to correspond to the full area of the BZ. This mismatch in the oscillation frequencies of the spectral and transport properties is, however, restricted to only certain parameter regimes. The high-frequency oscillations have been previously identified in the experiment [44–47] and dubbed the Brown-Zak (B-Z) oscillations. We discuss this phenomenon in more detail in Sec. III B 3, and in Ref. [48] which is devoted to this very topic. In Appendix L we check that no  $p/q = 1$  oscillations are present in thermodynamic potentials.

We also cross-check the results of our finite  $B_z$  calculation against the reference  $B_z = 0$  results, in the limit of low field. As the results are obtained numerically in rather different ways, this is a stringent test of our formalism and implementations. In Fig. 6 we show the DMFT results at  $U = 2.5D$ , at four different levels of doping ( $n = 1$  is half-filling), at  $B_z = 0$  and at three smallest possible fields in a finite  $B_z$  calculation with  $L = q = 1999$ . At high temperatures, small field does not significantly affect the result, and finite-field results are on top of the zero-field result, thus validating our numerics. At low temperature, the effect of the field becomes observable, but the results do tend towards the  $B_z = 0$  result as the field is decreased.

Next, we inspect the effect of the magnetic field on the temperature dependence of  $\sigma_{xx}^{-1}(\nu = 0)$  on Fig. 7. At low temperature, the behavior drastically depends on the precise choice of the magnetic field. At high temperature the behavior is weakly modified, and one still observes roughly linear dependence. At very high fields, the values appear increased by a constant prefactor, which means that the slope of the linear dependence is also increased. This can be more easily confirmed by looking at the linear scale plots in Fig. 8. The effect of the magnetic field appears somewhat insensitive to the strength of the interaction, and the overall trend appears similar in all three panels on the left side of Fig. 7. We are able to roughly collapse the curves at three different values of  $U$  by

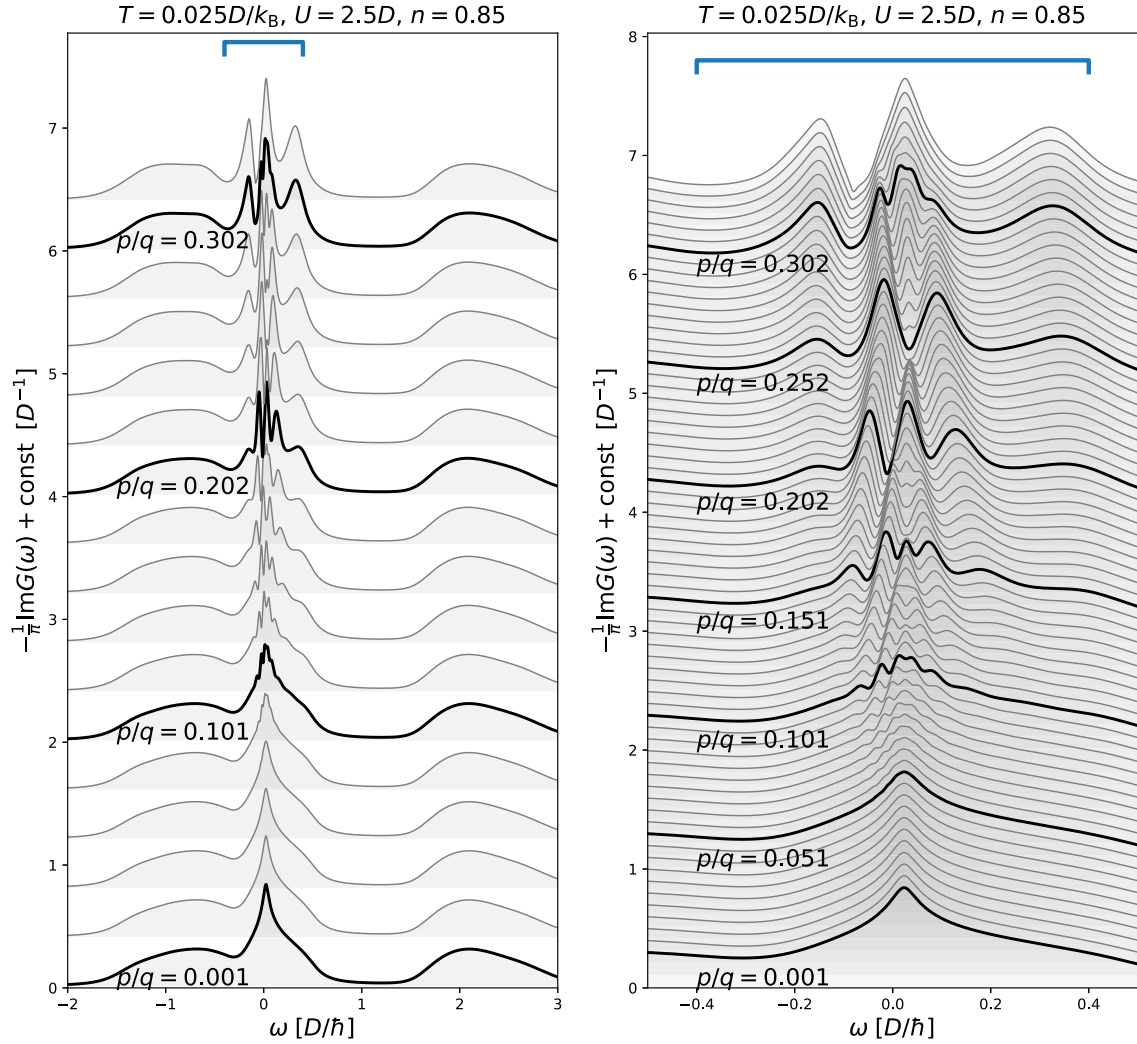


FIG. 4. Local density of states as a function of magnetic field. Left: full frequency range. Right: quasiparticle part of the spectrum. The result is obtained with the DMFT(NRG). The parameters are  $U = 2.5D$ ,  $\langle n_\sigma \rangle = 0.425$ ,  $T = 0.025D/k_B$ . The calculation was performed with  $L = q = 997$ .

simply rescaling the temperature  $T \rightarrow T/T^*(U)$ , with  $T^*(U)$  roughly a linear function of  $U$ . The scaling appears particularly valid between  $U = 2.5$  and  $U = 4$ , while the  $U = 1$  curves somewhat deviate.

Finally, in Fig. 9 we present the magnetic-field dependence of the conductivity, at a fixed temperature and doping. At low temperature one observes increasingly strong oscillations as magnetic field is increased. At low fields, the oscillations are relatively small and regular, which corresponds to the SdH regime, while at strong fields the oscillations cover multiple orders of magnitude, and exhibit no simple pattern as a function of the magnetic field. (This is the quantum limit dominated by the lowest Landau levels).

## 2. Hall conductivity and resistivity

In Fig. 10 we show results for direct current  $\sigma^{xy}$ ,  $1/\sigma^{xx}$  as well as  $\rho^{xy}$  and  $\rho^{xx}$ . We see that  $\sigma^{xy}$  exhibits a nonmonotonic dependence on the magnetic field, and also some oscillation, similar to  $\sigma^{xx}$ . The difference appears to be that when  $\sigma^{xx}$  has

a local maximum,  $\sigma^{xy}$  has a local extremum in the value of its first derivative. The results presented in this plot correspond to the high-frequency oscillation regime, where the maxima in  $\sigma^{xx}$  coincide with  $p/q = 1/q$ . This behavior is in line with the experimental observations in Ref. [45]. We also see that, as expected,  $\sigma^{xy}$  tends to zero as magnetic field is decreased. The effect of  $\sigma^{xy}$  on  $\rho^{xx}$  is not negligible, and one clearly has  $\rho^{xx} \neq 1/\sigma^{xx}$ . Nevertheless, the oscillatory behavior of  $\rho^{xx}$  appears very similar to that of  $1/\sigma^{xx}$  and in phase with it.

We further study the behavior of  $\sigma^{xy}$  in the limit of  $U = 0$  where the calculation can be performed at low numerical cost. The results are presented in Fig. 11. First we look at the temperature dependence (upper panel). We see that  $\sigma^{xy}$  falls off exponentially with increasing temperature. At  $T = 0$  the result corresponds to the Chern number of the topological insulator, whenever the chemical potential falls in an energy gap. We see that decreasing field produces gaps with ever larger Chern numbers. On the middle panel we look at this dependence more closely, and see that at a given chemical potential, the Chern number grows in a power-law fashion



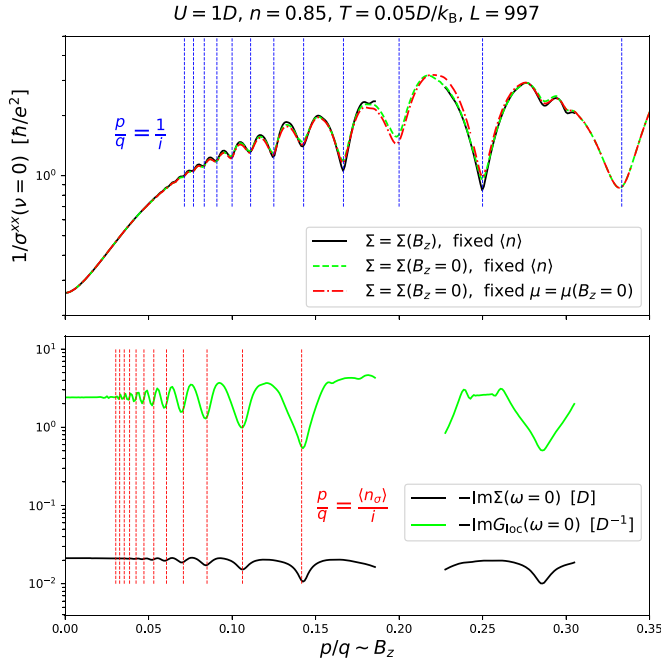


FIG. 5. Upper panel: conductivity obtained with the full DMFT(NRG) calculation (black line), and the simplified calculation where the self-energy is taken from the zero-field DMFT(NRG) calculation, and the chemical potential is either corrected to fix the overall density (lime line) or not (red line). Vertical lines indicate  $p/q = 1/i$  with  $i$  integer, which coincides with the dips in the inverse conductivity. Lower panel: dependence on the magnetic field of the density of states at the Fermi level (lime line) and the scattering rate (black line). Vertical lines indicate  $p/q = \langle n_\sigma \rangle / i$ , which roughly coincides with the dips in both the scattering rate and the density of states at the Fermi level.

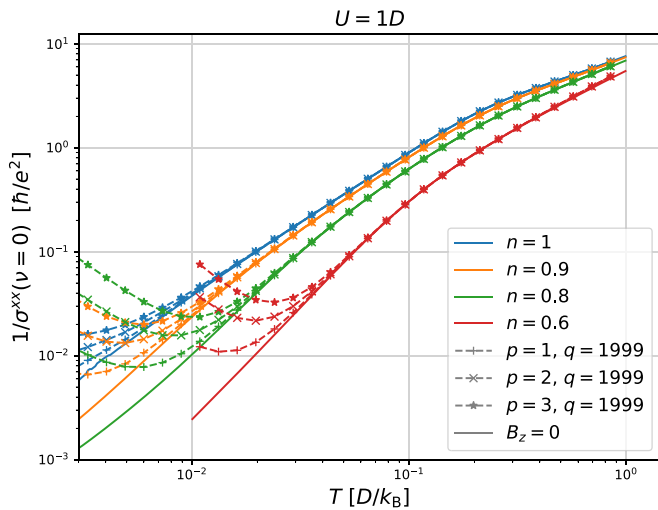


FIG. 6. Cross-check between the zero-field formalism and the finite-field formalism at weak fields. Solid lines are the  $B_z = 0$  DMFT(NRG) result, obtained within the zero-field formalism, at different values of density. We keep  $U = 2.5D$  fixed. Dashed lines with symbols are obtained within finite  $B_z$  formalism, at three lowest values of the field, at  $L = q = 1999$ .

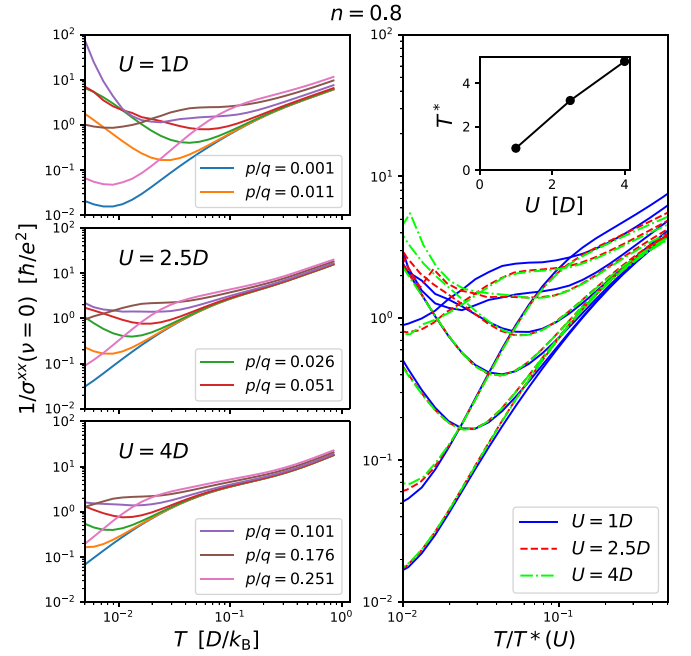


FIG. 7. Left panels: the  $T$  dependence of the inverse conductivity at different values of the field and fixed coupling and density. Right panel: the same results with rescaled temperature  $T \rightarrow T/T^*(U)$ .  $T^*(U)$  is given in the inset.

with  $1/B_z$ . It is clear that this law does not have a well-defined limiting behavior at  $B_z = 0$ , as in the absence of magnetic field there are no gaps and strictly  $\sigma^{xy} = 0$ . This is an indication of the fractal structure of the density of states at low fields: the gaps become smaller and smaller, but more and more numerous, and fully disappear only strictly at  $B_z = 0$ . However, this ill-defined behavior is corrected at finite values of the interaction (Fig. 10), and one observes a downturn of  $\sigma^{xy}$  at a finite value of the field, and  $\sigma^{xy}$  tends to zero smoothly as  $B_z \rightarrow 0$ .

Finally, we study the dependence of  $\sigma^{xy}$  on the chemical potential, at several different values of the field and  $T = 0$ , in the bottom panel of Fig. 11. One has  $\sigma^{xy}(\mu) = -\sigma^{xy}(-\mu)$ . The plateaus in the value of Hall conductivity are indications of gaps in the density of states and are always found at integer values. We benchmark our implementation with the data in Ref. [38] in Appendix M.

### 3. Quantum oscillations of $1/\sigma^{xx}$

As already noted in Sec. III B 1, the conductivity displays oscillatory behavior as a function of magnetic field. We start by inspecting the region of the phase diagram where notable oscillatory behavior is present. We define a characteristic  $(p/q)^*(T; n, U)$  (denoted by shaded circles in Fig. 9) as the value of magnetic field at which the first extremum in  $1/\sigma^{xx}(B_z \sim p/q)$  occurs ( $1/\sigma^{xx}$  initially grows, so the first extremum is always a maximum). Oscillations in the slope of  $1/\sigma^{xx}(B_z \sim p/q)$  might survive even below this characteristic value of the field [or inversely at temperatures higher than  $T((p/q)^*)$ ]; the amplitude of oscillations dies out with temperature exponentially, as in Lifshitz-Kosevich law [43] (see Fig. 12; the oscillatory part of  $1/\sigma^{xx}(p/q)$  is extracted

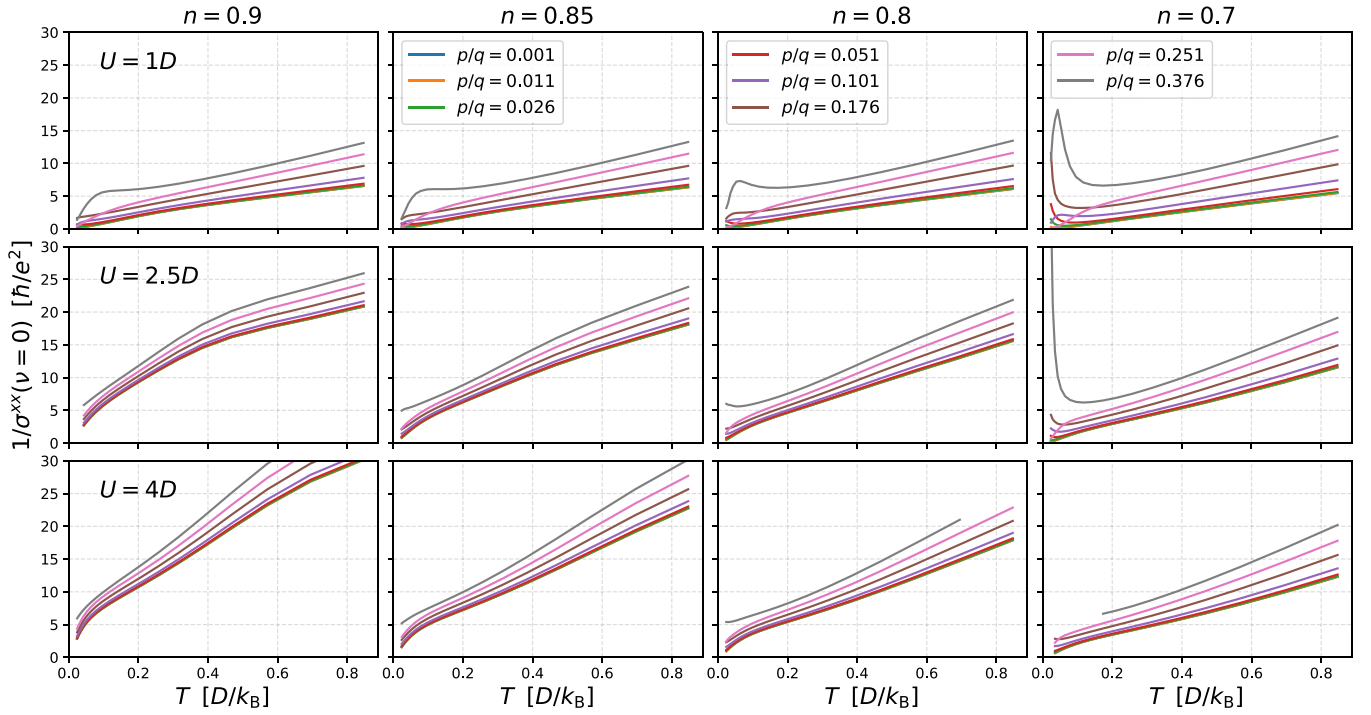


FIG. 8. Inverse conductivity on the linear scale. Columns are different dopings, rows are different values of interaction. Different curves are different values of the field.

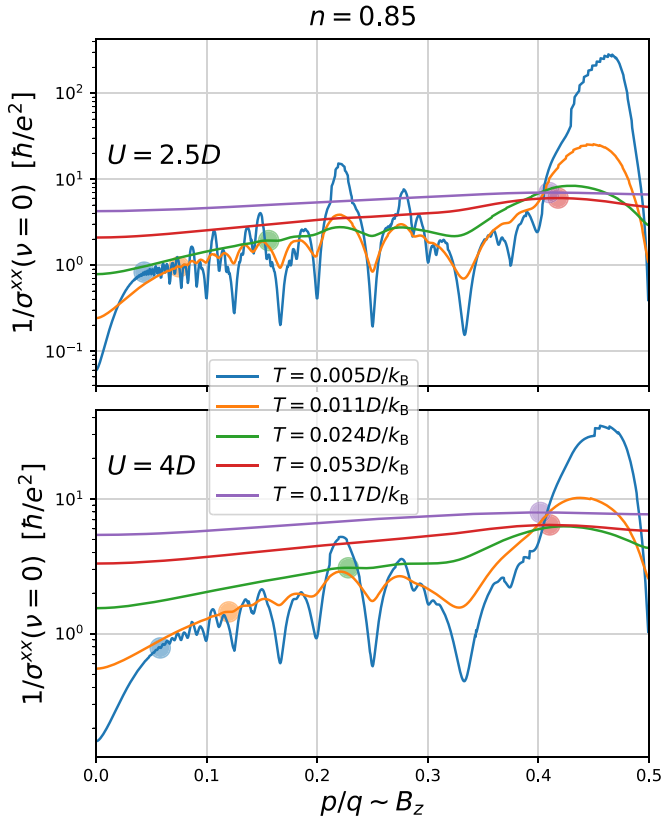


FIG. 9. Magnetic-field dependence of the inverse conductivity at two values of coupling constant, and various temperatures. Shaded circles correspond to the first extremum  $(p/q)^*$  (see text).

by subtracting from the full result the average value in the range  $[p/q - f(p/q), p/q + f(p/q)]$ , where  $f \sim p^{0.7}$ . The quantity  $T((p/q)^*)$  is presented in Fig. 13. We denote the doping with  $\delta = 1 - n$ .

We see that there is always roughly a plateau in  $T((p/q)^*)$ , followed by a kink and a near saturation of  $(p/q)^*(T)$  at high temperature. This is because above a certain temperature, no oscillations are present at any value of magnetic field,

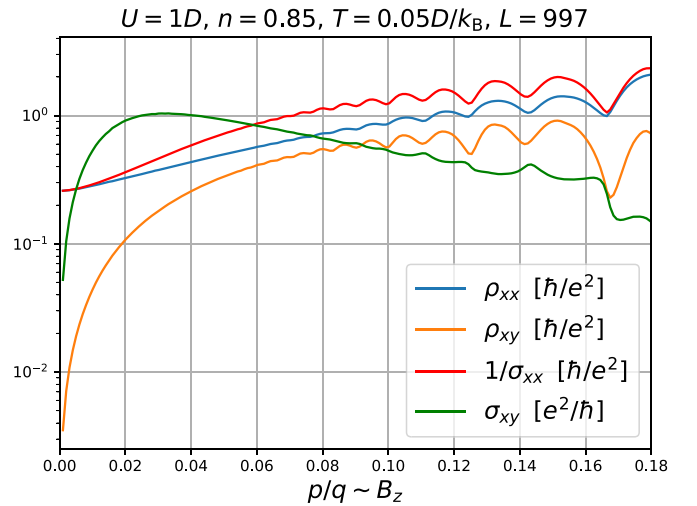


FIG. 10. Different components of the conductivity and resistivity tensors, showing the effect of the Hall component on the relation between the longitudinal resistivity  $\rho^{xx}$  and the inverse longitudinal conductivity  $1/\sigma^{xx}$ .

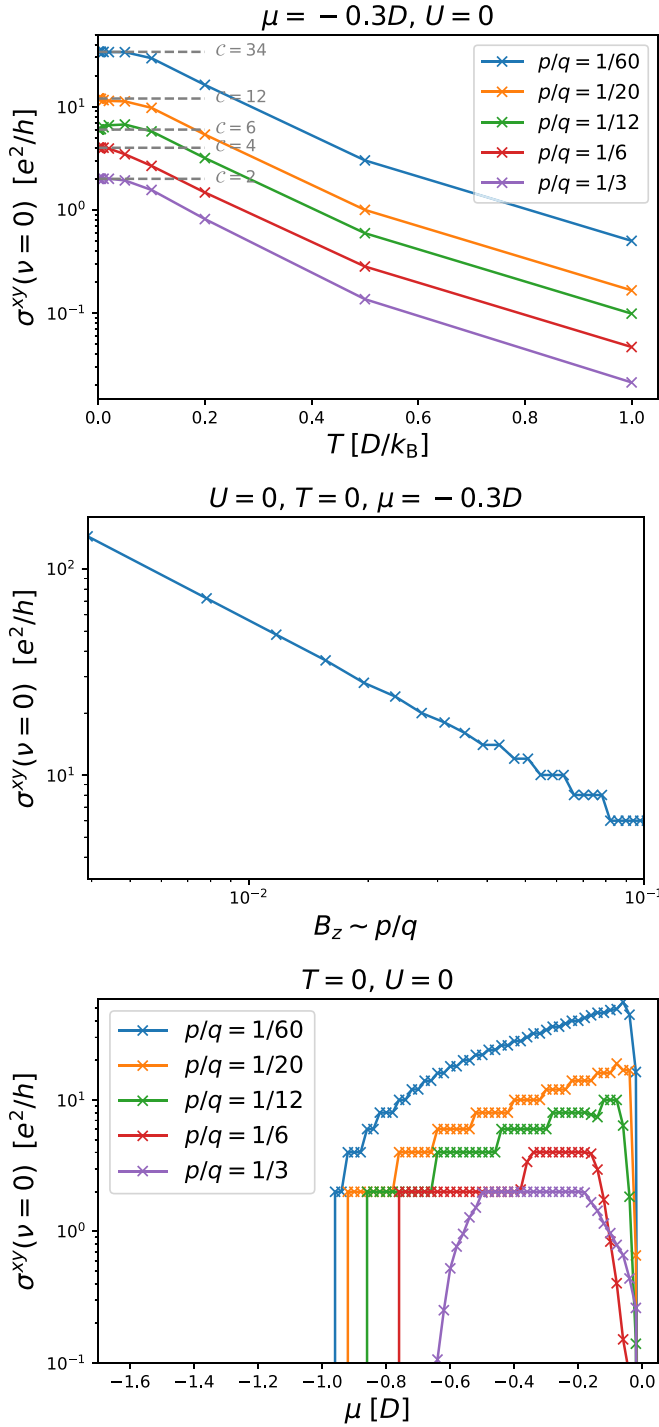


FIG. 11. Hall conductivity at  $U = 0$ . Top: temperature dependence of the Hall conductivity for a selection of magnetic fields. Gray lines indicate the value at  $T = 0$ , which is the Chern number for the corresponding topological insulator. Center: field dependence of the Hall conductivity at zero temperature. Bottom: chemical potential dependence of the Hall conductivity for a selection of magnetic fields.

and there remains at most a single maximum below  $p/q = 0.5$ . The maximum can persist at a roughly fixed  $p/q$  up to some temperature, and then ultimately moves to  $p/q = \frac{1}{2}$ . The shape of  $(p/q)^*(T)$  appears nearly universal for all  $\delta, U$ . We

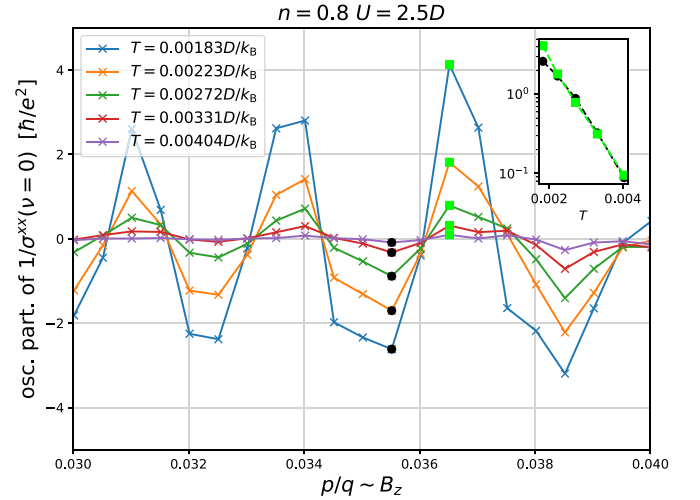


FIG. 12. Zoom-in on the oscillatory part of the magnetic-field dependence of inverse conductivity, in a range of weak fields. Different curves are different temperatures. Lime and black points denote the apparent antinodes of the wave, i.e., the amplitude of oscillation, up to a sign. Inset: dependence of the amplitude of oscillation vs temperature, on the logarithm scale, revealing exponential decay with  $T$ .

are able to roughly collapse all the curves on the left panel in Fig. 13 by rescaling the temperature as  $T \rightarrow T \times U^{c(\delta)}$  (right panel), with  $c(\delta)$  given in the inset. It is clear that the bigger the doping and the lower the interaction, the oscillations will persist up to a higher temperature, and start at a lower value of the field. It is interesting that roughly  $(p/q)^* \sim T^{2/3}$  in the regime where multiple oscillation periods are observed.

The oscillations have a fixed period when  $\sigma^{xx}$  is plotted as a function of inverse magnetic field. When this period is inversely proportional to the surface area of the Fermi sea, this corresponds to the well-known Shubnikov–de Haas effect. However, in our results, we observe in some regimes of parameters an additional oscillation frequency. This is documented in Fig. 14 where we present the Fourier transform of  $(\sigma^{xx})^{-1}(B_z^{-1} = q/p)$ . The presented part of each oscillation spectrum is normalized to 1. In the left panel we show the temperature dependence of the oscillation spectrum as a function of temperature, at fixed doping and coupling constant. At low temperature one observes peaks at roughly integer multiples of the density  $\langle n_\sigma \rangle$  which corresponds to the SdH effect. However, at intermediate temperature, there is an additional frequency corresponding to the full area of the BZ, and its higher harmonics [48]. At even higher temperature, before the oscillatory behavior is erased by thermal effects, the  $p/q = 1$  peak in the spectrum becomes dominant. In the right panel we inspect the effect of doping on the oscillation spectrum, at a fixed temperature. The SdH peak is present at all dopings, and is always found at  $p/q \approx \langle n_\sigma \rangle$ . The doping appears to reduce the  $p/q = 1$  peak, which is no longer the dominant peak at  $\delta > 0.2$ . At very low doping, it is not possible to distinguish between the  $p/q = 1$  peak and the second harmonic of the SdH peak, as  $\langle n_\sigma \rangle$  approaches 0.5. However, it is unexpected in the SdH effect that the second harmonic is stronger than the first harmonic (fundamental), which indicates a presence of a

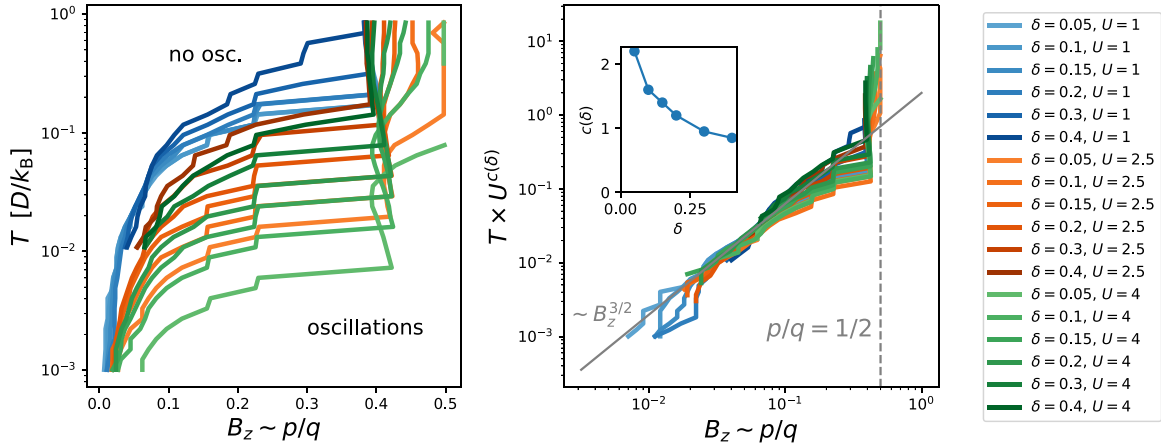


FIG. 13. The  $(B_z, T)$  phase diagram for the quantum oscillations. The diagram indicates the minimal magnetic field for observing significant quantum oscillations (nonmonotonic behavior) at a given temperature. Left: results for a set of model parameters. Right: rescaled results showing reasonable overlap.

separate mechanism which contributes to the amplitude of the peak at  $p/q = 1$ . In the next section, we are able to trace the origin of these high-frequency oscillations; the full description of the observed phenomenology and its relationship to experiments is presented in a separate publication (Ref. [48]).

#### 4. Oscillations of the current vertex

At the level of the DMFT, the magnetic field enters the calculation of conductivity through the self-energy and the current vertex  $v$ . As we have concluded in Sec. III B 1, the dependence of conductivity on the self-energy is of secondary importance, and cannot possibly account for the observed  $p/q = 1$  frequency oscillations, as the self-energy oscillates with the frequency  $p/q = \langle n_\sigma \rangle$ . The  $p/q = 1$  oscillations then must come from the current vertex. This was already suggested in previous experimental works [45,46], where the

$p/q = 1$  frequency oscillations have been linked to periodic changes in the velocity of magnetic minibands, featuring spikes at  $p/q = 1/q$ .

We first discuss which part of  $v^{xx}(\varepsilon, \varepsilon')$  plays a role at a given choice of parameters. First, by inspecting Eq. (70) we see that the  $\omega$  integrand will generally have two peaks, centered around  $\omega^*/\omega'^*$  such that  $\omega^{*(l)} + \mu - \varepsilon^{(l)} - \text{Re}\Sigma(\omega^{*(l)}) = 0$ . The width of those peaks is roughly proportional to  $\text{Im}\Sigma(\omega^{*(l)})$ . When the two peaks are further apart than is their width, the contribution of the integral will be very small. Additionally, if they fall outside of the thermal window, they will not contribute. Assuming in a most simple way  $\omega^{*(l)} = \mu - \varepsilon^{(l)}$ , and that the contribution is negligible if  $|\varepsilon - \varepsilon'| > \Gamma$ , with  $\Gamma$  playing the role of the width of the peaks [say roughly  $\Gamma \approx -\text{Im}\Sigma(\omega = 0)$ ], and taking that the thermal window is a hard cutoff  $|\omega^{*(l)}| < T$ , we can isolate the relevant values of  $v^{xx}(\varepsilon, \varepsilon')$ , which determine the value of the overall

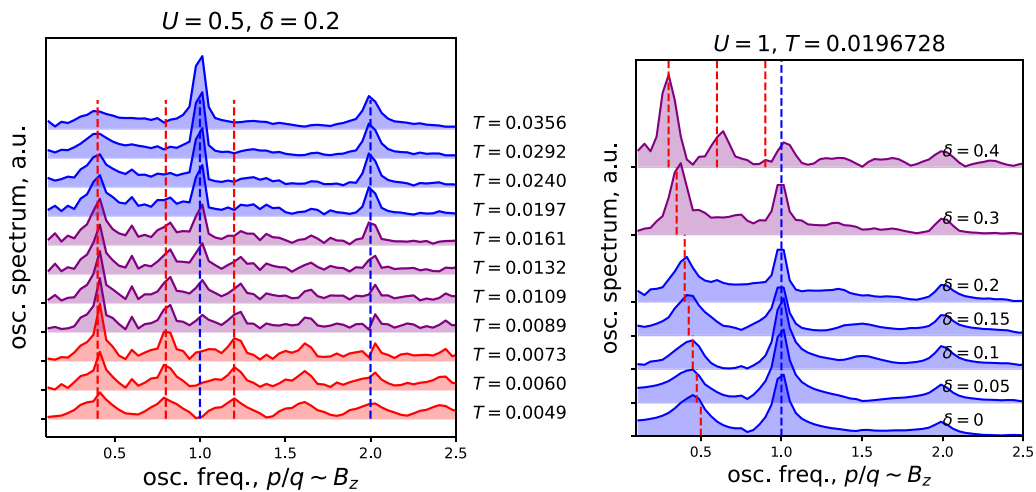


FIG. 14. Fourier spectra of the oscillatory component of the inverse dc conductivity. All spectra are normalized to 1. Left: temperature dependence at fixed electron density. Right: density dependence at fixed temperature. Both panels: vertical red dashed lines correspond to SdH frequency  $p/q = \langle n_\sigma \rangle$  and its higher harmonics; vertical blue dashed lines correspond to  $p/q = 1$  oscillation frequency and its higher harmonics.



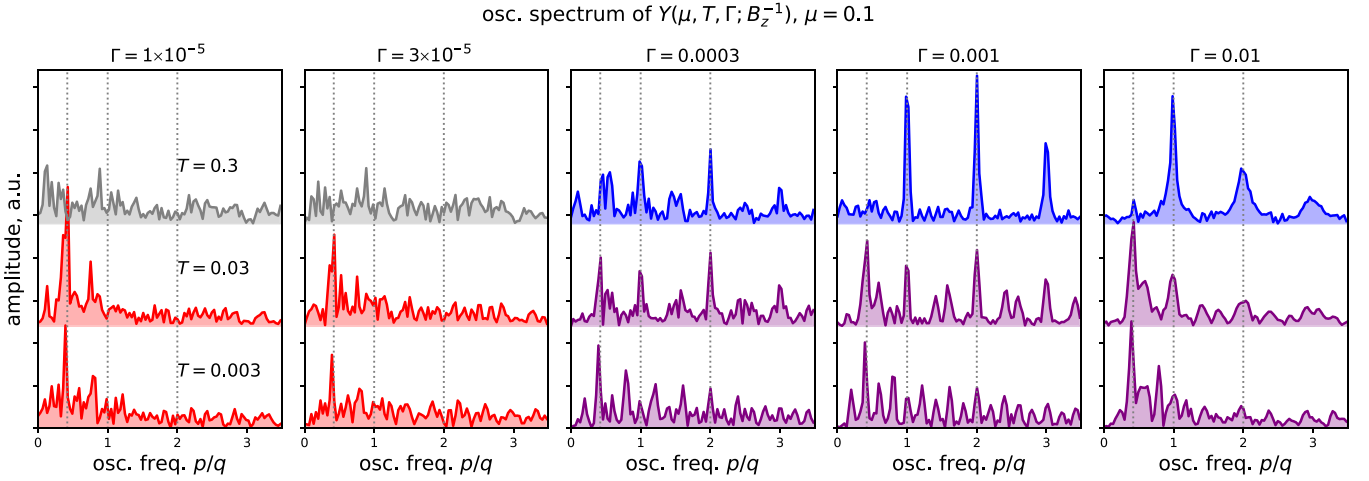


FIG. 15. Oscillation spectra of the current vertex (as quantified by  $Y$ ) at various  $\Gamma$ ,  $T$ . Spectra are colored gray where no pronounced peaks are observed, red where the standard SdH  $p/q = \langle n_\sigma \rangle$  peaks and its higher harmonics are observed, purple where we also observe the  $p/q = 1$  peaks, but the SdH peaks are dominant, and blue where  $p/q = 1$  peak is stronger than  $p/q = \langle n_\sigma \rangle$  peak.

integral. We define a quantity

$$Y(\mu, T, \Gamma; B_z) = \int d\varepsilon \int d\varepsilon' v^{xx}(\varepsilon, \varepsilon'; B_z) \theta(\Gamma - |\varepsilon - \varepsilon'|) \times [\theta(T - |\varepsilon - \mu|) + \theta(T - |\varepsilon' - \mu|)] \quad (84)$$

and inspect its oscillation spectrum as a function of  $B_z^{-1}$ . The results are presented in Fig. 15. We see that at low  $T$  and low  $\Gamma$ , the oscillations resemble the SdH effect. However, increasing  $\Gamma$  leads to an onset of  $p/q = 1$  oscillations, which, with an increase of  $T$ , eventually become dominant. To better understand this behavior, in Fig. 16 we show the spectrum as a function of  $\mu$ , at a fixed low temperature. We see how  $p/q = \langle n_\sigma \rangle$  peak and its harmonics move with changing  $\mu$ , as expected. On the contrary, the  $p/q = 1, 2, 3 \dots$  peaks (when present in the spectrum), do not move with changing  $\mu$ . The main insight is that roughly  $Y(\mu, T + \delta T) \approx Y(\mu, T, \dots) + Y(\mu + \delta\mu, T, \dots) + Y(\mu - \delta\mu, T, \dots)$ . At high temperature,

the contributions from different  $\mu$  will interfere destructively, and the  $p/q = \langle n_\sigma \rangle$  peak will wash out. On the other hand, the  $p/q = 1$  will accumulate, and become the dominant peak, which is precisely what we find.

### 5. Conductivity in the finite-lifetime approximation (FLA)

In the previous sections we have concluded that the high-frequency (Brown-Zak, B-Z) oscillations of conductivity originate from the current vertex. Therefore, it is expected that B-Z oscillations are observed even in the most simple models that feature no variability in the self-energy whatsoever. In this section we calculate conductivity in the finite-lifetime approximation (FLA), where the self-energy is assumed to be a local, frequency-independent, and purely imaginary quantity, i.e.,

$$\Sigma_{ij}^{\text{FLA}}(\omega + i0^+) = -i\Gamma\delta_{ij}, \quad (85)$$

where  $\Gamma$  is the scattering rate. At a fixed  $\mu = -0.1D$ , we construct the Green's function, and evaluate the Kubo

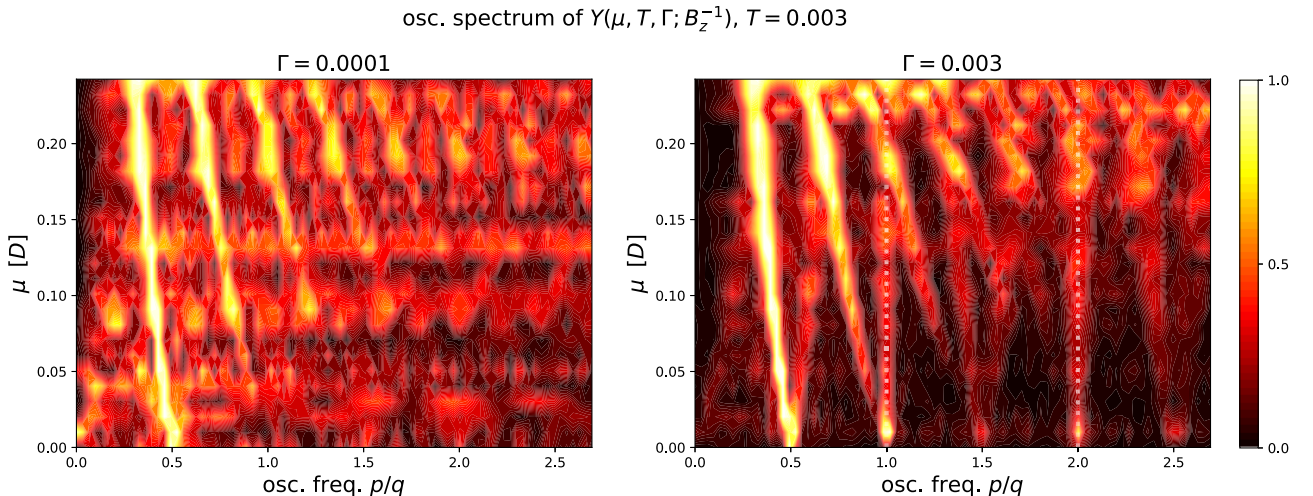


FIG. 16. Evolution of the oscillation spectrum of the current vertex (as quantified by  $Y$ ) with chemical potential, for two values of  $\Gamma$ .

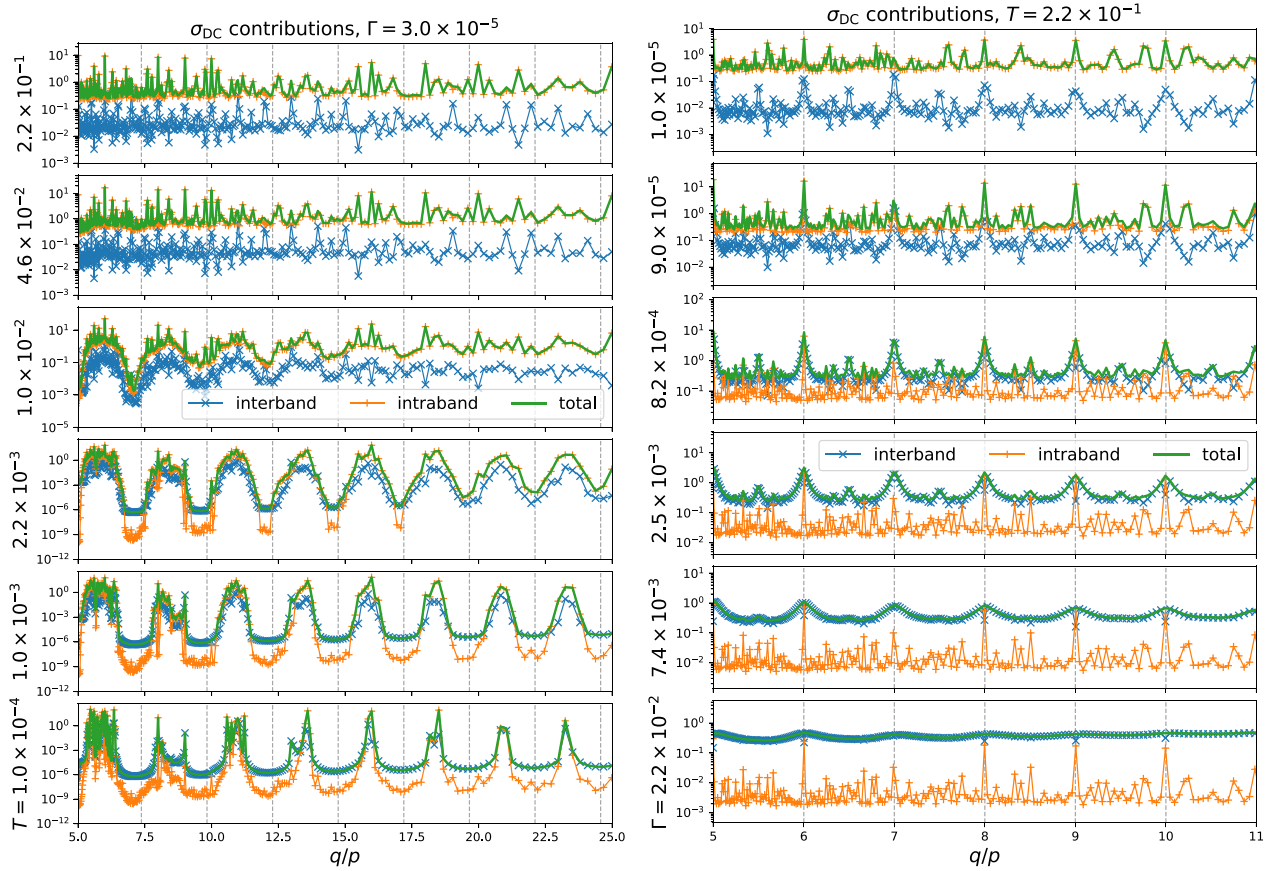


FIG. 17. Longitudinal dc conductivity within FLA: the total result and the contributions from interband and intraband processes. Left: different plots correspond to different temperatures at a fixed scattering rate. Right: different plots correspond to different  $\Gamma$ 's at a fixed temperature.

bubble (70). We are in particular interested in the trends with respect to temperature and scattering rate, and we wish to inspect the relative contributions of  $\varepsilon \approx \varepsilon'$  and  $\varepsilon \neq \varepsilon'$  terms in the double integral. We split the contributions by  $d = |\varepsilon - \varepsilon'|$ : the contributions with  $d > 0.0003$  we consider “interband” contributions, where the particle and the hole of the particle-hole pair reside in different bands; the contributions with  $d < 0.0003$  we consider “intraband” contributions, where the particle and the hole reside either in the same band, or two different bands which are very close in energy. The choice for the threshold value 0.0003 is made based on the finite-energy resolution that we can achieve and the systematic error made in energy levels due to finite lattice size.

The results are shown in Fig. 17 as a function of inverse magnetic field, i.e.,  $q/p$ . On the plots on the left, we take a small value for the scattering rate  $\Gamma \approx 3 \times 10^{-5}$ , and show the two contributions to conductivity as well as the total result at several different temperatures. At low temperature, the dips in conductivity roughly coincide with  $q/p = 0.407/i$ , with  $i$  integer (denoted with vertical gray dashed lines). This clearly corresponds to SdH oscillations, and signals that the occupancy at  $\mu = -0.1D$  is about  $\langle n_\sigma \rangle = 0.407$ . It is immediately clear that with increasing temperature, the SdH oscillations subside, and what is left is apparently a fractal-like behavior which cannot be fully resolved with our current resolution.

At low temperature, both intraband and interband processes contribute, while at high temperature, the intraband processes are dominant.

On the plots on the right in Fig. 17, we take a high temperature  $T \approx 0.215$  and show results for different values of  $\Gamma$ . As  $\Gamma$  is increased, the interband processes contribute increasingly, and ultimately become fully dominant; the fractal behavior is replaced by regular oscillations, with maxima coinciding with  $q/p = q/1$ . These are the high-frequency (or B-Z) oscillations, which appear only when the scattering rate is sufficiently high.

We illustrate the trends with respect to temperature and the scattering rate on Fig. 18(a) where we plot the oscillation spectra obtained by the Fourier transform of the data in the range of the field  $p/q \in [0.03, 0.15]$ . The results show clearly that at low  $\Gamma$ , high-frequency oscillations are never observed, but that at sufficiently high  $\Gamma$ , they are observed above some threshold temperature, but up to indefinite temperature: note that the highest temperature that we show is 10 in units of half-bandwidth, with no sign of weakening of the high-frequency oscillations. In contrast, the SdH oscillations subside simply due to increasing temperature. All oscillations disappear at very high scattering rate, and there seems to be a well-defined upper cutoff  $\Gamma$  for the observation of any oscillations. These findings are summarized in the rough phase diagram of the FLA model in Fig. 18(b).



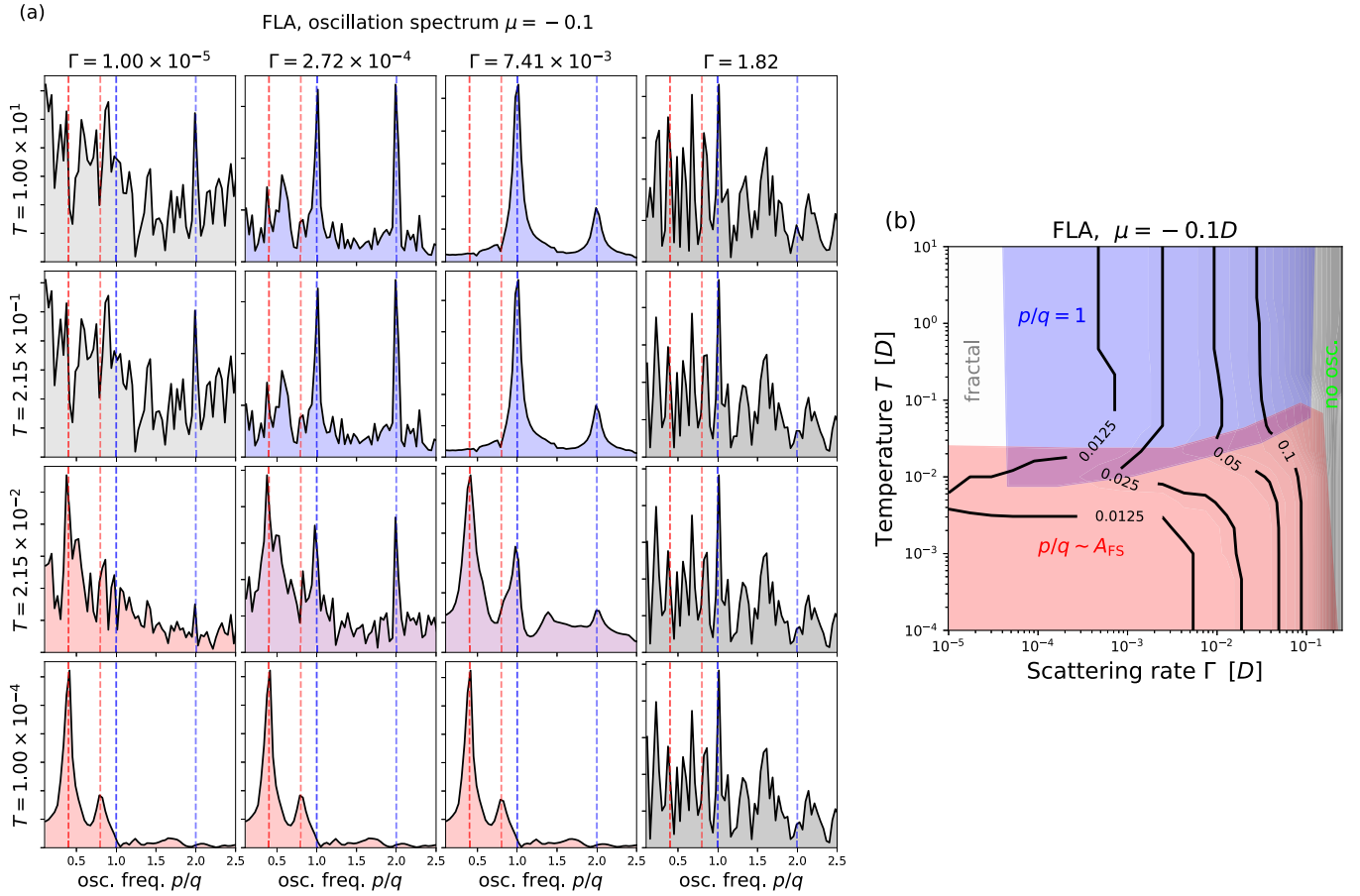


FIG. 18. (a) Oscillation spectra of longitudinal dc conductivity obtained within the FLA, at different  $\Gamma$  and  $T$ . Coloring is analogous to Fig. 15. (b) The phase diagram of the FLA toy model. Grayscale color coding in the background and the black contours correspond to the onset field for the nonmonotonous behavior  $(p/q)^*$ .

It is also interesting to compare the doping dependence of the quantum oscillation phenomenology in FLA and DMFT. On Fig. 19 we show the color plot of  $\log_{10} \sigma^{xx}(\nu = 0)$  in the doping-field plane, at a high temperature where SdH oscillations are already thermally washed out. We see opposite trends in the two plots: in FLA, the oscillations are the strongest close to half-filling ( $\mu = 0$ ), while in DMFT, the oscillatory features become stronger in the empty-band limit ( $\langle n_\sigma \rangle \rightarrow 0$ ). The difference must be due to the fact that in the Hubbard model, the scattering rate is maximal at half-filling and vanishes as the number of electrons goes to zero. In FLA, the scattering rate is simply held fixed at all dopings. The FLA result on Fig. 19 is in solid agreement with the experimental results in Ref. [45]. This indicates that the scattering rate in experiment is not vanishing with doping, as one would have in the pure Hubbard model. The additional scattering in experiment probably comes from phonons, or even impurities.

#### IV. CONCLUSIONS AND PROSPECTS

In this paper we have identified several important features of the DMFT results for conductivity in the square-lattice Hubbard model in a perpendicular magnetic field. First, the  $T$ -linear resistivity at high temperature is not strongly affected by magnetic field. At high temperature, varying the interaction

also does not strongly affect the resistivity, but rather sets the temperature scale in a linear fashion. Next, we observe that the effect of the magnetic field comes mainly through the current-vertex factor (which only contains kinetic effects), and not the self-energy (which involves dynamic effects and defines the energy and momentum windows with significant contribution in the integration). We are able to reproduce the SdH effect and observe quantum oscillations in  $1/\sigma^{xx}(B^{-1})$  with the expected frequency  $B_z \sim p/q = \langle n_\sigma \rangle$ . However, we also observe oscillations on a different, higher frequency  $B_z \sim p/q = 1$ , independently of doping. For this behavior, the prerequisites appear to be moderate scattering rate, moderate temperature and relatively high magnetic field flux per unit cell. Our observations are in line with the experimental results of recent experiments on moiré (graphene superlattice) systems [44–46].

For the future work it will be necessary to investigate how much of the observed phenomenology is representative of the exact solution, and how much is an artifact of the DMFT approximation. At the level of DMFT the two important simplifications are (1) the self-energy is fully local (which means that the Green's function is diagonal in the eigenbasis of the noninteracting Hamiltonian), and (2) the vertex corrections cancel. This question can in principle be addressed with cluster DMFT calculations [67], but these may

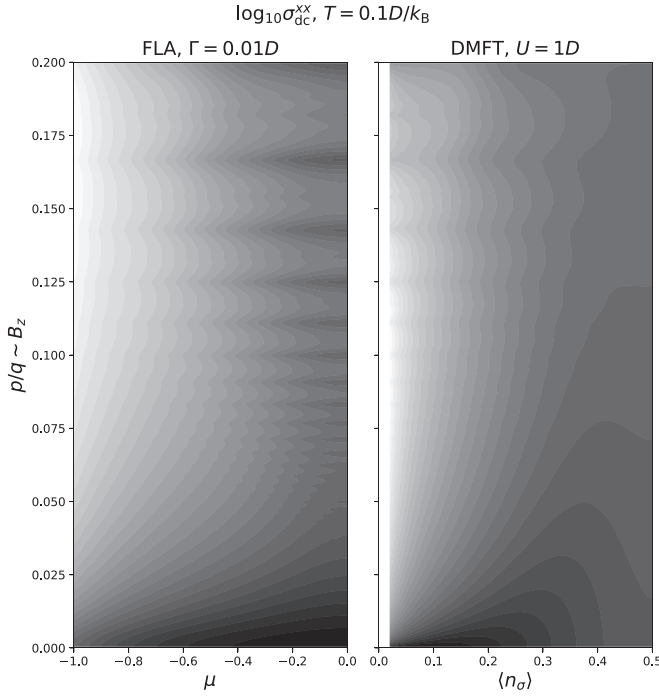


FIG. 19. The doping-field dependence of longitudinal dc conductivity within FLA and DMFT. Color code is logarithmic: white is  $-2.40$  and  $-3.12$ , respectively; black is  $0.98$  and  $1.03$ , respectively.

not be trivial to formulate or execute. Additionally, analytical continuation of self-energy data might be difficult [or an exact diagonalization (ED) solver might be used, which introduces additional systematic error]. Finally, calculation of vertex corrections in cluster DMFT schemes is notoriously difficult [68–72]. Another possibility is to use recently developed DiagMC technique which requires no analytical continuation [73–77], and can access the thermodynamic limit directly. As the observed phenomena are not restricted to very high values of the coupling and can already be observed at  $U = 0.5 - 1D$ , a DiagMC calculation with only several orders could be sufficient to work out the generic effect of self-energy nonlocality and vertex corrections.

#### ACKNOWLEDGMENTS

Computations were performed on the PARADOX supercomputing facility (Scientific Computing Laboratory, Center for the Study of Complex Systems, Institute of Physics Belgrade). J.V. acknowledges funding provided by the Institute of Physics Belgrade, through the grant by the Ministry of Education, Science, and Technological Development of the Republic of Serbia, as well as by the Science Fund of the Republic of Serbia, under the Key2SM project (PROMIS program, Grant No. 6066160). R.Ž. is supported by the Slovenian Research Agency (ARRS) under Program No. P1-0044 and Projects No. J1-1696 and No. J1-2458.

#### APPENDIX A: PEIERLS PHASE IN LANDAU GAUGE [PROOF OF EQ. (9)]

For the following derivation, we introduce  $\mathbf{r}(\alpha) = a(x(\alpha), y(\alpha)) = a[\mathbf{r}_i + \alpha(\mathbf{r}_j - \mathbf{r}_i)]$  and  $d\mathbf{r} = a d\alpha$ , with  $\mathbf{d} = \mathbf{r}_j - \mathbf{r}_i$ , while keeping  $\mathbf{r}_i = (x_i, y_i)$  dimensionless and  $x_i, y_i$  integers. The Peierls phase for the uniform magnetic field per-

pendicular to the lattice  $\mathbf{B} = (0, 0, B_z)$ , in the Landau gauge (7) can be expressed as

$$\begin{aligned} f_{ij} &= \frac{e}{\hbar} \int_{\mathbf{r}_i}^{\mathbf{r}_j} \mathbf{A}(\mathbf{r}) \cdot d\mathbf{r} \\ &= \frac{ea}{\hbar} \int_0^1 d\alpha \mathbf{A}(\mathbf{r}(\alpha)) \cdot \mathbf{d} \\ &= \frac{ea^2}{\hbar} B_z \int_0^1 d\alpha x(\alpha) \mathbf{e}_y \cdot \mathbf{d} \\ &= \frac{ea^2}{\hbar} B_z (y_j - y_i) \int_0^1 d\alpha (x_i + \alpha d_x) \\ &= \frac{ea^2}{\hbar} B_z (y_j - y_i) \left[ x_i + d_x \int_0^1 d\alpha \alpha \right] \\ &= \frac{ea^2}{\hbar} B_z (y_j - y_i) \left[ x_i + d_x \frac{\alpha^2}{2} \Big|_0^1 \right]. \end{aligned}$$

We finally have

$$\begin{aligned} f_{ij} &= \frac{ea^2}{\hbar} B_z (y_j - y_i) \left[ x_i + \frac{x_j - x_i}{2} \right] \\ &= \frac{ea^2}{\hbar} \frac{B_z}{2} (y_j - y_i) (x_i + x_j). \end{aligned} \quad (\text{A1})$$

When doing real-space calculations on a finite cyclic lattice, it is necessary to always consider the shortest distance between the sites and take instead the following periodicized expression:

$$f_{ij}^{\text{fin. latt.}} = \frac{ea^2}{\hbar} B_z (y_j \ominus y_i) \left[ x_i + \frac{x_j \ominus x_i}{2} \right], \quad (\text{A2})$$

where  $\ominus$  denotes the shortest distance on a finite cyclic lattice.

#### APPENDIX B: PROOF OF UNIT-CELL SIZE

We prove now that in the Landau gauge, the size of the unit cell in the  $x$  direction is  $q$ . Consider that we shift both  $\mathbf{r}_i$  and  $\mathbf{r}_j$  by  $q\mathbf{e}_x = (q, 0)$  [we remind the reader that we use dimensionless  $\mathbf{r}_i = (x_i, y_i)$  as arguments of  $f$ ]. We must show that the additional phase shift must be an integer number times  $2\pi$ :

$$\begin{aligned} f_{\mathbf{r}_i+q\mathbf{e}_x, \mathbf{r}_j+q\mathbf{e}_x} &= \frac{ea^2}{\hbar} \frac{B_z}{2} (y_j - y_i) (x_i + q + x_j + q) \\ &= f_{\mathbf{r}_i, \mathbf{r}_j} + \frac{ea^2}{\hbar} \frac{B_z}{2} (y_j - y_i) 2q. \end{aligned} \quad (\text{B1})$$

We now apply  $B_z = 2\pi \frac{p}{q} (\frac{ea^2}{\hbar})^{-1}$ :

$$\begin{aligned} f_{\mathbf{r}_i+q\mathbf{e}_x, \mathbf{r}_j+q\mathbf{e}_x} &= f_{\mathbf{r}_i, \mathbf{r}_j} + \frac{2\pi p}{2} (y_j - y_i) 2q \\ &= f_{\mathbf{r}_i, \mathbf{r}_j} + 2\pi p (y_j - y_i). \end{aligned} \quad (\text{B2})$$

As  $p(y_j - y_i)$  is an integer, the condition (10) indeed satisfies periodicity along the  $x$  direction.

## APPENDIX C: PROOF OF EQ. (14)

Here we rewrite in momentum space the kinetic term in the Hamiltonian (12) to reach Eq. (14):

$$\begin{aligned}
H_{\text{kin},\sigma} &= -t \frac{1}{N} \sum_{\mathbf{k}, \mathbf{k}'} \sum_{i, \mathbf{u} \in \{\mathbf{e}_x, \mathbf{e}_y\}} e^{i2\pi \frac{\mathbf{u} \cdot \mathbf{x}_i}{L}} e^{-i\mathbf{k} \cdot \mathbf{r}_i} c_{\mathbf{k},\sigma}^\dagger e^{i\mathbf{k}' \cdot (\mathbf{r}_i + \mathbf{u})} c_{\mathbf{k}',\sigma} + \text{H.c.} \\
&= -2t \sum_{\mathbf{k}, \sigma} \cos k_x n_{\mathbf{k},\sigma} - t \frac{1}{N} \sum_{\mathbf{k}, \mathbf{k}'} \sum_i e^{i2\pi \frac{\mathbf{x}_i}{L}} e^{-i\mathbf{k} \cdot \mathbf{r}_i} c_{\mathbf{k},\sigma}^\dagger e^{i\mathbf{k}' \cdot (\mathbf{r}_i + \mathbf{e}_y)} c_{\mathbf{k}',\sigma} + \text{H.c.} \\
&= -2t \sum_{\mathbf{k}, \sigma} \cos k_x n_{\mathbf{k},\sigma} - t \frac{1}{N} \sum_{\mathbf{k}, \mathbf{k}'} \sum_i e^{i2\pi \frac{\mathbf{r}_i \cdot \mathbf{e}_x}{L}} e^{-i\mathbf{k} \cdot \mathbf{r}_i} c_{\mathbf{k},\sigma}^\dagger e^{i\mathbf{k}' \cdot (\mathbf{r}_i + \mathbf{e}_y)} c_{\mathbf{k}',\sigma} + \text{H.c.} \\
&= -2t \sum_{\mathbf{k}, \sigma} \cos k_x n_{\mathbf{k},\sigma} - t \frac{1}{N} \sum_{\mathbf{k}, \mathbf{k}'} e^{i\mathbf{k}' \cdot \mathbf{e}_y} c_{\mathbf{k},\sigma}^\dagger c_{\mathbf{k}',\sigma} \sum_{i,\sigma} e^{i\mathbf{r}_i \cdot (\mathbf{k}' - \mathbf{k} + 2\pi \frac{\mathbf{e}_x}{L})} + \text{H.c.} \\
&= -2t \sum_{\mathbf{k}, \sigma} \cos k_x n_{\mathbf{k},\sigma} - t \sum_{\mathbf{k}, \mathbf{k}'} e^{i\mathbf{k}' \cdot \mathbf{e}_y} c_{\mathbf{k},\sigma}^\dagger c_{\mathbf{k}',\sigma} \delta_{\mathbf{k}', \mathbf{k} - 2\pi \frac{\mathbf{e}_x}{L}} + \text{H.c.} \\
&= -2t \sum_{\mathbf{k}, \sigma} \cos k_x n_{\mathbf{k},\sigma} - t \sum_{\mathbf{k}, \sigma} e^{i\mathbf{k}_y} c_{\mathbf{k},\sigma}^\dagger c_{\mathbf{k} - 2\pi \frac{\mathbf{e}_x}{L}, \sigma} + \text{H.c.} \tag{C1}
\end{aligned}$$

APPENDIX D: PERIODICITY WITH  $k_y$ 

We prove here the periodicity of the noninteracting eigenproblem along the  $k_y$  axis, as stated in Eqs. (24) and (25). We start by reordering rows and columns of the Hamiltonian (15): one can achieve that by redefining  $|\tilde{\mathbf{k}}, l, \sigma\rangle \equiv |\mathbf{k} + 2\pi l \frac{\mathbf{e}_y}{q}, \sigma\rangle$ , or simply  $|\tilde{\mathbf{k}}, lp \bmod q, \sigma\rangle \rightarrow |\tilde{\mathbf{k}}, l, \sigma\rangle$ . In that case, the Hamiltonian reads as

$$\begin{aligned}
[\tilde{H}_{0,\tilde{\mathbf{k}},\sigma}]_{l,l'} &= \left( -\mu_\sigma - 2t \cos \left( \tilde{k}_x + 2\pi l \frac{p}{q} \right) \right) \delta_{l,l'} \\
&\quad - t (e^{ik_y} \delta_{l,l' \oplus 1} + e^{-ik_y} \delta_{l \oplus 1, l'}). \tag{D1}
\end{aligned}$$

This transformation does not affect the eigenvectors and eigenvalues.

Now, we apply a unitary transformation defined by  $[U_{\tilde{\mathbf{k}}}]_{ll'} = \delta_{ll'} e^{-il\tilde{k}_y}$  and apply it to the Hamiltonian as

$$\check{H}_{0,\tilde{\mathbf{k}},\sigma} \equiv U_{\tilde{\mathbf{k}}} \tilde{H}_{0,\tilde{\mathbf{k}},\sigma} U_{\tilde{\mathbf{k}}}^\dagger. \tag{D2}$$

The transformed Hamiltonian  $\check{H}_{0,\tilde{\mathbf{k}},\sigma}$  has the same eigenvalues as  $\tilde{H}_{0,\tilde{\mathbf{k}},\sigma}$ , and the original eigenvectors can be obtained from the eigenvectors of  $\check{H}_{0,\tilde{\mathbf{k}},\sigma}$  as  $|m, \tilde{\mathbf{k}}, \sigma\rangle = U_{\tilde{\mathbf{k}}}^\dagger |\check{m}, \tilde{\mathbf{k}}, \sigma\rangle$ . As  $U_{\tilde{\mathbf{k}}}$  is diagonal, the element-wise equation for  $\check{H}_{\tilde{\mathbf{k}},\sigma}$  reads as

$$[\check{H}_{0,\tilde{\mathbf{k}},\sigma}]_{ll'} = [U_{\tilde{\mathbf{k}}}]_{ll} [\tilde{H}_{0,\tilde{\mathbf{k}},\sigma}]_{ll'} [U_{\tilde{\mathbf{k}}}]_{l'l'}^*. \tag{D3}$$

The diagonal elements remain unchanged, and we must consider two special cases for the off-diagonal elements: (a)  $|l - l'| = q - 1$ , and (b)  $|l - l'| = 1$ . The two cases correspond to whether the hopping between momenta winds around the BZ or not. In the latter case, we have for

$$\begin{aligned}
[\check{H}_{0,\tilde{\mathbf{k}},\sigma}]_{l>1, l'=l-1} &= e^{-il\tilde{k}_y} e^{ik_y} e^{i(l-1)\tilde{k}_y} \\
&= e^{i(1-l)\tilde{k}_y} e^{i(l-1)\tilde{k}_y} \\
&= 1 \\
&= [\check{H}_{0,\tilde{\mathbf{k}},\sigma}]_{l<q-1, l'=l+1}. \tag{D4}
\end{aligned}$$

But in the case when there is winding around the BZ, we get

$$\begin{aligned}
[\check{H}_{0,\tilde{\mathbf{k}},\sigma}]_{l=q-1, l'=0} &= e^{-i(q-1)\tilde{k}_y} e^{-ik_y} \\
&= e^{-iq\tilde{k}_y} \\
&= [\check{H}_{0,\tilde{\mathbf{k}},\sigma}]_{l=0, l'=q-1}^*. \tag{D5}
\end{aligned}$$

These are the only elements of the matrix that depend on  $\tilde{k}_y$ , which means that the blocks of the Hamiltonian are invariant under a transformation

$$\tilde{\mathbf{k}} \rightarrow (\tilde{k}_x, \tilde{k}_y + 2\pi C/q), \tag{D6}$$

where  $C \in \mathbb{Z}$ .

For the basis-change matrix elements, this periodicity means

$$\begin{aligned}
&\mathbf{H}_{0,\tilde{\mathbf{k}},\sigma}, [\alpha_{\mathbf{k},\sigma}]_{lp \bmod q, m} \\
&\xrightarrow{\text{permute}} \tilde{\mathbf{H}}_{0,\tilde{\mathbf{k}},\sigma}, [\alpha_{\mathbf{k},\sigma}]_{l, m} \\
&\xrightarrow{\text{unitary tr.}} \check{\mathbf{H}}_{0,\tilde{\mathbf{k}},\sigma}, e^{-ik_y l} [\alpha_{\mathbf{k},\sigma}]_{lm} \\
&\xrightarrow{\text{translate}} \check{\mathbf{H}}_{0,\tilde{\mathbf{k}}+(2\pi C/q)\mathbf{e}_y, \sigma}, e^{-ik_y l} [\alpha_{\mathbf{k},\sigma}]_{lm} \\
&\xrightarrow{\text{inv. unit. tr.}} \check{\mathbf{H}}_{0,\tilde{\mathbf{k}}+(2\pi C/q)\mathbf{e}_y, \sigma}, e^{-ik_y l} [\alpha_{\mathbf{k},\sigma}]_{lm} e^{i(k_y + 2\pi C/q)l} \\
&= e^{i(2\pi C/q)l} [\alpha_{\mathbf{k},\sigma}]_{lm} \\
&\xrightarrow{\text{permute back}} \mathbf{H}_{0,\mathbf{k}+(2\pi C/q)\mathbf{e}_y, \sigma}, e^{i(2\pi C/q)l} [\alpha_{\mathbf{k},\sigma}]_{lp \bmod q, m}. \tag{D7}
\end{aligned}$$

## APPENDIX E: DECOMPOSITION INTO DIAMAGNETIC AND PARAMAGNETIC CURRENTS

The current operator can be divided into the paramagnetic and diamagnetic parts

$$\mathbf{j}_r = \mathbf{j}_{r,P} + \mathbf{j}_{r,D}, \tag{E1}$$

where we use Eq. (46) with

$$\mathbf{y}_{\mathbf{r},\mathbf{P}} = (1, 1), \quad (\text{E2})$$

$$\mathbf{y}_{\mathbf{r},\mathbf{D}} = \mathbf{y}_{\mathbf{r}} - \mathbf{y}_{\mathbf{r},\mathbf{P}}. \quad (\text{E3})$$

Because the inversion symmetry is preserved along the  $x$  axis, the diamagnetic part of  $j^x$  is going to be zero. This does not hold along the  $y$  axis, so there will be nonzero paramagnetic and diamagnetic parts in  $j^y$ , but  $\langle \mathbf{j}_{\mathbf{r},\mathbf{P}} \rangle = -\langle \mathbf{j}_{\mathbf{r},\mathbf{D}} \rangle$  so that the total current is zero. This must hold as the total current is a physical observable, and thus a gauge-invariant quantity. Using the gauge-invariant Green's function, this can be easily proven: up to the constant prefactor, the thermal average of the paramagnetic part is simply

$$\begin{aligned} \langle \mathbf{j}_{\mathbf{r},\mathbf{P}} \rangle &= iG_{\mathbf{r}+\mathbf{e}_y,\mathbf{r}}(\tau=0^-) - iG_{\mathbf{r},\mathbf{r}+\mathbf{e}_y}(\tau=0^-) \\ &= i(e^{if_{\mathbf{r}+\mathbf{e}_y,\mathbf{r}}} - e^{-if_{\mathbf{r},\mathbf{r}+\mathbf{e}_y}})\tilde{G}_{\mathbf{r},\mathbf{r}+\mathbf{e}_y}(\tau=0^-) \\ &= i(e^{-i\frac{e\mathbf{a}^2}{\hbar}B_z x} - e^{i\frac{e\mathbf{a}^2}{\hbar}B_z x})\tilde{G}_{\mathbf{r},\mathbf{r}+\mathbf{e}_y}(\tau=0^-), \end{aligned} \quad (\text{E4})$$

and similarly

$$\langle \mathbf{j}_{\mathbf{r},\mathbf{D}} \rangle = i(e^{i\frac{e\mathbf{a}^2}{\hbar}B_z x} - e^{-i\frac{e\mathbf{a}^2}{\hbar}B_z x})\tilde{G}_{\mathbf{r},\mathbf{r}+\mathbf{e}_y}(\tau=0^-) = -\langle \mathbf{j}_{\mathbf{r},\mathbf{P}} \rangle. \quad (\text{E5})$$

## APPENDIX F: PROOF OF GAUGE INVARIANCE OF THE KUBO BUBBLE

We start with the expression for the site-space matrix (operator) for the current coupled to a vanishing external gauge field  $\mathbf{A}^{\text{ext}}$ , and in the presence of a rotary gauge field  $\mathbf{A}$  describing a perpendicular magnetic field. The total gauge field is  $\mathbf{A}^{\text{tot}} = \mathbf{A}^{\text{ext}} + \mathbf{A}$ . The corresponding contributions to the Peierls phase (which is additive as well) yield  $\mathbf{f}^{\text{tot}} = \mathbf{f}^{\text{ext}} + \mathbf{f}$ :

$$\begin{aligned} j_{\mathbf{r}}^{\eta} &= -\frac{\partial \mathbf{H}_{\text{kin}}}{\partial \mathbf{A}_{\mathbf{r}}^{\text{ext},\eta}} \Big|_{\mathbf{A}^{\text{ext}} \rightarrow 0} \\ &= -\frac{\partial (e^{i\mathbf{f}^{\text{tot}}} \circ \mathbf{H}_{\text{kin}}[\mathbf{A}^{\text{tot}} = 0])}{\partial \mathbf{A}_{\mathbf{r}}^{\text{ext},\eta}} \Big|_{\mathbf{A}^{\text{ext}} \rightarrow 0} \\ &= -\frac{\partial e^{i\mathbf{f}^{\text{tot}}}}{\partial \mathbf{A}_{\mathbf{r}}^{\text{ext},\eta}} \Big|_{\mathbf{A}^{\text{ext}} \rightarrow 0} \circ \mathbf{H}_{\text{kin}}[\mathbf{A}^{\text{tot}} = 0] \\ &= -i \frac{\partial \mathbf{f}^{\text{ext}}}{\partial \mathbf{A}_{\mathbf{r}}^{\text{ext},\eta}} \Big|_{\mathbf{A}^{\text{ext}} \rightarrow 0} \circ e^{i\mathbf{f}} \circ \mathbf{H}_{\text{kin}}[\mathbf{A}^{\text{tot}} = 0]. \end{aligned} \quad (\text{F1})$$

Expressed in terms of second-quantized operators, for the general TB Hamiltonian

$$\begin{aligned} j_{\mathbf{r}}^{\eta} &= -\sum_{\mathbf{u}} t_{\mathbf{r},\mathbf{r}+\mathbf{u}} \frac{\partial f_{\mathbf{r},\mathbf{r}+\mathbf{u}}^{\text{ext}}}{\partial \mathbf{A}_{\mathbf{r}}^{\text{ext},\eta}} \Big|_{\mathbf{A}^{\text{ext}} \rightarrow 0} \\ &\quad \times (ie^{if_{\mathbf{r},\mathbf{r}+\mathbf{u}}} c_{\mathbf{r}}^{\dagger} c_{\mathbf{r}+\mathbf{u}} - ie^{-if_{\mathbf{r},\mathbf{r}+\mathbf{u}}} c_{\mathbf{r}+\mathbf{u}}^{\dagger} c_{\mathbf{r}}), \end{aligned} \quad (\text{F2})$$

where the sum over  $\mathbf{u}$  goes over all sites, and we have omitted the spin indices and the sum over spin for the sake of brevity.

The current-current correlation function is then

$$\begin{aligned} \Lambda_{\mathbf{r},\mathbf{r}'}^{\eta,\eta'}(\tau) &= \sum_{\mathbf{u},\mathbf{u}'} t_{\mathbf{r},\mathbf{r}+\mathbf{u}} t_{\mathbf{r}',\mathbf{r}'+\mathbf{u}'} \frac{\partial f_{\mathbf{r},\mathbf{r}+\mathbf{u}}^{\text{ext}}}{\partial \mathbf{A}_{\mathbf{r}}^{\text{ext},\eta}} \Big|_{\mathbf{A}^{\text{ext}} \rightarrow 0} \frac{\partial f_{\mathbf{r}',\mathbf{r}'+\mathbf{u}'}^{\text{ext}}}{\partial \mathbf{A}_{\mathbf{r}'}^{\text{ext},\eta'}} \Big|_{\mathbf{A}^{\text{ext}} \rightarrow 0} \\ &\quad \times \langle c_{\mathbf{r}+\mathbf{u},\sigma}^{\dagger}(\tau) c_{\mathbf{r}+(1-b)\mathbf{u},\sigma}(\tau) c_{\mathbf{r}'+b'\mathbf{u}',\sigma'}^{\dagger}(0) c_{\mathbf{r}'+(1-b')\mathbf{u}',\sigma'}(0) \rangle. \end{aligned} \quad (\text{F3})$$

The dynamic and disconnected part is

$$\begin{aligned} \Lambda_{\mathbf{r},\mathbf{r}'}^{\eta,\eta'}(\tau) &= \sum_{\mathbf{u},\mathbf{u}'} t_{\mathbf{r},\mathbf{r}+\mathbf{u}} t_{\mathbf{r}',\mathbf{r}'+\mathbf{u}'} \frac{\partial f_{\mathbf{r},\mathbf{r}+\mathbf{u}}^{\text{ext}}}{\partial \mathbf{A}_{\mathbf{r}}^{\text{ext},\eta}} \Big|_{\mathbf{A}^{\text{ext}} \rightarrow 0} \frac{\partial f_{\mathbf{r}',\mathbf{r}'+\mathbf{u}'}^{\text{ext}}}{\partial \mathbf{A}_{\mathbf{r}'}^{\text{ext},\eta'}} \Big|_{\mathbf{A}^{\text{ext}} \rightarrow 0} \\ &\quad \times \sum_{b,b' \in \{0,1\}} (-1)^{b+b'+1} e^{i(-1)^b f_{\mathbf{r},\mathbf{r}+\mathbf{u}}} e^{i(-1)^{b'} f_{\mathbf{r}',\mathbf{r}'+\mathbf{u}'}} \\ &\quad \times \sum_{\sigma} [-G_{\mathbf{r}+(1-b)\mathbf{u},\mathbf{r}'+b'\mathbf{u}',\sigma}(\tau)] G_{\mathbf{r}'+(1-b')\mathbf{u}',\mathbf{r}+b\mathbf{u},\sigma}(-\tau), \end{aligned} \quad (\text{F4})$$

where the Green's functions are obtained with  $\mathbf{A}^{\text{ext}} = 0$ . We now rewrite in terms of the gauge-invariant Green's function

$$\begin{aligned} \Lambda_{\mathbf{r},\mathbf{r}'}^{\eta,\eta'}(\tau) &= \sum_{\mathbf{u},\mathbf{u}'} t_{\mathbf{r},\mathbf{r}+\mathbf{u}} t_{\mathbf{r}',\mathbf{r}'+\mathbf{u}'} \frac{\partial f_{\mathbf{r},\mathbf{r}+\mathbf{u}}^{\text{ext}}}{\partial \mathbf{A}_{\mathbf{r}}^{\text{ext},\eta}} \Big|_{\mathbf{A}^{\text{ext}} \rightarrow 0} \frac{\partial f_{\mathbf{r}',\mathbf{r}'+\mathbf{u}'}^{\text{ext}}}{\partial \mathbf{A}_{\mathbf{r}'}^{\text{ext},\eta'}} \Big|_{\mathbf{A}^{\text{ext}} \rightarrow 0} \\ &\quad \times \sum_{b,b' \in \{0,1\}} (-1)^{b+b'} e^{i(-1)^b f_{\mathbf{r},\mathbf{r}+\mathbf{u}}} e^{i(-1)^{b'} f_{\mathbf{r}',\mathbf{r}'+\mathbf{u}'}} \\ &\quad \times e^{if_{\mathbf{r}+(1-b)\mathbf{u},\mathbf{r}'+b'\mathbf{u}'}} e^{if_{\mathbf{r}'+b\mathbf{u},\mathbf{r}+(1-b')\mathbf{u}'}} \\ &\quad \times \sum_{\sigma} \tilde{G}_{\mathbf{r}+(1-b)\mathbf{u},\mathbf{r}'+b'\mathbf{u}',\sigma}(\tau) \tilde{G}_{\mathbf{r}'+(1-b')\mathbf{u}',\mathbf{r}+b\mathbf{u},\sigma}(-\tau). \end{aligned} \quad (\text{F5})$$

The sum over  $b, b'$  yields four terms with exponential prefactors,

$$\begin{aligned} b=0, b'=0 &: e^{if_{\mathbf{r},\mathbf{r}+\mathbf{u}}} e^{if_{\mathbf{r}',\mathbf{r}'+\mathbf{u}'}} e^{if_{\mathbf{r}+\mathbf{u},\mathbf{r}'}} e^{if_{\mathbf{r}'+\mathbf{u}',\mathbf{r}}}, \\ b=0, b'=1 &: e^{if_{\mathbf{r},\mathbf{r}+\mathbf{u}}} e^{if_{\mathbf{r}',\mathbf{r}'+\mathbf{u}'}} e^{if_{\mathbf{r}+\mathbf{u},\mathbf{r}'+\mathbf{u}'}} e^{if_{\mathbf{r}',\mathbf{r}}}, \\ b=1, b'=0 &: e^{if_{\mathbf{r}+\mathbf{u},\mathbf{r}}} e^{if_{\mathbf{r}',\mathbf{r}'+\mathbf{u}'}} e^{if_{\mathbf{r},\mathbf{r}'}} e^{if_{\mathbf{r}'+\mathbf{u}',\mathbf{r}+\mathbf{u}}}, \\ b=1, b'=1 &: e^{if_{\mathbf{r}+\mathbf{u},\mathbf{r}}} e^{if_{\mathbf{r}',\mathbf{r}'+\mathbf{u}'}} e^{if_{\mathbf{r},\mathbf{r}'+\mathbf{u}'}} e^{if_{\mathbf{r}',\mathbf{r}+\mathbf{u}}}. \end{aligned} \quad (\text{F6})$$

and each factor above is gauge invariant. Therefore, what determines whether the Kubo bubble is gauge invariant are the factors of the type  $\frac{\partial f_{\mathbf{r},\mathbf{r}+\mathbf{u}}^{\text{ext}}}{\partial \mathbf{A}_{\mathbf{r}}^{\text{ext},\eta}} \Big|_{\mathbf{A}^{\text{ext}} \rightarrow 0}$  which clearly do not depend on the choice of the gauge for  $\mathbf{A}$ . A vanishing uniform electric field  $\mathbf{E} = \partial_t \mathbf{A}^{\text{ext}}$ , can be achieved by letting  $\mathbf{A}^{\text{ext}}(\mathbf{r}, t) \rightarrow \mathbf{A}^{\text{ext}}$ , i.e., by having a constant and uniform vector potential. The only gauge freedom for the external electric field then corresponds to choosing the inertial reference frame, which is a trivial transformation that our calculation is certainly invariant to; the slowly varying field approximation holds, and we have

$$\frac{\partial}{\partial \mathbf{A}_{\mathbf{r}}^{\text{ext},\eta}} \int_{\mathbf{r}}^{\mathbf{r}+\mathbf{u}} \mathbf{A}^{\text{ext}}(\tilde{\mathbf{r}}) \cdot d\tilde{\mathbf{r}} = \frac{\partial}{\partial \mathbf{A}_{\mathbf{r}}^{\text{ext},\eta}} (\mathbf{A}^{\text{ext}} \cdot \mathbf{u}) = u^{\eta} \quad (\text{F7})$$

which clearly does not depend on the precise choice of the uniform  $\mathbf{A}^{\text{ext}}$ . We therefore conclude that for the calculation of the linear response to a spatially uniform  $\mathbf{q} = 0$  electric field, the Kubo bubble (47) is gauge invariant.

We also emphasize that the bubble for the charge-charge correlation function is trivially gauge invariant because  $G_{ij}G_{ji} = \tilde{G}_{ij}\tilde{G}_{ji}$ .

## APPENDIX G: CURRENT OPERATOR IN MOMENTUM SPACE

Here we derive the current operator in momentum space. The general form is

$$j_{\mathbf{q}=0}^\eta = \frac{it}{N} \frac{e}{ac\hbar} \sum_{\sigma} \sum_{\tilde{\mathbf{k}}, m, m'} v_{\tilde{\mathbf{k}}, m, m', \sigma}^\eta c_{\tilde{\mathbf{k}}, m, \sigma}^\dagger c_{\tilde{\mathbf{k}}, m', \sigma} \quad (\text{G1})$$

The goal of this section is to get expressions for the vertex factors  $v_{\tilde{\mathbf{k}}, m, m', \sigma}^\eta$ . We start with the current along the  $x$  direction. The local contribution is given in Eq. (46). After plugging this in Eq. (53) and applying the basis transformation from Eq. (37), we obtain

$$\begin{aligned} j_{\mathbf{q}=0}^x &= \frac{it}{N} \frac{e}{ac\hbar} \sum_{\sigma} \sum_{\tilde{\mathbf{k}}, m, \tilde{\mathbf{k}}', m'} c_{\tilde{\mathbf{k}}, m, \sigma}^\dagger c_{\tilde{\mathbf{k}}', m', \sigma} \sum_{l, l'} [\alpha_{\tilde{\mathbf{k}}, \sigma}]_{l, m} [\alpha_{\tilde{\mathbf{k}}', \sigma}]_{l', m'}^* \frac{1}{N} \sum_{\mathbf{r}} e^{-i(\tilde{\mathbf{k}}+l\frac{2\pi}{q}\mathbf{e}_x)\cdot\mathbf{r}} e^{i(\tilde{\mathbf{k}}'+l'\frac{2\pi}{q}\mathbf{e}_x)\cdot(\mathbf{r}+\mathbf{e}_x)} + \text{H.c.} \\ &= \frac{it}{N} \frac{e}{ac\hbar} \sum_{\sigma} \sum_{\tilde{\mathbf{k}}, m, \tilde{\mathbf{k}}', m'} c_{\tilde{\mathbf{k}}, m, \sigma}^\dagger c_{\tilde{\mathbf{k}}', m', \sigma} \sum_{l, l'} [\alpha_{\tilde{\mathbf{k}}, \sigma}]_{l, m} [\alpha_{\tilde{\mathbf{k}}', \sigma}]_{l', m'}^* e^{i(\tilde{\mathbf{k}}'+l'\frac{2\pi}{q}\mathbf{e}_x)\cdot\mathbf{e}_x} \delta_{\tilde{\mathbf{k}}, \tilde{\mathbf{k}}'} \delta_{l, l'} + \text{H.c.} \\ &= \frac{it}{N} \frac{e}{ac\hbar} \sum_{\sigma} \sum_{\tilde{\mathbf{k}}, m, m'} c_{\tilde{\mathbf{k}}, m, \sigma}^\dagger c_{\tilde{\mathbf{k}}, m', \sigma} \sum_l [\alpha_{\tilde{\mathbf{k}}, \sigma}]_{l, m} [\alpha_{\tilde{\mathbf{k}}, \sigma}]_{l, m'}^* e^{i(\tilde{\mathbf{k}}+l\frac{2\pi}{q}\mathbf{e}_x)\cdot\mathbf{e}_x} + \text{H.c.} \\ &= \frac{it}{N} \frac{e}{ac\hbar} \sum_{\sigma} \sum_{\tilde{\mathbf{k}}, m, m'} c_{\tilde{\mathbf{k}}, m, \sigma}^\dagger c_{\tilde{\mathbf{k}}, m', \sigma} e^{i\tilde{k}_x} \sum_l [\alpha_{\tilde{\mathbf{k}}, \sigma}]_{l, m} [\alpha_{\tilde{\mathbf{k}}, \sigma}]_{l, m'}^* e^{il\frac{2\pi}{q}} + \text{H.c.} \\ &= \frac{it}{N} \frac{e}{ac\hbar} \sum_{\sigma} \sum_{\tilde{\mathbf{k}}, m, m'} \left[ c_{\tilde{\mathbf{k}}, m, \sigma}^\dagger c_{\tilde{\mathbf{k}}, m', \sigma} e^{i\tilde{k}_x} \sum_l [\alpha_{\tilde{\mathbf{k}}, \sigma}]_{l, m} [\alpha_{\tilde{\mathbf{k}}, \sigma}]_{l, m'}^* e^{il\frac{2\pi}{q}} - c_{\tilde{\mathbf{k}}, m', \sigma}^\dagger c_{\tilde{\mathbf{k}}, m, \sigma} e^{-i\tilde{k}_x} \sum_l [\alpha_{\tilde{\mathbf{k}}, \sigma}]_{l, m}^* [\alpha_{\tilde{\mathbf{k}}, \sigma}]_{l, m'} e^{-il\frac{2\pi}{q}} \right]. \quad (\text{G2}) \end{aligned}$$

We are free to swap  $m$  and  $m'$  in the last term:

$$\begin{aligned} j_{\mathbf{q}=0}^x &= \frac{it}{N} \frac{e}{ac\hbar} \sum_{\sigma} \sum_{\tilde{\mathbf{k}}, m, m'} \left[ c_{\tilde{\mathbf{k}}, m, \sigma}^\dagger c_{\tilde{\mathbf{k}}, m', \sigma} e^{i\tilde{k}_x} \sum_l [\alpha_{\tilde{\mathbf{k}}, \sigma}]_{l, m} [\alpha_{\tilde{\mathbf{k}}, \sigma}]_{l, m'}^* e^{il\frac{2\pi}{q}} - c_{\tilde{\mathbf{k}}, m, \sigma}^\dagger c_{\tilde{\mathbf{k}}, m', \sigma} e^{-i\tilde{k}_x} \sum_l [\alpha_{\tilde{\mathbf{k}}, \sigma}]_{l, m} [\alpha_{\tilde{\mathbf{k}}, \sigma}]_{l, m'}^* e^{-il\frac{2\pi}{q}} \right] \\ &= \frac{it}{N} \frac{e}{ac\hbar} \sum_{\sigma} \sum_{\tilde{\mathbf{k}}, m, m'} c_{\tilde{\mathbf{k}}, m, \sigma}^\dagger c_{\tilde{\mathbf{k}}, m', \sigma} \sum_l [\alpha_{\tilde{\mathbf{k}}, \sigma}]_{l, m} [\alpha_{\tilde{\mathbf{k}}, \sigma}]_{l, m'}^* \left[ e^{i\tilde{k}_x} e^{il\frac{2\pi}{q}} - e^{-i\tilde{k}_x} e^{-il\frac{2\pi}{q}} \right], \quad (\text{G3}) \end{aligned}$$

and we can simply read off Eq. (55).

Along the  $y$  direction, similarly we have

$$\begin{aligned} N \frac{ac\hbar}{e} j_{\mathbf{q}=0}^y &= it \sum_{\sigma} \sum_{\tilde{\mathbf{k}}, m, \tilde{\mathbf{k}}', m'} c_{\tilde{\mathbf{k}}, m, \sigma}^\dagger c_{\tilde{\mathbf{k}}', m', \sigma} \sum_{l, l'} [\alpha_{\tilde{\mathbf{k}}, \sigma}]_{l, m} [\alpha_{\tilde{\mathbf{k}}', \sigma}]_{l', m'}^* \frac{1}{N} \sum_{\mathbf{r}} e^{2i\pi \frac{e}{q} \mathbf{r} \cdot \mathbf{e}_x} e^{-i(\tilde{\mathbf{k}}+l\frac{2\pi}{q}\mathbf{e}_x)\cdot\mathbf{r}} e^{i(\tilde{\mathbf{k}}'+l'\frac{2\pi}{q}\mathbf{e}_x)\cdot(\mathbf{r}+\mathbf{e}_y)} + \text{H.c.} \\ &= it \sum_{\sigma} \sum_{\tilde{\mathbf{k}}, m, \tilde{\mathbf{k}}', m'} c_{\tilde{\mathbf{k}}, m, \sigma}^\dagger c_{\tilde{\mathbf{k}}', m', \sigma} \sum_{l, l'} [\alpha_{\tilde{\mathbf{k}}, \sigma}]_{l, m} [\alpha_{\tilde{\mathbf{k}}', \sigma}]_{l', m'}^* \frac{1}{N} \sum_{\mathbf{r}} e^{i(\tilde{\mathbf{k}}'+l'\frac{2\pi}{q}\mathbf{e}_x - \tilde{\mathbf{k}} - l\frac{2\pi}{q}\mathbf{e}_x + p\frac{2\pi}{q}\mathbf{e}_x)\cdot\mathbf{r}} e^{i(\tilde{\mathbf{k}}'+l'\frac{2\pi}{q}\mathbf{e}_x)\cdot\mathbf{e}_y} + \text{H.c.} \\ &= it \sum_{\sigma} \sum_{\tilde{\mathbf{k}}, m, \tilde{\mathbf{k}}', m'} e^{i\tilde{k}_y} c_{\tilde{\mathbf{k}}, m, \sigma}^\dagger c_{\tilde{\mathbf{k}}', m', \sigma} \sum_{l, l'} [\alpha_{\tilde{\mathbf{k}}, \sigma}]_{l, m} [\alpha_{\tilde{\mathbf{k}}', \sigma}]_{l', m'}^* \delta_{\tilde{\mathbf{k}}, \tilde{\mathbf{k}}'} \delta_{l, l'} + \text{H.c.} \\ &= it \sum_{\sigma} \sum_{\tilde{\mathbf{k}}, m, m'} e^{i\tilde{k}_y} c_{\tilde{\mathbf{k}}, m, \sigma}^\dagger c_{\tilde{\mathbf{k}}, m', \sigma} \sum_l [\alpha_{\tilde{\mathbf{k}}, \sigma}]_{l, m} [\alpha_{\tilde{\mathbf{k}}, \sigma}]_{l, m'}^* + \text{H.c.} \\ &= it \sum_{\sigma} \sum_{\tilde{\mathbf{k}}, m, m'} \left[ e^{i\tilde{k}_y} c_{\tilde{\mathbf{k}}, m, \sigma}^\dagger c_{\tilde{\mathbf{k}}, m', \sigma} \sum_l [\alpha_{\tilde{\mathbf{k}}, \sigma}]_{l, m} [\alpha_{\tilde{\mathbf{k}}, \sigma}]_{l, m'}^* - e^{-i\tilde{k}_y} c_{\tilde{\mathbf{k}}, m', \sigma}^\dagger c_{\tilde{\mathbf{k}}, m, \sigma} \sum_l [\alpha_{\tilde{\mathbf{k}}, \sigma}]_{l, m}^* [\alpha_{\tilde{\mathbf{k}}, \sigma}]_{l, m'} \right] \\ &= it \sum_{\sigma} \sum_{\tilde{\mathbf{k}}, m, m'} c_{\tilde{\mathbf{k}}, m, \sigma}^\dagger c_{\tilde{\mathbf{k}}, m', \sigma} \left[ e^{i\tilde{k}_y} \sum_l [\alpha_{\tilde{\mathbf{k}}, \sigma}]_{l, m} [\alpha_{\tilde{\mathbf{k}}, \sigma}]_{l, m'}^* - e^{-i\tilde{k}_y} \sum_l [\alpha_{\tilde{\mathbf{k}}, \sigma}]_{l, m} [\alpha_{\tilde{\mathbf{k}}, \sigma}]_{l, m'}^* \right] \quad (\text{G4}) \end{aligned}$$

and we can immediately recognize Eq. (56).

We can use the property of the basis change matrix elements (23) to work out a symmetry of  $v^x$  with respect to momentum inversion:

$$v_{-\tilde{\mathbf{k}}, m, m', \sigma}^x = \sum_l [\alpha_{-\tilde{\mathbf{k}}, \sigma}]_{l, m} [\alpha_{-\tilde{\mathbf{k}}, \sigma}]_{l, m'}^* \left[ e^{-i\tilde{k}_x} e^{il\frac{2\pi}{q}} - e^{i\tilde{k}_x} e^{-il\frac{2\pi}{q}} \right] \quad (\text{G5})$$

$$= \sum_l [\alpha_{\tilde{\mathbf{k}}, \sigma}]_{q-l, m} [\alpha_{\tilde{\mathbf{k}}, \sigma}]_{q-l, m'}^* \left[ e^{-i\tilde{k}_x} e^{il\frac{2\pi}{q}} - e^{i\tilde{k}_x} e^{-il\frac{2\pi}{q}} \right]. \quad (\text{G6})$$

We now make a change of variables,  $l' = q - l$ ,  $l = q - l'$ :

$$v_{-\tilde{\mathbf{k}},m,m',\sigma}^x = \sum_{l'} [\alpha_{\tilde{\mathbf{k}},\sigma}]_{l',m} [\alpha_{\tilde{\mathbf{k}},\sigma}]_{l',m'}^* [e^{-i\tilde{k}_x} e^{i(q-l')\frac{2\pi}{q}} - e^{i\tilde{k}_x} e^{-i(q-l')\frac{2\pi}{q}}] = \sum_{l'} [\alpha_{\tilde{\mathbf{k}},\sigma}]_{l',m} [\alpha_{\tilde{\mathbf{k}},\sigma}]_{l',m'}^* [e^{-i\tilde{k}_x} e^{-il'\frac{2\pi}{q}} - e^{i\tilde{k}_x} e^{il'\frac{2\pi}{q}}]. \quad (\text{G7})$$

Therefore,

$$v_{-\tilde{\mathbf{k}},m,m',\sigma}^x = -v_{\tilde{\mathbf{k}},m,m',\sigma}^x. \quad (\text{G8})$$

Furthermore, by noting that  $v$  can be more simply written as

$$v_{\tilde{\mathbf{k}},m,m',\sigma}^x = -2i \sum_l [\alpha_{\tilde{\mathbf{k}},\sigma}]_{l',m} [\alpha_{\tilde{\mathbf{k}},\sigma}]_{l',m'}^* \sin\left(\tilde{k}_x + l\frac{2\pi}{q}\right), \quad (\text{G9})$$

we can easily prove

$$v_{\tilde{\mathbf{k}},m,m',\sigma}^x = -(v_{\tilde{\mathbf{k}},m',m,\sigma}^x)^*. \quad (\text{G10})$$

The matrix  $[v_{\tilde{\mathbf{k}},\sigma}^x]_{mm'}$  is hence anti-Hermitian, which also implies  $\text{Re} v_{\tilde{\mathbf{k}},m,m}^x = 0$ . Also, by using Eq. (21), it is easily proven that

$$v_{(\tilde{k}_x, -\tilde{k}_y),m,m',\sigma}^x = v_{(\tilde{k}_x, \tilde{k}_y),m',m,\sigma}^x. \quad (\text{G11})$$

## APPENDIX H: DERIVATION FOR $\Lambda_{\mathbf{q}=0}^{\eta,\eta',\text{disc}}(i\nu)$

The disconnected part of Eq. (57) reads as

$$\Lambda_{\mathbf{q}=0}^{\eta\eta',\text{disc}}(i\nu) = \frac{1}{2\hbar} \int_{-\beta\hbar}^{\beta\hbar} d\tau e^{i\nu\tau} \frac{t^2 e^2}{c\hbar^2} \frac{1}{N} \sum_{\sigma} \sum_{\tilde{\mathbf{k}},m_1,m'_1,m_2,m'_2} v_{\tilde{\mathbf{k}},m_1,m'_1,\sigma}^{\eta} v_{\tilde{\mathbf{k}},m_2,m'_2,\sigma}^{\eta'} G_{\tilde{\mathbf{k}},m'_2,m_1\sigma}(-\tau) G_{\tilde{\mathbf{k}},m'_1,m_2,\sigma}(\tau). \quad (\text{H1})$$

We now apply inverse Fourier transform to the Green's functions

$$G(\tau) = \frac{1}{\beta} \sum_{i\omega} e^{-i\omega\tau} G(i\omega), \quad (\text{H2})$$

to obtain

$$\Lambda_{\mathbf{q}=0}^{\eta\eta',\text{disc}}(i\nu) = \frac{t^2 e^2}{c\hbar^2} \frac{1}{N} \sum_{\sigma} \sum_{\tilde{\mathbf{k}},m_1,m'_1,m_2,m'_2} v_{\tilde{\mathbf{k}},m_1,m'_1,\sigma}^{\eta} v_{\tilde{\mathbf{k}},m_2,m'_2,\sigma}^{\eta'} \frac{1}{\beta^2} \sum_{i\omega,i\omega'} G_{\tilde{\mathbf{k}},m'_2,m_1\sigma}(i\omega) G_{\tilde{\mathbf{k}},m'_1,m_2,\sigma}(i\omega') \frac{1}{2\hbar} \int_{-\beta\hbar}^{\beta\hbar} d\tau e^{i(\nu+\omega-\omega')\tau}, \quad (\text{H3})$$

where  $\int_{-\beta\hbar}^{\beta\hbar} d\tau e^{i(\nu+\omega-\omega')\tau} = 2\beta\hbar \delta_{\nu+\omega-\omega'}$ , which immediately yields Eq. (58).

## APPENDIX I: PROOF THAT DMFT SELF-ENERGY IS DIAGONAL IN THE NONINTERACTING EIGENBASIS

The following shows that a local self-energy is also diagonal in the basis of  $|\tilde{\mathbf{k}}, m, \sigma\rangle$  states. We have

$$[\Sigma_{\tilde{\mathbf{k}},\sigma}(z)]_{ll'} = \langle \tilde{\mathbf{k}}, l, \sigma | \Sigma_{\sigma} | \tilde{\mathbf{k}}, l', \sigma \rangle = \sum_i [w_{\sigma}]_{(\tilde{\mathbf{k}},l),i}^* [w_{\sigma}]_{(\tilde{\mathbf{k}},l'),i} \Sigma_{ii,\sigma}(z) = \Sigma_{\sigma}(z) \sum_i [w_{\sigma}]_{(\tilde{\mathbf{k}},l),i}^* [w_{\sigma}]_{(\tilde{\mathbf{k}},l'),i} = \Sigma_{\sigma}(z) \delta_{ll'}, \quad (\text{I1})$$

where  $w_{\sigma}$  is the basis change matrix, for the transformation from site space to  $\tilde{\mathbf{k}}, l$  space. We can, therefore, write

$$[\Sigma_{\tilde{\mathbf{k}},\sigma}(z)]_{mm'} = \langle \tilde{\mathbf{k}}, m, \sigma | \Sigma_{\sigma} | \tilde{\mathbf{k}}, m', \sigma \rangle = \sum_l [\alpha_{\tilde{\mathbf{k}},\sigma}^{-1}]_{m,l}^* [\alpha_{\tilde{\mathbf{k}},\sigma}^{-1}]_{m',l} \Sigma_{ll,\sigma}(z) = \Sigma_{\sigma}(z) \delta_{mm'}, \quad (\text{I2})$$

which immediately yields Eq. (63).

## APPENDIX J: CALCULATION OF LOCAL GREEN'S FUNCTION IN DMFT USING THE NONINTERACTING DENSITY OF STATES

Here we prove Eq. (65):

$$\begin{aligned} G_{ii,\sigma}(z) &= \langle i, \sigma | \mathbf{G}_{\sigma}(z) | i, \sigma \rangle \\ &= \frac{1}{N} \sum_{\tilde{\mathbf{k}},m} \sum_{l,l'} e^{-i(\tilde{\mathbf{k}}+l\frac{2\pi}{q}\mathbf{e}_x)\cdot\mathbf{r}_i} e^{i(\tilde{\mathbf{k}}+l'\frac{2\pi}{q}\mathbf{e}_x)\cdot\mathbf{r}_i} [\alpha_{\tilde{\mathbf{k}},\sigma}]_{l,m} [\alpha_{\tilde{\mathbf{k}},\sigma}]_{l',m}^* \langle \tilde{\mathbf{k}}, m, \sigma | \mathbf{G}_{\sigma}(z) | \tilde{\mathbf{k}}, m, \sigma \rangle \\ &= \frac{1}{N} \sum_{\tilde{\mathbf{k}},m} \sum_{l,l'} e^{-i((l-l')\frac{2\pi}{q}\mathbf{e}_x)\cdot\mathbf{r}_i} [\alpha_{\tilde{\mathbf{k}},\sigma}]_{l,m} [\alpha_{\tilde{\mathbf{k}},\sigma}]_{l',m}^* \langle \tilde{\mathbf{k}}, m, \sigma | \mathbf{G}_{\sigma}(z) | \tilde{\mathbf{k}}, m, \sigma \rangle. \end{aligned} \quad (\text{J1})$$



Because we know that  $G_{ii}(z)$  must be uniform, we can define

$$\begin{aligned}
 G_{\text{loc},\sigma}(z) &= \frac{1}{N} \sum_i G_{ii,\sigma}(z) \\
 &= \frac{1}{N^2} \sum_{\tilde{\mathbf{k}},m} \sum_{l,l'} [\alpha_{\tilde{\mathbf{k}},\sigma}]_{l,m} [\alpha_{\tilde{\mathbf{k}},\sigma}]_{l',m}^* \sum_i e^{-i((l-l')\frac{2\pi}{q}\mathbf{e}_x) \cdot \mathbf{r}_i} \langle \tilde{\mathbf{k}}, m, \sigma | \mathbf{G}_\sigma(z) | \tilde{\mathbf{k}}, m, \sigma \rangle \\
 &= \frac{1}{N^2} \sum_{\tilde{\mathbf{k}},m} \sum_{l,l'} [\alpha_{\tilde{\mathbf{k}},\sigma}]_{l,m} [\alpha_{\tilde{\mathbf{k}},\sigma}]_{l',m}^* N \delta_{ll'} \langle \tilde{\mathbf{k}}, m, \sigma | \mathbf{G}_\sigma(z) | \tilde{\mathbf{k}}, m, \sigma \rangle \\
 &= \frac{1}{N} \sum_{\tilde{\mathbf{k}},m} \langle \tilde{\mathbf{k}}, m, \sigma | \mathbf{G}_\sigma(z) | \tilde{\mathbf{k}}, m, \sigma \rangle \sum_l |[\alpha_{\tilde{\mathbf{k}},\sigma}]_{l,m}|^2 \\
 &= \frac{1}{N} \sum_{\tilde{\mathbf{k}},m} \langle \tilde{\mathbf{k}}, m, \sigma | \mathbf{G}_\sigma(z) | \tilde{\mathbf{k}}, m, \sigma \rangle.
 \end{aligned} \tag{J2}$$

Therefore, we can identify

$$G_{ii,\sigma}(z) = \frac{1}{N} \sum_{\tilde{\mathbf{k}},m} \frac{1}{\hbar z - \varepsilon_{\tilde{\mathbf{k}},m,\sigma} - \Sigma_\sigma(z)} = \int d\varepsilon \frac{\rho_0(\varepsilon)}{\hbar z - \varepsilon - \Sigma_\sigma(z)}. \tag{J3}$$

#### APPENDIX K: CONDUCTIVITY EXPRESSION IN DMFT: PROOF OF EQS. (70) AND (71)

Starting from Eq. (67), we first perform the Hilbert transform of the Green's function

$$G(i\omega) = -\frac{1}{\pi} \int d\varepsilon \frac{\text{Im}G(\varepsilon + i0^+)}{i\omega - \varepsilon}, \tag{K1}$$

where  $\varepsilon$  and  $i\omega$  have the units of frequency. We obtain

$$\Lambda_{\mathbf{q}=0}^{\eta\eta',\text{disc}}(i\nu) = \frac{t^2 e^2}{c\hbar^2 \pi^2} \sum_\sigma \frac{1}{\beta} \sum_{i\omega} \int d\varepsilon \int d\varepsilon' v_\sigma^{\eta\eta'}(\varepsilon, \varepsilon') \int d\omega \int d\omega' \frac{\text{Im}G(\varepsilon, \omega)}{i\omega + i\nu - \omega} \frac{\text{Im}G(\varepsilon', \omega')}{i\omega - \omega'}. \tag{K2}$$

Now we apply the partial fraction expansion  $\frac{1}{z-a} \frac{1}{z-b} = \frac{1}{a-b} (\frac{1}{z-a} - \frac{1}{z-b})$ :

$$\begin{aligned}
 \Lambda_{\mathbf{q}=0}^{\eta\eta',\text{disc}}(i\nu) &= \frac{t^2 e^2}{c\hbar^2 \pi^2} \sum_\sigma \frac{1}{\beta} \sum_{i\omega} \int d\varepsilon \int d\varepsilon' v_\sigma^{\eta\eta'}(\varepsilon, \varepsilon') \int d\omega \int d\omega' \text{Im}G(\varepsilon, \omega) \text{Im}G(\varepsilon', \omega') \\
 &\quad \times \frac{1}{-i\nu + \omega - \omega'} \left[ \frac{1}{i\omega + i\nu - \omega} - \frac{1}{i\omega - \omega'} \right].
 \end{aligned} \tag{K3}$$

We apply  $\frac{1}{\beta} \sum_{i\omega} \frac{1}{\hbar(i\omega - z)} = n_F(z)$ :

$$\Lambda_{\mathbf{q}=0}^{\eta\eta',\text{disc}}(i\nu) = \frac{t^2 e^2}{c\hbar \pi^2} \sum_\sigma \int d\varepsilon \int d\varepsilon' v_\sigma^{\eta\eta'}(\varepsilon, \varepsilon') \int d\omega \int d\omega' \text{Im}G(\varepsilon, \omega) \text{Im}G(\varepsilon', \omega') \frac{1}{-i\nu + \omega - \omega'} [n_F(-i\nu + \omega) - n_F(\omega')]. \tag{K4}$$

The bosonic frequency does nothing in the argument of  $n_F$  so we can rewrite

$$\Lambda_{\mathbf{q}=0}^{\eta\eta',\text{disc}}(i\nu) = \frac{t^2 e^2}{c\hbar \pi^2} \sum_\sigma \int d\varepsilon \int d\varepsilon' v_\sigma^{\eta\eta'}(\varepsilon, \varepsilon') \int d\omega \int d\omega' \text{Im}G(\varepsilon, \omega) \text{Im}G(\varepsilon', \omega') \frac{1}{-i\nu + \omega - \omega'} [n_F(\omega) - n_F(\omega')]. \tag{K5}$$

Formal continuation to the real axis is performed by replacing  $i\nu \rightarrow \nu$ :

$$\Lambda_{\mathbf{q}=0}^{\eta\eta',\text{disc}}(\nu) = \frac{t^2 e^2}{c\hbar \pi^2} \sum_\sigma \int d\varepsilon \int d\varepsilon' v_\sigma^{\eta\eta'}(\varepsilon, \varepsilon') \int d\omega \int d\omega' \text{Im}G(\varepsilon, \omega) \text{Im}G(\varepsilon', \omega') \frac{1}{-\nu + \omega - \omega'} [n_F(\omega) - n_F(\omega')]. \tag{K6}$$

As we are interested in the real part of the conductivity, and having in mind  $\text{Im} \Lambda^{\eta, \eta'}(\nu = 0) = 0$ , we get

$$\begin{aligned} \text{Re} \sigma_{\mathbf{q}=0}^{\eta, \eta', \text{disc}}(\nu) &= c \frac{\text{Im} \Lambda_{\mathbf{q}=0}^{\eta, \eta', \text{disc}}(\nu)}{\nu} \\ &= \frac{t^2 e^2}{\hbar \pi^2} \sum_{\sigma} \text{Im} \int d\varepsilon \int d\varepsilon' v_{\sigma}^{\eta, \eta'}(\varepsilon, \varepsilon') \int d\omega \int d\omega' \text{Im} G(\varepsilon, \omega) \text{Im} G(\varepsilon', \omega') \frac{1}{-\nu + \omega - \omega'} \frac{[n_F(\omega) - n_F(\omega')]}{\nu}. \end{aligned} \quad (\text{K7})$$

For the longitudinal conductivity specifically,  $v^{\eta\eta}$  is purely real, so the imaginary part comes from the delta-peak part of the  $\omega, \omega'$  integrals through  $\int dx \frac{1}{x-y+i0} = \mathcal{P} \int dx \frac{1}{x-y} + i\pi \delta(x-y)$ . In the limit  $\nu \rightarrow 0$  we get Eq. (70).

For Hall conductivity the imaginary part comes from the principal part of the integral, and one can estimate it through [38]  $\mathcal{P} \int d\omega \int d\omega' \frac{1}{\nu - \nu + \omega - \omega'} = \mathcal{P} \int d\omega \int d\omega' \frac{1}{\nu} \frac{-\nu + \omega - \omega'}{(-\nu + \omega - \omega')^2} = -\int d\omega \int d\omega' \frac{1}{(-\nu + \omega - \omega')^2} + \int d\omega \int d\omega' \frac{1}{\nu} \frac{\omega - \omega'}{(-\nu + \omega - \omega')^2}$ . In the limit  $\nu \rightarrow 0$  the second term cancels exactly due to the antisymmetry of the integrand with respect to the exchange  $\omega \leftrightarrow \omega'$ , and we get Eq. (71).

## APPENDIX L: OSCILLATIONS IN THERMODYNAMIC PROPERTIES

With the NRG impurity solver, it is possible to directly calculate the thermodynamic properties of the lattice problem (i.e., without any integrations over parameters such as  $T$  or  $\mu$ , which is error prone). This is based on Eq. (46) from Ref. [58], which relates the lattice grand potential (Landau free energy)  $\Omega = F - \mu N_{\text{tot}} = E - TS - \mu N_{\text{tot}}$  ( $N_{\text{tot}}$  is total number of particles) and the impurity grand potential  $\Phi_{\text{imp}} = F_{\text{imp}} - \mu n_{\text{imp}}$ :

$$\begin{aligned} \frac{\Omega}{N} &= \Omega_{\text{imp}} - k_B T \sum_{i\omega, \sigma} \left( \int_{-\infty}^{+\infty} d\epsilon \rho_0(\epsilon) \right. \\ &\quad \times \ln \{ [i\omega \hbar + \mu - \Sigma_{\sigma}(i\omega) - \epsilon] G_{\sigma}(i\omega) \} \Big), \end{aligned} \quad (\text{L1})$$

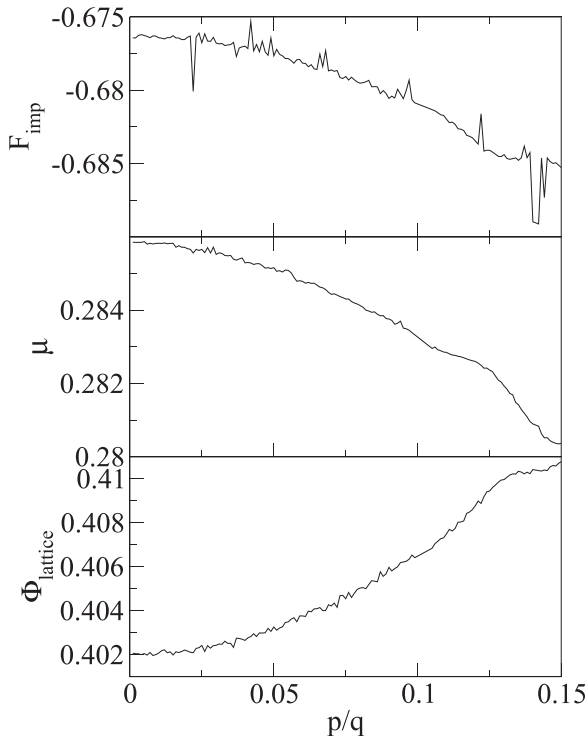


FIG. 20. Dependence of total free energy and its components on the magnetic field.

where  $G_{\sigma}$  is the local Green's function. This may be analytically continued to the real axis to give [78,79]

$$\begin{aligned} \frac{\Omega}{N} &= \Omega_{\text{imp}} + \frac{1}{\pi} \sum_{\sigma} \int_{-\infty}^{+\infty} d\epsilon \rho_0(\epsilon) \int_{-\infty}^{+\infty} d\omega \\ &\quad \times \text{Im} \ln \{ [\hbar\omega + \mu - \Sigma_{\sigma}(\omega) - \epsilon] G_{\sigma}(\omega) \} n_F(\omega), \end{aligned} \quad (\text{L2})$$

with the Fermi-Dirac distribution  $n_F(\omega) = 1/(1 + \exp[\hbar\omega/Tk_B])$ . The impurity free energy can be directly calculated in the NRG using the full-density-matrix approach.

We consider the case shown in Fig. 5 which exhibited significant transport oscillations at the high frequency, while the self-energy and the Green's function showed instead oscillations at the SdH frequency. In fact, at this temperature, the Fourier transform of the oscillatory part of the inverse conductivity shows no component at the SdH frequency, it is already thermally washed out. Indeed, we find no remnants of the SdH/dHvA oscillations in the thermodynamic properties either. In Fig. 20 we plot three elements that enter the full thermodynamic potential: impurity free energy  $F_{\text{imp}}$ , the chemical potential  $\mu$  (which enters as  $-\mu n_{\text{imp}}$  with constant  $n_{\text{imp}} = n = 0.85$ ), and the lattice contribution from the double integration  $\Phi_{\text{lattice}}$ . None of these show any clear oscillations;

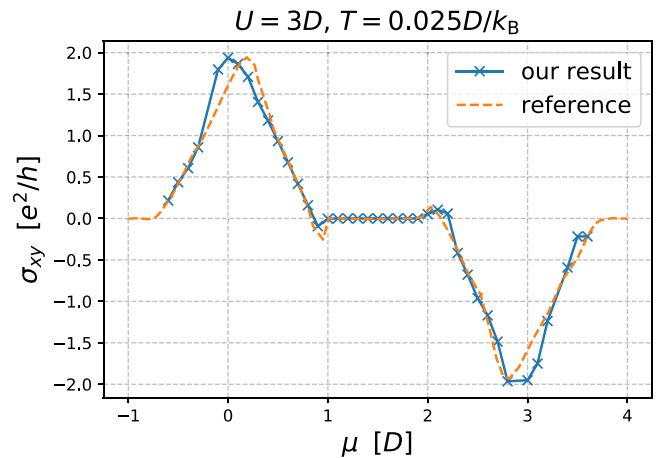


FIG. 21. Benchmark with the data from Markov *et al.* [38]. Our data: DMFT(NRG solver). Reference data: DMFT(exact diagonalization solver with five bath sites)+Padé analytical continuation used to obtain continuous spectra.

if they exist, they are below the numerical uncertainty. We only observe a weak quadratic dependence on the magnetic field in all three contributions. This confirms yet again that the high-frequency quantum oscillations show up exclusively in the transport properties through the vertex factors, thus they are, in this sense, a purely kinetic effect.

## APPENDIX M: BENCHMARK

To benchmark our formalism and implementation, we cross-check our  $\sigma^{xy}(\nu = 0)$  results with the data from Ref. [38]. We perform a chemical potential scan at a fixed  $U =$

$3D$  and  $T = 0.025D/k_B$ , which corresponds to the (doped) Mott insulator regime. The results are shown in Fig. 21. The agreement is solid. Neither of the curves fully satisfy  $\sigma^{xy}(\nu = 0; \mu) = -\sigma^{xy}(\nu = 0; -\mu)$ , which reveals the extent of the systematic error bars. The biggest difference is the position of the two peaks in the curves, which can be attributed to the difference in the impurity solvers used (we have used NRG [62–65], directly on the real axis; in Ref. [38] they used exact diagonalization with five bath sites, and Padé analytical continuation to obtain continuous spectra). We reproduce the change of sign of  $\sigma^{xy}(\nu = 0)$  as chemical potential crosses the edge of the Hubbard band into the Mott gap (at around  $\mu = 1$  and 2), which appears to be a robust feature of the solution.

- 
- [1] H. Takagi, B. Batlogg, H. L. Kao, J. Kwo, R. J. Cava, J. J. Krajewski, and W. F. Peck, *Phys. Rev. Lett.* **69**, 2975 (1992).
  - [2] B. Keimer, S. A. Kivelson, M. R. Norman, S. Uchida, and J. Zaanen, *Nature (London)* **518**, 179 (2015).
  - [3] A. Legros, S. Benhabib, W. Tabis, F. Laliberté, M. Dion, M. Lizaire, B. Vignolle, D. Vignolles, H. Raffy, Z. Z. Li, P. Auban-Senzier, N. Doiron-Leyraud, P. Fournier, D. Colson, L. Taillefer, and C. Proust, *Nat. Phys.* **15**, 142 (2018).
  - [4] T. Pruschke, D. L. Cox, and M. Jarrell, *Phys. Rev. B* **47**, 3553 (1993).
  - [5] M. Jarrell and T. Pruschke, *Phys. Rev. B* **49**, 1458 (1994).
  - [6] D. Bergeron, V. Hankevych, B. Kyung, and A.-M. S. Tremblay, *Phys. Rev. B* **84**, 085128 (2011).
  - [7] X. Deng, J. Mravlje, R. Žitko, M. Ferrero, G. Kotliar, and A. Georges, *Phys. Rev. Lett.* **110**, 086401 (2013).
  - [8] J. Vučičević, D. Tanasković, M. J. Rozenberg, and V. Dobrosavljević, *Phys. Rev. Lett.* **114**, 246402 (2015).
  - [9] E. Perepelitsky, A. Galatas, J. Mravlje, R. Žitko, E. Khatami, B. S. Shastry, and A. Georges, *Phys. Rev. B* **94**, 235115 (2016).
  - [10] J. Kokalj, *Phys. Rev. B* **95**, 041110(R) (2017).
  - [11] J. Vučičević, J. Kokalj, R. Žitko, N. Wentzell, D. Tanasković, and J. Mravlje, *Phys. Rev. Lett.* **123**, 036601 (2019).
  - [12] E. W. Huang, R. Sheppard, B. Moritz, and T. P. Devereaux, *Science* **366**, 987 (2019).
  - [13] A. Vranić, J. Vučičević, J. Kokalj, J. Skolimowski, R. Žitko, J. Mravlje, and D. Tanasković, *Phys. Rev. B* **102**, 115142 (2020).
  - [14] P. T. Brown, D. Mitra, E. Guardado-Sanchez, R. Nourafkan, A. Reymbaut, C.-D. Hébert, S. Bergeron, A.-M. S. Tremblay, J. Kokalj, D. A. Huse, P. Schauß, and W. S. Bakr, *Science* **363**, 379 (2018).
  - [15] H. Terletska, J. Vučičević, D. Tanasković, and V. Dobrosavljević, *Phys. Rev. Lett.* **107**, 026401 (2011).
  - [16] J. Vučičević, H. Terletska, D. Tanasković, and V. Dobrosavljević, *Phys. Rev. B* **88**, 075143 (2013).
  - [17] W. Witczak-Krempa, P. Ghaemi, T. Senthil, and Y. B. Kim, *Phys. Rev. B* **86**, 245102 (2012).
  - [18] J. D. Rameau, T. J. Reber, H.-B. Yang, S. Akhanjee, G. D. Gu, P. D. Johnson, and S. Campbell, *Phys. Rev. B* **90**, 134509 (2014).
  - [19] S. A. Hartnoll, *Nat. Phys.* **11**, 54 (2014).
  - [20] W. Thomson, *Proc. R. Soc. London* **8**, 546 (1857).
  - [21] K. v. Klitzing, G. Dorda, and M. Pepper, *Phys. Rev. Lett.* **45**, 494 (1980).
  - [22] D. J. Thouless, M. Kohmoto, M. P. Nightingale, and M. den Nijs, *Phys. Rev. Lett.* **49**, 405 (1982).
  - [23] Q. Niu, D. J. Thouless, and Y.-S. Wu, *Phys. Rev. B* **31**, 3372 (1985).
  - [24] Z. F. Ezawa, *Quantum Hall Effects* (World Scientific, Singapore, 2008).
  - [25] D. C. Tsui, H. L. Stormer, and A. C. Gossard, *Phys. Rev. Lett.* **48**, 1559 (1982).
  - [26] R. B. Laughlin, *Phys. Rev. Lett.* **50**, 1395 (1983).
  - [27] L. Schubnikow and W. J. De Haas, *Proc. R. Netherlands Acad. Arts Sci.* **33**, 130 (1930).
  - [28] D. Schoenberg, *Magnetic Oscillations in Metals* (Cambridge University Press, Cambridge, UK, 1984).
  - [29] D. LeBoeuf, N. Doiron-Leyraud, J. Levallois, R. Daou, J.-B. Bonnemaison, N. E. Hussey, L. Balicas, B. J. Ramshaw, R. Liang, D. A. Bonn, W. N. Hardy, S. Adachi, C. Proust, and L. Taillefer, *Nature (London)* **450**, 533 (2007).
  - [30] P. Moetakef, D. G. Ouellette, J. R. Williams, S. J. Allen, L. Balents, D. Goldhaber-Gordon, and S. Stemmer, *Appl. Phys. Lett.* **101**, 151604 (2012).
  - [31] S. E. Sebastian and C. Proust, *Annu. Rev. Condens. Matter Phys.* **6**, 411 (2015).
  - [32] P. Voruganti, A. Golubentsev, and S. John, *Phys. Rev. B* **45**, 13945 (1992).
  - [33] W. Ding, R. Žitko, and B. S. Shastry, *Phys. Rev. B* **96**, 115153 (2017).
  - [34] W. O. Wang, J. K. Ding, B. Moritz, Y. Schattner, E. W. Huang, and T. P. Devereaux, *Phys. Rev. Research* **3**, 033033 (2021).
  - [35] A. Auerbach, *Phys. Rev. B* **99**, 115115 (2019).
  - [36] P. G. Wijesinghe and K. W. Gamalath, *Int. Lett. Chem., Phys. Astron.* **82**, 21 (2019).
  - [37] F. F. Assaad and M. Imada, *Phys. Rev. Lett.* **74**, 3868 (1995).
  - [38] A. A. Markov, G. Rohringer, and A. N. Rubtsov, *Phys. Rev. B* **100**, 115102 (2019).
  - [39] W. O. Wang, J. K. Ding, B. Moritz, E. W. Huang, and T. P. Devereaux, *npj Quantum Mater.* **5**, 51 (2020).
  - [40] A. Sherman, *Phys. Lett. A* **379**, 1912 (2015).
  - [41] S. Acheche, L.-F. Arsenault, and A.-M. S. Tremblay, *Phys. Rev. B* **96**, 235135 (2017).
  - [42] A. Khurana, *Phys. Rev. Lett.* **64**, 1990 (1990).

- [43] I. M. Lifshitz and A. M. Kosevich, *Zh. Éksp. Teor. Fiz.* **29**, 730 (1955) [*Sov. Phys.-JETP* **2**, 636 (1956)].
- [44] B. Hunt, J. D. Sanchez-Yamagishi, A. F. Young, M. Yankowitz, B. J. LeRoy, K. Watanabe, T. Taniguchi, P. Moon, M. Koshino, P. Jarillo-Herrero, and R. C. Ashoori, *Science* **340**, 1427 (2013).
- [45] R. K. Kumar, X. Chen, G. H. Auton, A. Mishchenko, D. A. Bandurin, S. V. Morozov, Y. Cao, E. Khestanova, M. B. Shalom, A. V. Kretinin, K. S. Novoselov, L. Eaves, I. V. Grigorieva, L. A. Ponomarenko, V. I. Fal'ko, and A. K. Geim, *Science* **357**, 181 (2017).
- [46] R. K. Kumar, A. Mishchenko, X. Chen, S. Pezzini, G. H. Auton, L. A. Ponomarenko, U. Zeitler, L. Eaves, V. I. Fal'ko, and A. K. Geim, *Proc. Natl. Acad. Sci. U.S.A.* **115**, 5135 (2018).
- [47] J. Barrier, P. Kumaravadivel, R. K. Kumar, L. A. Ponomarenko, N. Xin, M. Holwill, C. Mullan, M. Kim, R. V. Gorbachev, M. D. Thompson, J. R. Prance, T. Taniguchi, K. Watanabe, I. V. Grigorieva, K. S. Novoselov, A. Mishchenko, V. I. Fal'ko, A. K. Geim, and A. I. Berdyugin, *Nat. Commun.* **11**, 5756 (2020).
- [48] J. Vučičević and R. Žitko, *Phys. Rev. Lett.* **127**, 196601 (2021).
- [49] R. Peierls, *Z. Phys.* **80**, 763 (1933).
- [50] G. H. Wannier, *Rev. Mod. Phys.* **34**, 645 (1962).
- [51] E. Y. Andrei, D. K. Efetov, P. Jarillo-Herrero, A. H. MacDonald, K. F. Mak, T. Senthil, E. Tutuc, A. Yazdani, and A. F. Young, *Nat. Rev. Mater.* **6**, 201 (2021).
- [52] N. R. Cooper, J. Dalibard, and I. B. Spielman, *Rev. Mod. Phys.* **91**, 015005 (2019).
- [53] J. Dalibard, F. Gerbier, G. Juzeliūnas, and P. Öhberg, *Rev. Mod. Phys.* **83**, 1523 (2011).
- [54] P. G. Harper, *Proc. Phys. Soc. London A* **68**, 874 (1955).
- [55] D. R. Hofstadter, *Phys. Rev. B* **14**, 2239 (1976).
- [56] K.-T. Chen and P. A. Lee, *Phys. Rev. B* **84**, 205137 (2011).
- [57] M. Berciu and A. M. Cook, *Europhys. Lett.* **92**, 40003 (2010).
- [58] A. Georges, G. Kotliar, W. Krauth, and M. J. Rozenberg, *Rev. Mod. Phys.* **68**, 13 (1996).
- [59] M. Potthoff and W. Nolting, *Eur. Phys. J. B* **8**, 555 (1999).
- [60] M. Potthoff and W. Nolting, *Phys. Rev. B* **59**, 2549 (1999).
- [61] M. Potthoff and W. Nolting, *Phys. Rev. B* **60**, 7834 (1999).
- [62] K. G. Wilson, *Rev. Mod. Phys.* **47**, 773 (1975).
- [63] H. R. Krishna-murthy, J. W. Wilkins, and K. G. Wilson, *Phys. Rev. B* **21**, 1003 (1980).
- [64] R. Bulla, T. A. Costi, and T. Pruschke, *Rev. Mod. Phys.* **80**, 395 (2008).
- [65] R. Žitko and T. Pruschke, *Phys. Rev. B* **79**, 085106 (2009).
- [66] J. Vučičević, N. Wentzell, M. Ferrero, and O. Parcollet, *Phys. Rev. B* **97**, 125141 (2018).
- [67] T. Maier, M. Jarrell, T. Pruschke, and M. H. Hettler, *Rev. Mod. Phys.* **77**, 1027 (2005).
- [68] N. Lin, E. Gull, and A. J. Millis, *Phys. Rev. B* **80**, 161105(R) (2009).
- [69] N. Lin, E. Gull, and A. J. Millis, *Phys. Rev. B* **82**, 045104 (2010).
- [70] N. Lin, E. Gull, and A. J. Millis, *Phys. Rev. Lett.* **109**, 106401 (2012).
- [71] T. Sato, K. Hattori, and H. Tsunetsugu, *Phys. Rev. B* **86**, 235137 (2012).
- [72] H. Sato, M. Arita, Y. Utsumi, Y. Mukaegawa, M. Sasaki, A. Ohnishi, M. Kitaura, H. Namatame, and M. Taniguchi, *Phys. Rev. B* **89**, 155137 (2014).
- [73] A. Taheridehkordi, S. H. Curnoe, and J. P. F. LeBlanc, *Phys. Rev. B* **99**, 035120 (2019).
- [74] J. Vučičević and M. Ferrero, *Phys. Rev. B* **101**, 075113 (2020).
- [75] A. Taheridehkordi, S. H. Curnoe, and J. P. F. LeBlanc, *Phys. Rev. B* **101**, 125109 (2020).
- [76] A. Taheridehkordi, S. H. Curnoe, and J. P. F. LeBlanc, *Phys. Rev. B* **102**, 045115 (2020).
- [77] J. Vučičević, P. Stipsić, and M. Ferrero, *Phys. Rev. Research* **3**, 023082 (2021).
- [78] U. Brandt and C. Mielsch, *Z. Phys. B* **82**, 37 (1991).
- [79] A. M. Shvaika and J. K. Freericks, *Phys. Rev. B* **67**, 153103 (2003).

# Analytical solution for time integrals in diagrammatic expansions: Application to real-frequency diagrammatic Monte Carlo

J. Vučković,<sup>1</sup> P. Stipsić<sup>1,2</sup> and M. Ferrero<sup>3,4</sup>

<sup>1</sup>*Scientific Computing Laboratory, Center for the Study of Complex Systems, Institute of Physics Belgrade, University of Belgrade, Pregrevica 118, 11080 Belgrade, Serbia*

<sup>2</sup>*Faculty of Physics, University of Belgrade, Studentski trg 12, 11001 Belgrade, Serbia*

<sup>3</sup>*CPHT, CNRS, Ecole Polytechnique, Institut Polytechnique de Paris, Route de Saclay, 91128 Palaiseau, France*

<sup>4</sup>*Collège de France, 11 place Marcelin Berthelot, 75005 Paris, France*



(Received 19 November 2020; accepted 25 March 2021; published 29 April 2021)

Recent years have seen a revived interest in the diagrammatic Monte Carlo (DiagMC) methods for interacting fermions on a lattice. A promising recent development allows one to now circumvent the analytical continuation of dynamic observables in DiagMC calculations within the Matsubara formalism. This is made possible by symbolic algebra algorithms, which can be used to analytically solve the internal Matsubara frequency summations of Feynman diagrams. In this paper, we take a different approach and show that it yields improved results. We present a closed-form analytical solution of imaginary-time integrals that appear in the time-domain formulation of Feynman diagrams. We implement and test a DiagMC algorithm based on this analytical solution and show that it has numerous significant advantages. Most importantly, the algorithm is general enough for any kind of single-time correlation function series, involving any single-particle vertex insertions. Therefore, it readily allows for the use of action-shifted schemes, aimed at improving the convergence properties of the series. By performing a frequency-resolved action-shift tuning, we are able to further improve the method and converge the self-energy in a nontrivial regime, with only 3–4 perturbation orders. Finally, we identify time integrals of the same general form in many commonly used Monte Carlo algorithms and therefore expect a broader usage of our analytical solution.

DOI: [10.1103/PhysRevResearch.3.023082](https://doi.org/10.1103/PhysRevResearch.3.023082)

## I. INTRODUCTION

Finding controlled solutions of the Hubbard model is one of the central challenges in condensed matter physics [1–4]. Many common approaches to this problem rely on the stochastic (Monte Carlo) summation of various expansions and decompositions of relevant physical quantities. However, Monte Carlo (MC) algorithms are often plagued by two notorious problems: the fermionic sign problem and the analytical continuation of frequency-dependent quantities in calculations based on the Matsubara formalism [5–8] (alternatively, the dynamical sign problem in the Kadanoff-Baym and Keldysh formalism calculations [9–23]). In diagrammatic Monte Carlo (DiagMC) methods [24–38] (as opposed to determinantal methods such as continuous-time interaction-expansion quantum Monte Carlo (CTINT) or, auxiliary-field quantum Monte Carlo (CTAUX) [39–42]), an additional problem is often the slow (or absence of) convergence of the series with respect to the perturbation order. In recent years, several works have started to address the problems of obtaining

real-frequency quantities [43–51] and series convergence in DiagMC [52–57].

In Refs. [43,52], it has been shown that a convenient transformation of the interaction-expansion series can be used to significantly improve its convergence and sometimes allows one to converge the electronic self-energy with only a few perturbation orders where it would have otherwise been impossible. The method relies on a transformation of the action which affects the bare propagator at the cost of an additional expansion, i.e., more diagram topologies need to be taken into account. Alternatively, this transformation can be viewed as a Maclaurin expansion of the bare propagator with respect to a small chemical potential shift. The resulting convergence speedup comes from an increased convergence radius of the transformed series.

In a separate line of work, DiagMC methods have been proposed that are based on the Matsubara formalism that do not require an ill-defined analytical continuation [47]. Such methods have so far been implemented for the calculation of the self-energy [48,49] and the dynamical spin susceptibility [50]. The algorithms differ in some aspects, but all rely on the symbolic algebra solution of the internal Matsubara frequency summations appearing in Feynman diagrams. However, this approach has some downsides. First, numerical regulators are needed to properly evaluate Bose-Einstein distribution functions and diverging ratios that appear in the analytical expressions, and also poles on the real axis (effec-



tive broadening of the real-frequency results). In the case of finite cyclic lattice calculations, multiple precision algebra is needed in order to cancel divergences even with relatively large regulators [48]. Most importantly, in the Matsubara summation algorithm, applying the series transformation from Refs. [43,52] would require a separate analytical solution for each of the additional diagram topologies, which are very numerous, and the calculation would become rather impractical. More generally, treating any distinct diagram requires that the Matsubara frequency summations be performed algorithmically beforehand. This makes it difficult to devise MC sampling algorithms that go to indefinite perturbation orders, unless the Matsubara summation part is sufficiently optimized so that it no longer presents a prohibitive performance penalty if performed at the time of the Monte Carlo sampling.

In this paper, we show that it can be advantageous to start from the imaginary-time domain formulation of Feynman diagrams. A diagram contribution then features a multiple imaginary-time integral, rather than sums over Matsubara frequencies. The multiple integral can be solved analytically and we present a general solution. This analytical solution, although equivalent to the analytical Matsubara summation, has a simpler and more convenient form that does not feature Bose-Einstein distribution functions or diverging ratios. As a result, numerical regulators are not needed and the need for multiple precision arithmetic may arise only at very high perturbation orders. The numerical evaluation yields a sum of poles of various orders on a uniform grid on the real axis. The ability to separate contributions of poles of different orders allows one to formally extract the real-frequency result without any numerical broadening. Finally, the analytical solution is general and applies to all diagram topologies that would appear in the transformed series proposed in Refs. [43,52] or any other diagrammatic series for single-time correlation functions. This paves the way for real-frequency diagrammatic algorithms formulated in real space that are not *a priori* limited to small perturbation orders (similarly to CTINT or CTAUX [42]).

In this work, we apply the analytical time integral to the momentum-space DiagMC for the calculation of the self-energy, and implement and thoroughly test the method. We reproduce the self-energy results from Ref. [52] and supplement them with real-axis results, free of the uncontrolled systematic error that would otherwise come from the analytical continuation. Furthermore, we show that even if a full convergence is not possible with a single choice of the action-tuning parameter, one can choose the optimal tuning parameter for each frequency independently [46]. Such a frequency-resolved resummation can be used to improve the solution and in some cases systematically eliminate the non-physical features that appear in the result due to the truncation of the series at a finite order.

The paper is organized as follows. In Sec. II, we define the model and the basic assumptions of our calculations. In Sec. III, we introduce our method in detail. First, in Sec. III A, we present the analytical solution of the general multiple-time integral that appears in the time-domain formulation of Feynman diagrams and discuss the numerical evaluation of the final expression. Then, in Sec. III B, we show the analytical solution for the Fourier transform of the Maclaurin expansion

of the bare propagator, which is essential for our DiagMC algorithm. In Sec. III C, we discuss in detail how our analytical solutions can be applied in the context of DiagMC for the self-energy. In Sec. IV, we discuss our results and benchmarks and then give closing remarks in Sec. V. Additional details of the analytical derivations and further benchmarks and examples of the calculations can be found in the appendices.

## II. MODEL

We solve the Hubbard model given by the Hamiltonian

$$H = - \sum_{\sigma,ij} t_{ij} c_{\sigma,i}^{\dagger} c_{\sigma,j} + U \sum_i n_{\uparrow,i} n_{\downarrow,i} - \mu \sum_{\sigma,i} n_{\sigma,i}, \quad (1)$$

where  $\sigma \in \{\uparrow, \downarrow\}$ ,  $i, j$  enumerate lattice sites,  $t_{ij}$  is the hopping amplitude between the sites  $i$  and  $j$ ,  $U$  is the on-site coupling constant, and  $\mu$  is the chemical potential. We only consider the Hubbard model on the square lattice with the nearest-neighbor hopping  $t$  and next-nearest-neighbor hopping  $t'$ . The bare dispersion is given by

$$\varepsilon_{\mathbf{k}} = -2t(\cos k_x + \cos k_y) - 4t' \cos k_x \cos k_y. \quad (2)$$

We define  $D = 4t$ , which will be used as the unit of energy unless stated otherwise. We restrict to thermal equilibrium and paramagnetic phases with full lattice symmetry.

## III. METHODS

The idea of DiagMC algorithms is to stochastically compute the coefficients of a perturbation series describing some physical quantity. We will focus on expansions in the coupling constant  $U$  and a shift in the chemical potential  $\delta\mu$ . The calculation of each coefficient involves the evaluation of many Feynman diagrams expressed in terms of the bare propagator, in our case taken as a function of momentum and two imaginary times. The evaluation of a diagram then boils down to a sum over multiple momentum variables and a multiple imaginary-time integral that is always of the same generic form. The goal of this section is to find a general analytical solution for these time integrals and reformulate the perturbation series as a function of a complex frequency  $z$ .

### A. Analytical solution of time integrals

We are interested in analytically solving  $(N-1)$ -fold integrals over  $\{\tau_{i=2\dots N}\}$  of the form

$$\mathcal{I}_{\mathbf{X}}(i\Omega_{\eta}) = \prod_{i=2}^N \int_0^{\tau_{i+1}} d\tau_i \tau_i^{l_i} e^{\tau_i(i\Omega_{\eta}\delta_{r,i} + \omega_i)}, \quad (3)$$

where the parameters of the integrand are given by

$$\mathbf{X} = (r, \{l_2 \dots l_N\}, \{\omega_2 \dots \omega_N\}). \quad (4)$$

The argument  $r$  is an integer and determines which of the times  $\tau_i$  is multiplied by the external Matsubara frequency  $i\Omega_{\eta}$  in the exponential. The frequency  $i\Omega_{\eta}$  can be any Matsubara frequency, either fermionic or bosonic, depending on  $\eta$ ;  $i\Omega_{\eta=-1} \equiv i\omega \equiv i(2m+1)\pi T$  and  $i\Omega_{\eta=1} \equiv i\nu \equiv 2im\pi T$ , with  $m \in \mathbb{Z}$ . The integer powers of  $\tau_i$  outside of the exponent are given by  $l_i \geq 0$ , and the parameters  $\omega_i$  may be complex.



The limit of the outermost integration is the inverse temperature  $\tau_{N+1} \equiv \beta$ . We denote by  $\delta_{x,y}$  the Kronecker delta (it will be used throughout this paper, also in the shortened version  $\delta_x \equiv \delta_{x,0}$ ). The reason for our choice to label times starting from 2 will become clear later.

The main insight is that upon applying the innermost integral, one gets a number of terms, but each new integrand has the same general form  $\sim \tau^n e^{\tau z}$ . The solution therefore boils down to a recursive application of

$$\int_0^{\tau_f} \tau^n e^{\tau z} d\tau = \sum_{k=0}^{n+1} (-)^k C_{nk} \frac{\tau_f^{n+1-k-B_{nk}} e^{B_{nk} z \tau_f}}{z^{k+B_{nk}}}, \quad (5)$$

with  $B_{nk} = 1 - \delta_{k,n+1}$  and  $C_{nk} = \frac{n!}{(n-k+\delta_{k,n+1})!}$  (for the proof, see Appendix D), and

$$\lim_{z \rightarrow 0} \int_0^{\tau_f} \tau^n e^{\tau z} d\tau = \frac{\tau_f^{n+1}}{n+1}. \quad (6)$$

The number of terms obtained after each integration is apparently  $1 + (1 - \delta_z)(n+1)$ , and we can enumerate all terms obtained after the full integration by a set of integers,  $\{k_i\}_{i=2,\dots,N}$ , where  $k_i \geq 0$  denotes the choice of the term of the integral  $i$  (over  $d\tau_i$ ).

For a given choice of  $\{k_i\}$ , the propagation of exponents  $[n$  and  $z$  in Eqs. (5) and (6)] across successive integrals can be fully described by a simple set of auxiliary quantities. We denote the exponent of  $e$  in the integration  $i$  as  $\tilde{z}_i$ , and it is given by

$$\tilde{z}_i \equiv z_i + b_{i-1} \tilde{z}_{i-1}, \quad \tilde{z}_2 \equiv z_2, \quad (7)$$

$$z_i \equiv \delta_{i,r} i\Omega_\eta + \omega_i, \quad (8)$$

where we introduced  $b_i \equiv B_{n_i, k_i}$ . The meaning of  $b_i$  can be understood by looking at Eq. (5): The exponent of  $e$  that enters the integral on the left-hand side survives in all but the last term ( $k = n+1$ ) on the right-hand side. Therefore,  $b_i = 1$  means that the exponent propagates from integration  $i$  to integration  $i+1$ , while  $b_i = 0$  means it does not, and the calculation of the recursive  $\tilde{z}_i$  is reset with each  $b_i = 0$ . The auxiliary quantity  $n_i$  are the exponents of  $\tau_i$  and is specified below.

We will need to obtain a more convenient expression for the exponent  $\tilde{z}_i$ , where  $i\Omega_\eta$  appears explicitly. Straightforwardly, we can write

$$\tilde{z}_i = i\Omega_\eta h_i + \tilde{\omega}_i, \quad (9)$$

with auxiliary quantities

$$\tilde{\omega}_i \equiv \omega_i + b_{i-1} \tilde{\omega}_{i-1}, \quad \tilde{\omega}_2 \equiv \omega_2, \quad (10)$$

and

$$h_i \equiv \begin{cases} 0, & i < r \\ 1, & i = r \\ b_{i-1} h_{i-1}, & i > r. \end{cases} \quad (11)$$

To be able to determine whether the exponent in the integrand,  $\tilde{z}_i$ , is zero and then employ Eq. (6) if needed, we can now use

$$\delta_{\tilde{z}_i} = \begin{cases} 1, & h_i = 0 \wedge \tilde{\omega}_i = 0 \\ 0 & \text{otherwise.} \end{cases} \quad (12)$$

It is important to note that at the time of integration,  $i\Omega_\eta$  is unspecified and whether  $\tilde{z}_i$  is zero cannot be tested by numerical means, unless  $i\Omega_\eta$  does not appear in  $\tilde{z}_i$ . With the convenient rewriting of Eq. (7) as Eq. (9), one can tell whether  $i\Omega_\eta$  appears in  $\tilde{z}_i$  by looking at  $h_i$ . If  $i\Omega_\eta$  does appear in  $\tilde{z}_i$  (i.e.,  $h_i = 1$ ), we cannot use Eq. (6) even if one can find such  $i\Omega_\eta$  that cancels  $\tilde{\omega}_i$ . This is because we are working towards an analytical expression which ought to be general for all possible  $i\Omega_\eta$ .

The exponent of  $\tau$  that will be carried over from integration  $i$  to integration  $i+1$  depends on the choice of the term from the integral  $i$ , and is given by  $\text{Pos}(n_i - k_i)$ , where  $\text{Pos}$  denotes the positive part of the number  $[\text{Pos}(x) = (x + |x|)/2]$ .  $n_i$  denotes the maximum exponent that can be carried over from integration  $i$ , and is obtained as

$$n_i = \begin{cases} \delta_{\tilde{z}_i} + l_i + \text{Pos}(n_{i-1} - k_{i-1}), & i > 2 \\ \delta_{\tilde{z}_i} + l_i, & i = 2. \end{cases} \quad (13)$$

In the case of Eq. (5), the maximal exponent that can be carried over to the next integration coincides with the exponent that entered the integral [the integral given by Eq. (5) does not raise the power of  $\tau$ ], so the definition of  $n_i$  coincides with the meaning of  $n$  in Eq. (5). In the case of the integral given by Eq. (6),  $n_i$  rather denotes the exponent after the integration, i.e.,  $n+1$ .

After the last integration, it can happen that  $i\Omega_\eta$  appears in the exponent of  $e$  (this is signaled by  $h_N b_N = 1$ ). We can then use the property  $e^{i\Omega_\eta \beta} = (-1)^{\delta_{\eta,-1}}$  to eliminate it from this exponent. Then, the solution for the integral can be continued to the whole of the complex plane  $i\Omega_\eta \rightarrow z$ , and can be written as (introducing the additional superscript  $\eta$  because the fermionic/bosonic nature of the expression can no longer be inferred from the external Matsubara frequency)

$$\begin{aligned} \mathcal{I}_X^\eta(z) &= \sum_{\{b_i \in [\delta_{\tilde{z}_i}, 1]\}_{i=2,\dots,N}} e^{b_N \beta \tilde{\omega}_N} \sum_{\{k_i \in [0, (1-\delta_{\tilde{z}_i}) n_i]\}_{i: b_i=1}} \\ &\times \prod_{i: \delta_{\tilde{z}_i}=1} \frac{1}{n_i} \\ &\times (-1)^{b_N h_N \delta_{\eta,-1} + \sum_{i=2}^N k_i} \times \beta^{n_N+1-b_N-k_N} \\ &\times \prod_{i: h_i=0 \wedge \tilde{\omega}_i \neq 0} \frac{C_{n_i, k_i}}{\tilde{\omega}_i^{k_i+b_i}} \prod_{i: h_i=1} \frac{C_{n_i, k_i}}{(z + \tilde{\omega}_i)^{k_i+b_i}}. \end{aligned} \quad (14)$$

Note that we have expressed the sum over  $\{k_i\}$  as a sum over  $\{b_i\}$  and a partial (inner) sum over  $\{k_i\}$ . This is not necessary, being that  $b_i$  is a function of  $k_i$ . Each  $b_i$  is fully determined by  $k_i$ , but not the other way around, so the inner sum over  $k_i$  in Eq. (14) goes over values that are allowed by the corresponding  $b_i$ . We present this form of Eq. (14) to emphasize that the factor  $e^{b_N \beta \tilde{\omega}_N}$  depends only on  $\{b_i\}$ , and can thus be pulled out of the inner  $\{k_i\}$  sum. The notation “ $i: b_i = 1$ ” means that we only consider indices  $i$  such that  $b_i = 1$ . We therefore only sum over those  $k_i$  for which the corresponding  $b_i = 1$ . The remaining  $k_i$  are fixed to  $n_i + 1$ , which is the only possibility if  $b_i = 0$ . The notation is applied analogously in other products over  $i$ .

TABLE I. Illustration of the calculation of a single term in Eq. (14). Rows correspond to successive integrations over  $d\tau_i$ . The second to fourth columns are parameters of the integrand. The choice of the term is colored red. The remaining columns are auxiliary quantities, the integrand before and after each integration. The prefactors that are “collected” after each integration are written in blue. The full contribution is written in the last column and then simplified to the form of a term in Eq. (16).

$i$	$\delta_{r,i}$	$l_i$	$\omega_i$	$k_i$	$b_i$	$n_i$	$\tilde{\omega}_i$	$h_i$	$\delta_{z_i}$	Integrand	Integral	Total
2	0	0	1	0	1	0	1	0	0	$e^{\tau_2 1}$	$\frac{1}{1}e^{\tau_3 1} - \frac{1}{1}1$	
3	0	1	2	1	1	1	3	0	0	$\tau_3 e^{\tau_3(2+1)}$	$\frac{1}{3}\tau_4 e^{\tau_4 3} - \frac{1}{3^2}e^{\tau_4 3} + \frac{1}{3^2}1$	
4	1	0	1	1	0	0	4	1	0	$e^{\tau_4(i\Omega_\eta+1+3)}$	$\frac{1}{i\Omega_\eta+4}e^{\tau_5(i\Omega_\eta+4)} - \frac{1}{i\Omega_\eta+4}1$	$\frac{1}{1}(-\frac{1}{3^2})(-\frac{1}{i\Omega_\eta+4})\frac{1}{1}\frac{1}{4}\beta e^{\beta 4}$
5	0	0	0	0	1	1	0	0	1	$e^{\tau_5 0}$	$\frac{1}{1}\tau_6^1$	$\rightarrow \frac{\beta e^{4\beta}/36}{[z-(-4)]^1}$
6	0	0	4	0	1	1	4	0	0	$\tau_6 e^{\tau_6 4}$	$\frac{1}{4}\beta e^{\beta 4} - \frac{1}{4^2}e^{\beta 4} + \frac{1}{4^2}1$	

The only remaining step is to expand the product of poles in Eq. (14) into a sum of poles (see Ref. [48] for more details),

$$\prod_{\gamma} \frac{1}{(z - z_{\gamma})^{m_{\gamma}}} = \sum_{\gamma} \sum_{r=1}^{m_{\gamma}} \frac{1}{(z - z_{\gamma})^r} \times (-1)^{m_{\gamma}-r} \sum_{C\{p_{\gamma'} \neq \gamma \in \mathbb{N}_0\}: \sum_{\gamma'} p_{\gamma'} = m_{\gamma}-r} \times \prod_{\gamma' \neq \gamma} \frac{(m_{\gamma'} + p_{\gamma'} - 1)!}{p_{\gamma'}! (m_{\gamma'} - 1)!} \frac{1}{(z_{\gamma} - z_{\gamma'})^{m_{\gamma'} + p_{\gamma'}}}, \quad (15)$$

and the final expression has the form

$$\mathcal{I}_{\mathbf{X}}^{\eta}(z) = \sum_{j,p \in \mathbb{N}} \frac{\mathcal{A}_{j,p}}{(z - \mathcal{Z}_j)^p}. \quad (16)$$

In order to illustrate our solution, we present in tabular form (Table I) a summary of all intermediate steps, integrand parameters, and auxiliary quantities that are used in calculating the contribution for a single choice of  $\{k_i\}$ , in an example with  $N = 6$  and  $r = 4$ .

Also note that if  $r \notin [2, N]$  (no Matsubara frequency appearing in any exponent), the result of the integral is a number, rather than a frequency-dependent quantity. In that case, the integral can be straightforwardly generalized to the case of real time, where integrations go to some externally given time  $t$  (instead of  $\beta$ ), and the resulting expression is a function of that time. The step given by Eq. (15) is then not needed. See Appendix A for details.

#### Numerical evaluation of the analytical expression and relation to other algorithms

The implementation of Eq. (14) is rather straightforward and much simpler than the algorithmic Matsubara summations in our previous work [48]. Indeed, most of the calculations just require the numerical evaluation of an analytical expression and it is not necessary to implement a dedicated symbolic algebra to manipulate the expressions. The only exception is the last step, Eq. (15). This transformation was the centerpiece of the algorithm in Ref. [48] and was applied recursively many times, leading to complex bookkeeping and data structures. Ultimately, the result was a symbolic expression that was stored, and a separate

implementation was needed for the comprehension and numerical evaluation of such a general symbolic expression. In the present context, however, Eq. (15) is applied only once to produce numbers, and is simple to implement.

The other important point is that we analytically treat cases with  $\delta_{z_i} = 1$  by employing Eq. (6). With the frequency-summation algorithms [48,49], one cannot take into account possible cancellations of the  $\omega_i$  terms in Eq. (10) without computing a large number of separate analytical solutions. When untreated, these cancellations yield diverging ratios in the final expressions, which need to be regularized. On the contrary, in Eq. (14), the ratio  $1/\tilde{\omega}_i^{k_i+b_i}$  cannot have a vanishing denominator and its size will, in practice, be limited by the energy resolution. This will also allow us to have the final result in the form of a sum of poles on an equidistant grid on the real axis, and extract the real-axis results without any numerical pole broadening (see Sec. III C 2 and Appendix B).

It is interesting to compare the computational effort for the numerical evaluation of our analytical solution to the straightforward numerical integration. In the most straightforward integration algorithm, one would discretize the imaginary-time interval  $[0, \beta]$  with  $N_{\tau}$  times, and then perform the summation which has the complexity  $O(N_{\tau}^{N-1})$  for each external  $\tau$ , so that overall  $O(N_{\tau}^N)$ . With our algorithm, we do not have to go through all of the configurations of internal times, but we do need to go through all of the possible permutations of the internal times, and for each permutation there is at least  $2^{N-1}$  terms to be summed over. So the number of terms one has to sum grows at least as  $O[(N-1)!2^{N-1}]$ . At sufficiently high  $N$ , this number is bound to outgrow the exponential  $N_{\tau}^N$ , whatever the  $N_{\tau}$ . This will happen, however, only at very large  $N$ . For example, if  $N_{\tau} = 30$ , the analytical solution becomes slower at around  $N = 40$ . Moreover, one actually needs a much larger  $N_{\tau}$ , especially at low temperature. In any case, the additional computational effort can be understood as coming from the difference in the information content of the result, which is a lot more substantial in the case of the analytical solution.

At orders  $N < 6$  (within context of DiagMC), we find that the implementation of our algorithm is significantly more efficient than our current implementation of the Matsubara summations from Ref. [48], and at  $N = 6$ , they are about equally efficient. However, we anticipate that further optimizations will be possible at the level of Eq. (14).

## B. Expansion of the bare propagator

The central quantity is the Green's function defined in Matsubara formalism as

$$G_{\sigma\mathbf{k}}(\tau - \tau') = -\langle T_{\tau} c_{\sigma\mathbf{k}}(\tau) c_{\sigma\mathbf{k}}^{\dagger}(\tau') \rangle = \begin{cases} -\langle c_{\sigma\mathbf{k}}(\tau) c_{\sigma\mathbf{k}}^{\dagger}(\tau') \rangle, & \tau > \tau' \\ \langle c_{\sigma\mathbf{k}}^{\dagger}(\tau') c_{\sigma\mathbf{k}}(\tau) \rangle, & \tau' > \tau, \end{cases} \quad (17)$$

where  $\tau, \tau' \in [0, \beta]$ . The noninteracting Green's function (or the bare propagator) in the eigenbasis of the noninteracting Hamiltonian has a very simple general form,

$$G_0(\varepsilon, i\omega) \equiv \frac{1}{i\omega - \varepsilon}, \quad (18)$$

and for the plane wave  $\mathbf{k}$ , the propagator is  $G_{0,\mathbf{k}}(i\omega) = G_0(\varepsilon_{\mathbf{k}} - \mu, i\omega)$ .

As we will discuss below, the diagrammatic series for the self-energy will, in general, be constructed from different powers of the bare propagator,

$$G_0^l(\varepsilon, i\omega) \equiv \frac{1}{(i\omega - \varepsilon)^l}. \quad (19)$$

Indeed, these powers naturally arise after expanding the bare propagator in a Maclaurin series,  $\frac{1}{z+x} = \sum_{n=0}^{\infty} \frac{(-x)^n}{z^{n+1}}$ , around a small chemical potential shift,

$$G_0(\varepsilon, i\omega) = \sum_{l=1}^{\infty} (-\delta\mu)^{l-1} G_0^l(\varepsilon + \delta\mu, i\omega). \quad (20)$$

This series converges (for all  $i\omega$ ) if  $\delta\mu$  is smaller in amplitude than the first Matsubara frequency:  $|\delta\mu| < \pi T$ . Nevertheless, this expression will become a part of a larger series with additional expansion parameters, which may result in a modified convergence radius of the overall series with respect to  $\delta\mu$ .

We anticipate that the Feynman diagrams will be formulated in the imaginary-time domain, so it is essential to work out the Fourier transform of  $G_0^l(\varepsilon, i\omega)$ . We present the full derivation in Appendix E and here only write the final solution,

$$G_0^l(\varepsilon, \tau - \tau') = s_{\tau, \tau'} e^{-\varepsilon(\tau - \tau')} n_F(s_{\tau, \tau'} \varepsilon) \sum_{\zeta=0}^{l-1} \sum_{\varsigma=0}^{l-\zeta-1} c_{l\zeta\varsigma}^{s_{\tau, \tau'}}(\varepsilon) \tau^{\zeta} \tau'^{\varsigma}, \quad (21)$$

with  $s_{\tau, \tau'} = \text{sgn}(\tau' - \tau)$ . In our notation,  $l$  in  $G_0^l$  is a superscript index, rather than the power of  $G_0$  [although these meanings coincide in the case of  $G_0^l(\varepsilon, i\omega)$ ]. The Fermi function is defined as  $n_F(\varepsilon) = 1/(e^{\beta\varepsilon} + 1)$  and the coefficients that go with the  $\tau^{\zeta} \tau'^{\varsigma}$  terms are

$$c_{l\zeta\varsigma}^{-}(\varepsilon) = \sum_{n=0}^{l-\zeta-\varsigma-1} \frac{n!(-1)^{l+\varsigma-1}[-n_F(\varepsilon)]^n \beta^{l-\varsigma-\zeta-1}}{(l-\varsigma-\zeta-1)!(\varsigma+\zeta)!} \times \begin{Bmatrix} l-\varsigma-\zeta-1 \\ n \end{Bmatrix} \begin{pmatrix} \varsigma+\zeta \\ \zeta \end{pmatrix}, \quad (22)$$

and  $c_{l\zeta\varsigma}^{+}(\varepsilon) = (-1)^{l-1} c_{l\zeta\varsigma}^{-}(-\varepsilon)$ . Here we make use of binomial coefficients  $\binom{n}{k} = \frac{n!}{k!(n-k)!}$  and the Stirling number of the second kind,  $\{n\}_k = \sum_{i=0}^k \frac{(-1)^i}{k!} \binom{k}{i} (k-i)^n$ .

## C. Application to DiagMC

In the following, we apply the analytic time integral and the expansion of the bare propagator in the context of DiagMC. We discuss two kinds of self-energy series (Hartree shifted and bare) and the corresponding implementation details. Note that some symbols will be redefined with respect to previous sections.

### 1. Hartree-shifted series

In this section, we discuss the construction of the self-energy series, where all tadpolelike insertions are omitted in the topologies of the diagrams. Rather, the full Hartree shift is absorbed in the bare propagator. The diagrams are therefore expressed in terms of the Hartree-shifted bare propagator,

$$G_{0,\mathbf{k}}^{\text{HF}}(i\omega) = G_0(\tilde{\varepsilon}_{\mathbf{k}}, i\omega), \quad (23)$$

with the Hartree-shifted dispersion defined as

$$\tilde{\varepsilon}_{\mathbf{k}} = \varepsilon_{\mathbf{k}} - \mu + U \langle n_{\sigma} \rangle, \quad (24)$$

where  $\langle n_{\sigma} \rangle$  is the average site occupation per spin.

After constructing the tadpoleless topologies, we are free to expand all propagators that appear in the diagrams according to Eq. (20):

$$G_{0,\mathbf{k}}^{\text{HF}}(i\omega) = \sum_{l=1}^{\infty} (-\delta\mu)^{l-1} G_0^l(\tilde{\varepsilon}_{\mathbf{k}} + \delta\mu, i\omega). \quad (25)$$

In the frequency domain, this step can be viewed as introducing new topologies: we now have diagrams with any number of single-particle-vertex ( $\delta\mu$ ) insertions on any of the propagator lines. Each arrangement of these additional single-particle vertices on the diagram does require a separate solution by the symbolic algebra algorithm, as presented in Refs. [48,49]. Nevertheless, as a  $\delta\mu$  vertex cannot carry any momentum or energy, the formal effect of it is that it just raises the power  $l$  of the propagator that passes through it. In the imaginary-time domain, it turns out that the contribution of the  $\delta\mu$ -dressed diagrams is readily treatable by the analytical expression (14) and we no longer have to view the  $\delta\mu$  insertions as changes to topology, but rather as additional internal degrees of freedom to be summed over. This is illustrated in Fig. 1.

Up to the Hartree shift, the self-energy expansion can now be made in powers of the interaction  $U$  and the small chemical-potential shift  $\delta\mu$ ,

$$\Sigma_{\mathbf{k}}^{(\text{HF})}(\tau) = \sum_N (-U)^N \times \sum_{l_1, \dots, l_{2N-1}=1}^{\infty} (-\delta\mu)^{\sum_j (l_j-1)} \sum_{\Upsilon_N} D_{\Upsilon_N, \mathbf{k}, \{l_j\}, \delta\mu}(\tau), \quad (26)$$

where  $j$  enumerates the propagators, of which there are  $N_{\text{prop}} = 2N - 1$ ,  $N$  is the perturbation order in  $U$ , each  $l_j$  goes from 1 to  $\infty$ ,  $\Upsilon_N$  enumerates distinct topologies of the diagram at order  $N$  (without any  $\delta\mu$  or Hartree insertions), and  $D$  is the contribution of the diagram. The general form of the

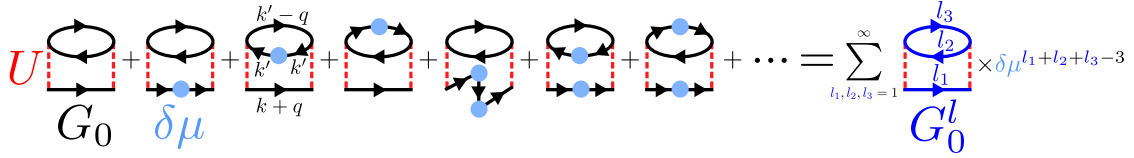


FIG. 1. Illustration of the use of the  $G_0^l(\varepsilon, \tau - \tau')$  propagator. The entire series of diagrams with all possible  $\delta\mu$  insertions can be captured by a single diagram with additional degrees of freedom.

diagram contribution is

$$D_{\Upsilon_N, \mathbf{k}, \{l_j\}, \delta\mu}(\tau) = (-1)^{N_{\text{bub}}} \prod_{i=2}^{N-1} \int_0^\beta d\tau_i \sum_{\mathbf{k}_1 \dots \mathbf{k}_N} \prod_{j=1}^{2N-1} G_0^{l_j}(\bar{\varepsilon}_{\mathbf{k}_j}, \tilde{\tau}_j - \tilde{\tau}'_j), \quad (27)$$

with  $\bar{\varepsilon}_{\mathbf{k}} \equiv \varepsilon_{\mathbf{k}} + \delta\mu$ . We denote  $N_{\text{bub}}$  as the number of closed fermion loops in the diagram;  $\tau_1 \dots \tau_{N-1}$  are internal times, and we fix  $\tau_{i=1} = 0$ ;  $\tau$  is the external time,  $\mathbf{k}$  is the external momentum,  $\mathbf{k}_1 \dots \mathbf{k}_N$  are the independent internal momenta,  $j$  indexes the propagator lines, and  $\tilde{\mathbf{k}}$  are the corresponding

linear combinations of the momenta  $\tilde{\mathbf{k}}_j \equiv \sum_{\lambda=0}^N \tilde{s}_{j\lambda} \mathbf{k}_\lambda$ , where  $\tilde{s}_{j\lambda} \in \{-1, 0, 1\}$ , and we index with 0 the external momentum  $\mathbf{k}_0 \equiv \mathbf{k}$ .  $\tilde{\tau}_j$  and  $\tilde{\tau}'_j$  are the outgoing and incoming times for the propagator  $j$ , and take values in  $\{\tau_1 \dots \tau_N\}$ , where we denote with index  $N$  the external time  $\tau_N \equiv \tau$ . The coefficients  $\tilde{s}_{j\lambda}$ , times  $\tilde{\tau}_j$ ,  $\tilde{\tau}'_j$ , and the number  $N_{\text{bub}}$  are implicit functions of the topology  $\Upsilon_N$ . Throughout the paper, we assume normalized  $\mathbf{k}$  sums,  $\sum_{\mathbf{k}} \equiv \frac{1}{N_{\mathbf{k}}} \sum_{\mathbf{k}}$ , where  $N_{\mathbf{k}}$  is the number of lattice sites.

We can perform the Fourier transform of the external time to obtain the contribution of the diagram in the Matsubara-frequency domain,

$$D_{\Upsilon_N, \mathbf{k}, \{l_j\}, \delta\mu}(i\omega) = (-1)^{N_{\text{bub}}} \prod_{i=2}^N \int_0^\beta d\tau_i e^{i\omega\tau_N} \sum_{\mathbf{k}_1 \dots \mathbf{k}_N} \prod_{j=1}^{2N-1} G_0^{l_j}(\bar{\varepsilon}_{\mathbf{k}_j}, \tilde{\tau}_j - \tilde{\tau}'_j). \quad (28)$$

The Green's function  $G_0^l(\varepsilon, \tau - \tau')$  is discontinuous at  $\tau = \tau'$ , so to be able to perform the  $\tau$  integrations analytically, we first need to split the integrals into ordered parts,

$$\int_0^\beta d\tau_2 \dots \int_0^\beta d\tau_N = \sum_{(\tau_{p_2} \dots \tau_{p_N}) \in \mathcal{P}(\{\tau_2 \dots \tau_N\})} \int_0^\beta d\tau_{p_N} \int_0^{\tau_{p_N}} d\tau_{p_{N-1}} \dots \int_0^{\tau_{p_4}} d\tau_{p_3} \int_0^{\tau_{p_3}} d\tau_{p_2}, \quad (29)$$

where  $\mathcal{P}$  denotes all  $(N-1)!$  permutations of the time indices.  $p$  labels the permutation and  $p_i$  is the permuted index of vertex  $i$ .

Let us rewrite the contribution of the diagram, with propagators written explicitly using the expression (21),

$$D_{\Upsilon_N, \mathbf{k}, \{l_j\}, \delta\mu}(i\omega) = (-1)^{N_{\text{bub}}} \sum_{\mathbf{k}_1 \dots \mathbf{k}_N} \sum_{(\tau_{p_2} \dots \tau_{p_N}) \in \mathcal{P}(\{\tau_2 \dots \tau_N\})} (-1)^{N_{\text{fwd}}(p)} \prod_j n_F(s_j \bar{\varepsilon}_{\tilde{\mathbf{k}}_j}) \sum_{\zeta_j=0}^{l_j-1} \sum_{s_j=0}^{l_j-\zeta_j-1} c_{l_j, \zeta_j, s_j}^{s_j}(\bar{\varepsilon}_{\tilde{\mathbf{k}}_j}) \prod_{j \in \mathcal{J}_i(i=1)} \delta_{\zeta_j} \prod_{j \in \mathcal{J}_o(i=1)} \delta_{s_j} \\ \times \int_0^\beta d\tau_{p_N} \int_0^{\tau_{p_N}} d\tau_{p_{N-1}} \dots \int_0^{\tau_{p_4}} d\tau_{p_3} \int_0^{\tau_{p_3}} d\tau_{p_2} e^{i\omega\tau_N} \prod_{i=2}^N \tau_i^{\sum_{j \in \mathcal{J}_i(i)} \zeta_j + \sum_{j \in \mathcal{J}_o(i)} s_j} e^{\tau_i (\sum_{j \in \mathcal{J}_o(i)} \bar{\varepsilon}_{\tilde{\mathbf{k}}_j} - \sum_{j \in \mathcal{J}_i(i)} \bar{\varepsilon}_{\tilde{\mathbf{k}}_j})}, \quad (30)$$

where  $\mathcal{J}_{i/o}(i)$  is the set of incoming/outgoing propagators  $j$  of the vertex  $i$ , which depends on the topology  $\Upsilon_N$ . We also introduced shorthand notation  $s_j = s_{\tilde{\tau}_j, \tilde{\tau}'_j}$ . Practically,  $s_j$  depends on whether  $p(i(j)) > p(i'(j))$  or the other way around, where  $i(j)/i'(j)$  is the outgoing/incoming vertex of propagator  $j$  in the given permutation  $p$ . The total number of forward-facing propagators is  $N_{\text{fwd}}(p) = \sum_j \delta_{-1, s_j}$ , which depends on the permutation and the topology. The products of  $\delta_{\zeta_j}$  and  $\delta_{s_j}$  are there to ensure that the time  $\tau_1 = 0$  is not raised to any power other than 0, as such terms do not contribute.

Now we can apply the analytic solution for the time integrals [Eq. (14)] to arrive at the final expression:

$$D_{\Upsilon_N, \mathbf{k}, L, \delta\mu}(z) = (-1)^{N_{\text{bub}}} \sum_{\{\tilde{l}_j \geq 0\}: \sum_j \tilde{l}_j = L} \sum_{\mathbf{k}_1 \dots \mathbf{k}_N} \sum_{(\tau_{p_2} \dots \tau_{p_N}) \in \mathcal{P}(\{\tau_2 \dots \tau_N\})} (-1)^{N_{\text{fwd}}(p)} \\ \times \prod_j n_F(s_j \bar{\varepsilon}_{\tilde{\mathbf{k}}_j}) \sum_{\zeta_j=0}^{\tilde{l}_j} \sum_{s_j=0}^{\tilde{l}_j-\zeta_j} c_{\tilde{l}_j+1, \zeta_j, s_j}^{s_j}(\bar{\varepsilon}_{\tilde{\mathbf{k}}_j}) \prod_{j \in \mathcal{J}_i(i=1)} \delta_{\zeta_j} \prod_{j \in \mathcal{J}_o(i=1)} \delta_{s_j} \mathcal{I}_{\mathbf{X}}^{\eta=-1}(z), \\ \mathbf{X} = \left( p(N), \left\{ \sum_{j \in \mathcal{J}_i(i(p_r))} \zeta_j + \sum_{j \in \mathcal{J}_o(i(p_r))} s_j \right\}_{r=2 \dots N}, \left\{ \sum_{j \in \mathcal{J}_o(i(p_r))} \bar{\varepsilon}_{\tilde{\mathbf{k}}_j} - \sum_{j \in \mathcal{J}_i(i(p_r))} \bar{\varepsilon}_{\tilde{\mathbf{k}}_j} \right\}_{r=2 \dots N} \right), \quad (31)$$



where  $i(p_i)$  is the vertex index  $i$  of the permuted index  $p_i$  and we have introduced a new expansion variable  $L = \sum_j (l_j - 1)$  and a convenient variable  $\tilde{l}_j = l_j - 1$ , so that

$$\Sigma_{\mathbf{k}}^{(\text{HF})}(z) = \sum_{K=2}^{\infty} \sum_{N=2}^K \sum_{L=0}^{K-N} (-U)^N (-\delta\mu)^L \sum_{\Upsilon_N} D_{\Upsilon_N, \mathbf{k}, L, \delta\mu}(z), \quad (32)$$

which is the series that we implement and use in practice. The meaning of  $K$  is the number of all independent (internal and external) times in the diagram. Note that in  $\mathcal{D}$ , we perform only  $N - 1$  integrations over time. Those are the times associated with  $N$  interaction vertices, minus the one that is fixed to zero. The integrations of the times associated with  $\delta\mu$  insertions have already been performed in Eq. (21), and there are  $L$  such integrals. Overall, the number of independent times is  $K = N + L$ . Ultimately, we group contributions by the expansion order  $K$  and look for convergence with respect to this parameter.

## 2. Numerical implementation of DiagMC and relation to other algorithms

The expression (31) is very convenient for numerical evaluation. First, we restrict the values of  $\bar{\epsilon}_{\mathbf{k}}$  to a uniform grid on the real axis with the step  $\Delta\omega$  ( $\bar{\epsilon}_{\mathbf{k}} = j\Delta\omega$ ). These appear in  $\omega_2, \dots, \omega_K$  as terms with integer coefficients, which means that  $\{\omega_i\}$  entering  $\mathcal{I}_{\mathbf{X}}$  will also be restricted to the same uniform grid. The final result therefore has the form

$$D_{\Upsilon_N, \mathbf{k}, L, \delta\mu}(z) = \sum_{j \in \mathbb{Z}, p \in \mathbb{N}} \frac{\mathcal{A}_{j,p}}{(z - j\Delta\omega)^p}. \quad (33)$$

This form allows us to reinterpret the finite-lattice results as that of the thermodynamic limit and extract  $D_{\Upsilon_N, \mathbf{k}, L, \delta\mu}(\omega + i0^+)$  without any numerical broadening (see Appendix B for details).

In our present implementation, we perform a flat-weight (uniform) MC sampling over internal momenta  $\{\mathbf{k}_i\}$ , do a full summation of all the other sums, and accumulate the amplitudes  $\mathcal{A}_{j,p}$ . There are, however, other options. For example, one may sample  $\{\mathbf{k}_i\}, \{p_i\}, \{b_i\}$  and use  $P \equiv \prod_j n_{\mathbf{F}}(s_j \bar{\epsilon}_{\mathbf{k}_j}) e^{b_N \beta \tilde{\omega}_N}$  as the weighting function. We have thoroughly checked that the factor  $P$  closely correlates with the contribution to  $\mathcal{A}_{j,p}$  coming from a given choice of the  $\{\mathbf{k}_i\}, \{p_i\}, \{b_i\}$  variables (with other variables summed over), and thus  $P$  could be a good choice for a weighting function. However, this requires additional operations related to move proposals and trials, and we have not yet been able to make such an algorithm more efficient than the flat-weight MC. Nevertheless, it is apparent that our approach offers more flexibility than the algorithmic Matsubara summations (AMS). In AMS, no convenient weighting function can be defined for the Monte Carlo, so one either does the flat-weight summation [48] or uses the whole contribution to the result as the weight, which comes at the price of having to repeat the calculation for each frequency of interest [49] (on the contrary, in Ref. [48], as well as in this paper, the entire frequency dependence of the self-energy is obtained in a single MC run). At present, it is unclear which scheme is best—whether one should evaluate

$D(z)$  one  $z$  at a time or capture all  $z$  at once as we do here. This choice, as well as the choice of the weighting function, likely needs to be made on a case-by-case basis, as it is probable that in different regimes, different approaches will be optimal. In that sense, the added flexibility of our time-integration approach in terms of the choice of the weighting function may prove valuable in the future.

Concerning floating-point arithmetic, it is important that the factor  $e^{b_N \beta \tilde{\omega}_N}$  stemming from  $\mathcal{I}_{\mathbf{X}}$  can always be absorbed into the product of  $n_{\mathbf{F}}$  functions in the second row of Eq. (31). This can be understood as follows. A given  $\bar{\epsilon}_{\mathbf{k}_j}$  can, at most, appear twice as a term in  $\tilde{\omega}_N$ , once with sign  $+1$  and once with sign  $-1$ , corresponding to the incoming  $\tilde{\tau}'_j$  and outgoing  $\tilde{\tau}_j$  ends of the propagator  $j$ . In that case, the exponent cancels. The other possibility is that it appears only once, in which case it must correspond to the later time in the given permutation. If the later time is the outgoing end of the propagator, then the propagator is forward facing and the sign in front is  $s = -1$ ; if it is the incoming end, then the propagator is backward facing and the sign in front is  $s = 1$ . In both cases, we can make use of

$$e^{s\beta\epsilon} n_{\mathbf{F}}(s\epsilon) = n_{\mathbf{F}}(-s\epsilon). \quad (34)$$

Therefore, no exponentials will appear in the final expression. A product of  $n_{\mathbf{F}}$  functions is, at most, 1 and the coefficients  $c$  are not particularly big. Then, the size of the pole amplitudes that come out of Eq. (14) is determined by the energy resolution  $(1/\Delta\omega)$  and temperature  $(\beta^{n_N+1-b_N-k_N})$ . In our calculations so far, the amplitudes remain relatively small. Our approach ensures that we do not have very large canceling terms, such as we had in Ref. [48]. Indeed, we have successfully implemented Eq. (31) without the need for multiple-precision floating-point types.

Compared to the Matsubara-frequency summation algorithm [47–49], Eq. (31) presents an improved generality. Equation (31) is valid for any number and arrangement of instantaneous (i.e., frequency-independent) insertions, i.e., any choice of  $\{\tilde{l}_j\}$ . In contrast, the algorithmic Matsubara summation has to be performed for each choice of  $\{\tilde{l}_j\}$  independently, and the resulting symbolic expressions need to be stored. For example, at  $N = 4$ , we have 12  $\Upsilon_N$  topologies. Therefore, at  $L = 0$ , the number of analytical solutions to prepare is 12. However, at  $L = 2$ , this number is 336, i.e., 28-fold bigger (we can place  $L = 2$  insertions on  $2N - 1 = 7$  fermionic lines in  $7 \times 6/2 + 7 = 28$  ways, times 12  $\Upsilon_N$  topologies, i.e., 336).

## 3. Bare series

We are also interested in constructing a bare series where tadpole insertions are present in diagram topologies. Tadpole (or Hartree) insertions are instantaneous and an evaluation of their amplitudes can be done relatively simply by various means. At the level of the Hubbard model, the Hartree insertions factor out: For each Hartree diagram, the internal momentum summations and time integrations can be performed beforehand and only once, leading to a significant speedup.

In the expression (31), there is no difference between a Hartree insertion and a chemical-potential vertex insertion. Therefore, the inclusion of the Hartree insertions can be en-

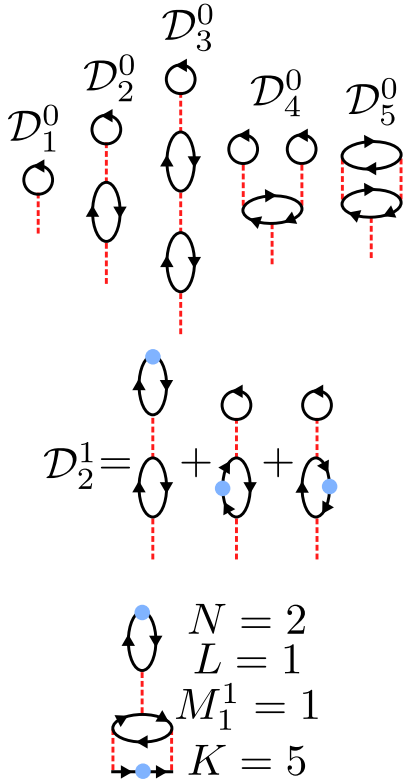


FIG. 2. Top: Illustration of possible Hartree diagrams, without any  $\delta\mu$  insertions. Middle: Amplitude of a Hartree diagram with a single  $\delta\mu$  insertion. Bottom: An example of a diagram dressed with both Hartree and  $\delta\mu$  insertions, and the values of the parameters  $N, L, \{M_i^L\}, K$  that it falls under (with  $M_{i \neq 1}^{L \neq 1} = 0$ ).

tirely accounted for in the resummation of the  $D_{\Upsilon_N, \mathbf{k}, L, \delta\mu}(z)$  contributions from the previous section, with the replacement

$$\bar{\varepsilon}_{\mathbf{k}} \equiv \varepsilon_{\mathbf{k}} - \mu + \delta\mu \quad (35)$$

(i.e., full Hartree shift excluded).

Note that the expansion of the propagators in  $\delta\mu$  is performed in Hartree insertions as well, so we need to account for possible additional  $\delta\mu$  insertions inside the Hartree diagrams. As before, our expansion order will be  $K$ , which is the total number of independent times, with each time associated to a single interaction or a  $\delta\mu$  vertex, including those within Hartree insertions.

We will for now focus on the series up to  $K = 5$ . As the number of interactions in  $\Upsilon_N$  is at least two, we can have, at most, three interaction vertices in a Hartree insertion. There are only five such Hartree diagrams (Fig. 2). We can evaluate these five amplitudes with very little effort by making use of spatial and temporal Fourier transforms.

Before we proceed with the calculation of the amplitudes  $\mathcal{D}$  of possible Hartree insertions relevant for the series up to  $K = 5$ , we define some auxiliary quantities. We first define the bare density,

$$n_0^{\bar{l}} = \sum_{\mathbf{k}} G_0^{l=1+\bar{l}}(\bar{\varepsilon}_{\mathbf{k}}, \tau = 0^-), \quad (36)$$

and the real-space propagator,

$$G_{0,\mathbf{r}}^{l=1+\bar{l}} = \sum_{\mathbf{k}} e^{i\mathbf{k}\cdot\mathbf{r}} G_0^{l=1+\bar{l}}(\bar{\varepsilon}_{\mathbf{k}}, \tau = 0^-). \quad (37)$$

We will also need the polarization bubble diagram,

$$\chi_{0,\mathbf{r}}^{\bar{l}_1, \bar{l}_2}(\tau) = G_{0,\mathbf{r}}^{l=1+\bar{l}_1}(\tau) G_{0,-\mathbf{r}}^{l=1+\bar{l}_2}(-\tau), \quad (38)$$

$$\chi_{0,\mathbf{q}=0}^{\bar{l}_1, \bar{l}_2}(i\nu = 0) = \sum_{\mathbf{r}} \int d\tau \chi_{0,\mathbf{r}}^{\bar{l}_1, \bar{l}_2}(\tau), \quad (39)$$

and the second-order self-energy diagram (up to the constant prefactor),

$$\Sigma_{2,\mathbf{r}}^{\bar{l}_1, \bar{l}_2, \bar{l}_3}(\tau) = G_{0,\mathbf{r}}^{l=1+\bar{l}_1}(\tau) \chi_{0,\mathbf{r}}^{\bar{l}_2, \bar{l}_3}(\tau), \quad (40)$$

which can be Fourier transformed to yield  $\Sigma_{2,\mathbf{k}}^{\bar{l}_1, \bar{l}_2, \bar{l}_3}(i\omega)$ .

We can now calculate the amplitudes of the possible Hartree insertions with a number  $L$  of  $\delta\mu$  insertions on them, in any arrangement

$$\mathcal{D}_1^L = (-) n_0^L, \quad (41)$$

$$\mathcal{D}_2^L = (-)^2 \sum_{\substack{\bar{l}_1, \bar{l}_2, \bar{l}_3 \\ \bar{l}_1 + \bar{l}_2 + \bar{l}_3 = L}} n_0^{\bar{l}_1} \chi_{0,\mathbf{q}=0}^{\bar{l}_2, \bar{l}_3}(i\nu = 0), \quad (42)$$

$$\mathcal{D}_3^L = (-)^3 \sum_{\substack{\bar{l}_1, \dots, \bar{l}_5 \\ \sum_i \bar{l}_i = L}} n_0^{\bar{l}_1} \chi_{0,\mathbf{q}=0}^{\bar{l}_2, \bar{l}_3}(i\nu = 0) \chi_{0,\mathbf{q}=0}^{\bar{l}_4, \bar{l}_5}(i\nu = 0), \quad (43)$$

$$\mathcal{D}_4^L = (-)^3 \sum_{\substack{\bar{l}_1, \dots, \bar{l}_3 \\ \sum_i \bar{l}_i = L}} \binom{2+\bar{l}_3}{2} n_0^{\bar{l}_1} n_0^{\bar{l}_2} n_0^{2+\bar{l}_3}, \quad (44)$$

$$\mathcal{D}_5^L = (-)^2 \sum_{\substack{\bar{l}_1, \dots, \bar{l}_5 \\ \sum_i \bar{l}_i = L}} T \sum_{i\omega} e^{-i\omega 0^-} \sum_{\mathbf{k}} G_{0,\mathbf{k}}^{l=1+\bar{l}_1}(i\omega) \Sigma_{2,\mathbf{k}}^{\bar{l}_2, \bar{l}_3, \bar{l}_4}(i\omega) G_{0,\mathbf{k}}^{l=1+\bar{l}_5}(i\omega). \quad (45)$$

As we are restricting to  $K \leq 5$  calculations, the  $\mathcal{D}_{3\dots 5}^L$  insertions can only be added once, and only with  $L = 0$ . We now define  $M_i^L$  as the number of insertions of  $\mathcal{D}_i^L$  tadpoles, and we define  $N_i$  as the number of interaction vertices contained in the tadpole  $\mathcal{D}_i$  (regardless of  $L$ , we have  $N_1 = 1, N_2 = 2, N_3 = N_4 = N_5 = 3$ ).



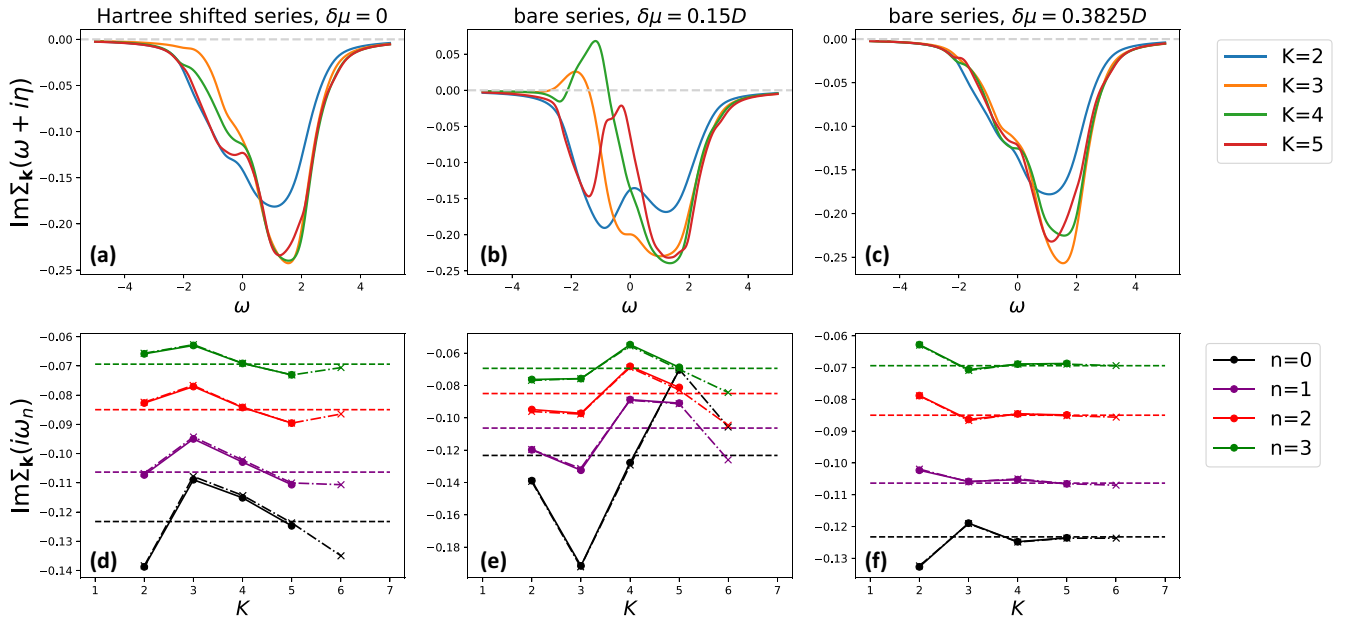


FIG. 3. DiagMC solution for the Hubbard model on a square lattice. Parameters of the model are  $t' = -0.3t$ ,  $\mu = 0$ ,  $U = 1D$ , and  $T = 0.125D$ , which corresponds to  $\langle n_\sigma \rangle \approx 0.3625$ . Top row: Imaginary part of self-energy at  $\mathbf{k} = (\pi/4, \pi)$  on the real axis (with broadening  $\eta = 0.3D$ ) obtained with three different series, up to perturbation order  $K$ . Bottom row: Illustration of convergence with respect to perturbation order  $K$ , using values of the imaginary part of the self-energy at the lowest four Matsubara frequencies,  $i\omega_{n=0\dots3}$ . Full lines are our result, dash-dotted lines with crosses are the analogous result with a numerical  $\tau$ -integration algorithm from Ref. [52], and horizontal dashed lines are the determinantal QMC result on a  $16 \times 16$  lattice from Ref. [52].

The series can now be resummed as

$$\Sigma_{\mathbf{k}}^{(\text{HF})}(z) = \sum_{K=2}^{\infty} \sum_{N=2}^K \sum_{L=0}^{K-N} \sum_{\substack{\{M_i^{L'}\} = 0 \\ N+L+\sum_{i,L'} M_i^{L'}(N_i+L')=K}}^{K-N-L} (-U)^{N+\sum_{i,L'} M_i^{L'} N_i} (-\delta\mu)^{L+\sum_{i,L'} M_i^{L'} L'} \prod_{i,L'} (\mathcal{D}_i^{L'})^{M_i^{L'}} \Omega(L, \{M_i^{L'}\}) \times \sum_{\Upsilon_N} D_{\Upsilon_N, \mathbf{k}, L+\sum_{i,L'} M_i^{L'}}(z), \quad (46)$$

where  $\Omega(L, \{M_i^{L'}\})$  is the combinatorial prefactor which counts all the possible ways the selected single-particle vertices  $\delta\mu, \{\mathcal{D}_i\}$  can be arranged. This corresponds to the number of permutations of the multisets,

$$\Omega(L, \{M_i^{L'}\}) = \frac{(L + \sum_{i,L'} M_i^{L'})!}{L! \prod_{i,L'} M_i^{L'}!}. \quad (47)$$

We emphasize that Eq. (46) is fully general, but at orders  $K \geq 5$ , additional Hartree insertions  $\mathcal{D}$  [compared to Eqs. (41)–(45)] need to be considered.

Finally, we stress that our analytical time-integral solution and action-shift tuning scheme in DiagMC are not restricted to the treatment of the Hubbard Hamiltonian. See Appendix F for a discussion of DiagMC in the case of a general Hamiltonian with two-body interactions.

#### IV. RESULTS

##### A. Convergence speedup with $\delta\mu$ expansion in the bare series

Here we focus on supplementing the results from Ref. [52] with real-frequency self-energies calculated without any numerically ill-defined analytical continuation.

The model parameters are  $t' = -0.3t$ ,  $\mu = 0$ ,  $U = 1.0D$ ,  $T = 0.125D$ , and  $\langle n_\sigma \rangle = 0.3625$ . In Ref. [52], the calculation was performed with the Hartree-shifted series with  $\delta\mu = 0$ , as well as with the bare series, with two values of  $\delta\mu$ , namely,  $0.15D$  and  $0.3825D$ . We repeat these calculations with our method. We use lattice size  $32 \times 32$ , and project the dispersion onto a uniform energy grid, as described in Ref. [48] and discussed in Sec. III C 2. In Fig. 3, we show our results and compare them with the results of Ref. [52].

In the upper row of Fig. 3 are the real-frequency self-energies calculated up to order  $K \leq 5$ . We are keeping a finite broadening  $\eta = 0.3D$  to smoothen the curves. As discussed in Appendix B, in our method, numerical pole broadening is not a formal necessity. However, there is still a significant amount of statistical noise in our real-frequency result (although the imaginary-frequency result is already very well converged). It is important to note that some of the noisy features in our real-frequency result may be artifacts of the finite-lattice size that would not vanish with increasing number of MC steps. However, by comparing the result with a  $256 \times 256$  lattice calculation (Appendix C), we check that already at  $\eta = 0.2D$ , no such artifact should be visible. It appears that for the given

external  $\mathbf{k}$  and broadening  $\eta = 0.2D$ , increasing the lattice size further from  $32 \times 32$  brings no new information, but it also does not present an additional cost: at  $\eta = 0.2D$ , our  $256 \times 256$  lattice calculation appears equally well converged as the  $32 \times 32$  lattice calculation, with the equal number of MC steps and a similar runtime, and yields a result that is on top of the  $32 \times 32$  calculation.

In the bottom row of Fig. 3, we show the change in the imaginary part of the self-energy at the first four Matsubara frequencies, as a function of the maximal order  $K$ . Full-line and dots are the result of our calculations. The dash-dotted lines with crosses are data points taken from Ref. [52]. The horizontal dashed lines are the  $16 \times 16$ -lattice determinantal QMC result, also from Ref. [52].

The excellent agreement with the results from Ref. [52] serves as a stringent test of our implementation. In the  $\delta\mu = 0.3825D$  calculation, even on the real axis, the self-energy does appear well converged by order  $K = 5$ , although there is some discrepancy between  $K = 4$  and  $K = 5$  at around  $\omega = 1.5D$ .

### B. $\omega$ -resolved resummation

We can now go one step further by resumming the series presented in Figs. 3(a) and 3(c) for each  $\omega$  individually, using an  $\omega$ -dependent optimal shift  $\delta\mu^*(\omega)$ . The results are shown in Figs. 4 and 5.

We determine the optimal  $\delta\mu^*(\omega)$  by minimizing the spread of the  $\text{Im}\Sigma(\omega + i\eta)$  results between orders  $K = 3$  and  $K = 5$ . This spread as a function of  $\omega$  and  $\delta\mu$  is color plotted in Figs. 4 and 5. We have results for a discrete set of  $\delta\mu \in \{\delta\mu_i\}$ , so the optimal  $\delta\mu^*(\omega)$  is *a priori* a discontinuous curve. As this is clearly unsatisfactory, we smoothen the curve (shown with the blue line on the top panels in Figs. 4 and 5). However, we do not have results for each precise value of this optimal  $\delta\mu^*(\omega)$ . One could take, for each  $\omega$ , the available  $\delta\mu_i$  that is closest to  $\delta\mu^*(\omega)$ , but this would, again, result in a discontinuous curve. To avoid this, we average the available results as

$$\Sigma(\omega) = \frac{\sum_i \Delta\delta\mu_i \Sigma(\omega; \delta\mu_i) w(\delta\mu^*(\omega), \delta\mu_i)}{\sum_i \Delta\delta\mu_i w(\delta\mu^*(\omega), \delta\mu_i)}, \quad (48)$$

where  $\Delta\delta\mu_i$  is the size of the  $\delta\mu$  step in the available results at the  $i$ th value (allows for nonuniform grids). We use a narrow Gaussian weighting kernel,

$$w(\delta\mu^*(\omega), \delta\mu_i) = e^{-(\delta\mu_i - \delta\mu^*(\omega))^2 / W^2}. \quad (49)$$

The width of the kernel  $W$  is chosen such that it is as narrow as possible, while still encompassing at least 3–4  $\delta\mu_i$  points, so that the final result is reasonably smooth as a function of  $\omega$ ;  $W$  is therefore determined according to the resolution in  $\delta\mu$ . We use  $W = 0.05$  and  $\Delta\delta\mu_i \approx 0.02$  and have checked that the results are insensitive to the precise choice of this numerical parameter.

The results of the averaging around the optimal  $\delta\mu^*(\omega)$  are shown in the middle and bottom panels of Figs. 4 and 5. In both cases, the  $\omega$ -resolved resummation helps to converge the result. In the case of the bare series, the convergence is now almost perfect, and already order  $K = 3$  is on top of the exact result. In the case of the Hartree-shifted series, the results are

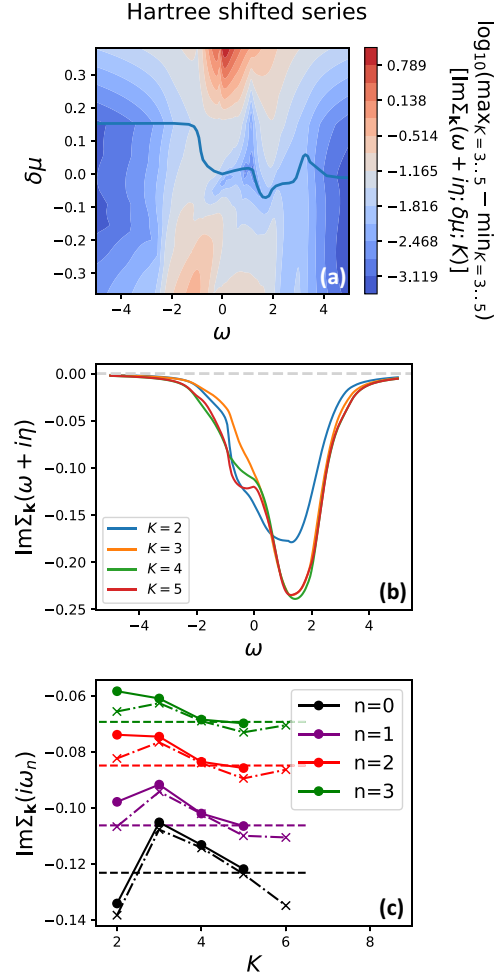


FIG. 4. Results of the Hartree-shifted series with  $\omega$ -resolved resummation, to be compared to Figs. 3(a) and 3(d) (all parameters are the same). Top panel: Color plot of the spread of the imaginary part of the self-energy at a given  $\omega + i\eta$  between orders  $K = 3$  and  $5$ , in a calculation with a given  $\delta\mu$ . The blue line smoothly connects the minima of the spread (at each  $\omega$ ), and defines the  $\omega$ -dependent optimal shift  $\delta\mu^*(\omega)$  used in the resummation. Middle and bottom panels are analogous to Figs. 3(a) and 3(d). In the bottom panel, the dash-dotted and dashed lines are the same as in Fig. 3(d).

not perfectly converged at  $\omega < 0$ , yet the  $K = 5$  calculation is practically on top of the exact result on the imaginary axis, and presents an improvement to the  $\delta\mu = 0$  series in Fig. 3(a). Note that the improvement in convergence is seen on the imaginary axis, as well.

### C. Removing nonphysical features

In this section, we focus on the parameters case discussed in Ref. [48]. We calculate the Hartree-shifted series with parameters of the model  $t' = 0$ ,  $\mu - U\langle n_\sigma \rangle = -0.1D$ ,  $T = 0.1D$ , and employ various  $\delta\mu$  shifts. The lattice size is again  $32 \times 32$  and we focus on the self-energy at  $\mathbf{k} = (0, \pi)$ . Note that in Hartree-shifted series, the quantity that enters the calculation is  $\mu - U\langle n_\sigma \rangle$ , rather than  $\mu$ . If  $\langle n \rangle$  is calculated,  $\mu$  can be estimated *a posteriori*. In our calculation, we fix

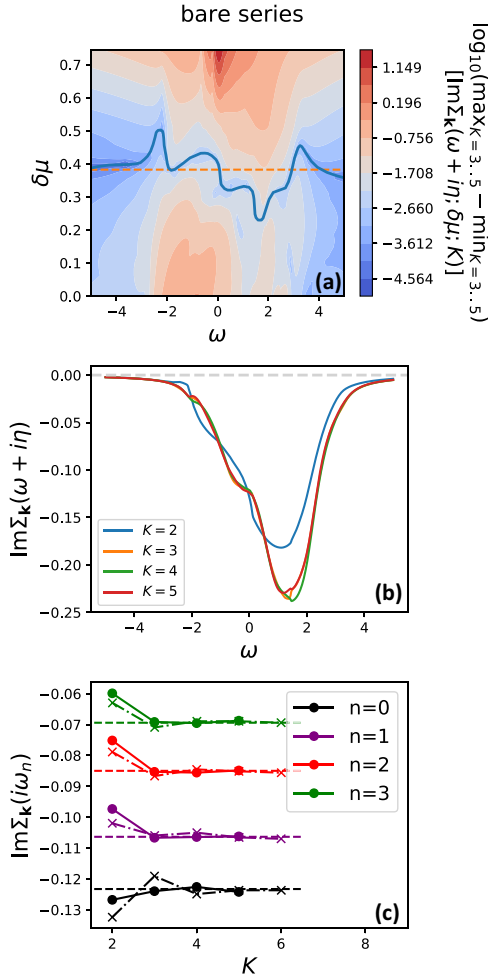


FIG. 5. Results of the bare series with  $\omega$ -resolved resummation, to be compared to Figs. 3(c) and 3(f) (all parameters are the same). The top panel is analogous to Fig. 4(a). The horizontal orange dashed line denotes the value of  $\delta\mu$  used in Figs. 3(c) and 3(f) to best converge the imaginary-axis result. The middle and bottom panels are analogous to Figs. 3(c) and 3(f). In the bottom panel, the dash-dotted and dashed lines are the same as in Fig. 3(f).

$\mu - U \langle n_\sigma \rangle$ , and  $\langle n_\sigma \rangle$  is then  $U$  dependent. Roughly, as given in Ref. [48], at  $U = 1$ , we have  $\langle n_\sigma \rangle \approx 0.455$ .

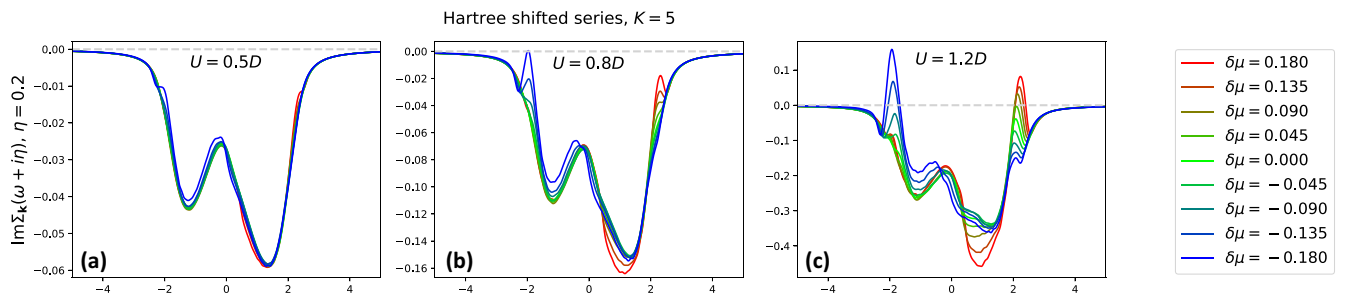


FIG. 6. Imaginary part of the self-energy on the real axis (with broadening  $\eta$ ), at different values of coupling constant  $U$ , obtained with our method at  $K = 5$  using different chemical-potential shifts  $\delta\mu$ . The parameters of the calculation are the same as in Ref. [48], i.e.,  $t' = 0$ ,  $\mu - U \langle n_\sigma \rangle = -0.1D$ ,  $T = 0.1D$ . The self-energy is calculated at  $\mathbf{k} = (0, \pi)$ . Passing of the curves above the gray dashed line indicates breaking of causality.

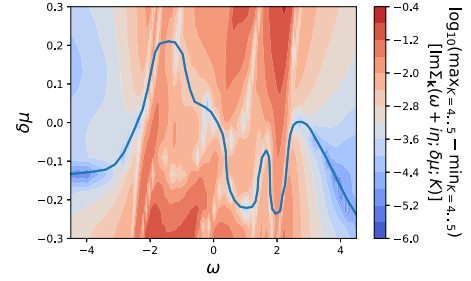


FIG. 7. Analogous to Fig. 4(a), for the parameters of the model corresponding to Fig. 6. The blue line is the optimal  $\delta\mu^*$ , to be used in Fig. 8.

The results are presented in Fig. 6 for three values of  $U$ . At low  $U$ , the series is well converged by  $K = 5$ , and the result is entirely insensitive to the choice of  $\delta\mu$ , as expected. At intermediate and high  $U$ , the result can be strongly  $\delta\mu$  sensitive. The  $\delta\mu$  dependence of the result, however, strongly varies with  $\omega$ . It appears that for a given  $\omega$ , there are ranges of the  $\delta\mu$  value where the result (at fixed order  $K$ ) is insensitive to the precise choice of  $\delta\mu$ . This presents an alternative way of choosing an optimal  $\delta\mu$  (a similar idea was employed in a different context in Ref. [58]).

The striking feature at large  $U$  is the causality violations at  $|\omega| \approx 2$  that were previously discussed in Ref. [48] (note that the broadening somewhat masks the extent of the problem). The dips in the self-energy spectrum appear to happen only at certain values of  $\delta\mu$ : at  $\omega = -2$ , the problem is present at  $\delta\mu$  large and negative, and at  $\omega = 2$ , at  $\delta\mu$  large and positive. In particular, at  $\omega = 2$ , the result appears to vary uniformly with  $\delta\mu$ , and one cannot select an optimal  $\delta\mu$  based on the sensitivity of the result to the  $\delta\mu$  value. We therefore repeat the procedure from the previous section and select the optimal  $\delta\mu^*(\omega)$  based on the level of convergence between orders  $K = 4$  and  $K = 5$ . The spread of the results and a smooth choice of  $\delta\mu^*(\omega)$  are presented in Fig. 7.

In Fig. 8, the results of the averaging are shown and compared to the  $\delta\mu = 0$  results at the highest available orders  $K = 4$  and  $K = 5$ , at three values of  $U$ . The convergence is visibly better around our  $\delta\mu^*$  than with  $\delta\mu = 0$  at problematic frequencies  $|\omega| \approx 2$ . More importantly, the non-physical features are clearly absent. At  $U = 1$ , in the  $\delta\mu = 0$

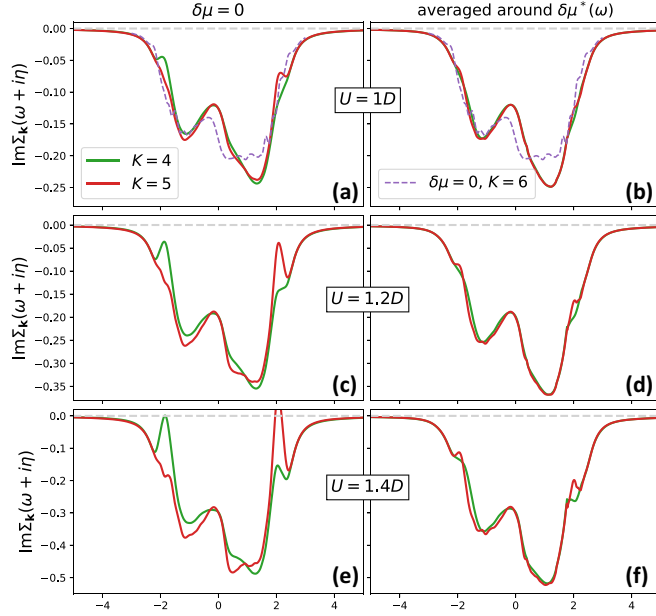


FIG. 8. Imaginary part of self-energy, real-frequency results (with broadening  $\eta$ ). Right column: obtained with the  $\omega$ -resolved resummation for the model parameters from Fig. 6, using the optimal  $\delta\mu^*(\omega)$  from Fig. 7; to be compared to the standard  $\delta\mu = 0$  calculation in the left column. Purple dashed lines in the top row are the  $K = 6$  calculation with  $\delta\mu = 0$ .

calculation, the causality is not yet violated, but the dip at  $\omega = 2$  is already starting to appear, which is clearly an artifact of the series truncation which should be removed systematically. It is important that the intermediate frequency behavior that we obtained by averaging results around the optimal  $\delta\mu$  is indeed the correct one, and it will not change much further with increasing orders. We show in the top panels the  $K = 6$ , the  $\delta\mu = 0$  result of which has been benchmarked against a fully converged imaginary-axis result in Fig. 9 (the converged result was obtained with the  $\Sigma$ Det method [59,60] at order

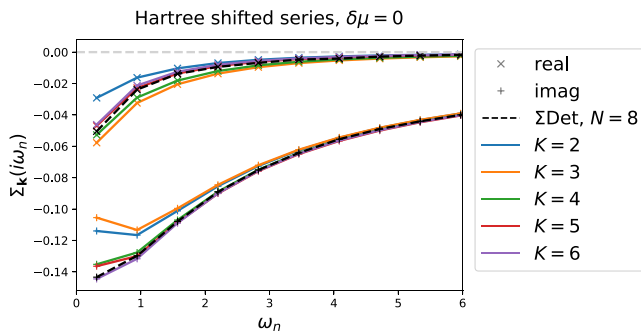


FIG. 9. Matsubara-frequency self-energy result, with model parameters as in Fig. 6. Crosses are the real part, pluses are the imaginary part, and lines are eye guides. Solid lines are the Hartree-shifted series with  $\delta\mu = 0$  at different maximal  $K$ . The same result was obtained with both the algorithm presented in this work and the algorithmic Matsubara summation method from Ref. [48] (the two methods were compared diagram by diagram). Black dashed lines are the  $\Sigma$ Det result at maximal order  $N = 8$ .

8). Clearly, the improved convergence between orders 4 and 5 that we have achieved by choosing  $\delta\mu$  appropriately does indeed mean an improved final result. However, our procedure does not improve the result at around  $\omega = 0$ , where the optimal  $\delta\mu$  does appear to be close to 0. The  $K = 6$ ,  $\delta\mu = 0$  result shown in the upper panels of Fig. 8 is still a bit different from the  $K = 5$ ,  $\delta\mu \approx \delta\mu^*(\omega)$  results around  $\omega = 0$ .

In the case of  $U = 1D$ , it is interesting that a large negative  $\delta\mu$  does bring the  $\omega \approx 0$  result at order  $K = 5$  much closer to the exact value. This can be anticipated from Fig. 6, where we show the corresponding results for  $U = 0.8D$  and  $U = 1.2D$ . Also, by looking at the color plot in Fig. 7, we see that at  $\omega = 0$ , there is indeed a local minimum in the spread at around  $\delta\mu = -0.2$ , which could be used as the optimal  $\delta\mu^*$ . This minimum, however, cannot be continuously connected with the other minima that we observe at  $\omega < 0$ , so we chose a different trajectory in the  $(\omega, \delta\mu)$  space. It would be interesting for future work to inspect the behavior at even more negative  $\delta\mu$ , where another continuous trajectory  $\delta\mu^*(\omega)$  might be found.

## V. DISCUSSION, CONCLUSIONS, AND PROSPECTS

In this paper, we have derived an analytical solution for the multiple-time integral that appears in the imaginary-time Feynman diagrams of an interaction series expansion. The solution is general for any diagram with a single external time or no external times. We find this generality to be a great advantage compared to the recently proposed algorithmic solutions of the corresponding Matsubara-frequency summations. Our analytical solution allowed us to develop a very flexible DiagMC algorithm that can make use of the possibility to optimize the series with shifted actions. As a result, we were able to almost perfectly converge a real-frequency self-energy in just 3–4 orders of perturbation, in a nontrivial regime and practically in the thermodynamic limit.

More importantly, the fact that one does not have to prepare a solution for each diagram topology individually opens the possibility to develop algorithms more akin to CTINT and allow the MC sampling to go to indefinite perturbation orders. In fact, upon a simple inspection of CTINT and continuous-time hybridization-expansion quantum Monte Carlo in the segment picture (segment-CTHYB) equations [42], it becomes clear that our solution can, in principle, be applied there, so as to reformulate these methods in real frequency. This would, however, come at the price of having to break into individual terms the determinant that captures all the contributions to the partition function at a given perturbation order. In turn, this may lead to a more significant sign problem, and an effective cap on the perturbation orders that can be handled in practice. On the other hand, it is not entirely clear how much of the sign problem comes from summing the individual terms and how much from the integration of the internal times, and we leave such considerations for future work. In any case, DiagMC algorithms based on hybridization expansion have been proposed before (see Refs. [23,28,61]), where our analytical solution may be applied.

Our solution also trivially generalizes to real-time integrals and may have use in Keldysh and Kadanoff-Baym [9]



calculations, where the infamous dynamical sign problem arises precisely due to oscillating time integrands. There have been recent works [62,63] with imaginary-time propagation of randomized walkers where our solution may also find application.

Finally, we emphasize that avoiding analytical continuation could be beneficial at high temperature where the Matsubara frequencies become distant from the real axis, and thus noisy imaginary-axis correlators contain little information [64,65]. The high-temperature regime is particularly relevant for optical lattice simulations of the Hubbard model [66]. In that context, we anticipate our method will find application in the calculation of conductivity and other response functions.

### ACKNOWLEDGMENTS

We thank Fedor Šimkovic for useful discussions and for sharing his diagram topology data. Computations were performed on the PARADOX supercomputing facility (Scientific Computing Laboratory, Center for the Study of Complex Systems, Institute of Physics Belgrade) and the ALPHA cluster (Collège de France). This work was also granted access to the HPC resources of TGCC and IDRIS under the Allocations No. A0090510609 and No. A0070510609 attributed by GENCI (Grand Equipement National de Calcul Intensif). J.V. acknowledges funding provided by the Institute of Physics Belgrade, through the grant by the Ministry of Education, Science, and Technological Development of the Republic of Serbia, as well as by the Science Fund of the Republic of Serbia, under the Key2SM project (PROMIS program, Grant No. 6066160). M.F. acknowledges support by the Simons Foundation. We also acknowledge support by the European Research Council for the European Union Seventh Framework Program (FP7/2007-2013) with ERC Grant No. 319286 (QMAC).

### APPENDIX A: REAL-TIME INTEGRATION

Let us consider the following special case of the integral given by Eq. (3), which is relevant for real-time integrations featuring integrands of the form  $e^{itE}$ :

$$\tilde{\mathcal{I}}_{\{l_2 \dots l_N\}, \{E_2 \dots E_N\}}(t) = \prod_{i=2}^N \int_0^{t_{i+1}} dt_i t_i^{l_i} e^{it_i E_i}, \quad (\text{A1})$$

with  $t_{N+1} \equiv t$ . This corresponds to the case  $r \notin [2, N]$  in Eq. (3), and  $\omega_i = iE_i$ , and we will define  $\tilde{E}_i$  analogously to  $\tilde{\omega}_i$ . The result is then obtained straightforwardly from Eq. (14),

$$\begin{aligned} \tilde{\mathcal{I}}_{\{l_2 \dots l_N\}, \{E_2 \dots E_N\}}(t) &= \sum_{\{b_i \in [\delta_{z_i}, 1]\}_{i=2 \dots N}} e^{it \tilde{E}_N b_N} \sum_{\{k_i \in [0, (1 - \delta_{z_i}) n_i]\}_{i: b_i=1}} \\ &\times (-1)^{\sum_{i=2}^N k_i} \prod_{i: \delta_{z_i}=1} \frac{1}{n_i} \\ &\times t^{n_N+1-b_N-k_N} \prod_{i: E_i \neq 0} \frac{C_{n_i, k_i}}{(i \tilde{E}_i)^{k_i+b_i}}, \quad (\text{A2}) \end{aligned}$$

which has the following general form:

$$\tilde{\mathcal{I}}(t) = \sum_{j: p \in \mathbb{N}_0} \mathcal{Z}_{p,j} t^p e^{it \varepsilon_j}. \quad (\text{A3})$$

### APPENDIX B: EXTRACTING REAL-AXIS RESULTS WITHOUT POLE BROADENING

In this section, we show how the results on the real axis can be extracted without any numerical broadening of the poles. Rather, we make use of the pole amplitudes by interpreting the result as being representative of the thermodynamic limit, where poles on the real axis merge into a branch cut, and thus we consider that the pole amplitude is a continuous function of the real frequency. We extract the imaginary part of the contribution  $[\text{Im} D(\omega)]$ , and then the Hilbert transform can be used to reconstruct the real part.

The procedure relies on the following construction: A function  $f(z)$  which is analytic everywhere in the upper half of the complex plane ( $z^+ = x + iy$  with  $y > 0$ ) and decays to zero with  $|z^+|$  satisfies the relation

$$f(z^+) = -\frac{1}{\pi} \int dx' \frac{\text{Im} f(x' + i0^+)}{z^+ - x'}. \quad (\text{B1})$$

After applying the  $p$ th derivative with respect to  $x$  (i.e., the real part of  $z^+$ ) on both sides of the equation, one obtains

$$\begin{aligned} \partial_x^p f(z^+) &= -\frac{1}{\pi} \int dx' \partial_x^p \frac{\text{Im} f(x' + i0^+)}{z^+ - x'} \\ &= -\frac{1}{\pi} \int dx' (-1)^p (p+1)! \frac{\text{Im} f(x' + i0^+)}{(z^+ - x')^{p+1}}. \quad (\text{B2}) \end{aligned}$$

We can now move the constant prefactors to the left-hand side and rename  $p+1 \rightarrow p$ . Just above the real axis, we have

$$\frac{(-1)^p \pi}{p!} \partial_x^{p-1} f(x + i0^+) = \int dx' \frac{\text{Im} f(x' + i0^+)}{(x - x' + i0^+)^p}. \quad (\text{B3})$$

We can now discretize the expression on a uniform  $x$  grid with the step  $\Delta x$ , say,  $x_j = j \Delta x$ , and we see that the right-hand side has the form of a sum of poles of order  $p$ , equidistant along the real axis, and with amplitudes  $\mathcal{A}_j = \text{Im} f(x_j + i0^+)$ ,

$$\frac{(-1)^p \pi}{p!} \tilde{\partial}_j^{p-1} \mathcal{A}_j \approx \text{Im} \sum_{j'} \Delta x \frac{\mathcal{A}_{j'}}{(x_j - x_{j'} + i0^+)^p}, \quad (\text{B4})$$

where  $\tilde{\partial}$  is the finite-difference approximation for the derivative along the  $x$  axis. Clearly, the imaginary part of the entire sum of  $p$ -order poles at a certain point  $x_j$  can be estimated by looking only at the  $(p-1)$ th derivative of the amplitudes of these poles at  $x_j$ , as given in the above expression.

The expression (B4) can be readily applied in our case [Eq. (33)] where the real axis is the frequency axis  $\omega$ , with step  $\Delta \omega$  and  $\omega_j = j \Delta \omega$ , and the sum of the poles determines our diagram contribution  $D$ . In general we have poles of various orders, but we can group the poles by order and treat their contributions separately. We therefore have

$$\text{Im} D(\omega_j + i0^+) \approx \frac{\pi}{\Delta \omega} \sum_p \frac{(-1)^p}{p!} \tilde{\partial}_j^{p-1} \mathcal{A}_{j,p}. \quad (\text{B5})$$

In the case of simple poles only, the contribution at any  $\omega_j$  is simply proportional to the amplitude of the pole  $\mathcal{A}_{j,1}$ . Other-

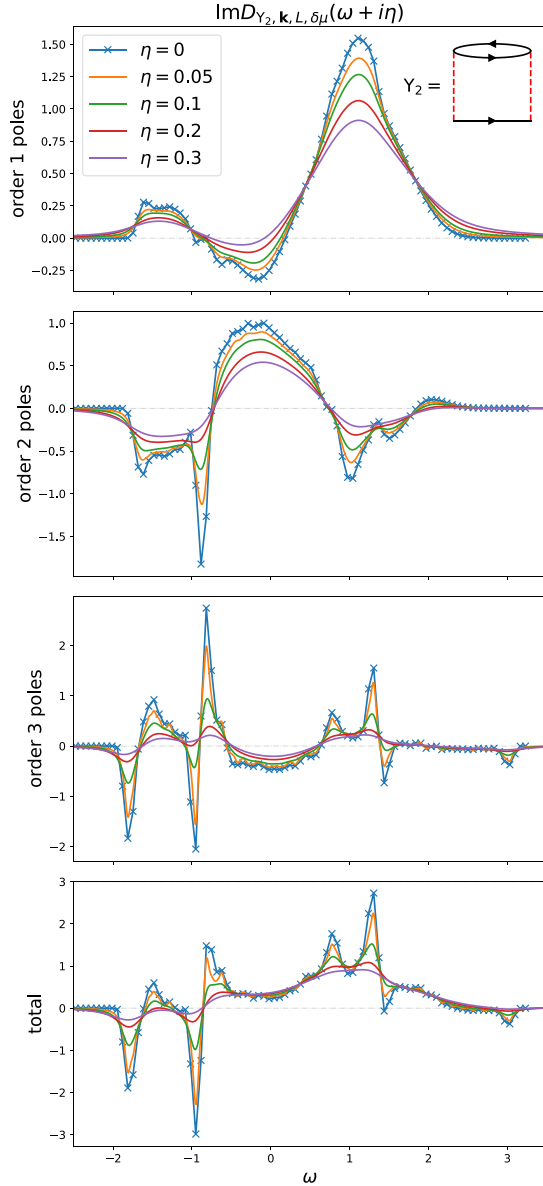


FIG. 10. Illustration of a  $\eta = 0^+$  result obtained from Eq. (31) without any numerical broadening, based only on pole amplitudes. The diagram used is the second-order diagram (illustrated in the top panel), with  $L = 2$ . In the propagators, we take  $\delta\mu = 0$ . The rest of the parameters are  $\mu - U\langle n_\sigma \rangle = -0.1D$ ,  $T = 0.1D$ , and the external momentum is  $\mathbf{k} = (0, \pi)$ . The top three panels are contributions from first-, second-, and third-order poles, respectively. The bottom panel is the total result. Lines with  $\eta > 0$  are obtained with numerical broadening. The crosses on the  $\eta = 0$  result denote the available frequencies (in between, we assume linear interpolation).

wise, the procedure requires that the pole amplitudes form a reasonably smooth function of the real frequency. Additionally, the energy resolution is a measure of the systematic error made in this procedure.

To avoid statistical noise and noisy features coming from the finite size of the lattice (see next section), we test our method on the example of a  $N = 2$ ,  $L = 2$  diagram, which we can solve with the full summation of Eq. (31), on a lattice

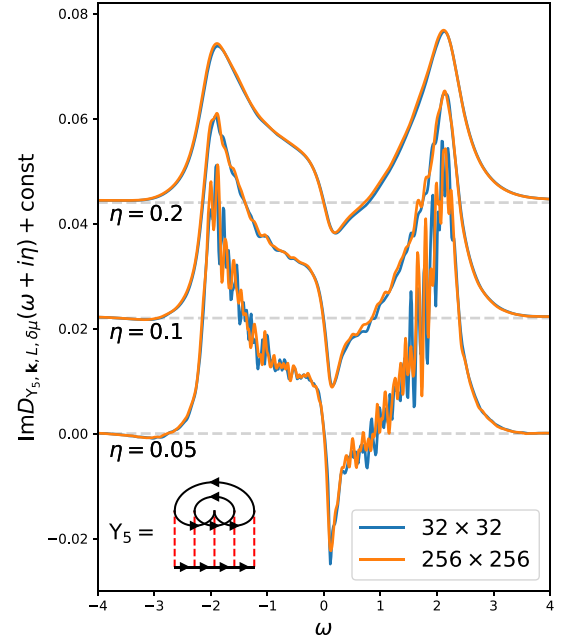


FIG. 11. Comparison of the real-frequency imaginary self-energy result for a single fifth-order diagram (illustrated in the bottom-left corner), for the lattice sizes  $32 \times 32$  and  $256 \times 256$ , at three different levels of broadening. The calculation is in both cases performed with the same number of MC steps and took similar time. The parameters are  $L = 0$ ,  $\delta\mu = 0$ ,  $\mu - U\langle n_\sigma \rangle = -0.1D$ ,  $T = 0.1D$ , and the external momentum is  $\mathbf{k} = (0, \pi)$ .

of the size  $96 \times 96$ . This diagram produces poles up to order 3. The result is shown in Fig. 10. In the first three panels, we show the contribution from the poles of each order, and in the bottom panel, we show the total result.

### APPENDIX C: CONVERGENCE WITH LATTICE SIZE

In this section we discuss the convergence of the result with respect to the lattice size. In Fig. 11, we compare the results for a single  $N = 5$ ,  $L = 0$  diagram on the lattices of size  $32 \times 32$  and  $256 \times 256$ . We observe that the result is almost exactly the same at broadening level  $\eta = 0.2$ , which brings further confidence in the results in the main part of the paper.

In Fig. 12, we illustrate how the size of the lattice determines the highest energy resolution that one can have, under requirement that the results form a continuous curve on the real axis and are, therefore, representative of the thermodynamic limit. We perform the full summation for the second-order diagram with  $L = 0$ , with various sizes of the lattice and various resolutions. Clearly, the bigger the lattice, the higher the energy resolution one can set without affecting the smoothness of the results.

The numerical parameters of the calculation are therefore the size of the lattice, the energy resolution, and the broadening (the resolution and the broadening can be tuned *a posteriori*), and one can tune them to get the optimal ratio between performance and the error bar. If the pole amplitudes  $\mathcal{A}_{jp}$  are a relatively smooth function of  $j$ , no broadening is then needed at all.



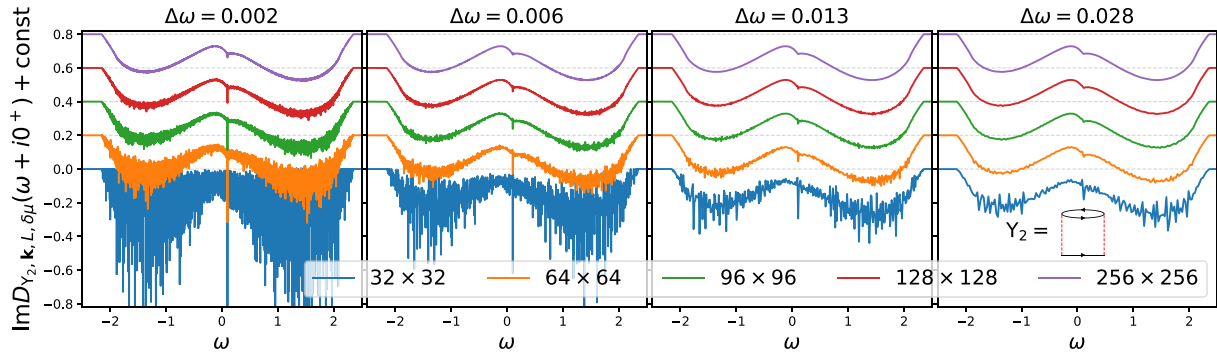


FIG. 12. Real-frequency result ( $\eta = 0^+$ ) for the contribution of the lowest-order diagram (illustrated in the rightmost panel) at various lattice sizes and frequency resolutions, obtained with full summation (gray code). The step of the uniform energy grid is denoted  $\Delta\omega$ . The parameters are  $L = 0$ ,  $\delta\mu = 0$ ,  $\mu - U\langle n_\sigma \rangle = -0.1D$ ,  $T = 0.1D$ , and the external momentum is  $\mathbf{k} = (0, \pi)$ .

#### APPENDIX D: DERIVATION OF EQ. (5)

After applying  $n$  times the partial integration over the integral from the left-hand side of Eq. (5), we get

$$\begin{aligned}
 \int_0^{\tau_f} \tau^n e^{\tau z} d\tau &= \frac{1}{z^{n+1}} \int_0^{\tau_f} \tau^n e^{\tau} d\tau \\
 &= \frac{1}{z^{n+1}} \left[ e^{z\tau_f} (z\tau_f)^n - n e^{z\tau_f} (z\tau_f)^{n-1} + \dots + (-1)^n n! \int_0^{\tau_f} \tau^0 e^{\tau} d\tau \right] \\
 &= \frac{1}{z^{n+1}} \left[ \frac{n!}{(n-0)!} (-1)^0 e^{z\tau_f} (z\tau_f)^{n-0} + (-1)^1 \frac{n!}{(n-1)!} e^{z\tau_f} (z\tau_f)^{n-1} + \dots + (-1)^n \frac{n!}{(n-n)!} \int_0^{\tau_f} \tau^0 e^{\tau} d\tau \right] \\
 &= \frac{1}{z^{n+1}} \left[ \frac{n!}{(n-0)!} (-1)^0 e^{z\tau_f} (z\tau_f)^{n-0} + (-1)^1 \frac{n!}{(n-1)!} e^{z\tau_f} (z\tau_f)^{n-1} + \dots + (-1)^n \frac{n!}{(n-n)!} (z\tau_f)^0 (e^{z\tau_f} - 1) \right] \\
 &= \frac{1}{z^{n+1}} e^{z\tau_f} \sum_{k=0}^n (-1)^k (z\tau_f)^{n-k} \frac{n!}{(n-k)!} - (-1)^n \frac{n!}{z^{n+1}}, \tag{D1}
 \end{aligned}$$

which can be readily identified with the right-hand side of Eq. (5).

#### APPENDIX E: DERIVATION OF EQ. (21)

We are looking for a solution of the Fourier transform

$$G_0^l(\varepsilon, \tau) = \frac{1}{\beta} \sum_{i\Omega_\eta} \frac{e^{-i\Omega_\eta \tau}}{(i\Omega_\eta - \varepsilon)^l}. \tag{E1}$$

For any  $\tau$ , we can express the sum above as a contour integral, and we find

$$\begin{aligned}
 G_0^l(\varepsilon, \tau) &= -\text{Res}_{z=\varepsilon} \frac{e^{-z\tau}}{(z-\varepsilon)^l} \frac{\eta^{\lfloor \frac{\tau}{\beta} \rfloor} e^{\lfloor \frac{\tau}{\beta} \rfloor \beta z}}{1 - \eta e^{-\beta z}} dz \\
 &= -\frac{\eta^{\lfloor \frac{\tau}{\beta} \rfloor}}{(l-1)!} \frac{d^{l-1}}{dz^{l-1}} \frac{e^{-\beta z \lfloor \frac{\tau}{\beta} \rfloor}}{1 - \eta e^{-\beta z}} \Big|_{z=\varepsilon}, \tag{E2}
 \end{aligned}$$

where  $\lfloor \dots \rfloor$  denotes the integer part (floor function), and  $\{x\} \equiv x - \lfloor x \rfloor$  denotes the fractional part.

We see that it will be useful to have an expression for derivatives of  $(1 - \eta e^z)^{-1}$ . They have the general form

$$\frac{d^k}{dz^k} \frac{1}{1 - \eta e^z} = \sum_{n=0}^k C_n^k \frac{(e^z)^n}{(1 - \eta e^z)^{n+1}}. \tag{E3}$$

By deriving this expression on both sides, one obtains a recursion for the coefficients  $C_n^k$ ,

$$C_n^{k+1} = n C_n^k + \eta n C_{n-1}^k, \tag{E4}$$

with holds for  $k > -1$  and  $n > 0$  with  $C_0^0 = 1$ . That can be rewritten

$$\frac{\eta^n}{n!} C_n^{k+1} = n \frac{\eta^n}{n!} C_n^k + \frac{\eta^{n-1}}{(n-1)!} C_{n-1}^k. \tag{E5}$$

If we define  $S_n^k = \frac{\eta^n}{n!} C_n^k$ , we have the recursion  $S_n^{k+1} = n S_n^k + S_{n-1}^k$ , which is the recursion for the Stirling numbers of the second kind. This allows one to have the following important result:

$$\begin{aligned}
 \frac{d^k}{dz^k} \frac{1}{1 - \eta e^z} &= \sum_{n=0}^k \eta^n n! \left\{ \begin{matrix} k \\ n \end{matrix} \right\} \frac{(e^z)^n}{(1 - \eta e^z)^{n+1}} \\
 &= \sum_{n=0}^k \eta^n n! \left\{ \begin{matrix} k \\ n \end{matrix} \right\} \frac{e^{-z}}{(e^{-z} - \eta)^{n+1}}. \tag{E6}
 \end{aligned}$$

With this, one obtains the following expression:

$$G_0^l(\varepsilon, \tau) = -e^{\varepsilon\beta(1-\{\frac{\tau}{\beta}\})} \eta^{\lfloor \frac{\tau}{\beta} \rfloor + 1} (-\beta)^{l-1} \times \sum_{m=0}^{l-1} \sum_{n=0}^{l-m-1} \frac{n!}{(l-m-1)!m!} \left\{ \begin{matrix} l-m-1 \\ n \end{matrix} \right\} \times \left( \frac{1}{\eta e^{\varepsilon\beta} - 1} \right)^{n+1} \left\{ \frac{\tau}{\beta} \right\}^m, \quad (\text{E7})$$

which already satisfies the (anti)periodicity properties of the Green's function.

To make use of the result given by Eq. (E7), we need to express  $G_0^l(\varepsilon, \tau)$  as a function of two times  $G_0^l(\varepsilon, \tau, \tau') \equiv G_0^l(\varepsilon, \tau - \tau')$ , with  $\tau, \tau' \in [0, \beta]$ . We first consider  $\tau \geq \tau'$ . By substituting  $(\tau - \tau')^m = \sum_{\zeta=0}^m (-1)^{m-\zeta} \binom{m}{\zeta} \tau^\zeta \tau'^{m-\zeta}$  into Eq. (E7) and substituting  $m - \zeta$  with  $\zeta$ , we get

$$G_0^l(\varepsilon, \tau - \tau') = \eta e^{\varepsilon(\tau' - \tau)} n_\eta(-\varepsilon) \sum_{\zeta=0}^{l-1} \sum_{\varsigma=0}^{l-\zeta-1} c_{l,\zeta,\varsigma}^-(\varepsilon) \tau^\zeta \tau'^\varsigma, \quad (\text{E8})$$

with  $c_{l,\zeta,\varsigma}^-(\varepsilon)$  as defined in Eq. (22). The result for  $\tau < \tau'$  can then be easily obtained by proving the property  $G_0^l(\varepsilon, \tau) = (-1)^l G_0^l(-\varepsilon, -\tau)$ ,

$$\begin{aligned} G_0^l(\varepsilon, -\tau) &= \frac{1}{\beta} \sum_{n=-\infty}^{\infty} \frac{e^{i\Omega_n \tau}}{(i\Omega_n - \varepsilon)^l} \\ &= \frac{1}{\beta} \sum_{n=-\infty}^{\infty} \frac{e^{-i\Omega_n \tau}}{(-i\Omega_n - \varepsilon)^l} \\ &= (-1)^l \frac{1}{\beta} \sum_{n=-\infty}^{\infty} \frac{e^{-i\Omega_n \tau}}{(i\Omega_n + \varepsilon)^l} \\ &= (-1)^l G_0^l(-\varepsilon, \tau), \end{aligned}$$

which implies that in the definition (21), we must have

$$c_{l,\zeta,\varsigma}^+(\varepsilon) = (-1)^{l-1} c_{l,\varsigma,\zeta}^-(\varepsilon). \quad (\text{E9})$$

## APPENDIX F: GENERAL HAMILTONIAN CASE

It is important to show that our method is not restricted to a specific choice of Hamiltonian. The local density-density interaction and the single band of the Hubbard Hamiltonian bring many simplifications, but none of them are necessary for our imaginary-time integral solution or the chemical-potential tuning scheme.

Consider the general Hamiltonian

$$H = \sum_{\alpha} (\varepsilon_{\alpha} - \mu) + \sum_{\alpha_1 \alpha_2 \alpha_3 \alpha_4} U_{\alpha_1 \alpha_2 \alpha_3 \alpha_4} c_{\alpha_1}^{\dagger} c_{\alpha_2} c_{\alpha_3}^{\dagger} c_{\alpha_4}. \quad (\text{F1})$$

The  $\alpha$  are the eigenstates of the noninteracting Hamiltonian, e.g., a combined momentum, band, and spin index. The self-energy can be now expressed as a

series,

$$\begin{aligned} \Sigma_{\alpha, \alpha'}^{(\text{HF})}(\tau) &= \sum_N \sum_{\Upsilon_N} \prod_{j=1}^{2N-1} \sum_{l_j=1}^{\infty} \sum_{\alpha_{j,1} \dots \alpha_{j,l_j}} \prod_{n=1}^{l_j-1} \sum_{\mathbf{V}_{j,n}} \\ &\times [\mathbf{V}_{j,n}]_{\alpha_{j,n} \alpha_{j,n+1}} \prod_{i=1}^N U_{\alpha_{j_1}(i) \alpha_{j_2}(i) \alpha_{j_3}(i) \alpha_{j_4}(i)} \\ &\times \prod_{m=1}^{N-1+\sum_j(l_j-1)} \int_0^{\beta} d\tau_m G_0(\bar{\varepsilon}_{\alpha_{j,n}}, \tilde{\tau}_{j,n} - \tilde{\tau}'_{j,n}). \end{aligned} \quad (\text{F2})$$

Similarly as before,  $\Upsilon_N$  enumerates topologies without any instantaneous insertions (Hartree or chemical potential) at perturbation order  $N$  (the number of interaction vertices). The fermionic lines in the  $\Upsilon_N$  topology are enumerated with  $j$ . On each fermionic line, we make any number  $l_j - 1$  of instantaneous insertions with amplitudes  $\mathbf{V}_{j,n}$  (interaction amplitudes in Hartree insertions are included in  $\mathbf{V}$ ;  $n$  enumerates the insertions at the fermionic line  $j$ ). In general, Hartree insertions may contain off-diagonal terms in the  $\alpha$  basis and are therefore a matrix in the  $\alpha$  space. However, it is necessary that chemical-potential shifts are diagonal in this basis, as we want to have the bare propagator diagonal in this basis as well. Otherwise, the form of  $G_0$  from Eq. (18) would no longer hold. Nevertheless, one may still have a separate chemical-potential shift for each state,  $\delta\mu_{\alpha}$ . After making insertions, the number of fermionic lines increases to  $\sum_j l_j$ . The fermionic lines are now enumerated with  $j, n$ , and the corresponding states are  $\alpha_{j,n}$ . The index  $i$  enumerates the interaction vertices outside of any Hartree insertions. We denote  $\alpha_{j,1\dots 4}(i)$  as the single-particle states at four terminals of each interaction vertex. The interaction vertices at incoming ( $i = 1$ ) and outgoing ( $i = N$ ) terminals of the self-energy diagram are  $\alpha_{j_1}(i = N) = \alpha$ ,  $\alpha_{j_2}(i = 1) = \alpha'$ . With  $m$ , we enumerate all times to be integrated over. With each interaction vertex  $i > 1$ , we associate one time, and there is a time associated to each instantaneous insertion of which there are  $\sum_j(l_j - 1)$ . We assume that the incoming time corresponding to the vertex  $i = 1$  is 0. The times on the terminals of each bare propagator  $j, n$  are  $\tilde{\tau}_{j,n}$  and  $\tilde{\tau}'_{j,n}$  and they take on values from the set  $\{\tau_m\}_{m=0\dots N-1+\sum_j(l_j-1)}$ , with the external incoming time fixed,  $\tau_0 \equiv 0$ .  $\tilde{\tau}_{j,n}$ ,  $\tilde{\tau}'_{j,n}$ , and  $\alpha_{j,1\dots 4}(i)$  are implicit functions of topology  $\Upsilon_N$ . Finally,  $\bar{\varepsilon}_{\alpha_{j,n}} \equiv \varepsilon_{\alpha_{j,n}} - \mu + \delta\mu_{\alpha_{j,n}}$ . We can now focus only on the time-integral part and proceed completely analogously to Eqs. (27)–(31).

It is worth noting that with general interactions, pulling the coupling constant in front of the diagram contribution is impossible, as the frequency dependence of the contribution of each diagram will depend on the precise form of  $U_{\alpha_1 \alpha_2 \alpha_3 \alpha_4}$ . In the most general case, one must set specific values for  $U_{\alpha_1 \alpha_2 \alpha_3 \alpha_4}$  and  $\delta\mu_{\alpha}$  before performing the Monte Carlo summation. One can then choose the variables that will be sampled stochastically and the ones that will be fully summed over. In the end, the contributions can be easily grouped by total number of independent times ( $K$ ), including those in Hartree insertions. The integration of times in Hartree insertions can always be performed beforehand. Therefore, in the fully

general case, the number of integrations to be performed at the time of Monte Carlo sampling is  $N - 1 + \sum_j (l_j - 1)$ . In the case of purely density-density interactions (as is the case in the Hubbard model) or spin-spin interactions in the absence of external magnetic fields, this simplifies further because instantaneous insertions lead to expressions of the type  $\frac{1}{(i\omega - \varepsilon)^l}$  for which we can work out the temporal Fourier transform analytically [Eq. (21)] and the remaining number of integrations to perform is  $N - 1$  [as we do in Eq. (31)]. In the general case, when Hartree insertions are not diagonal in the  $\alpha$  basis, one has expressions of the type  $\frac{1}{i\omega - \varepsilon_1} \frac{1}{i\omega - \varepsilon_2} \cdots \frac{1}{i\omega - \varepsilon_l}$ . In

principle, one could prepare the analytical Fourier transforms for a general function of this form, but it might be increasingly involved at large  $l$ , so we assume one would do these integrations at the level of the Monte Carlo, when  $\varepsilon_{1\dots l}$  are already specified.

We finally emphasize that even more general constructions are possible, even in bases other than the noninteracting eigenbasis. In such cases, the  $G_0$ 's are nondiagonal and may have a continuous real-frequency dependence, instead of being a single pole. We leave such considerations for future work.

- 
- [1] The Hubbard model at half a century, *Nat. Phys.* **9**, 523 (2013).
- [2] J. P. F. LeBlanc, A. E. Antipov, F. Becca, I. W. Bulik, Garnet Kin-Lic Chan, Chia-Min Chung, Y. Deng, M. Ferrero, T. M. Henderson, C. A. Jiménez-Hoyos, E. Kozik, Xuan-Wen Liu, A. J. Millis, N. V. Prokof'ev, M. Qin, G. E. Scuseria, Hao Shi, B. V. Svistunov, L. F. Tocchio, I. S. Tupitsyn, S. R. White, S. Zhang, Bo-Xiao Zheng, Z. Zhu, and E. Gull (Simons Collaboration on the Many-Electron Problem), Solutions of the Two-Dimensional Hubbard Model: Benchmarks and Results from a Wide Range of Numerical Algorithms, *Phys. Rev. X* **5**, 041041 (2015).
- [3] G. Rohringer, H. Hafermann, A. Toschi, A. A. Katanin, A. E. Antipov, M. I. Katsnelson, A. I. Lichtenstein, A. N. Rubtsov, and K. Held, Diagrammatic routes to nonlocal correlations beyond dynamical mean field theory, *Rev. Mod. Phys.* **90**, 025003 (2018).
- [4] T. Schäfer, N. Wentzell, F. Šimkovic, Y.-Y. He, C. Hille, M. Klett, C. J. Eckhardt, B. Arzhang, V. Harkov, F.-M. Le Régent, A. Kirsch, Y. Wang, A. J. Kim, E. Kozik, E. A. Stepanov, A. Kauch, S. Andergassen, P. Hansmann, D. Rohe, Y. M. Vil'k, J. P. F. LeBlanc, S. Zhang, A.-M. S. Tremblay, M. Ferrero, O. Parcollet, and A. Georges, Tracking the Footprints of Spin Fluctuations: A MultiMethod, MultiMessenger Study of the Two-Dimensional Hubbard Model, *Phys. Rev. X* **11**, 011058 (2021).
- [5] A. W. Sandvik, Stochastic method for analytic continuation of quantum Monte Carlo data, *Phys. Rev. B* **57**, 10287 (1998).
- [6] O. F. Syljuåsen, Using the average spectrum method to extract dynamics from quantum Monte Carlo simulations, *Phys. Rev. B* **78**, 174429 (2008).
- [7] S. Fuchs, T. Pruschke, and M. Jarrell, Analytic continuation of quantum Monte Carlo data by stochastic analytical inference, *Phys. Rev. E* **81**, 056701 (2010).
- [8] K. Ghanem and E. Koch, Extending the average spectrum method: Grid point sampling and density averaging, *Phys. Rev. B* **102**, 035114 (2020).
- [9] H. Aoki, N. Tsuji, M. Eckstein, M. Kollar, T. Oka, and P. Werner, Nonequilibrium dynamical mean-field theory and its applications, *Rev. Mod. Phys.* **86**, 779 (2014).
- [10] J. K. Freericks, Quenching Bloch oscillations in a strongly correlated material: Nonequilibrium dynamical mean-field theory, *Phys. Rev. B* **77**, 075109 (2008).
- [11] M. Eckstein and M. Kollar, Nonthermal Steady States after an Interaction Quench in the Falicov-Kimball Model, *Phys. Rev. Lett.* **100**, 120404 (2008).
- [12] M. Schiró and M. Fabrizio, Real-time diagrammatic Monte Carlo for nonequilibrium quantum transport, *Phys. Rev. B* **79**, 153302 (2009).
- [13] P. Werner, T. Oka, and A. J. Millis, Diagrammatic Monte Carlo simulation of nonequilibrium systems, *Phys. Rev. B* **79**, 035320 (2009).
- [14] M. Eckstein, M. Kollar, and P. Werner, Thermalization after an Interaction Quench in the Hubbard Model, *Phys. Rev. Lett.* **103**, 056403 (2009).
- [15] M. Schiró and M. Fabrizio, Time-Dependent Mean Field Theory for Quench Dynamics in Correlated Electron Systems, *Phys. Rev. Lett.* **105**, 076401 (2010).
- [16] P. Werner, T. Oka, M. Eckstein, and A. J. Millis, Weak-coupling quantum Monte Carlo calculations on the Keldysh contour: Theory and application to the current-voltage characteristics of the Anderson model, *Phys. Rev. B* **81**, 035108 (2010).
- [17] M. Eckstein and P. Werner, Nonequilibrium dynamical mean-field calculations based on the noncrossing approximation and its generalizations, *Phys. Rev. B* **82**, 115115 (2010).
- [18] M. Schiró and M. Fabrizio, Quantum quenches in the Hubbard model: Time-dependent mean-field theory and the role of quantum fluctuations, *Phys. Rev. B* **83**, 165105 (2011).
- [19] P. Werner and M. Eckstein, Phonon-enhanced relaxation and excitation in the Holstein-Hubbard model, *Phys. Rev. B* **88**, 165108 (2013).
- [20] M. Eckstein and P. Werner, Nonequilibrium dynamical mean-field simulation of inhomogeneous systems, *Phys. Rev. B* **88**, 075135 (2013).
- [21] G. Cohen, D. R. Reichman, A. J. Millis, and E. Gull, Green's functions from real-time bold-line Monte Carlo, *Phys. Rev. B* **89**, 115139 (2014).
- [22] G. Cohen, E. Gull, D. R. Reichman, and A. J. Millis, Green's Functions from Real-Time Bold-Line Monte Carlo Calculations: Spectral Properties of the Nonequilibrium Anderson Impurity Model, *Phys. Rev. Lett.* **112**, 146802 (2014).
- [23] G. Cohen, E. Gull, D. R. Reichman, and A. J. Millis, Taming the Dynamical Sign Problem in Real-Time Evolution of Quantum Many-Body Problems, *Phys. Rev. Lett.* **115**, 266802 (2015).
- [24] N. V. Prokof'ev and B. V. Svistunov, Polaron Problem by Diagrammatic Quantum Monte Carlo, *Phys. Rev. Lett.* **81**, 2514 (1998).
- [25] A. S. Mishchenko, N. V. Prokof'ev, A. Sakamoto, and B. V. Svistunov, Diagrammatic quantum Monte Carlo study of the Fröhlich polaron, *Phys. Rev. B* **62**, 6317 (2000).

- [26] N. Prokof'ev and B. Svistunov, Bold Diagrammatic Monte Carlo Technique: When the Sign Problem Is Welcome, *Phys. Rev. Lett.* **99**, 250201 (2007).
- [27] N. V. Prokof'ev and B. V. Svistunov, Bold diagrammatic Monte Carlo: A generic sign-problem tolerant technique for polaron models and possibly interacting many-body problems, *Phys. Rev. B* **77**, 125101 (2008).
- [28] E. Gull, D. R. Reichman, and A. J. Millis, Bold-line diagrammatic Monte Carlo method: General formulation and application to expansion around the noncrossing approximation, *Phys. Rev. B* **82**, 075109 (2010).
- [29] E. Kozik, K. Van Houcke, E. Gull, L. Pollet, N. Prokof'ev, B. Svistunov, and M. Troyer, Diagrammatic Monte Carlo for correlated fermions, *Europhys. Lett.* **90**, 10004 (2010).
- [30] K. V. Houcke, E. Kozik, N. Prokof'ev, and B. Svistunov, Diagrammatic Monte Carlo, *Phys. Proc.* **6**, 95 (2010).
- [31] L. Pollet, Recent developments in quantum Monte Carlo simulations with applications for cold gases, *Rep. Prog. Phys.* **75**, 094501 (2012).
- [32] K. Van Houcke, F. Werner, E. Kozik, N. Prokof'ev, B. Svistunov, M. J. H. Ku, A. T. Sommer, L. W. Cheuk, A. Schirotzek, and M. W. Zwierlein, Feynman diagrams versus Fermi-gas Feynman emulator, *Nat. Phys.* **8**, 366 (2012).
- [33] S. A. Kulagin, N. Prokof'ev, O. A. Starykh, B. Svistunov, and C. N. Varney, Bold Diagrammatic Monte Carlo Method Applied to Fermionized Frustrated Spins, *Phys. Rev. Lett.* **110**, 070601 (2013).
- [34] S. A. Kulagin, N. Prokof'ev, O. A. Starykh, B. Svistunov, and C. N. Varney, Bold diagrammatic Monte Carlo technique for frustrated spin systems, *Phys. Rev. B* **87**, 024407 (2013).
- [35] R. Rossi, T. Ohgoe, E. Kozik, N. Prokof'ev, B. Svistunov, K. Van Houcke, and F. Werner, Contact and Momentum Distribution of the Unitary Fermi Gas, *Phys. Rev. Lett.* **121**, 130406 (2018).
- [36] R. Rossi, Determinant Diagrammatic Monte Carlo Algorithm in the Thermodynamic Limit, *Phys. Rev. Lett.* **119**, 045701 (2017).
- [37] K. Van Houcke, F. Werner, T. Ohgoe, N. V. Prokof'ev, and B. V. Svistunov, Diagrammatic Monte Carlo algorithm for the resonant Fermi gas, *Phys. Rev. B* **99**, 035140 (2019).
- [38] K. Chen and K. Haule, A combined variational and diagrammatic quantum Monte Carlo approach to the many-electron problem, *Nat. Commun.* **10**, 3725 (2019).
- [39] A. N. Rubtsov and A. I. Lichtenstein, Continuous-time quantum Monte Carlo method for fermions: Beyond auxiliary field framework, *J. Expt. Theor. Phys. Lett.* **80**, 61 (2004).
- [40] A. N. Rubtsov, V. V. Savkin, and A. I. Lichtenstein, Continuous-time quantum Monte Carlo method for fermions, *Phys. Rev. B* **72**, 035122 (2005).
- [41] E. Gull, P. Werner, O. Parcollet, and M. Troyer, Continuous-time auxiliary-field Monte Carlo for quantum impurity models, *Europhys. Lett.* **82**, 57003 (2008).
- [42] E. Gull, A. J. Millis, A. I. Lichtenstein, A. N. Rubtsov, M. Troyer, and P. Werner, Continuous-time Monte Carlo methods for quantum impurity models, *Rev. Mod. Phys.* **83**, 349 (2011).
- [43] R. E. V. Profumo, C. Groth, L. Messio, O. Parcollet, and X. Waintal, Quantum Monte Carlo for correlated out-of-equilibrium nanoelectronic devices, *Phys. Rev. B* **91**, 245154 (2015).
- [44] A. Moutenet, P. Seth, M. Ferrero, and O. Parcollet, Cancellation of vacuum diagrams and the long-time limit in out-of-equilibrium diagrammatic quantum Monte Carlo, *Phys. Rev. B* **100**, 085125 (2019).
- [45] C. Bertrand, O. Parcollet, A. Maillard, and X. Waintal, Quantum Monte Carlo algorithm for out-of-equilibrium Green's functions at long times, *Phys. Rev. B* **100**, 125129 (2019).
- [46] C. Bertrand, S. Florens, O. Parcollet, and X. Waintal, Reconstructing Nonequilibrium Regimes of Quantum Many-Body Systems from the Analytical Structure of Perturbative Expansions, *Phys. Rev. X* **9**, 041008 (2019).
- [47] A. Taheridehkordi, S. H. Curnoe, and J. P. F. LeBlanc, Algorithmic Matsubara integration for Hubbard-like models, *Phys. Rev. B* **99**, 035120 (2019).
- [48] J. Vučičević and M. Ferrero, Real-frequency diagrammatic Monte Carlo at finite temperature, *Phys. Rev. B* **101**, 075113 (2020).
- [49] A. Taheridehkordi, S. H. Curnoe, and J. P. F. LeBlanc, Optimal grouping of arbitrary diagrammatic expansions via analytic pole structure, *Phys. Rev. B* **101**, 125109 (2020).
- [50] A. Taheridehkordi, S. H. Curnoe, and J. P. F. LeBlanc, Algorithmic approach to diagrammatic expansions for real-frequency evaluation of susceptibility functions, *Phys. Rev. B* **102**, 045115 (2020).
- [51] M. Maček, P. T. Dumitrescu, C. Bertrand, B. Triggs, O. Parcollet, and X. Waintal, Quantum Quasi-Monte Carlo Technique for Many-Body Perturbative Expansions, *Phys. Rev. Lett.* **125**, 047702 (2020).
- [52] W. Wu, M. Ferrero, A. Georges, and E. Kozik, Controlling Feynman diagrammatic expansions: Physical nature of the pseudogap in the two-dimensional Hubbard model, *Phys. Rev. B* **96**, 041105(R) (2017).
- [53] R. Rossi, F. Šimkovic IV, and M. Ferrero, Renormalized perturbation theory at large expansion orders, *Europhys. Lett.* **132**, 11001 (2020).
- [54] F. Šimkovic IV, R. Rossi, and M. Ferrero, Efficient one-loop-renormalized vertex expansions with connected determinant diagrammatic Monte Carlo, *Phys. Rev. B* **102**, 195122 (2020).
- [55] F. Šimkovic IV, J. P. F. LeBlanc, A. J. Kim, Y. Deng, N. V. Prokof'ev, B. V. Svistunov, and E. Kozik, Extended Crossover from a Fermi Liquid to a Quasiantiferromagnet in the Half-Filled 2D Hubbard Model, *Phys. Rev. Lett.* **124**, 017003 (2020).
- [56] A. J. Kim, F. Šimkovic IV, and E. Kozik, Spin and Charge Correlations across the Metal-to-Insulator Crossover in the Half-Filled 2D Hubbard Model, *Phys. Rev. Lett.* **124**, 117602 (2020).
- [57] C. Lenihan, A. J. Kim, F. Šimkovic IV, and E. Kozik, Entropy in the Non-Fermi-Liquid Regime of the Doped 2D Hubbard Model, *Phys. Rev. Lett.* **126**, 105701 (2021).
- [58] T. Ayral, J. Vučičević, and O. Parcollet, Fierz Convergence Criterion: A Controlled Approach to Strongly Interacting Systems with Small Embedded Clusters, *Phys. Rev. Lett.* **119**, 166401 (2017).
- [59] A. Moutenet, W. Wu, and M. Ferrero, Determinant Monte Carlo algorithms for dynamical quantities in fermionic systems, *Phys. Rev. B* **97**, 085117 (2018).
- [60] F. Šimkovic IV and E. Kozik, Determinant Monte Carlo for irreducible Feynman diagrams in the strongly correlated regime, *Phys. Rev. B* **100**, 121102(R) (2019).

- [61] E. Eidelstein, E. Gull, and G. Cohen, Multiorbital Quantum Impurity Solver for General Interactions and Hybridizations, *Phys. Rev. Lett.* **124**, 206405 (2020).
- [62] A. A. Kunitsa and So Hirata, Grid-based diffusion Monte Carlo for fermions without the fixed-node approximation, *Phys. Rev. E* **101**, 013311 (2020).
- [63] M. Hutcheon, Stochastic nodal surfaces in quantum Monte Carlo calculations, *Phys. Rev. E* **102**, 042105 (2020).
- [64] J. Vučković, J. Kokalj, R. Žitko, N. Wentzell, D. Tanasković, and J. Mravlje, Conductivity in the Square Lattice Hubbard Model at High Temperatures: Importance of Vertex Corrections, *Phys. Rev. Lett.* **123**, 036601 (2019).
- [65] E. W. Huang, R. Sheppard, B. Moritz, and T. P. Devereaux, Strange metallicity in the doped Hubbard model, *Science* **366**, 987 (2019).
- [66] P. T. Brown, D. Mitra, E. Guardado-Sanchez, R. Nourafkan, A. Reymbaut, Charles-David Hébert, S. Bergeron, A.-M. S. Tremblay, J. Kokalj, D. A. Huse, P. Schauß, and W. S. Bakr, Bad metallic transport in a cold atom Fermi-Hubbard system, *Science* **363**, 379 (2018).